学位論文

Measurement of the Higgs boson couplings using the $WW^* \to \ell\nu\ell\nu$ final state

($WW^* \to \ell\nu\ell\nu$終状態を用いた
ヒッグスボソン結合定数の測定)

平成 26 年 7 月　　博士（理学）申請

東京大学大学院理学系研究科
物理学専攻

吉原　圭亮

MEASUREMENT OF THE HIGGS BOSON COUPLINGS USING THE $WW^* \to \ell\nu\ell\nu$ FINAL STATE

Keisuke Yoshihara

A Dissertation submitted in partial fulfillment of

the requirements for the Degree of Doctor of Science

Graduate School of Science, The University of Tokyo

July 2014

Abstract

The discovery of a Higgs boson with a mass of approximately 125 GeV was reported by the ATLAS and CMS collaborations in July 2012 [1, 2], which has opened up a new era in understanding the nature of electroweak symmetry breaking and possibly completing the Standard Model of particle physics. The center of physics analysis is property measurement of the Higgs boson, which allows us to investigate underlying physics beyond the Standard Model. This thesis presents measurements of the Higgs couplings in the $H \to WW^* \to \ell\nu\ell\nu$ final state, using the full Run-I pp collision data recorded by the ATLAS at the LHC, corresponding to 4.5 fb^{-1} of $\sqrt{s} = 7$ TeV data collected in 2011 and 20.3 fb^{-1} of $\sqrt{s} = 8$ TeV data collected in 2012. The $H \to WW^* \to \ell\nu\ell\nu$ is one of the most sensitive channels to the coupling measurement through both gluon-gluon fusion (ggF) and vector boson fusion (VBF) production processes. The analysis adopted several enhanced techniques on the background estimation to attain a substantially better sensitivity to the measurement; the study of the W+jets process, being one of the most important backgrounds, is fully described. The coupling strength is represented by signal strength μ that is defined as the ratio of cross section times branching fraction in data to that in theoretical prediction. The result presented in this thesis supersedes the previous measurement [3, 4], owing to optimizations of selection of physics objects and improvements of the modeling of backgrounds. The observed excess of the inclusive production is about 6 σ that is large enough to claim the discovery of the $H \to WW^*$ decay, and the corresponding signal strengths for individual production processes are:

$$\mu_{\mathrm{ggF}} = 1.15^{+0.18}_{-0.18}(\mathrm{stat.})^{+0.23}_{-0.19}(\mathrm{syst.}),$$

$$\mu_{\mathrm{VBF+VH}} = 1.36^{+0.41}_{-0.45}(\mathrm{stat.})^{+0.32}_{-0.24}(\mathrm{syst.}).$$

Furthermore the couplings to fermions and weak bosons are each extracted, introducing coupling scale factors κ_F for fermions and κ_V for weak bosons. The measured scale factors are:

$$\kappa_V = 1.08^{+0.11}_{-0.11} = 1.08^{+0.07}_{-0.08}(\mathrm{stat.})^{+0.08}_{-0.07}(\mathrm{syst.}),$$

$$\kappa_F = 1.00^{+0.32}_{-0.24} = 1.00^{+0.24}_{-0.18}(\mathrm{stat.})^{+0.22}_{-0.15}(\mathrm{syst.}).$$

which are consistent with the values predicted by Standard Model.

Acknowledgement

This thesis would not have been materialized without the help from many people who gave their support in different ways.

First and foremost, I would like to express my sincere gratitude to my supervisor Prof. T. Kawamoto for providing a great opportunity to participate in the ATLAS experiment and for the continuous support of my research and of my life at CERN. His guidance helped me in all the time of research and writing of this thesis. I could not have imagined having a better advisor.

My sincere thanks also goes to Dr. T. Masubuchi, who has supported me throughout my research with his patience and knowledge while allowing me the room to work in my own way. I have worked very closely with him over three years having sleepless night, in particular in the discovery phase. The discovery of the Higgs boson is irreplaceable memory. I would also like to thank Prof. T. Kobayashi, Prof. S. Asai, Prof. J. Tanaka, and Prof. Y. Enari for leading our group and giving enormous advices about how to conduct research and about how to survive in large collaboration represented by the ATLAS group.

I am deeply grateful to all members involved in "Team W+jets", Prof. J. Kroll, Dr. J. Alison, Dr. C. Mills, Dr. D. Schaefer, Dr. L. Galtieri, T. Kishimoto, Dr. O. Arnaez, and C. Lester for continuous and long discussions on this topic. They have made lots of meaningful suggestions and have given me ideas to improve my works. I would like to add one more special thanks to Prof. J. Kroll again who will be my supervisor at University of Pennsylvania in the near future for his proof reading of this thesis, and for making lots of suggestions on it. I am very much indebted to ATLAS-Higgs HWW organizers during my stay at CERN : Dr. T. Masubuchi, Dr. C. Mills, Prof. J. Kroll, Prof. C. Hays, Prof. B.D. Micco, Dr. T.M. Hong, Dr. M. Chelstowska, Prof. P. Savard, and Prof. J. Qian, and editorial board members, Prof. D. Froidevaux, Prof. A. Nisati, Prof. J. Baptiste, Prof. B. Malaescu, and Prof. R. Teuscher, and (co-) editors of supporting documentations with total > 1000 pages, Dr. L. Ma, Dr. M. Chelstowska, J.M. Miguens, Dr. R. Polifka, Dr. L. Yuan, Dr. D. Schaefer, Prof. C. Hays, D.C. Hall, Dr. J. Griffiths, Dr. P.J. Hsu, S. Gadatsch, Dr. C. Mills for their continuous efforts on this analysis!

I would also like to thank all other members, including secretaries in the University of Tokyo and ICEPP, Prof. S. Komamiya, Prof. H. Sakamoto, Prof. N. Kanaya, Prof. K. Terashi, Prof. T. Namba, Prof. K. Nakamura (KEK), Prof. T. Mashimo, Prof. I. Ueda, Prof. T. Nakamura (KEK), Dr. S. Yamamoto, Dr. Y. Kataoka, Dr. Y. Takashi, Dr. K. Hanawa, Dr. T. Kubota (Melbourne), Masako Shiota, Ritsuko Anbiru, Yoshie Tezuka, Yoko Takemoto, and Akiko Miyazono, and the same-grade (or younger) colleagues, Yuki Fuji, Shingo Kazama, Akira Miyazaki, Yuichi Sasaki, Yohei Yamaguchi, Yoichi Ninomiya, Aine Kobayashi, Masahiro Morinaga, Yuto Minami, and Takashi Goto for supportive and friendly atomosphere.

On a more personal note, I would like to thank my room mates in Thoiry, France, Yutaro, Andrew, Nil, and Bastian for sharing a precious time with me! I am also very thankful for "my lovely friends", Katarina and Filip for making me happy and making my Europe life fulfilling, especially travelling Amalfi, Sorrento, and Capri together was so wonderful!! I would also like to thank Kohei who was always my playmate in Geneva and he is still my young star!!

Last but not least, I would like to thank my family: my parents for giving birth to me at the first place and infinite supports, and my wife's parents for all support, ... And of course my wife, Seiko, for all her love and support!

Executive Summary

The Standard Model of particle physics (SM) is a fundamental and elegant theory of elementary particles and their interactions. It has been tested in various aspects by many experiments, and has been accomplished as a local gauge invariant theory. In the SM there was a theoretical obstacle when considering mass of weak bosons, since all particles in the theory are massless. In 1960's it has been demonstrated by R. Brout, F. Englert, and P. Higgs that the weak bosons acquire their own mass interacting with a scalar boson, so-called the Higgs boson, through the Brout-Englert-Higgs (BEH) mechanism [5–7]. However the Higgs boson had not been observed for more than 50 years. In July 2012 the ATLAS and CMS collaborations reported the discovery of new particle consistent with the Higgs boson predicted by the SM [1, 2]. In the SM the BEH mechanism must be responsible for mass of weak bosons, but the discovery of the Higgs boson via gluon-gluon fusion (ggF) process also implies the presence of Yukawa coupling, namely couplings to fermions. Thus, as a next step, measurements of the Higgs boson couplings to fermions and weak bosons are of special importance.

From the beginning of the LHC experiment, the $H \to WW^* \to \ell\nu\ell\nu$ channel led Higgs boson search due to the large branching fraction of $H \to WW^*$. In fact this channel was most sensitive to the search in the mass region of $114 < m_{\mathrm{H}} < 158$ GeV that was not excluded by previous experiments. Also this channel was sensitive to other scenarios (i.e. non-SM scenarios) represented by fermiophobic scenario [8, 9], 4th generation scenario [10], and no Higgs boson scenario [11] in early 2011. Even after the discovery of the Higgs boson with a mass of approximately 125 GeV in 2012, this channel continues to lead efforts to the measurement of the couplings to fermions and weak bosons.

This thesis presents the latest measurement of the Higgs couplings using $WW^* \to \ell\nu\ell\nu$ final state through the ggF and VBF production processes. The most crucial part of the analysis is background estimation because the analysis suffers from many backgrounds. Most of the SM processes such as WW and top ($t\bar{t}, Wt$) production processes enter a signal region as backgrounds. One of the most significant backgrounds is W+jets background, where a W boson produced in association with a jet that is misidentified as a lepton. Since the large uncertainty on this background makes it an important limitation to the experimental sensitivity, the study of systematic uncertainty on this background is a crucial part of the analysis.

Author's Contribution

Since early 2011, I have been an active member of the $H \to WW^* \to \ell\nu\ell\nu$ analysis group in the ATLAS collaboration. I spent three years at CERN that taught me the importance of being "on the ground" in the large collaboration. During my stay at CERN, I had a chance to contribute to the discovery of the Higgs boson, which is one of the best and irreplaceable experiences. Since the discovery, I have stayed in this analysis to study and measure the Higgs boson couplings to fermions and weak bosons.

My main contributions to the collaboration are as follows:

- I have studied cavern background (e.g. neutrons) to the TGC detector that is a subsystem of the ATLAS Muon Spectrometer (for qualification for the ATLAS authorship). I measured the rate of such backgrounds comparing to simulation. This study is very important since the contamination of the backgrounds increases the trigger rate significantly. More details can be found in the cavern background note [12] (ATLAS Internal).

- I have studied performance of leptons (electrons and muons). I have been responsible for the leptons in the analysis group as a contact person since early 2011. I have particularly worked closely with e/gamma group to study efficiency for electron identification focusing on the efficiency for the low E_{T} electron that is quite important for the low mass ($m_{\mathrm{H}} < 140$ GeV) Higgs analysis because the sub-leading lepton in the final state tends to have lower E_{T}. The studies of leptons are described in Chapter 4. More details can be found in the electron performance paper [13, 14] and $H \to WW^*$ object note [15] (ATLAS Internal).

- I have worked extensively on extending and improving a data-driven technique for the W+jet estimate. The rate of hadronic jets misidentified as leptons may not be accurately described in the simulation, because these events are due to rare fragmentation processes or interactions with the detector. This background is therefore determined from data using control samples dominated by the W+jets events. The W+jets background is described in Chapter 6. Furthermore the detailed study of the sample composition of the misidentified lepton can be found in Appendix B. More details can be found in the $H \to WW^*$ background note [16] (ATLAS Internal).

- I have contributed to introducing same sign control region method (SS CR) for the normalization of diboson backgrounds ($WZ/ZZ/W\gamma/W\gamma^*$). In particular I have developed a dedicated correlation model between the signal region and the control region. The SS CR is described in Chapter 7. More details can be found in the $H \to WW^*$ background note [16] (ATLAS Internal).

- I am leading efforts to documenting object selection and background estimation as a co-editor of the object note [15] and background note [16] for a paper being prepared for publication.

Thesis Organization

This thesis is organized as follows:

Chapter1 Introduction:
Physics motivations and goals of this thesis are presented starting from a basic introduction to the SM and Higgs boson physics.

Part I: Experimental Apparatus and Physics Object

- Chapter 2 LHC and ATLAS Detector:
  The LHC and ATLAS detector are briefly summarized.
- Chapter 3 Event and Object Reconstruction:
  Event and object reconstruction for all physics objects including triggers used in the analysis are summarized.
- Chapter 4 Determination of Lepton Selection:
  Reconstruction and important studies of leptons are summarized including the optimization and systematic uncertainties.

Part II: Analysis for the Measurement of the Higgs Boson Couplings

- Chapter 5 $H \to WW^* \to \ell\nu\ell\nu$ Analysis:
  The $H \to WW^* \to \ell\nu\ell\nu$ analysis is briefly summarized.
- Chapter 6 Fake Backgrounds:
  A data-driven technique for the W+jets/QCD backgrounds estimation called fake factor method is described. The systematic uncertainties on those backgrounds are summarized.
- Chapter 7 Modeling of Same Sign Backgrounds:
  An introduction to the Same Sign Control Region (SS CR) is given. Systematic uncertainties on this control region are briefly summarized. Also the correlation model of signal region and this control region is discussed.

Part III: Result and Conclusion

- Chapter 8 Results:
  Results of the couplings of the Higgs boson are presented. Also some compatibility tests are made.
- Chapter 9 Conclusion:
  Concluding remarks.

For those who want to grasp shortly the outline of the whole contents in this thesis, please go through Chapter 1 Introduction, Chapter 5 $H \to WW^* \to \ell\nu\ell\nu$ Analysis, Chapter 8 Results, and Chapter 9 Conclusion.

For those (I assume LHC colleagues) who want to get the whole procedure of specific topics, please go to Chapter 4 Determination of Lepton Selection, Chapter 6 Fake backgrounds, and Chapter 7 Modeling of Same Sign Backgrounds.

Contents

Chapter 1

Introduction

The Higgs boson was the final piece of the puzzle in the Standard Model of particle physics (SM). On 4th July 2012, the ATLAS and CMS collaborations announced that they had each observed a new particle, most likely "*the SM Higgs boson*", with a mass of approximately 125 GeV [1,2]. The discovery implies that we finally reached a portal of new era in understanding the nature of electroweak symmetry breaking and possibly completing the SM. The major focus of physics analysis at the LHC now is therefore the measurement of the properties of the Higgs boson including mass [17], spin-parity [18], and couplings [4]. In this thesis, the measurements of the couplings using the $H \to WW^* \to \ell\nu\ell\nu$ final state are presented with the full Run-I pp collision data corresponding to 20.3 fb^{-1} of $\sqrt{s} = 8$ TeV and 4.5 fb^{-1} of 7 TeV, recorded by the ATLAS at the LHC. There are some advantages to using the $H \to WW^* \to \ell\nu\ell\nu$ channel as follows:

- a large branching fraction of $H \to WW^*$ ($\sim$22 %),
- leptonic final state ($WW^* \to \ell\nu\ell\nu$) allows for rejecting a large amount of QCD.

Those advantages make this channel sensitive to the coupling measurements via ggF and VBF (see Section 1.3.2), even with the limited data set in Run-I. The remainder of this chapter is a brief introduction to the SM and the Higgs physics, which will provide an idea of how the analysis can be important.

1.1 The Standard Model and Mass of Gauge Bosons

The SM is a relativistic quantum field theory that incorporates three (out of four) fundamental interactions in nature: electromagnetic, weak, and strong interactions. The three interactions are described in a local gauge symmetry based on SU(3)$\otimes$SU(2)$\otimes$U(1), where all interactions are propagated via massless gauge bosons. Nevertheless it is well-known fact that the symmetry must be broken since weak vector bosons have their own masses, so the question is what endows them with masses. The answer can be given by introducing the Brout-Englert-Higgs (BEH) mechanism [5–7] in the electroweak theory. In this section, a brief introduction to the electroweak theory and BEH mechanism is given.

1.1.1 Spontaneous Symmetry Breaking

The global U(1) symmetry is a simple example of the Spontaneous Symmetry Breaking (SSB) [19–22]. The U(1) transformation of a complex field ϕ can be expressed as:

$$\phi(x) \to e^{i\alpha}\phi(x), \tag{1.1}$$

where α is a constant and hence a global parameter that is independent of space-time, and that introduces a global symmetry. The Lagrangian of this complex scalar field is expressed as follows:

$$\begin{aligned} \mathcal{L} &= \partial_\mu\phi\partial^\mu\phi^* - V, \\ V(\phi) &= \mu^2\phi\phi^* + \lambda(\phi\phi^*)^2, \end{aligned} \tag{1.2}$$

where $\phi\phi^*$ is a mass term with a mass μ, and $(\phi\phi^*)^2$ term symbolizes a four-point configuration for the self interaction of the field ϕ with a coupling constant λ. The potential has a parabola-shape with $\mu^2 > 0$.

For the SSB, the sign of the mass term is however chosen negative ($\mu^2 < 0$), which ends up with a Mexican hat (or wine bottle) potential. In this case the ground state (i.e. vacuum) can be defined as $\phi(x) = v$, and the local maximum of the potential at $\phi(x) = 0$ is unstable. The field will condense into a stable ground state that is not an unique ground state for this system. The minima of this system are then degenerate, in other words, there exists many states with the same vacuum energy. The different orientations in the complex plane define different states, and applying the U(1) transformation to any of the vacuum states will rotate it to a different orientation, describing a different physical state. To analyze the Lagrangian, it is necessary to define a perturbative expansion around the ground state. This can be achieved by writing ϕ as:

$$\phi(x) = \frac{1}{\sqrt{2}}(v + \eta(x) + i\xi(x)), \tag{1.3}$$

where $v = (\sqrt{\frac{-\mu^2}{\lambda}})$ is a non-zero value of the ground state (vacuum expectation value), and where $\eta(x)$ and $\xi(x)$ are real fields while $\phi(x)$ is a complex field. When this expression is plugged into the Lagrangian, the Lagrangian is rewritten as follows:

$$\mathcal{L} = \frac{1}{2}(\partial_\mu\eta)^2 - (\lambda v^2)\eta^2 + \frac{1}{2}(\partial_\mu\xi)^2 - 0\cdot\xi^2 + \cdots . \tag{1.4}$$

The Lagrangian now shows that there is a mass term with a positive coefficient for the η field, with a mass given by $m_\eta^2 = \lambda v^2$. There is however no mass term for the ξ field. The particle associated with this massless field is called a "Goldstone boson", that always shows up in the SSB of a global symmetry. The Goldstone boson can be interpreted as a freedom in the ground state plane. This was demonstrated by J. Goldstone, and the existence of the Goldstone boson in the (global) SSB is referred to as Goldstone theorem [23, 24].

1.1.2 Brout-Englert-Higgs Mechanism

The Goldstone bosons that appeared upon the breaking of a global symmetry, however, will not be found in spontaneously broken "local" symmetry, meaning that the Goldstone theorem breaks down in the local symmetry. The Brout-Englert-Higgs mechanism (referred to as Higgs mechanism) gives an idea of how the SSB works in the local gauge symmetry, and of how a field with a non-zero ground state can be a source of massive gauge bosons [25,26]. The cornerstone in the BEH mechanism is the assumption of a new scalar field, the BEH field, whose non-zero vacuum expectation value locally breaks the U(1) gauge symmetry of the Lagrangian. This is implemented in the Lagrangian in a similar fashion for the case of global symmetry breaking. The Lagrangian for ϕ^4 theory with the simple Abelian U(1) gauge symmetry is:

$$\begin{aligned} \mathcal{L} &= D^\mu \phi D_\mu \phi^* - \mu^2 \phi\phi^* - \lambda(\phi\phi^*)^2 - \frac{1}{4} F^{\mu\nu} F_{\mu\nu}, \\ D_\mu &= \partial_\mu + iqA_\mu, \end{aligned} \tag{1.5}$$

where $F^{\mu\nu}F_{\mu\nu}$ is the kinetic term for the gauge field. The gauge field A_μ interacts with the field ϕ in such a way that the Lagrangian is invariant under the gauge transformations of $\phi(x) \to q^{i\alpha(x)}\phi(x)$ and $A_\mu \to A_\mu + \frac{1}{q}\partial_\mu \alpha(x)$. Then a mass term would break the gauge invariance of the Lagrangian. In the BEH mechanism $\phi(x)$ is the BEH field satisfying $\mu^2 < 0$, so that the potential has the Mexican hat shape. To analyze the Lagrangian in a perturbative expansion, it is, as in the global U(1) symmetry case, necessary to expand around a variable field that is small for perturbations around the ground state. Therefore the field can be again written out, similar to the global symmetry case:

$$\phi(x) = \frac{1}{\sqrt{2}}(v + \rho(x) + i\xi(x)), \tag{1.6}$$

where v is vacuum expectation value, and $\rho(x)$ and $\xi(x)$ are real scalar fields. Plugging this into the Lagrangian gives:

$$\begin{aligned} \mathcal{L} = &\frac{1}{2}(\partial_\mu \rho)^2 - \lambda v^2 \rho^2 + \frac{1}{2}(\partial_\mu \xi)^2 \\ &+ qvA_\mu \partial^\mu \xi + \frac{1}{2} q^2 v^2 A_\mu A^\mu - \frac{1}{4} F^{\mu\nu} F_{\mu\nu} + \cdots . \end{aligned} \tag{1.7}$$

The term $q^2v^2A_\mu A^\mu$ shows that the gauge field A_μ has become massive, due to its interaction with the constant part of the BEH field. The term $\lambda v^2\rho^2$ also represents that one of the components in the BEH field $\rho(x)$ is massive, while the other component $\xi(x)$ seems to be a massless Goldstone mode, like in the global case. $\xi(x)$ is however not a physical particle but it arises from a freedom to pick up a gauge. Looking at the term including the ξ field, one can rewrite it as:

$$\begin{aligned} \mathcal{L} &= \frac{1}{2}(\partial_\mu \xi)^2 + qvA_\mu \partial^\mu \xi + \frac{1}{2} q^2 v^2 A_\mu A^\mu, \\ &= \frac{1}{2} q^2 v^2 [A_\mu + \frac{1}{qv}(\partial_\mu \xi)]^2 = \frac{1}{2} q^2 v^2 A'_\mu A'^\mu, \\ &\text{where } A_\mu \to A'_\mu = A_\mu + \frac{1}{qv}\partial_\mu \xi. \end{aligned} \tag{1.8}$$

This choice of gauge ($A_\mu \rightarrow A'_\mu$) is referred to as '*unitary gauge*' [27, 28]. Then the Lagrangian becomes:

$$\begin{aligned}\mathcal{L} =& \frac{1}{2}(\partial_\mu \rho)^2 - \lambda v^2 \rho^2 + \frac{1}{2} q^2 v^2 A'_\mu A'^\mu - \frac{1}{4} F^{\mu\nu} F_{\mu\nu} \\ &+ q^2 v A'_\mu A'^\mu \rho + \frac{1}{2} q^2 A'_\mu A'^\mu \rho^2 - \lambda v \rho^3 - \frac{1}{4} \lambda \rho^4.\end{aligned} \tag{1.9}$$

The Lagrangian now clearly shows that there is a massive gauge field (the third term), and that the BEH field has one massive component (the second term). There are no massless particles in this theory, and the field $\xi(x)$ has completely disappeared from the Lagrangian. With a similar treatment it is possible to expand the BEH mechanism to the SU(2)⊗U(1) symmetry of the electroweak theory.

One can notice the presence of interaction terms ($A'_\mu A'^\mu \rho$, $A'_\mu A'^\mu \rho^2$, ρ^3, and ρ^4) that correspond to the self-couplings of the scalar massive boson (shown by dashed line with H) and its couplings to the gauge boson A'_μ (shown by wavy line) as shown in Figure 1.1.

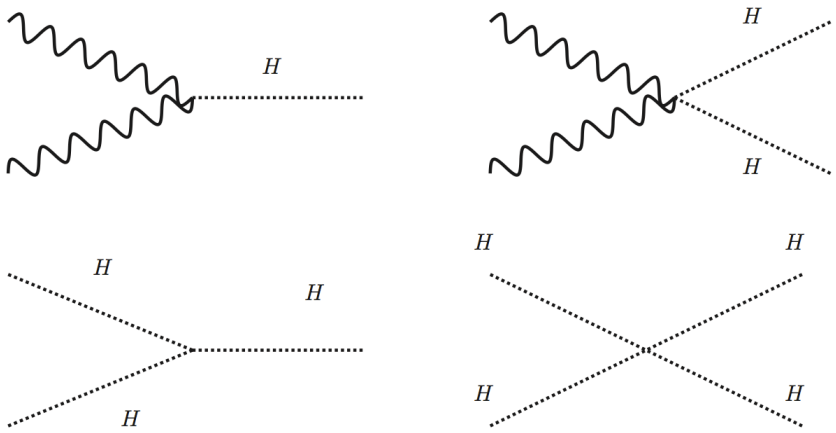

Figure 1.1: Schematic view of the self-interactions of the scalar massive boson (dashed line, ρ field in the text but is referred to as "H" in this figure) and its interactions with the gauge bosons (wavy line) in the U(1) gauge theory.

The discussion here is still in the context of the U(1) symmetry, but the scalar massive boson corresponds to the Higgs boson when considering the Glashow-Weinberg-Salam (GWS) theory discussed in Section 1.1.3. Only the term $A'_\mu A'^\mu \rho$ is relevant to the measurement currently performed at the LHC. The others will be subjects of the *High Luminosity LHC* (HL-LHC) [29] in the near future.

1.1.3 Glashow-Weinberg-Salam Model

The theories, namely the SSB and BEH mechanism, are applicable to the Glashow-Weinberg-Salam (GWS) model [30–32] that describes the electroweak interactions. The Lagrangian for the GWS theory is written as:

$$\begin{aligned} \mathcal{L} &= (D^\mu\phi)^\dagger(D^\mu\phi) - V(\phi), \\ D_\mu &= \partial_\mu + \frac{i}{2}g'YB_\mu + \frac{i}{2}g\vec{\tau}\cdot\vec{W}_\mu. \end{aligned} \tag{1.10}$$

where Y denotes hypercharge. The kinetic term ($F^{\mu\nu}F_{\mu\nu}$) is not shown here. In the presence of the gauge fields, the fields are transformed into the unitary gauge, so that the field can be written as:

$$\phi(x) = \frac{1}{\sqrt{2}}\begin{pmatrix} 0 \\ v + h(x) \end{pmatrix}. \tag{1.11}$$

The only difference from the U(1) gauge theory is that the BEH field is now a SU(2) doublet. $V(\phi)$ term will again obtain the mass term for the massive scalar boson and the self-interactions. And $(D^\mu\phi)^\dagger(D^\mu\phi)$ term will give rise to the masses of the gauge bosons and their interactions with the massive scalar. $(D^\mu\phi)^\dagger(D^\mu\phi)$ term finally leads to:

$$\begin{aligned} (D^\mu\phi)^\dagger(D^\mu\phi) = &\frac{1}{2}(\partial_\mu h)^2 + {m_W}^2{W^+}_\mu W^{-\mu} + \frac{1}{2}g^2{W^+}_\mu W^{-\mu}(vh + \frac{h^2}{2}) \\ &+ \frac{1}{2}{m_Z}^2 Z_\mu Z^\mu + \frac{1}{4}(g^2 + g'^2)Z_\mu Z^\mu(vh + \frac{h^2}{2}), \end{aligned} \tag{1.12}$$

where ${m_W}^2 = \frac{1}{4}g^2v^2$ and ${m_Z}^2 = \frac{1}{4}(g^2 + g'^2)v^2$ denote masses of the W and Z bosons. As illustrated in Figure 1.2, the couplings of the massive scalar boson to the WW and ZZ can be then expressed as $g_{hWW} \propto g \cdot m_W \propto m_W^2/v$ and $g_{hZZ} \propto g \cdot m_Z/\cos\theta_W \propto m_Z^2/v$ where $\cos\theta_W$ indicates 'Weinberg angle' defined as the ratio of those masses, m_W/m_Z. It is now clear that the couplings to the gauge bosons are proportional to the squared mass of each gauge boson (m_W^2 or m_Z^2). The g_{hWW} and g_{hZZ} (referred to in general as 'Feynman rules') are used for the calculation of the matrix element $\mathcal{M}$ for individual decay width (or cross sections) of the Higgs boson.

Recently the ATLAS and CMS also reported their discovery of the Higgs decay into fermionic channels [33–35], meaning that the BEH mechanism can also give rise to masses of the fermions. The formalization will not be presented here but it can be found, for instance, in [36, 37].

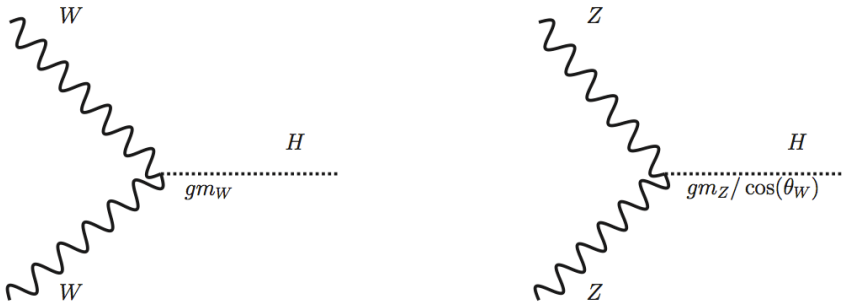

Figure 1.2: Schematic view of the scalar massive boson (H) interactions with the weak gauge bosons in the GWS theory.

1.2 The Standard Model Processes as 'Backgrounds'

In the last 50 years, the SM predictions have been tested and well-verified by many experiments, as can be seen in the electroweak global fit [38] that includes more than 20 experimental input parameters. It is no exaggeration to say that the result of the global fit including the Higgs mass measured by the ATLAS and CMS, is exactly our current understanding of the SM.

At the LHC, the cross section measurements of several important benchmark SM production processes have been performed since 2010. Given that a huge amount of the SM processes can contribute as 'backgrounds' to the Higgs analyses, and that the cross section of the Higgs production is smaller than that of the SM processes, further cross checks of the cross sections for these SM production processes at new energy scale at the LHC is obviously meaningful.

The most relevant cross section measurements, namely the measurements using a similar phase space (possibly opposite sign dilepton final state) to that used in the $H \to WW^* \to \ell\nu\ell\nu$ analysis, are summarized below:

- "Measurement of the WW production in $\sqrt{s} = 7$ TeV pp collisions with the ATLAS detector and limits on anomalous gauge couplings" [39, 40]",
- "Measurement of the $t\bar{t}$ production cross-section using $e\mu$ events with b-tagged jets in pp collisions at $\sqrt{s} = 7$ and 8 TeV with the ATLAS detector" [41],
- "Measurement of the cross section for associated production of a top quark and a W boson at $\sqrt{s} = 8$ TeV with the ATLAS detector" [42],
- "Measurement of the t-channel single top-quark production cross section in pp collisions at $\sqrt{s} = 7$ TeV with the ATLAS detector" [43],

- "Measurement of the $W \to \ell\nu$ and $Z/\gamma^* \to \ell\ell$ production cross sections in proton proton collision at $\sqrt{s} = 7$ TeV with the ATLAS detector" [44],
- "Measurement of the low-mass Drell-Yan differential cross section at $\sqrt{s} = 7$ TeV using the ATLAS detector" [45],
- "Measurements of the $W\gamma$ and $Z\gamma$ Production in pp collisions at $\sqrt{s} = 7$ TeV with the ATLAS Detector at the LHC" [46],
- "Measurement of WZ Production in Proton-Proton Collisions at $\sqrt{s} = 7$ TeV with the ATLAS Detector" [47],
- "Measurement of ZZ production in pp collisions at $\sqrt{s} = 7$ TeV with the ATLAS detector and limits on anomalous ZZZ and $ZZ\gamma$ couplings" [48].

In addition to those described above, measurements of production (or differential) cross section of the W/Z processes in association with heavy flavors are also important for understanding the W+jets "background" in the analysis due to large fraction of W+heavy flavors.

- "Measurement of differential production cross-sections for a Z boson in association with b-jets in 7 TeV proton-proton collisions with the ATLAS detector" [49],
- "Measurement of the production of a W boson in association with a charm quark in pp collisions at $\sqrt{s} = 7$ TeV with the ATLAS detector" [50],
- "Measurement of the cross-section for W boson production in association with b-jets in pp collisions at $\sqrt{s} = 7$ TeV with the ATLAS detector" [51].

It is very impressive and evident that theoretical predictions (all calculated at the NLO or higher order) and experimentally measured cross sections, are in good agreement for all the SM processes as shown in Figure 1.3. Our understanding on the SM processes at $\sqrt{s} = 7$ and 8 TeV including the description of Monte Carlo samples are good enough to proceed measurements of the Higgs boson properties. In the analysis, the SM backgrounds are independently evaluated by defining dedicated "control" regions where we normalize individual backgrounds to data. The background estimation techniques and expected yields of the backgrounds in the signal region are presented in detail in Chapter 5.

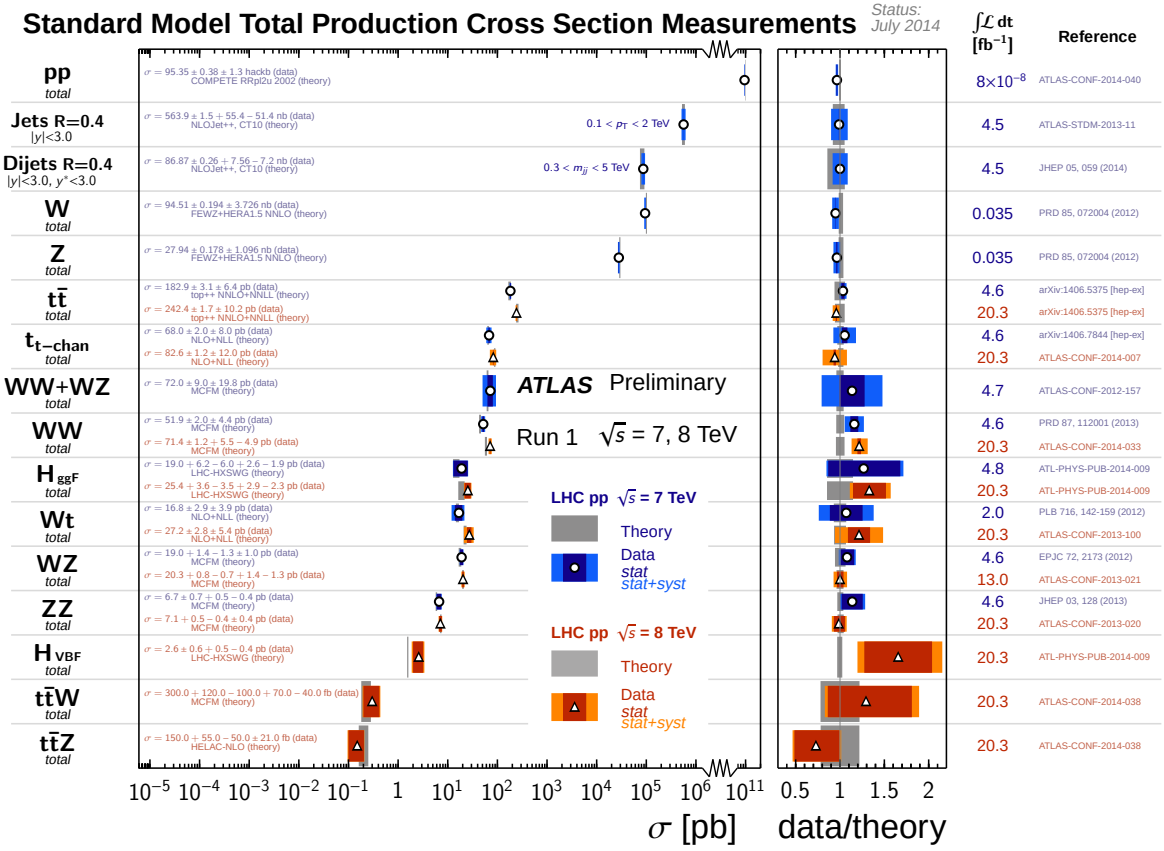

Figure 1.3: Detailed summary of several SM total and fiducial production cross section measurements, corrected for leptonic branching fractions, compared to the corresponding theoretical expectations [52]. All theoretical expectations were calculated at NLO or higher. The W and Z vector-boson inclusive cross sections were measured with 35 fb^{-1} of integrated luminosity from the 2010 data set. All other measurements were performed using the 2011 data set or the 2012 data set. The dark-color error bar represents the statistical uncertainty. The lighter color error bar represents the full uncertainty, including systematics and luminosity uncertainties. The data/theory ratio, luminosity used and reference for each measurement are also shown. Uncertainties for the theoretical predictions are quoted from the original ATLAS papers [53].

1.3 Higgs Phenomenology at the LHC

In this section the Higgs production and decay are briefly described. Our best knowledge on them has been well summarized in detail in the Yellow Report [54–56].

1.3.1 Higgs Production Processes

At the LHC, four major production modes are accessible, the gluon-gluon fusion (ggF), the vector boson fusion (VBF), the production in association with a vector boson (VH), and the production in association with a pair of top/bottom quarks (ttH/bbH). From the analysis point of view, our main focus in Run-I was on the measurement of the ggF and VBF modes because of their large cross sections.

1.3.1.1 ggF Higgs production process

The dominant production mode at the LHC is the ggF as illustrated in Figure 1.4.

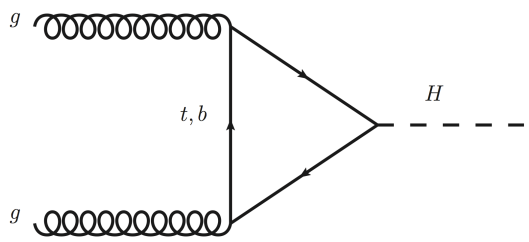

Figure 1.4: Diagram contributing to the ggF production at the LO.

The largest contribution comes from the top quark because of the largest Yukawa coupling. Since the ggF cross section makes up approximately 90 % of the total production cross section, the discovery of the Higgs boson with a cross section which is consistent with the SM expectation would indicate the existence of the ggF production. Hence the discovery had indirectly confirmed that the Higgs boson couples to fermions. The ggF cross section has been calculated up to the next-to-next-to-leading order (NNLO) in QCD [57–62]. Furthermore the NNLO calculation has been improved by resumming the soft-gluon contributions up to next-to-next-to leading logarithm (NNLL) [63]. The theoretical calculation of the ggF process is available at the NNLO+NNLL including the NLO EW correction [64,65]. More details can be found in [66–68]. The uncertainty on the cross section has two primary origins from uncalculated higher-order QCD radiative correction (QCD scale) and from our limited knowledge of the parton distribution functions (PDFs) that are of order ~ 10 % in total.

1.3.1.2 VBF Higgs production process

The second dominant SM Higgs boson production mode at the LHC is the VBF process as illustrated in Figure 1.5.

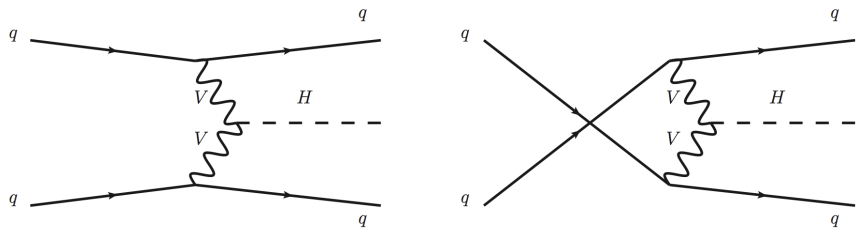

Figure 1.5: Diagrams of t-, u-channel contributions to the VBF production at the LO.

The VBF process is typically associated with two jets in the forward and backward regions of the detector. The s-channel $qq \to qqH$ production contribution is suppressed after requiring the presence of the two jets, so-called VBF selection requirements. The VBF process provides information about the direct coupling to weak gauge bosons. Experimental observation of the VBF production would therefore imply that the Higgs boson is responsible for the SSB in the GWS theory as discussed in Section 1.1. Since the LO matrix element contains only EW vertices, the LO calculation is already a good approximation. The approximate NNLO QCD correction [69] and the full NLO corrections for the QCD and EW [70–72] are also applied to the LO calculation.

1.3.1.3 VH and ttH Higgs production processes

The other modes at the LHC are the VH and ttH processes as illustrated in Figure 1.6.

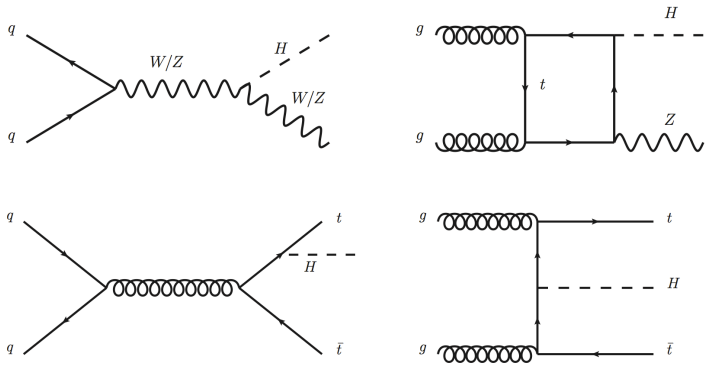

Figure 1.6: Diagrams of the VH process (top left) and the ttH process (bottom) at the LO. The top right is an example of an EW correction to the ggF production ($gg \to HZ$).

In the VH process, the presence of a vector boson provides triggerable leptons (or neutrinos as missing transverse energy) in event. This is especially crucial in the search for $H \to b\bar{b}$ decay due to the huge $b\bar{b}$ background at the LHC, making it unrealistic to trigger on the b-jets from the Higgs boson decay. It is also important to search and measure the VH production in other decay channels, such as the $WH \to WWW$ and $ZH \to ZZZ$ channels, because the Higgs boson can couple purely to either the W or Z boson that can allow us to study the custodial symmetry [73, 74]. In the ttH process, the Higgs boson can purely couple to top quarks via ttH vertex, meaning that the production rate can provide relevant information on the top Yukawa coupling.

In summary, the cross sections of the production modes at $\sqrt{s} = 8$ TeV and the inclusive cross sections at $\sqrt{s} = 7$ TeV, 8 TeV, and 14 TeV are shown in Figure 1.7.

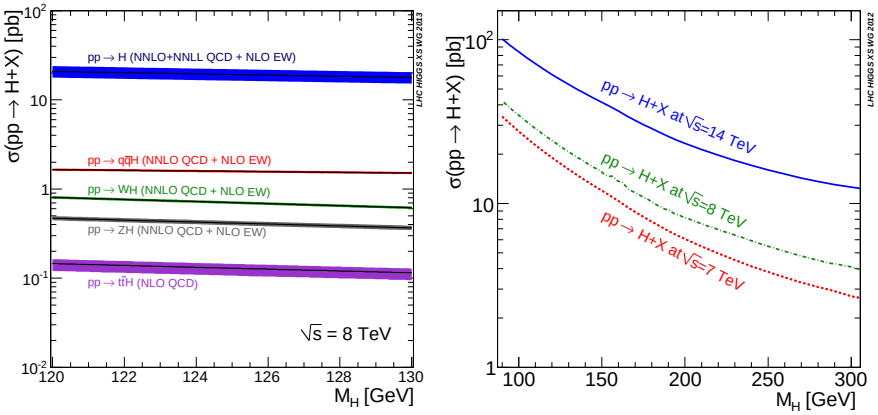

Figure 1.7: Production cross section of the SM Higgs boson for each mode at $\sqrt{s} = 8$ TeV (left) and $\sqrt{s}$ dependence (right) as a function of m_{H} [75].

1.3.2 Higgs Decay Processes

1.3.2.1 Decay into weak bosons

The general expression of the two-body differential width is expressed as:

$$\frac{d\Gamma}{d\Omega} = \frac{|\mathcal{M}|^2}{32\pi^2 M}|p_f|S, \tag{1.13}$$

where $\mathcal{M}$, $|p_f|$, and S denote the matrix element, the momentum of produced particles ($\frac{1}{2}m_{\mathrm{H}}(\sqrt{1-4m_f^2/m_{\mathrm{H}}^2})$), and the number of identical particles, respectively. The S is equal to 1 for the $H \to WW$ decay and 2 for the $H \to ZZ$ decay. The complete matrix element (that is obtained from 'Feynman rules' as discussed in Section 1.1.3) is written as follows:

$$i\mathcal{M}_{H\to WW} = \sum_{\lambda,\rho} igm_W g_{\mu\nu}\epsilon_{1\lambda}{}^{*\mu}\epsilon_{2\rho}{}^{*\nu} \tag{1.14}$$

where ϵ denotes the helicity states of the W boson, and λ and ρ are corresponding indices of ϵ. Using the Equations 1.13 and 1.14, the partial decay width for the two on-shell WW can be written as:

$$\begin{aligned}\Gamma_{H\to WW} &= \int d\Omega \frac{d\Gamma}{d\Omega}, \\ &= \frac{g^2}{64\pi}\frac{{m_{\mathrm{H}}}^3}{{m_W}^2}\sqrt{1-4\frac{{m_W}^2}{{m_{\mathrm{H}}}^2}}(1-4\frac{{m_W}^2}{{m_{\mathrm{H}}}^2}+12\frac{{m_W}^2}{{m_{\mathrm{H}}}^2}).\end{aligned} \tag{1.15}$$

Given that the mass of the Higgs boson is about 125 GeV, it is necessary to take into account the case that one of the weak bosons or both are off-shell. This case has been calculated, for example, in [76], and has been simulated by HDECAY [77] that provides proper off-shell WW decays and includes the complete NLO QCD and EW corrections.

1.3.2.2 Decay into fermions and $\gamma\gamma$

The SM Higgs boson has other decay channels as well. In the $H \to \gamma\gamma$ decay [78], the decay is possible only through W boson or (top) quark loop processes, since the photon is massless gauge boson. Similar to the $H \to \gamma\gamma$ decay, the $H \to gg$ decay is also possible through quark loop. In the fermionic decays, the decay width is determined based on the Yukawa coupling that is proportional to the squared mass of fermions, so that the decay is dominated by bottom quark pairs because the light Higgs boson (e.g. $m_{\mathrm{H}} = 125$ GeV) cannot go into top quark pairs. The partial width is obtained as follows:

$$\Gamma_{H\to ff} = \frac{g^2 N_c}{32\pi m_W^2} m_{\mathrm{H}} m_f^2 \sqrt{1-\frac{4m_f^2}{m_{\mathrm{H}}^2}}, \tag{1.16}$$

where N_c denotes the number of colors that is equal to three for quarks and one for leptons.

1.3.2.3 Total width and branching fractions

The total width of the Higgs boson is computed by putting together all the partial widths. Figure 1.8 shows the total width as a function of the mass of the Higgs boson. The total width blows up around 160 GeV that is the threshold of the (two on-shell) WW production. At m_{H} =125 GeV, the total width is about 4 MeV that makes it difficult to directly measure the width due to detector, while around 600 GeV, the width is order of 100 GeV. The branching fraction (BR) is defined as fraction with respect to the total width, i.e. Γ_i/Γ_{tot} (i: individual channels). The BRs for individual channels between $m_{\mathrm{H}} = 120$-130 GeV are also shown in Figure 1.8. It shows that the BR of the $H\to WW^*$ is 22 % at $m_{\mathrm{H}} = 125$ GeV. It is also clear that the branching fraction to the WW strongly depends on the mass of the Higgs boson. This implies that the signal strength (defined as the ratio of $\sigma\times$BR in data to that in the SM expectation) has also dependence on the mass. [1]

[1] The mass of the Higgs boson is determined by other high resolution channels $H \to \gamma\gamma$ and $H \to ZZ^* \to 4\ell$ because the $H\to WW^*\to \ell\nu\ell\nu$ channel is not sensitive to the mass measurement due to worse mass resolution (i.e. two neutrinos in the final state).

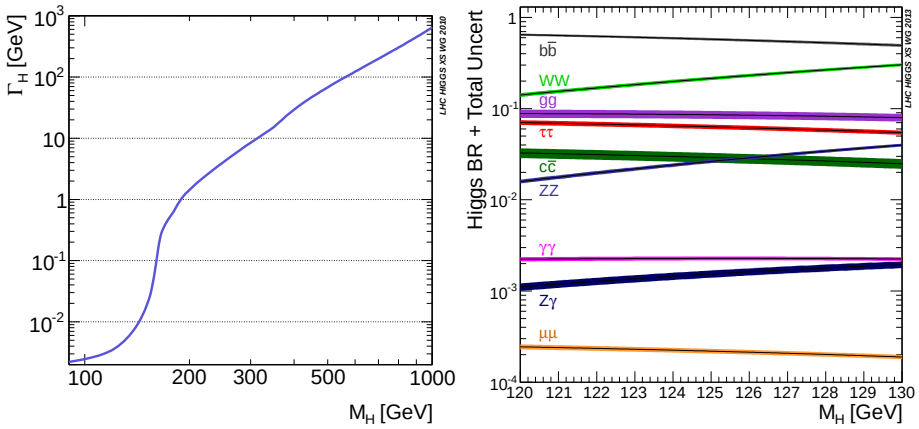

Figure 1.8: Total width of the SM Higgs boson (left) and branching fractions for individual channels (right), as a function of m_{H} [75].

At the end of this section, the $\sigma \times$BR is shown in Figure 1.9 that provides more straightforward information about the size of the Higgs boson signal for each decay channel. Given the Higgs mass of approximately 125 GeV, the $WW \to \ell^+\nu\ell^-\nu$ (shown in blue) has the third largest signal yield. One needs to consider that the fact that the $WW \to \ell^\pm\nu q\bar{q}$ channel suffers from a huge amount of the backgrounds, and that the $\tau\tau$ channel will decay further hadronically or leptonically. Hence the $WW \to \ell^+\nu\ell^-\nu$ channel will be better than those channels in the signal/background ratio.

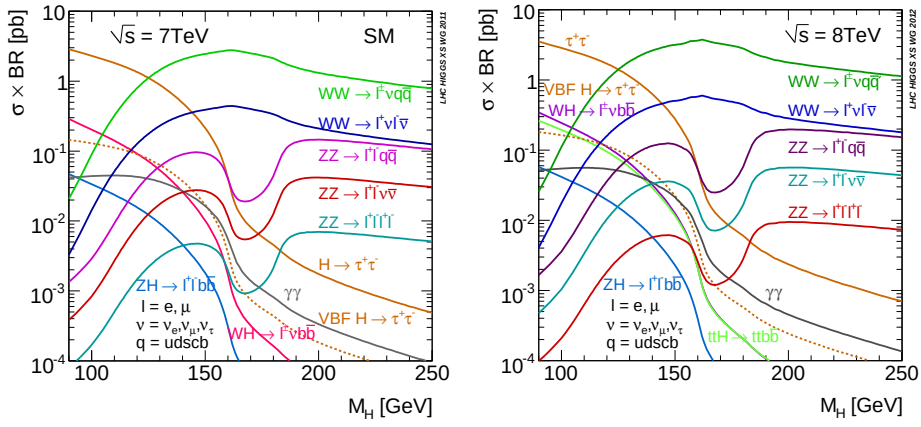

Figure 1.9: The SM Higgs boson production cross section times branching fraction at $\sqrt{s} = 7$ TeV (left) and 8 TeV (right) as a function of m_{H} [75].

1.4 History of Higgs Search

The Higgs search has a long history since the BEH mechanism was proposed in 1964 [79]. The mass of the Higgs boson had been constrained by many theoretical considerations, however it could not be specified by theories. The first experimental limit on the Higgs mass was made by LEP [80] and SLD [81] in mass plane of W boson and top quark. The two dimensional mass plane allowed for an indirect measurement of the Higgs mass because the Higgs boson can contributes to measured quantities of W boson and top quark via loop corrections. LEP and SLD measured W boson mass whereas they deduced top quark mass from electroweak measurements. This indirect measurement was updated making stronger constraint by LEP2 [82] and Tevatron [83, 84] with the direct measurement of the mass of top quark from the Tevatron. The constraint from these indirect measurements is shown in Figure 1.10.

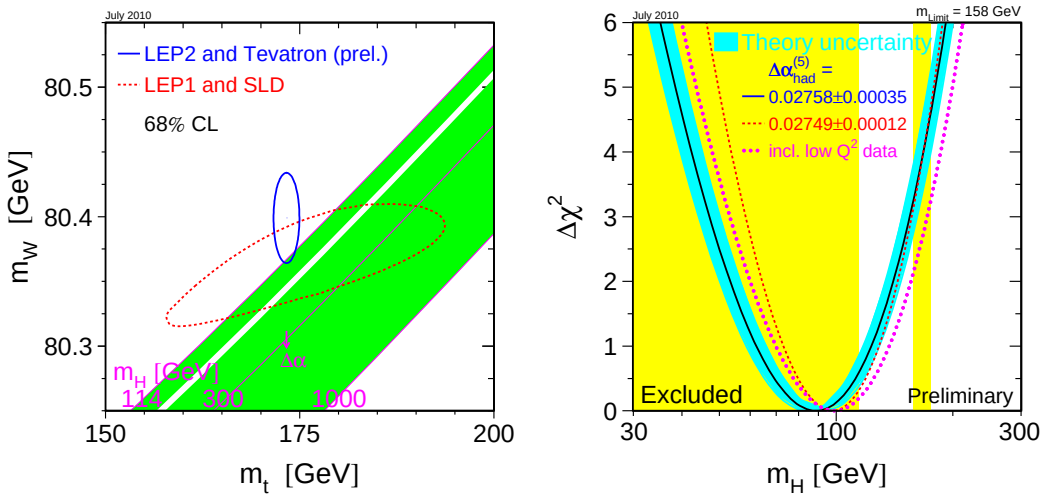

Figure 1.10: (Left): Indirect constraints on the Higgs mass in the W boson mass and top quark mass plane obtained from the LEP, Tevatron, and SLD. The shaded band represents the SM relationship for the masses as a function of m_{H}. The arrow labeled $\Delta\alpha$ shows the variation of this relation with one of the SM parameters that gives an additional uncertainty to the band. (Right): Direct search and indirect constraints on the Higgs mass in the $\Delta\chi^2$ (from the global fit) and m_{H} plane. The line is the result of the fit using data at the Z pole, and the direct determinations of m_t, m_W and Γ_{W}. The band represents uncertainty on theory due to higher order corrections. The yellow band represents the 95% CL exclusion limit on m_{H} from the LEP (up to 114.4 GeV) and Tevatron (158-175 GeV) in July 2010 [85].

In parallel the direct searches were also performed using the Higgs production in association with a vector boson (VH mode) by the LEP/LEP2. In 2000, the LEP2 finally

obtained a lower limit of $m_{\mathrm{H}} > 114.4$ GeV. After the shutdown of the LEP2, the lead in the Higgs searches was taken by the Tevatron. As the analyzed Tevatron luminosity accumulated, the CDF [86] and D0 experiments [87] at the Tevatron started excluding a range of the Higgs masses between 156 GeV and 177 GeV. The constraint on the Higgs mass from these direct measurements is also shown in Figure 1.10.

In 2010, the LHC turned on and started data-taking with the center of mass energy of 7 TeV. The ATLAS and CMS experiments had each accumulated ~ 5 fb^{-1} in 2011. By the end of 2011 the ATLAS excluded a range of the Higgs masses between 131 GeV and 237 GeV, and between 251 GeV and 453 GeV [1], and eventually in July 2012, the discovery of a new boson that was most likely the SM Higgs boson was reported by the ATLAS and CMS. Figure 1.11 shows 95% CL upper limit on the signal strength μ and local p_0 value as a function of m_{H}. The largest excess over the background prediction can be seen around m_{H} = 125 GeV. The discovery opened up new era in understanding the nature of electroweak symmetry breaking. The center of physics analysis is moving from "the search for the Higgs boson" to "the measurement of its properties". The measurement allows for investigating underling physics beyond the Standard Model.

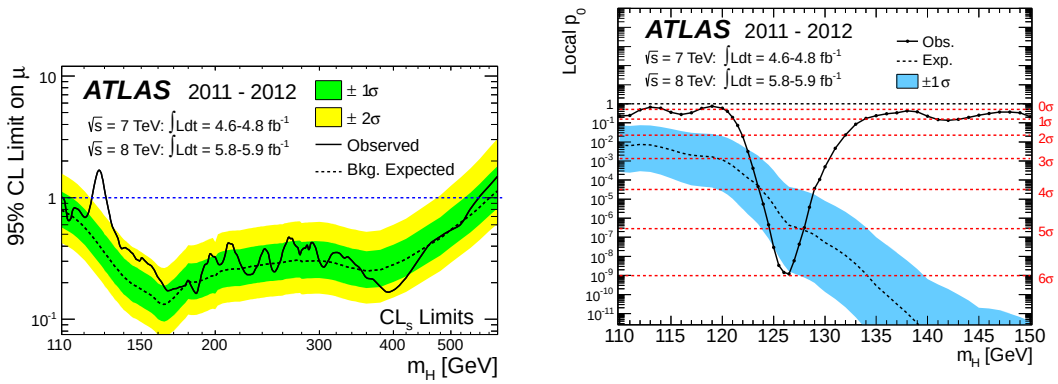

Figure 1.11: Results of the Higgs boson search using $H \to \gamma\gamma$, $H \to ZZ^* \to 4\ell$, and $H \to WW^* \to \ell\nu\ell\nu$ channels [1]. (Left): Observed 95% CL upper limit (solid line) on the signal strength as a function of m_{H} and the expectation (dashed line) under the background-only hypothesis. The dark and light shaded bands show the plus/minus one sigma and plus/minus two sigma uncertainties on the background-only expectation. (Right): Observed local p_0 (solid line) as a function of m_{H} in the low mass range. The dashed curve shows the expected local p_0 under the hypothesis of a SM Higgs boson signal at that mass with its plus/minus one sigma band. The horizontal dashed lines indicate the p-values corresponding to significances of 1 to 6 sigma.

1.5 Coupling Measurements using the $H \to WW^* \to \ell\nu\ell\nu$

The $H \to WW^* \to \ell\nu\ell\nu$ channel had played a leading role in the Higgs search since the turn-on of the LHC, and contributed to the discovery. Even after the discovery the $H \to WW^* \to \ell\nu\ell\nu$ analysis is leading efforts on the property measurements. For example, the spin-0 nature of the new boson has been tested in the $H \to WW^* \to \ell\nu\ell\nu$ channel by comparing with a spin-2 model that can be separated from the spin-0 by dilepton kinematics because the spin-2 makes larger angle between the leptons in the final state [88]. Also the $H \to WW^* \to \ell\nu\ell\nu$ provided the first measurement of the Higgs couplings to weak bosons [3].

The updated analysis presented in this thesis aims at measuring the couplings more accurately. The precise measurement is possible only in understanding of all the Standard Model processes, since the analysis suffers from many backgrounds such as Standard Model WW, top ($t\bar{t}, Wt$), W+jets and other diboson ($WZ, ZZ, W\gamma^{(*)}$), referred to as "other VV", backgrounds. One of the most significant backgrounds is the W+jets background, where a W boson produced in association with a jet that is misidentified as a lepton, due to its large systematic uncertainty (that was 40-60%), making it an important limitation to the experimental sensitivity. The previous analysis [3] was thus optimized making the W+jets background as small as possible, however it was found that the analysis was limited by large statistical uncertainty as shown in Table 1.1.

Table 1.1: Leading uncertainties on the signal strength μ in the previous analysis [3].

Category	Source	Uncertainty, up (%)	Uncertainty, down (%)
Statistical	Observed data	+21	−21
Theoretical	Signal yield and acceptance	+15	−11
Theoretical	WW normalization	+12	−12
Experimental	Objects and DY estimation	+9	−8
Experimental	MC statistics	+7	−7
Experimental	W+jets estimation	+5	−5
Others	luminosity, other backgrounds	+6	−6
Total		+32	−29

To improve the statistics in a given integrated luminosity, the analysis presented in this thesis employs looser lepton selection as suggested by the lepton optimization (see Chapter 4), but the looser selection increases the W+jets and other VV backgrounds by more than a factor of two. Figure 1.12 shows distribution of transverse mass m_{T} of the dilepton system (for the 0-jet analysis) that is used as a final discriminant in this analysis. As can be seen in this figure, the W+jets (light blue) and other VV (magenta) are now the second largest backgrounds (the largest is Standard Model WW background). Several improvements have been made on the modeling of these backgrounds, such as Z+jets fake factor method and SS CR method, in order to reduce the systematic uncertainties on these backgrounds. These new methods are described in detail in Chapter 6 and 7.

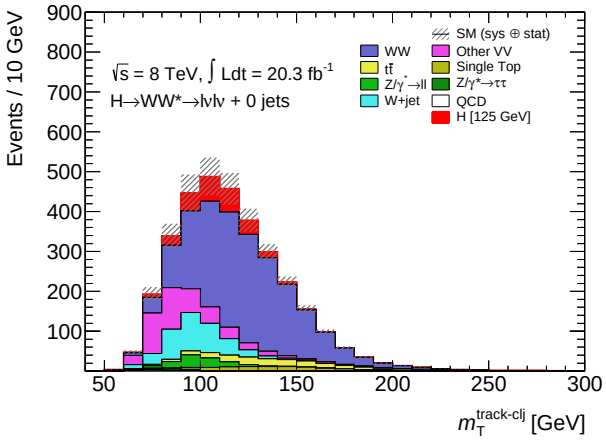

Figure 1.12: Transverse mass of the dilepton system (m_{T}) [89] for 0-jet analysis. m_{T} is used as final discriminant in the analysis.

The goal of this thesis is to perform more precise measurements of the Higgs couplings represented by signal strength μ that is defined as the ratio of cross section times branching fraction in data to that in theoretical prediction given by:

$$\mu = \frac{(\sigma \cdot \mathrm{BR}(\mathrm{H} \to \mathrm{WW}^* \to \ell\nu\ell\nu))_{\ \mathrm{data}}}{(\sigma \cdot \mathrm{BR}(\mathrm{H} \to \mathrm{WW}^* \to \ell\nu\ell\nu))_{\ \mathrm{Theory(SM)}}}, \tag{1.17}$$

where σ is cross section of the Higgs production and $\mathrm{BR}(H \to WW^* \to \ell\nu\ell\nu)$ is branching fraction of the Higgs decay into $WW^* \to \ell\nu\ell\nu$. Assuming that there is no contribution from beyond the Standard Model (BSM) particles that can couple to the Higgs boson, the signal strength is expected to be unity, while if there exists the BSM particle, one can see a deviation on the signal strength. The results presented in this thesis supersede the previous measurement by $> 50\%$ on the experimental sensitivity. The large improvement is achieved owing to optimizations of selection of physics objects (see Chapter 4) and better modeling of the W+jets and VV backgrounds (see Chapter 6, 7).

The signal strength is measured for the individual processes μ_{ggF} and μ_{VBF}, optimizing the analysis to each production process. The comparison of individual signal strengths is meaningful because the coupling strengths of these production processes are different. The ggF production includes the Higgs coupling with top quark (or bottom quark), namely Yukawa coupling, as well as the coupling with weak bosons. While the VBF production contains only electroweak (EW) vertices in the leading order, thus the VBF indicates the couplings with purely weak bosons. Eventually the coupling to fermions and weak bosons are each extracted by introducing new parameterization of the coupling strengths (κ_F and κ_V). The results of these coupling strengths are also shown and discussed in Chapter 8.

Part I

Experimental Apparatus and Physics Objects

Chapter 2

LHC and ATLAS Detector

2.1 Large Hadron Collider

The Large Hadron Collider (LHC) [90, 91] is a superconducting hadron accelerator outside of Geneva, Switzerland. The machine was installed in the existing 27 km tunnel that was initially constructed in 1984-1989 for the Large Electron-Positron (LEP) experiment [80] by European Organization for Nuclear Research (CERN). Four main experiments [92] were installed in four interaction points (IPs) located between 50 m and 150 m underground as shown in Figure 2.1.

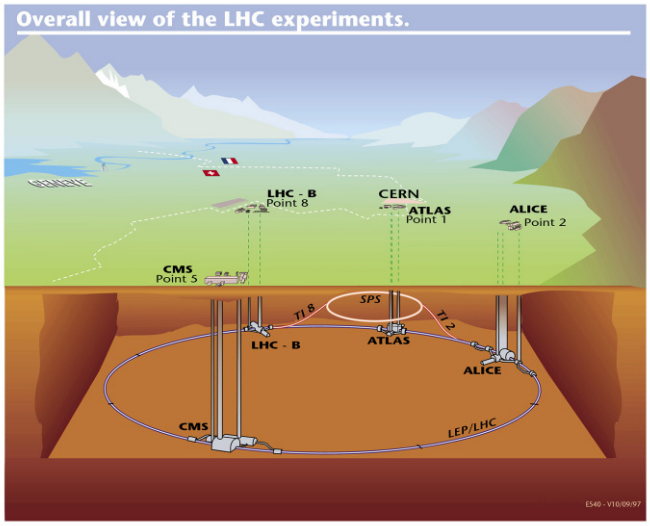

Figure 2.1: Locations of the four main experiments (ALICE, ATLAS, CMS, and LHCb) at the LHC [93]. They are located between 50m and 150m underground. The SPS, the final link in the pre-acceleration chain, and its connection tunnels to the LHC are also shown.

The ATLAS [94–97] and the CMS [98] are general purpose detectors designed to survey the new energy scale, targeting searches for a Higgs boson and beyond the Standard Model (BSM) particles in addition to precision measurements of the Electroweak Symmetry Breaking (EWSB). The LHCb [99] experiment is dedicated to study CP violation through heavy flavor physics. The ALICE [100] is an experiment focused on the physics of strongly interacting matter and the $quark-gluon\ plasma$ at an extreme energy density and temperature through heavy ion collisions at the LHC.

2.1.1 Proton injector chain

The LHC is only the final stage of a series of machines used to accelerate the protons to increasingly higher energies. The protons are initially obtained from ionized hydrogen atoms, and are accelerated away from the bound electrons by electric fields, forming into bunches. The protons start their journey to the LHC in a linear particle accelerator (LINAC2), where they are accelerated up to 50 MeV. The beam is then fed into the first circular accelerator *Proton Synchrotron Booster* (PSB). The *Proton Synchrotron* (PS) then raises the beam energy from 1.4 GeV to 25 GeV. From the PS the bunched beam is injected into the *Super Proton Synchrotron* (SPS). The beam energy is then increased to 450 GeV in the SPS. The beam from the SPS is finally injected into the LHC [101]. The injector chain is summarized in Figure 2.2.

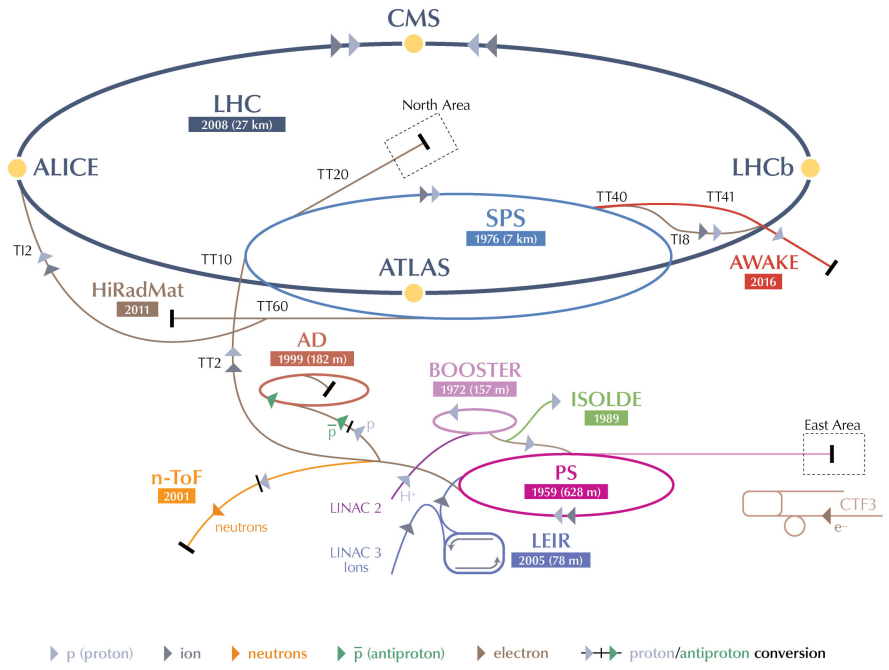

Figure 2.2: The proton injector chain for the LHC at CERN [102].

2.1.2 LHC parameters

The LHC is the most powerful tool for particle physics research, and is designed to collide proton beams at $\sqrt{s} = 14$ TeV with a maximum instantaneous luminosity of $10^{34}\text{cm}^{-2}\text{s}^{-1}$. It can also collide heavy (Pb) ions at $\sqrt{s} = 2.8$ TeV per nucleon with a peak luminosity of $10^{-27}\text{cm}^{-2}\text{s}^{-1}$. During 2010 and 2011 the energy of proton beams circulated in opposite directions was 3.5 TeV, producing collisions at a center-of-mass energy of 7 TeV. In 2012, the energy was increased to 4 TeV per beam, producing collisions at 8 TeV. The beam structure is composed of proton bunches, nominally with 115 billion protons in each. A bunch train is composed of 36 bunches with 50 ns bunch spacing, after which there is a 345 ns gap before the next bunch train. In total, there were 1380 colliding bunches in each in the LHC ring. The beam parameters are summarized in Table 2.1.2.

Table 2.1: The LHC proton beam parameters [103].

	Design	2012 Run
Proton energy [GeV]	7000	4000
Bunch spacing [ns]	25	50
Number of bunches	2808	1380
Number of particles per bunch	1.15×10^{11}	$\sim 1.7 \times 10^{11}$
Peak luminosity [$\text{cm}^{-2}\text{s}^{-1}$]	1.0×10^{34}	7.7×10^{33}
Magnetic field on the dipoles [T]	8.33	4.76
Beam current [A]	0.582	0.369
Bunch length [cm]	7.55	≥ 9
Transverse beam size at IP [μm]	16.7	19
Crossing angle at IP [μrad]	285	290

2.1.3 Pileups

Due to the high instantaneous luminosity, there are approximately 20 (9) expected interactions, inelastic scatterings, per bunch crossing in 2012 (2011) [104]. This effect is called pileup and is classified into two categories, In-time pileup and Out-of-time pileup. The In-time pileup accounts for multiple interactions in the same bunch crossing. The additional interactions are mostly caused by soft collisions and are not interesting in most of physics analyses. The Out-of-time pileup accounts for overlaps of electronic signals between bunch crossings. Both pileups can be a common issue in physics analysis. In the $H\rightarrow WW^*\rightarrow \ell\nu\ell\nu$ analysis, Drell-Yan background is, for instance, increased by a factor of >3 in same flavor (ee and $\mu\mu$) channels due to worse energy resolution of missing transverse energy ($E_{\text{T}}^{\text{miss}}$) caused by the higher pileup in 2012. Hence the objects (lepton, jet, and $E_{\text{T}}^{\text{miss}}$ etc) used in the analysis must be robust against the pileups, and the effect of pileups must be corrected to obtain the physical quantities. (See Section 3.2.2)

2.2 ATLAS Detector

2.2.1 Overview

The ATLAS (*A Toroidal Lhc ApparatuS*) detector is a multipurpose detector and is designed to cover almost 4π rad in solid angle for providing excellent physics performance in the difficult environment of the LHC. The size of the detector is over 25 m in height and about 44 m in length as shown in Figure 2.3.

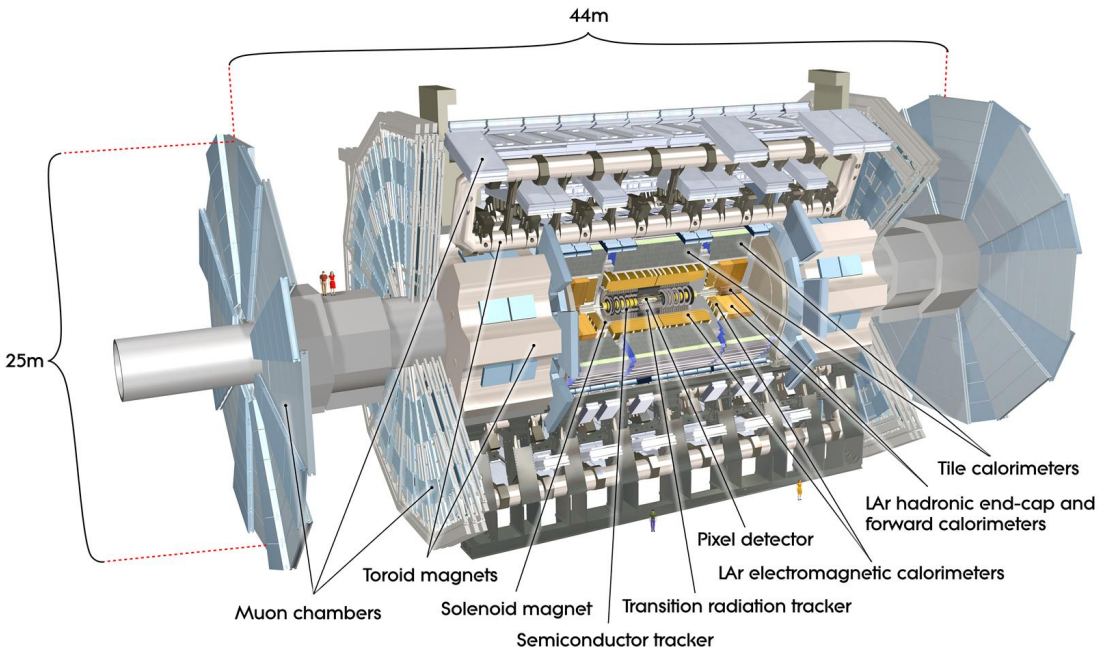

Figure 2.3: Cut-away view of the ATLAS detector and subsystems [105]. The dimensions of the detector are over 25 m in height and about 44 m in length. The overall weight of the detector is approximately 7000 tons.

The ATLAS employs a right-handed coordinate system with its origin at the interaction point (IP). The beam direction defines the z-axis, the positive x-axis points from the IP toward the center of the LHC ring and the positive y-axis points upwards. Cylindrical coordinates (r, ϕ) are used in the transverse plane and the pseudo-rapidity η is defined instead of the polar angle θ as $\eta = -\ln \tan(\theta/2)$.

The ATLAS detector is made up of a barrel region and two endcaps, with each region consisting of several detector subsystems. Closest to the IP is the Inner Detector (ID) [106,107], which consists of two silicon detectors, the Pixel Detector [108] and the Semi-

Conductor Tracker (SCT) [109–111], and the Transition Radiation Tracker (TRT) [112–114], all immersed in a 2 T magnetic field provided by a superconducting solenoid magnet. The ID is surrounded by barrel and endcap liquid argon electromagnetic (EM) calorimeters. The EM calorimeters are surrounded by hadronic calorimeters. In the barrel region, the Tile Calorimeter is composed of steel and scintillating tiles, with a central barrel and two extended barrel regions, And the endcap region ($|\eta| > 1.5$) is covered by the Hadronic Endcap Calorimeter (HEC) based on liquid argon. Furthermore the forward region ($3.2 < |\eta| < 4.9$) is covered by a liquid argon Forward Calorimeter (FCal). The calorimeters are surrounded by the Muon Spectrometer (MS) that is relied on the air-core toroid magnet system. The η coverages and typical resolutions of each subsystem are summarized in Table 2.2.

Table 2.2: The η coverage and typical resolution of each subsystem in the ATLAS detector [96].

Detector component	Typical Resolution	η coverage	
		Precision	Trigger
Tracking	$\sigma_{p_T}/p_T = 0.05 \times p_T(\text{GeV}) \oplus 1\%$	$0.0 < \|\eta\| < 2.5$	
EM calorimeter	$\sigma_E/\text{E} = 10/\sqrt{E}(\text{GeV}) \oplus 0.7\%$	$0.0 < \|\eta\| < 3.2$	$0.0 < \|\eta\| < 2.5$
Hadronic calorimeter			
barrel and endcap	$\sigma_E/\text{E} = 50/\sqrt{E}(\text{GeV}) \oplus 3\%$	$0.0 < \|\eta\| < 3.2$	$0.0 < \|\eta\| < 3.2$
forward	$\sigma_E/\text{E} = 100/\sqrt{E}(\text{GeV}) \oplus 10\%$	$3.1 < \|\eta\| < 4.9$	$3.1 < \|\eta\| < 4.9$
Muon spectrometer	$\sigma_{p_T} = 10\%$ at $p_T = 1$ TeV	$0.0 < \|\eta\| < 2.7$	$0.0 < \|\eta\| < 2.4$

2.2.2 Inner Detectors

In order to measure the momentum of charged particles and to determine the location of primary and secondary vertices (that are originated from heavy flavor and τ decays) against a high occupancy environment expected in every event at the LHC, a good spatial resolution is crucial. For this purpose the ID consists of three independent but complementary subsystems (Pixel, SCT, and TRT) that are all immersed in a superconducting solenoid magnet. The layout of the ID in the barrel region is illustrated in Figure 2.4.

The precision tracking detectors (the Pixel and the SCT) cover the region $|\eta| < 2.5$. In the barrel region they are arranged on concentric cylinders around the beam axis while in the endcap they are mounted on disks perpendicular to the beam axis. The highest granularity is achieved around the vertex region using the Pixel that is the closest detector to the IP. The Pixel is segmented in r-ϕ and z with typically three layers crossed by each track. All pixel sensors that consist of 80.4 million readout channels, have a minimum pixel size in r-$\phi \times z$ of $50{\times}400$ μm^2. The typical spatial resolutions are 10 μm in r-ϕ and 115 μm in the longitudinal direction that is z for the barrel and r for the endcap region.

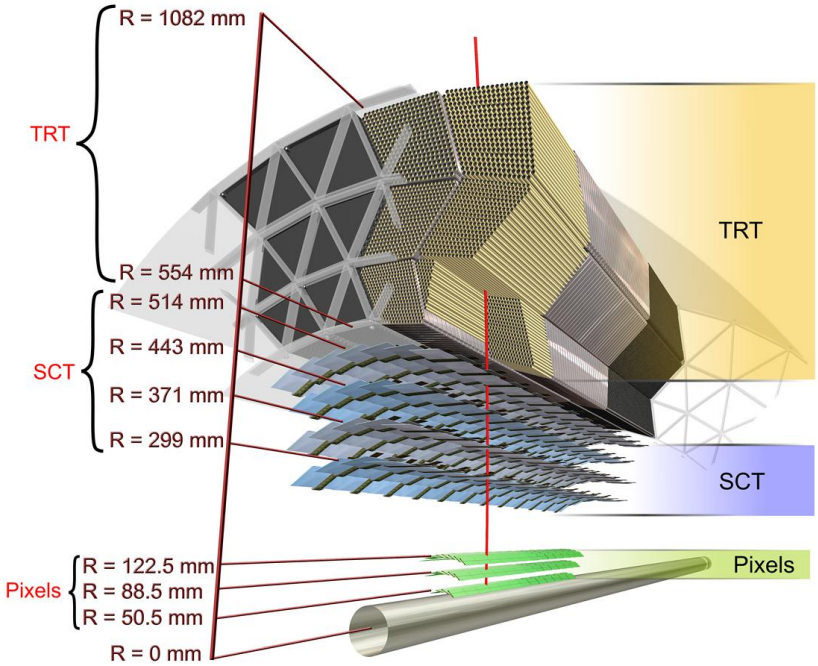

Figure 2.4: Cut-away view of the ATLAS inner detector system [105] that consists of the Pixel, SCT, and TRT in the barrel region, being crossed by one high-energy particle (red-line).

The SCT is the second innermost detector that consists of eight strip layers (four space points) crossed by each track. The SCT module consists of two layers of silicon strip sensors with a strip pitch of 80 μm. The two layers in each module are rotated by $\pm$20 mrad each other to measure both coordinates, r-ϕ and z. The typical spatial resolutions per module are 17 μm in r-ϕ and 580 μm in the longitudinal direction that is z for the barrel and r for the endcap region. The total number of readout channels in the SCT is approximately 6.3 million.

The TRT is the outermost detector that consists of a barrel ($|\eta| < 1.0$) and two endcaps ($1.0 < |\eta| < 2.0$) modules. The TRT uses transition radiation (TR) that is in general emitted by a particle when it comes across a boundary of two media with different indices of refraction. The probability of the TR emission is proportional to the lorentz boost factor (γ) that is sensitive to a mass of the incident particle. The barrel contains 73 layers (144 cm long gas-filled straw tubes) that are oriented parallel to the beam axis, whereas the endcap contains 160 layers (37 cm long gas-filled straw tubes) that are arranged radially in wheels. Typically 36 hits per track are provided by the TRT, which enables to perform precision tracking up to the region $|\eta| = 2.0$. Also the TRT can be used for the electron identification distinguishing electrons from heavier particles. The TRT provides r-ϕ information with an

accuracy of 130 μm per straw. The total number of TRT readout channels is approximately 0.35 million.

In summary, the combination of the inner detector system gives very robust pattern recognition and high precision in both r-ϕ and z. The TRT also contributes significantly to the momentum measurement by the large number of hits and longer measured track length. The achieved spatial resolution of charged particles in r-ϕ is typically $\sigma_{p_T}/p_T = 0.05\ \%\ p_T \oplus 1\ \%$ in $|\eta| < 2.5$. And the vertex reconstruction is accurate enough (typically 15 μm in r-ϕ) to observe secondary vertices that are mostly enhanced by the innermost layer of the Pixel (called B-layer). The configuration of the inner detector system with its η coverage is summarized in Figure 2.5.

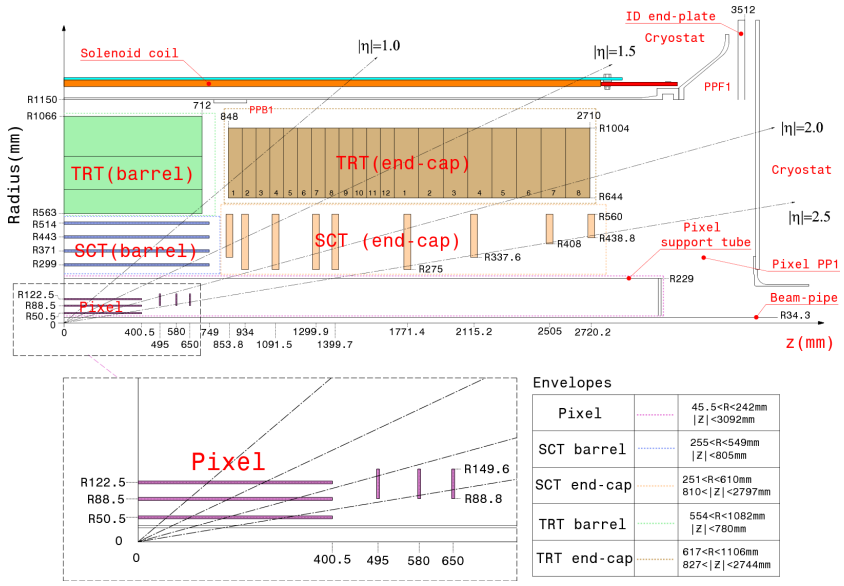

Figure 2.5: Schematic view of a quarter-section of the ATLAS inner detector system [105], showing each subsystem, Pixel, SCT, and TRT with their active dimensions. The IP is located at $(r,\ \phi) = (0,\ 0)$.

2.2.3 Calorimeters

The calorimeter system is designed to measure the energy of electrons, photons, and hadrons. The system covers the range up to $|\eta| < 4.9$, and it consists of mainly two types of calorimeters: electromagnetic (EM) and hadronic calorimeters that are sensitive to the electromagnetic and hadronic interactions, respectively. A cut-away view of the calorimeter system is shown in Figure 2.6.

All calorimeters are so-called sampling calorimeters made of absorbers and active sensors. When an incident particle hits the absorber inside a calorimeter, the particle interacts with the absorber generating a shower. A part of energies from the shower is then "sam-

pled" by the sensors. The energy of the full shower can be inferred and determined from the "sampled" energy. The calorimeter system must provide good containment for those showers to limit energy leakages, called "punch-through", into the muon system. To satisfy this requirement a total thickness of the calorimeter can be an important consideration. Together with a large η coverage up to $|\eta| < 4.9$, it must be ensured to reconstruct physics objects, particularly jet and $E_{\mathrm{T}}^{\mathrm{miss}}$ objects.

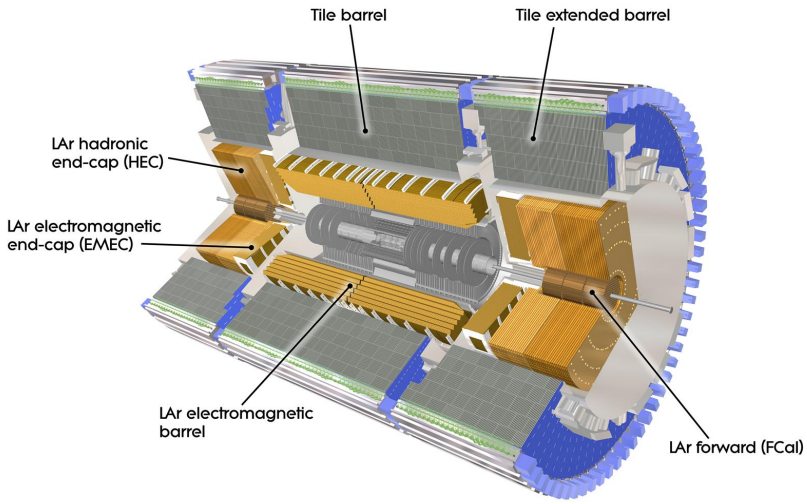

Figure 2.6: Cut-away view of the calorimeter system [105].

The EM calorimeter consists of a barrel ($|\eta| < 1.475$) and two endcaps ($1.375 < |\eta| < 3.2$) with a transition region ($1.37 < |\eta| < 1.52$). The EM calorimeter is a lead-liquid argon detector (LAr) with accordion-shaped absorbers (lead) and electrodes (kapton) in a combination with liquid argon as active medium providing uniform coverage in ϕ and fast readout. In the barrel region, the EM calorimeter is segmented in depth into three longitudinal layers varying granularity as shown in Figure 2.7.

The first (innermost) layer has a finest granularity in η that is used for the precision measurement of the EM showers discriminating photons from π^0s. The largest energy deposit can be observed in the second layer that has a thickness of $\sim$ 16 X_0. The third layer is mainly used for distinguishing the EM and hadronic showers. For the regions of $|\eta| < 1.8$, a presampler detector that provides a measurement of the energy lost in front of the EM calorimeters, is also placed to correct for the energy for better performance in energy resolution. In the endcap region, the calorimeter is segmented into two longitudinal layers with a coarse lateral granularity. With this configuration, a total thickness of >22 radiation lengths (X_0) in the barrel and of >24 X_0 in the endcap is achieved.

The hadronic calorimeters surround the EM calorimeters. The hadronic calorimeter (Tile HCal) in the range of $|\eta| < 1.7$ uses steel as absorber material and scintillating tiles as

active media. The scintillation photons are guided to photomultiplier tubes by wavelength-shifting fibres. The granularity of the hadronic calorimeters is coarser than that of the EM calorimeter because the hadronic showers are typically wider than the EM showers. In the endcap region, the Hadronic Endcap Calorimeters (HEC) are placed and they cover the region $1.5 < |\eta| < 3.2$ with the LAr active media. With this configuration, a total thickness of >10 interaction lengths (λ) that is sufficient to reduce the "punch-through" events, is achieved. Figure 2.9 shows interaction lengths as a function of $|\eta|$.

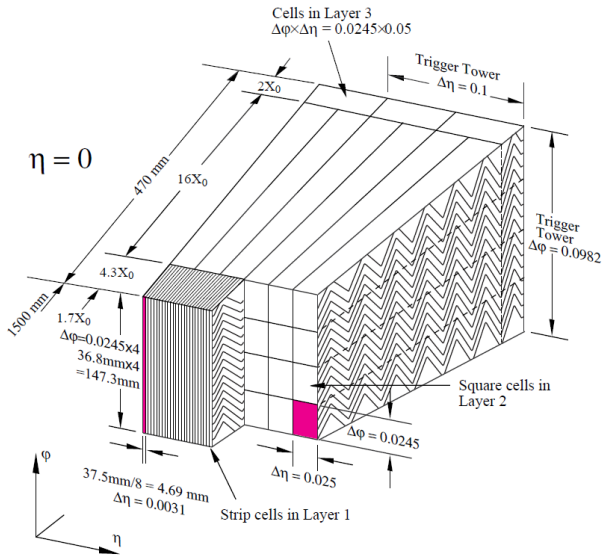

Figure 2.7: Sketch of an accordion-shaped barrel module of the EM calorimeter [105]. The granularity in η and ϕ of the cells of each of the three layers and of the trigger towers is also shown.

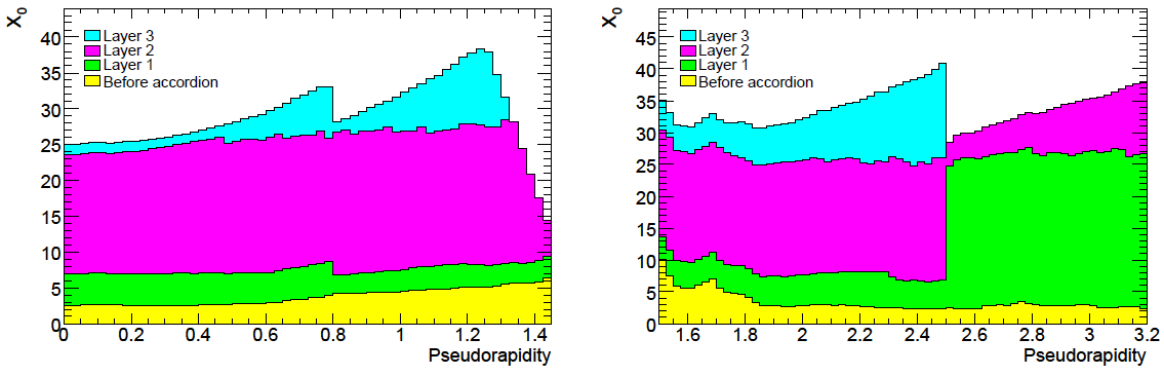

Figure 2.8: Cumulative amount of material (in units of radiation length) in front of the EM calorimeters and in the EM calorimeters themselves for the barrel (left) and endcaps (right) regions as a function of $|\eta|$ [105].

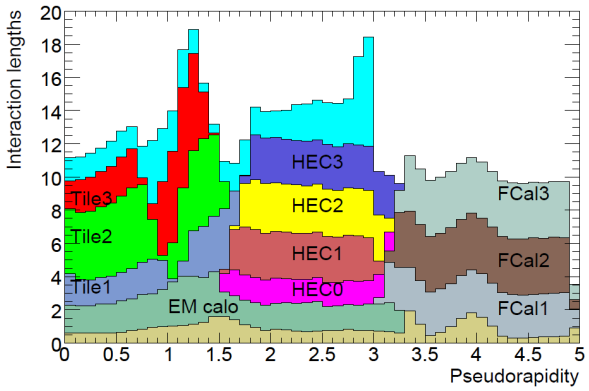

Figure 2.9: Cumulative amount of material (in units of interaction length) in front of the EM calorimeters, in the EM calorimeters themselves, in hadronic calorimeters, and the total amount of material in front of the active layer of muon spectrometer (light blue), as a function of $|\eta|$ [105].

The calorimeter system also keeps its coverage at higher η region ($3.1 < |\eta| < 4.9$) provided by the forward calorimeter (FCal). The aim of covering the high η region is to trigger the VBF topology (See Section 1.3.1) that has two forward/backward jets in event. The first layer is dedicated to the measurement of the EM showers while the second and third layers are dedicated to the hadronic showers. This is achieved by constructing last two layers with tungsten instead of steel.

2.2.4 Muon Spectrometer

The outermost detector in the ATLAS is the Muon Spectrometer (MS) system. The system covers the range of $|\eta| < 2.7$ and it consists of two precision tracking chambers, two trigger chambers and air-core toroid magnet system. The layout of the MS is shown in Figure 2.10.

The muon tracks are reconstructed using precision chambers that consist of three layers of the Monitored Drift Tubes (MDT) and the Cathode Strip Chambers (CSC). The momenta are then measured from the deflection of the muon trajectory in the magnetic field generated by the air-core toroid system. Since the precision chambers require a wide time window of about 700 μs, the MS system needs to have independent trigger chambers to provide fast responses to issue muon triggers. Hence the MS system also has such trigger chambers that consist of three layers of the Resistive Plate Chambers (RPC) and three layers of the Thin Gap Chambers (TGC). The TGC and RPC provide the ATLAS level-1 triggers with correct bunch crossing in every 25 ns. The TGC and RPC are also used to measure the muon trajectories in ϕ coordinate.

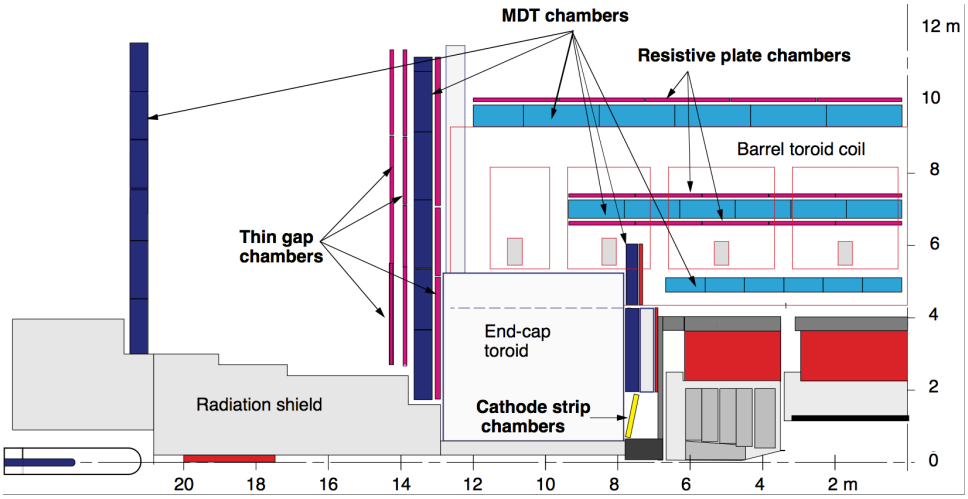

Figure 2.10: The ATLAS muon spectrometer [115].

2.2.5 Magnet system

The magnet system in the ATLAS detector consists of four superconducting magnets. A superconducting solenoid is placed parallel to the beam axis, and is designed to provide the ID with a 2 T axial field that is enough to bend and measure momenta of charged particles from around the IP. The solenoid is also designed to be as thin as possible to reduce the unnecessary material (that corresponds to 0.66 X_0) in front of the EM calorimeter.

There are also three large air-core toroidal magnets that lie outside the calorimeter but in the MS. One is dedicated to the barrel and the others to the endcaps. These magnets are placed concentrically behind the calorimeter and produce a 0.5 T toroidal field in the barrel and 1 T in the endcap. Each of three magnets consists of eight coils that are arranged radially and symmetrically around the beam axis. In the barrel region, each coil is immersed in their own cryostat whereas in the each endcap the coils are housed all together in a single but large cryostat. The bending power can be tunable by rotating the coil systems in the endcap with respect to the system in the barrel. Each endcap is now rotated 22.5 degrees to be optimal and to provide the radial overlap.

2.2.6 Trigger system

The trigger system is of crucial importance to the physics analyses at the LHC. During the LHC running, a bunch of protons collide inside the ATLAS every 25 ns. Neither the data acquisition system nor the resources for doing off-line analysis are capable of handling such amounts of data. Therefore a trigger system is required to select only rare processes of primary interest to the physics analyses to be written to disk and analyzed further off-line. In general those interesting events are characterized by large momentum transfer in the

hard process, namely high p_{T} jets, leptons, and large missing transverse energy ($E_{\mathrm{T}}^{\mathrm{miss}}$). Figure 2.11 shows cross sections of primary processes in pp collisions.

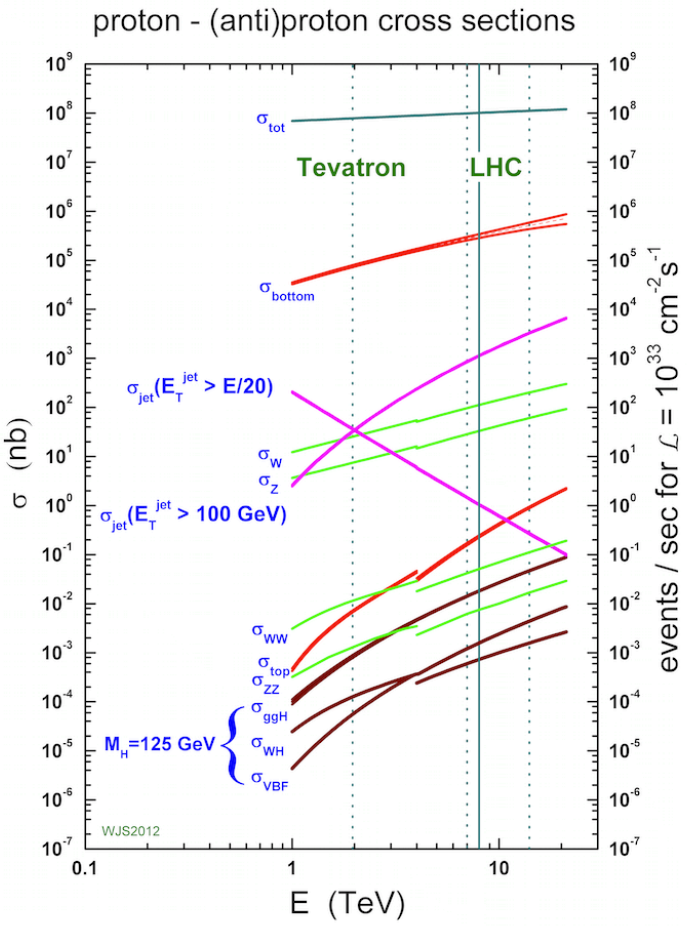

Figure 2.11: Cross section as a function of $\sqrt{s}$ in pp collision [116]. The cross sections are calculated either at NLO or NNLO QCD correction, using MSTW2008 parton distributions, with the exception of the total hadronic cross section which is based on parametrization of the Particle Data Group. The discontinuity in some of the cross sections at 4 TeV is due to the switch from $p\bar{p}$ to pp collisions.

Roughly speaking, the ggF process (σ_{ggH}) is produced with the probability of $1/10^{10}$ at $\sqrt{s} = 8$ TeV in pp collisions. Hence the order of 10^{10} soft pp collisions have to be rejected by triggering and off-line analysis. In the current trigger system, the order of 10^5-10^6 reduction has been achieved by the trigger system, meaning that W/Z events ($\sigma_{W/Z}$) are mostly recorded by the (lepton) trigger system for physics analysis.

The trigger system consists of three levels of event selection: Level-1(L1), Level-2(L2), and Event Filter (EF) where the L2 and EF form the High-Level Trigger (HLT). A schematic

overview of the trigger system is shown in Figure 2.12.

The L1 trigger performs as an initial event selection. The L1 is hardware-based and it uses limited information from a subset of detectors to look for signatures: the RPC and TGC for high p_T muons, and all the calorimeter systems with a low granularity for electrons/photons, jets, and τ, selecting an event with large $E_{\mathrm{T}}^{\mathrm{miss}}$ and large total transverse energy. The L1 sends information about those triggered signatures with their coordinate in ϕ and η to the L2. The information about the coordinate is called $Regions-of-Interest$ (ROI). The maximum L1 acceptance that can be handled by the detector readout is 75 $\mathrm{kH_Z}$, and the L1 decision must reach the front-end electronics within 2.5 μm after corresponding bunch crossing is occurred. All data selected by the L1 are held in the Readout Buffers (ROB) until they are processed by the L2.

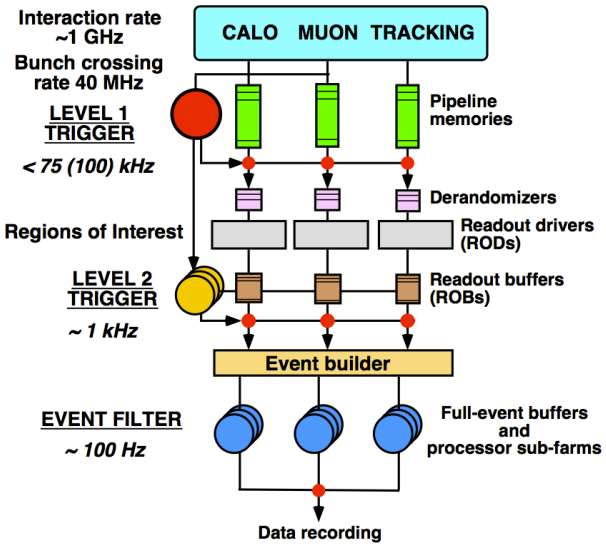

Figure 2.12: Block diagram of the ATLAS trigger system [94].

The L2 trigger is software-based and it uses the ROI information, energy, and the type of signatures, and provides more sophisticated selections based on the full detector information that was not available in the L1 such as reconstructed track information from the ID and better information on energy deposition etc, to reduce the event rate to below 3.5 $\mathrm{kH_Z}$, with an average event processing time of approximately 40 ms.

The EF performs as the final off-line selection on the events that passed the L2 selection to further select events down to a rate which can be recorded for subsequent off-line analysis. It reduces the event rate to approximately 200 $\mathrm{H_Z}$, with an average event processing time of order four seconds.

2.2.7 Luminosity monitoring

Besides the main detector, there are two luminosity detectors in the ATLAS: Beam Condition Monitor (BCM) and LUminosity measurement using Cherenkov Integrating Detector (LUCID). They measure instantaneous/integrated luminosities and calibrate data quantity recorded by the ATLAS.

The LUCID, located at $z = \pm$ 17 m from the IP, consists of twenty aluminum tubes surrounding the beampipe. The LUCID performs online luminosity monitoring of the instantaneous luminosity and beam conditions by counting inelastic pp scatterings since the LUCID is based on the principle that the number of pp scattering in a bunch crossing is proportional to the number of particles detected in this detector. This holds true even when most of the detected particles originate from secondary interactions.

The BCM, located at $z = \pm$ 1.84 m from the IP, consists of four small diamond sensors arranged around the beampipe in a cross pattern on each side of the IP. The BCM performs bunch-by-bunch luminosity measurement in the ID by counting in-time and out-of-time collisions, and by distinguishing particles in pp collisions from beam-background particles using timing information. The BCM also provides a beam-abort signal when the beam losses start to risk damaging the ID.

Chapter 3

Event and Object Reconstruction

Since the $H \to WW^* \to \ell\nu\ell\nu$ analysis is binned in jet multiplicity, obtaining robust jet definition against pileup jets is crucial. In addition, as the Higgs signature contains two genuine isolated high p_{T} leptons and two neutrinos in the final state, leptons and missing transverse energy ($E_{\mathrm{T}}^{\mathrm{miss}}$) are also key objects regardless of the Higgs production process. Furthermore b-tagging is of special importance to reduce/control the top backgrounds ($t\bar{t}$, single top) that are dominant in the $\geq$1 jet analysis.

In this chapter lepton triggers are firstly presented since any events used in the analysis are collected with those triggers. The reconstruction of the physics objects, except for leptons (See Chapter 4), used in the analysis are then briefly summarized, starting from the reconstruction of tracks and vertices that are primary objects for the reconstruction of all the other physics objects (electrons, muons, jets, and $E_{\mathrm{T}}^{\mathrm{miss}}$).

3.1 Lepton Triggers

This section focuses on lepton triggers since the analysis relies on those trigger. The overall trigger system is summarized in Section 2.2.6. In the analysis, luminosity prescaled triggers referred to as "supporting triggers" [117, 118], are also used but they are only for the modeling of the W+jets/QCD backgrounds. Hence the detail of those triggers are presented in Chapter 6.

3.1.1 Electron triggers

At the Level 1 trigger (L1), e/gamma objects are identified by making use of trigger tower [119] as illustrated in Figure 3.1. The trigger tower consists of the calorimeter cells with a reduced granularity of $\Delta\eta \times \Delta\phi = 0.1 \times 0.1$. The towers are used for measuring the transverse energy E_{T} in the clusters (with a precision of the order of $\sim$ 1 GeV) that are formed by identifying local maxima using a *sliding window* algorithm [119] based on a 4×4 group of trigger towers. A trigger is fired if the central 2×2 trigger towers contain at least one pair of neighboring towers with a combined energy that satisfies a certain threshold.

Finally the positions of the triggered e/gamma objects, referred to as Region of Interests (ROI), are determined and the ROI information is sent to the Level 2 trigger (L2).

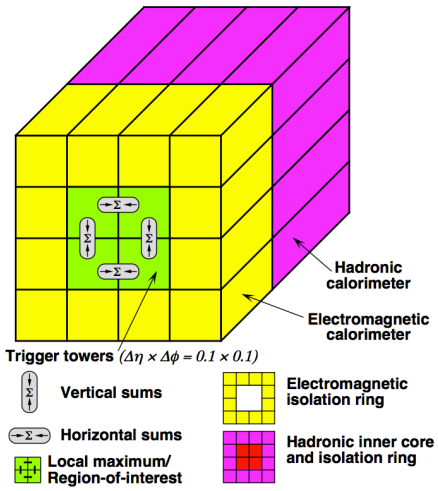

Figure 3.1: Schematic view of trigger tower [105].

At the L2, fast calorimeter and tracking reconstruction algorithms that are mostly the same as the off-line electron reconstruction described in Section 4.1.1 but using only the highest E_{T} seed cluster in the second layer, are used. Finally at the EF, the full off-line reconstruction and identification algorithms described in Section 4.1.1 and 4.1.2, are applied.

3.1.2 Muon triggers

At the L1 trigger, an initial selection based on the reduced granularity information from a subset of the detectors is made. The transverse momentum of muons are roughly estimated from the hit patterns along the muon trajectory using only trigger chambers, the RPC in the barrel and the TGC in the endcap. The muons from the limited p_{T} measurements are classified into six p_{T} categories, and the position information and hit patterns, namely ROIs, based on the classification are sent to the L2.

At the L2, muons are further selected using fast L2 muon algorithms. The candidates from the L1 are refined by using both the trigger and precision chambers. The trajectory of the candidate is identified by fast fitting, while the p_{T} is reconstructed by Look Up Tables (LUT) to achieve reasonable resolution in sufficiently short time allowed at the L2. Subsequently the reconstructed tracks in the ID are combined with the tracks reconstructed by the precision chambers, to refine the track parameters. Finally at the EF, the full off-line reconstruction algorithm with the isolation requirement, is applied as described in Section 4.2.1.

3.1.3 Off-line triggers

The data sample used in the analysis was collected with primary electron and muon triggers in 2011 with center mass energy of $\sqrt{s} = 7$ TeV and integrated luminosity of 4.5 fb^{-1}, and 2012 with center mass energy of $\sqrt{s} = 8$ TeV and integrated luminosity of 20.3 fb^{-1}. For the different flavor ($e\mu$,μe) analysis, all electron and muon triggers are "OR"-ed, and for the same flavor (ee,$\mu\mu$) analysis, either electron or muon triggers are used.

In 2012 the dilepton triggers are "OR"-ed because of their gain in acceptance, the dilepton trigger thresholds also allow for the loosening of the lepton p_{T} thresholds from 25 GeV $\rightarrow$ 22 GeV for the leading lepton. In the ee and μe channels, however, the dilepton trigger thresholds are too high for any contribution to events with a sub-leading electron below 15 GeV. Table 3.1 presents combined gain from lowering the leading and sub-leading lepton p_{T} when dilepton triggers are included (for both cut selections, reference point is same cut but with single lepton trigger).

Table 3.1: Signal efficiency gains from adding dilepton triggers. Efficiency gains are computed for the ggF Higgs signal in 0 jet analysis.

Channel	p_{T}>25,10	p_{T}>22,10
ee channel	2.6%	9.1%
$\mu\mu$ channel	9.0%	18.5%
$e\mu$ channel	1.6%	8.3%
μe channel	2.1%	8.2%

While no dilepton triggers are considered in 2011 due to the fact that the trigger threshold is lower than the leading lepton p_{T} requirement, retaining a high trigger efficiency. Table 3.2 shows all the triggers used in the analysis. The definitions of the triggers are changed through the years 2011 and 2012 according to the LHC running conditions, in other words, the increasing luminosity and therefore worsening pileup conditions.

For electron triggers, numbers after `EF_e` in the trigger names mean p_{T} threshold values that are set to give an efficiency of 90 % relative to the trigger plateau efficiency at the given threshold value in the EF in units of GeV. `vh` denotes a cut on the hadronic core isolation ($<$ 1 GeV) at the L1. This is similar to the hadronic leakage cut (see Section 4.1.2) but as it uses a fixed energy cut, it causes an inefficiency at very high p_{T} ($p_{\mathrm{T}}>$ 300 GeV). The `i` after `vh` indicates a cut on the track isolation at the EF (Ptcone20/$p_{\mathrm{T}} < 0.1$). The `T` before `vh` denotes a change of the E_{T} threshold from 2EM7VH to 2EM10VH at the L1 in 2011, but it does not imply anything in 2012. The `L2StarB` trigger was added during the 2012 data taking in order to recover the efficiency in the endcap. Finally `medium`, `medium1`, and `loose1` denote the tightness of the electron identification. For `medium1`, additional cuts (on shower shapes and tracking variables) are applied to `medium`.

For muon triggers, the suffixes `medium` and `tight` are added for triggers seeded by MU11 and MU15, respectively. The `i` on `EF_mu24i_tight` indicates a cut on the track isolation at the EF (Ptcone20/$p_{\mathrm{T}} < 0.12$). The `_EFFS` on `EF_mu18_tight_mu8_EFFS` indicates that additional muons are searched for by "full-scan" information rather than relying on only the ROI information. This results in no L1 seed for the second (or third) muon as can be seen in Table 3.2.

Table 3.2: Trigger setup for 2011 and 2012 analysis. The definitions of the triggers are changed through the years 2011 and 2012 according to the LHC running conditions.

Primary single lepton triggers in 2011

	Offline trigger	L1 seed	Period
elec	`EF_e20_medium`	EM14	B - J
	`EF_e22_medium`	EM16	K
	`EF_e22vh_medium1`	EM16VH	L - M
muon	`EF_mu18_MG`	MU10	B - I
	`EF_mu18_MG_medium`	MU11	J - M

Primary single lepton and dilepton triggers in 2012

	Offline trigger	L1 seed	Period
elec	`EF_e24vhi_medium1`	EM18VH	A - L
	`EF_e60_medium1`	EM30	A - L
	`EF_2e12Tvh_loose1`	2EM10VH	A - L
	`EF_2e12Tvh_loose1_L2StarB`	2EM10VH	D - L (data only)
muon	`EF_mu24i_tight`	MU15	A - L
	`EF_mu36_tight`	MU15	A - L
	`EF_mu18_tight_mu8_EFFS`	MU15	A - L
elec-muon	`EF_e12Tvh_medium1_mu8`	EM10VH_MU6	A - L

3.1.4 Trigger efficiency

The trigger efficiencies have been measured using tag-and-probe method (see Section 4.3.1), and have been found to be ∼90 % for electrons, and ∼90 % (∼70 %) for muons in the endcap (barrel). Any differences between data and simulation in efficiency are corrected for by calculating scale factors (SF) for individual leptons. Using the individual SFs, the per-event SF is also calculated as follows:

$$\mathrm{SF} = \frac{\mathrm{Eff}_{data}}{\mathrm{Eff}_{MC}} = \frac{1-(1-\epsilon_{MC}^{lead}\times \mathrm{SF}^{lead})\times(1-\epsilon_{MC}^{sub}\times \mathrm{SF}^{sub})}{1-(1-\epsilon_{MC}^{lead})\times(1-\epsilon_{MC}^{sub})}, \tag{3.1}$$

where ϵ_{MC}^{lead} and ϵ_{MC}^{sub} are trigger efficiencies for the leading and sub-leading leptons, and SF^{lead} and SF^{sub} are individual scale factors for the leading and sub-leading leptons. The

'OR'ing of the dilepton triggers increases the complexity of the efficiency calculation as follows:

$$\text{Eff} = \epsilon_{single} + \epsilon_{di-lep} - \epsilon_{single} \cdot \epsilon_{di-lep} \tag{3.2}$$

$$= (\epsilon_1^s + \epsilon_2^s - \epsilon_1^s\epsilon_2^s) + (\epsilon_1^d\epsilon_2^d) - (\epsilon_1^s + \epsilon_2^s - \epsilon_1^s\epsilon_2^s) \cdot (\epsilon_1^d\epsilon_2^d), \tag{3.3}$$

where ϵ_{single} and ϵ_{di-lep} are the per-event efficiencies from the single lepton triggers and dilepton triggers. The superscripts s and d denote the single lepton trigger and dilepton trigger, and the subscripts 1 and 2 denote the leading and sub-leading leptons. Using these symbols, the uncertainty on the per-event efficiency is expressed as:

$$(\Delta\text{Eff})^2 = [\sigma_1^s(1-\epsilon_2^s)(1-\epsilon_{di-lep}) + \sigma_1^d\epsilon_2^d(1-\epsilon_{single})]^2 \tag{3.4}$$

$$+ [\sigma_2^s(1-\epsilon_1^s)(1-\epsilon_{di-lep}) + \sigma_2^d\epsilon_1^d(1-\epsilon_{single})]^2, \tag{3.5}$$

where $\sigma_{1,2}^d$ is the uncertainty, for instance, on either `e12Tvh_medium1` or `mu8` in $e\mu$ final state. In order to reduce the complexity, a simplification is made for events that are triggered by both single lepton and dilepton triggers. For those events, the uncertainties for the single lepton triggers are used. And for events that fire only the dilepton triggers, the uncertainties for the dilepton triggers are applied. In practice the events that have the leading lepton p_{T} = 22-25 GeV, are not accessible by the single lepton triggers because of its trigger plateau threshold ($p_{\text{T}} > 25$ GeV). Therefore the uncertainties for the dilepton triggers are considered for those events. The uncertainties are treated as uncorrelated between the leading and sub-leading leptons when the leptons fire different triggers while are treated as correlated when the leptons fire the same trigger.

3.2 Tracks and vertices

3.2.1 Track reconstruction

Track reconstruction [120–123] is based on two algorithms referred to as "inside-out" and "outside-in" algorithms. The former starts the reconstruction from the innermost detector, namely the Pixel, whereas the latter from the outermost detector, the TRT.

inside-out algorithm: In the inside-out algorithm, the track reconstruction starts from forming track-seeds using all three layers of the Pixel and the first layer of the SCT. Simultaneously a fast primary vertex search is performed to further constrain the seeds. Then the seeds provide directional information to build roads for the further search of associated hits in the remaining layers of the SCT to one track candidate. However the seeded track finding results in a very high number of track candidates. Many of these track candidates share silicon hits including fake tracks that do not originate from one single particle. In the second stage, the ambiguities between real and fake tracks are resolved by placing a score on the track quality [124] with more sophisticated fitting that includes global χ^2 and Kalman filter algorithms [125]. In the final stage, the tracks reconstructed in the silicon detectors are extended into the TRT by associating extra hits in the TRT. The tracks are

refitted with the additional hits in the TRT and compared to the silicon-only tracks in the fitting score. If the score is improved by the TRT hits, then the extended track is taken, otherwise the original silicon-only track is taken instead as a real track. The tracks reconstructed by the inside-out algorithm are required to have $p_{\mathrm{T}} > 400$ MeV and $|\eta| < 2.5$.

back-tracking algorithm: After the inside-out algorithm, the outside-in algorithm referred to as the back-tracking, is also performed. The back-tracking algorithm is a track search starting from segments reconstructed in the TRT. The algorithm is designed to reconstruct secondaries that are defined as particles produced in the interactions of primaries. Since heavy flavor/τ decays and photon conversions have secondaries, it is crucial to identify those tracks in this algorithm. If there are no tracks associating to the silicon detectors, the tracks are classified as the TRT-standalone tracks.

3.2.2 Vertex reconstruction

Primary vertices are then reconstructed using the reconstructed tracks based on the 'vertex finding' algorithm [126]. Firstly the algorithm selects the reconstructed tracks that are compatible with tracks originated from the interaction point (IP). Then a vertex seed is obtained from a global maximum in the z position of the reconstructed tracks at the beamline. An iterative χ^2 fit is then performed using the seed and the nearby tracks. Each track carries a weight that is a measurement of its compatibility with the fitted vertex depending on the χ^2. Bad χ^2 tracks, defined as more than 7 σ far from the vertex, are used again to seed a new vertex and the whole procedure is repeated until no unassociated tracks are left. Each primary vertex is finally required to have more than two associated tracks.

Reconstruction efficiency

The vertex reconstruction efficiency depends on the pileups. The efficiency decreases with the higher pileup because of an increased number of fake tracks, which results in the worse resolution of the vertex position, namely an increased number of fake vertices. Figure 3.2 shows the vertex reconstruction efficiency and fake probability as a function of the average number of interactions per bunch crossing, referred to as $< \mu >$, that is from the calorimeter readout including both in-time and out-of-time pileups (see also Section 2.1.3). The reconstruction efficiency for the robust selection with having more than two associated tracks (shown in green) is higher by ~ 5 % thanks to the smaller contamination of the fake tracks in the denominator sample. Hence the analysis also requires more than two associated tracks when defining the vertex.

NPV and $< \mu >$ rescaling

Since it is hard to generate the $< \mu >$ distribution correctly in simulation, the difference between data and MC in the μ is corrected by '$< \mu >$-rescaling'. As illustrated in Figure 3.3, the $< \mu >$-rescaling also improves the NPV distribution.

The remaining difference is further corrected for by reweighting the $< \mu >$ distribution to data. These corrections affect most of the physics objects such as leptons, $E_{\mathrm{T}}^{\mathrm{miss}}$ and jets. The impact of the scaling in the analysis is further discussed in Section 8.3.2

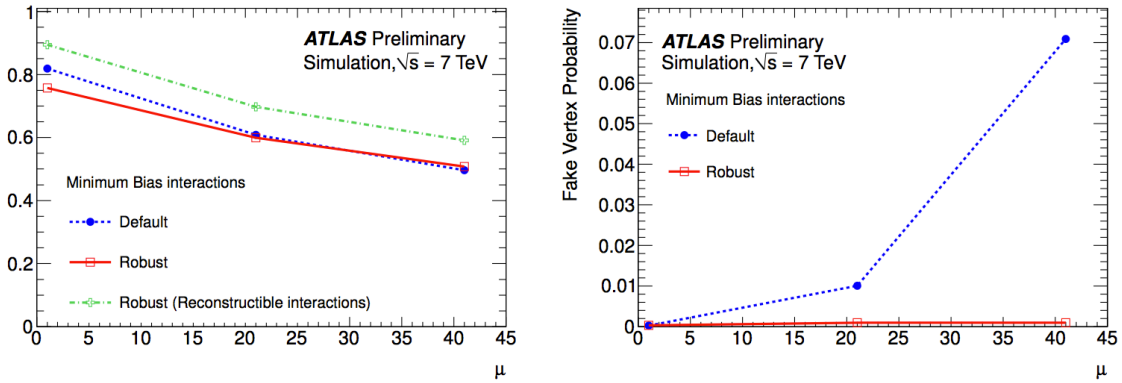

Figure 3.2: The vertex reconstruction efficiency (left) and fake probability (right) as a function of μ in minimum bias MC sample. These are shown both using default track selection (blue, dashed) and with robust track requirements (red, solid). The reconstruction efficiency with the robust track requirements is shown for reconstructible interactions (green, dot-dased), defined as having at least two stable charged primary particles with $|\eta| < 2.5$ and $p_{\mathrm{T}} > 400$ MeV [122].

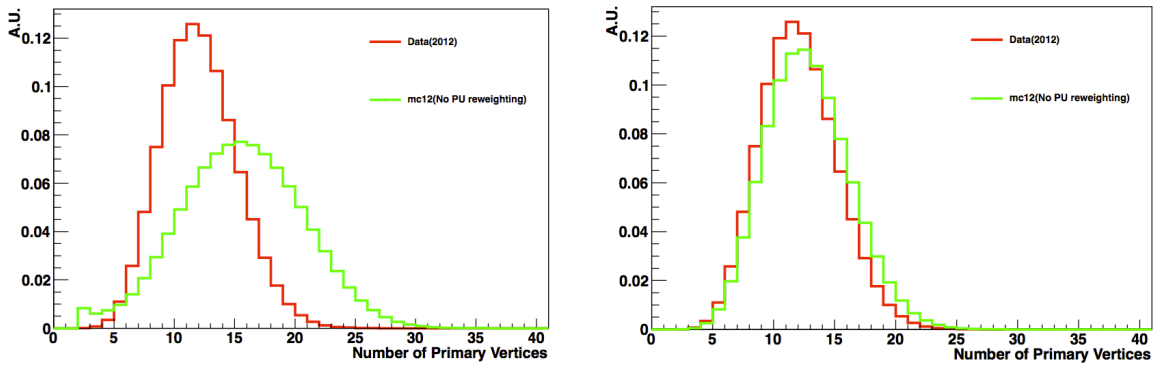

Figure 3.3: NPV distribution before (left) and after (right) the $< \mu >$-rescaling. Since the number of interactions per crossing ($< \mu >$) is highly correlated with NPV, the NPV distribution can be improved by the μ-rescaling. The remaining difference in $< \mu >$ is further corrected for by another reweighting referred to as 'pileup reweighting'.

3.3 Jets

3.3.1 Reconstruction

Jets used in the analysis are reconstructed from the topological clusters (topo-clusters) using the anti-k_t algorithm [127] that is designed to form jets by an iterative sorting algorithm. Jets defined by the algorithm are not influenced by soft QCD radiations. The jet finding procedure starts from a creation of the topo-clusters that are built from the calorimeter cells with a large energy deposit above a certain threshold. The cells neighboring the seeded topo-cluster are added iteratively to the cluster. The anti-k_t algorithm is then applied to the topo-cluster to form an "anti-k_t jet". This can be expressed as Equation 3.6 by introducing a distance parameter d_{ij} between the objects.

$$d_{ij} = \min(p_{\mathrm{T},i}^{-2}, p_{\mathrm{T},j}^{-2}) \frac{\Delta R_{ij}^2}{R^2}, \tag{3.6}$$

where $p_{\mathrm{T},i}$ is a transverse momentum of object i, and R is a distance parameter that is set to be 0.4 in the analysis. The algorithm iteratively calculates the d_{ij} values looking for the smallest d_{ij}. Once the smallest is found, both objects i and j are combined. The calculation is repeated until finding the final smallest d_{ij} that corresponds to $p_{\mathrm{T},i}$. This means that the object i is stable and is defined as a jet.

3.3.2 Calibration

The topo-clusters are reconstructed at the EM energy scale. Hence the clusters need to be calibrated/scaled to 'jet energy scale (JES)', using the local cluster weighting (LCW) method. The LCW can classify the topo-clusters as either electromagnetic or hadronic based on the measured energy density and the longitudinal shower depth since hadrons are supposed to have a lower energy density and a longer shower depth in the EM calorimeter compared to electrons. The jet energy corrections are derived according to this classification from the truth jets that are generated from single charged/neutral pion in simulation, and that are reconstructed using the same anti-k_t algorithm. The correction is further weighted by pileup correction, etc accordingly, to get the final jet energy correction [15].

To derive the systematic uncertainties on the JES the jet p_{T} in data is compared to the one in simulation by exploiting the p_{T} balance between the jet p_{T} and the p_{T} of a reference object as follows:

$$\Delta(\mathrm{JES}) \;=\; < p_{\mathrm{T}}^{jet}/p_{\mathrm{T}}^{ref} >_{data} / < p_{\mathrm{T}}^{jet}/p_{\mathrm{T}}^{ref} >_{MC}, \tag{3.7}$$

Firstly, di-jets events are exploited to test the p_{T} balance between a central jet ($|\eta|$ <0.8) and a forward jet (0.8< $|\eta|$ <4.5) (referred to as 'di-jet η-intercalibration'). After the intercalibration, γ+jet and Z+jet events are exploited as references to test the direct p_{T} balance (DB), and to evaluate the uncertainties in the region $|\eta|$ >1.2. Finally events where a system of low p_{T} jets recoils against a high p_{T} jet are used to calibrate jets up to the TeV scale. The low p_{T} jets are required to be within $|\eta|$ <2.8 while the leading jet is within

$|\eta|$ <1.2. In addition to the main JES uncertainties discussed above, other uncertainties are also evaluated:

- pileup (in-time and out-of-time) uncertainty,
- close-by-jet uncertainty that accounts for the presence of non-isolated jets,
- jet flavor composition uncertainty to accounts for the difference in response between gluon and quark jets,
- heavy flavor response that accounts for the difference in energy scale for b-jet,
- different pileup simulation sample (`PYTHIA6.4` vs `PYTHIA8`) [128, 129]) in the jet calibration,

Figure 3.4 shows the total JES uncertainty for 2012 as a function of η ($p_{\mathrm{T}} = 40$ GeV) and as a function of p_{T} ($|\eta| = 0$). The uncertainty at the lowest p_{T} is ∼4% and at the highest η is ∼7%. The impact on the final result is discussed in Chapter 8.

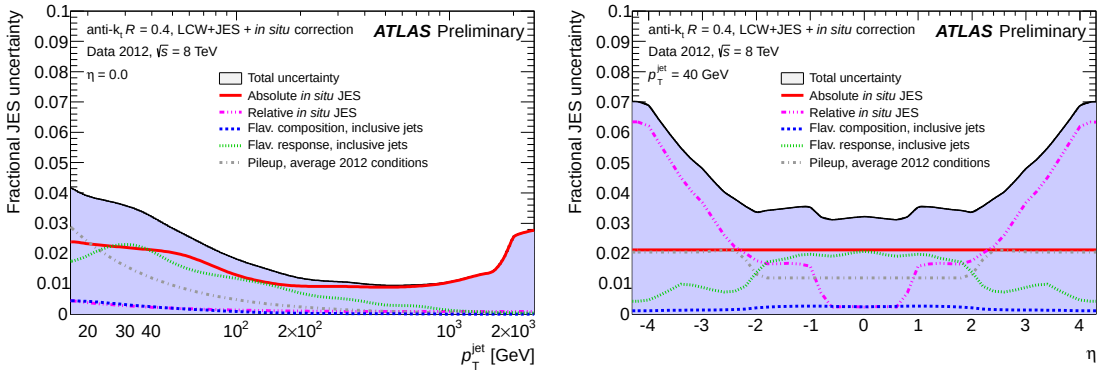

Figure 3.4: Fractioal jet energy scale systematic uncertainty components as a function of p_{T} for anti-k_t jets at $|\eta|$=0.0 (left) and as a function of η for anti-k_t jets at $p_{\mathrm{T}} = 40$ GeV with R=0.4 calibrated using the LCW+JES calibration sheme. The total uncertainty (all components summed in quadrature) is shown as a filled blue region. Average 2012 pileup conditions were used, and topology dependent components were taken from inclusive di-jets sample [130].

3.3.3 Jet vertex fraction

Even after pileup correction (namely pileup subtraction [131, 132]) in the jet calibration, a large amount of pileup jets remain non-negligible, which results in the increased number of reconstructed jets. In order to further reject the pileup jets, tracking information is used to calculate a discriminant variable referred to as jet vertex fraction (JVF).

The JVF is defined for each jet as the ratio of the scalar p_{T} sum of the tracks (p_{T}> 500

MeV) associated with the jet from the primary vertex (PV) with the largest $\sum p_{\mathrm{T}}^2$, to the scalar p_{T} sum of all associated tracks from all primary vertices:

$$\mathrm{JVF} = \frac{\sum_k p_{\mathrm{T}}^{\mathrm{track}_k}(\mathrm{PV}_0)}{\sum_l p_{\mathrm{T}}^{\mathrm{track}_l}(\mathrm{PV}_0) + \sum_{n\geq 1}(\sum_l p_{\mathrm{T}}^{\mathrm{track}_l}(\mathrm{PV}_n))}, \tag{3.8}$$

where PV_0 is the primary vertex (PV) with the largest $\sum p_{\mathrm{T}}^2$ of constituent tracks, and $\mathrm{PV}_n (n \geq 1)$ corresponds to primary vertices from other smaller pp interactions in the event. In other words the JVF is the fraction of p_{T} from tracks associated with the PV from the hardest pp collision in event. Figure 3.5 shows JVF distribution. The JVF = 0 indicates that all associated tracks originate from pileup vertices, while the JVF = 1 indicates that all associated tracks originate from the hard-scatter vertex. The JVF = -1 is assigned to jets which do not have associated tracks. A cut on the JVF ($|\mathrm{JVF}| > 0.5$ is used in the analysis for jets with $25 < p_{\mathrm{T}} < 50$ GeV and $|\eta| < 2.4$) can help to reduce the pileup jets, but enhance jets from hard scattering, which depends on the number of reconstructed primary vertices in the event.

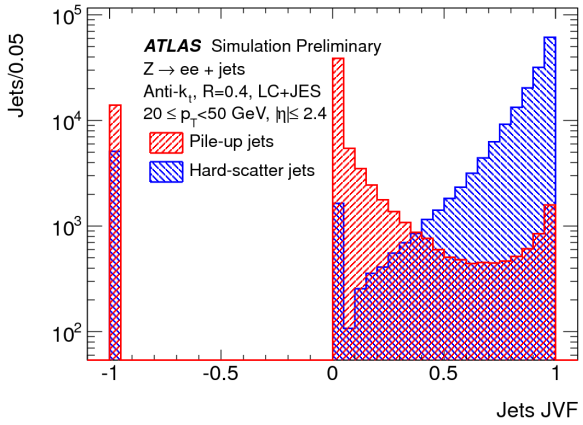

Figure 3.5: JVF distribution for hard scatter (blue) and pileup (red) jets with $20 \leq p_{\mathrm{T}} < 50$ GeV in simulated $Z \to ee$ events. The JVF = 0 indicates that all associated tracks originate from pileup vertices, while the JVF = 1 indicates that all associated tracks originate from the hard-scatter vertex. The JVF = -1 is assigned to jets which do not have associated tracks [131].

3.3.4 Heavy flavor tagging

In the analysis it is essential to identify b-jets efficiently, namely high b-tagging efficiency for real b-jets while retaining the misidentification efficiency for c and light flavors at low rate. The sufficient performance of the b-tagging allows to reduce top backgrounds and to define dedicated top control region. The b-tagging is performed based on the multivariate (MVA) tagging algorithm referred to as MV1 algorithm [133, 134]. The MV1 uses all available information that is sensitive to the b-jet identification such as vertexing parameters (transverse impact parameter significance d_0/σ_{d_0} and longitudinal impact parameter z_0) [135], secondary vertices [136] that generate displaced tracks, and topology of weak $b-$ and $c-$hadron decays, as input. The b-tagging efficiency is derived from $t\bar{t}$ events in the dilepton decay channel classifying the final states into four channels, two lepton flavor channels ($e\mu$ and $ee + \mu\mu$ channels) and two jet bins (two jets and three jets channels). The MV1 can exploit the per-event flavor correlations between the possible combinations of two or three jets (for two jets case: b-jet vs b-jet, b-jet vs non b-jet, non b-jet vs non b-jet), taking into account the p_{T} dependence. Finally four channels are combined and all single systematic variations are treated as fully correlated in the combination, except for the theory uncertainty for which 50% correlation is assumed due to the different effect in each channel. For the $H\to WW^*\to \ell\nu\ell\nu$ analysis, 85% efficiency operating point is chosen to maximize the rejection of top backgrounds.

The uncertainties on the b-jet identification that potentially change the flavor composition, are decomposed into 6 uncorrelated components using eigenvector method [15] instead of varying each source of uncertainties. The eigenvector method can reduce the number of variations (108 variations) to the handleable numbers (10 variations). For each source of uncertainties one covariance matrix is constructed with dimension corresponding to the number of bins (10 bins) and the total covariance matrix is obtained as a sum of these individual component matrices. The eigenvectors which solve the total covariance matrix can be seen as "directions" in which independent variations are carried out. This leads to the 6 uncorrelated parameters related to the b-jet tagging in the final fit. The total uncertainty is between 2-9%.

3.3.5 Jet Selection

The jet selection used in the analysis is summarized below:

- $|\eta| < 4.5$,
- $p_{\mathrm{T}} > 25$ GeV for $|\eta| < 2.4$ and $p_{\mathrm{T}} > 30$ GeV for $|\eta| \geq 2.4$,
- $|JVF| > 0.5$ for jet with $p_{\mathrm{T}} < 50$ GeV and $|\eta| < 2.4$,
- b-jet: MV1 algorithm (85% operating point) for the same jets but with $p_{\mathrm{T}} > 20$ GeV.

3.4 Missing Transverse Energy and Momentum

Due to the presence of two neutrinos in the final state and the inability of the ATLAS detector to detect them, the missing transverse energy is an important observable for the analysis. Two types of variables $E_{\mathrm{T}}^{\mathrm{miss}}$ and $\boldsymbol{p}_{\mathbf{T}}^{\mathbf{miss}}$ have been developed and used for different purposes in the analysis.

3.4.1 $E_{\mathrm{T}}^{\mathrm{miss}}$ reconstruction

The $E_{\mathrm{T}}^{\mathrm{miss}}$ reconstruction [137] uses energy deposits in the calorimeters and muons reconstructed in muon spectrometer (MS) as follows:

$$E_{x(y)}^{\mathrm{miss}} = E_{x(y)}^{\mathrm{miss},\ calo} + E_{x(y)}^{\mathrm{miss},\ \mu}, \tag{3.9}$$

where each term is calculated as the negative vector sum of the reconstructed and calibrated objects in the region $|\eta| < 4.5$. The muon term accounts for all muons that include segment tagged (ST) muons (see Section 4.2.1) to recover the contribution from low p_{T} muons. The calo term includes all physics objects reconstructed in the calorimeters, namely electrons, photons, hadronically decaying τ leptons, and jets, as well as energy deposits not associated with any such objects, referred to as 'soft term'. Splitting the calo term the Equation 3.9 can be rewritten as:

$$E_{x(y)}^{\mathrm{miss}} = (E_{x(y)}^{\mathrm{miss},\ e} + E_{x(y)}^{\mathrm{miss},\ \gamma} + E_{x(y)}^{\mathrm{miss},\ \tau} + E_{x(y)}^{\mathrm{miss},\ jets} + E_{x(y)}^{\mathrm{miss,\ softTerm}}) + E_{x(y)}^{\mathrm{miss},\ \mu}, \tag{3.10}$$

$$E_{\mathrm{T}}^{\mathrm{miss}} = \sqrt{(E_{x}^{\mathrm{miss}})^2 + (E_{y}^{\mathrm{miss}})^2}, \tag{3.11}$$

where each term in the calo term is calculated in that order, which allows to avoid any double counting of those objects. The soft term is calculated from the topological clusters (see Section 3.3.1) and tracks not associated to other parent objects, subtracting any overlap between the topological clusters and tracks, and the energy losses for muons in the calorimeters. The uncertainties on each term such as energy scale and resolution are calculated and propagated to the $E_{\mathrm{T}}^{\mathrm{miss}}$ calculation [137].

The performance of the $E_{\mathrm{T}}^{\mathrm{miss}}$ is strongly dependent on the pileup conditions. The degradation of the performance due to the pileups can be serious issue in most of analyses. In 2012 the $H \to WW^* \to \ell\nu\ell\nu$ analysis also suffers from the higher pileups, which results in a factor of 3-5 increase of the Z/DY backgrounds. It is clear that the increased Z/DY backgrounds make the analysis insensitive in ee and $\mu\mu$ channels without solving the issue, or at least improving the situation. Indeed the situation has been much improved by introducing a cut on new variable referred to as f_{recoil} (see Section 5.4.3). The cut reduces the Z/DY backgrounds significantly and they remain very small in the signal region.

Also from the $E_{\mathrm{T}}^{\mathrm{miss}}$ side, the jet term and soft term are recalculated using primary vertex information to suppress the degradation of the performance. For the jet term, the jet vertex fraction (JVF) (see Section 3.3.3) is applied to each jet, which makes the jet

term more robust against the pileups. Similarly for the soft term, the fraction of p_{T} from tracks matched to the soft term, referred to as 'soft term vertex fraction (STVF), has been calculated to mitigate the impact of the pileups. In the analysis the STVF $E_{\mathrm{T}}^{\mathrm{miss}}$ is not used but instead the $\boldsymbol{p}_{\mathbf{T}}^{\mathbf{miss}}$ (see Section 3.4.2) is used.

3.4.2 $\boldsymbol{p}_{\mathbf{T}}^{\mathbf{miss}}$ reconstruction

Since the $E_{\mathrm{T}}^{\mathrm{miss}}$ has dependence on the pileups, the missing transverse momentum $\boldsymbol{p}_{\mathbf{T}}^{\mathbf{miss}}$ [138] has been considered for the analysis because of its little dependence on the pileups. The $\boldsymbol{p}_{\mathbf{T}}^{\mathbf{miss}}$ is calculated from the reconstructed tracks defined in Section 3.2.1 with the quality cuts shown in Table 3.3. Regardless of the quality cuts above, all electron and muon tracks defined in Table 3.4 are taken into account in the $\boldsymbol{p}_{\mathbf{T}}^{\mathbf{miss}}$ calculation.

Table 3.3: Definition of tracks used in the $\boldsymbol{p}_{\mathbf{T}}^{\mathbf{miss}}$ calculation.

Quality cuts for track selection
· track $p_{\mathrm{T}} > 500$ MeV (all tracks associated to primary vertices)
· $\lvert\eta\rvert < 2.5$ that corresponds to the coverage of inner detector (ID)
· $\lvert d_0\rvert < 1.5$ mm (d_0: transverse impact parameter w.r.t. primary vertex)
· $\lvert z_0 \sin\theta\rvert < 1.5$ mm (z_0: longitudinal impact parameter w.r.t. primary vertex)
· Number of Pixel hits ≥ 1
· Number of SCT hits ≥ 6

Table 3.4: Definition of lepton tracks used in the $\boldsymbol{p}_{\mathbf{T}}^{\mathbf{miss}}$ calculation.

Electron track selection
· $E_{\mathrm{T}}^{cluster} > 10$ GeV
· $\lvert\eta\rvert < 2.47$
· cut-based Medium++ identification (see Section 4.1.2)
· $\lvert z_0 \sin\theta\rvert < 1.5$ mm (z_0: longitudinal impact parameter w.r.t. primary vertex)
· lower p_{T} electron is removed if ΔR(electron, electron) < 0.10
· electron is removed if ΔR(electron, jet) < 0.30

Muon track selection
· $p_{\mathrm{T}} > 6$ GeV
· $\lvert\eta\rvert < 2.50$
· Staco muons (see Section 4.2.1)
· $\lvert z_0 \sin\theta\rvert < 1.5$ mm (z_0: longitudinal impact parameter w.r.t. primary vertex)

In addition, anti-id leptons used for data-driven W+jets background estimate (see Section 6.3.1 and 6.3.2) are considered since the anti-id leptons particularly anti-id electrons

cannot pass the selection for electron track by definition because of the requirement of cut-based Medium++ veto. Without including the anti-id leptons in the calculation, the W+jets background is significantly (30-40 %) underestimated in the signal region. The impact of the anti-id correction on $\boldsymbol{p}_{\mathbf{T}}^{\mathbf{miss}}$ and m_{T} distributions are shown in Figure 3.6. Furthermore tracks that correspond to bremsstrahlung photons subsequently converting into $e^{+}e^{-}$ pairs inside the inner detector (or earlier), are removed if the tracks are within the electron cone defined as ΔR (electron, track) < 0.05, excluding the electron track itself, while no bremsstrahlung cut is applied to muons because the bremsstrahlung photons cannot convert into muons.

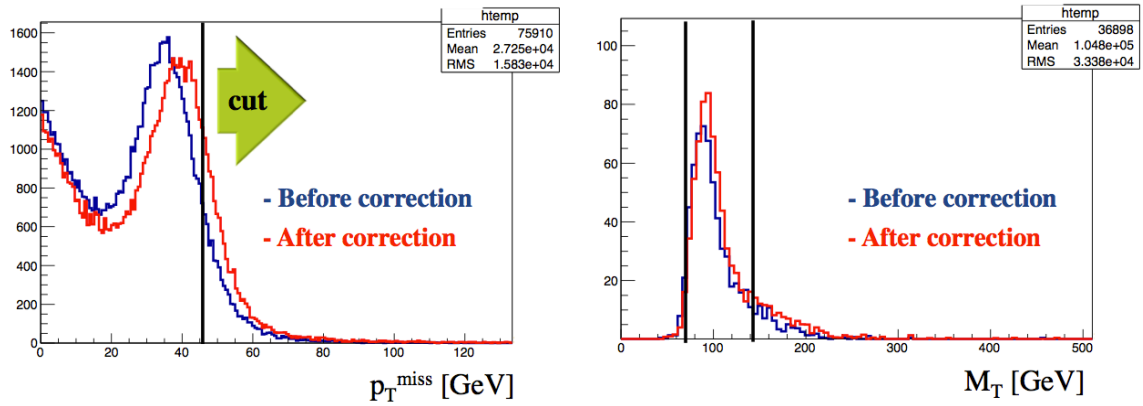

Figure 3.6: $\boldsymbol{p}_{\mathbf{T}}^{\mathbf{miss}}$ and m_{T} distributions showing the impact of anti-id correction on the $\boldsymbol{p}_{\mathbf{T}}^{\mathbf{miss}}$ calculation. Without including the anti-id correction, about 30-40% underestimate of the data-driven W+jets backgrounds is expected.

The $\boldsymbol{p}_{\mathbf{T}}^{\mathbf{miss}}$ defined above is however only used in the same flavor (ee,$\mu\mu$) analysis. In addition to the $\boldsymbol{p}_{\mathbf{T}}^{\mathbf{miss}}$ a new missing transverse momentum referred to as $\boldsymbol{p}_{\mathbf{T}}^{\mathbf{miss,\ jetCorr}}$ is also defined by replacing all tracks in jet cone (ΔR(jet, tracks)<0.4) and electron tracks with the reconstructed objects defined in Section 3.3.1 and 4.1.1 as expressed below:

$$\boldsymbol{p}_{\mathbf{T}}^{\mathbf{miss,\ jetCorr}} = -\boldsymbol{p}_{\mathbf{T}}^{\mathbf{miss}} + \sum_{j\ (\mathrm{jet})} \Big(\sum_{k} \boldsymbol{p}_{\mathrm{T}}^{j,k}(\mathrm{trk}) - \boldsymbol{p}_{\mathrm{T}}^{j}(\mathrm{cal})\Big) + \sum_{l\ (\mathrm{ele})} \big(\boldsymbol{p}_{\mathrm{T}}^{l}(\mathrm{trk}) - \boldsymbol{p}_{\mathrm{T}}^{l}(\mathrm{cal})\big) \quad (3.12)$$

where $p_{\mathrm{T}}^{j,k}(\mathrm{trk})$ and $p_{\mathrm{T}}^{j}(\mathrm{cal})$ in the second term indicate all tracks associated to jet j and jet j reconstructed in the calorimeter, and $p_{\mathrm{T}}^{l}(\mathrm{trk})$ and $p_{\mathrm{T}}^{l}(\mathrm{cal})$ in the third term indicate electron track l and electron l calibrated in the calorimeter, respectively.

Since mis-measured tracks that make a longer tail at higher $\boldsymbol{p}_{\mathbf{T}}^{\mathbf{miss,\ jetCorr}}$ still remain non-negligible, further removals are applied in the following order:

- track is removed if ΔR(track, jet) < 0.40 with jet p_{T}> 10 GeV and $p_{\mathrm{T}}^{\mathrm{trk}} > 1.4 \cdot p_{\mathrm{T}}^{\mathrm{jet}}$,
- track is removed if the track with $p_{\mathrm{T}}^{\mathrm{trk}} > 100$ GeV does not match to any reconstructed objects.

For events that do not have jets, the jet replacement is not made by definition, namely the $\boldsymbol{p}_{\mathbf{T}}^{\mathbf{miss,\ jetCorr}}$ is identical to the $\boldsymbol{p}_{\mathbf{T}}^{\mathbf{miss}}$ definition. In addition to the robustness against the pileups, the $\boldsymbol{p}_{\mathbf{T}}^{\mathbf{miss,\ jetCorr}}$ also shows its better performance in resolution as shown in Figure 3.7, so that the $\boldsymbol{p}_{\mathbf{T}}^{\mathbf{miss,\ jetCorr}}$ is also used to reconstruct a final discriminant dilepton m_{T} for the signal extraction.

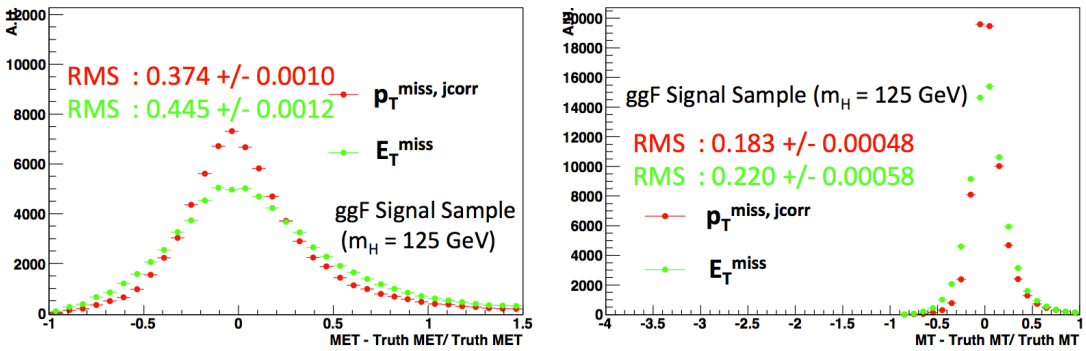

Figure 3.7: Comparison of missing transverse energy resolution between $E_{\mathrm{T}}^{\mathrm{miss}}$ and $\boldsymbol{p}_{\mathbf{T}}^{\mathbf{miss,\ jetCorr}}$ in ($E_{\mathrm{T}}^{\mathrm{miss}}$- truth $E_{\mathrm{T}}^{\mathrm{miss}}$ / truth $E_{\mathrm{T}}^{\mathrm{miss}}$) (left) and in dilepton (m_{T} - truth m_{T} / m_{T}) (right) distributions.

Chapter 4

Determination of Lepton Selection

Leptons are important ingredients in the $H \to WW^* \to \ell\nu\ell\nu$ analysis. In order to maximize the analysis sensitivity, lepton selection must be optimized. The efficiencies for those optimized leptons are then measured using tag-and-probe method, in order to correct for the mis-modeling in simulation. In this chapter the reconstruction of leptons are firstly presented. The lepton optimization is then discussed. Finally lepton selection criteria and corresponding lepton efficiencies are summarized.

4.1 Electrons

4.1.1 Reconstruction

Central electrons ($|\eta| < 2.5$) are reconstructed based on the energy deposited in the EM calorimeter, being associated to the reconstructed tracks in the inner detectors (ID) [139]. [1]

The electron reconstruction starts with a creation of seed clusters having a transverse energy $E_{\mathrm{T}} > 2.5$ GeV. The seed clusters are searched for by a *sliding − window* algorithm [119] in the middle layer of the EM calorimeter that has the largest radiation length ($X_0 > 16$), using a window size of 3×5 in units of 0.025×0.025 in $\eta \times \phi$ space.

The reconstructed tracks with $E_{\mathrm{T}} > 1$ GeV that is larger than the default track p_{T} (namely 400 MeV) for taking into account the energy losses at material surface, are then loosely matched to the seed clusters satisfying $\Delta\eta(\mathrm{cl, track}) < 0.05$. In case that several tracks are matched to the same cluster, the one with the smallest $\Delta R = \sqrt{\Delta\eta^2 + \Delta\phi^2}$ distance to the cluster is chosen. After the loose matching, the electron tracks, in most of the cases the TRT-standalone tracks defined in Section 3.2.1, are refit by an optimized electron track fitter, referred to as the Gaussian Sum Filter (GSF) algorithm [140] that is a non-linear generalization of the Kalman filter [125]. With the GSF, the electron track parameters will

[1] On the other hand the associated track is not required for forward electrons ($2.5 < |\eta| < 4.9$) because of the ID coverage ($|\eta| < 2.5$), and those electrons are not used in the analysis.

be more accurately determined by accounting for the non-linear bremsstrahlung effects. [2]

The electron cluster is then rebuilt using a larger number of clusters, 3×7 (5×5) longitudinal towers in the barrel (endcaps), in order to determine the cluster energy summing four different contributions: energy deposit in the material in front of the EM calorimeter, energy deposit in the cluster, external energy deposit outside the cluster (lateral leakage), and energy deposit beyond the EM calorimeter (longitudinal leakage). The four-momentum is finally computed using information from both the final cluster and the best track matched to the original seed cluster. The electron energy is given by the cluster energy. The ϕ and η directions are taken from the corresponding track parameters at the vertex, except for the TRT-standalone tracks for which the cluster-based directions are used.

4.1.2 Identification

Even after the reconstruction, the purity of real electrons is still very low and it suffers from a huge amount of non-real electrons that originate from hadrons, photon conversions, and semi-leptonic decays of heavy flavors. A sufficient rejection of those backgrounds, while retaining high efficiency for real electrons, is therefore crucial. [3] The electron identification plays an important role against those backgrounds. Figure 4.1 shows two examples of the shower shape variables used in the identification.

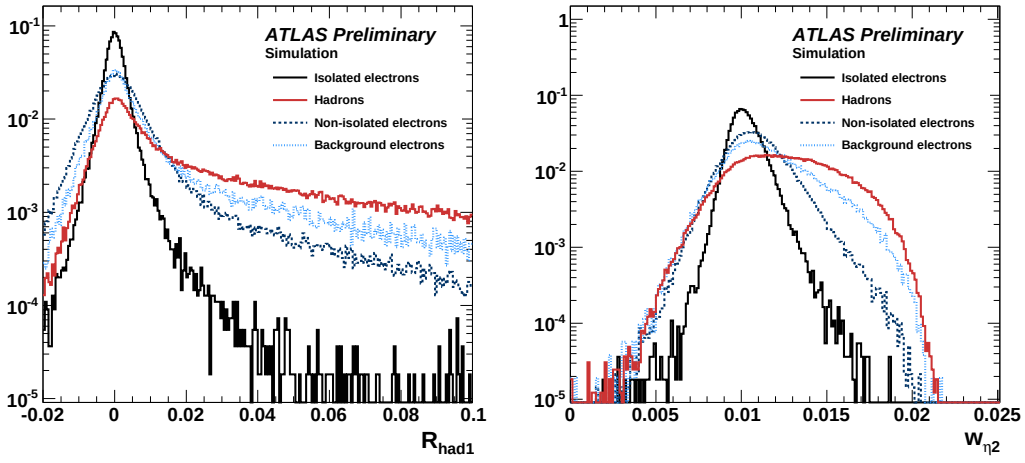

Figure 4.1: Comparison of shower shape variables between isolated electrons and "background" electrons in simulation. The left (right) figure shows R_{had1} ($W_{\eta 2}$) distribution over inclusive E_{T}. The contribution from real electrons is labeled as "Isolated" electrons. Conversions and electrons from semi-leptonic decays of heavy flavors are referred to as "Background" and "Non-Isolated" electrons, respectively [141].

[2] Note that the GSF electrons are only available in the 2012 analysis.

[3] In the $H \to WW^* \to \ell\nu\ell\nu$ analysis the misidentified electrons result in either W+jets/QCD or $W + \gamma$ background that potentially limits the experimental sensitivity.

The hadronic leakage variable R_{had1} is used that is defined as the ratio of the longitudinal energy leakage into the first layer of the hadronic calorimeter to the total energy deposited in the EM calorimeter, to discriminate real electrons from hadrons. The lateral shower width in the second layer of the EM calorimeters, referred to as $W_{\eta 2}$, is also useful to separate real electrons from hadrons as the hadronic shower generally tend to be wider than the EM shower. In total there are 22 discriminating variables used as input for the identification. All discriminating variables are summarized in Table 4.1.

For the identification, there are two types of identifications: cut-based and likelihood identifications. The cut-based identification [14,142], which is based on rectangular cuts on these variables, has been used for identifying electrons in 2011. The identifications *tight*, *medium*, and *loose* are subsets of each other. With increasing tightness, more variables are added. On the other hand, in order to deal with the higher pileup condition in 2012, likelihoods techniques have been also developed [143]. The likelihoods are one of the multivariate (MVA) techniques that are used extensively in physics analyses to separate signal from background, since they allow the simultaneous evaluation of several properties. The likelihoods are chosen because of its simplicity in construction. The likelihoods make use of signal and background probability density functions (PDF) of discriminating variables. Based on these PDFs that are obtained from data, an overall probability is calculated for the event or object to be signal(-like) or background(-like). The signal and background probabilities for a given electron are combined into a discriminant on which a cut is made. The choice of the cut value determines the signal efficiency/background rejection of the likelihood.

The identification operating point for electrons has been optimized (see Section 4.4) for each E_{T} bin due to the fact that the background composition highly depends on E_{T}. Both likelihood and cut-based identifications are used in the $H \to WW^* \to \ell\nu\ell\nu$ analysis. The *very tight* identification that is the tightest operating point in the likelihoods, has been designed/optimized to have roughly the same signal efficiency as the cut-based *tight* but to have better rejection against hadrons and conversions. For the lower E_{T} ($E_{\mathrm{T}} < 25$ GeV), the *very tight* is preferred to cope with a large amount of the W+jets/QCD backgrounds that arise from the electron misidentification, whereas the cut-based *medium* with some additional cuts is preferred to keep the signal efficiency as high as possible, since the W+jets/QCD backgrounds remain small in high E_{T} ($E_{\mathrm{T}} >$ 25 GeV).

4.1.3 Isolation

In order to further reject hadrons, two types of isolations: track isolation and calorimeter isolation, are used. The isolations are good discriminants for the background rejection even after the identification because they are uncorrelated with the identification variables, so a substantial improvement is expected from the isolations.

Calorimeter isolation: The calorimeter isolation is defined as the sum of the transverse energy E_{T} deposited in the calorimeter cells in a cone size of Δ R ($= \sqrt{\Delta\eta^2 + \Delta\phi^2}$)

Table 4.1: Definition of electron discriminating variables [14, 141, 142].

Type	Description	Variable name
Hadronic leakage	· Ratio of E_{T} in the first layer of the hadronic calorimeter to E_{T} of the EM cluster in the range of $\lvert\eta\rvert < 0.8$ and $\lvert\eta\rvert > 1.37$	R_{had1}
	· Ratio of E_{T} in the hadronic calorimeter to E_{T} of the EM cluster in the range of $\lvert\eta\rvert > 0.8$ and $\lvert\eta\rvert < 1.37$	R_{had}
Third layer of EM calorimeter	· Ratio of the energy in the third layer to the total energy	f_3
Middle layer of EM calorimeter	· Lateral shower width in the second layer in 3×5 cells	$W_{\eta 2}$
	· Ratio of the energy in 3×3 cells over the energy in 3×7 cells centered at the electron cluster position	R_ϕ
	· Ratio of the energy in 3×7 cells over the energy in 7×7 cells centered at the electron cluster position	R_η
Strip layer of	· Shower width in overall strips within $\Delta\eta \times \Delta\phi \sim 0.0625\times0.2$ corresponding typically to 20 strips in η	W_{stot}
	· Ratio of the energy difference between the largest and second largest energy deposits in the cluster over the sum of these energies	E_{ratio}
	· Ratio of the energy in the strip layer to the total energy	f_1
Track quality	· Number of hits in the B-Layer (the innermost layer of the Pixel)	N_{blayer}
	· Number of hits in the Pixel detector	N_{pixel}
	· Number of total hits in the Pixel and SCT detectors	N_{Si}
	· Transverse impact parameter	d_0
	· Significance of transverse impact parameter defined as the ratio of d_0 and its uncertainty	σ_{d_0}
	· Momentum lost by the track between the perigee [126] and the last measured point divided by original momentum	$\Delta p/p$
TRT	· Total number of hits in the TRT	N_{TRT}
	· Ratio of the number of high-threshold hits to the total number of hits in the TRT	F_{HT}
Track-cluster matching	· $\Delta\eta$ between the cluster position in the first (strip) layer and the extrapolated track	$\Delta\eta 1$
	· $\Delta\phi$ between the cluster position in the middle layer and the extrapolated track	$\Delta\phi 2$
	· Defined as $\Delta\phi 2$ but the track momentum is rescaled to the cluster energy before extrapolating the track to the middle layer of the calorimeter	$\Delta\phi_{Res}$
	· Ratio of the cluster energy to the track momentum	E/p
Conversion	· Veto electron candidates matched to reconstructed photon conversions	!isConv

= 0.3 around the electron, excluding the contribution of the electron itself. In 2011 the cell-based algorithm [144] (Etcone) has been used, whereas in 2012, the algorithm has been replaced with the new algorithm [145] based on topological cluster (topoEtcone). Figure 4.2 shows a comparison of the Etcone and topoEtcone isolations where signal (red) events are collected with the Z tag-and-probe, and backgrounds (green) are collected with `EF_g20_etcut` trigger that enhances QCD or γ+jet like events. The signal and background definitions will be described later on in Section 4.3.

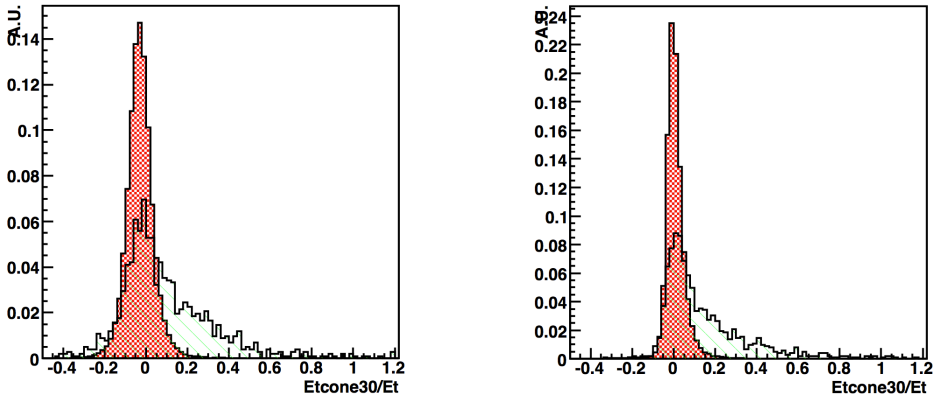

Figure 4.2: Isolation distributions for Etcone (left) and topoEtcone (right) divided by E_{T} with a cone size of $\Delta\mathrm{R} = 0.3$ for electrons that pass the cut-based *tight* with $E_{\mathrm{T}} > 15$ GeV. The signal (real) electrons collected with Z tag-and-probe and background electrons collected with `EF_g20_etcut` trigger are shown as red and green, respectively.

The isolation energy for topoEtcone is computed by summing the energy of uncalibrated topological clusters with only positive energy deposited in the cone around the electron, which acts as a noise suppression keeping only the cells with an energy deposit coherently spread over neighboring cells [145]. The isolation energy is corrected for the leakage and corrected on event by event basis for energy deposits from the underlying event [146]. Figure 4.3 shows signal efficiency versus background rejection for the Etcone and topoEtcone.

The performance of the Etcone gets worse in increased pileup ($\mu > 20$) environment, whereas the topoEtcone is more robust against the pileup and is better in the background rejection for a given signal efficiency. It is also found that the smaller cone size is better at higher signal efficiency (namely high E_{T}), while the larger is better at the lower signal efficiency (namely low E_{T}).

Track isolation: The track isolation is defined as the sum of the transverse momentum of the tracks with p_{T}>400 MeV (900 MeV in 2011) in a given cone $\Delta\mathrm{R}$ around the electron, excluding the contribution of the electron itself. The tracks must come from the primary vertex and be of good quality satisfying at least four hits in the Pixel and SCT detectors, which makes the track isolation better than the calorimeter one in the background rejection and in robustness against the pileup. Figure 4.4 shows a comparison of the track

isolation between 2011 and 2012.

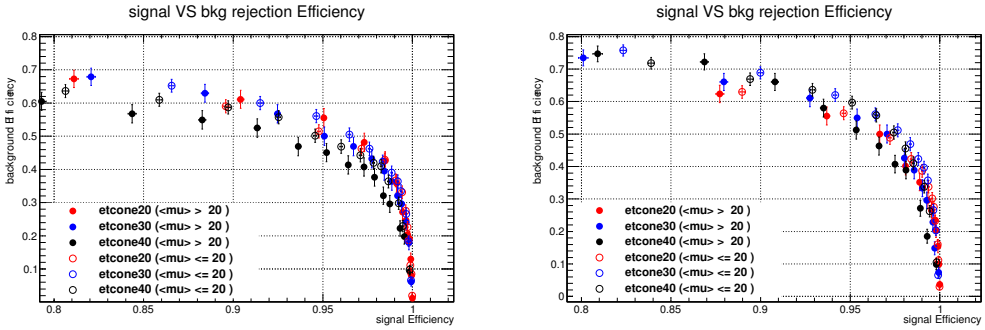

Figure 4.3: Signal efficiency versus background rejection for Etcone (left) and topoEtcone (right) for electrons that pass the cut-based *tight* with $E_{\mathrm{T}} > 20$ GeV. The cone size is explicitly labeled as etconeXX (XX = 20, 30, and 40) where XX = 20, for instance, denotes a cone size of $\Delta\mathrm{R} = 0.2$. The topoEtcone is more robust against the pileups regardless of the cone size, and is better in the rejection.

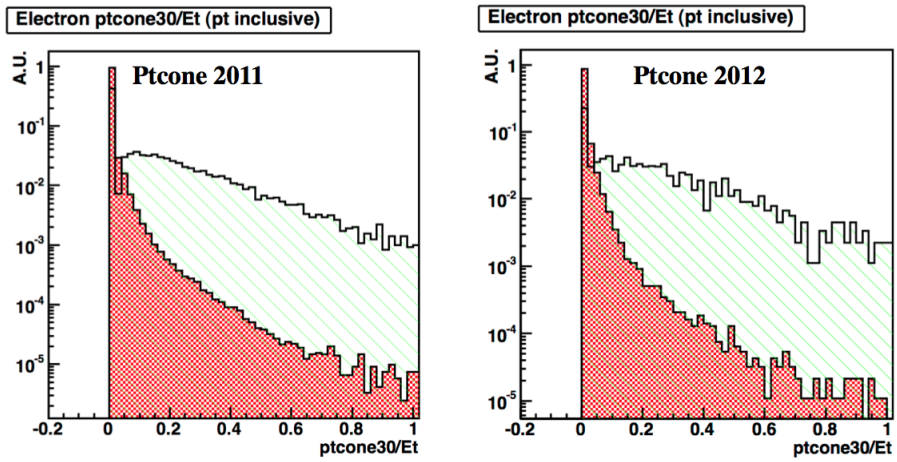

Figure 4.4: Isolation distributions for Ptcone for 2011 (left) and 2012 (right) divided by E_{T} with a cone size of $\Delta\mathrm{R} = 0.3$ for electrons that pass the cut-based *tight* with $E_{\mathrm{T}} > 15$ GeV. The signal (real) electrons collected with Z tag-and-probe and background electrons collected with EF_g20_etcut trigger are shown as red and green, respectively.

Also the performance of the track isolation in 2012 is improved compared to that in 2011 in the background rejection as shown in Figure 4.5. This is due to the lower p_{T} threshold for each track from 900 MeV to 400 MeV in the isolation energy calculation. Since the track isolation is the best discriminant against the W+jets/QCD backgrounds, the lepton optimization (see Section 4.4) rather relies on it. The signal efficiency for the isolations at actual operating points in the analysis are presented in Section 4.7.

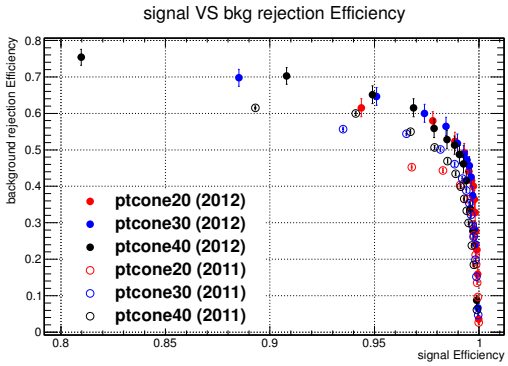

Figure 4.5: Signal efficiency versus background rejection for Ptcone for electrons that pass the cut-based *tight* with $E_{\mathrm{T}} > 20$ GeV. The cone size is explicitly labeled as ptconeXX (XX = 20, 30, and 40) where XX = 20, for instance, denotes a cone of $\Delta\mathrm{R} = 0.2$. The topoEtcone is more robust against the pileup regardless of cone size, and is better in the background rejection.

4.1.4 Energy scale and resolution

Electron energy scale and resolution [119] are determined from the $Z \to ee$ or $J/\psi \to ee$ resonances. The mis-calibration is defined as the difference in energy response between data and simulation, and is parametrized as follows:

$$E_i^{data} = E_i^{mc}(1 + \alpha_i), \tag{4.1}$$

where E_i^{data} and E_i^{MC} are the electron energy in data and simulation for a given η region i, and α_i represents the deviation from the optimal calibration. For Z and J/ψ decays, the effect of electron mis-calibration on the invariant mass is expressed as:

$$m_{ij}^{data} = m_{ij}^{MC}(1 + \alpha_{ij}) \sim m_{ij}^{MC}(1 + \frac{\alpha_i + \alpha_j}{2}), \tag{4.2}$$

where m_{ij} is the invariant mass for a pair of reconstructed electrons, and α_{ij} is the induced shift on the mass peak in given η bins i and j. The second order terms are neglected by assuming that the angle between the two electrons is known.

The energy resolution is parametrized under the assumption that the resolution curve is well modeled in simulation as follows:

$$\frac{\sigma_E}{E} = \frac{a}{\sqrt{E}} \oplus \frac{b}{E} \oplus c, \tag{4.3}$$

where a, b, and c denote the sampling term, the noise term, and a constant term, respectively. The constant term is determined by fitting the invariant mass using a Breit-Wigner convoluted with a Crystal Ball function. The intrinsic width of the Z or J/ψ is fixed and the experimental resolution is described by the Crystal Ball.

The total uncertainty on the energy scale is <0.05 %, and the total uncertainty on the energy resolution is at most <0.5 %, so the scale and resolution uncertainties are not our concern due to the fact that the uncertainty on the identification and isolation is much larger ($\sim$ a few percent level).

4.2 Muons

4.2.1 Reconstruction

The muon reconstruction [147–150] is performed using both Muon Spectrometer (MS) and Inner Detector (ID). The configuration of the MS and ID is described in Section 2.2.4 and Section 2.2.2, respectively. The triggering and coordinate measurement are provided by the RPC in the barrel ($|\eta| < 1.05$) and by the TGC in the endcap ($1.0 < |\eta| < 2.4$). The precision momentum measurement with a typical resolution of < 3 % over a wide p_{T} range and up to 10 % at $p_{\mathrm{T}} = 1$ TeV in the transverse plane is performed by the MDT in $|\eta| < 2.0$ and by the CSC up to $|\eta| < 2.7$. An independent measurement of the muon momentum is also performed up to $|\eta| < 2.5$ by the ID that provides coordinate measurements with high resolution for the track reconstruction inside the solenoid magnet. The reconstruction is performed according to the available information provided by the ID and MS (and calorimeter). The following three are the most relevant algorithms:

stand-alone (SA) muons: the muon trajectory is reconstructed using only MS information. The direction of flight and the vetexing parameter (impact parameter) of the muon with respect to the interaction point (IP) are determined by extrapolating the MS track back to the beam axis, taking into account the energy loss in the calorimeters.
combined (CB) muons: the muon trajectory is reconstructed independently in the MS and ID. The statistical combination of the track parameters of the SA and ID muon tracks is performed using the covariance matrices. The combined measurement improves the momentum resolution and reduces the fake tracks including secondaries from heavy flavor decays. This type of muons has the highest purity than other types of muons.
segment-tagged (ST) muons: the muon track is identified by the ID if the track extrapolated to the MS is associated with at least one track segment in the MDT or CSC. The ST muons can recover the reconstruction efficiency of in particular the low p_{T} muons since the ST muons cannot be identified as CB muons.

The three types of muons are reconstructed based on Staco [151] algorithm and they are relevant to the analysis. (There is another algorithm referred to as MuID [152] that provides muons refit by full hit information from the MS and ID.) In addition, there is another type of muons referred to as 'calorimeter-tagged (CaloTag) muons'. The CaloTag muons do not use the MS but instead use the calorimeter assuming that the muon candidate is a minimum ionizing particle (MIP). The CaloTag has the lowest purity than any others but recovers the reconstruction efficiency in the region which is not covered by the MS. Given that large fake background in the analysis, the CaloTag is not considered for now.

4.2.2 Isolation

Similar to the electron isolations described in Section 4.1.3, a substantial improvement is expected from the isolations in the analysis.

Calorimeter isolation: The calorimeter isolation is also used to reject background dominated by the muons from heavy flavor decays. For the calorimeter isolation, a pileup correction has been developed [15]. The correction is derived from the Z tag-and-probe method (see Section 4.3.1). The isolation median distribution for 'probe' muons is fit using a quadratic function of the number of primary vertices (NPV) in event. The functional form can be seen in Equation 4.4.

$$E_{T,\text{corrected}}^{\text{coneXX}} = E_{\text{T}}^{\text{coneXX}} - a[\eta]\, N_{PV}^2 - b[\eta]\, N_{PV} - c[\eta] \tag{4.4}$$

where a, b, and c are discrete functions of η which are obtained from the fitting the median distribution as a function of NPV in bins of η. The 'median' is chosen rather than 'mean' to account for the non-gaussian tails on the isolation. To account for a decrease of the vertex reconstruction efficiency at the higher NPV, there is a small quadratic term included in the equation. The Etcone versus NPV can be seen in Figure 4.6. The difference in slope between 2011 and 2012 is mainly due to the application of the noise suppression in 2012, as well as the change of the muon definition through the years 2011 and 2012.

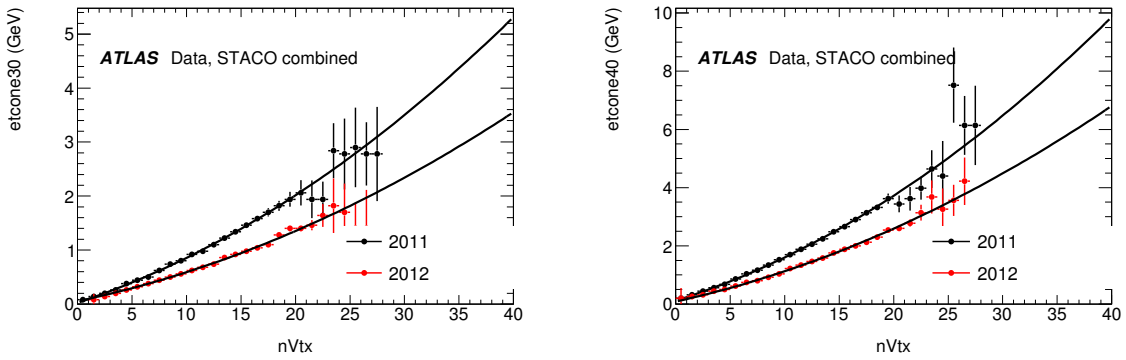

Figure 4.6: Quadratic calorimeter isolation corrections for 2011 and 2012. The difference in slope between 2011 and 2012 is mainly due to the application of the noise suppression in 2012, as well as the change of the muon definition through the years 2011 and 2012. The left and right figures show Etcone30 (ΔR = 0.3) and Etcone40 (ΔR = 0.4), respectively.

Track isolation: For muons the track isolation defined in Section 4.1.3 is also used. The isolation efficiencies are presented later in Section 4.7.

4.2.3 Momentum scale and resolution

Muon momentum resolution and scale are determined from $Z \to \mu\mu$, $J/\psi \to \mu\mu$, and $\Upsilon \to \mu\mu$ resonances. A fractional momentum resolution is parametrized by the quadratic

sum of two terms:

$$\frac{\sigma_{p_{\mathrm{T}}}}{p_{\mathrm{T}}} = a \oplus b \cdot p_{\mathrm{T}}, \tag{4.5}$$

where a is a constant term to account for the effect of multiple scattering, and b indicates the intrinsic resolution from the spatial resolution of the detectors and any residual misalignment. When the momentum scale "s" is taken into account, the equation is rewritten as follows:

$$p_{\mathrm{T}}^{Cor} = p_{\mathrm{T}}^{MC} \cdot s(\eta)(1 + \Delta a(\eta) G(0,1) + \Delta b(\eta) G(0,1) p_{\mathrm{T}}^{MC}), \tag{4.6}$$

where $G(0,1)$ denotes a random seed with mean 0 and width 1, and the correction factors $s(\eta)$, $\Delta a(\eta)$, and $\Delta b(\eta)$ are derived for a given η region. The correction of the muon momentum is computed as the average of the ID and MS momentum correction weighted by the inverse square of their resolution. The correction is determined by fitting the invariant mass distribution using the template derived from the $Z \to \mu\mu$ in simulation. It is found that the total uncertainty on the momentum scale correction is <0.2 %.

4.3 Tag-and-Probe

The efficiency is not measured as a single quantity but is factorized into individual efficiencies such as those related to triggers, reconstructions, identifications, and isolations:

$$\epsilon_{\mathrm{total}} = \epsilon_{\mathrm{rec.}} \times \epsilon_{\mathrm{id.}} \times \epsilon_{\mathrm{add.}} \times \epsilon_{\mathrm{trig.}}, \tag{4.7}$$

where $\epsilon_{\mathrm{total}}$ is the total efficiency of lepton, $\epsilon_{\mathrm{rec.}}$ is the reconstruction efficiency given the presence of the clusters (see Section 4.1.1), $\epsilon_{\mathrm{id.}}$ is the identification efficiency with respect to the reconstructed leptons, $\epsilon_{\mathrm{add.}}$ is the efficiency for additional cuts such as isolations and impact parameters with respect to the reconstructed and identified leptons, $\epsilon_{\mathrm{trig.}}$ is trigger efficiency with respect to fully identified leptons used in the analysis.

For the purpose of measuring those individual efficiencies from data, the tag-and-probe method has been extensively used to select clean and unbiased samples from well-known resonances. The most popular and widely used sample at the LHC is $Z \to \ell\ell$ resonance due to its fairly large statistics even at lower p_{T} ($p_{\mathrm{T}} > 10$ or 15 GeV) and its simplicity of triggering without any bias. The tag-and-probe method can be further extended to much lower p_{T} ($p_{\mathrm{T}} > 7$ GeV for electrons and > 6 GeV for muons) with $J/\psi \to \ell\ell$ resonance even though the available statistics are quite limited due to the triggering with low p_{T} leptons.

The tag-and-probe is also used to collect signal sample for the lepton optimization where the efficiencies are measured for leptons with $p_{\mathrm{T}} > 10$ GeV that corresponds to the lepton p_{T} threshold used in the $H \to WW^* \to \ell\nu\ell\nu$ analysis.

4.3.1 Tag and probe definition

As an example of the tag-and-probe method, one can consider the efficiency for electron identification using $Z \to ee$ decays in which there are exactly two oppositely charged elec-

trons. One of the two electrons is firstly chosen as "*tag*"electron with very strict selection criteria. The other that passes minimal selection criteria is then considered as a "*probe*"electron candidate used for the efficiency measurement. Table 4.2 summarizes selection criteria for those electrons for identification efficiency measurement. Note that the definition of the probe changes according to the individual measurements.

Table 4.2: Definition of tag and probe electrons.

Tag electron selection in 2012

· $E_{\mathrm{T}}^{cluster} > 20$ GeV
· $\|\eta\| < 2.47$ (excluding crack region $1.37 < \|\eta\| < 1.52$)
· track quality cut
· cut-based Tight++ identification (see Section 4.1.2)
· $\|d_0/\sigma_{d_0}\| < 3$ (d_0: transverse impact parameter w.r.t. primary vertex)
· $\|z_0 \sin\theta\| < 0.4$ mm (z_0: longitudinal impact parameter w.r.t. primary vertex)
· Ptcone40/$p_{\mathrm{T}} < 0.06$ (track isolation with $\Delta\mathrm{R} = 0.4$)
· topoEtconeEt30/$E_{\mathrm{T}} < 0.16$ (calorimeter isolation with $\Delta\mathrm{R} = 0.3$)
· lower E_{T} electron is removed if ΔR(electron, electron) < 0.10
· `EF_e24vhi_medium1` || `EF_e60_medium1`

Probe electron selection in 2012 (for identification efficiency)

· $E_{\mathrm{T}}^{cluster} > 10$ GeV
· $\|\eta\| < 2.47$ (excluding crack region $1.37 < \|\eta\| < 1.52$)
· track quality cut
· (targeting) identification for numerators OR no identification for denominators
· lower E_{T} electron is removed if ΔR(electron, electron) < 0.10
· no trigger requirement

The primary single lepton triggers (`EF_e24vhi_medium1` and `EF_e60_medium1`) are used to collect events from $Z \to ee$, and are imposed on only tag candidates. While the triggers are not required for probe candidates to avoid possible trigger bias from the requirements, such as `medium1`, `i` (Ptcone20/$p_{\mathrm{T}} < 0.10$), and $E_{\mathrm{T}} > 24$ GeV on `EF_e24vhi_medium1`, that make the triggers tighter than the probe definition, otherwise the biased probes will end up with higher efficiency in the measurement. Similarly the primary dilepton triggers such as `EF_2e12Tvh_loose1` is not used in the measurement due to `loose1` that also causes bias on the probe definition.

It is possible that the probe candidates also pass the tag selection criteria at some rate, turning the probe into another tag. This is not the case for the probes with $E_{\mathrm{T}} < 25$ GeV since the trigger plateau threshold for the primary single electron trigger `EF_e24vhi_medium1` ($E_{\mathrm{T}} = 25$ GeV) is above the E_{T} requirement for the probes. In other words, the tag and probe are defined exclusively due to the trigger requirement in event. While if the probe passes tag's selection criteria with $E_{\mathrm{T}} < 25$ GeV, all possible tag and probe combinations

are taken into account, so more than one pair of the tag and probe electrons in event are considered for the measurement.

4.3.2 Background evaluation and systematic uncertainties

In order to ensure that the probes are likely real electrons from Z bosons, an invariant mass m_{ee} for an oppositely charged pair of the probe and tag electrons is required to be within the Z mass window defined as $|m_Z - m_{ee}| < 10$ GeV. The cut on the invariant mass m_{ee} significantly increases the purity of $Z \to ee$ events. However, even after the window cut, background electrons represented by hadrons faking electrons, electrons from heavy flavor decays, and photon conversions (see Section 4.1.2), still contaminate mainly in the probe samples. In case of the $Z \to ee$ tag-and-probe, the background electrons are dominated by the W+jet background where a jet is misidentified as a probe electron. At smaller rate, there also exists the QCD background, namely double fake background, where another jet is also misidentified as a tag electron paired with the jet faking probe. Figure 4.7 shows m_{ee} distributions with probe E_{T} = 10-15 GeV and E_{T} = 25-30 GeV before identification requirements.

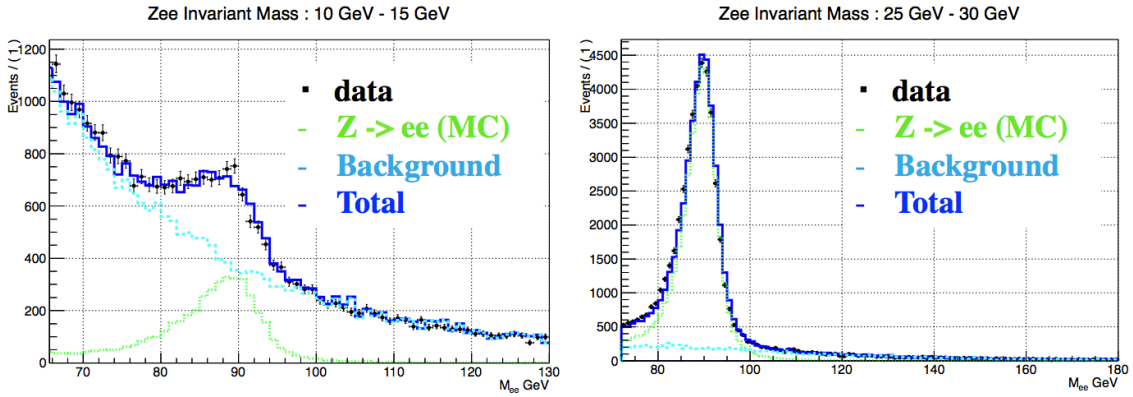

Figure 4.7: Invariant mass m_{ee} distributions for pairs of the probe and tag electrons, where no identification cut is applied to the probe electrons. The E_{T} cut is applied to the probe electrons: 10-15 GeV (left) and 25-30 GeV (right).

The backgrounds significantly increase with lower probe E_{T}. Given that the efficiency measurement is made in a region $|m_Z - m_{ee}| < 10$ GeV, the signal-background ratio S/B is less than 50 % for the probe E_{T}= 10-15 GeV, so the backgrounds must be subtracted as properly as possible using signal and background templates (or combined fits of background and signal analytical models to data). For the signal template, $Z \to ee$ events are generated in simulation. In order to avoid selecting undesired pairs of tag and probe electrons in simulation, for instance a pair of a jet faking probe and a tag from $Z \to ee$, and the other electron from $Z \to ee$ is out of acceptance, generator-level information is also used to select electrons originating only from $Z \to ee$ decays when forming the template. For

the background template, probes are chosen with two additional requirements that enhance jets/photons faking electrons and significantly reduce real electrons from Z decays:

- cut-based loose++ veto
- same charge as the tag electron

Both signal and background templates are normalized to data simultaneously in the region $60 < m_{ee} < 120$ GeV. The normalized background are then subtracted from data when counting the number of probes for the efficiency.

In order to assess systematic uncertainties on the background estimation, several variations are considered:

- isolation requirements for tag electrons are varied to Ptcone20/p_{T}< 0.10 that is identical to the isolation cut on the trigger. The variation can change the composition of the backgrounds between the W+jets and QCD backgrounds since the tighter isolation on tag electron possibly reduce the QCD background but enhance more the W+jet background in the background template. So the variation results in the shape variation for the background template.
- Z mass range is also varied to be wider $|m_Z - m_{ee}| < 20$ GeV and to be narrower $|m_Z - m_{ee}| < 5$ GeV, which potentially increases/decreases the background contamination in the signal region used for the measurement. The wider mass range is more sensitive to the background mis-modeling.
- fit range for the signal and background templates are varied to be $70 < m_{ee} < 140$ GeV, keeping χ^2/ndof value reasonable (less than 4). The variation can change the overall normalization of the background template.

All those uncertainties are added in quadrature to compute the total systematic uncertainty.

4.3.3 Efficiencies and scale factors

The efficiency is finally measured using the selected probes as the fraction of them. For the identification efficiency, only acceptance cuts ($E_{\mathrm{T}} > 10$ GeV and $|\eta| < 2.47$) are applied to the reconstructed electrons for denominators, whereas the identification cut is also added to the denominator selection criteria for numerators. Then the efficiency can be written as follows:

$$\epsilon_{\mathrm{id.}}^{\mathrm{data}} = \frac{N_{\mathrm{rec.+id.}}^{\mathrm{data}} - N_{\mathrm{rec.+id.}}^{\mathrm{bkg}}}{N_{\mathrm{rec.}}^{\mathrm{data}} - N_{\mathrm{rec.}}^{\mathrm{bkg}}}, \tag{4.8}$$

$$\epsilon_{\mathrm{id.}}^{\mathrm{MC}} = \frac{N_{\mathrm{rec.+id.}}^{\mathrm{MC}}}{N_{\mathrm{rec.}}^{\mathrm{MC}}}, \tag{4.9}$$

where $N_{\text{rec.}}$ is the number of denominators and $N_{\text{rec.+id.}}$ is the number of numerators. The background subtraction is not made to the simulated $Z \to ee$ events but the generator-level matching like the signal template is applied to select real electron pairs. Finally any difference in efficiency between data and simulation are corrected for by taking the ratio of those efficiencies as scale factor:

$$\text{SF}_{\text{id.}}^{(i,j)} = \epsilon_{\text{id.}}^{\text{data}(i,j)} / \epsilon_{\text{id.}}^{\text{MC}(i,j)} \qquad (\text{where } i: \ E_{\text{T}} \text{ bin}, \ j: \ \eta \text{ bin}). \tag{4.10}$$

The efficiencies and corresponding scale factors are evaluated as a function of E_{T} and η, and all scale factors from the individual measurements (reconstruction, identification, isolation etc) are put together for the final electron efficiency used in the analysis.

Figure 4.8 shows efficiencies for electron identification comparing with both cut-based and likelihood identifications. The efficiency for the VeryTight likelihood is very close to that for the cut-based Tight++.

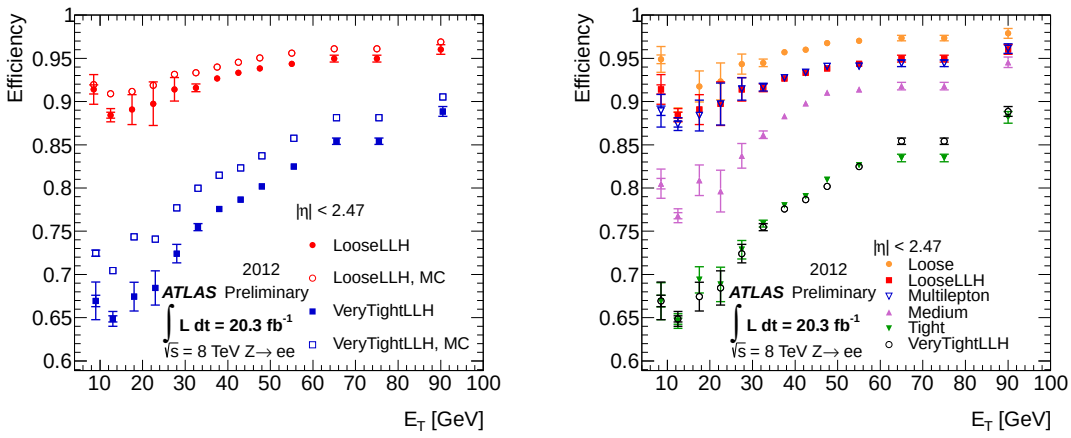

Figure 4.8: Comparison of likelihood identification efficiency between data and simulation as a function of E_{T} (left) and identification efficiency for the various cut-based and LH identifications as a function of E_{T} (right) [153].

4.4 Optimization Strategy

4.4.1 General Strategy

In order to maximize the experimental sensitivity, lepton optimization has been performed focusing on identifications, isolations, and impact parameters. Since the W+jets background is significant in the signal region and has relatively large systematic uncertainty, the optimization criteria below, are defined explicitly including the effect of the W+jets

systematics on the significance:

$$\text{signif} = \frac{\mathrm{N_{Sig}}}{\sqrt{\mathrm{N_{Sig}} + \mathrm{N_{Bkg(non-Wjet)}} + \mathrm{N_{Bkg(Wjet)}} + \Delta^2_{\mathrm{(non-Wjet)}} + \Delta^2_{\mathrm{Wjet}}}}, \tag{4.11}$$

where N_{Sig} is signal yield, $N_{\mathrm{Bkg(non-Wjet)}}$ is total background yield without W+jets, $N_{\mathrm{Bkg(Wjet)}}$ is W+jets yield, $\Delta_{i\mathrm{(non-Wjet)}}$ is the impact of the total backgrounds without W+jets ($N_{\mathrm{Bkg}}(\mathrm{non-Wjet}) \times \sigma_{\mathrm{non-Wjet}}$), and Δ_{Wjet} is the impact of the W+jets background ($N_{\mathrm{Bkg}}(\mathrm{Wjet}) \times \sigma_{\mathrm{Wjet}}$). These yields and uncertainties are obtained from the previously published results [3], adding several improvements that have been considered for this updated analysis such as dilepton triggers and lowering lepton p_{T} ($p_{\mathrm{T}}^{\mathrm{lead}} = 22$ GeV and $p_{\mathrm{T}}^{\mathrm{sub}} = 10$ GeV). Equation 4.11 can be rewritten to be more complete form as:

$$\text{signif} = \frac{\epsilon \times N_{\mathrm{Sig}}}{\sqrt{\epsilon \times (N_{\mathrm{Sig}} + N_{\mathrm{Bkg(non-Wjet)}}) + f \times N_{\mathrm{Bkg(Wjet)}} + \mathrm{Unc}(\epsilon, \mathrm{f})^2 + \mathrm{Corr}(\epsilon, \mathrm{f})}}, \tag{4.12}$$

$$\mathrm{Unc}(\epsilon, \mathrm{f})^2 = (\epsilon \times \sigma_{\mathrm{(non-Wjet)}} N_{\mathrm{Bkg(non-Wjet)}})^2 + (f \times \sigma_{\mathrm{Wjet}} N_{\mathrm{Bkg(Wjet)}})^2, \tag{4.13}$$

$$\mathrm{Corr}(\epsilon, \mathrm{f})^2 = \sum_i (N_i^j \times \sum_{j \neq k}^{m} N_i^k)^2, \tag{4.14}$$

where

(I) ϵ is a ratio of the signal (either signal or non-Wjet) efficiency at the selection point being considered to the pre-optimized efficiency,

(II) f is a ratio of the background (W+jets) efficiency at the selection point being considered to the pre-optimized background efficiency that approximates the ratio of the W+jets fake factors,

(III) σ_{Wjet} is uncertainty on the W+jets, and $\sigma_{\mathrm{(non-Wjet)}}$ is uncertainty on the non-Wjet. The non-Wjet uncertainty is defined for each background,

(IV) $\mathrm{Unc}(\epsilon, \mathrm{f})$ is total background uncertainty where the W+jets is scaled by f, and the non-Wjet is scaled by ϵ,

(V) $\mathrm{Corr}(\epsilon, \mathrm{f})$ is correlation term between signal regions [4] as a function of ϵ and f, which makes the optimization more realistic. In this term i denotes either W+jets or non-Wjet background, j is index of each signal region, and m is the number of signal region. Without this term, the systematic uncertainty will end up with zero when splitting into infinite number of signal regions.

[4] the signal region is split into two $m_{\ell\ell}$ bins ($10 < m_{\ell\ell} < 30$, $30 < m_{\ell\ell} < 55$ GeV), and four $p_{\mathrm{T}}^{\mathrm{sub}}$ bins (10-15,15-20, 20-25, 25- GeV).

The significance is computed in two-dimensional map of isolation variables "Etcone vs Ptcone" for each signal region. The two-dimensional optimization is useful as it can take into account the correlation automatically between the isolations. The computed significances for each signal region are finally combined and the optimal operating point is extracted for the analysis. The optimization is made for each sub-leading lepton p_{T} ($p_{\mathrm{T}}^{\mathrm{sub}}$) bin because the impact of the W+jets background is strongly dependent on $p_{\mathrm{T}}^{\mathrm{sub}}$. At lower $p_{\mathrm{T}}^{\mathrm{sub}}$, the W+jets background increases rapidly, while the W+jets background remains small at higher $p_{\mathrm{T}}^{\mathrm{sub}}$.

This optimization procedure is extremely powerful as it can simulate well-approximated analysis sensitivity without full machinery, while taking into account the correlation between the isolations (as well as the correlation between the signal regions). This optimization procedure is applied to both electron and muon optimizations. Given that $e\mu$ and μe channels are the most sensitive channels in the analysis, only those two channels (μe for electrons, and $e\mu$ for muons) are considered in the optimization.

There is one limitation in this method due to the fact that all background processes except for the W+jets are considered as true-lepton backgrounds. This assumption is not accurate for some background like the $W + \gamma$ background where photon is faking electron. In practice, since the conversion rate is like neither ϵ nor f, it would be better to reduce the conversion background as much as possible. This will be a crucial point when considering the identification for higher p_{T} (see Section 4.5.1).

4.4.2 Signal and background efficiencies

To define ϵ and f, it is necessary to measure signal and background efficiencies for each isolation operating points. The efficiencies are measured using signal and background samples. The definition of the samples are summarized in Table 4.3.

The signal efficiency is measured in data using Z tag-and-probe method (see Section 4.3.1) with a narrow Z mass range defined as $|m_{\ell\ell} - m_Z| < 10$ GeV in order to suppress the contamination of background leptons (No background subtraction made in the optimization).

The background efficiency is measured in data using multijet/QCD-enriched samples collected with e/gamma and MCP supporting triggers that are also used in the di-jets fake factor evaluation (see Section B.1). To further reduce the contamination of true leptons from $Z \to \ell\ell$ or $W \to \ell\nu$ decays, a event veto referred to as 'EW veto' is applied to the background samples. The EW veto is defined as:

- $|m_{\ell\ell} - m_Z| > 15$ GeV for leptons from $Z \to \ell\ell$ decays
- $m_{\mathrm{T}}(\mathrm{lep}, \mathrm{E}_{\mathrm{T}}^{\mathrm{miss}}) < 30$ GeV for leptons from $W \to \ell\nu$ decays

The background contamination is negligibly small after the EW veto. Measured signal efficiency and background rejection are shown for each $p_{\mathrm{T}}^{\mathrm{sub}}$ bin (10-15, 15-20, 20-25, 25-) in

Table 4.3: Definition of signal and background samples.

Electron selection in 2012
· $E_{\mathrm{T}}^{cluster} > 10$ GeV
· $\|\eta\| < 2.47$ (excluding crack region $1.37 < \|\eta\| < 1.52$)
· track quality cut
· being considered identification (see Section 4.1.2)
· $\|d_0/\sigma_{d_0}\| < 3$ (d_0: transverse impact parameter w.r.t. primary vertex)
· $\|z_0 \sin\theta\| < 1.0$ mm (z_0: longitudinal impact parameter w.r.t. primary vertex)
· overlap removals (see Section 6.3.3)
· Signal: `EF_e24vhi_medium1`, `EF_e60_medium1`, and `EF_2e12Tvh_loose1` triggers
· Background:`EF_g24_etcutEF_g20_etcut`, `EF_e11_etcut`, and `EF_e5_etcut` triggers
· being considered isolation selection (Etcone and Ptcone)

Muon selection in 2012
· $p_{\mathrm{T}} > 10$ GeV
· $\|\eta\| < 2.50$
· track quality cut
· $\|d_0/\sigma_{d_0}\| < 3$ (d_0: transverse impact parameter w.r.t. primary vertex)
· $\|z_0 \sin\theta\| < 1.0$ mm (z_0: longitudinal impact parameter w.r.t. primary vertex)
· overlap removals (see Section 6.3.3)
· Signal: `EF_mu24i_tight`, `EF_mu36_tight`, and `EF_mu18_tight_mu8_EFFS` triggers
· Background:`EF_mu6` and `EF_mu15` triggers
· being considered isolation selection (Etcone and Ptcone)

Figure 4.9 and 4.10. ϵ and f are finally computed by taking the ratio of the two operating points, being scanned operating point and Moriond operating point.

4.5 Electron Optimization

4.5.1 Identification

The identification optimization is made by comparing either the (Very) Tight likelihood or cut-based Medium++, to the cut-based Tight++ in a given isolation operating point. The signal efficiency ratio ϵ in Equation 4.11 can be expressed explicitly including identification and isolation terms as follows:

$$\epsilon = \frac{\mathrm{eff}_{\mathrm{sub}}^{\mathrm{op}}}{\mathrm{eff}_{\mathrm{sub}}^{\mathrm{pre}}} \sim \frac{\mathrm{eff}_{\mathrm{id}}^{\mathrm{op}}}{\mathrm{eff}_{\mathrm{id}}^{\mathrm{pre}}} \times \frac{\mathrm{eff}_{\mathrm{iso}}^{\mathrm{op}}}{\mathrm{eff}_{\mathrm{iso}}^{\mathrm{pre}}}, \tag{4.15}$$

where superscript 'op' is a selection operating point being considered and 'pre' is the selection operating point used in the previous result. Only sub-leading lepton is considered

in the low E_{T} optimization, and muon efficiencies are fixed. Similarly, f can be written as follows:

$$f = \frac{\mathrm{eff}_{\mathrm{sub}}^{\mathrm{op}}}{\mathrm{eff}_{\mathrm{sub}}^{\mathrm{pre}}} \sim \frac{\mathrm{eff}_{\mathrm{id}}^{\mathrm{op}}}{\mathrm{eff}_{\mathrm{id}}^{\mathrm{pre}}} \times \frac{\mathrm{eff}_{\mathrm{iso}}^{\mathrm{op}}}{\mathrm{eff}_{\mathrm{iso}}^{\mathrm{pre}}}. \tag{4.16}$$

Note that the correlation between the identification and isolation is not taken into account in the Equations above. Since it is difficult to make signal sample without the identification requirement as discussed in Sections 4.3.1 and 4.4.2. For the identification term, signal and background efficiency ratios is obtained from the identification efficiency measurement, by taking the ratio of "being considered" identification efficiency to the cut-based Tight++ efficiency. Measured signal and background ratio is summarized in Table 4.4. The numbers are calculated taking into account the small effects caused by the difference in input variables. [5]

Table 4.4: Signal efficiency and background efficiency ratio for electron identification.

Signal efficiency ratio w.r.t. cut-based Tight++

E_{T}[GeV]	LH Tight/ Tight++	LH Very Tight/ Tight++	Medium++/ Tight++
10-15	1.18	1.03	1.19
15-20	1.13	1.03	1.14
20-25	1.12	1.02	1.12
25-	-	-	1.11

Background efficiency ratio w.r.t. cut-based Tight++

E_{T}[GeV]	LH Tight/ Tight++	LH Very Tight/ Tight++	Medium++/ Tight++
10-15	1.09	0.83	1.59
15-20	1.16	0.89	1.59
20-25	1.16	0.87	1.55
25-	-	-	1.60

[5] $|d_0/\sigma - d_0|$ cut is not included in the cut-based. This is explicitly added in the cut-based Tight++ to perform fair comparison. Also the cut-based Medium++ is modified to include conversion flag and B-Layer hit requirements at $|\eta| > 2.37$. With this additional η requirement full η acceptance used in the analysis is covered.

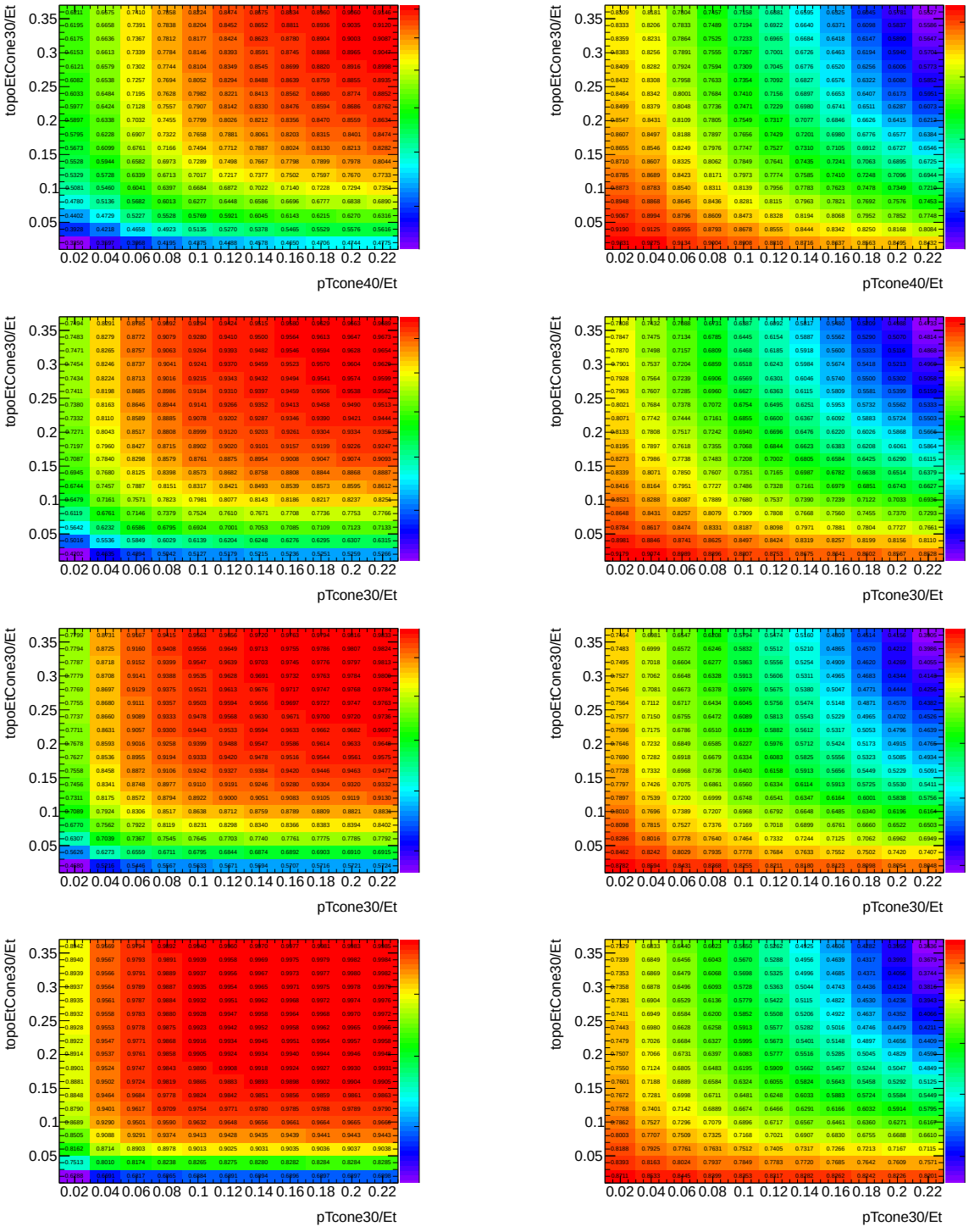

Figure 4.9: Electron signal efficiency (left) and background rejection (right) after the identification applied in μe channel. Top of them are for 10-15, 2nd for 15-20, 3rd for 20-25, and the bottom for > 25 GeV.

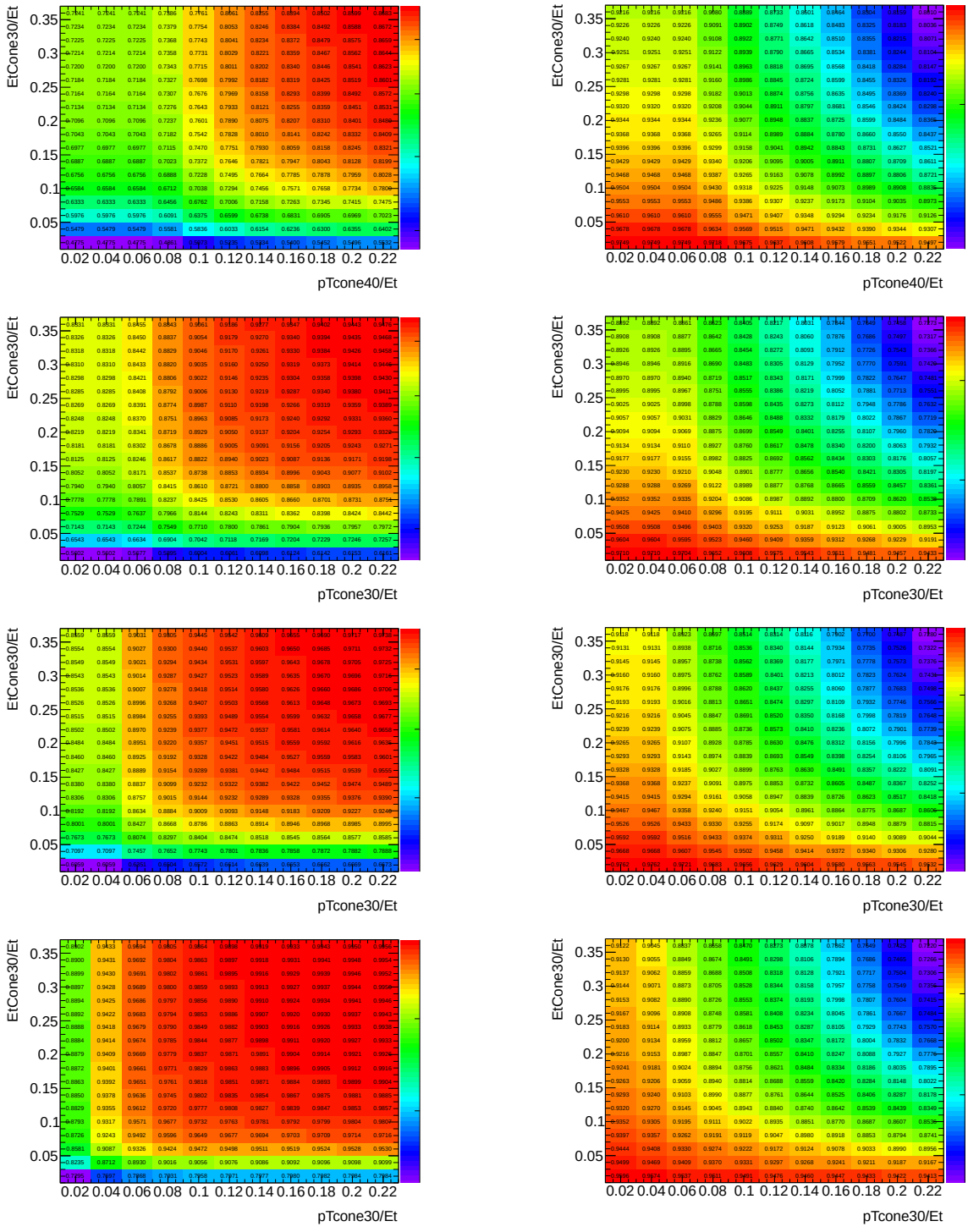

Figure 4.10: Muon signal efficiency (left) and background rejection (right) after the identification applied in μe channel. Top of them are for 10-15, 2nd for 15-20, 3rd for 20-25, and the bottom for > 25 GeV.

Trigger bias

The efficiency loss from "`medium1`" identification on `EF_e12Tvh_medium1_mu8` dilepton trigger, needs to be taken into account when comparing the likelihood and cut-based identifications because the likelihood identification is not a subset of the "`medium1`". This is particularly important in the low E_{T}, 10-25 GeV optimization since the likelihood is considered.

While there is no "`medium1`" bias from the single lepton triggers such as `EF_e24vhi_medium1` and `EF_e60_medium1` because the cut-based identifications, which are a subset of "`medium1`", are used above 25 GeV. In order to include the loss from the triggers in the optimization, the loss can be quantitatively evaluated using Z tag-and-probe method in data for the signal efficiency and using multijet/QCD samples in data for the background efficiency.

Figure 4.11 shows the signal and background efficiencies with/without the cut-based Medium++ requirement, assuming that Medium++ $\sim$ `medium1`. The change in the signal efficiency caused by the cut-based Medium++ is also summarized in Table 4.5.

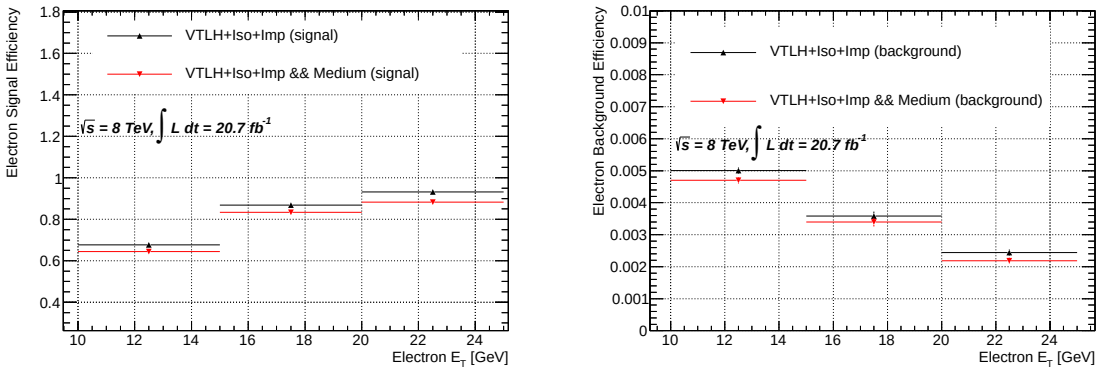

Figure 4.11: Plots show the comparison of electron efficiencies in data for Very Tight likelihood and the AND of the Very Tight likelihood and cut-based Medium++ after isolations, impact parameters, and exactly two leptons requirements. The left and right plots are signal and background efficiencies as a function of E_{T}, respectively. About 5 % loss can be seen depending on E_{T} in 10-25 GeV. For the $E_{\mathrm{T}} > 25$ GeV, the bias is not expected since the cut-based Medium++ is a subset of `medium1`.

Other bias

In addition to the loss caused by the trigger, the variables which has been further added in the likelihood (but not in the cut-based Tight++ or Medium++) have to be taken into account in the optimization. In fact, there are several new variables included in the likelihood such as Δp, $\Delta\phi_{\mathrm{Res}}$, σ_{d_0} (see Section 4.1.2). Especially evaluating the impact of d_0

Table 4.5: Table shows expected event loss caused by `medium1` on `EF_e12Tvh_medium1_mu8` for each E_{T} bin. The event loss is not expected below 15 GeV by definition because events are collected with only single muon triggers. Also the event loss is not expected above 25 GeV since the likelihood is not considered.

E_{T}[GeV]	expected event loss from "`medium1`"
10-15	0.0%(by definition)
15-20	0.92%
20-25	0.79%
25-	0.0%(by definition)

significance is important because it is one of the variables that has less correlation among other variables. In order to make a fair comparison between the Very Tight likelihood and the cut-based Tight++ in the signal and the background efficiency, the d_0 significance in the likelihood is taken into account in the optimization. The numbers in Table 4.4 are already corrected for the d_0 significance.

Identification optimization

The comparisons of the significances between the identifications are made in the 2-D map taking into account any bias discussed above. Table 4.6 and Figure 4.12 are the results for each E_{T} bin.

Table 4.6: Comparison of Electron identification in significance for each E_{T} bin. The significance is calculated in a given isolation operating point (optimal operating point) in μe channel for 10-25 GeV, and in $e\mu$+μe channels for 25- GeV.

E_{T}[GeV]	Very Tight LH	Tight++
10-15	0.418	0.359
15-20	0.733	0.701
20-25	0.851	0.841
	Medium++	Tight++
> 25	1.778	1.730

For 10-25 GeV, the improvements from the likelihood identification in significance in μe channel are $\sim$ 15 % in 10-15 GeV, $\sim$ 3 % in 15-20 GeV, and $\sim$ 1 % in 20-25 GeV at the optimal isolation operating point, which results in 1.5 % improvement in overall E_{T}. For 25- GeV, the cut-based Medium++ is considered since the W+jets background is smaller. The improvement from the cut-based Medium++ in significance in $e\mu$+μe channels are $\sim$ 2.8 % in 25- GeV.

In order to avoid non-negligible increase of the $W + \gamma$ background with the cut-based

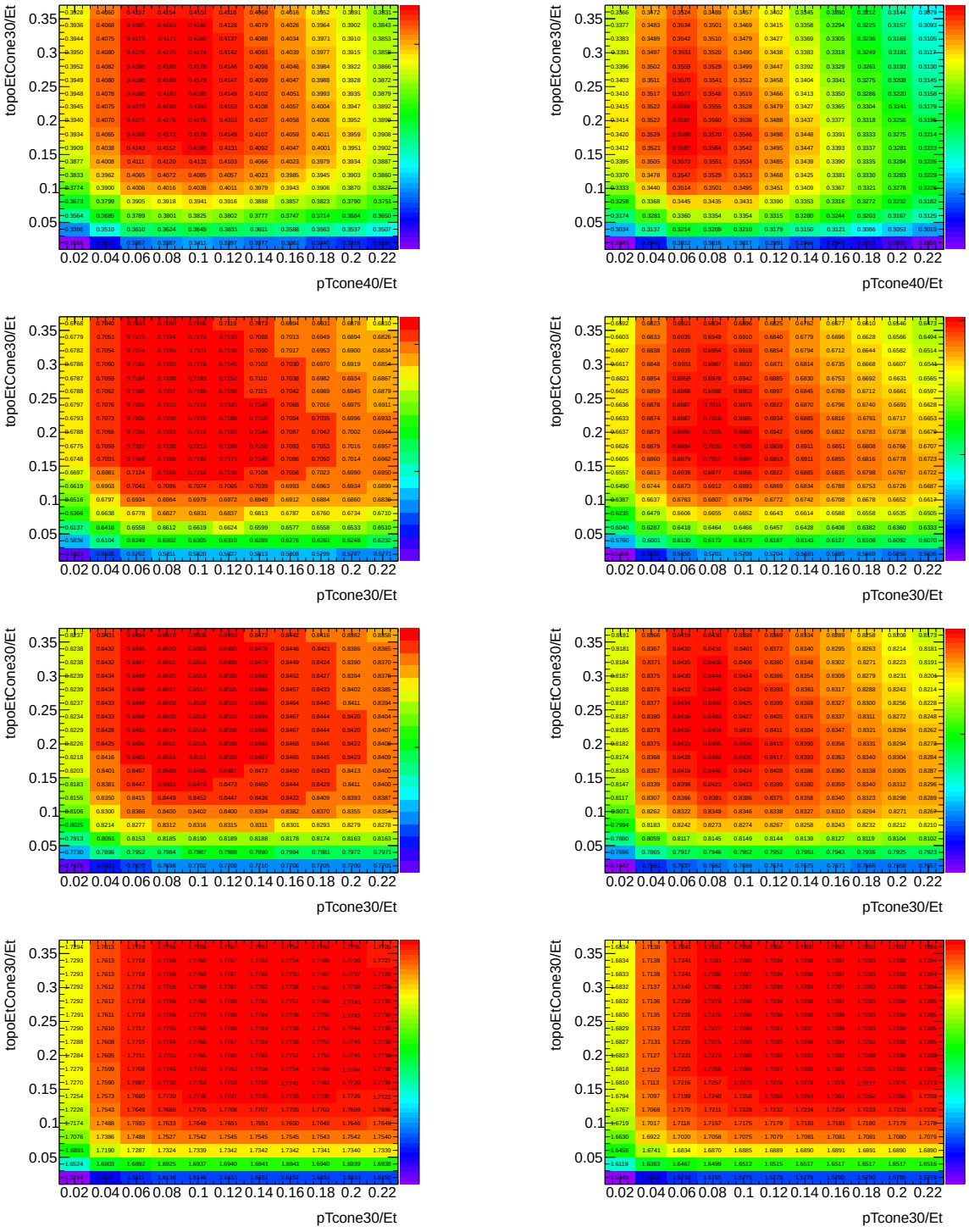

Figure 4.12: Comparison of the identifications in 2-dimensional map. Top three plots are comparison of the Very Tight likelihood (left) and Tight++ (right) for E_{T} = 10-15 GeV (top), 15-20 GeV (2nd), and 20-25 GeV (3rd) in μe channel. Bottom plots are comparison of the modified Medium++ (left) and Tight++ (right) for $E_{\mathrm{T}} > 25$ GeV in $e\mu$+μe channels.

Medium++, the conversion flag and B-Layer hit in the inner detector are additionally required on the top of the cut-based Medium++, at high η ($|\eta|$ >2.37) to cover full η acceptance. [6] The gain from the modified Medium++ in the signal efficiency is $\sim$ 10 %, while retaining the $W+\gamma$ rejection similar to the cut-based Tight++. The comparison of the cut-based Medium++ and Tight++ in significance is also found in Figure 4.12 and in Table 4.6. Also the comparison in cutflow between the modified Medium++ and Tight++ above 25 GeV for $e\mu$ channel is found in Tables 4.9 and 4.10. From the table it is clear that the rate of the $W+\gamma$ background does not change much between the two identifications. The final electron identification criteria as a function of E_{T} are found in Table 4.7.

Table 4.7: Electron identification as a function of E_{T}.

E_{T}[GeV]	Electron identification
10-15	Very Tight LH
15-20	Very Tight LH
20-25	Very Tight LH
> 25	(Modified) cut-based Medium++

4.5.2 Isolation

The isolation optimization is of crucial importance since the isolations are the most powerful discriminants against the W+jets background. The electron isolations are particularly important since most of the W+jets backgrounds originate from non-prompt electrons rather than non-prompt muons. Since the previous publication, there has also been a lot of improvements considered to mitigate the impact of the W+jets background. The optimization is therefore made step by step verifying the impact of each improvement that can be seen as a change of the optimal operating points.

- step1: the same configuration as previous publication but adding dilepton triggers and lowering E_{T},
- step2: change from Di-jet fake factor to Z+jets fake factor (see Chapter 6)
- step3: add m_{ll} split and SS CR method (see Chapter 7)

The first item is just a statistical improvement, which is roughly 10 % in total. The second and third items are more important in terms of the W+jets background because they can change the isolation operating points to be looser than those for the previous analysis. More specifically, for the second item, the change from the di-jet fake factor to the Z+jets fake factor in 10-25 GeV are taken into account, which implies the total systematic uncertainty on the W+jets background is reduced from 45 % to 20-45 % depending on E_{T}.

[6] Both are already required in full η region by default in the cut-based Tight++. Also this effect is taken into account in Table 4.4.

The Z+jets fake factor has a big impact in 10-20 GeV, while it has less impact in $E_{\mathrm{T}} > 20$ GeV due to large EW contamination and statistical uncertainty in the measurement. The Z+jets fake factor is discussed in detail in Chapter 6. For the third item, m_{ll} split at 30 GeV in signal region and the SS CR method are taken into account. Briefly the SS CR is one of the control regions in which the non-WW dibosons ($W+\gamma^{(*)}/WZ/Z+\gamma^{(*)}/ZZ$) normalization is determined from same sign data but subtracting out the W+jets background that is pre-dominant background in this region. The step-by-step changes in significance are verified and shown in Figure 4.13. [7] At the second and third steps, the optimal operating points are apparently moved to be looser due to smaller impact of the W+jets background.

A summary of isolation cuts is found in Table 4.8. The optimization suggests that the analysis should rely on the track isolation rather than the calorimeter isolation because the track isolation is more powerful in the background rejection while keeping higher signal efficiency. There is however an upper limit on the cut value on the track isolation due to the trigger isolation (Ptcone20/$p_{\mathrm{T}} < 0.10$) on `EF_e24vhi_medium1`. The track isolation is therefore set to be a subset of the trigger isolation at higher p_{T}.

Table 4.8: Electron isolation and impact parameters as a function of E_{T}.

E_{T}[GeV]	topoEtcone30	ptcone	$\lvert d_0/\sigma_{d_0}\rvert$	$\lvert z_0 \sin\theta\rvert$
10-15	topoEtConeCor30/E_{T} <0.20	Ptcone40/p_{T} <0.06	3	0.4 mm
15-20	topoEtConeCor30/E_{T} <0.24	Ptcone30/p_{T} <0.08	3	0.4 mm
20-25	topoEtConeCor30/E_{T} <0.28	Ptcone30/p_{T} <0.10	3	0.4 mm
25-	topoEtConeCor30/E_{T} <0.28	Ptcone30/p_{T} <0.10	3	0.4 mm

[7] Note that the cut-based Tight++ is used in the step-by-step optimization for E_{T} = 10-25 GeV but the optimal points are finally chosen from the Figure 4.12 with the optimal identification defined in Table 4.7.

Table 4.9: Event yields and predictions for $e\mu$ channel with the cut-based Tight++ in $E_{\mathrm{T}} > 25$ GeV. Only statistical uncertainties are shown in this table.

	Signal [125 GeV]	WW	$WZ/ZZ/W\gamma$	$W\gamma$	$W\gamma^*$	WZ	ZZ	$t\bar{t}$	Single Top	Z+jets	W+jets	Total Bkg.	Observed	Data/MC
blinding	352.61 ± 2.01	5813.28 ± 18.74	2113.36 ± 13.82	729.45 ± 10.75	332.49 ± 6.05	854.91 ± 6.19	196.51 ± 0.75	32099.93 ± 64.52	3013.26 ± 10.97	28773.58 ± 84.01	11242.09 ± 37.76	83055.50 ± 115.36		
lepton p_{T}	335.65 ± 1.96	5723.46 ± 18.60	1816.44 ± 12.56	581.08 ± 9.62	244.80 ± 5.30	811.50 ± 6.04	179.06 ± 0.72	31757.35 ± 64.20	2985.79 ± 10.87	23870.63 ± 78.33	6518.01 ± 30.71	72671.68 ± 108.73		
Scale factors														
OS leptons	335.30 ± 1.96	5707.86 ± 18.57	917.75 ± 8.92	298.92 ± 6.90	120.08 ± 3.69	404.84 ± 4.25	93.92 ± 0.55	31659.81 ± 64.10	2950.44 ± 9.55	23612.59 ± 73.58	4245.61 ± 26.02	69094.06 ± 103.52		
$m_{\ell\ell} > 12,10$ GeV	331.59 ± 1.95	5698.50 ± 18.56	878.60 ± 8.62	270.49 ± 6.57	111.56 ± 3.58	403.23 ± 4.24	93.32 ± 0.55	31618.50 ± 64.06	2948.07 ± 9.55	23594.73 ± 73.56	4195.40 ± 25.90	68933.81 ± 103.42		
Z veto (for $ee,\mu\mu$)	331.59 ± 1.95	5698.50 ± 18.56	878.60 ± 8.62	270.49 ± 6.57	111.56 ± 3.58	403.23 ± 4.24	93.32 ± 0.55	31618.50 ± 64.06	2948.07 ± 9.55	23594.73 ± 73.56	4195.40 ± 25.90	68933.81 ± 103.42		
Scale factors														
$E_{\mathrm{T,rel}}^{\mathrm{miss}} > 45,25$ GeV	217.81 ± 1.59	3595.25 ± 14.71	448.31 ± 6.38	149.81 ± 4.87	63.53 ± 2.68	217.23 ± 3.13	17.74 ± 0.29	18328.05 ± 48.69	1828.81 ± 7.40	3010.73 ± 24.75	1060.32 ± 13.40	28271.47 ± 58.95		
Z validation region (incl)	331.59 ± 1.95	5698.50 ± 18.56	878.60 ± 8.62	270.49 ± 6.57	111.56 ± 3.58	403.23 ± 4.24	93.32 ± 0.55	31618.50 ± 64.06	2948.07 ± 9.55	23594.73 ± 73.56	4195.40 ± 25.90	68933.81 ± 103.42		
Top validation region (incl)	10.65 ± 0.36	139.54 ± 3.05	24.92 ± 1.56	8.31 ± 1.21	2.04 ± 0.54	13.65 ± 0.82	0.92 ± 0.07	16079.82 ± 45.70	1278.06 ± 5.36	105.68 ± 4.35	207.52 ± 7.47	17835.55 ± 46.94		
Scale factors														
0j: jet veto	123.24 ± 1.23	2354.36 ± 11.95	221.68 ± 4.71	89.20 ± 3.79	42.95 ± 2.05	81.55 ± 1.88	7.98 ± 0.22	304.86 ± 6.21	175.17 ± 1.97	2034.39 ± 21.00	547.65 ± 8.66	5638.11 ± 26.90		
0j: $\Delta\phi_{\ell\ell,MET} > 1.57$	122.29 ± 1.23	2325.18 ± 11.88	216.24 ± 4.67	87.95 ± 3.77	42.60 ± 2.04	78.96 ± 1.85	6.73 ± 0.21	298.02 ± 6.14	172.85 ± 1.96	1387.93 ± 18.32	479.90 ± 7.98	4880.11 ± 24.57		
0j: $p_{\mathrm{T},\ell\ell}$ >45,30 GeV	111.56 ± 1.17	1961.45 ± 10.91	176.26 ± 4.24	72.34 ± 3.41	34.68 ± 1.85	65.45 ± 1.69	3.79 ± 0.17	275.06 ± 5.91	159.90 ± 1.65	63.88 ± 4.75	297.77 ± 5.88	2934.32 ± 15.22		
0j: $m_{\ell\ell} < 50$ GeV	93.60 ± 1.07	545.47 ± 5.72	106.60 ± 3.52	55.16 ± 2.98	25.17 ± 1.57	24.59 ± 1.02	1.68 ± 0.12	55.57 ± 2.74	33.12 ± 0.75	14.92 ± 1.50	128.09 ± 3.85	883.78 ± 8.38		
0j: $\Delta\phi_{\ell\ell} < 1.8$	88.62 ± 1.04	515.08 ± 5.55	102.62 ± 3.46	53.39 ± 2.92	24.74 ± 1.56	23.00 ± 0.99	1.49 ± 0.11	54.41 ± 2.71	32.38 ± 0.74	1.20 ± 0.48	99.89 ± 3.40	805.57 ± 7.90		
0j: $m_{\ell\ell} < 30$ hipt	34.66 ± 0.65	165.10 ± 3.15	37.21 ± 2.15	22.27 ± 1.87	9.01 ± 0.94	5.59 ± 0.48	0.33 ± 0.05	16.39 ± 1.56	10.01 ± 0.41	0.00 ± 0.00	14.72 ± 1.32	243.44 ± 4.34		
0j: $m_{\ell\ell} > 30$ hipt	34.68 ± 0.66	278.71 ± 4.08	19.72 ± 1.40	7.49 ± 1.14	3.16 ± 0.54	8.34 ± 0.61	0.73 ± 0.08	29.75 ± 1.99	17.17 ± 0.54	0.03 ± 0.03	23.15 ± 1.49	368.52 ± 5.01		
0j: $m_{\ell\ell} < 30$ lowpt	11.84 ± 0.38	36.05 ± 1.46	40.31 ± 2.22	22.04 ± 1.86	11.96 ± 1.10	6.13 ± 0.52	0.19 ± 0.03	3.49 ± 0.65	2.18 ± 0.19	0.63 ± 0.35	36.72 ± 2.15	119.38 ± 3.51		
0j: $m_{\ell\ell} > 30$ lowpt	7.43 ± 0.30	35.23 ± 1.45	5.38 ± 0.65	1.59 ± 0.50	0.62 ± 0.24	2.94 ± 0.34	0.24 ± 0.06	4.77 ± 0.72	3.02 ± 0.23	0.54 ± 0.32	25.30 ± 1.73	74.23 ± 2.49		
0j: $0.75 \cdot m_{\mathrm{H}} \leq m_{\mathrm{T}} \leq m_{\mathrm{H}}$	51.86 ± 0.80	220.08 ± 3.66	29.79 ± 1.80	14.47 ± 1.52	5.50 ± 0.72	9.38 ± 0.63	0.45 ± 0.06	16.12 ± 1.47	8.96 ± 0.39	0.16 ± 0.13	44.05 ± 2.22	319.16 ± 4.89		
0j: Z validation region	160.66 ± 1.40	3644.76 ± 14.90	376.80 ± 5.90	139.39 ± 4.74	67.01 ± 2.55	135.40 ± 2.40	35.00 ± 0.37	412.13 ± 7.18	234.07 ± 2.69	17221.42 ± 59.24	2229.07 ± 18.52	24118.25 ± 64.56		
Scale factors														
0j: WW control region	15.96 ± 0.45	709.74 ± 6.57	33.15 ± 1.59	7.65 ± 1.12	4.37 ± 0.66	19.69 ± 0.92	1.44 ± 0.11	82.49 ± 3.29	52.73 ± 0.94	27.63 ± 2.04	78.43 ± 3.01	984.17 ± 8.41		
0j: WW Old control region	0.11 ± 0.04	895.84 ± 7.41	40.28 ± 1.87	11.52 ± 1.38	5.61 ± 0.75	22.45 ± 1.01	0.70 ± 0.05	159.90 ± 4.40	87.77 ± 1.23	6.41 ± 1.00	60.90 ± 2.79	1251.11 ± 9.38		
0j: WW validation region	0.00 ± 0.00	653.82 ± 6.33	30.07 ± 1.61	8.19 ± 1.15	4.68 ± 0.69	16.72 ± 0.89	0.48 ± 0.04	128.68 ± 3.94	68.29 ± 1.09	2.83 ± 0.65	37.46 ± 2.10	921.17 ± 8.02		
Scale factors														
1j: one jet	61.32 ± 0.84	915.42 ± 7.42	142.47 ± 3.36	37.58 ± 2.38	13.65 ± 1.27	84.40 ± 1.99	6.84 ± 0.16	3014.38 ± 19.67	879.74 ± 5.18	705.72 ± 10.61	254.08 ± 6.55	5911.79 ± 25.21		
1j: SMT veto	61.02 ± 0.83	910.34 ± 7.40	141.15 ± 3.35	37.43 ± 2.38	13.57 ± 1.26	83.46 ± 1.98	6.69 ± 0.15	2660.71 ± 18.46	806.34 ± 5.05	702.89 ± 10.59	246.82 ± 6.42	5468.24 ± 24.20		
1j: b-jet veto	56.81 ± 0.80	844.39 ± 7.09	132.37 ± 3.23	34.89 ± 2.30	12.65 ± 1.22	78.55 ± 1.91	6.28 ± 0.15	673.69 ± 9.32	249.29 ± 3.64	653.83 ± 10.19	203.89 ± 5.61	2757.46 ± 17.21		
1j: $Z \to \tau\tau$ veto	56.55 ± 0.80	821.00 ± 6.99	129.14 ± 3.19	34.26 ± 2.27	12.34 ± 1.20	76.47 ± 1.89	6.08 ± 0.15	647.94 ± 9.14	239.44 ± 3.61	556.61 ± 9.55	198.26 ± 5.47	2592.40 ± 16.63		
1j: $m_{\ell\ell} < 50$ GeV	45.24 ± 0.72	185.03 ± 3.30	48.28 ± 2.09	17.18 ± 1.59	7.49 ± 0.93	21.18 ± 0.98	2.44 ± 0.09	138.13 ± 4.38	50.39 ± 1.69	260.46 ± 5.73	86.26 ± 3.46	768.56 ± 9.06		
1j: $\Delta\phi_{\ell\ell} < 1.8$	39.97 ± 0.67	162.09 ± 3.08	43.19 ± 2.02	16.02 ± 1.54	7.18 ± 0.91	18.32 ± 0.93	1.66 ± 0.08	126.88 ± 4.21	47.24 ± 1.68	32.58 ± 1.98	51.95 ± 2.51	463.91 ± 6.66		
1j: $m_{\ell\ell} < 30$ hipt	15.96 ± 0.42	51.36 ± 1.73	19.66 ± 1.44	9.24 ± 1.16	3.83 ± 0.65	6.13 ± 0.56	0.47 ± 0.04	39.96 ± 2.43	14.04 ± 0.49	2.59 ± 0.55	12.20 ± 1.16	139.80 ± 3.58		
1j: $m_{\ell\ell} > 30$ hipt	16.42 ± 0.43	86.97 ± 2.27	14.47 ± 1.07	3.47 ± 0.73	1.63 ± 0.45	8.65 ± 0.64	0.72 ± 0.06	66.14 ± 3.06	26.04 ± 1.20	16.10 ± 1.39	11.35 ± 1.19	221.08 ± 4.52		
1j: $m_{\ell\ell} < 30$ lowpt	4.60 ± 0.23	11.29 ± 0.81	7.07 ± 0.87	3.07 ± 0.69	1.73 ± 0.46	1.97 ± 0.27	0.30 ± 0.03	9.46 ± 1.08	3.55 ± 1.03	3.63 ± 0.68	15.94 ± 1.39	50.93 ± 2.46		
1j: $m_{\ell\ell} > 30$ lowpt	2.99 ± 0.18	12.47 ± 0.85	1.98 ± 0.32	0.24 ± 0.17	0.00 ± 0.00	1.57 ± 0.27	0.17 ± 0.02	11.32 ± 1.15	3.61 ± 0.24	10.26 ± 1.10	12.45 ± 1.26	52.10 ± 2.24		
1j: $0.75 \cdot m_{\mathrm{H}} \leq m_{\mathrm{T}} \leq m_{\mathrm{H}}$	21.55 ± 0.50	52.32 ± 1.76	15.55 ± 1.22	6.22 ± 0.98	1.63 ± 0.43	7.26 ± 0.58	0.44 ± 0.04	34.55 ± 2.18	12.90 ± 0.47	2.18 ± 0.50	15.69 ± 1.39	133.19 ± 3.43		
1j: Z validation region	104.38 ± 1.09	1485.36 ± 9.46	307.11 ± 4.79	76.30 ± 3.44	30.13 ± 1.88	161.30 ± 2.72	39.38 ± 0.34	4452.00 ± 23.85	1336.93 ± 6.13	4575.36 ± 36.04	1098.58 ± 12.75	13255.33 ± 46.69		
Scale factors														
1j: WW control region	0.03 ± 0.01	403.87 ± 4.91	46.71 ± 1.84	9.44 ± 1.19	2.91 ± 0.59	32.84 ± 1.27	1.53 ± 0.07	340.37 ± 6.48	122.29 ± 1.78	16.04 ± 1.47	42.93 ± 2.53	972.21 ± 9.01		
Scale factors														
1j: Top control region	4.15 ± 0.23	64.34 ± 2.12	8.69 ± 0.87	2.53 ± 0.62	0.93 ± 0.35	4.84 ± 0.50	0.39 ± 0.05	1896.54 ± 15.61	532.56 ± 3.43	41.47 ± 2.51	42.15 ± 3.07	2585.75 ± 16.63		

Table 4.10: Event yields and predictions for $e\mu$ channel with the cut-based Medium++ in $E_{\mathrm{T}} > 25$ GeV. Only statistical uncertainties are shown in this table.

	Signal [125 GeV]	WW	$WZ/ZZ/W\gamma$	$W\gamma$	$W\gamma^*$	WZ	ZZ	$t\bar{t}$	Single Top	Z+jets	W+jets	Total Bkg.	Observed	Data/MC
blinding	417.39 ± 2.55	6179.52 ± 19.33	2198.02 ± 14.05	786.25 ± 11.20	346.66 ± 5.73	866.68 ± 6.20	198.44 ± 0.76	33702.40 ± 66.70	3227.70 ± 8.27	30384.46 ± 92.93	12039.60 ± 38.94	87731.71 ± 123.45		
lepton p_{T}	399.22 ± 2.50	6089.92 ± 19.19	1899.32 ± 12.81	638.24 ± 10.11	255.42 ± 4.95	824.03 ± 6.06	181.63 ± 0.73	33367.90 ± 66.38	3198.65 ± 8.21	25505.74 ± 87.81	7319.03 ± 32.17	77380.57 ± 117.27		
Scale factors														
OS leptons	386.33 ± 2.31	6067.38 ± 19.16	965.66 ± 9.17	333.28 ± 7.31	126.09 ± 3.48	410.97 ± 4.26	95.33 ± 0.56	33249.80 ± 66.27	3159.23 ± 7.92	25195.85 ± 83.01	4715.11 ± 27.10	73353.02 ± 111.94		
$m_{\ell\ell} > 12,10$ GeV	382.24 ± 2.30	6057.42 ± 19.14	923.49 ± 8.86	302.87 ± 6.98	116.60 ± 3.35	409.28 ± 4.25	94.73 ± 0.56	33207.34 ± 66.23	3156.72 ± 7.92	25176.50 ± 82.99	4661.44 ± 26.97	73182.90 ± 111.84		
Z veto (for $ee,\mu\mu$)	382.24 ± 2.30	6057.42 ± 19.14	923.49 ± 8.86	302.87 ± 6.98	116.60 ± 3.35	409.28 ± 4.25	94.73 ± 0.56	33207.34 ± 66.23	3156.72 ± 7.92	25176.50 ± 82.99	4661.44 ± 26.97	73182.90 ± 111.84		
Scale factors														
$E_{\mathrm{T,rel}}^{\mathrm{miss}} > 45, 25$ GeV	249.39 ± 1.87	3823.94 ± 15.18	473.54 ± 6.57	167.16 ± 5.17	67.25 ± 2.54	221.02 ± 3.15	18.12 ± 0.29	19249.52 ± 50.35	1954.88 ± 6.19	3204.51 ± 27.87	1147.08 ± 13.67	29853.48 ± 61.73		
Z validation region (incl)	382.24 ± 2.30	6057.42 ± 19.14	923.49 ± 8.86	302.87 ± 6.98	116.60 ± 3.35	409.28 ± 4.25	94.73 ± 0.56	33207.34 ± 66.23	3156.72 ± 7.92	25176.50 ± 82.99	4661.44 ± 26.97	73182.90 ± 111.84		
Top validation region (incl)	14.24 ± 0.53	147.94 ± 3.14	25.65 ± 1.56	8.56 ± 1.23	1.93 ± 0.47	14.19 ± 0.84	0.97 ± 0.07	16887.43 ± 47.25	1380.69 ± 5.15	111.89 ± 4.64	207.66 ± 7.43	18761.27 ± 48.45		
Scale factors														
0j: jet veto	135.80 ± 1.36	2509.95 ± 12.34	241.86 ± 4.96	99.12 ± 4.02	48.40 ± 2.15	85.95 ± 1.93	8.39 ± 0.22	318.45 ± 6.41	183.04 ± 1.88	2162.69 ± 23.07	606.74 ± 9.00	6022.73 ± 28.89		
0j: $\Delta\phi_{\ell\ell,MET} > 1.57$	134.74 ± 1.35	2478.78 ± 12.27	235.99 ± 4.92	97.85 ± 4.00	47.92 ± 2.14	83.14 ± 1.90	7.08 ± 0.21	311.02 ± 6.33	180.74 ± 1.87	1475.75 ± 19.65	530.87 ± 8.28	5213.15 ± 25.94		
0j: $p_{\mathrm{T},\ell\ell}$ >45,30 GeV	122.52 ± 1.28	2089.64 ± 11.27	190.82 ± 4.43	79.37 ± 3.59	38.77 ± 1.93	68.65 ± 1.73	4.03 ± 0.18	286.44 ± 6.09	167.17 ± 1.78	74.62 ± 6.37	325.86 ± 6.08	3134.54 ± 16.26		
0j: $m_{\ell\ell} < 50$ GeV	101.34 ± 1.14	581.73 ± 5.91	115.31 ± 3.67	59.90 ± 3.12	27.95 ± 1.63	25.66 ± 1.04	1.81 ± 0.13	58.83 ± 2.83	34.94 ± 0.79	19.52 ± 3.47	137.47 ± 4.00	947.80 ± 9.22		
0j: $\Delta\phi_{\ell\ell} < 1.8$	96.06 ± 1.11	549.14 ± 5.73	111.26 ± 3.62	58.22 ± 3.07	27.47 ± 1.61	23.98 ± 1.01	1.60 ± 0.12	57.60 ± 2.80	34.09 ± 0.78	4.96 ± 3.12	107.29 ± 3.54	864.34 ± 8.75		
0j: $m_{\ell\ell} < 30$ hipt	37.63 ± 0.71	176.48 ± 3.25	40.78 ± 2.26	24.25 ± 1.97	10.35 ± 1.00	5.83 ± 0.49	0.35 ± 0.05	17.21 ± 1.60	10.56 ± 0.44	3.81 ± 3.09	16.09 ± 1.38	264.93 ± 5.47		
0j: $m_{\ell\ell} > 30$ hipt	37.72 ± 0.69	297.18 ± 4.22	22.17 ± 1.51	8.61 ± 1.22	4.04 ± 0.62	8.71 ± 0.62	0.81 ± 0.09	31.73 ± 2.07	18.36 ± 0.57	0.18 ± 0.15	25.92 ± 1.57	395.54 ± 5.21		
0j: $m_{\ell\ell} < 30$ lowpt	12.54 ± 0.40	38.42 ± 1.51	42.73 ± 2.29	23.75 ± 1.95	12.39 ± 1.07	6.40 ± 0.53	0.19 ± 0.03	3.88 ± 0.68	2.21 ± 0.19	0.63 ± 0.35	39.28 ± 2.25	127.15 ± 3.64		
0j: $m_{\ell\ell} > 30$ lowpt	8.17 ± 0.32	37.06 ± 1.49	5.58 ± 0.67	1.61 ± 0.51	0.68 ± 0.26	3.04 ± 0.35	0.25 ± 0.06	4.79 ± 0.74	2.96 ± 0.23	0.33 ± 0.24	26.00 ± 1.75	76.72 ± 2.53		
0j: $0.75 \cdot m_{\mathrm{H}} \leq m_{\mathrm{T}} \leq m_{\mathrm{H}}$	55.96 ± 0.86	234.27 ± 3.78	33.02 ± 1.92	16.14 ± 1.62	6.57 ± 0.80	9.81 ± 0.64	0.49 ± 0.06	17.14 ± 1.53	9.48 ± 0.41	1.18 ± 0.87	47.73 ± 2.30	342.82 ± 5.14		
0j: Z validation region	176.55 ± 1.54	3882.26 ± 15.39	412.01 ± 6.24	155.28 ± 5.03	77.27 ± 2.72	142.47 ± 2.46	36.99 ± 0.38	429.61 ± 7.40	245.14 ± 2.17	18340.71 ± 66.11	2495.55 ± 19.43	25805.28 ± 71.30		
Scale factors														
0j: WW control region	18.56 ± 0.54	760.92 ± 6.81	36.03 ± 1.68	8.65 ± 1.19	5.11 ± 0.71	20.74 ± 0.94	1.53 ± 0.11	85.23 ± 3.38	56.94 ± 1.08	30.24 ± 2.18	87.84 ± 3.09	1057.20 ± 8.72		
0j: WW Old control region	0.89 ± 0.19	949.17 ± 7.63	43.69 ± 1.96	12.99 ± 1.47	6.19 ± 0.78	23.78 ± 1.04	0.74 ± 0.05	166.41 ± 4.55	90.12 ± 1.30	9.46 ± 2.91	69.66 ± 2.88	1328.51 ± 10.06		
0j: WW validation region	0.45 ± 0.14	691.12 ± 6.51	32.72 ± 1.70	9.47 ± 1.24	5.03 ± 0.70	17.72 ± 0.92	0.50 ± 0.04	134.17 ± 4.07	69.17 ± 1.12	5.71 ± 2.81	43.76 ± 2.20	976.66 ± 8.71		
Scale factors														
1j: one jet	71.65 ± 1.02	971.22 ± 7.65	147.78 ± 3.43	42.23 ± 2.54	14.16 ± 1.17	84.58 ± 1.98	6.81 ± 0.16	3165.37 ± 20.34	944.06 ± 4.23	757.47 ± 12.72	272.55 ± 6.66	6258.45 ± 26.61		
1j: SMT veto	71.26 ± 1.02	965.96 ± 7.63	146.24 ± 3.42	42.09 ± 2.53	14.05 ± 1.16	83.47 ± 1.97	6.63 ± 0.16	2794.27 ± 19.08	864.15 ± 4.06	754.92 ± 12.71	265.50 ± 6.53	5791.03 ± 25.58		
1j: b-jet veto	66.00 ± 0.97	896.05 ± 7.31	137.01 ± 3.30	39.50 ± 2.45	13.05 ± 1.11	78.25 ± 1.90	6.21 ± 0.15	709.28 ± 9.66	260.60 ± 2.34	703.54 ± 12.32	224.65 ± 5.76	2931.14 ± 18.66		
1j: $Z \to \tau\tau$ veto	65.61 ± 0.96	871.50 ± 7.21	133.94 ± 3.27	38.88 ± 2.43	12.82 ± 1.11	76.22 ± 1.88	6.02 ± 0.15	682.56 ± 9.48	249.90 ± 2.29	601.32 ± 11.74	218.77 ± 5.62	2758.00 ± 18.08		
1j: $m_{\ell\ell} < 50$ GeV	51.23 ± 0.81	196.98 ± 3.41	50.72 ± 2.16	19.74 ± 1.73	7.56 ± 0.85	20.98 ± 0.97	2.43 ± 0.10	145.30 ± 4.53	53.08 ± 1.09	275.80 ± 6.33	92.64 ± 3.59	814.52 ± 9.54		
1j: $\Delta\phi_{\ell\ell} < 1.8$	45.25 ± 0.75	172.52 ± 3.18	45.38 ± 2.08	18.43 ± 1.67	7.20 ± 0.83	18.08 ± 0.92	1.67 ± 0.08	133.47 ± 4.36	49.44 ± 1.04	34.68 ± 2.11	56.43 ± 2.59	491.91 ± 6.76		
1j: $m_{\ell\ell} < 30$ hipt	17.98 ± 0.47	54.64 ± 1.78	21.42 ± 1.52	10.77 ± 1.27	3.96 ± 0.62	6.23 ± 0.56	0.45 ± 0.04	42.20 ± 2.50	15.20 ± 0.53	2.81 ± 0.58	13.65 ± 1.20	149.92 ± 3.72		
1j: $m_{\ell\ell} > 30$ hipt	18.73 ± 0.49	92.33 ± 2.33	14.40 ± 1.07	3.83 ± 0.77	1.51 ± 0.38	8.32 ± 0.63	0.73 ± 0.06	69.76 ± 3.17	27.24 ± 0.75	17.00 ± 1.49	12.32 ± 1.20	233.05 ± 4.57		
1j: $m_{\ell\ell} < 30$ lowpt	5.23 ± 0.26	12.25 ± 0.84	7.57 ± 0.89	3.55 ± 0.74	1.73 ± 0.40	1.98 ± 0.27	0.31 ± 0.03	9.72 ± 1.12	2.97 ± 0.34	3.70 ± 0.70	17.27 ± 1.44	53.48 ± 2.33		
1j: $m_{\ell\ell} > 30$ lowpt	3.31 ± 0.20	13.30 ± 0.89	1.99 ± 0.31	0.27 ± 0.17	0.00 ± 0.00	1.54 ± 0.25	0.18 ± 0.03	11.79 ± 1.20	4.03 ± 0.34	11.16 ± 1.18	13.18 ± 1.31	55.46 ± 2.36		
1j: $0.75 \cdot m_{\mathrm{H}} \leq m_{\mathrm{T}} \leq m_{\mathrm{H}}$	23.71 ± 0.54	56.11 ± 1.83	16.04 ± 1.24	6.59 ± 1.01	1.84 ± 0.43	7.14 ± 0.58	0.47 ± 0.04	35.78 ± 2.24	14.49 ± 0.63	2.49 ± 0.57	17.04 ± 1.41	141.96 ± 3.55		
1j: Z validation region	121.12 ± 1.31	1576.77 ± 9.76	316.73 ± 4.88	86.28 ± 3.67	30.05 ± 1.70	161.40 ± 2.71	39.00 ± 0.34	4677.29 ± 24.65	1437.20 ± 5.21	4901.25 ± 40.76	1231.74 ± 13.37	14140.99 ± 50.93		
Scale factors														
1j: WW control region	1.26 ± 0.28	426.71 ± 5.05	47.42 ± 1.85	10.44 ± 1.25	3.02 ± 0.54	32.47 ± 1.26	1.48 ± 0.07	357.02 ± 6.72	128.92 ± 1.60	21.10 ± 3.82	49.14 ± 2.60	1030.31 ± 9.90		
Scale factors														
1j: Top control region	5.15 ± 0.32	68.29 ± 2.18	9.18 ± 0.88	2.53 ± 0.62	1.04 ± 0.35	5.19 ± 0.52	0.41 ± 0.05	1991.60 ± 16.13	577.48 ± 3.25	44.20 ± 2.70	40.16 ± 3.02	2730.90 ± 17.11		

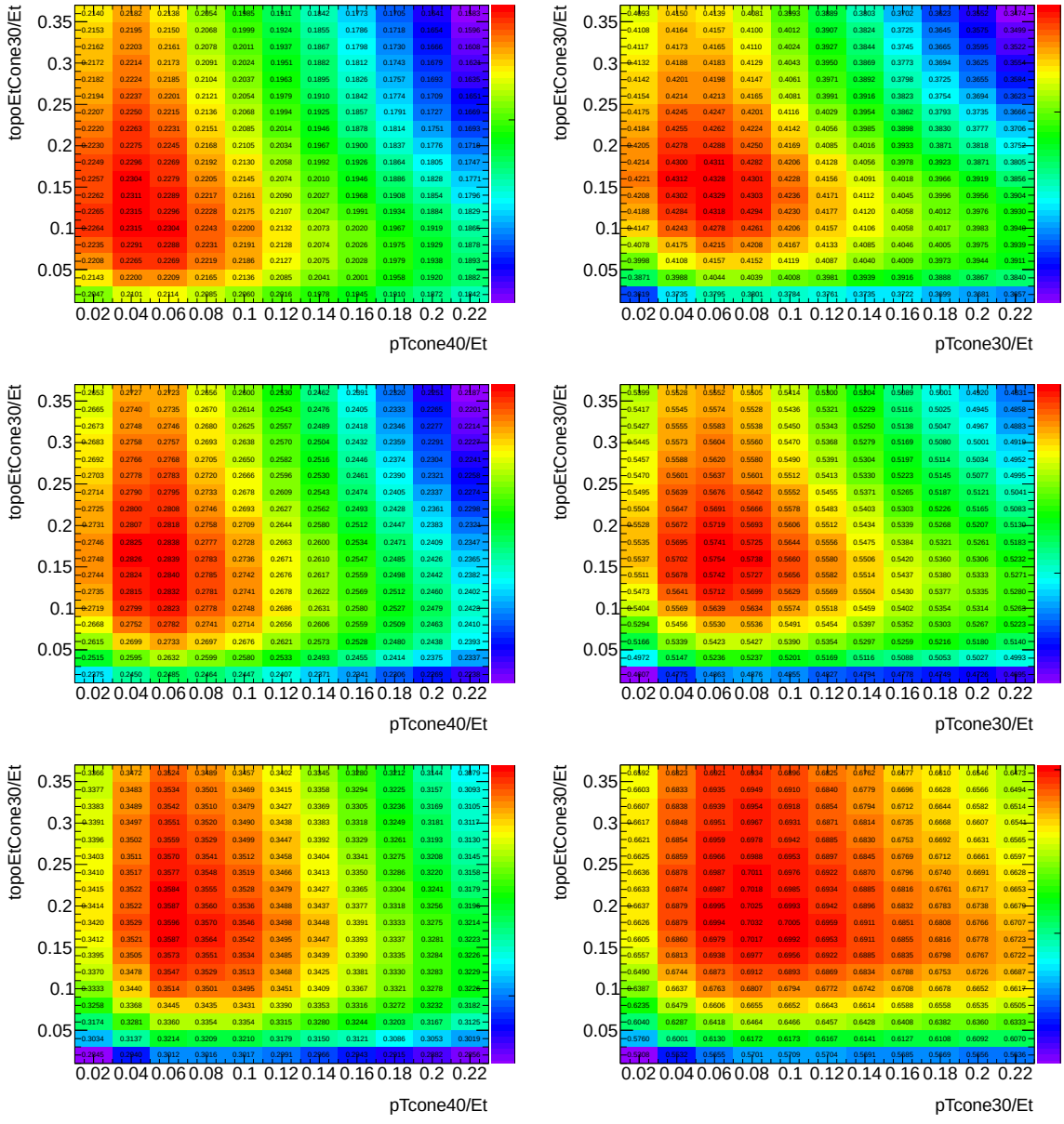

Figure 4.13: Step-by-step isolation optimization: isolation map at the first step (top), at the second step (middle), and at the third step (bottom) in μe channel. As examples, only E_{T} = 10-15 (left) and 15-20 GeV (right) are shown where the impact of the W+jets are relatively large.

4.5.3 Vertex Requirements

The electron track impact parameter resolutions are significantly improved in 2012 due to the new Gaussian Sum Filter (GSF) algorithm based on a non-linear generalization of the Kalman Fitter, where the error distributions in the track reconstruction are approximated as weighted gaussian sums. After the loose matching between tracks and electromagnetic clusters, the candidate electron or photon conversion tracks above 1 GeV in the event are refit with the GSF algorithm (see Section 4.1.1).

While in the 2011 reconstruction, there is no special treatment applied to the electron tracking. All tracks are fit using a pion particle hypothesis. An electron can lose a significant amount of its initial energy due to bremsstrahlung effects when interacting with the material in the inner detector and surrounding infrastructure. The lack of special treatment results in poorly determined track parameters, particularly in the bending plane, and a significant dependence of electron tracking parameters on the amount of material encountered.

The optimization of vertex parameters, namely d_0 significance and z_0 impact parameters, benefits by the GSF improvements. In addition, the cut on z_0 is changed into a cut on $z_0 \sin\theta$ to take into account the fact that more forward tracks have a longer projection on the z-axis and thus a larger uncertainty. The difference of this change is significant at higher η as shown in Figure 4.14. Also d_0 significance and $z_0 \sin\theta$ distributions just after the isolations are shown in Figure 4.15. After the isolation, both vertexing parameters do not work well as good discriminants because most of background electrons originated from light flavors such as charged/neutral pions are rejected by the isolations.

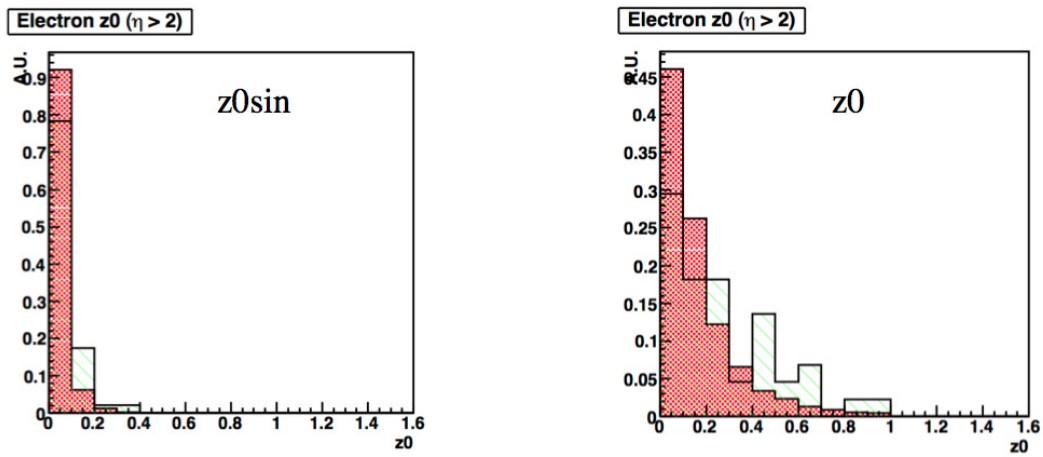

Figure 4.14: Comparison of z_0 and $z_0 \sin\theta$ impact parameters in $|\eta| > 2.0$, where the red is prompt electrons and the green is non-prompt (hadron background) electrons.

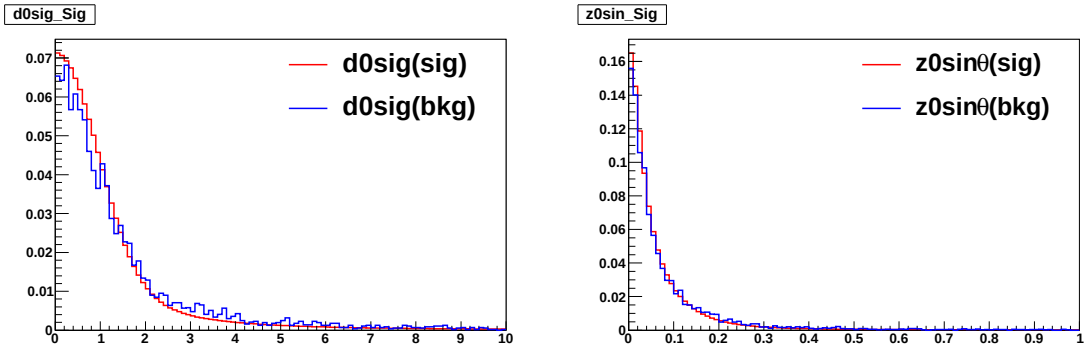

Figure 4.15: d_0 significance and $z_0 \sin\theta$ after isolation cuts. Red and blue solid lines are real and background electrons, respectively.

For the d_0 significance and z_0 parameter optimizations, the same procedure as the identification or isolation is applied. In order to assess the effect of pile-up, the optimization was made in the beginning of 2012, with the variations of the average mu ($< \mu >$). From Figure 4.16, it was found that the vertexing parameters are robust against high pileups, and that the optimal point does not change between low and high $< \mu >$.

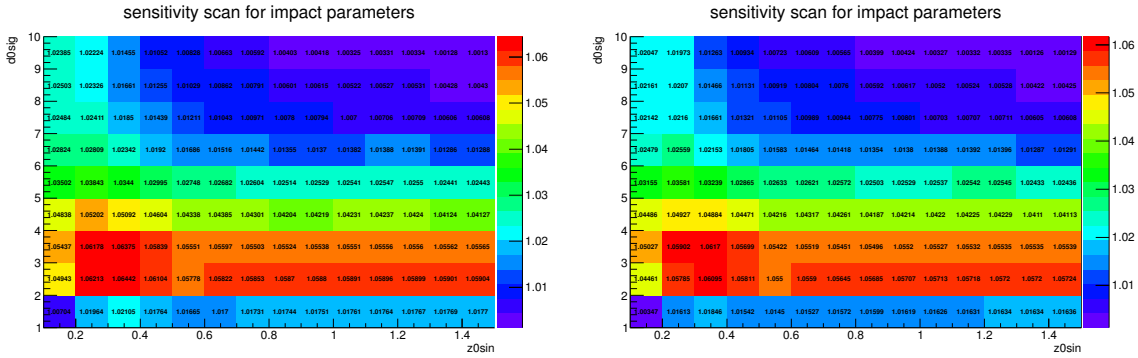

Figure 4.16: Significance in 2-dimensional map of vertexing parameters for electrons. The left and the right show significances with $< \mu >< 20$ and $< \mu >> 20$, respectively.

According to the updated isolation and identification operating points, the impact parameters optimization is also repeated. Since the Very Tight likelihood already includes d_0 significance as input to create the PDFs, the optimization of the d_0 significance is just a confirmation whether or not further cut on the d_0 significance on the top of the likelihood works better. The updated 2-D map in d_0 significance versus $z_0 \sin\theta$ is shown in Figure 4.17. It is found that further cut on the d_0 significance works better. A summary of impact parameter cuts is also found in Table 4.8.

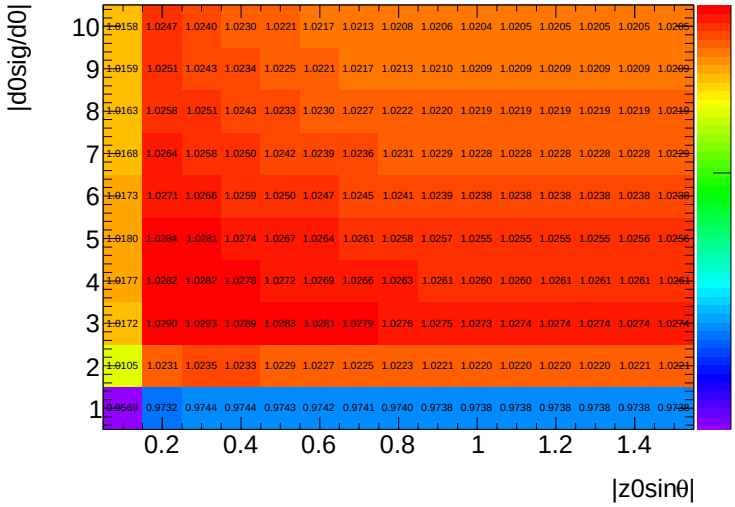

Figure 4.17: Significance in 2-dimensional map of vertexing parameters for electrons.

4.6 Muon Optimization

4.6.1 Isolation

The procedure of muon optimization is the same as the electron optimization. In order to verify all the changes from the previous analysis, the step-by-step optimization is also made as shown in Figure 4.18. For muons, the optimization suggests that the calorimeter isolation should be tightened as well as since the identification is not applied to the muon selection. The cut value on the calorimeter isolation is only about 50 % compared to the one for electrons. Also as discussed in the electron optimization, note that there is an upper limit on the cut value on the track isolation to be a subset of the trigger isolation (Ptcone20/$p_{\mathrm{T}} < 0.12$) on `EF_mu24i_tight`. A summary of muon isolation selection is found in Table 4.11.

Table 4.11: Muon isolation and impact parameters as a function of p_{T}.

p_{T}[GeV]	Etcone30	ptcone	$\lvert d_0/\sigma_{d_0}\rvert$	$\lvert z_0 \sin\theta\rvert$
10-15	EtConeCor30/p_{T} <0.06	Ptcone40/p_{T} <0.06	3	1.0 mm
15-20	EtConeCor30/p_{T} <0.12	Ptcone30/p_{T} <0.08	3	1.0 mm
20-25	EtConeCor30/p_{T} <0.18	Ptcone30/p_{T} <0.12	3	1.0 mm
25-	EtConeCor30/p_{T} <0.30	Ptcone30/p_{T} <0.12	3	1.0 mm

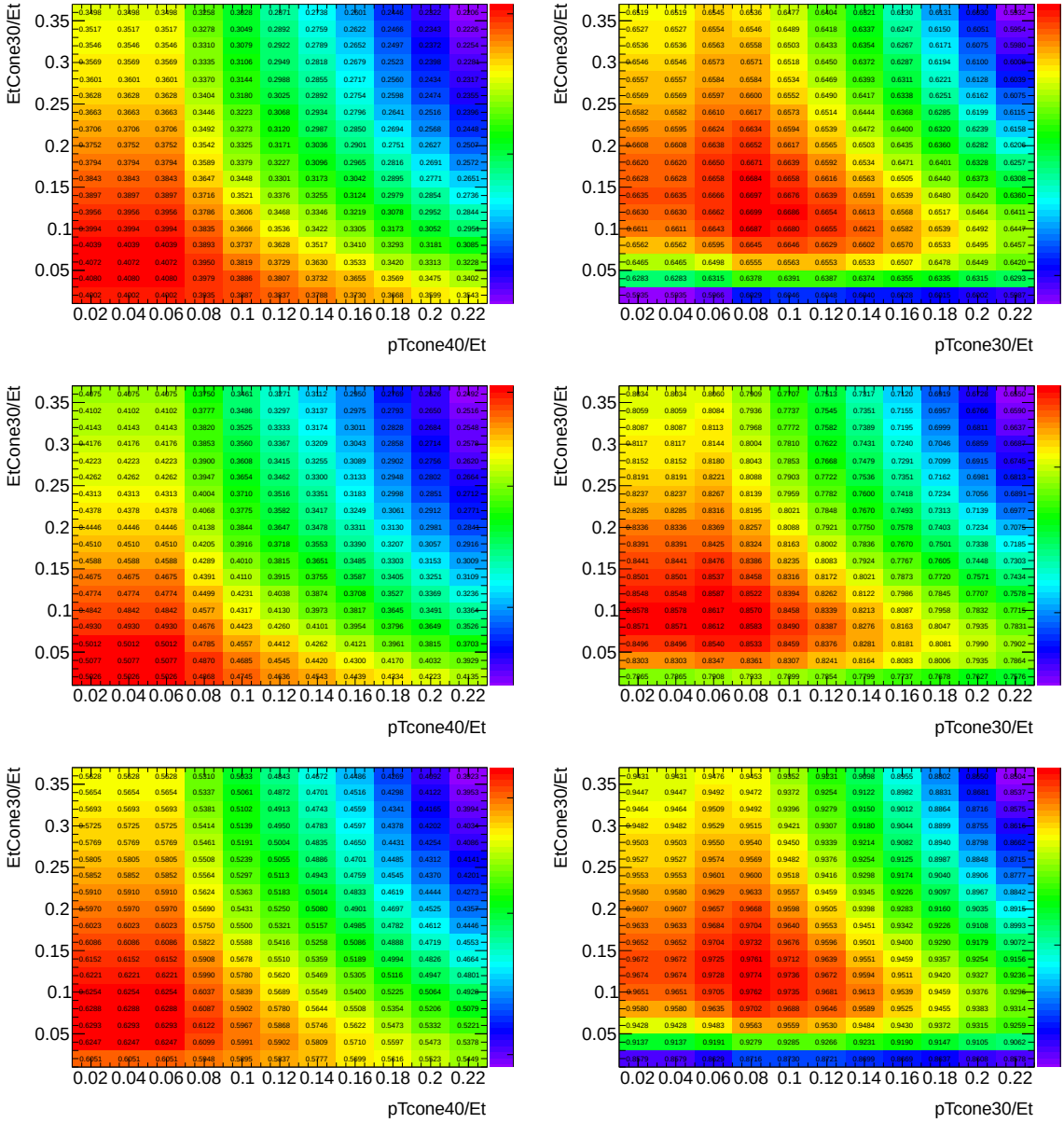

Figure 4.18: Step-by-step isolation optimization: isolation map at the first step (top), at the second step (middle), and at the third step (bottom) in $e\mu$ channel. As examples, only p_{T} = 10-15 (left) and 15-20 GeV (right) are shown where the impact of the W+jets are relatively large.

4.6.2 Vertex Requirements

For muons, the d_0 significance is particularly important since it is very sensitive to muons from heavy flavor decays that make longer tail in transverse direction, and that are not rejected much by the isolations. Since those background muons are dominant source of the fake background like the W+jets, the d_0 significance needs to be tightened.

While the $z_0 \sin\theta$ is less sensitive to those background muons because the background muons do not produce longer tail on beam axis. [8] Figure 4.19 shows d_0 significance and $z_0 \sin\theta$ distributions after the isolations, where red and blue solid lines are real and background muons, respectively.

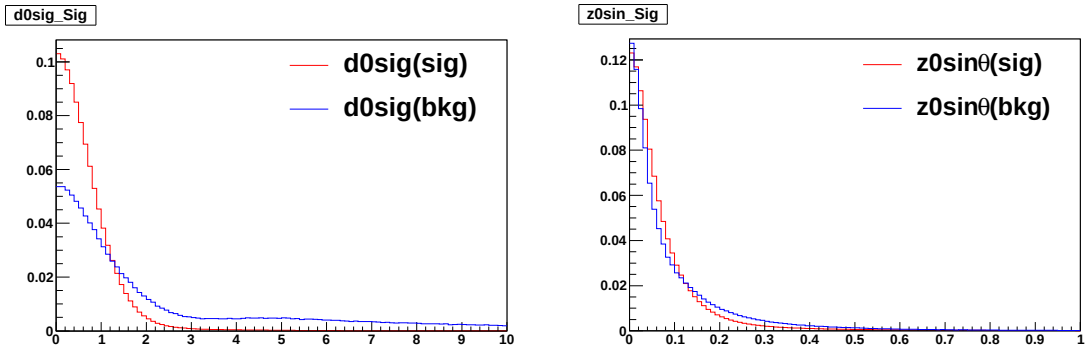

Figure 4.19: d_0 significance and $z_0 \sin\theta$ after isolation cuts. Red and blue solid lines are real and background muons, respectively. Even after the isolations, d_0 is still sensitive to muons from heavy flavor decays, while $z_0 \sin\theta$ is less sensitive to those backgrounds.

The muon vertexing parameters are also optimized. In order to take into account the correlation between the impact parameters and isolations, the optimization is made just after isolation cuts. Figure 4.20 is the result of the optimization.

The optimization suggests that d_0 significance is very sensitive in the analysis, while the analysis is less sensitive to the $z_0 \sin\theta$. For the z_0, the looser operating point ($|z_0 \sin\theta| < 1$ mm) than the electron's one is taken as a cut value. A summary of impact parameter cuts is also found in Table 4.11.

4.7 Additional Selection Efficiency

After evaluating the identification efficiency, the efficiency for all additional selections that are specific for each physics analysis, is also measured using the Z tag-and-probe. The

[8] Strictly speaking, secondaries make longer tails in both transverse and beam direction but it is harder to discriminate the secondaries from primary particles using z_0 impact parameter.

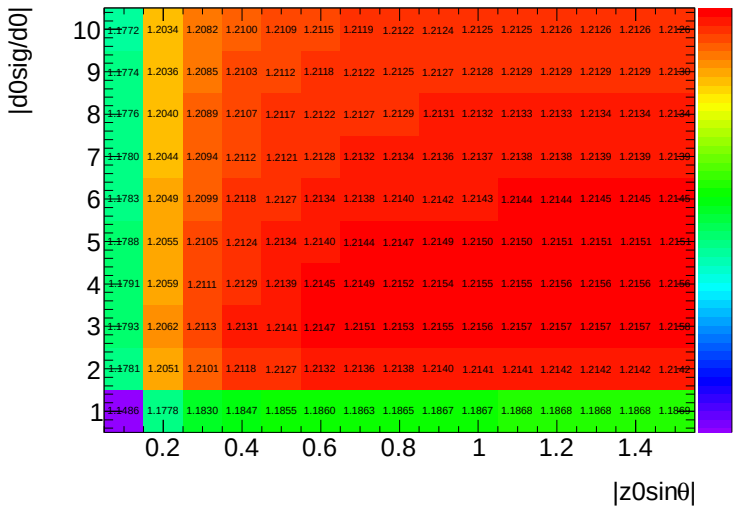

Figure 4.20: Significance in 2-dimensional map of vertexing parameters for muons.

efficiency can be written as follows:

$$\epsilon_{\text{add.}}^{\text{data}} = \frac{N_{\text{rec.+id.+add.}}^{\text{data}} - N_{\text{rec.+id.+add.}}^{\text{bkg}}}{N_{\text{rec.+id.}}^{\text{data}} - N_{\text{rec.+id.}}^{\text{bkg}}}, \tag{4.17}$$

$$\epsilon_{\text{add.}}^{\text{MC}} = \frac{N_{\text{rec.+id.+add.}}^{\text{MC}}}{N_{\text{rec.+id.}}^{\text{MC}}}, \tag{4.18}$$

where $N_{\text{rec.+id.}}$ is the number of denominators and $N_{\text{rec.+id.+add.}}$ is the number of numerators. The identification must be required for both the numerator and denominator to take into account the correlation between the identification and additional selection when measuring the efficiency for the additional selection. As is done for the identification, the scale factor is also evaluated as a function of p_{T} to correct for possible mis-modeling in simulation.

4.7.1 Electron isolation and vertexing parameter

For electrons, the followings are considered as additional selection:

- calorimeter isolation (topoEtcone30/E_{T})
- track isolation (Ptcone40/p_{T} for 10-15 GeV and Ptcone30/p_{T} for $p_{\text{T}} > 15$ GeV)
- longitudinal impact parameter ($|z_0 \sin\theta| < 0.4$ mm)
- transverse impact parameter significance ($|d_0/\sigma_{d_0}| < 3$)

- conversion flag and B-Layer hits at $2.37 < |\eta| < 2.47$ for $p_{\mathrm{T}} > 25$ GeV (see Section 4.5.1),

Figure 4.21 shows comparison of data and simulation in isolation distributions. The overall agreement looks reasonable except for lower tail of the calorimeter isolation. Given that the calorimeter isolation cut is made at higher tail (topoEtcone30/E_{T}< 0.20 or higher depending on E_{T}), the difference in efficiency between data and simulation ends up small but the small mis-modeling is corrected for by scale factor.

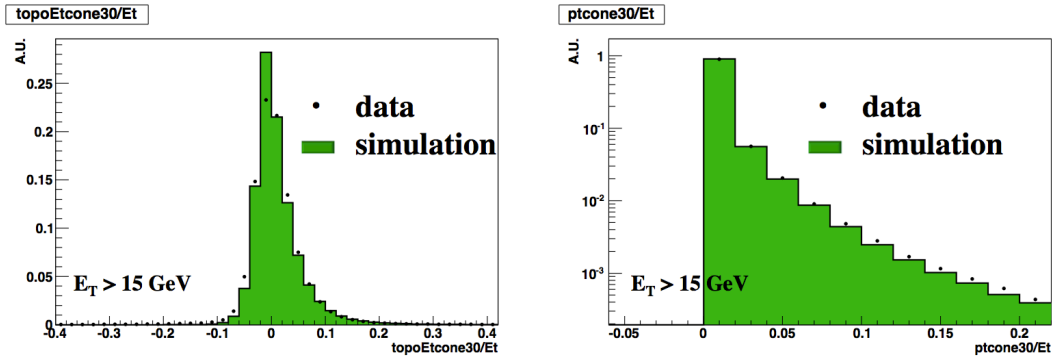

Figure 4.21: Comparison of calorimeter isolation (left) and track isolation (right) distributions between data and simulation. Both data and simulation are collected with Z tag-and-probe method, and are normalized to unit area.

Figure 4.22 shows invariant mass m_{ee} (tag and probe pairs) distributions with probe p_{T} = 10-15 GeV after the identification where the background is modeled with same sign events as defined in Section 4.3.1. Even for denominator samples, the background contamination is less than 3 %. The contamination remains much smaller (∼0.5 %) in the numerator.

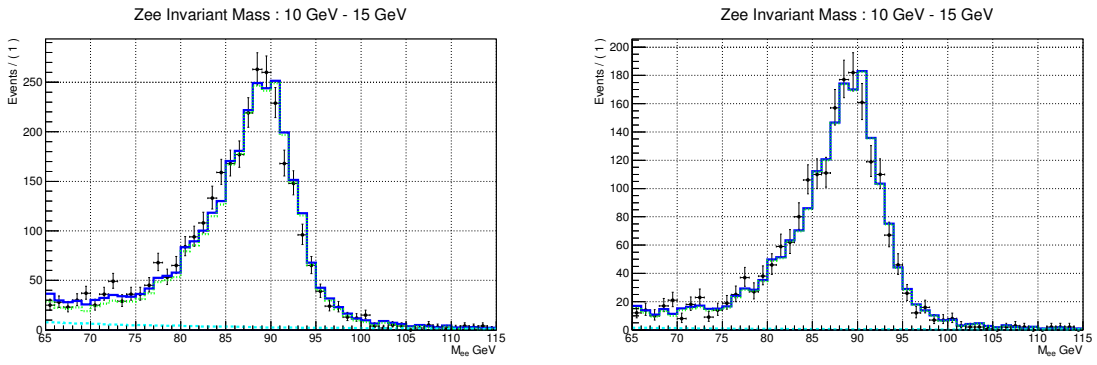

Figure 4.22: Invariant mass m_{ee} distributions with probe p_{T} = 10-15 GeV before (left) and after (right) passing all additional selections. Here green and light blue line show expected signal and background, respectively.

Figure 4.23 shows the efficiency and corresponding scale factor. In overall, the efficiency is well modeled in simulation, which results in less than 2 % deviation from unity on the scale factor. The bump at $p_{\mathrm{T}} = 25$ GeV is due to the requirements of conversion flag and B-Layer hits at $2.37 < |\eta| < 2.47$ for $p_{\mathrm{T}} > 25$ GeV (see Section 4.5.1). To assess the uncertainty on the scale factor, two systemtic uncertainties are considered:

- Z mass range is varied to be wider $|m_Z - m_{ee}| < 20$ GeV and to be narrower $|m_Z - m_{ee}| < 5$ GeV to see the background fluctuation that is $\lesssim 1$ % effect.
- pileup dependence is also evaluated by varying $< \mu >$ ($< \mu > \geq 20$ and $< \mu > < 20$). The vertexing parameter resolution is expected to decrease with increased pileups. Also isolation energy is expected to increase with higher pileups.

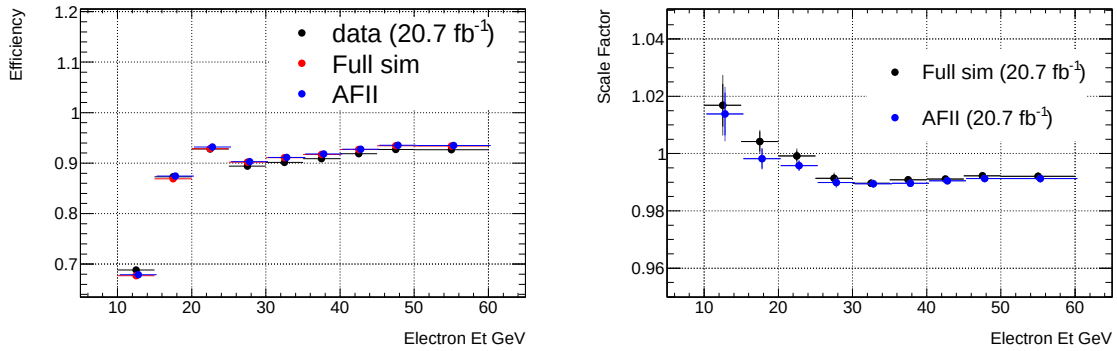

Figure 4.23: Electron efficiency for all the additional selections (left) and corresponding scale factors (right) as a function of p_{T}. Conversion bit and B-Layer requirements are also taken into account above 25 GeV.

Table 4.12 summarizes the uncertainties on the scale factor for individual components.

Table 4.12: Electron additional selection scale factor and corresponding uncertainties.

E_{T}	scale factor	stat.	bkg variation	pile-up
10-15	1.0169	0.0075	0.0106	0.0090
15-20	1.0042	0.0035	0.0040	0.0070
20-25	0.9992	0.0018	0.0026	0.0070
25-30	0.9914	0.0014	0.0020	0.0060
30-35	0.9897	0.0010	0.0013	0.0050
35-40	0.9908	0.0008	0.0009	0.0050
40-45	0.9911	0.0007	0.0009	0.0050
45-50	0.9922	0.0009	0.0011	0.0050

4.7.2 Muon isolation and vertexing parameter

For muons, the followings are considered as additional selection:

- calorimeter isolation (Etcone30/E_{T})
- track isolation (Ptcone40/p_{T} for 10-15 GeV and Ptcone30/p_{T} for $p_{\mathrm{T}} > 15$ GeV)
- longitudinal impact parameter ($|z_0 \sin\theta| < 1.0$ mm)
- transverse impact parameter significance ($|d_0/\sigma_{d_0}| < 3$)

Figure 4.24 shows invariant mass $m_{\mu\mu}$ (tag and probe pairs) distributions with probe p_{T}= 10-15 GeV after the identification where the background is modeled with same sign events as well. For denominator samples, the background contamination is less than 1 % and is smaller for numerator samples.

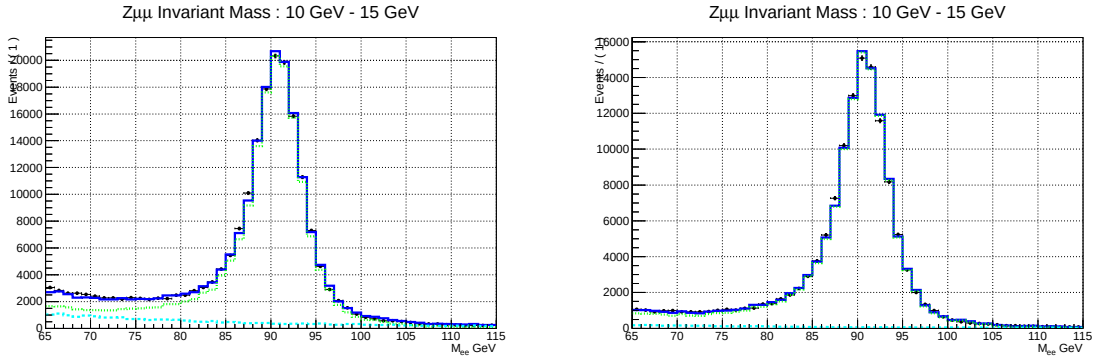

Figure 4.24: Invariant mass $m_{\mu\mu}$ distributions with probe p_{T} = 10-15 GeV before (left) and after (right) passing all additional selections. Here green and light blue line show expected signal and background, respectively.

Figure 4.25 shows the efficiency and corresponding scale factor. In overall, the efficiency is well modeled in simulation except for the lowest p_{T} muons. This is due to the mis-modeling of the calorimeter isolation. The systematic uncertainty is evaluated in the same way as is done for electrons, and is summarized in Table 4.13.

4.8 Summary of Lepton Selection and Uncertainties

4.8.1 Electron Selection and Efficiency

The optimized electron definition used in the analysis is summarized in Tables 4.14.

The efficiency for electrons that pass all the optimized selection criteria, with respect to truth electrons from the Higgs signal sample, is shown in Figure 4.26. The overall efficiency is $\sim$ 70 %. Finally all electron systematics that are relevant to the analysis are summarized in Table 4.15.

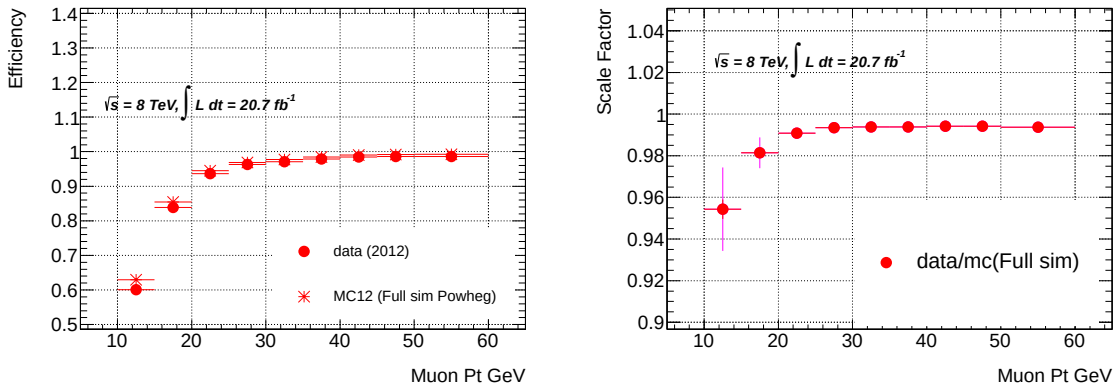

Figure 4.25: Muon efficiency for all the additional selections (left) and corresponding scale factors (right) as a function of p_{T}.

Table 4.13: Muon additional cuts scale factor and corresponding uncertainties.

p_{T}	scale factor	stat.	bkg variation	pile-up
10-15	0.9543	0.0046	0.0221	0.0100
15-20	0.9814	0.0023	0.0074	0.0090
20-25	0.9909	0.0010	0.0023	0.0060
25-30	0.9934	0.0005	0.0008	0.0050
30-35	0.9939	0.0004	0.0007	0.0050
35-40	0.9938	0.0003	0.0005	0.0050
40-45	0.9941	0.0002	0.0003	0.0050
45-50	0.9942	0.0002	0.0003	0.0050

Table 4.14: Electron selection as a function of E_{T}. ΔR for isolations is set to be 0.3, except for track isolation for 10-15 GeV in which $\Delta\mathrm{R} = 0.4$ is used. "CBL" refers to the conversion flag and B-Layer hit requirements extended to all η (within the electron acceptance coverage).

E_{T} GeV	PID	Cal Iso (ΔR<0.3)	Trk Iso (ΔR<0.3)	Vertex
10-15	Very Tight LH	$\Sigma E_{\mathrm{T}}^{\mathrm{cal}}/E_{\mathrm{T}} < 0.20$	$\Sigma p_{\mathrm{T}}^{\mathrm{trk}}/E_{\mathrm{T}} < 0.06$	$d_0/\sigma_{d_0} < 3.0$, $z_0 \sin\theta < 0.4$ mm
15-20		$\Sigma E_{\mathrm{T}}^{\mathrm{cal}}/E_{\mathrm{T}} < 0.24$	$\Sigma p_{\mathrm{T}}^{\mathrm{trk}}/E_{\mathrm{T}} < 0.08$	
20-25		$\Sigma E_{\mathrm{T}}^{\mathrm{cal}}/E_{\mathrm{T}} < 0.28$	$\Sigma p_{\mathrm{T}}^{\mathrm{trk}}/E_{\mathrm{T}} < 0.10$	
> 25	Medium++ with "CBL"			

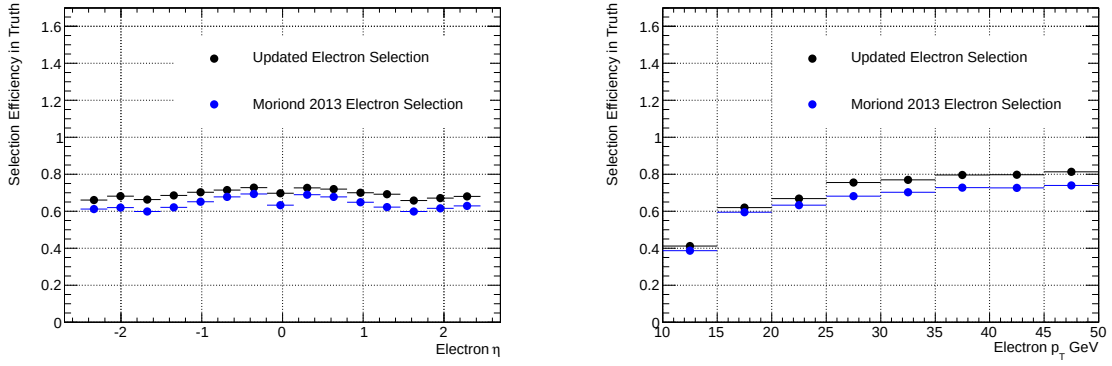

Figure 4.26: Electron selection efficiencies with respect to truth electrons for a 125 GeV Higgs signal versus η (left) and p_T (right). Only statistical uncertainty is shown.

Table 4.15: Updated electron selection efficiencies and total uncertainties (relative) for a 125 GeV Higgs signal sample. All uncertainties are added in quadrature. (Not included energy scale and resolution).

E_{T}	Total eff.	Iso. unc.	ID+Rec. unc.	Total unc.
10-15	0.412	0.016	0.016	0.022
15-20	0.619	0.009	0.024	0.025
20-25	0.668	0.008	0.027	0.028
25-30	0.755	0.007	0.014	0.016
30-35	0.770	0.007	0.005	0.009
35-40	0.796	0.006	0.003	0.007
40-45	0.798	0.006	0.002	0.006
45-	0.813	0.006	0.002	0.006

4.8.2 Muon Selection and Efficiency

The optimized muon definition used in the analysis is summarized in Tables 4.16.

Table 4.16: Muon selection as a function of p_{T}. ΔR for isolations is set to be 0.3, except for track isolation for 10-15 GeV in which $\Delta\mathrm{R} = 0.4$ is used.

p_{T} GeV	Cal Iso	Trk Iso	IP
10-15	$\Sigma E_{\mathrm{T}}^{\mathrm{cal}}/p_{\mathrm{T}} < 0.06$	$\Sigma p_{\mathrm{T}}^{\mathrm{trk}}/p_{\mathrm{T}} < 0.06$	$d_0/\sigma_{d_0} < 3.0$, $z_0 \sin\theta < 1.0$ mm
15-20	$\Sigma E_{\mathrm{T}}^{\mathrm{cal}}/p_{\mathrm{T}} < 0.12$	$\Sigma p_{\mathrm{T}}^{\mathrm{trk}}/p_{\mathrm{T}} < 0.08$	
20-25	$\Sigma E_{\mathrm{T}}^{\mathrm{cal}}/p_{\mathrm{T}} < 0.18$	$\Sigma p_{\mathrm{T}}^{\mathrm{trk}}/p_{\mathrm{T}} < 0.12$	
> 25	$\Sigma E_{\mathrm{T}}^{\mathrm{cal}}/p_{\mathrm{T}} < 0.30$		

The efficiency for muons that pass all the optimized selection criteria, with respect to truth muons from the Higgs signal sample, is shown in Figure 4.27. The overall efficiency is ~ 70 %. Finally all electron systematics that are relevant to the analysis are summarized in Table 4.17.

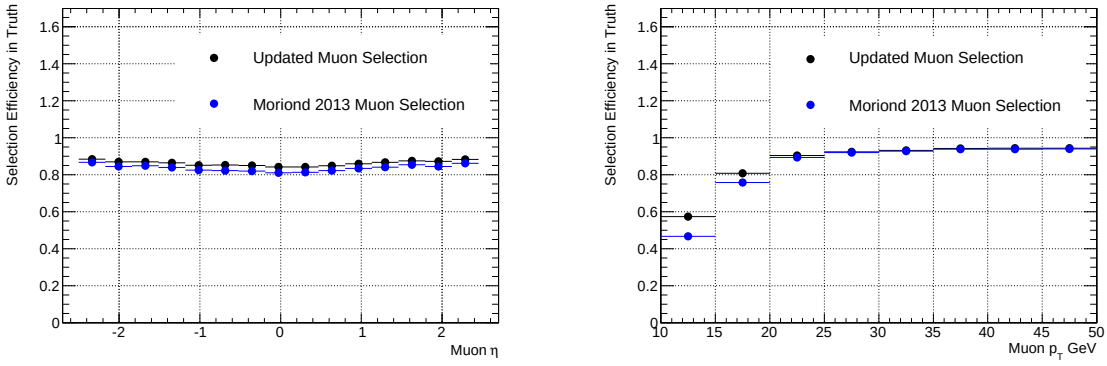

Figure 4.27: Muon selection efficiencies with respect to truth muons for a 125 GeV Higgs versus η (left) and p_{T} (right). Only statistical uncertainty is shown.

Table 4.17: Updated muon selection efficiencies and total uncertainties (relative) for a 125 GeV Higgs signal sample. All uncertainties are added in quadrature. (Not included energy scale and resolution).

p_{T}	Total eff.	Iso. unc.	ID+Rec. unc.	Total unc.
10-15	0.574	0.027	< 0.005	< 0.027
15-20	0.808	0.012	< 0.005	< 0.013
20-25	0.904	0.007	< 0.005	< 0.009
25-30	0.924	0.006	< 0.005	< 0.008
30-35	0.932	0.006	< 0.005	< 0.008
35-40	0.942	0.005	< 0.005	< 0.007
40-45	0.943	0.005	< 0.005	< 0.007
45-	0.944	0.005	< 0.005	< 0.007

Part II

Analysis for the Measurement of the Higgs Boson Couplings

Chapter 5

$H \to WW^* \to \ell\nu\ell\nu$ Analysis

The $H \to WW^* \to \ell\nu\ell\nu$ ($\ell = e, \mu$) analysis is particulary sensitive to the coupling measurement via gluon fusion (ggF) and vector boson fusion (VBF) production processes. This is due to: (1) the second largest branching fraction to WW^* for the SM Higgs boson with a mass of $m_H = 125$ GeV, and (2) the dilepton decay mode of the W pair ($WW \to \ell\nu\ell\nu$) that occurs in 5 % of WW events, allows Higgs candidates to be identified with a good (10 % or better) signal-to-background ratio (S/B).

In this chapter the overview of the $H \to WW^* \to \ell\nu\ell\nu$ analysis is presented starting from signature of $H \to WW^* \to \ell\nu\ell\nu$ and analysis classification as an "Introduction (Section 5.1)". After the introduction, the following topics are discussed: "Analysis Strategy (Section 5.2)", "Monte Carlo Simulation (Section 5.3)", "Event Selection (Section 5.4)", "Background Estimation (Section 5.5)", and "Systematic Uncertainties (Section 5.6)". Since the modeling of the W+jets background is different from other backgrounds, the W+jets background is separately discussed in next Chapter 6. Furthermore the diboson (other VV) backgrounds are also discussed separately after the W+jets background in Chapter 7 as the modeling of the diboson backgrounds is deeply related to the W+jets background.

5.1 Introduction

A typical signature of the $H \to WW^* \to \ell\nu\ell\nu$ for the ggF and VBF production processes is illustrated in Figure 5.1. Regardless of the Higgs boson production processes, the signature contains two genuine isolated high p_{T} leptons from W boson decays and a large missing transverse energy ($E_{\mathrm{T}}^{\mathrm{miss}}$) from two neutrinos in the final state. In the ggF production process, there is no jet in the final state in the leading order (LO) but possibly there is one jet (or two jets) that arises from initial state gluon radiation. On the other hand, the VBF signature is characterized by two forward/backward jets in the final state, making a high invariant mass (m_{jj}) and a large rapidity gap (Δy_{jj}) as illustrated in Figure 5.2.

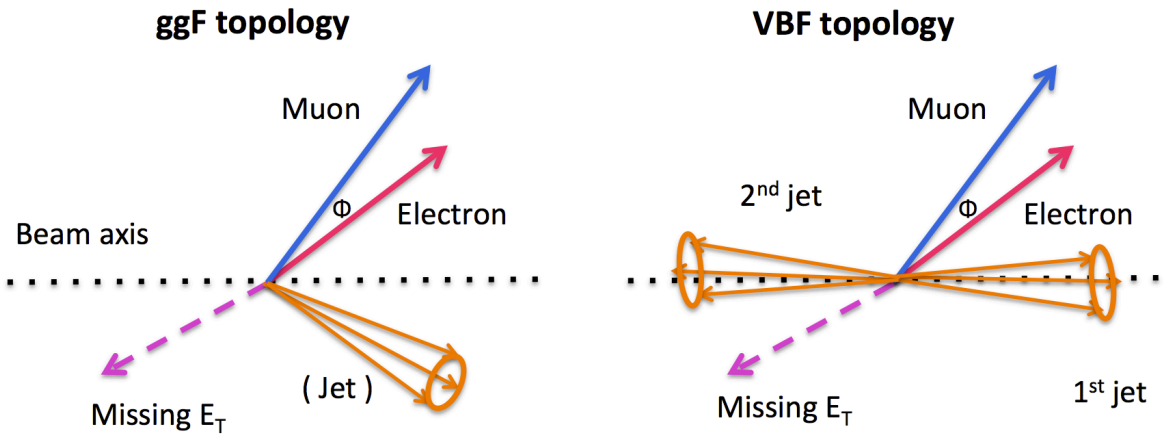

Figure 5.1: Typical signature of the Higgs boson in the $H \to WW^* \to \ell\nu\ell\nu$ analysis. Two genuine high p_{T} leptons and large $E_{\mathrm{T}}^{\mathrm{miss}}$ in the $WW \to \ell\nu\ell\nu$ final state. The left is topology of the ggF process where one jet can arise from initial state gluon radiation. The right is topology of the VBF process that is characterized by two forward jets.

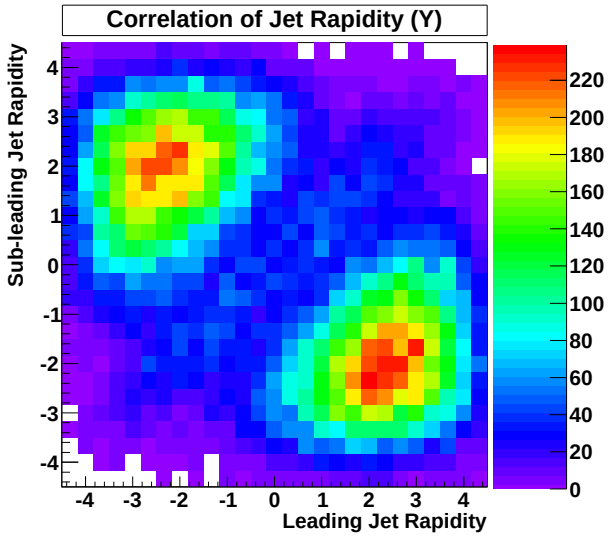

Figure 5.2: Correlation of forward/backward jets rapidities in the VBF production process.

The goal of the analysis is to measure the signal strength defined in Equation 1.17. In order to measure individual signal strengths for each production process (i.e. μ_{ggF} and μ_{VBF}), the analysis is optimized for each process by separating into bins of jet multiplicity. The 0-1 jet analysis is designed to select $H \to WW^*$ events from the ggF process. The 0-1 jet analysis is referred to in the following as "**ggF 0-jet**" and "**ggF 1-jet**" analyses. The 2-jets analysis aims at selecting $H \to WW^*$ events mainly from the VBF process while

containing some $H \to WW^*$ events from the ggF process as background (denoted as "**VBF analysis**"). Since the contribution from the ggF process remains non-negligible in the 2-jet analysis, the "**ggF 2-jets**" analysis is also defined to be orthogonal to the VBF analysis. Similarly the contribution of the VBF process remains non-negligible ($\sim 10\%$) in the ggF 1-jet analysis. The VBF 1-jet is however not treated as separated analysis but the VBF signal is profiled as one of free parameters when performing the statistical analysis (See Section 8.3.4).

In order to maximize the experimental sensitivity to the measurement, the analysis is further separated into four lepton flavor channels ($ee, \mu\mu, e\mu, \mu e$) as listed in Table 5.1, where $e\mu$ channel is defined as events that have a leading electron and a sub-leading muon, while μe channel as events that have a leading muon and a sub-leading electron.

Table 5.1: Analysis classification for 2011 and 2012 data set.

Year (luminosity)	ggF 0-jet	ggF 1-jet	ggF 2-jets	VBF ($N_{\text{jet}} \geq 2$)
2011 (4.5 fb^{-1})	$ee, \mu\mu, e\mu, \mu e$	$ee, \mu\mu, e\mu, \mu e$	-	$ee, \mu\mu, e\mu, \mu e$
2012 (20.3 fb^{-1})	$ee, \mu\mu, e\mu, \mu e$	$ee, \mu\mu, e\mu, \mu e$	$e\mu, \mu e$	$ee, \mu\mu, e\mu, \mu e$

The same flavor channel ($ee, \mu\mu$) has very different background composition from the different flavor channel ($e\mu, \mu e$). In particular the Z/DY process is significant background in the same flavor while this background remains small in the different flavor. It is also worth noting that the different flavor is further split into $e\mu$ and μe channels because the background composition and shape are different, in particular the W+jets background. In the $e\mu$ channel, the W+jets is dominated by fake muons from heavy flavor decays, whereas in the μe channel the W+jets is mainly due to fake electrons that overlapping with charged or neutral pions. One more note is that the ggF 2-jet analysis is only considered for the 2012 different flavor due to little sensitivity to the same flavor (and the 2011 analysis).

Table 5.2 summarizes expected significance to show contributions from individual analyses. The largest contribution is from the ggF 0-1 jet different flavor analysis, and the same flavor addes only $\sim 6\%$ to the sensitivity. In comparison to the ggF 0-1 jet different flavor analysis, it is also clear that the 2011 and ggF 2-jet analyses (see Appendix A) have less sensitivity. Therefore the remainder of this chapter focuses on the main analyses, namely **ggF 0-1 jet (2012)** and **VBF (2012)**.

On the other hand, the final results presented in Chapter 8 also include the remaining analyses (i.e. 2011 and ggF 2-jets) to fully exploit the sensitivity of this analysis. Adding small contributions, for example from the 2011 analysis, is particularly important for the VBF analysis, since the significance is not large enough to claim the VBF observation.

Table 5.2: Expected local significance (in sigma) based on p_0 in a given Higgs mass hypothesis $m_{\mathrm{H}} = 125$ GeV for individual analyses: different flavor (DF) and same flavor (SF) ggF 0-jet, ggF 1-jet, ggF 2-jets, and VBF analyses. The ggF 2-jets analysis is only considered for 2012 different flavor data set. The results will be presented in detail in Chapter 8.

	DF (2012)	SF (2012)	DF (2011)	SF (2011)
ggF 0-jet	3.50	1.25	1.34	0.65
ggF 1-jet	2.39	0.94	0.92	0.44
ggF 2-jet	1.25	-	-	-
VBF	2.02	1.18	0.79	0.36

Last comment on the selection of physics objects, the optimization of the physics objects is made focusing on the ggF 0-1 jet analysis due to the largest sensitivity of this analysis. In order to easily keep orthogonality across the analyses, the ggF 2-jets and VBF analyses also use the same physics objects as used in the ggF 0-1 jet analysis. This is quite important in the combination of all the analyses, otherwise it is hard to avoid any double counting of the Higgs signals.

5.2 Analysis Strategy

The analysis starts from data set with two oppositely signed leptons splitting into four lepton flavor channels ($ee, \mu\mu, e\mu, \mu e$). The missing transverse energy ($E_{\mathrm{T}}^{\mathrm{miss}}$) corresponding to the two neutrinos is then imposed, except for the VBF different flavor analysis. [1] The composition of this data set as a function of jet multiplicity (after selection requirement of the analysis-dependent missing transverse energy) is illustrated in Figure 5.3.

The background composition is strongly dependent on lepton flavor and jet multiplicity. Numerous background processes contribute to this data set, including top ($t\bar{t}$ and Wt), SM WW, $Z/\gamma^* \to \ell\ell$, WZ, $W\gamma^{(*)}$, ZZ, and W+jets/QCD. These can be grouped into categories based on the properties of the final state which allows these events to pass the signal region selection.

- The $t\bar{t}$, Wt, and SM WW have two W bosons in the final state, similar to the signal. The presence of jets, especially those tagged as b-jets, is used to discriminate against top, and properties of spin correlation are used to reduce WW.

- $Z/\gamma^* \to ee/\mu\mu$, which is relevant mostly to the same flavor analysis, has a high cross section but can be rejected through $E_{\mathrm{T}}^{\mathrm{miss}}$ and $M_{\ell\ell}$ requirements, because $E_{\mathrm{T}}^{\mathrm{miss}}$ is

[1] In the VBF different flavor analysis, no requirement of $E_{\mathrm{T}}^{\mathrm{miss}}$ is optimal because the $E_{\mathrm{T}}^{\mathrm{miss}}$ rejects a large amount of signal as well as backgrounds. One can imagine that the dominant background processes (e.g. WW and $t\bar{t}$ processes) have real $E_{\mathrm{T}}^{\mathrm{miss}}$, and the backgrounds with no $E_{\mathrm{T}}^{\mathrm{miss}}$ or softer $E_{\mathrm{T}}^{\mathrm{miss}}$ spectrum (e.g. Drell-Yan and QCD processes) are not as important in the VBF different flavor analysis.

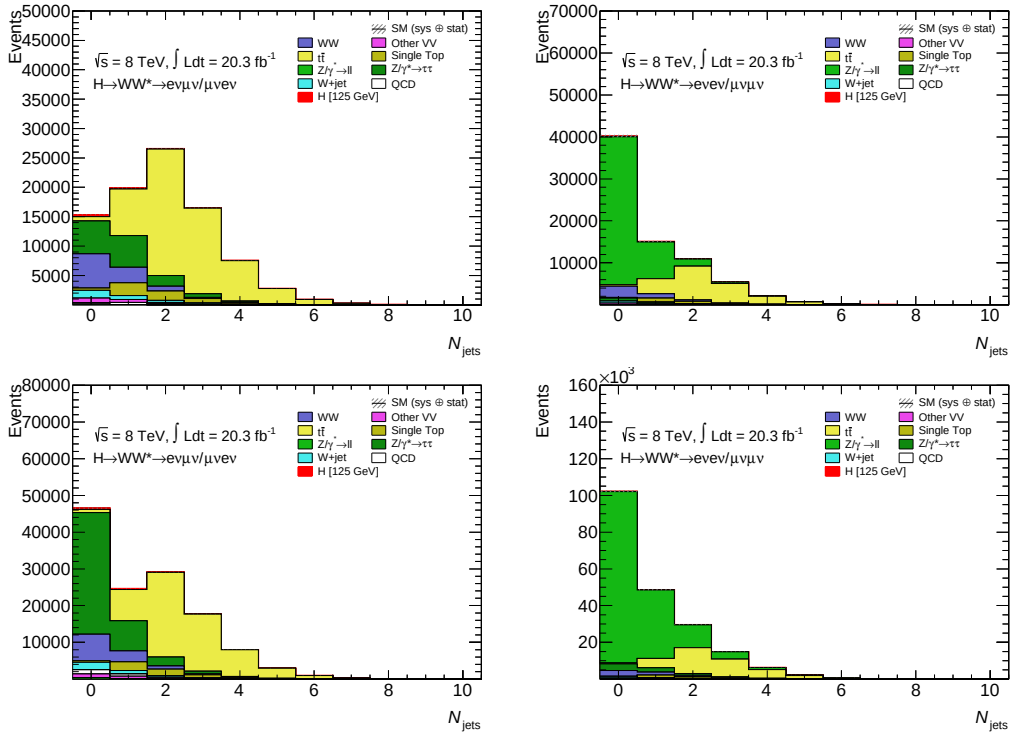

Figure 5.3: Jet multiplicity distributions after the dilepton pre-selection and analysis-specific missing transverse energy selection for the different flavor (left) and same flavor (right) lepton pairs. The top pair of plots shows the background composition for the ggF different flavor (top left) and the ggF same flavor analyses. The bottom pair shows the equivalent for the VBF analysis.

mainly produced through mis-measurement of momenta. This is primarily the effect of relatively poor resolution for soft jets and particles, which can produced by pileup interactions as well as the primary one.

- Two or more real leptons are produced by the $Z/\gamma^* \to \tau\tau$ and "Non-WW" diboson processes WZ, $W\gamma^{(*)}$, and ZZ. These have a smaller cross section but more signal-like kinematics because of their asymmetric lepton p_{T} particularly in the case of $W\gamma^{(*)}$.

- Finally W+jets/QCD also pass the signal region selection under the rare condition that a jet is misidentified as an isolated lepton. The W+jets is particularly important background since it has similar kinematics to the signal, the size of this background is large, and the uncertainty on the fake rate is large.

The lepton flavor and jet multiplicity dependent selections are applied to cope with those individual backgrounds. The main purpose of these selections is to reject a huge amount of $Z/\gamma^* \to \tau\tau$, $Z/\gamma^* \to ee/\mu\mu$ as well as top backgrounds. In the VBF analysis, for instance, several selection requirements based on the VBF specific topology (e.g. m_{jj} and

Δy_{jj}) are imposed. [2] Furthermore the selection requirements of the dilepton kinematics are imposed to deal with the largest SM WW background and to extract the signal based on spin correlations as illustrated in Figure 5.4.

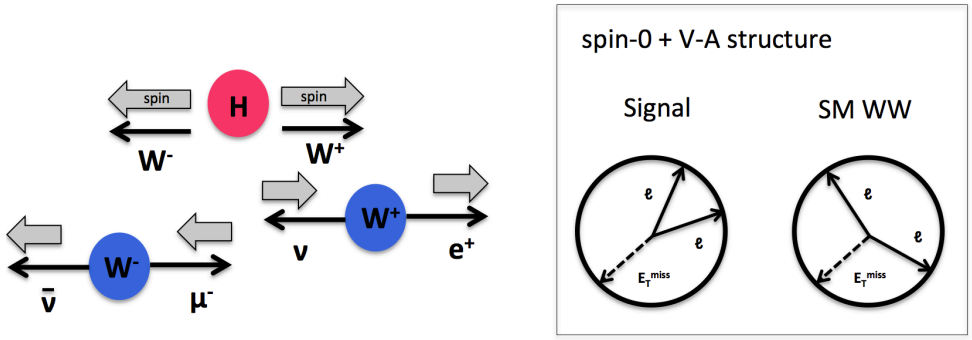

Figure 5.4: Spin correlation in the $(H \to)WW^*$ system. The two leptons from the Higgs boson tend to make small lepton angle due to angular momentum (or helicity) conservation, while the two leptons from the SM WW process tend to make larger angle.

In comparison to the SM WW process, the two leptons from the signal tend to make smaller opening angle due to the fact that the Higgs boson is a spin-0 particle [88]. The spin-0 particle produces correlations between the two leptons based on V-A structure of electroweak interaction in the WW^* system leading the two leptons in the same direction. Hence certain cuts on the dilepton kinematics such as those $\Delta\phi_{\ell\ell}$ and $m_{\ell\ell}$ can descriminate the signal from the continuum SM WW background efficiently. The comparison of signal and SM WW in $\Delta\phi_{\ell\ell}$ distribution is illustrated in Figure 5.5. The signal tends to have small $\Delta\phi_{\ell\ell}$, whereas the SM WW does not.

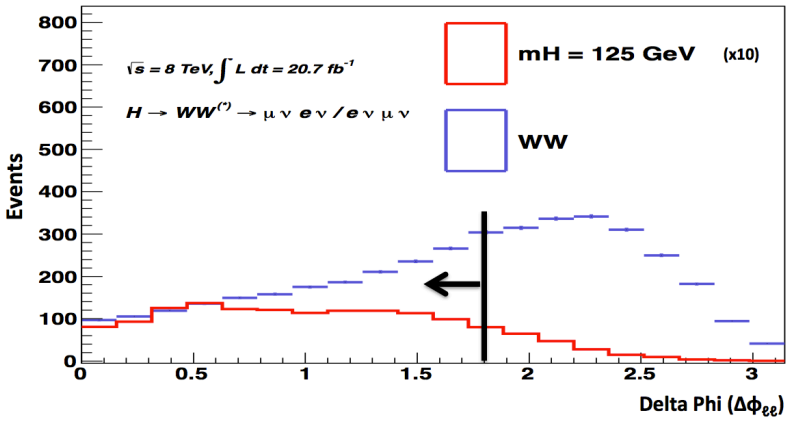

Figure 5.5: Comparison of $\Delta\phi_{\ell\ell}$ distributions between the signal (red) and SM WW (blue). Spin correlation in the $(H \to)WW^*$ system leads to small opening angle in $\Delta\phi_{\ell\ell}$.

[2] Strictly, the m_{jj} and Δy_{jj} are not imposed but are used as input variables of the BDT analysis.

Due to the presence of the two neutrinos in the final state and worse energy resolution of the missing transverse energy compared to leptons or photons, it is difficult to make a narrow peak of the Higgs boson from decay products. Instead of invariant mass, transverse mass of the dilepton system (m_{T}) that also have mass information, is used as a final discriminant to extract the signals. The m_{T} [89] is defined as:

$$m_{\mathrm{T}} = \sqrt{(E_{\mathrm{T}}^{\ell\ell} + E_{\mathrm{T}}^{\mathrm{miss}})^2 - |\boldsymbol{p}_{\mathrm{T}}^{\ell\ell} + \boldsymbol{E}_{\mathrm{T}}^{\mathrm{miss}}|^2}, \tag{5.1}$$

where $\boldsymbol{p}_{\mathrm{T}}^{\ell\ell}$ is vector sum of p_{T} of the two leptons, and $\boldsymbol{E}_{\mathrm{T}}^{\mathrm{miss}}$ ($E_{\mathrm{T}}^{\mathrm{miss}}$) is vector (scalar) sum of $E_{\mathrm{T}}^{\mathrm{miss}}$. Also $E_{\mathrm{T}}^{\ell\ell}$ can be rewritten as $E_{\mathrm{T}}^{\ell\ell} = \sqrt{|\boldsymbol{p}_{\mathrm{T}}^{\ell\ell}|^2 + m_{\ell\ell}^2}$ where $\boldsymbol{p}_{\mathrm{T}}^{\ell\ell}$ is p_{T} of the dilepton system.

For all the ggF analyses, m_{T} based on $\boldsymbol{p}_{\mathbf{T}}^{\mathbf{miss,\ jetCorr}}$ (see Section 3.4.2) is used as a discriminating variable. Making use of $\boldsymbol{p}_{\mathbf{T}}^{\mathbf{miss,\ jetCorr}}$ for the m_{T} improves the resolution of this observable. To obtain signal strength (μ), the m_{T} distribution is fit using the binned likelihood $\mathcal{L}$ (see Section 8.2), in which all the signal and control regions, and all the systemtatic uncertainties (experimental uncertainties and theoretical uncertainties), treated as nuisance parameters (NP), are put together.

The VBF analysis uses a Boosted Decision Trees (BDT) technique. The final signal region is defined by a cut on the BDT value, and is subdivided into bins by BDT score. The BDT analysis has a higher expected sensitivity compared to the cut-based analysis, because it can benefit from knowledge of the correlations between all variables (see Section 5.4.4). To obtain signal strength the BDT score is fit using the binned likelihood, in which all the signal and control regions as well as systematics are put together.

5.3 Monte Carlo Simulation

In this analysis many processes of the SM contribute to the signal regions as backgrounds. For the modeling of signal and backgrounds, the Monte Carlo (MC) event generators are used [154]. The MC generators are built up by a few main steps: "Hard process" and "Parton shower and Hadronization". The first step is simulating the hard process. This step is responsible for the simulation and calculation of the matrix element based on the fixed order perturbation theory. The Parton Distribution Functions (PDFs) describe partons coming into the process and the perturbation theory gives a probabilistic distribution of the outgoing partons. The second step is parton showering evolution that starts from the hard process and works downwards to a lower momentum scale at which perturbation theory breaks down, namely the lower cut-off threshold. Subsequently to the parton shower process, hadronization is simulated. The hadronization takes account of the confinement of a system of partons into hadrons, which are seen in the detector. All the MC generators used in the analysis are listed in Table 5.3. For example, "Alpgen [155]"+"Herwig [156]" denotes the generator that uses Alpgen for the hard process and Herwig for the parton shower and hadronization.

The signal production includes the dominant ggF production process, the VBF production process, and WH/ZH process. Other small contributions from the ttH and bbH are neglected. The contribution from $H \to \tau\tau$ in the signal region is explicitly investigated, and it is found to be negligible. For most processes, separate programs are used to generate the hard scattering and parton showering/hadronization. Pythia [128], Pythia8 [129] or Herwig [156] is used for the parton shower/hadronization modeling. [3] The ggF Higgs boson p_{T} spectrum in Powheg [158] is tuned to agree with the prediction from HqT [159]. Finite heavy quark mass effects in the ggF production process are also included [160].

For the background processes, the following generators are used:

- Continuum WW is modeled in Powheg. The small contribution from quark box diagram, which is not included in Powheg, is explicitly added by using gg2VV [161]. For ggF+2jet and VBF analyses, WW+jets is modeled in Sherpa because the 2nd jet in Powheg is not well modeled. The WW process with six electroweak couplings is modeled in Sherpa. This process is more important for the VBF analysis due to diagrams associated with two forward jets.

- $t\bar{t}$ process is modeled in Powheg. In 8 TeV, dilepton filter sample is generated to increase statistics, while the filter is not applied to 7 TeV sample. The relevant single-top production channels (s-channel, t-channel and Wt) are included.

- The inclusive Z/γ^* (Z/DY) process is generated with a dilepton invariant mass greater than 10 GeV. Low mass DY background is more important in this analysis because of the requirement of Z mass veto. To enhance statistics, a dilepton filter requiring at least one $p_{\mathrm{T}} > 20$ GeV lepton and two $p_{\mathrm{T}} > 7$ GeV leptons in $|\eta| < 3.0$ is imposed. Furthermore, VBF filter requiring at least two jets with $p_{\mathrm{T}} > 15$ GeV, $|\eta| < 5.0$, $m_{jj} > 200$ GeV, and $\Delta y_{jj} > 2.0$, sample is generated for VBF analysis. This QCD Z+jets is modeled in Alpgen. In addition, electroweak Z+jets process, which has no QCD coupling, is modeled in Sherpa.

- W+jets process modeled in Alpgen is only used for the evaluation of fake factor systematic uncertainties and for the subtraction from the QCD control region.

- For the $WZ^{(*)}$ and $W\gamma^*$ processes, interference between the $Z^{(*)}$ and the γ^* is included, and the boundary between the samples is at $m_{\ell\ell} = 7$ GeV. For the $W\gamma^*$, Sherpa is used with a lower invariant mass cut of $m_{\ell\ell} > 2m_{\ell}$ depending on decay of γ^*. For $WZ^{(*)}$, Powheg is used. To remove overlap with Sherpa sample, the events with $m_{Z/\gamma*} < 7$ GeV are removed from sample. A dilepton filter requiring at least two charged leptons with $p_{\mathrm{T}} > 5$ GeV and $|\eta| < 2.7$ is also applied in Powheg $WZ^{(*)}$ sample. The $Z^{(*)}Z^{(*)} \to 4\ell$ samples are modeled in Powheg and generated with an invariant mass cut of $m_{\ell\ell} > 4$ GeV. Electroweak WZ and ZZ processes with six electroweak couplings are generated in Sherpa.

[3] And the JIMMY [157] is used for the underlying event modeling.

- $W\gamma$ process is modeled in Alpgen. Kinematic criteria are also applied in the generation of $W(\to \ell\nu)\gamma$ events (the photon must have $p_{\mathrm{T}} > 8$ GeV and be separated from the charged lepton by $\Delta R > 0.25$and $W(\to \ell\nu)\gamma^*(\to \ell'\ell')$ events (at least two leptons have p_{T} larger than 5 GeV and $|\eta| < 3$ for the ee and $\mu\mu$ case, and $|\eta| < 5$ for the $\tau\tau$ case).

- $Z\gamma$ (the photon $p_{\mathrm{T}} > 7$ GeV) is generated by Sherpa.

For the Parton Distribution Function (PDF), the CT10 PDF set [162] is used for the Powheg, Sherpa and gg2VV samples, and CTEQ6L1 [163] is used for the Alpgen, AcerMC, Pythia8 and several Sherpa (in 7 TeV) samples, except for the Alpgen Z/γ^* sample that is reweighted to the MRSTMCal [164] PDF set. Acceptances and efficiencies are obtained for most processes from a full simulation [165] of the ATLAS detector using GEANT4 [166], including pileup simulation.

Table 5.3: MC generators and corresponding cross sections (given for $m_H = 125$ GeV) used to model the signal and background processes. The quoted cross section includes the branching ratio assuming the leptonic decay (e, μ, τ) of W/Z bosons.

Process	Generator	$\sigma \cdot$ Br(8TeV) (pb)	$\sigma \cdot$ Br(7TeV) (pb)
ggF $H \to WW$	Powheg [167]+Pythia8 [129]	0.435	0.341
VBF $H \to WW$	Powheg [168]+Pythia8	$36 \cdot 10^{-3}$	$28 \cdot 10^{-3}$
WH/ZH $H \to WW$	Pythia8 (Pythia6)	$25 \cdot 10^{-3}$	$21 \cdot 10^{-3}$
$q\bar{q}/g \to WW$	Powheg +Pythia6	5.68	4.68
$gg \to WW$	gg2WW [161]+Herwig [156]	0.20	0.14
QCD $WW + 2$ jets	Sherpa	0.568	-
EW $WW + 2$ jets	Sherpa	0.039	0.027
$t\bar{t}$ dileptonic	Powheg [169]+Pythia6	26.6	18.6
tW/tb leptonic	Powheg [169]+Pythia6	4.17	3.15
tqb leptonic	AcerMC [170]+Pythia6 [128]	28.4	20.7
inclusive W	Alpgen [155]+Herwig	$37 \cdot 10^3$	$31 \cdot 10^3$
inclusive $Z/\gamma^*(m_{ll} \geq 10GeV)$	Alpgen [155]+Herwig	$16.5 \cdot 10^3$	$14.9 \cdot 10^3$
EW Z/γ^*	Sherpa	5.36 (inc. t-ch)	2.26
$W(Z/\gamma^*)$	Powheg +Pythia8	12.7	10.8
$W(Z/\gamma^*)(m_{(Z/\gamma^*)} < 7$ GeV)	Sherpa	12.2	10.6
$Z^{(*)}Z^{(*)} \to 4l(2l2\nu)$	Powheg +Pythia8	0.73(0.50)	0.64(0.42)
EW $WZ + 2$ jets	Sherpa	$13 \cdot 10^{-3}$	$8.5 \cdot 10^{-3}$
EW $ZZ + 2$ jets $(4l, ll\nu\nu)$	Sherpa	$73 \cdot 10^{-5}(12 \cdot 10^{-4})$	$53 \cdot 10^{-5}(8.8 \cdot 10^{-4})$
$W\gamma$	Alpgen [155]+Herwig	369	313
$Z\gamma(p_{\mathrm{T}}^{\gamma} > 7GeV)$	Sherpa	163	-

5.4 Event Selection

5.4.1 Pre-selection

The trigger selection, object selection, and overlap removals are common for all analyses. The analysis uses single and dilepton triggers (see Section 3.1) to collect dilepton sample, and selects isolated leptons (see Section 4.8) and reconstructed jets (see Section 3.3.5) for analysis categorization. The overlap removals (see Section 6.3.3) are then required to prioritize the physics objects (lepton and jet) in case of a high proximity of two objects. The pre-selection that is also common for all analyses is applied after the overlap removals.

- exactly two opposite sign leptons,
- $p_{\mathrm{T}}^{\mathrm{lead}} > 22$ GeV, $p_{\mathrm{T}}^{\mathrm{sublead}} > 10$ GeV,
- $m_{\ell\ell} > 10$ (12) GeV for $e\mu + \mu e$ ($ee + \mu\mu$) lepton channel,
- $|m_{\ell\ell} - m_Z| > 15$ GeV for $ee + \mu\mu$,

where the lower $m_{\ell\ell}$ cut aims at rejecting low mass resonance of J/ψ and Υ decays as well as QCD background, and the fourth cut aims at rejecting $Z/\gamma^* \to \ell\ell$ resonance. After the pre-selection, the analysis-dependent $E_{\mathrm{T}}^{\mathrm{miss}}$ is imposed. Figures 5.6, 5.7, and 5.8 present the understanding of the objects after the pre-selection requirement where the backgrounds are normalized to the SM cross section. The agreement of data/SM is acceptable at this stage. The yellow band represents statistical uncertainty on simulation, the occasional discrepancies are covered by the relevant systematics which are not applicable at this stage.

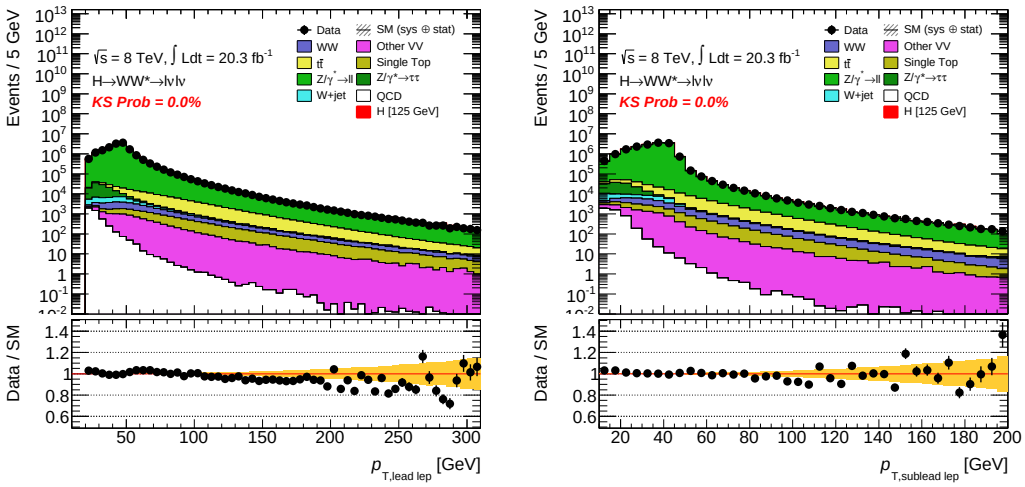

Figure 5.6: Leading lepton p_{T} (left) and sub-leading lepton p_{T} (right) after the pre-selection for all lepton flavors combined. The Data/ SM shows the ratio of data to the total background where yellow band represents the statistical uncertainty. No systematic uncertainty is displayed.

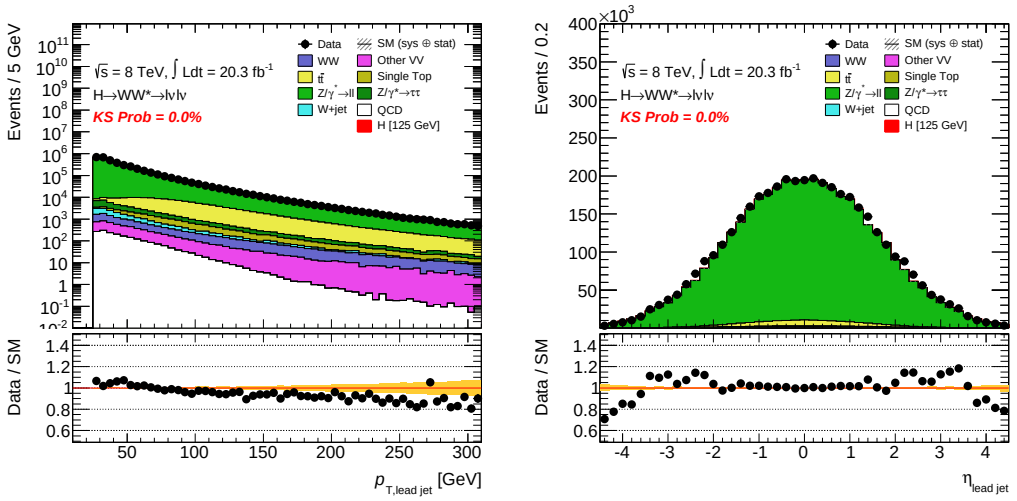

Figure 5.7: Leading jet p_{T} (left) and η (right) after the pre-selection for all lepton flavors combined. The Data/ SM shows the ratio of data to the total background where yellow band represents the statistical uncertainty. No systematic uncertainty is displayed.

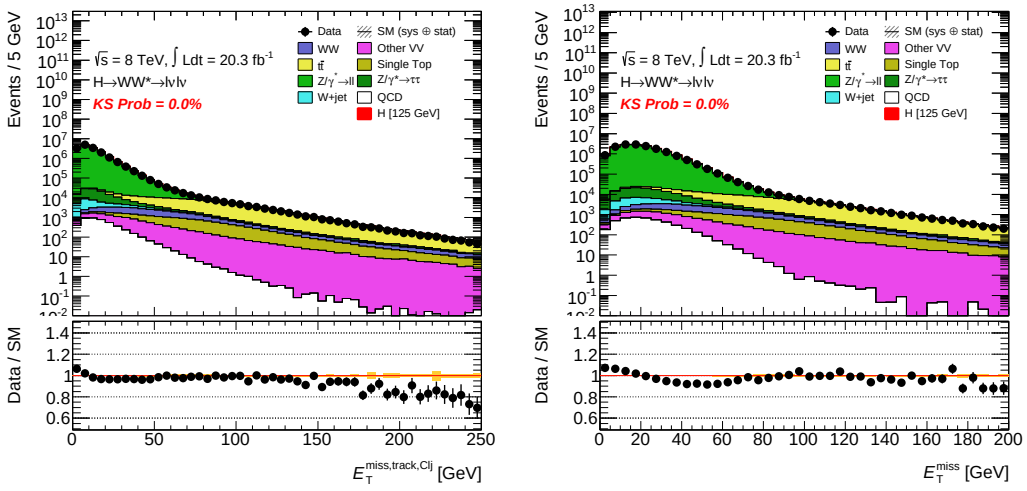

Figure 5.8: $\boldsymbol{p_{\mathrm{T}}^{\mathrm{miss,\ jetCorr}}}$ (left) and $E_{\mathrm{T}}^{\mathrm{miss}}$ (right) distributions after the pre-selection ($m_{\ell\ell}$) for all lepton flavors combined. The Data/ SM shows the ratio of data to the total background where yellow band represents the statistical uncertainty. No systematic uncertainty is displayed.

5.4.2 ggF 0-1 jet Different Flavor Selection

ggF 0-jet Different Flavor

The selection criteria in the 0-jet analysis exploit the dilepton kinematics resulting from spin correlations present in the $H\to WW^*\to \ell\nu\ell\nu$ (See Section 5.1). In addition to the pre-selection described in Section 5.4.1, the following requirements are imposed:

- $\boldsymbol{p_{\mathrm{T}}^{\mathbf{miss,\ jetCorr}}} > 20$ GeV,
- The opening angle between the dilepton system and the transverse missing energy, $\Delta\phi_{\ell\ell,E_{\mathrm{T}}^{\mathrm{miss}}}$, is required to be larger than $\pi/2$ to remove potential pathological events in which the $E_{\mathrm{T}}^{\mathrm{miss}}$ is pointing in the direction of the lepton pair (this criteria is more than 99 % efficient for signal),
- The transverse momentum of the dilepton system, $|\mathbf{p}_{\mathrm{T}}^{\ell\ell}| > 30$ GeV,
- The invariant mass of the dilepton system, $m_{\ell\ell} < 55$ GeV,
- The dilepton opening angle in the transverse plane, $\Delta\phi_{\ell\ell} < 1.8$ radians.

Figure 5.9 shows $m_{\ell\ell}$ distribution after $\mathbf{p}_{\mathrm{T}}^{\ell\ell}$ requirement and $\Delta\phi_{\ell\ell}$ distribution after $m_{\ell\ell}$ requirement. The signal has lower $m_{\ell\ell}$ and $\Delta\phi_{\ell\ell}$ due to the spin correlation. Also it is clearly presented that the $\Delta\phi_{\ell\ell}$ is a good discriminant against $Z/\mathrm{DY}\to\tau\tau$ which is the largest background after pre-selection requirement.

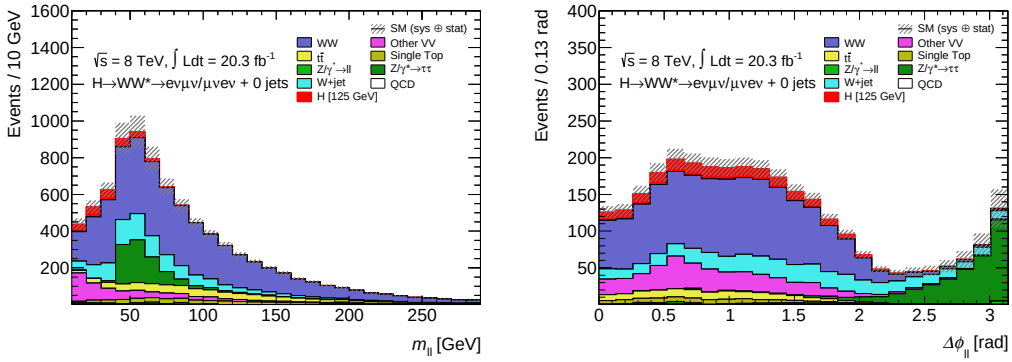

Figure 5.9: $m_{\ell\ell}$ distribution after $p_{\mathrm{T}}^{\ell\ell}$ requirement (left) and $\Delta\phi_{\ell\ell}$ distribution after $m_{\ell\ell}$ requirement (right). The signal has lower $m_{\ell\ell}$ and $\Delta\phi_{\ell\ell}$ due to the spin correlation in the $H\to WW^*\to \ell\nu\ell\nu$.

Figure 5.10 shows sub-leading lepton p_{T}, $m_{\ell\ell}$, $\Delta\phi_{\ell\ell}$, and m_{T} distributions after $\Delta\phi_{\ell\ell}$ requirement. The remaining backgrounds are dominated by the WW, non-WW dibosons (other VV), and W+jets backgrounds, and these backgrounds are strongly dependent on sub-leading lepton p_{T} and $m_{\ell\ell}$. The WW (both Ws are on-shell) tends to be in high p_{T} while the other VV and W+jets backgrounds tends to be in low p_{T} region. The other

VV and W+jets can be further separated in $m_{\ell\ell}$ since the contribution from other VV backgrounds are mostly in lower $m_{\ell\ell}$, while the W+jets background is mostly in higher $m_{\ell\ell}$, so the split in $m_{\ell\ell}$ and sub-leading lepton p_{T} helps the analysis discriminate those backgrounds efficiently. The signal region is split in $m_{\ell\ell}$ (10-30, 30-55) and $p_{\mathrm{T}}^{\mathrm{sub}}$ (10-15, 15-20, 20-) into 6 sub-regions. Figures 5.11 and 5.12 show m_{T} distributions and Table 5.4 shows expected signal and background counts for each sub-divisions (but $p_{\mathrm{T}}^{\mathrm{sub}}$ = 15-20 and 20- are combined).

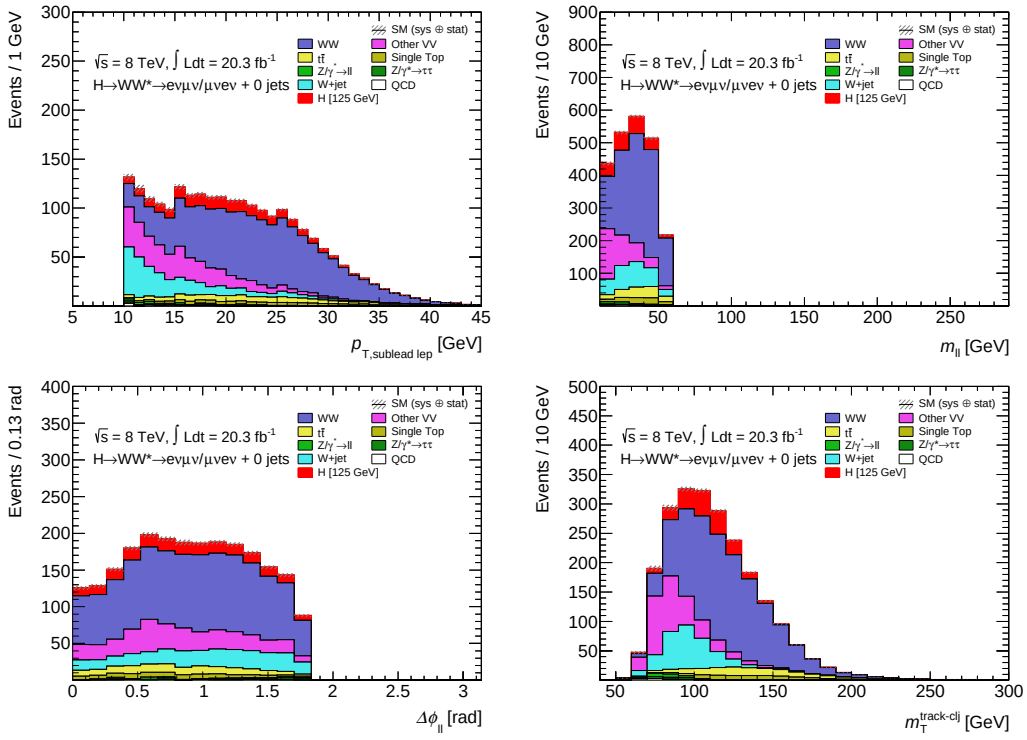

Figure 5.10: Sub-leading lepton p_{T} (top left), $m_{\ell\ell}$ (top right), $\Delta\phi_{\ell\ell}$ (bottom left), and m_{T} (bottom right) distributions after $\Delta\phi_{\ell\ell}$ requirement.

Table 5.4: Expected event counts in the 8 TeV ggF 0-jet analysis. Percentages are the fraction of the total background. The W+jets and QCD are from data-driven estimate.

	H	All Bkg.	S/B	WW	VV	$t\bar{t}$	$(W)t$	Z+jets	W+jets	QCD
$e\mu$ $m_{\ell\ell} < 30$, $p_T^{\text{sublead}} > 15$	41	330	0.125	228 (69%)	50 (15%)	18 (6%)	11 (3%)	3 (1%)	18 (5%)	0.9 (0.3%)
$e\mu$ $m_{\ell\ell} > 30$, $p_T^{\text{sublead}} > 15$	46	632	0.073	489 (77%)	33 (5%)	43 (7%)	25 (4%)	4 (1%)	35 (6%)	1.2 (0.2%)
$e\mu$ $m_{\ell\ell} < 30$, $p_T^{\text{sublead}} < 15$	14	172	0.081	54 (31%)	59 (34%)	5 (3%)	2 (1%)	4 (2%)	43 (25%)	4.3 (2.5%)
$e\mu$ $m_{\ell\ell} > 30$, $p_T^{\text{sublead}} < 15$	10	117	0.085	54 (46%)	10 (9%)	7 (6%)	4 (3%)	2 (2%)	39 (34%)	0.8 (0.7%)
μe $m_{\ell\ell} < 30$, $p_T^{\text{sublead}} > 15$	32	300	0.105	194 (65%)	57 (19%)	15 (5%)	9 (3%)	5 (2%)	21 (7%)	0.5 (0.2%)
μe $m_{\ell\ell} > 30$, $p_T^{\text{sublead}} > 15$	36	543	0.066	410 (76%)	33 (6%)	35 (6%)	20 (4%)	3 (1%)	41 (8%)	0.8 (0.1%)
μe $m_{\ell\ell} < 30$, $p_T^{\text{sublead}} < 15$	10	152	0.063	39 (25%)	64 (42%)	3 (2%)	2 (1%)	5 (3%)	40 (26%)	0.6 (0.4%)
μe $m_{\ell\ell} > 30$, $p_T^{\text{sublead}} < 15$	6	107	0.060	39 (37%)	17 (15%)	5 (4%)	2 (2%)	3 (3%)	41 (39%)	0.0 (0.0%)

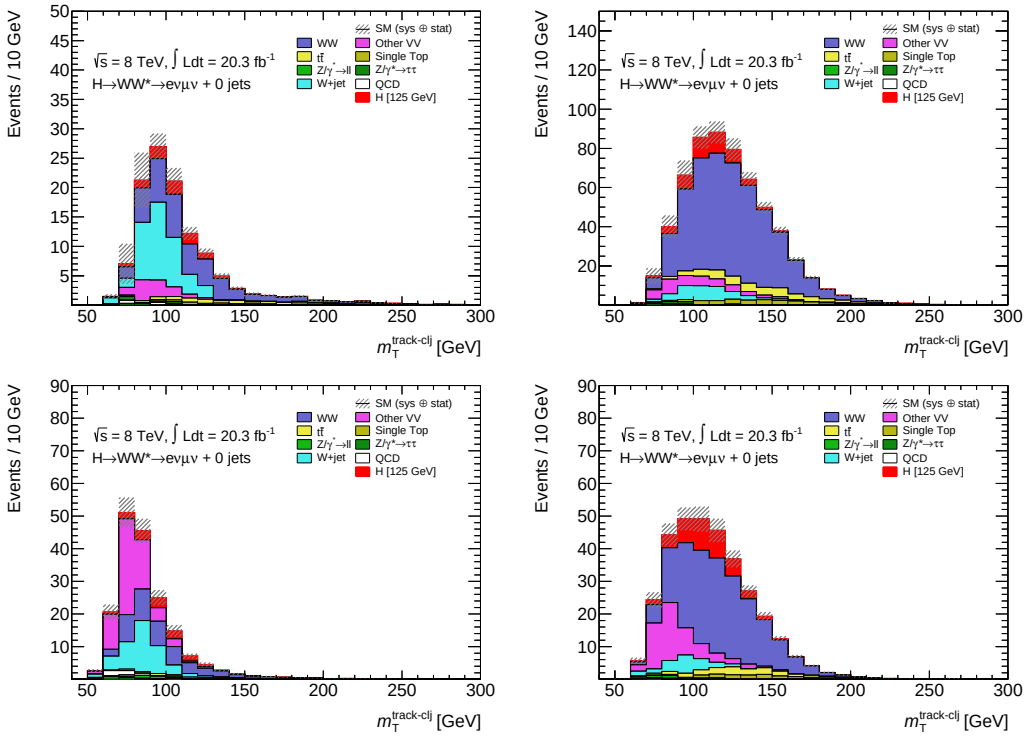

Figure 5.11: m_{T} distribution for each sub-divisions in the 0-jet $e\mu$ channel: $p_{\text{T}}^{\text{sub}}$ = 10-15 GeV and $m_{\ell\ell} > 30$ GeV (top left), $p_{\text{T}}^{\text{sub}} > 15$ GeV and $m_{\ell\ell} > 30$ GeV (top left), $p_{\text{T}}^{\text{sub}}$ = 10-15 GeV and $m_{\ell\ell} < 30$ GeV (bottom left), $p_{\text{T}}^{\text{sub}} > 15$ GeV and $m_{\ell\ell} < 30$ GeV (bottom right).

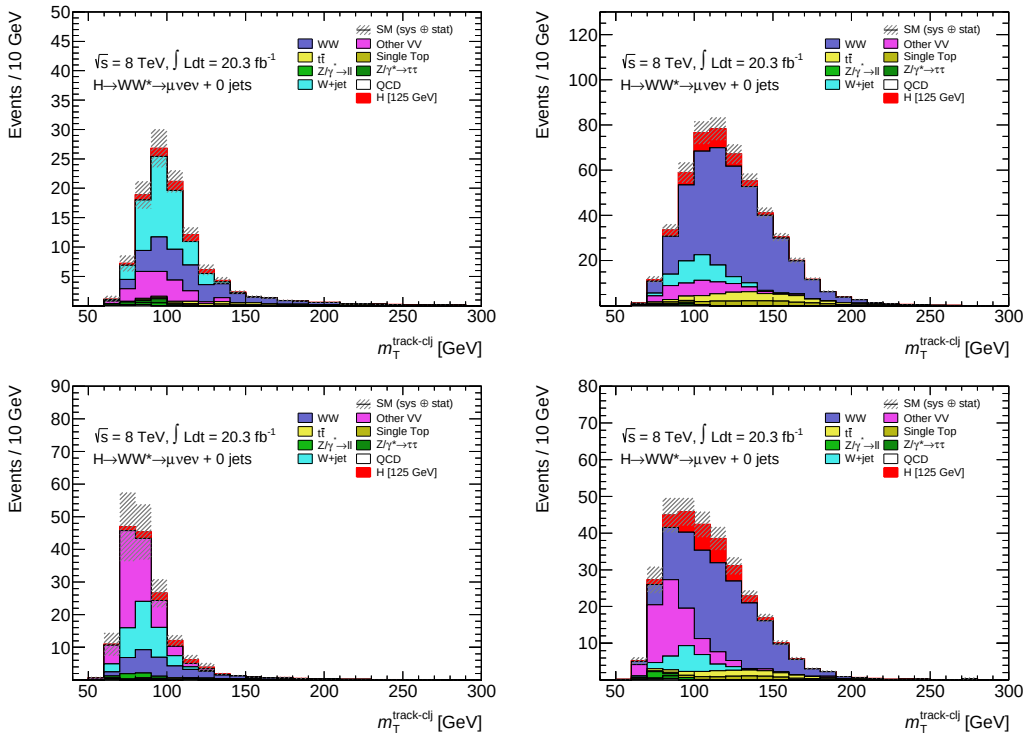

Figure 5.12: m_{T} distribution for each sub-divisions in the 0-jet μe channel: $p_{\mathrm{T}}^{\mathrm{sub}}$ = 10-15 GeV and $m_{\ell\ell} > 30$ GeV (top left), $p_{\mathrm{T}}^{\mathrm{sub}} > 15$ GeV and $m_{\ell\ell} > 30$ GeV (top left), $p_{\mathrm{T}}^{\mathrm{sub}}$ = 10-15 GeV and $m_{\ell\ell} < 30$ GeV (bottom left), $p_{\mathrm{T}}^{\mathrm{sub}} > 15$ GeV and $m_{\ell\ell} < 30$ GeV (bottom right).

ggF 1-jet Different Flavor

The selection of events satisfying the pre-selection (see Section 5.4.1) and containing exactly one selected jet is similar to the 0-jet analysis. In addition to the pre-selection, the following requirements are imposed:

- $\boldsymbol{p}_{\mathbf{T}}^{\mathbf{miss,\ jetCorr}} > 20$ GeV,
- b-jet veto: there should be no jet in the event with $p_T > 20$ GeV tagged as originating from a b-quark using the MV1 algorithm [133, 134] with an 85% efficient operating point,
- The $\tau\tau$ invariant mass, $m_{\tau\tau}$, is reconstructed using the approximation that the neutrinos are collinear with the visible products of the corresponding τ decays, and assuming that the leptons arise from $Z \to \tau\tau$ decays. If the energy fractions x_{τ_1} and x_{τ_2} carried by the putative visible decay products are positive (the collinear approximation does not always yield good solutions) and the invariant mass of the hypothetical $\tau\tau$ system satisfies $m_{\tau\tau} > m_Z - 25$ GeV, the event is rejected,
- Max $m_{\mathrm{T}}(W) > 50$ GeV [4] is required to reject the QCD and $Z/\gamma^* \to \tau\tau$ backgrounds,
- The event must pass the same cuts on $m_{\ell\ell}$ and $\Delta\phi_{\ell\ell}$ as those of the 0-jet analysis.

Figure 5.13 shows Max $m_{\mathrm{T}}(W)$ distribution after b-jet veto requirement and $\Delta\phi_{\ell\ell}$ distribution after $m_{\ell\ell}$ requirement. The $m_{\mathrm{T}}(W)$ cut removes most of the QCD background that has a large ($\sim 40\%$) uncertainty because it originates from the rare event of a jet faking a lepton. Similar to the 0-jet analysis, the signal has lower $\Delta\phi_{\ell\ell}$ due to the spin correlation.

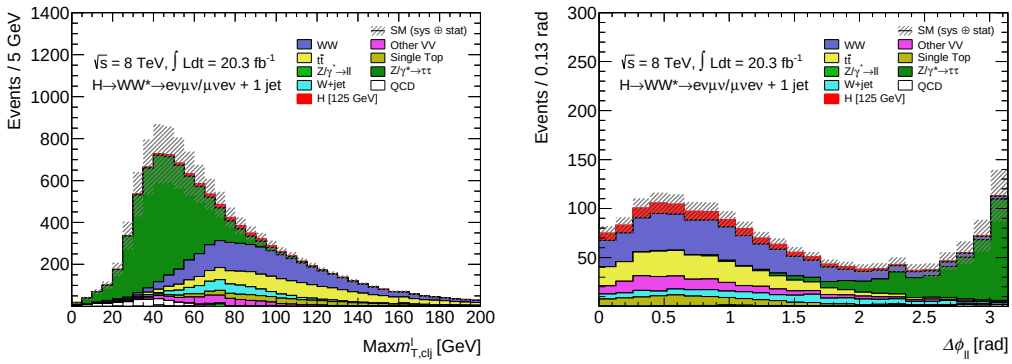

Figure 5.13: Max $m_{\mathrm{T}}(W)$ distribution after b-jet veto requirement (left) and $\Delta\phi_{\ell\ell}$ distribution after $m_{\ell\ell}$ requirement (right). The signal has lower $m_{\ell\ell}$ and $\Delta\phi_{\ell\ell}$ due to the spin correlation.

[4] The Max $m_{\mathrm{T}}(W)$ is the maximum of the two transverse masses formed with each charged lepton and the missing transverse energy. For W decays, m_{T} has a Jacobian distribution with an edge at $m_{\mathrm{T}} = m_{\mathrm{W}}$. Backgrounds such as QCD (multijet) production tend to have lower $m_{\mathrm{T}}(W)$.

Figure 5.14 shows sub-leading lepton p_{T}, $m_{\ell\ell}$, $\Delta\phi_{\ell\ell}$, and m_{T} distributions after $\Delta\phi_{\ell\ell}$ requirement. In comparison to the 0-jet analysis, the top backgrounds are larger, otherwise the background composition is similar to the 0-jet analysis. Similar to the 0-jet analysis, the signal region is split in $m_{\ell\ell}$ (10-30, 30-55) and $p_{\mathrm{T}}^{\mathrm{sub}}$ (10-15, 15-20, 20-25) into 6 sub-regions. Figures 5.15 and 5.16 show m_{T} distributions and Table 5.5 shows expected signal and background counts for each sub-divisions (but $p_{\mathrm{T}}^{\mathrm{sub}}$ = 15-20 and 20- are combined).

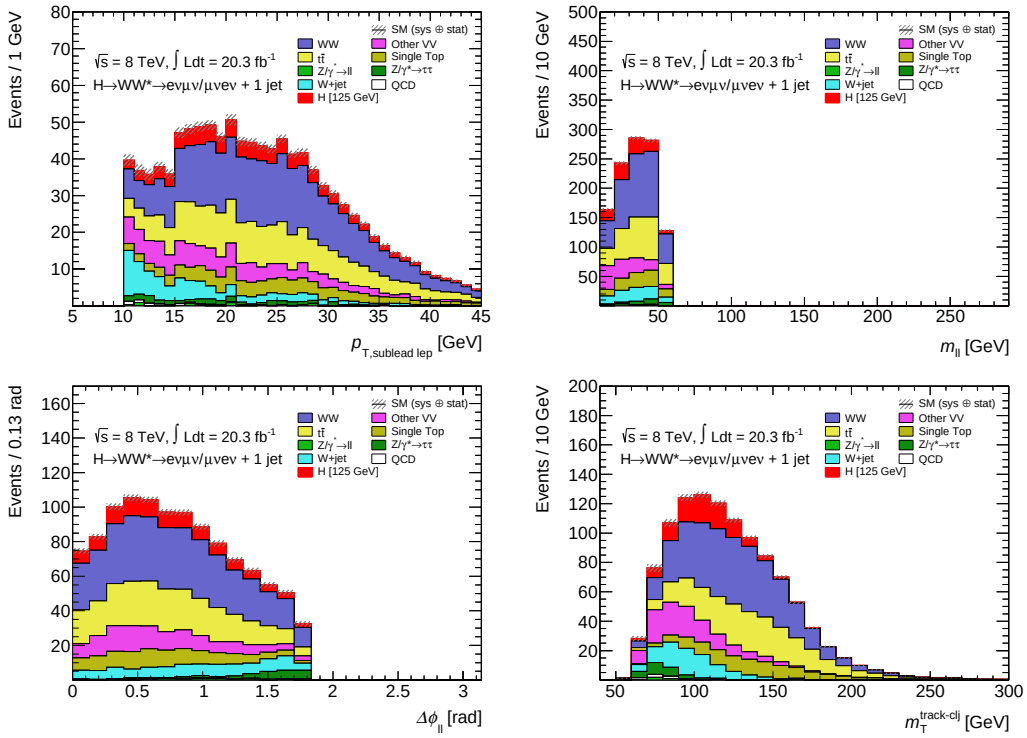

Figure 5.14: Sub-leading lepton p_{T} (top left), $m_{\ell\ell}$ (top right), $\Delta\phi_{\ell\ell}$ (bottom left), and m_{T} (bottom right) distributions after $\Delta\phi_{\ell\ell}$ requirement.

Table 5.5: Expected event counts in the 8 TeV ggF 1-jet analysis. Percentages are the fraction of the total background. The W+jets and QCD are from data-driven estimate.

	H	All Bkg.	S/B	WW	VV	$t\bar{t}$	$(W)t$	Z+jets	W+jets	QCD
$e\mu$ $m_{\ell\ell} < 30$, $p_T^{\mathrm{sublead}} > 15$	21	151	0.140	64 (42%)	23 (15%)	38 (25%)	15 (10%)	1 (0%)	10 (6%)	0.7 (0.5%)
$e\mu$ $m_{\ell\ell} > 30$, $p_T^{\mathrm{sublead}} > 15$	25	309	0.081	144 (47%)	19 (6%)	86 (28%)	33 (11%)	9 (3%)	17 (5%)	0.9 (0.3%)
$e\mu$ $m_{\ell\ell} < 30$, $p_T^{\mathrm{sublead}} < 15$	5	47	0.113	13 (27%)	11 (23%)	8 (17%)	3 (6%)	2 (3%)	9 (20%)	1.7 (3.6%)
$e\mu$ $m_{\ell\ell} > 30$, $p_T^{\mathrm{sublead}} < 15$	4	51	0.073	16 (31%)	4 (8%)	11 (22%)	4 (8%)	3 (6%)	11 (22%)	1.1 (2.1%)
μe $m_{\ell\ell} < 30$, $p_T^{\mathrm{sublead}} > 15$	17	133	0.132	56 (42%)	24 (18%)	31 (23%)	12 (9%)	2 (1%)	8 (6%)	0.5 (0.4%)
μe $m_{\ell\ell} > 30$, $p_T^{\mathrm{sublead}} > 15$	20	265	0.077	122 (46%)	20 (8%)	73 (27%)	27 (10%)	7 (3%)	16 (6%)	0.8 (0.3%)
μe $m_{\ell\ell} < 30$, $p_T^{\mathrm{sublead}} < 15$	3	37	0.089	9 (25%)	12 (32%)	5 (14%)	2 (4%)	2 (4%)	8 (20%)	0.2 (0.5%)
μe $m_{\ell\ell} > 30$, $p_T^{\mathrm{sublead}} < 15$	3	38	0.069	11 (29%)	5 (13%)	8 (21%)	3 (7%)	1 (4%)	10 (26%)	0.1 (0.3%)

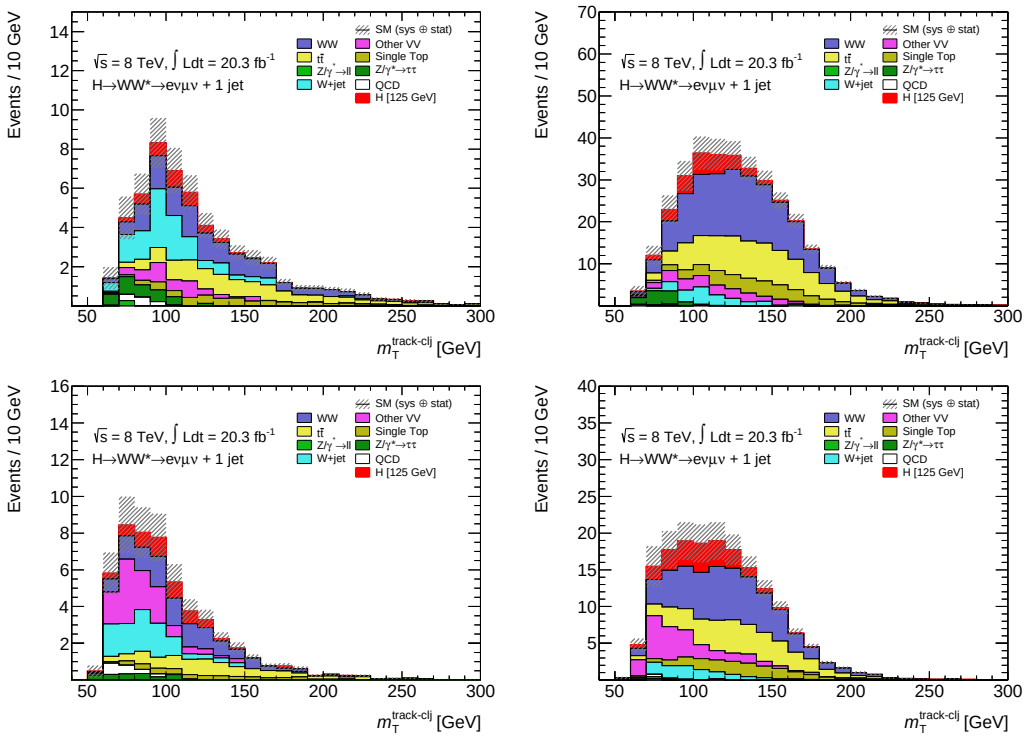

Figure 5.15: m_{T} distribution for each sub-divisions in the 1-jet $e\mu$ channel: $p_{\mathrm{T}}^{\mathrm{sub}}$ = 10-15 GeV and $m_{\ell\ell} > 30$ GeV (top left), $p_{\mathrm{T}}^{\mathrm{sub}} > 15$ GeV and $m_{\ell\ell} > 30$ GeV (top left), $p_{\mathrm{T}}^{\mathrm{sub}}$ = 10-15 GeV and $m_{\ell\ell} < 30$ GeV (bottom left), $p_{\mathrm{T}}^{\mathrm{sub}} > 15$ GeV and $m_{\ell\ell} < 30$ GeV (bottom right).

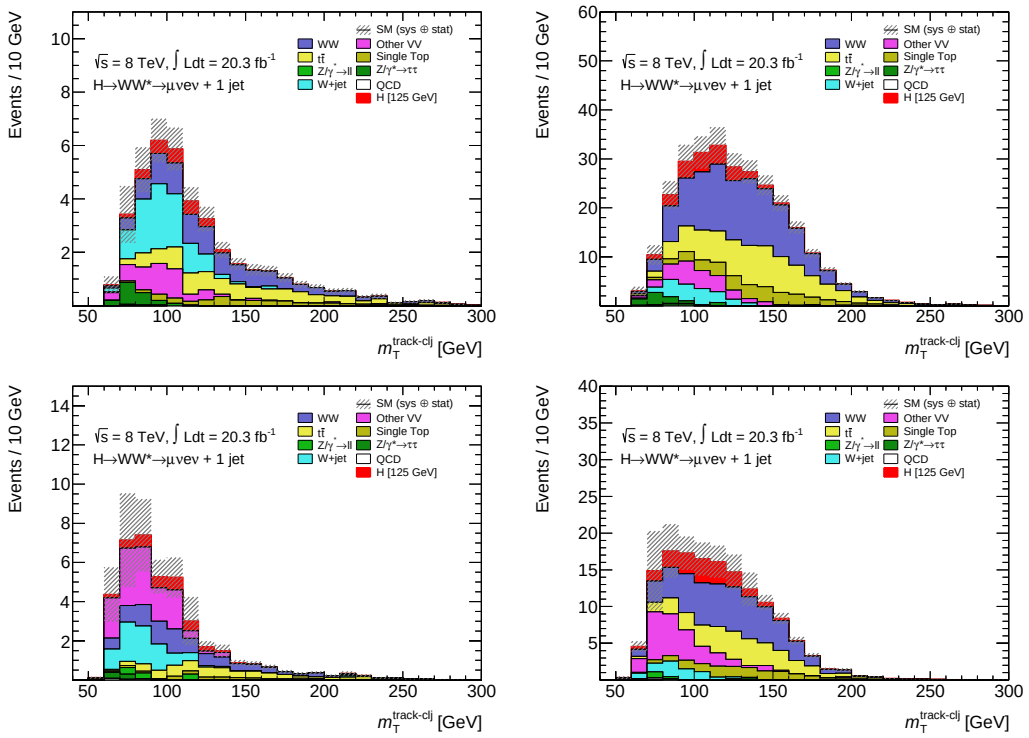

Figure 5.16: m_{T} distribution for each sub-divisions in the 1-jet μe channel: $p_{\mathrm{T}}^{\mathrm{sub}}$ = 10-15 GeV and $m_{\ell\ell} > 30$ GeV (top left), $p_{\mathrm{T}}^{\mathrm{sub}} > 15$ GeV and $m_{\ell\ell} > 30$ GeV (top left), $p_{\mathrm{T}}^{\mathrm{sub}}$ = 10-15 GeV and $m_{\ell\ell} < 30$ GeV (bottom left), $p_{\mathrm{T}}^{\mathrm{sub}} > 15$ GeV and $m_{\ell\ell} < 30$ GeV (bottom right).

5.4.3 ggF 0-1 jet Same Flavor Selection

The selection criteria in the same flavor ($ee, \mu\mu$) analysis is essentially the same as the different flavor analysis. Nevertheless one needs to more seriously consider a large contribution from resonance decay of $Z/\gamma^* \to \ell\ell$. The $Z/\gamma^* \to \ell\ell$ background increased by a factor of three in 2012 due to worse resoulution of missing transverse energy ($E_{\mathrm{T}}^{\mathrm{miss}}$) compared to 2011. The worse resolution arises from higher pileup in 2012 that affects soft term of the $E_{\mathrm{T}}^{\mathrm{miss}}$ calculation. The increased $Z/\gamma^* \to \ell\ell$ background makes the analysis very difficult, so that the analysis has little sensitivity. Therefore, to suppress the $Z/\gamma^* \to \ell\ell$ background, the following cuts are required in addition to the different flavor selection:

- $E_{\mathrm{T,rel}}^{\mathrm{miss}} > 40$ GeV,
- $|\boldsymbol{p}_{\mathbf{T}}^{\mathbf{miss}}| > 35$ GeV,
- $f_{\mathrm{recoil}} < 0.1$.

Note that $E_{\mathrm{T,rel}}^{\mathrm{miss}}$ is considered in the same flavor analysis as a missing transverse energy variable ($E_{\mathrm{T}}^{\mathrm{miss}}$). The $E_{\mathrm{T,rel}}^{\mathrm{miss}}$ is projection onto the axis defined by the nearest object:

$$E_{\mathrm{T,rel}}^{\mathrm{miss}} = E_{\mathrm{T}}^{\mathrm{miss}} \cdot \sin\Delta\phi \quad (\Delta\phi < \pi/2), \tag{5.2}$$

$$= E_{\mathrm{T}}^{\mathrm{miss}} \qquad (\Delta\phi > \pi/2), \tag{5.3}$$

where $\Delta\phi$ is the angle between the $E_{\mathrm{T}}^{\mathrm{miss}}$ and the nearest hard object (lepton or jet). This variable is sensitive to the mis-measured object, thus has an advantage of reducing the QCD and $Z/\gamma^* \to \ell\ell$ backgrounds. The $E_{\mathrm{T,rel}}^{\mathrm{miss}}$ is only considered for the same flavor analysis because it also rejects substantial signals. The risk of reducing the signals is still optimal due to a huge amount of $Z/\gamma^* \to \ell\ell$ background in the analysis. Furthermore track-based $|\boldsymbol{p}_{\mathbf{T}}^{\mathbf{miss}}|$ is also required in a combination with $E_{\mathrm{T,rel}}^{\mathrm{miss}}$. The combination helps to further reduce the $Z/\gamma^* \to \ell\ell$ background since the $|\boldsymbol{p}_{\mathbf{T}}^{\mathbf{miss}}|$ has less correlation with $E_{\mathrm{T,rel}}^{\mathrm{miss}}$.

The $Z/\gamma^* \to \ell\ell$ background is still large after the $|\boldsymbol{p}_{\mathbf{T}}^{\mathbf{miss}}|$ requirement, so a special cut based on soft hadronic recoil, referred to as f_{recoil}, is made to further reject the $Z/\gamma^* \to \ell\ell$ background. The missing transverse energy in the $Z \to \ell\ell$ events is in principle due to mis-measured objects (fake $E_{\mathrm{T}}^{\mathrm{miss}}$) because no neutrino exists in the event to balance the dilepton system, so the two leptons must be balanced by a hadronic recoil system. In fact the soft jets below the analysis jet threshold play a role in the recoil system since the jet veto, in particular for the 0-jet analysis, ensures that this recoil is not reconstructed as the jet used in the analysis. The f_{recoil} is defined as:

$$f_{\mathrm{recoil}} = \frac{|\sum_{\text{soft jets}} |\mathrm{JVF}| \cdot \vec{p}_{\mathrm{T}}|}{p_{\mathrm{T}}^{\ell\ell}}. \tag{5.4}$$

The f_{recoil} variable measures the strength of the recoil system relative to the dilepton system, with the $\boldsymbol{p}_{\mathrm{T}}$ of the soft jets weighted by the jet vertex fraction (JVF) to reduce the effects

of soft jets from pileup. The soft recoil system is reconstructed as the vector sum p_{T} of soft jets with $p_{\mathrm{T}} > 10$ GeV and $|\eta| < 4.5$ in the transverse quadrant opposite the dilepton system ($3\pi/4 < \Delta\phi(\ell\ell, \text{soft-jets}) < 5\pi/4$) as illustrated in Figure 5.17.

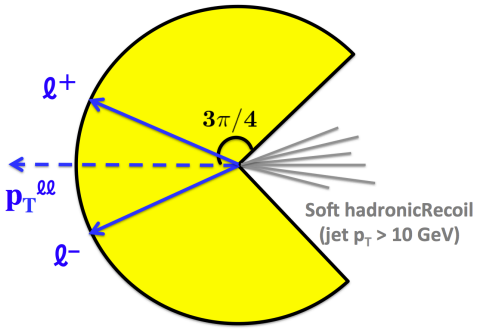

Figure 5.17: Schematic view of soft hadronic recoil system. The hadronic recoil system is reconstructed in the transverse quadrant opposite the dilepton system ($3\pi/4 < \Delta\phi(\ell\ell, \text{soft-jets}) < 5\pi/4$).

The f_{recoil} can be extended to the 1-jet analysis by substituting the p_{T} of the dilepton and "jets ($p_{\mathrm{T}} > 25$ GeV)" system for the p_{T} of the dilepton system in the denominator of the f_{recoil} definition. This modified variable is labeled $f_{\mathrm{recoil}}^{\mathrm{extended}}$. Figure 5.18 shows these variables and their discriminating power against $Z/\gamma^* \to ee/\mu\mu$ and other processes, including the signal.

For the same flavor analysis, the signal region is split neither in $m_{\ell\ell}$ nor $p_{\mathrm{T}}^{\mathrm{sub}}$ unlike the different flavor analysis. Only lepton flavor split (ee, $\mu\mu$) is used for final result since the statistics in the signal region is quite limited. Table 5.6 shows expected signal and background counts for the 0-jet and 1-jet same flavor analysis.

A cut on $f_{\mathrm{recoil}} = 0.1$ after all signal region selection except for $\Delta\phi_{\ell\ell}$ and $|\boldsymbol{p}_{\mathbf{T}}^{\mathbf{miss}}|$ obtains 90 % rejection against $Z/\gamma^* \to \ell\ell$ background while retaining 60-70 % signal (or non-$Z/\gamma^* \to \ell\ell$ background), so the contribution from the $Z/\gamma^* \to \ell\ell$ background ends up very small (< 10 %) compared to WW (or top) background in the end of cutflow. The f_{recoil} and $f_{\mathrm{recoil}}^{\mathrm{extended}}$ are used for the data-driven $Z/\gamma^* \to \ell\ell$ background estimation by measuring those cut efficiencies in data in relevant Z control regions. The data-driven $Z/\gamma^* \to \ell\ell$ background estimation is discussed in Section 5.5.1. Figures 5.19 and 5.20 show sub-leading lepton p_{T}, $m_{\ell\ell}$, $\Delta\phi_{\ell\ell}$, and m_{T} distributions after f_{recoil} (or $f_{\mathrm{recoil}}^{\mathrm{extended}}$) requirement.

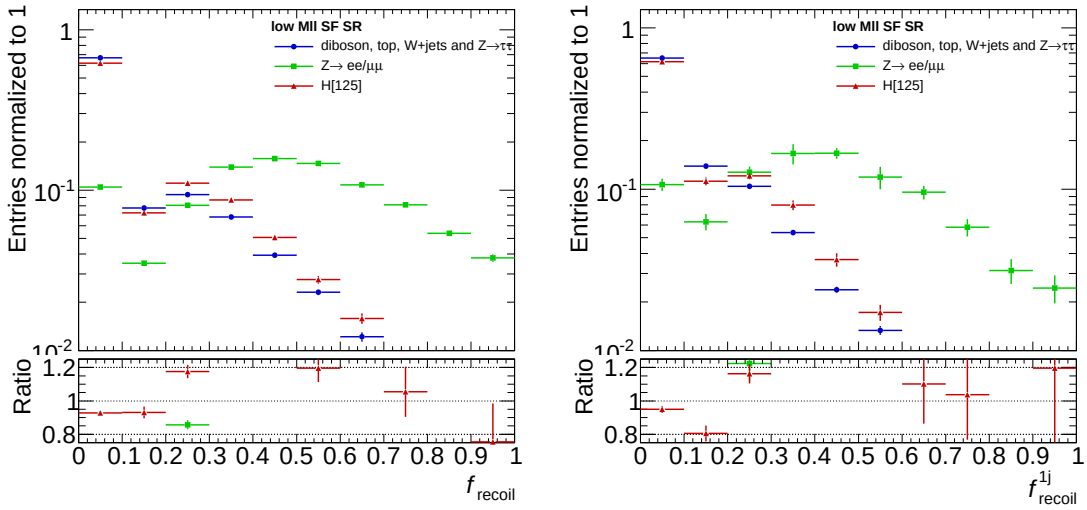

Figure 5.18: f_{recoil} variable in the 0-jet analysis (left) and $f^{\text{extended}}_{\text{recoil}}$ variable in the 1-jet analysis (right) for the signal, $Z/\gamma^* \to \ell\ell$ background, and non-$Z/\gamma^* \to \ell\ell$ backgrounds (i.e. top, $W+$ jets, $Z \to \tau\tau$, WW and other diboson backgrounds). For the f_{recoil} events pass all signal regions selection except for $|\boldsymbol{p}^{\text{miss}}_{\text{T}}|$, $\Delta\phi_{\ell\ell}$ and f_{recoil} itself, to allow for more statistics. The $p^{\ell\ell}_{\text{T}} > 30$ GeV threshold boosts the dilepton system, creating the shape difference visible. For the $f^{\text{extended}}_{\text{recoil}}$ events pass all signal region selection except for $\Delta\phi_{\ell\ell}$ and $f^{\text{extended}}_{\text{recoil}}$ itself.

Table 5.6: Expected event counts in the 8 TeV ggF 0-1 jet analysis. Percentages are the fraction of the total background.

ggF 0-jet same flavor signal region

	H	All Bkg.	S/B	WW	VV	$t\bar{t}$	$(W)t$	Z+jets	W+jets	QCD
ee	25	406	0.062	283 (70%)	34 (8%)	16 (4%)	12 (3%)	24 (6%)	38 (9%)	0.2 (0.0%)
$\mu\mu$	46	680	0.067	505 (74%)	34 (5%)	24 (4%)	19 (3%)	58 (8%)	41 (6%)	-0.1 (-0.0%)

ggF 1-jet same flavor signal region

	H	All Bkg.	S/B	WW	VV	$t\bar{t}$	$(W)t$	Z+jets	W+jets	QCD
ee	10	159	0.060	71 (45%)	17 (11%)	37 (24%)	16 (10%)	9 (6%)	8 (5%)	0.0 (0.0%)
$\mu\mu$	17	249	0.068	124 (50%)	12 (5%)	57 (23%)	26 (10%)	20 (8%)	9 (4%)	-0.0 (-0.0%)

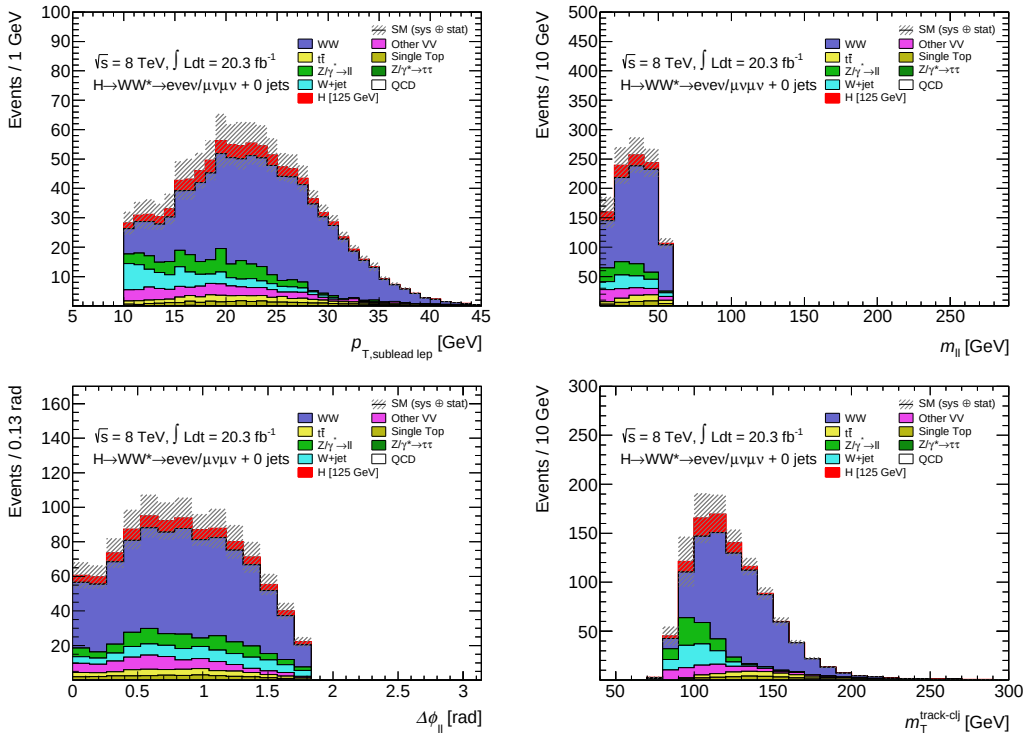

Figure 5.19: Sub-leading lepton p_{T} (top left), $m_{\ell\ell}$ (top right), $\Delta\phi_{\ell\ell}$ (bottom left), and m_{T} (bottom right) distributions after f_{recoil} requirement for 0-jet same flavor analysis.

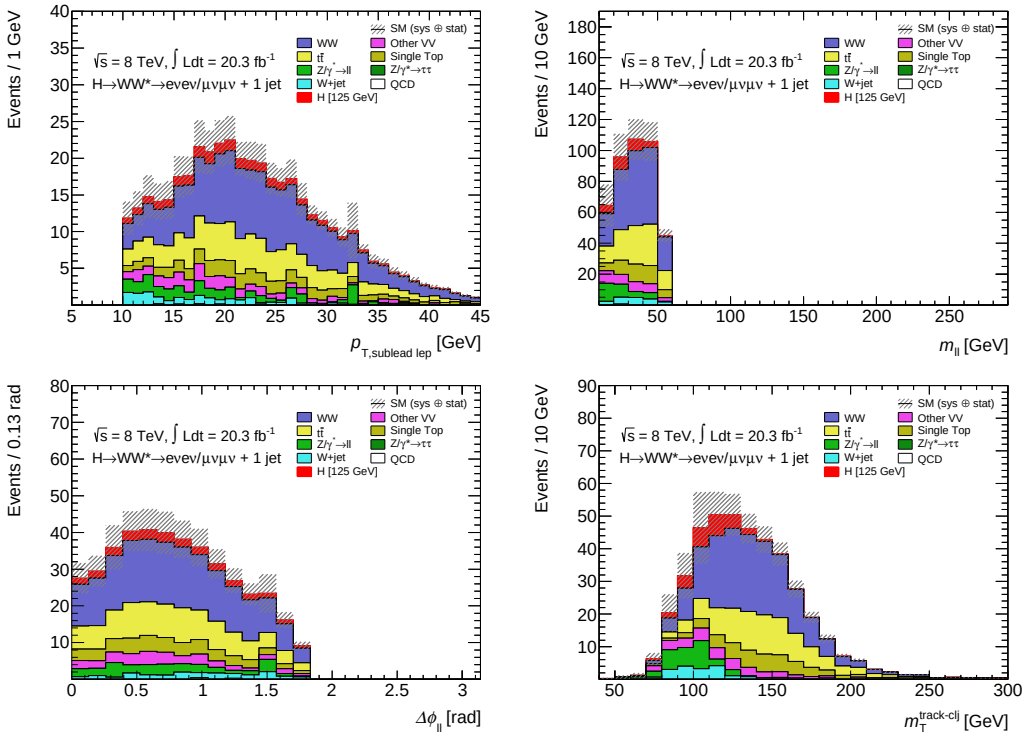

Figure 5.20: Sub-leading lepton p_{T} (top left), $m_{\ell\ell}$ (top right), $\Delta\phi_{\ell\ell}$ (bottom left), and m_{T} (bottom right) distributions after $f_{\mathrm{recoil}}^{\mathrm{extended}}$ requirement for 1-jet same flavor analysis.

5.4.4 VBF Selection

The VBF analysis employs multivariate analysis (MVA) based on Boosted Decision Tree (BDT) technique to fully exploit distinct VBF topology. A decision tree is a collection of cuts designed to classify events as signal-like or background-like. A given signal event is correctly identified if it is placed in a signal-dominated leaf, and vice-versa for background events. After the initial tree is built, another tree is grown to better separate the signal and background events that were misidentified by the first tree. This proceeds iteratively until there is a collection of a specified number of trees, in a process known as boosting. A weighted average is taken from all these trees to form a BDT output discriminant with values ranging between -1 and 1.

In this analysis, the BDT is trained using both different flavor ($e\mu, \mu e$) and same flavor ($ee, \mu\mu$) data set, since most of non-$Z/\gamma^* \to \ell\ell$ backgrounds are insensitive to lepton flavor, and adding extra same flavor specific variables did not offer a significant gain. On the other hand, training with all flavor channels gains in statistics of training samples. The BDT is trained with events that satisfy sub-leading lepton p_{T} ($p_{\mathrm{T}}^{\mathrm{sub}}$) > 15 GeV, but applied to all events ($p_{\mathrm{T}}^{\mathrm{sub}} > 10$ GeV) when fitting to the BDT output. A couple of cuts are made for the VBF analysis before the BDT training after the pre-selection described in Section 5.4.1:

- No missing transverse energy requirement for the different flavor channel, while $\boldsymbol{p}_{\mathbf{T}}^{\mathbf{miss,\ jetCorr}} > 40$ GeV and $E_{\mathrm{T}}^{\mathrm{miss}} > 45$ GeV are imposed for the same flavor channel,
- b-jet veto (see Section 5.4.2),
- $Z \to \tau\tau$ veto (see Section 5.4.2),
- CJV (Central Jet Veto): Events that have jets with $p_{\mathrm{T}} > 20$ GeV, lying between the two forward jets in η are rejected.
- OLV (Outside Lepton Veto): The two charged leptons must have rapidities Y ($= \frac{1}{2}\ln\left(\frac{E+p_z}{E-p_z}\right)$) that are between the tagging jets' rapidities.

The additional requirements above allow for having sample that is similar to the signal region in phase space. The data set that passes the criteria above are used to create the BDT with the following eight variables:

- $p_{\mathrm{T}}^{\mathrm{tot,track,jetCorr}}$: The total transverse momentum $p_{\mathrm{T}}^{\mathrm{tot}}$, the magnitude of $\boldsymbol{p}_{\mathrm{T}}^{l1} + \boldsymbol{p}_{\mathrm{T}}^{\mathrm{l2}} + \boldsymbol{p}_{\mathbf{T}}^{\mathbf{miss,\ jetCorr}} + \sum \boldsymbol{p}_{\mathrm{T}}^{\mathrm{jets}}$, suppresses events with significant soft gluon radiation that recoils against the two leptons and two jets system. For the missing transverse energy, jet-corrected track-based missing transverse energy $\boldsymbol{p}_{\mathbf{T}}^{\mathbf{miss,\ jetCorr}}$ is used.
- Δy_{jj}: The signal is characterized by a separation of the two tagging jets in rapidity,
- m_{jj}: invariant mass of the tag jets (m_{jj}),

- $\eta_{\text{lep}}^{\text{centrality}}$: It quantifies the exact positions of the leptons with respect to the two tagging jets in the η plane:

$$\eta_{\text{lep}}^{\text{centrality}} = \sum_{n=0,1} \text{OLV}_{\ell_n} = \sum_{n=0,1} 2 \cdot \frac{|\eta_{\ell_n} - \bar{\eta}|}{|\eta_{j_0} - \eta_{j_1}|}, \tag{5.5}$$

  where $\bar{\eta} = (\eta_{j_0} + \eta_{j_1})/2$ is the average η of the two tag jets. $\eta_{\text{lep}}^{\text{centrality}} > 1$ indicates a event that have outside leptons.

- $\sum_{\ell,j} M_{\ell j}$: The sum of the invariant mass of lepton and jet pairs. The VBF signal makes large opening angle between jet and lepton,

- $m_{\ell\ell}$: The invariant mass of dilepton system,

- $\Delta\phi_{\ell\ell}$: The opening angle of leptons in the ϕ plane,

- m_{T}: The transverse mass of dilepton system. For the missing transverse energy, jet-corrected track-based missing transverse energy $\boldsymbol{p}_{\mathbf{T}}^{\mathbf{miss,\ jetCorr}}$ is used.

First five are variables specific for the VBF analysis, and last three that are related to the spin correlation are common variables to the ggF analysis. Key input variables after pre-selection are shown in Figure 5.21 for the different flavor channel, and Figure 5.22 for the same flavor channel.

The BDT output distribution (BDT score) is then fit to get final result. The binning has been optimized for maximal expected significance while keeping reasonable MC statistics in each bin. The chosen configuration is four bins with boundaries at $[-0.48, 0.3, 0.78]$ over the range of $[-1, 1]$. The bin with the lowest BDT score contains the majority of background ($> 90\%$) and thus substantially smaller signal to background ratio. Hence it is negligible in terms of total significance and is excluded from the BDT fit, which also ensures orthogonality with the ggF 2-jets analysis. Table 5.7 shows expected signal and background counts in each bin of BDT, and Figure 5.23 shows corresponding BDT bins.

Table 5.7: Expected yield in each bin of BDT for the different flavor and same flavor channels (No normalization factors (NFs) are applied).

	vbf+vh [125 GeV]	ggf [125 GeV]	WW	$WZ/ZZ/W\gamma$	$t\bar{t}$	Single Top	$Z \to \ell\ell$+jets	$Z \to \tau\tau$+jets	W+jets/QCD	Total Bkg.(+ggf)
$e\mu + \mu e$										
Bin 1	4.27 ± 0.10	3.03 ± 0.07	5.99 ± 0.28	2.53 ± 0.49	11.52 ± 0.40	2.14 ± 0.18	0.19 ± 0.12	4.30 ± 0.59	5.31 ± 1.23	35.20 ± 1.25
Bin 2	4.23 ± 0.09	1.25 ± 0.05	2.06 ± 0.16	0.75 ± 0.28	2.36 ± 0.18	0.37 ± 0.05	0.00 ± 0.00	0.29 ± 0.07	0.69 ± 0.43	8.14 ± 0.49
Bin 3	3.12 ± 0.07	0.40 ± 0.03	0.53 ± 0.07	0.06 ± 0.06	0.33 ± 0.07	0.09 ± 0.03	0.00 ± 0.00	0.07 ± 0.04	0.01 ± 0.02	1.61 ± 0.16
$ee + \mu\mu$										
Bin 1	2.22 ± 0.07	1.48 ± 0.05	3.53 ± 0.22	0.89 ± 0.22	7.24 ± 0.32	1.24 ± 0.14	25.54 ± 2.26	1.94 ± 0.35	1.15 ± 0.55	43.48 ± 2.39
Bin 2	2.47 ± 0.07	0.62 ± 0.03	1.14 ± 0.12	0.30 ± 0.15	1.51 ± 0.14	0.31 ± 0.07	4.56 ± 0.57	0.31 ± 0.08	0.28 ± 0.19	9.20 ± 0.66
Bin 3	1.74 ± 0.06	0.18 ± 0.02	0.26 ± 0.05	0.02 ± 0.02	0.25 ± 0.06	0.05 ± 0.02	0.63 ± 0.19	0.01 ± 0.01	0.00 ± 0.00	1.42 ± 0.21

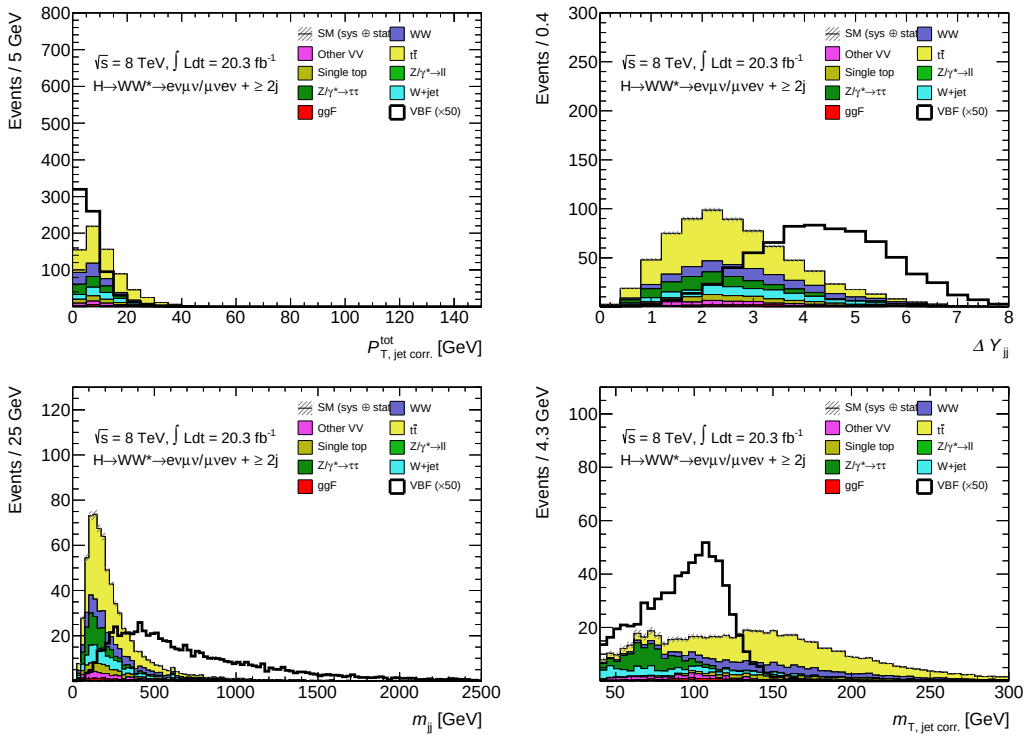

Figure 5.21: Distributions of $p_{\mathrm{T}}^{\mathrm{tot,track,jetCorr}}$, Δy_{jj}, m_{jj}, and m_{T} in different flavor channel after all pre-selection. The VBF signal is scaled by 50 times larger.

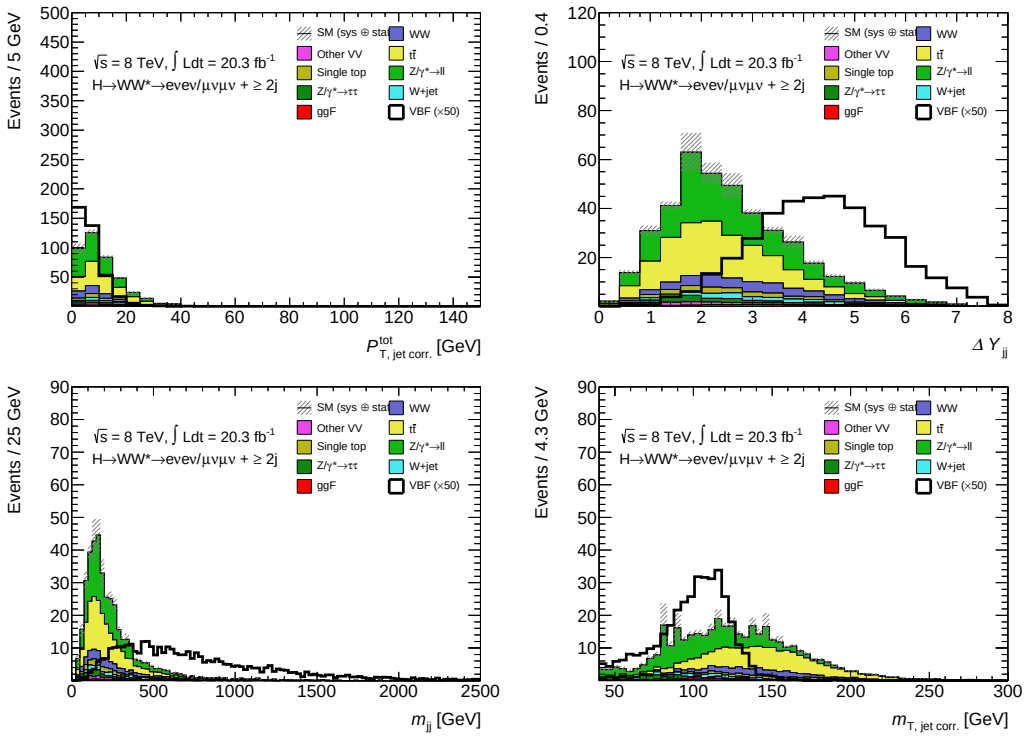

Figure 5.22: Distributions of $p_{\mathrm{T}}^{\mathrm{tot,track,jetCorr}}$, Δy_{jj}, m_{jj}, and m_{T} in same flavor channel after all pre-selection. The VBF signal is scaled by 50 times larger.

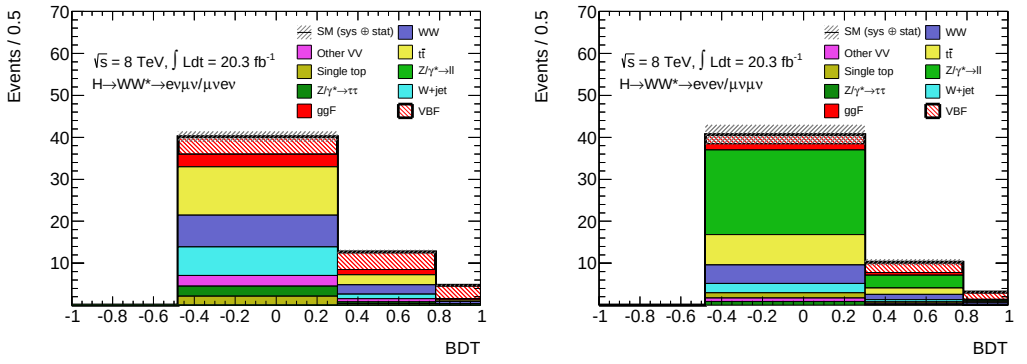

Figure 5.23: BDT score for the $e\mu$+μe (left) and ee+$\mu\mu$ (right) channels after the BDT > -0.48 cut. The MC is unblinded. The grey band contains only statistical uncertainties.

5.5 Background Estimation

In order to determine expected background yield in the signal region, some backgrounds are normalized to data in dedicated control regions, and other background normalizations are taken directly from MC cross section, except for the W+jets/QCD and the same flavor Z+jets backgrounds. These backgrounds are evaluated in data-driven methods.

5.5.1 ggF 0-1 jet analysis

Figure 5.24 shows schematic view of the extraction of the main backgrounds in the ggF 0-jet analysis.

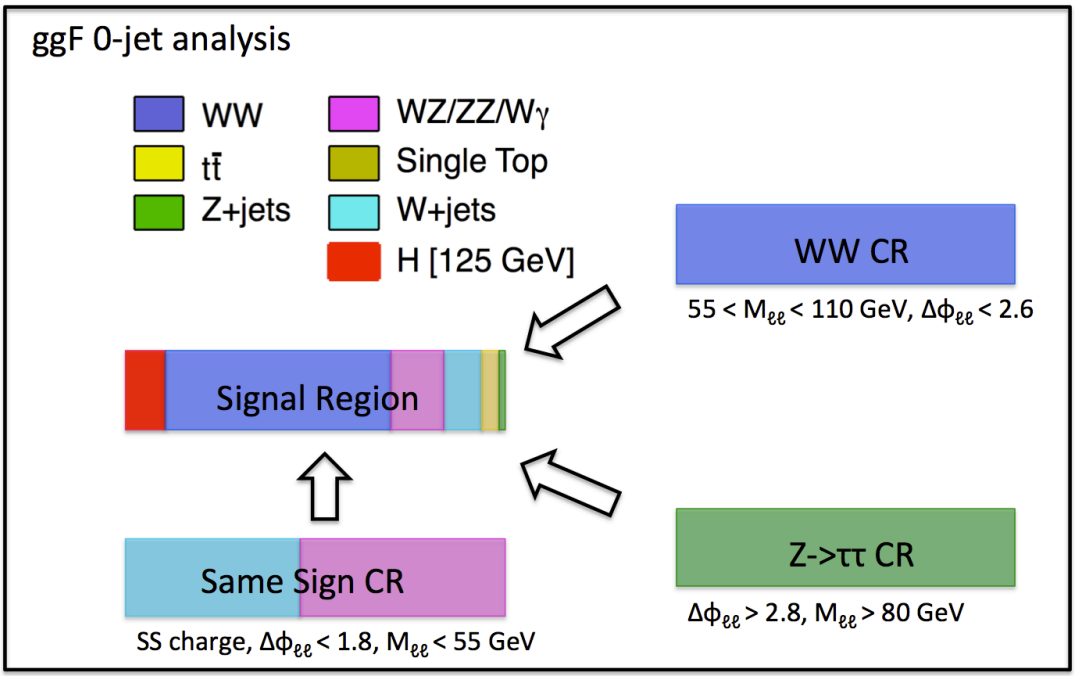

Figure 5.24: Schematic view of the extraction of the main backgrounds for ggF 0-jet analysis. Signal region is defined as "$\Delta\phi_{\ell\ell} < 1.8$ and $m_{\ell\ell} < 55$ GeV. Several backgrounds are normalized to data in dedicated control regions.

In the ggF 0-jet analysis, WW, $Z/\gamma^* \to \tau\tau$, and Same Sign (SS) control regions are defined. The SS control region is used to extract the normalization of the "non-WW" dibosons (VV). Other significant background is the W+jets background. The W+jets background is estimated by a data-driven method called fake factor method (see Chapter 6). Making use of the data-driven method is essential for this background, since it may not be accurately modeled by simulation. For the same flavor channel ($ee, \mu\mu$), the $Z/\gamma^* \to \ell\ell$ background is also of special importance, which is discussed in this section.

Figure 5.25 shows schematic view of the extraction of the main backgrounds in the ggF 1-jet analysis.

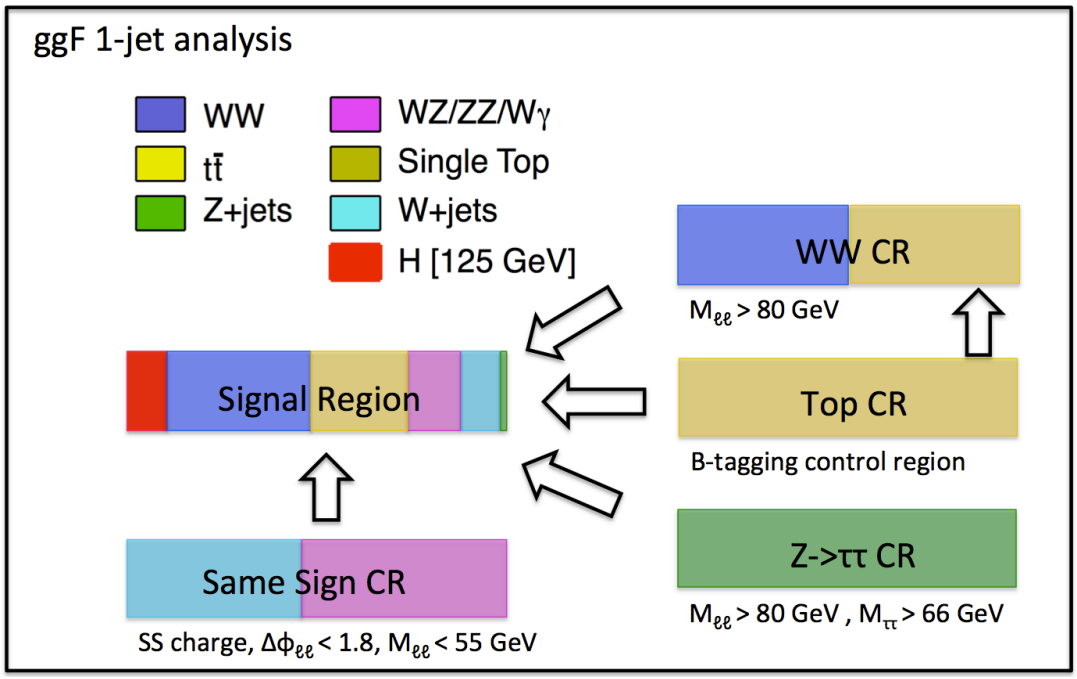

Figure 5.25: Schematic view of the extraction of the main backgrounds for the ggF 1-jet analysis. Signal region is defined as "$\Delta\phi_{\ell\ell} < 1.8$ and $m_{\ell\ell} < 55$ GeV. Several backgrounds are normalized to data in dedicated control regions. Several backgrounds are normalized to data in dedicated control regions.

In the ggF 1-jet analysis, the top control region is added, since the contribution from the top background is large. Otherwise the strategy of the background estimation is the same as the ggF 0-jet analysis. In the remaining section, each background estimation is described.

WW background

The background from continuum $WW^* \to \ell\nu\ell\nu$ production is the most important background in the analysis since it has the same final state ($WW^* \to \ell\nu\ell\nu$) and more than 10 times larger cross section than the Higgs signal cross section. The WW background is normalized using a control region which is defined to be orthogonal to the signal region but to be similar to the signal region in phase space. In order to define the control region, topological selection criteria, namely $m_{\ell\ell}$ and $\Delta\phi_{\ell\ell}$ are changed from the signal region definition described in Section 5.4.2:

0-jet

- $55 < m_{\ell\ell} < 110$ GeV,

- $\Delta\phi_{\ell\ell} < 2.6$ radians,

1-jet

- $m_{\ell\ell} > 80$ GeV,
- no $\Delta\phi_{\ell\ell}$ cut applied,

where the $\Delta\phi_{\ell\ell}$ cut intends to reduce the remaining $Z/\gamma^* \to \tau\tau$ contribution at high $\Delta\phi_{\ell\ell}$ for the 0-jet analysis but is not applied to the 1-jet analysis since the $Z/\gamma^* \to \tau\tau$ veto requirement already rejects most of the $Z/\gamma^* \to \tau\tau$. It is worth noting that the sub-leading lepton p_{T} is set to be $p_{\mathrm{T}}^{\mathrm{sublead}} > 15$ GeV for the WW control region to avoid the large W+jets contamination from events with $10 < p_{\mathrm{T}}^{\mathrm{sublead}} < 15$ GeV.

The normalization factor (NF) is derived from this control region. The NF is evaluated subtracting contribution from other backgrounds, and taking the ratio of the remaining data events to the WW yield predicted by MC. Since there is no significant difference between the $e\mu$ and μe channels and no physical reason to separate $e\mu$ and μe channels, the combined different flavor channel ($e\mu$+μe) is used to derive the NF. As $Z/\gamma^* \to \ell\ell$ contamination in the WW control region is large for the same flavor channels, The same normalization factor is applied to all lepton flavor channels ($ee, \mu\mu, e\mu, \mu e$). The resulting NFs are 1.22 ± 0.03(stat.) for 0-jet and 1.05 ± 0.05(stat.) for 1-jet, and is listed along with other NFs in Table 5.11.

The signal and control regions are fit simultaneously and the WW normalization is extrapolated from the control region to the signal region as extrapolation factor α ($N_{\mathrm{SR}} = \alpha N_{\mathrm{CR}}$). The theoretical uncertainties on the extrapolation factor α is the main source of systematic uncertainty on the WW background. The theoretical uncertainties are evaluated, varying the renormalization and factorization scales for QCD scale uncertainty, comparing different PDFs for PDF uncertainty, and comparing the extrapolation factors between generators for underlying/parton shower (UEPS) and matrix element modeling. These uncertainties (referred to as QCD scale, PDF, UEPS, and matching) are evaluated for each signal region, namely the same sub-leading lepton p_{T} and $m_{\ell\ell}$ configuration. In order to reduce the theoretical uncertainties, the control region is defined closely to the signal region in $m_{\ell\ell}$. The $m_{\ell\ell}$ boundary between signal and control region is optimized to keep both signal and control region acceptance, while ensuring similar kinematics in both regions.

For the WW background m_{T} shape variations are also evaluated as shape systematic uncertainty. The uncertainties on the WW background will be further discussed in Section 5.6.2.2 since they have large impact on the measured signal strength.

Figure 5.26 and 5.27 show kinematic distributions ($m_{\ell\ell}$, m_{T}, $\boldsymbol{p}_{\mathbf{T}}^{\mathbf{miss,\ jetCorr}}$, and sub-leading lepton p_{T}) of the WW control region for 0-1 jet analysis. Overall agreement between data/MC looks reasonable and the purity of the WW control region is 70% level for 0-jet and 40% for 1-jet.

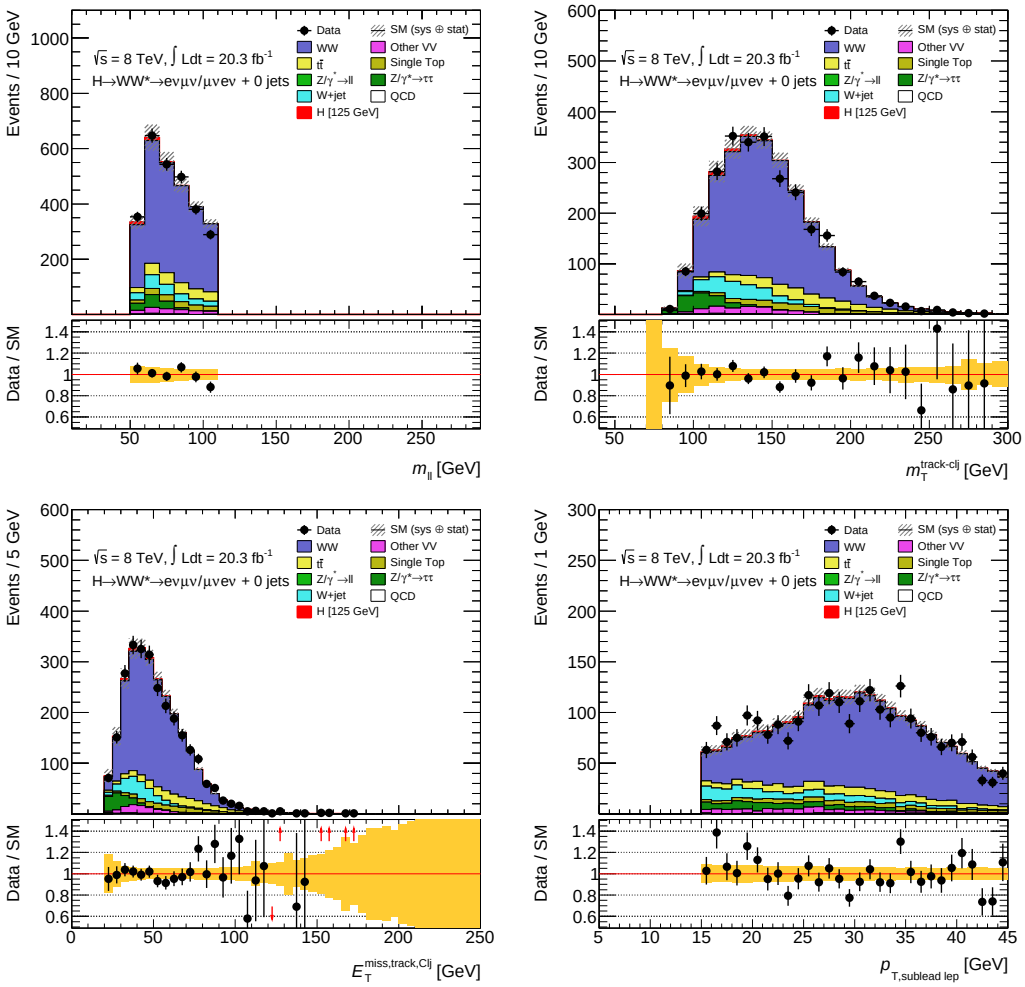

Figure 5.26: $m_{\ell\ell}$ (top left), m_{T} (top right), $\boldsymbol{p_{\mathrm{T}}^{\mathrm{miss,\ jetCorr}}}$ (bottom left), and sub-leading lepton p_{T} (bottom right) distributions in the WW control region for 0-jet analysis.

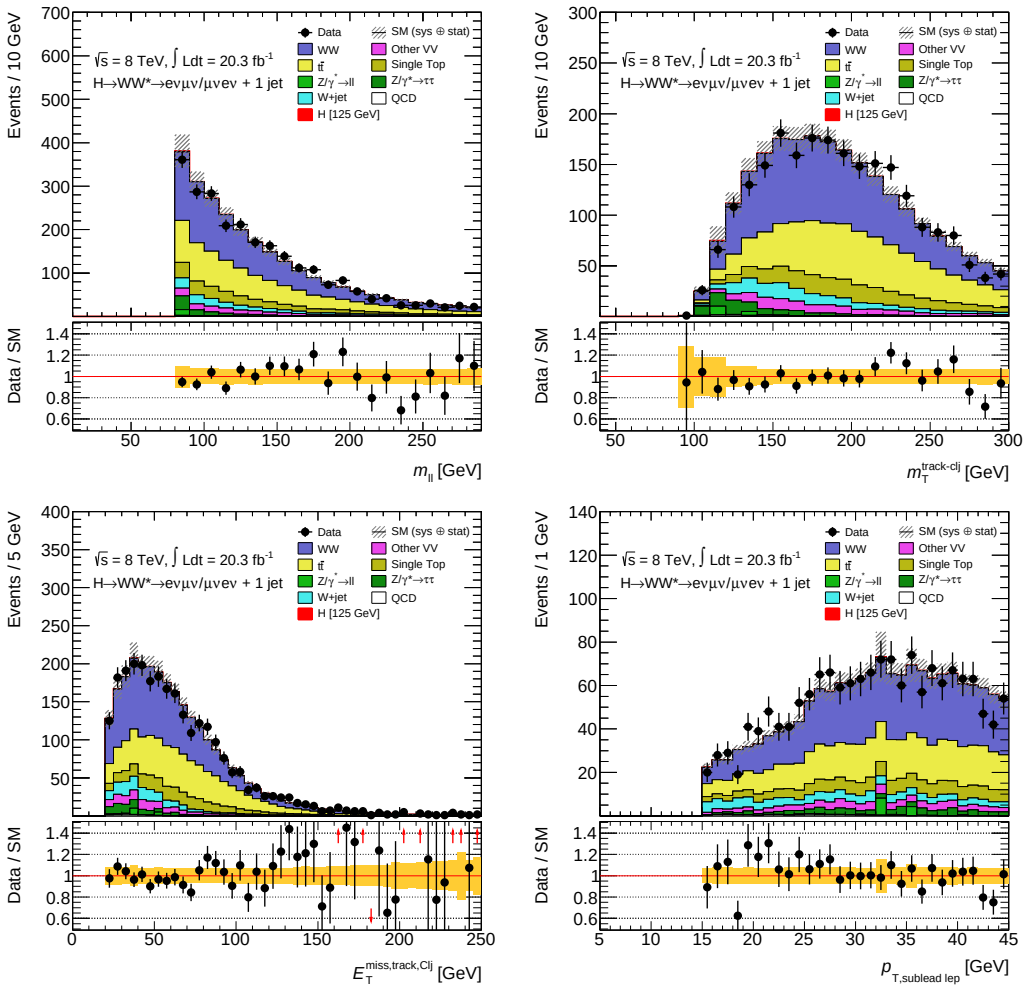

Figure 5.27: $m_{\ell\ell}$ (top left), m_{T} (top right), $\boldsymbol{p}_{\mathbf{T}}^{\mathbf{miss,\ jetCorr}}$ (bottom left), and sub-leading lepton p_{T} (bottom right) distributions in the WW control region for 1-jet analysis.

$Z/\gamma^* \to \tau\tau$ background

The $Z/\gamma^* \to \tau\tau$ background that is sub-dominant background in the signal region is estimated using MC but the cross section is normalized to data in an appropriate $Z/\gamma^* \to \tau\tau$ control region. In order to define the $Z/\gamma^* \to \tau\tau$ control region, some selection criteria such as those $Z/\gamma^* \to \tau\tau$ veto, $m_{\ell\ell}$, and $\Delta\phi_{\ell\ell}$ are changed from the signal region definition described in Section 5.4.2:

0-jet

- $m_{\ell\ell} < 80$ GeV,
- $\Delta\phi_{\ell\ell} > 2.8$ radians,

1-jet

- $m_{\ell\ell} < 80$ GeV,
- revert $Z/\gamma^* \to \tau\tau$ veto.

The purity of this control region is $\sim 90\%$ and 0.5% of the total Z/γ^* yield originates from the $Z/\gamma^* \to \ell\ell$ ($\ell = e, \mu$) component. The normalization factors (NF) are calculated, subtracting small contribution from other processes in the control region, and taking the ratio of background-subtracted data to MC cross section. Since there is no significant difference between the $e\mu$ and μe channels and no physical reason to separate $e\mu$ and μe channels, the combined different flavor channel ($e\mu$+μe) is used to derive the NF. Although $Z/\gamma^* \to \tau\tau$ is negligible in the same flavor channels, the NF derived from the different flavor dateset is applied to all lepton flavor channels ($ee, \mu\mu, e\mu, \mu e$). The resulting NFs are 1.01 ± 0.02(stat.) for 0-jet and 1.07 ± 0.04(stat.) for 1-jet, and is listed along with other NFs in Table 5.11.

Similar to the WW background, the uncertainties on the $Z/\gamma^* \to \tau\tau$ extrapolation from the control region to the signal region is evaluated from the variations of the PDF, QCD scale, UEPS (underlying event/parton shower) and matching (matching of parton shower to the matrix element). The total uncertainty that is dominated by the scale uncertainty is 8% for 0-jet and 12% for 1-jet.

Figure 5.28 and 5.29 show kinematic distributions ($m_{\ell\ell}$, m_{T}, $\boldsymbol{p}_{\mathbf{T}}^{\mathbf{miss,\ jetCorr}}$, and subleading lepton p_{T}) of the $Z/\gamma^* \to \tau\tau$ control region for 0-1 jet analysis. Overall agreement between data/MC looks reasonable.

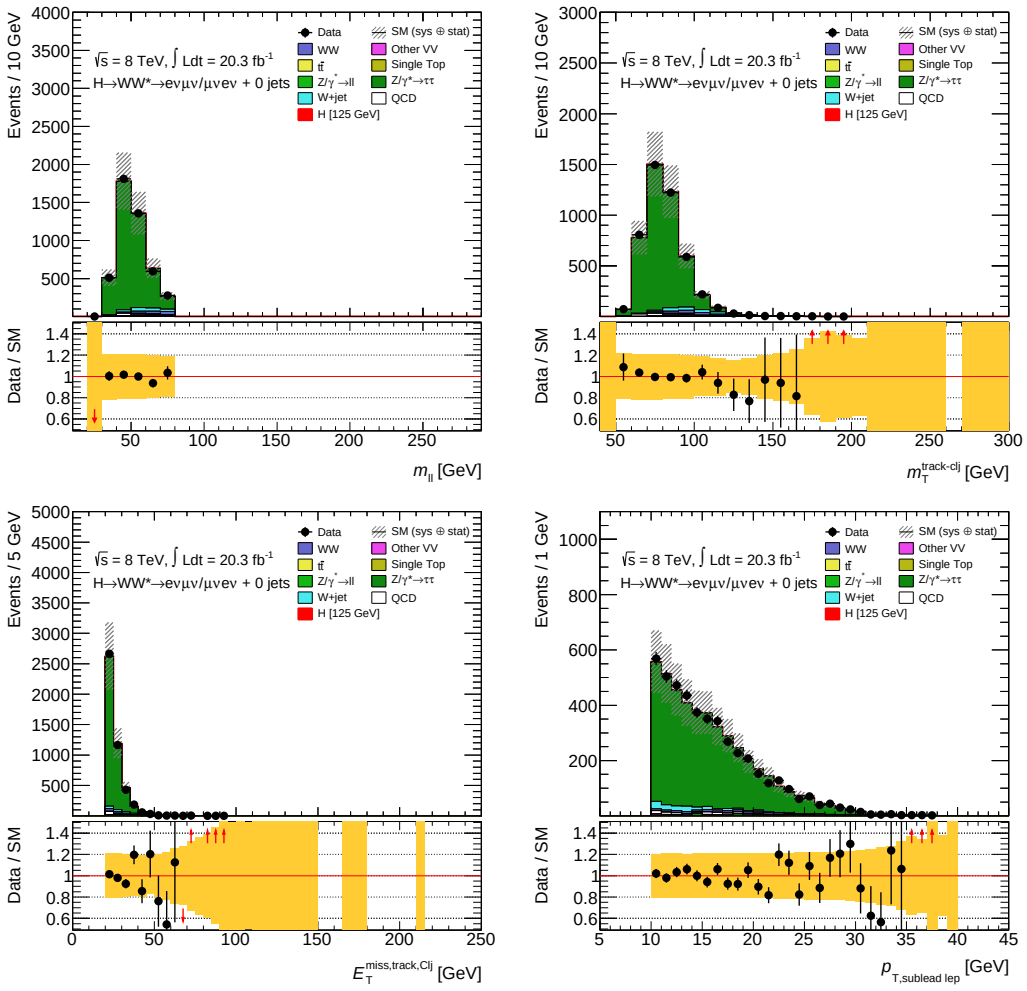

Figure 5.28: $m_{\ell\ell}$ (top left), m_{T} (top right), $\boldsymbol{p}_{\mathbf{T}}^{\mathbf{miss,\ jetCorr}}$ (bottom left), and sub-leading lepton p_{T} (bottom right) distributions in the $Z/\gamma^* \to \tau\tau$ control region for 0-jet analysis.

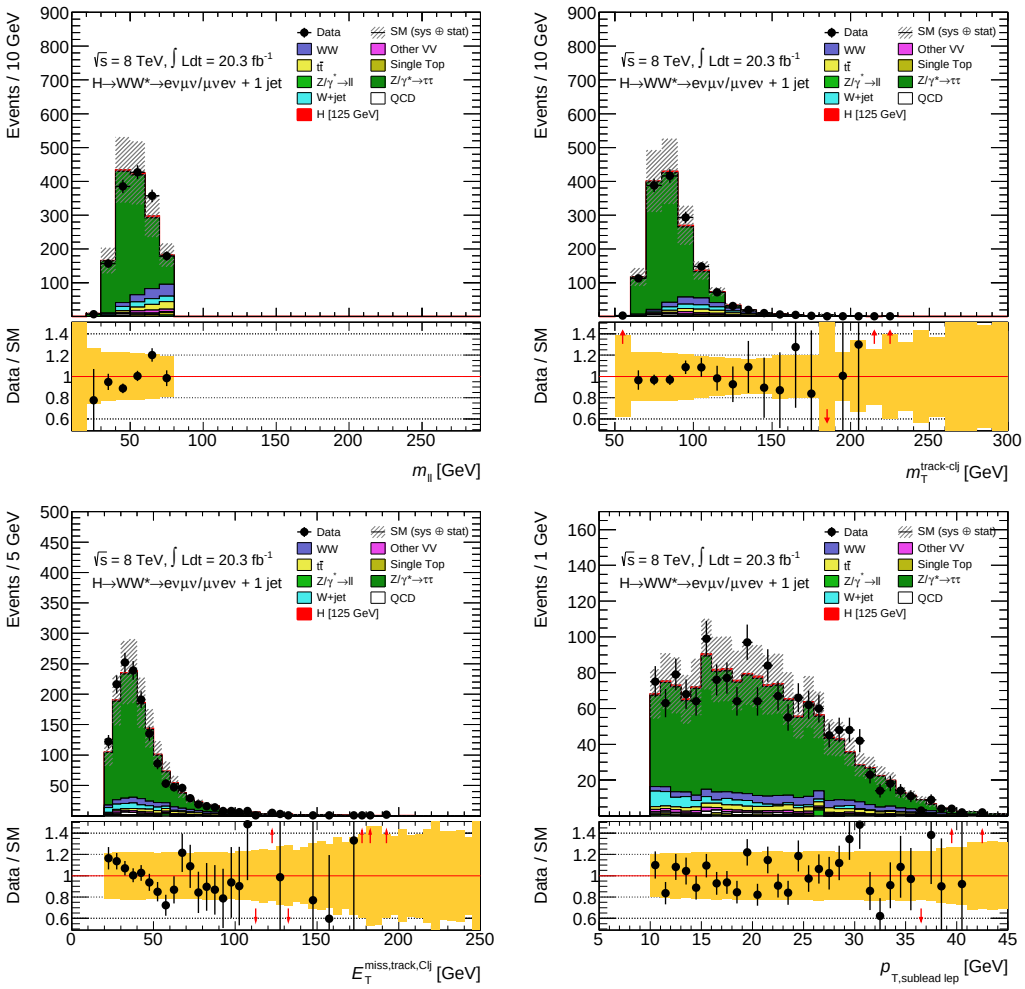

Figure 5.29: $m_{\ell\ell}$ (top left), m_{T} (top right), $\boldsymbol{p}_{\mathbf{T}}^{\mathbf{miss,\ jetCorr}}$ (bottom left), and sub-leading lepton p_{T} (bottom right) distributions in the $Z/\gamma^* \to \tau\tau$ control region for 1-jet analysis.

$Z/\gamma^* \to \ell\ell$ background

The $Z/\gamma^* \to \ell\ell$ background (Z/DY) arises mainly from mis-measured objects or associated soft pp collisions in event. This background is significant in the same flavor analysis. The soft hadronic recoil variable (f_{recoil}) described in Section 5.4.3, shows a clear difference in shape between the Z/DY and all other processes that have neutrino(s) in the final state (i.e. true missing transverse energy), including the signal as shown in Figure 5.18. Based on soft hadronic recoil, a data-driven technique called "Pacman method" has been developed for the Z/DY background estimation. For the Z/DY background estimate, the data-driven procedure is essential because f_{recoil} uses very soft jets ($p_{\text{T}} > 10$ GeV) which may not be accurately modeled in simulation. The Pacman method is illustrated in Figure 5.30.

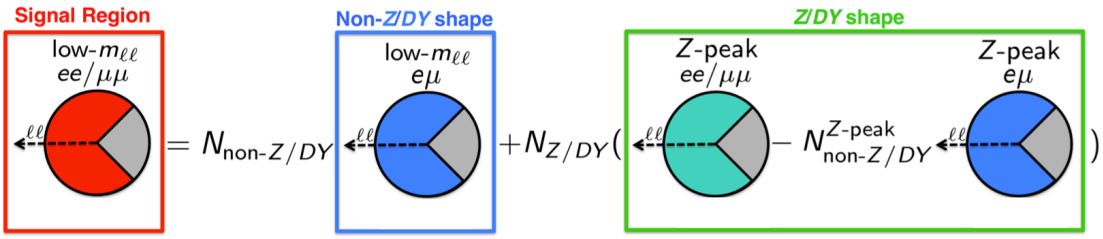

Figure 5.30: Schematic view of the Pacman method for the Z/DY background estimate.

In the Pacman method, the efficiency of f_{recoil} cut for Z/DY (green box) and non-Z/DY (blue box) events are independently measured in data. The Z/DY efficiency is calculated in the same flavor (SF) Z mass peak, $|m_{\ell\ell} - m_Z| < 15$ GeV (see green box in Figure 5.30). The purity of Z/DY events in this region is only $\sim 50\%$, thus the non-Z/DY contribution must be subtracted. The Z/DY efficiency is written as follows:

$$\epsilon^{\text{Z/DY}} = \frac{N0^{Z\text{peak}}_{\text{SF}} - \epsilon^{\text{non-Z/DY}}_{Z\text{peak}} \times N(\text{non-Z/DY})^{Z\text{peak}}_{\text{SF}}}{N^{Z\text{peak}}_{\text{SF}} - N(\text{non-Z/DY})^{Z\text{peak}}_{\text{SF}}}, \tag{5.6}$$

where $N0^{Z\text{peak}}_{\text{SF}}$ is the number of events that pass f_{recoil} cut in the same flavor Z peak, $N^{Z\text{peak}}_{\text{SF}}$ is the number of events before applying f_{recoil} cut in the same flavor Z peak, and $N(\text{non-Z/DY})^{Z\text{peak}}_{\text{SF}}$ is the number of non-Z/DY events in the same flavor Z peak. The normalization of the non-Z/DY contribution, $N(\text{non-DY})^{Z\text{peak}}_{\text{SF}}$, is taken from the MC cross section (but including data normalizations for WW, top and $Z/\gamma^* \to \tau\tau$ from the control regions), and has an associated uncertainty of $\sim 10\%$. The non-Z/DY efficiency, $\epsilon^{\text{non-Z/DY}}_{Z\text{peak}}$, is measured in data using different flavor data set in the Z peak. The non-Z/DY efficiency in the Z peak is written as:

$$\epsilon^{\text{non-Z/DY}}_{Z\text{peak}} = \frac{N0^{Z\text{peak}}_{\text{DF}}}{N^{Z\text{peak}}_{\text{DF}}}. \tag{5.7}$$

where DF denotes different flavor.

One can write the Z/DY background in the signal region (red box in Figure 5.30) as:

$$\mathrm{N0(Z/DY)}_{\mathrm{SF}}^{\mathrm{SR}} = \mathrm{N0}_{\mathrm{SF}}^{\mathrm{SR}} - \mathrm{N0(non\text{-}Z/DY)}_{\mathrm{SF}}^{\mathrm{SR}}. \tag{5.8}$$

Similarly one can write the Z/DY background in the signal region before the f_{recoil} cut using $\epsilon^{\mathrm{Z/DY}}$ (green box) and $\epsilon^{\mathrm{non\text{-}Z/DY}}$ (blue box) as:

$$\frac{\mathrm{N0(Z/DY)}_{\mathrm{SF}}^{\mathrm{SR}}}{\epsilon^{\mathrm{Z/DY}}} = N_{\mathrm{SF}}^{\mathrm{SR}} - \frac{\mathrm{N0(non\text{-}Z/DY)}_{\mathrm{SF}}^{\mathrm{SR}}}{\epsilon^{\mathrm{non\text{-}Z/DY}}}. \tag{5.9}$$

Then solve for $\mathrm{N0(Z/DY)}_{\mathrm{SF}}^{\mathrm{SR}}$ using Equations 5.8 and 5.9 as:

$$\mathrm{N0(Z/DY)}_{\mathrm{SF}}^{\mathrm{SR}} = \epsilon^{\mathrm{Z/DY}} \times \frac{N0_{\mathrm{SF}}^{\mathrm{SR}} - \epsilon^{\mathrm{non\text{-}Z/DY}} \times N_{\mathrm{SF}}^{\mathrm{SR}}}{\epsilon^{\mathrm{Z/DY}} - \epsilon^{\mathrm{non\text{-}Z/DY}}}. \tag{5.10}$$

$\epsilon^{\mathrm{non\text{-}Z/DY}}$ is the cut efficiency for non-Z/DY events in the low $m_{\ell\ell}$ signal region (blue box), and is obtained from the f_{recoil} data distribution of different flavor events that pass full same flavor selection. One can derive the cut efficiency for the non-Z/DY using different flavor data set since the relative fractions of each non-Z/DY process in the signal region are the same between different flavor and same flavor due to flavor universality.

The systematic uncertainties on $\epsilon^{\mathrm{non\text{-}Z/DY}}$ and $\epsilon_{Z\mathrm{peak}}^{\mathrm{non\text{-}Z/DY}}$ to account for the uncertainties on the extrapolation from the different flavor control sample to the same flavor signal region are evaluated, comparing several MC generators and data. The systematic uncertainties are then added in quadrature to the statistical uncertainty on the measured non-Z/DY efficiency. The same procedure is also applied to ϵ^{DY} to account for the extrapolation from the Z-peak control sample to the low $m_{\ell\ell}$ signal region. Figure 5.31 shows a comparison of Z/DY recoil shapes between Z peak and low $m_{\ell\ell}$ regions in MC.

Table 5.8 summarizes the systematic uncertainties on the cut efficiencies for the 0-jet and 1-jet analyses. One can expect a final uncertainty on the Z/DY background of $\sim 50\%$, dominated by the extrapolation uncertainty on ϵ^{DY}.

W+jets/QCD background

The W+jets background arises from events that have one fully identified lepton and one jet faking an identified lepton. Similarly the QCD background arises from events that have two jets faking identified leptons. Since the fake backgrounds are difficult to model in simulation, the data-driven method called "fake factor method" has been developed. The fake factor method is further discussed in detail in Chapter 6. This data-driven method is employed to both ggF and VBF analyses. The size of these backgrounds is very large in the signal region in particular in the region that contains sub-leading lepton with $p_{\mathrm{T}} <$

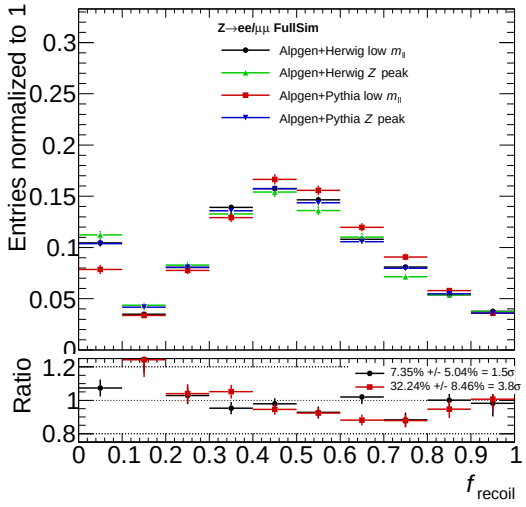

Figure 5.31: Comparison of Z/DY recoil shapes for the 0-jet between same flavor Z peak and signal low $m_{\ell\ell}$ regions events in MC.

Table 5.8: Z/DY and non-Z/DY efficiencies and uncertainties, used to estimate the Z/DY background in the 0-jet signal region with the Pacman method.

Sources	0-jet	1-jet
$\epsilon^{\text{non-DY}}$	0.69 ± 0.01	0.64 ± 0.02
DF $\to$ SF extrapolation	0.8%	1.2%
statistical uncertainty	1.8%	3.0%
total uncertainty	1.9%	3.2%
$\epsilon^{\text{non-DY}}_{Z\text{peak}}$	0.68 ± 0.02	0.66 ± 0.03
DF $\to$ SF extrapolation	1.9%	2.4%
statistical uncertainty	2.5%	3.9%
total uncertainty	3.1%	4.5%
ϵ^{DY}	0.14 ± 0.05	0.13 ± 0.04
Z peak $\to$ low $m_{\ell\ell}$ extrapolation	32%	16%
statistical uncertainty	9.4%	16%
total uncertainty	38%	32%
estimated DY yield in SF SR	88 ± 43	26 ± 12
statistical uncertainty	15%	29%
total uncertainty	49%	45%

15 GeV, which results in large impact on the final fit, so a sophisticated modeling of these backgrounds is very important.

VV background

The non-WW backgrounds ($WZ/ZZ^*/W\gamma^{(*)}/Z\gamma^{(*)}$) contribute to the signal region. These backgrounds are normalized in Same Sign control region by subtracting the W+jets background which is sub-dominant in this region. The SS control region is further discussed in Chapter 7.

Top background

Top quark events ($t\bar{t}$ and single top process Wt) are a significant background to the 0-1 jet analysis as shown in Table 5.4 and 5.5.

Top background in the 0-jet analysis

The top background in the 0-jet analysis is estimated using the jet-veto survival probability (JVSP) method [16, 171]. Pre-selected sample that passes pre-selection described in Section 5.4.1 and some additional cuts, $\boldsymbol{p}_{\mathbf{T}}^{\mathbf{miss,\ jetCorr}} > 20$ GeV and $\Delta\phi_{\ell\ell} < 2.8$, is used. The top background in the signal region after the jet veto cut is given by:

$$N_{\text{top,0j}}^{\text{Exp}} = (N_{\text{data}} - N_{\text{non-top}}) \times P_2^{\text{Exp}}, \tag{5.11}$$

where N_{data} is the total number of events in data after pre-selection and $N_{\text{non-top}}$ is contributions from non-top backgrounds in the pre-selected data sample (N_{data}). P_2^{Exp} is a data-driven fraction of top events which pass the jet veto in the pre-selected sample. Assuming that a $t\bar{t}$ event has two b-quarks and there is no correlation between the two b-quarks, the P_2 can be expressed as:

$$P_2 = P_1^2, \tag{5.12}$$

where P_1 is a single jet veto survival probability that can be obtained from a control sample requiring at least one b-jet. P_2^{Exp} is then written using P_1 as:

$$P_2^{\text{Exp}} = P_2^{\text{MC}} \times (\frac{P_1^{\text{Btag,data}}}{P_1^{\text{Btag,MC}}})^2, \tag{5.13}$$

where superscript "Btag" indicates that P_1 is measured in b-tagged control region, and P_2^{MC} is a fraction of top events that pass the jet veto. The top background in the signal region is rewritten using Equations 5.11 and 5.13 as:

$$N_{\text{top,0j}}^{\text{Exp}} = (N_{\text{data}} - N_{\text{non-top}}) \times (P_1^{\text{Btag,data}})^2 \times \frac{P_2^{\text{MC}}}{(P_1^{\text{Btag,MC}})^2}. \tag{5.14}$$

The efficiency for the remaining requirements on $p_{\text{T}}^{\ell\ell}$, $m_{\ell\ell}$,and $\Delta\phi_{\ell\ell}$ is taken from simulation. The ratio of the resulting prediction to the one from simulation alone is 1.11 ± 0.02(stat.). This ratio is applied as a correction to the predicted top background.

The total systematic uncertainty on the ratio term $\frac{P_2^{\mathrm{MC}}}{(P_1^{\mathrm{Btag,MC}})^2}$ is 8% in which experimental uncertainties contribute about 7% that is mostly coming from the jet energy scale and resolution, and in which theoretical uncertainties contribute about 4.5% including the PDF, QCD scale, UEPS, and matching uncertainties.

Top background in the 1-jet analysis

The top background in the 1-jet analysis is estimated using the b-tagged control region that can be expressed as:

$$N_{\mathrm{top}}^{\mathrm{data,1j-SR}} = N_{\mathrm{top}}^{\mathrm{MC,1j-SR}} \times \frac{N_{\mathrm{top}}^{\mathrm{data,1j-CR}}}{N_{\mathrm{top}}^{\mathrm{MC,1j-CR}}}, \tag{5.15}$$

where $N_{\mathrm{top}}^{\mathrm{1j-SR}}$ is the number of top background in the signal region and $N_{\mathrm{top}}^{\mathrm{1j-CR}}$ is the number of top background in the control region that contains at least one b-jet, otherwise passes the same requirements as the signal region. When introducing the b-tagging efficiency (ϵ_{tag}) and inefficiency ($1 - \epsilon_{\mathrm{tag}}$), the ratio $N^{\mathrm{1j-SR}}/N^{\mathrm{1j-CR}}$ is given by:

$$\frac{N_{\mathrm{top}}^{\mathrm{1j-SR}}}{N_{\mathrm{top}}^{\mathrm{1j-CR}}} = \frac{1 - \epsilon_{\mathrm{tag}}^{\mathrm{1j-CR}}}{\epsilon_{\mathrm{tag}}^{\mathrm{1j-CR}}}. \tag{5.16}$$

Substituting Equation 5.16 into Equation 5.15, the $N_{\mathrm{top}}^{\mathrm{data,1j-SR}}$ is expressed as:

$$N_{\mathrm{top}}^{\mathrm{data,1j-SR}} = N_{\mathrm{top}}^{\mathrm{data,1j-CR}} \times \frac{1 - \epsilon_{\mathrm{tag}}^{\mathrm{MC,1j-CR}}}{\epsilon_{\mathrm{tag}}^{\mathrm{MC,1j-CR}}}. \tag{5.17}$$

In practice the efficiency is not measured using MC but measured in data because the MC efficiency leads to large experimental uncertainty coming from mis-tagging efficiency, jet energy scale, and jet energy resolution. To reduce the uncertainty one can measure the b-tagging efficiency using $t\bar{t}$ events in data. The data-driven method is so-called tag-and-probe method where randomly chosen one b-jet is defined as "tag". Making use of the other jet as "probe" does not make any bias in jet composition. Substituting MC efficiency for data efficiency, the equation above can be expressed as:

$$N_{top}^{\mathrm{data,1j-SR}} = \frac{N_{top}^{\mathrm{data,1j-CR}}}{\epsilon_{\mathrm{tag}}^{\mathrm{data,2j-CR}} \times f_{\mathrm{corr}}} \times (1 - \epsilon_{\mathrm{tag}}^{\mathrm{data,2j-CR}} \times f_{\mathrm{corr}}), \tag{5.18}$$

$$f_{\mathrm{corr}} = \frac{\epsilon_{\mathrm{tag}}^{MC,1j-CR}}{\epsilon_{\mathrm{tag}}^{MC,2j-CR}}, \tag{5.19}$$

In this formalization, the experimental uncertainty on the MC efficiency is mostly canceled by taking the ratio, thus the systematic uncertainty is dominated by the theoretical uncertainties on f_{corr}. The theoretical uncertainty is evaluated by comparing several MC

samples, and it is found that the theoretical uncertainty propagated to the final measured top events is $\sim 4\%$.

Figure 5.32 shows $m_{\ell\ell}$, m_{T}, $\boldsymbol{p}_{\mathbf{T}}^{\mathbf{miss,\ jetCorr}}$, and sub-leading lepton p_{T} distributions for 1-jet analysis. Overall agreement between data/MC looks reasonable and the purity of the top control region is 90% level. The normalization factor (NF) is also calculated in the signal region as the ratio of estimated top events ($N_{\mathrm{top}}^{\mathrm{data,1j-SR}}$) to the predicted top events ($N_{\mathrm{top}}^{\mathrm{MC,1j-SR}}$), which is 1.03 ± 0.03(stat.).

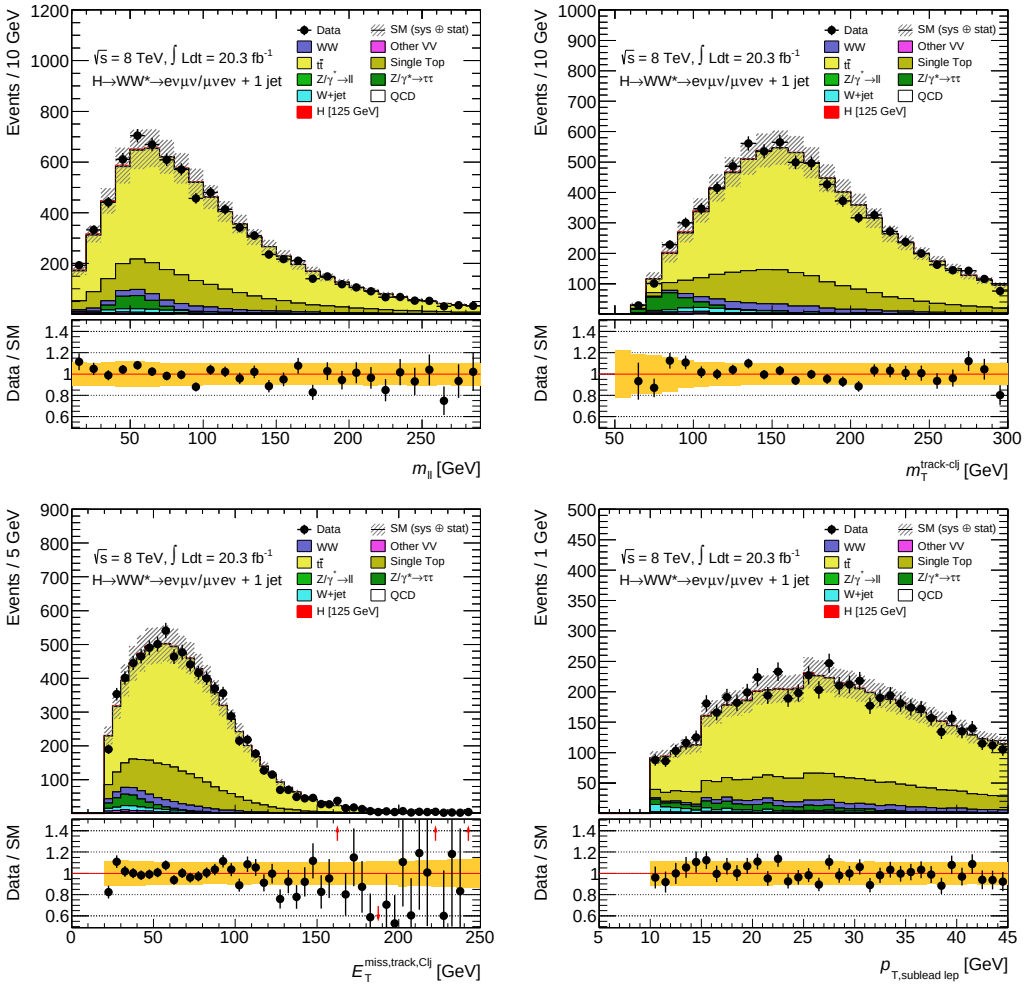

Figure 5.32: $m_{\ell\ell}$ (top left), m_{T} (top right), $\boldsymbol{p}_{\mathbf{T}}^{\mathbf{miss,\ jetCorr}}$ (bottom left), and sub-leading lepton p_{T} (bottom right) distributions in the top control region for 1-jet analysis.

5.5.2 VBF analysis

Figures 5.33 shows schematic view of the extraction of the main backgrounds in the VBF analysis.

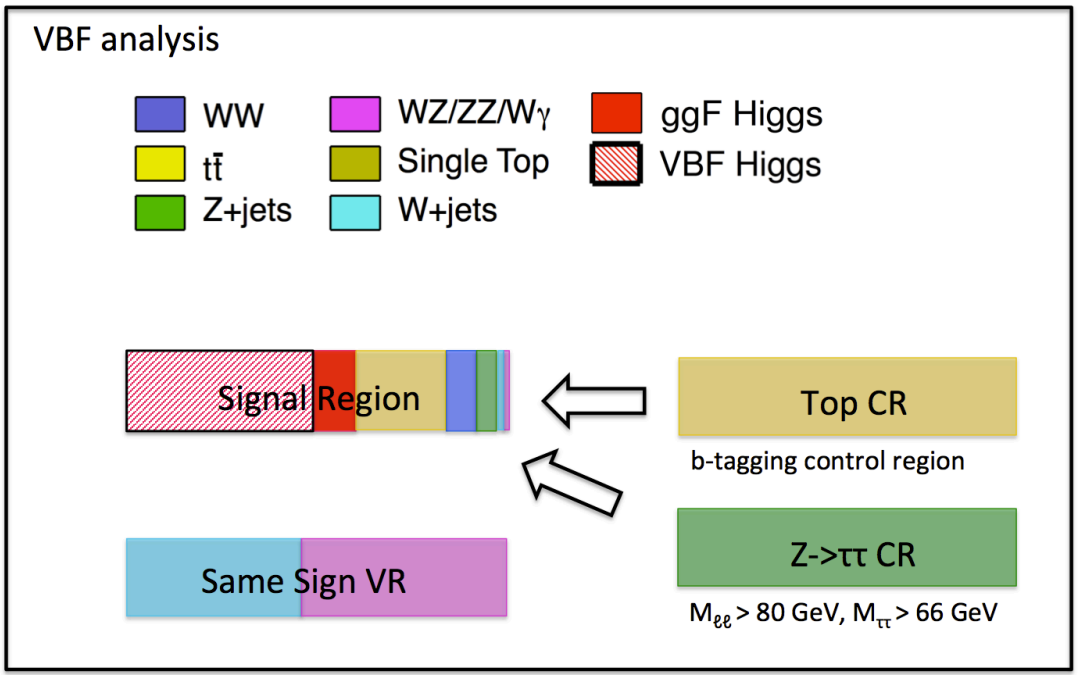

Figure 5.33: Schematic view of the extraction of the main backgrounds for the VBF analysis. Some backgrounds are normalized to data in dedicated control regions.

Top background

The top background is estimated using MC but the cross section is normalized to data in a b-tagged control region. The control region requires exactly one b-tagged jet, in order to make the flavor composition of tag jets closer to the one in the signal region. The control region is defined for each bin in the BDT score, but due to the lack of data statistics, the two bins with the highest BDT score share a combined normalization factor (NF). The resulting NFs from different flavor data set are 1.50±0.14(stat.) for the lowest bin and 1.34±0.38(stat.) for the highest two bins, and the NFs from same flavor data set are 1.67±0.20(stat.) for the lowest bin and 0.31±0.54(stat.) for the highest two bins. Figure 5.34 shows kinematic distributions for different flavor top control region.

The theoretical uncertainties are evaluated for the standard sources: the QCD scale, the PDF, the UEPS, and the matching using different MC generators. The uncertainties are derived for each bin of the BDT score. The total theoretical uncertainties for each bin are 10%, 12%, and 21% for each bin, that are dominated by the UEPS uncertainty, while other uncertainties are relatively small.

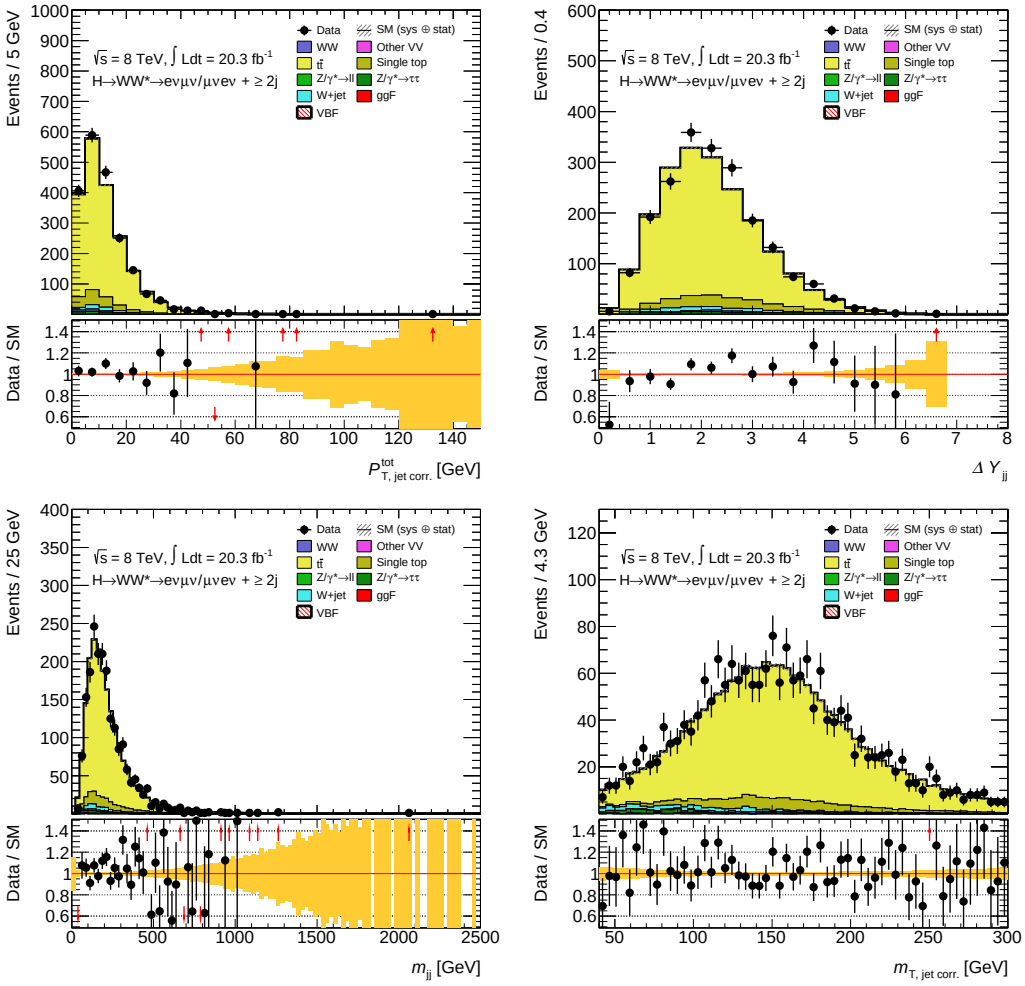

Figure 5.34: Distributions of $p_{\mathrm{T}}^{\mathrm{tot,track,jetCorr}}$, Δy_{jj}, m_{jj}, and m_{T} in different flavor top control region after all pre-selection.

$Z/\gamma^* \to \tau\tau$ background

The $Z/\gamma^* \to \tau\tau$ background is estimated using MC but the cross section is normalized to data in an appropriate $Z/\gamma^* \to \tau\tau$ control region. In order to define the $Z/\gamma^* \to \tau\tau$ control region, some selection criteria such as those $Z/\gamma^* \to \tau\tau$ veto and $m_{\ell\ell}$ are changed like the ggF analysis from the signal region definition described in Section 5.4.2:

- $m_{\ell\ell} < 80$ GeV,
- revert $Z/\gamma^* \to \tau\tau$ veto,
- BDT score > -0.48.

The cuts above increase the purity of the control region. The normalization factor (NF) is calculated using combined lepton flavor channels ($ee, \mu\mu, e\mu, \mu e$) due to lack of statistics. The resulting NF is 0.9±0.3(stat.). The systematic uncertainties are evaluated for standard sources: the PDF, the QCD scale, the UEPS, and the matching variations. Given the large statistical uncertainty (30%), the extrapolation uncertainty is negligible.

$Z/\gamma^* \to \ell\ell$ background

The $Z/\gamma^* \to \ell\ell$ (Z/DY) background is only relevant to the same flavor analysis. This background is estimated using a data-driven method, so-called ABCD method. Table 5.9 summarizes all regions used in the ABCD method.

Table 5.9: Summary of the regions used for the Z/DY estimation technique used in the SF channel of the VBF BDT analysis.

Region A (Signal Region) $E_{\mathrm{T}}^{\mathrm{miss}} > 45$ GeV $m_{\ell\ell} < 75$ GeV	**Region C** $E_{\mathrm{T}}^{\mathrm{miss}} > 45$ GeV $\lvert m_{\ell\ell} - m_Z \rvert < 15$ GeV
Region B 25 GeV $< E_{\mathrm{T}}^{\mathrm{miss}} < 45$ GeV $m_{\ell\ell} < 75$ GeV	**Region D** 25 GeV $< E_{\mathrm{T}}^{\mathrm{miss}} < 45$ GeV $\lvert m_{\ell\ell} - m_Z \rvert < 15$ GeV

The Z/DY shape is derived in data using a low $E_{\mathrm{T}}^{\mathrm{miss}}$ control region, referred to as "Region B". The Z/DY is normalized in the signal region (Region A) using the $E_{\mathrm{T}}^{\mathrm{miss}}$ cut

efficiency calculated from data in the Z peak (Region C and D). The Z/DY estimate in each BDT score bin i is given by:

$$\mathrm{N}^{\mathrm{SR},i}_{\mathrm{Z/DY}} = \mathrm{N}^{\mathrm{B},i}_{i\mathrm{Z/DY}} \cdot \frac{\mathrm{N}^{\mathrm{C}}_{\mathrm{Z/DY}}}{\mathrm{N}^{\mathrm{D}}_{\mathrm{Z/DY}}} \cdot f_{\text{non-closure}}, \tag{5.20}$$

where $\mathrm{N}_{\mathrm{Z/DY}} = (\mathrm{N}_{\mathrm{data}} - \mathrm{N}_{\text{non-Z/DY MC}})$, and $f_{\text{non-closure}}$ is the non-closure factor from MC that represents the difference in $E_{\mathrm{T}}^{\mathrm{miss}}$ cut efficiencies between Z peak and the low $m_{\ell\ell}$ ($m_{\ell\ell} < 75$ GeV) region, defined as:

$$f_{\text{non-closure}} = \frac{\mathrm{N_A}/\mathrm{N_B}}{\mathrm{N_C}/\mathrm{N_D}}. \tag{5.21}$$

Due to lack of events in data in the last BDT bin of Region B, a common normalization is used for the last two bins. The resulting NFs are 1.13 ± 0.14 for $-0.48 < \mathrm{BDT} < 0.3$ and 0.79 ± 0.23 for $0.3 < \mathrm{BDT} < 1.0$ The systematic uncertainties are evaluated by varying the QCD, the PDF, the UEPS, and the matching that is $\sim 11\%$ in total.

W+jets/QCD background

The W+jets/QCD backgrounds are estimated using the same data-driven method as is employed in the ggF 0-1 jet analysis.

VV background

For VV backgrounds fully MC-based estimation is employed since they remain small in the signal region. These backgrounds can be validated in the Same Sign region.

WW background

The WW background are categorized into processes containing only electroweak vertices "EW WW" and those containing a QCD vertex "QCD WW". Even though the cross section of QCD WW is much larger than that of EW WW, the contribution is compatible in the VBF phase space. The WW control region is not established due to large top background in a potential WW enriched region, thus the WW background is predicted by purely MC. The systematic uncertainty on the production cross section is evaluated by varying the QCD scale, the PDF, the UEPS, and the matching that is in total less than 2 %.

ggF background

The ggF process is an important background in the VBF analysis, since the cross section of the ggF process is 10 times higher than that of the VBF. The systematic uncertainty is evaluated by varying the QCD scale using the MCFM generator, that is $\sim 30\%$ uncertainty. The ggF uncertainty is further discussed in Section 5.6.2.1.

5.5.3 Background Summary

All significant sources of backgrounds are normalized using either fully data-driven estimates or the data in appropriate control regions. The WW, top, $Z/\gamma^* \to \tau\tau$, and VV ($W\gamma^{(*)}$, WZ, and ZZ) backgrounds are estimated using control regions in which one signal region criterion is reversed and others are loosened or dropped. The W+jets/QCD backgrounds are estimated using the fake factor method, which is discussed in Chapter 6. The $Z/\gamma^* \to \ell\ell$ background is estimated using a fully data-driven method based on Z/γ^*-enriched and -depleted regions. The background treatment is summarized in Table 5.10, and the set of all CR-derived normalization factors used in the analysis is summarized in Table 5.11.

Table 5.10: Methods of background estimation used in the 8 TeV analysis. The estimation procedures for various background processes are given in four categories: normalized using a control region (CR); data-driven estimate (Data); normalized using the MC (MC); and normalized using the MC, but validated in a control region (MC+VR). The "($e\mu$+μe)" indicates that the control region is defined in different flavor data set instead of same flavor data set for reasons of purity and/or statistics.

Channel	WW	Top	$Z/\gamma^* \to \tau\tau$	$Z/\gamma^* \to \ell\ell$	W+jets/QCD	VV
$N_{\text{jet}} = 0$						
$e\mu$+μe	CR	CR	CR	MC	Data	CR
ee+$\mu\mu$	CR ($e\mu$+μe)	CR ($e\mu$+μe)	CR ($e\mu$+μe)	Data	Data	MC+VR
$N_{\text{jet}} = 1$						
$e\mu$+μe	CR	CR	CR	MC	Data	CR
ee+$\mu\mu$	CR ($e\mu$+μe)	CR ($e\mu$+μe)	CR ($e\mu$+μe)	Data	Data	MC+VR
$N_{\text{jet}} \geq 2$						
$e\mu$+μe	MC	CR	CR	MC	Data	MC+VR
VBF						
$e\mu$+μe	MC	CR	CR ($e\mu$+μe +ee+$\mu\mu$)	MC	Data	MC+VR
ee+$\mu\mu$	MC	CR	CR ($e\mu$+μe +ee+$\mu\mu$)	Data	Data	MC+VR

Table 5.11: Normalization factors evaluated from control regions. Only statistical uncertainties are quoted. The VBF top NF is shown only for highest two bins.

	$N_{\text{jet}} = 0$	$N_{\text{jet}} = 1$	VBF ($e\mu$+μe)
WW	1.22 ± 0.03(stat.)	1.05 ± 0.05(stat.)	-
top	1.11 ± 0.02(stat.)	1.03 ± 0.03(stat.)	1.34±0.38(stat.)
$Z/\gamma^* \to \tau\tau$	1.01 ± 0.02(stat.)	1.07 ± 0.04(stat.)	0.90±0.30(stat.)
VV	0.93 ± 0.07(stat.)	0.96 ± 0.12(stat.)	-

5.6 Systematic Uncertainties

5.6.1 Experimental systematic uncertainty

5.6.1.1 Lepton

Systematic uncertainties related to electrons, except for uncertainties of isolation and impact parameter efficiencies, are summarized in Table 5.12. The efficiency of all additional cuts, (i.e. calorimeter isolation, track isolation, vertexing parameters, adding conversion bit and B-Layer at high η in $>$ 25 GeV) is also measured to correct possible mis-modeling in simulation. These additional cuts are a source of additional systematic uncertainties which is estimated with the Z tag-and-probe method and the final systematic uncertainty is presented in Section 4.8.

Table 5.12: Summary of electron systematic uncertainties. [119, 153]

Source of uncertainty	Size of uncertainty
Electron Efficiency	reconstruction: 0.1 - 1.0 % depending on E_{T} and η
	identification: 0.2 - 2.7 % depending on E_{T} and η
Electron Energy Scale	$\sim$ 0.4 % depending on E_T and η (except for crack region)
Electron Energy Resolution	about 1 % depending on E_T and η

An additional uncertainty is applied to photons misidentified as electrons. The electron from converted photon arises from $W\gamma$ events that are sub-dominant background in the 0-1 jet analysis. Table 5.13 summarizes the uncertainty to account for the mis-modeling of these electrons.

Table 5.13: Systematic uncertainty on converted electron as a function of p_{T}.

E_{T}	Uncertainty
10-15	25%
15-20	18%
20-	5%

Systematic uncertainties related to muons, except for uncertainties of isolation and impact parameter efficiencies, are summarized in the Table 5.14. Similar to the electrons, the systematic uncertainty due to additional cuts is evaluated using the Z tag-and-probe method and the final systematic uncertainty is presented in Section 4.8.

5.6.1.2 Jet

Jet systematic uncertainties are mostly relevant to the higher jet multiplicity analyses such as the ggF 2-jet and VBF analyses. Three sources of systematics are mainly considered: jet

Table 5.14: Summary of muon systematic uncertainties. [147]

Source of uncertainty	Size of the uncertainty
Muon Efficiency	< 0.46 % depending on p_{T} and η
Muon Energy Scale	< 0.50 % depending on p_{T} and η
Muon Energy Resolution	less than 1 % depending on p_{T} and η

energy scale/resolution (JES/JER), jet vertex fraction (JVF), and pileup. Also dedicated systematics for b-tagging is presented below.

Jet energy calibration uncertainties

The JES systematics are evaluated as a function of jet p_{T} and η that are at most 7% as shown in Section 3.3.1. The largest uncertainty on JES is coming from η modeling, which is $\sim$ 13% in the ggF 2-jet analysis, but the uncertainty gets smaller in the other analyses. The JER is an additional source of uncertainty and is added as uncorrelated source. The JER has some impact on the ggF 2-jet but otherwise it has less impact. The final impact on μ will be discussed in Section 8.3.2.

JVF uncertainty

The systematic uncertainty due to the application of JVF in the jet selection has been studied. The uncertainty is found to be negligible in case of signal and for any background estimation, the uncertainty can be canceled in usage of control regions. The most potentially sensitive selection is the Central Jet Veto (CJV) in the VBF analysis. A dedicated study shows a negligible effect of $\sim 0.5\%$.

Pileup uncertainty

The systematic uncertainty due to increased pileup especially in 2012 is evaluated by varying μ rescaling (see Section 3.2.2), pileup related JES uncertainties, and systematic uncertainties that can migrate across jet bins. The impact of μ scaling variation is at most 4% on the ggF 2-jet analysis that is compatible with statistical fluctuation. The variation of pileup related JES uncertainties affects $\sim 2\%$ on the ggF 2-jet analysis but has less impact on the other analyses. The effect of jet bin migration is also checked and found to be $< 1\%$ that is smaller than theory uncertainty on the ggF cross section, thus the uncertainty is neglected in the ggF analysis, while for the VBF analysis, the jet bin migration uncertainty of 1% is explicitely added because the theory uncertainty on the VBF production process is smaller than that on the ggF production process.

***b*-tagging uncertainty**

The uncertainties related to b-jet identification efficiency are decomposed into 6 uncorrelated components using so called eigenvector method (see Section 3.3.4). The 6 decomposed components of the uncertainty are ranging between 0.01%-0.6%, 0.01%-0.4%, 0.01%-0.7%, 0.6%-1.5%, 0.2%-4.8%, and 1.1%-7.8%. In addition, for the misidentified light or c-jets as a b-jets, the uncertainties are determined varying $\pm 1\sigma$ as a function of p_{T} and η. The uncertainty (1σ) on the light flavor is 9%-15% in the region $|\eta| < 1.1$, and 9%-19% at higher η bin, and the uncertainty on the c-jet is 6%-14% that is given in inclusive η range.

5.6.1.3 Missing transverse energy

Calorimeter-based missing transverse energy ($E_{\mathrm{T}}^{\mathrm{miss,CAL}}$)

The calorimeter missing transverse energy $E_{\mathrm{T}}^{\mathrm{miss,CAL}}$ that is only relevant to the ggF 0-1 jet same flavor analysis, is composed of all hard objects present in the event as well as the remaining part referred to as a "soft term" (see Section 3.4.1). The object related systematic variations are propagated into the $E_{\mathrm{T}}^{\mathrm{miss,CAL}}$. The only systematic source specific to the $E_{\mathrm{T}}^{\mathrm{miss,CAL}}$ calculation is the soft term systematic uncertainty. In order to derive the systematic uncertainty on the soft term of the $E_{\mathrm{T}}^{\mathrm{miss,CAL}}$, the $E_{\mathrm{T}}^{\mathrm{miss,CAL}}$ direction is decomposed into longitudinal and perpendicular directions with respect to the direction of the hard component of the $E_{\mathrm{T}}^{\mathrm{miss,CAL}}$. The systematic uncertainties are obtained from smearing and scaling both of these components, and those variations are treated as fully correlated uncertainties. The total uncertainty of $E_{\mathrm{T,rel}}^{\mathrm{miss}} > 45$ GeV cut (ggF 0-1 jet same flavor analysis) is 17%. The systematic uncertainty on the $E_{\mathrm{T}}^{\mathrm{miss}}$ (or $E_{\mathrm{T,rel}}^{\mathrm{miss}}$) is detailed in [15].

Track-based missing transverse momentum ($\boldsymbol{p}_{\mathbf{T}}^{\mathbf{miss}}$)

Similar to calorimeter missing transverse energy, the $\boldsymbol{p}_{\mathbf{T}}^{\mathbf{miss}}$ is composed of all hard object (electron, muon, and jet) and soft track term (see Section 3.4.2). As is the $E_{\mathrm{T}}^{\mathrm{miss,CAL}}$ case, the systematic uncertainties on the soft track term are derived in $Z \to \mu\mu$ events by decomposing $\boldsymbol{p}_{\mathbf{T}}^{\mathbf{miss}}$ direction into longitudinal and perpendicular directions, and by comparing several generators to account for the modeling of parton shower. For the $\boldsymbol{p}_{\mathbf{T}}^{\mathbf{miss,\ jetCorr}}$, an additional uncertainty is considered to account for tracks inside hard jets, which is as a function of p_{T} and η. The total uncertainty on the $\boldsymbol{p}_{\mathbf{T}}^{\mathbf{miss,\ jetCorr}}$ is $\sim 5\%$ and all those variations are treated as fully correlated uncertainties. The systematic uncertainty on the $\boldsymbol{p}_{\mathbf{T}}^{\mathbf{miss,\ jetCorr}}$ is detailed in [15].

5.6.2 Theoretical systematic uncertainty

Theoretical uncertainties (QCD scale, PDF, and modeling of underlying event and parton shower) are considered as uncertainties on cross sections of signal and background processes. The uncertainties on the Higgs signal are of special importance because of their large impact on the final result. Also the uncertainties on the WW production are important, since the WW is the largest and irreducible background in the main (ggF 0-1 jet) analysis. For the WW background in the ggF 0-1 jet analysis, the uncertainties are assigned on extrapolation

from the control region to the signal region, since the cross section of the WW background is normalized to data in the control region, while in the ggF 2-jets and VBF analyses, the uncertainty is considered on cross section rather than the extrapolation because the WW control region is not defined. In the remaining sections, uncertainties on both signal and WW productions are discussed, and others are detailed in [172].

5.6.2.1 Systematic uncertainty on the Higgs boson production

For the ggF analysis, since the analysis is separated into bins of jet multiplicity (0,1, $\geq$2), the signal cross section is calculated in each jet bin at the generator level to match the best available calculations of the veto efficiency of first and second jets. The uncertainty on the veto efficiencies to account for higher order corrections are 12% for the first jet and 14% for the second jet. These are treated as fully correlated to account for the jet bin migrations. For the signal acceptance the following variations are considered as theoretical uncertainties :

- QCD scale,
- PDF model uncertainties,
- underlying event and parton shower modeling (UEPS),
- mathcing of matrix element calculation to the parton shower.

These uncertainties are calculated in each signal regions and are summarized in Table 5.15. For the QCD scale, variations of renormalization and factorization scales ranging -50% to 200% are evaluated. The PDF uncertainties are evaluated for acceptances relative to the inclusive cross section, whereas others are calculated within jet bins. Different matching schemes of matrix element to the parton shower modeling are also calculated using generators with the same parton shower model (Herwig), which gives an estimate of the uncertainty due to the choice of matching scheme.

For the VBF process, the uncertainties on the signal acceptance (PDF, UEPS, QCD scale, matching) are also calculated. The uncertainty on the UEPS is 3.4%, the PDF uncertainty is 4.0%, the QCD scale is 3.0%, and the matching is 4.2%. To account for the difference among BDT bins, the BDT shape uncertainties are also evaluated and are summarized in Table 5.16. The uncertainties on those production processes are detailed in [172].

Table 5.15: Theoretical uncertainties in the ggF acceptance of each signal region. PDF uncertainties are evaluated for acceptances relative to the inclusive cross section, whereas others are calculated within jet bins. When the sign of an uncertainty is parenthesised, this means that the uncertainty is not statistically significant. In these cases, the statistical uncertainty on the generator difference is given, and the sign of the generator difference is parenthesised.

	m_{ll} (GeV)	$p_{T,l}^{\text{sublead}}$ (GeV)	Scale	PDF		UEPS		NLO-PS matching
				MSTW	68% CL	Pythia	Herwig	
$ee/\mu\mu$ channels								
0-jet	12–55	> 10	1.4%	1.9%	3.2%	+1.6%	+6.4%	−2.5%
1-jet	12–55	> 10	1.9%	1.8%	2.8%	(−)1.5%	+2.1%	(−)1.4%
$e\mu/\mu e$ channels								
0-jet	10–30	10–15	2.6%	1.8%	3.2%	−1.7%	+5.7%	−3.5%
	10–30	15–20	1.3%	1.9%	3.2%	(+)2.4%	+4.9%	−2.9%
	10–30	> 20	1.0%	1.9%	3.2%	−2.2%	(−)1.6%	(−)1.4%
	30–55	10–15	1.5%	1.8%	3.3%	(+)2.0%	+5.5%	−3.8%
	30–55	15–20	1.5%	1.9%	3.3%	(−)2.5%	(+)2.4%	−2.5%
	30–55	> 20	3.5%	1.9%	3.3%	−1.9%	−2.4%	(−)1.3%
1-jet	10–30	10–15	3.7%	1.7%	2.9%	+2.9%	+10.8%	−3.8%
	10–30	15–20	9.0%	1.7%	2.9%	(+)3.8%	(+)3.9%	(+)3.6%
	10–30	> 20	3.5%	1.8%	2.7%	(+)2.1%	(+)2.0%	(−)1.9%
	30–55	10–15	5.7%	1.7%	3.0%	(+)3.2%	+11.4%	−6.8%
	30–55	15–20	3.4%	1.9%	3.3%	(+)2.6%	+13.5%	+6.7%
	30–55	> 20	1.4%	1.8%	2.8%	(−)1.9%	(−)1.8%	(+)1.7%
≥2-jet	10–55	> 10	18%	2.0%	2.2%	(−)1.7%	(+)1.7%	−4.5%

Table 5.16: Theoretical uncertainties on the VBF Higgs production process, on the overall normalization in BDT (BDT norm.) and the BDT shape. μ_F and μ_R denote the variations of renormalization and factorization scales that are varied ranging [-50%, 200%].

Source	Description	BDT norm.	BDT shape
Scale	μ_F, μ_R in Powheg + Pythia	0.5%	[1%, 3%, 3%]
PDF	CT10 and NNPDF	4.0%	$< 2.0\%$
UEPS	Pythia v.s. Herwig	3.4%	[0.2%, 1.8%, 11%]
Matching	Powheg v.s. aMC@NLO	4.2%	-

5.6.2.2 Systematics on the Standard Model WW production

For the ggF 0-1 jet analysis, the WW background is normalized in the different flavor control region that is separated from the signal region at $m_{\ell\ell} = 55$ GeV. The followings are considered as the uncertainties on the extrapolation parameter α from the control region to the signal region:

- QCD scale,
- PDF model uncertainties,
- underlying event and parton shower modeling (UEPS),
- mathcing of matrix element calculation to the parton shower,
- EW corrections.

Table 5.17 summarizes the uncertainties on the extrapolation for NLO $q\bar{q}, qg \to WW$ processes. Note that the different flavor control region is also used in the same flavor analysis but the extrapolation uncertainties are separately calculated.

Table 5.17: Scale, UEPS, matching, higher order EW correction, and PDF uncertainties on the WW extrapolation parameters α for the NLO $q\bar{q}, qg \to WW$ processes. The correlations in the UEPS and matching uncertainties are shown explicitly, including the signed difference in the comparison. The different flavor (DF) signal regions are divided into $10 < m_{\ell\ell} < 30$ ("SR1") and $30 < m_{\ell\ell} < 55$ ("SR2"). The uncertainties on the uncertainties are also shown but only central values are used as the uncertainties.

$p_{\mathrm{T}}^{\mathrm{sublead}}$ [GeV]	α_i	Scale	UEPS	Matching	EW corr	PDFs	Total
$10-15$	$\alpha_{0j}^{\mathrm{DF}}$ (SR1)	0.73 ± 0.59	2.2 ± 0.29	0.44 ± 0.4	1.2 ± 0.33	0.96	2.8
	$\alpha_{0j}^{\mathrm{DF}}$ (SR2)	0.69 ± 0.63	1.5 ± 0.3	0.49 ± 0.41	0.82 ± 0.34	0.79	2.1
	$\alpha_{1j}^{\mathrm{DF}}$ (SR1)	3.1 ± 1.1	-2.4 ± 0.54	-3.4 ± 0.74	-0.85 ± 0.6	0.55	5.4
	$\alpha_{1j}^{\mathrm{DF}}$ (SR2)	3.2 ± 1	-2 ± 0.5	1.9 ± 0.68	-0.9 ± 0.56	0.55	4.5
$15-20$	$\alpha_{0j}^{\mathrm{DF}}$ (SR1)	1.2 ± 0.53	1.7 ± 0.26	0.9 ± 0.36	0.69 ± 0.3	0.79	2.6
	$\alpha_{0j}^{\mathrm{DF}}$ (SR2)	0.83 ± 0.46	1 ± 0.23	1 ± 0.32	0.47 ± 0.26	0.68	2
	$\alpha_{1j}^{\mathrm{DF}}$ (SR1)	1.6 ± 1	-3 ± 0.5	0.7 ± 0.7	-1.5 ± 0.57	0.48	3.9
	$\alpha_{1j}^{\mathrm{DF}}$ (SR2)	1.5 ± 0.83	-3 ± 0.41	2.4 ± 0.56	-1.6 ± 0.46	0.45	4.5
$20-$	$\alpha_{0j}^{\mathrm{DF}}$ (SR1)	0.72 ± 0.41	-1.9 ± 0.2	3.1 ± 0.28	-0.25 ± 0.23	0.61	3.8
	$\alpha_{0j}^{\mathrm{DF}}$ (SR2)	0.76 ± 0.29	-2.4 ± 0.14	3.9 ± 0.2	-0.4 ± 0.16	0.67	4.8
	$\alpha_{1j}^{\mathrm{DF}}$ (SR1)	1 ± 0.7	-3.6 ± 0.33	5.3 ± 0.46	-2.8 ± 0.38	0.62	7.1
	$\alpha_{1j}^{\mathrm{DF}}$ (SR2)	1.3 ± 0.48	-3.1 ± 0.23	5.6 ± 0.32	-2.7 ± 0.26	0.62	7.1
$10-$	$\alpha_{0j}^{\mathrm{SF}}$ (SR)	0.77 ± 0.23	-1.2 ± 0.12	2.4 ± 0.16	0.14 ± 0.13	1.1	2.9
	$\alpha_{1j}^{\mathrm{SF}}$ (SR)	0.81 ± 0.38	-2.3 ± 0.18	3.8 ± 0.25	-2.1 ± 0.21	0.86	5.1

The scale uncertainties are evaluated by varying the renormalization and factorization scales in aMC@NLO by a factor of two. The PDF uncertainties are evaluated comparing CT10 PDFs to the MSTW2008 and NNPDF2.3 PDFs. The UEPS uncertainty is evaluated by comparing the extrapolation parameter for the *Powheg+Pythia6* to that for *Powheg+Pythia8* and *Powheg+Herwig*. The Matching uncertainty is from comparison of Powheg +Herwig to MC@NLO+Herwig. The uncertainty on the EW correction is evaluated by comparison of the extrapolation with the NLO correction to the higher order calculation. The total uncertainty on the extrapolation varies 2.0-7.1%. For the $gg \to WW$ process, the relative uncertainty ($\Delta\alpha$) on the extrapolation (which is only 5.5% contribution in total WW cross section) is estimated to be 0.5% for 0-jet and 3.1% for 1-jet.

For the WW background, a shape uncertainty of the m_{T} distribution is also considered with three sources: the QCD scale, the UEPS, and the matching. The PDF shape uncertainties are small relative to those three, thus not included here. The shape uncertainties are considered for all subdivisions ($[m_{\ell\ell} < 30,\ m_{\ell\ell} > 30] \otimes [p_{\mathrm{T}}^{\mathrm{sublead}} :\ 10-15,\ 15-20,\ 20-] \otimes [0-\mathrm{jet},\ 1-\mathrm{jet}]$), 12 variations for each source of uncertainty. For each m_{T} shape comparison, envelopes are constructed by dividing one distribution by the other. Figure 5.35 shows m_{T} shape uncertainties, as an example, for the 0-jet low $m_{\ell\ell}$ ($m_{\ell\ell} < 30$) signal region. The final shape weights are made continuous by performing a piecewise linear interpolation which is visualized by looking at the bands themselves for each source of uncertainty. The variations are minimal at lower m_{T} (100-120 GeV), whereas they increase at higher m_{T} tail, which is up to $\sim 15\%$.

For the VBF analysis, the uncertainties for the QCD scale are separately evaluated for the production processes with zero (EW WW+2jets) or two QCD (QCD WW+2jets) vertices. In the former case a flat uncertainty of 10% is assigned, and in the latter case the uncertainty is 27%. The PDF uncertainties are at most 4 %, and the interference between processes is found to be negligible. An additional uncertainty is taken from the differences among several generators to cover remaining uncertainties, the UEPS, and the matching, which are in total [14%, 8%, 12%] for each BDT bin.

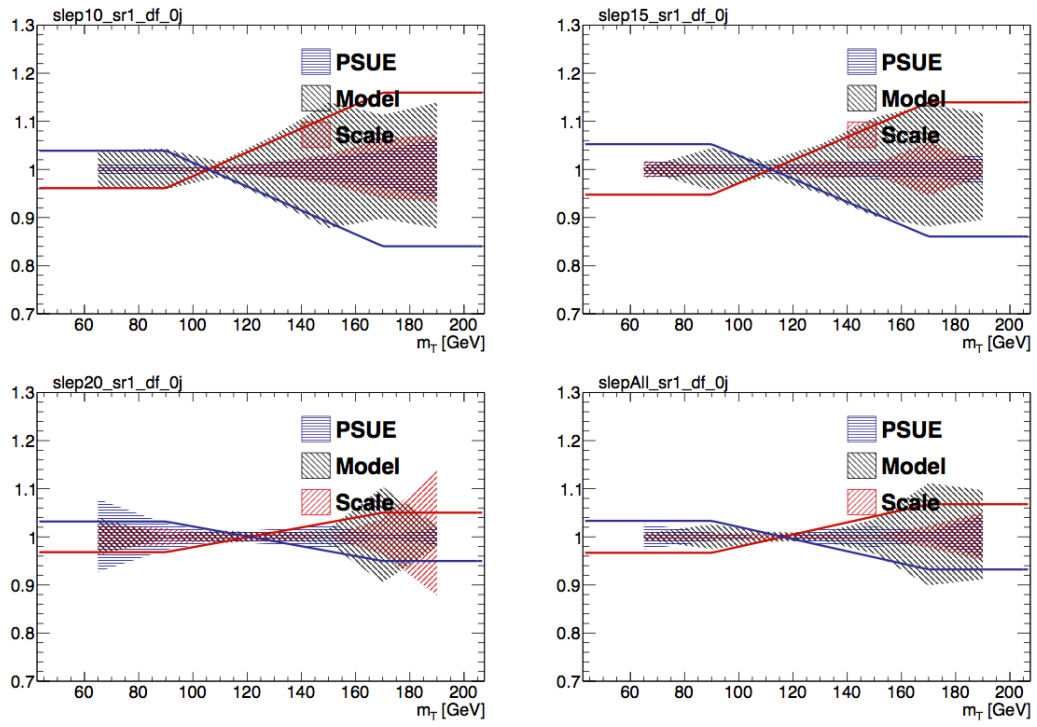

Figure 5.35: UEPS, matching, and scale envelopes for the 0-jet $10 < m_{\ell\ell} < 30$ GeV signal region. The linear envelope shows the global weight which parametrizes the three envelopes added in quadrature. However, a piecewise linear interpolation is used for each individual source of uncertainty instead of the linear envelope. The top left is for sub-leading lepton p_{T} = 10-15, top right for p_{T} = 15-20, bottom left for p_{T} = 20-, and bottom right for p_{T} = 10- just for reference.

Chapter 6

Fake Backgrounds

6.1 Introduction

Events in which W bosons are produced in association with jets give rise to background to WW events when the jet is misidentified as a lepton. The rate at which jets are misidentified as leptons may not be accurately described in simulation. A data-driven method to estimate this background is employed [173]. In this method, the QCD background can be similarly estimated as events in which two jets are misidentified as leptons. A description of the *Fake Factor Method* for predicting the W+jets/QCD backgrounds is presented in this chapter.

6.2 Fake Factor Method

6.2.1 Signal and Control Samples

In the *Fake Factor Method*, three samples are defined exclusively: signal sample ($N_{\text{id+id}}$), W+jets control sample ($N_{\text{id+anti-id}}$), QCD control sample ($N_{\text{anti-id+anti-id}}$).

The signal sample $N_{\text{id+id}}$ is identical to what is used in the standard analysis. In other words the sample is defined as events containing two fully identified leptons in data. It can also be rewritten, explicitly including the W+jets and the QCD backgrounds as:

$$N_{\text{id+id}} = N_{\text{id+id}}^{\text{QCD}} + N_{\text{id+id}}^{\text{W+jet}} + N_{\text{id+id}}^{\text{EW}} \tag{6.1}$$

where $N_{\text{id+id}}^{\text{QCD}}$ is the QCD background, $N_{\text{id+id}}^{\text{W+jet}}$ is the W+jets background, and $N_{\text{id+id}}^{\text{EW}}$ is all other backgrounds including the Higgs signal itself. The signal regions defined in the analysis is a subset of $N_{\text{id+id}}$ samples.

In order to estimate the W+jets background in the signal sample, the W+jets control sample is defined using an alternative lepton definition that enhances jets misidentified as leptons. Objects passing this alternative lepton definition are referred to in the following as anti-id objects. Events containing one fully identified lepton and one anti-id object constitute the W+jets control sample. These events are otherwise required to pass the full WW event selection, where the anti-id object is treated as if it were a fully identified lepton.

The W+jets control sample is expressed as:

$$N_{\text{id+anti-id}} = N^{\text{QCD}}_{\text{id+anti-id}} + N^{\text{W+jet}}_{\text{id+anti-id}} + N^{\text{EW}}_{\text{id+anti-id}} \tag{6.2}$$

where $N^{\text{QCD}}_{\text{id+anti-id}}$ is the QCD background, $N^{\text{W+jet}}_{\text{id+anti-id}}$ is the W+jets background, and $N^{\text{EW}}_{\text{id+anti-id}}$ is all other backgrounds including the Higgs signal itself in the W+jets control sample. Contaminations of $N^{\text{QCD}}_{\text{id+anti-id}}$ and $N^{\text{EW}}_{\text{id+anti-id}}$ are normally small depending on jet bins and lepton flavors but those backgrounds are subtracted from the W+jets control sample when predicting the W+jets background in the signal sample.

Similarly the QCD backgrounds are also estimated from data using events containing two anti-id objects. The two anti-id objects constitute the QCD control sample as:

$$N_{\text{anti-id+anti-id}} = N^{\text{QCD}}_{\text{anti-id+anti-id}} + N^{\text{W+jet}}_{\text{anti-id+anti-id}} + N^{\text{EW}}_{\text{anti-id+anti-id}} \tag{6.3}$$

where $N^{\text{QCD}}_{\text{anti-id+anti-id}}$ is the QCD background, $N^{\text{W+jet}}_{\text{anti-id+anti-id}}$ is the W+jets background, and $N^{\text{EW}}_{\text{anti-id+anti-id}}$ is all other backgrounds including the Higgs signal itself in the QCD control sample. Contaminations of $N^{\text{W+jet}}_{\text{anti-id+anti-id}}$ and $N^{\text{EW}}_{\text{anti-id+anti-id}}$ are normally small depending on jet bins and lepton flavors but those backgrounds are similarly subtracted from the QCD control sample when predicting the QCD background in the signal sample.

6.2.2 Fake Factor

The W+jets background is estimated from the W+jets control sample by applying an extrapolation factor, referred to in the following as a fake factor, which relates the W+jets control sample to the W+jets background in the signal sample (or which relates the QCD control sample to the QCD background in the W+jets control sample). The fake factor is expressed as:

$$f_l \equiv \frac{N_{\text{id}}}{N_{\text{anti-id}}} \quad (l = e \text{ or } \mu). \tag{6.4}$$

The fake factor, f_l, is independently defined for both electrons and muons, and it measures the ratio of the rate at which jets pass the full lepton identification requirements, to the rate at which they pass the anti-id requirement but fail the full lepton identification requirements. This fake factor is not exactly a fake rate and cannot be interpreted as a probability because the numerator samples are not a subset of the denominator samples (but the numerators and denominators are defined exclusively as shown in Table 6.2, 6.1, 6.4, and 6.3). The fake factor is measured in data using either di-jets or Z+jets events. The W+jets background in the signal sample is then calculated by scaling the number of events in the W+jets control sample using the measured fake factor:

$$N^{\text{W+jet}}_{\text{id+id}} = f_l \times N^{\text{W+jet}}_{\text{id+anti-id}} \tag{6.5}$$

$$= f_l \times (N_{\text{id+anti-id}} - N^{\text{EW}}_{\text{id+anti-id}} - N^{\text{QCD}}_{\text{id+anti-id}}), \tag{6.6}$$

where $N^{\text{EW}}_{\text{id+ anti-id}}$ is subtracted out using simulation and $N^{\text{QCD}}_{\text{id+anti-id}}$ is subtracted using $N_{\text{anti-id+anti-id}}$ events. The QCD subtraction from the W+jets control sample is discussed in detail in Section 6.7.

6.3 Anti-id Lepton Definitions and Overlap Removals

6.3.1 Anti-id Electron Definition

The `id` electron (numerator) and `anti-id` electron (denominator) definitions are shown in Table 6.1 and 6.2. The optimization procedure for `id` electrons can be found in Chapter 4. The denominator selection is defined by loosening isolation cuts and reverting the identification such that prompt electrons from W and Z bosons are suppressed, and that the contribution from misidentified jets is enhanced.

Table 6.1: Definition of the id electron (numerator).

Identified Electron
Author 1 or 3 (default algorithm of electron reconstruction [14])
$p_T > 10$ GeV
$\|\eta\| < 2.47$, excluded crack region ($1.37 < \|\eta\| < 1.52$)
$\|z_0 \sin\theta\| < 0.4$ mm, $\|d_0/\sigma_{d_0}\| < 3$
topoEtCone30Corr$/E_{\mathrm{T}} < 0.20$, PtCone40$/p_{\mathrm{T}} < 0.06$ (10-15 GeV)
topoEtCone30Corr$/E_{\mathrm{T}} < 0.24$, PtCone30$/p_{\mathrm{T}} < 0.08$ (15-20 GeV)
topoEtCone30Corr$/E_{\mathrm{T}} < 0.28$, PtCone30$/p_{\mathrm{T}} < 0.10$ (20- GeV)
VeryTight Likelihood $(10 - 25$ GeV)
Medium++ with conversion bit and b-layer requirement (25$-$ GeV)

Table 6.2: Definition of the anti-id electron (denominator).

Anti-id Electron
Author 1 or 3 (default algorithm of electron reconstruction [14])
$p_T > 10$ GeV
$\|\eta\| < 2.47$, excluded crack region ($1.37 < \|\eta\| < 1.52$)
$\|z_0 \sin\theta\| < 0.4$ mm, $\|d_0/\sigma_{d_0}\| < 3$
$N_{hits}^{SCT} + N_{hits}^{Pixel} \geq 4$
topoEtCone30Corr$/E_{\mathrm{T}} < 0.30$
PtCone30$/p_{\mathrm{T}} < 0.16$
Fails isEM Medium++
Fails the identified electron

6.3.2 Anti-id Muon Definition

The `id` muon and `anti-id` muon definitions are shown in Table 6.3 and 6.4. The optimization procedure for `id` electrons can be found in Chapter 4. The denominator selection is

defined by loosening isolation cuts and removing d_0 significance such that prompt muons from W and Z bosons are suppressed, and that the contribution from misidentified jets is enhanced.

Table 6.3: The definition of id muon (numerator).

Identified Muon Definition
STACO Combined Muon
$p_T > 10$ GeV
$\|\eta\| < 2.5$
$\|z_0 \sin\theta\| < 1$ mm, $\|d_0/\sigma_{d_0}\| < 3$
EtCone30Corr/$p_{\mathrm{T}} < 0.06$, PtCone40/$p_{\mathrm{T}} < 0.06$ (10-15 GeV)
EtCone30Corr/$p_{\mathrm{T}} < 0.12$, PtCone30/$p_{\mathrm{T}} < 0.08$ (15-20 GeV)
EtCone30Corr/$p_{\mathrm{T}} < 0.18$, PtCone30/$p_{\mathrm{T}} < 0.12$ (20-25 GeV)
EtCone30Corr/$p_{\mathrm{T}} < 0.30$, PtCone30/$p_{\mathrm{T}} < 0.12$ (25- GeV)

Table 6.4: The definition of anti-id muon (denominator).

Anti-id Muon Definition
STACO Combined Muon
$p_T > 10$ GeV
$\|\eta\| < 2.5$
$\|z_0 \sin\theta\| < 1$ mm
d_0 Impact Parameter Requirements Removed
EtCone30Corr/$p_{\mathrm{T}} < 0.15$ (10-15 GeV)
EtCone30Corr/$p_{\mathrm{T}} < 0.25$ (15-20 GeV)
EtCone30Corr/$p_{\mathrm{T}} < 0.30$ (20- GeV)
Track isolation cuts Removed
Fails the identified muon selection

6.3.3 Overlap Removal Procedure in W+jets/QCD estimation

The proper overlap removal between leptons and jets is of crucial importance for W+jets /QCD background estimations since the anti-id objects are less isolated. The anti-id objects are often overlapping with the jets defined in Section 3.3.1 ($p_{\mathrm{T}} > 25$ (30) GeV for $|\eta| < (\geq)$ 2.4). The procedure of overlap removals for standard analyses and for W+jet /QCD control samples is summarized in Table 6.5 and 6.6, where `id` denotes id objects and `anti-id` denotes anti-id objects.

Table 6.5: Summary of overlap removals in standard analysis.

	Overlap removals in standard analysis
dR (μ(id), e(id)) < 0.1	electron is removed if it overlaps with muon
dR (e(id), e(id)) < 0.1	electron is removed if it overlaps with higher E_{T} electron
dR (e(id), jet) < 0.3	jet is removed if it overlaps with electron
dR (μ(id), jet) < 0.3	muon is removed if it overlaps with jet

Table 6.6: Summary of overlap removals in W+jet /QCD control sample.

	Overlap removals in W+jet /QCD control sample
dR (μ(id), e(id)) < 0.1	electron is removed if it overlaps with muon
dR (μ(id), e(anti-id)) < 0.1	electron is removed if it overlaps with muon
dR (μ(anti-id), e(id)) < 0.1	electron is removed if it overlaps with muon
dR (μ(anti-id), e(anti-id)) < 0.1	electron is removed if it overlaps with muon
dR (e(id), e(id)) < 0.1	electron is removed if it overlaps with higher E_T electron
dR (e(anti-id), e(anti-id)) < 0.1	electron is removed if it overlaps with higher E_T electron
dR (e(anti-id), e(id)) < 0.1	electron is removed if it overlaps with higher E_T electron
dR (e(id), jet) < 0.3	jet is removed if it overlaps with electron
dR (e(anti-id), jet) < 0.3	jet is removed if it overlaps with electron
dR (μ(id), jet) < 0.3	muon is removed if it overlaps with jet
dR (μ(anti-id), jet) < 0.3	jet is removed if it overlaps with muon

In the W+jet /QCD estimate, the overlap removals for denominators are added. Note that μ-jet overlap removal is not symmetric between the anti-id and the id objects. An identified muon overlapping with a jet is removed in the W+jet /QCD control sample to keep consistency with standard analysis. It is found that the effect of this incompatibility is negligible in the W+jet /QCD control sample. In same flavor analysis, soft jets are defined with lower threshold (jet $p_T > 10$ GeV). If the jet is overlapping with the identified electron or the anti-identified electron/muon, the jet is removed from the jet counting. Without this procedure, the jet would be double counted since the jet is already counted as the anti-id muon in the W+jet /QCD control sample. Similarly, in VBF analysis, central jets are defined with lower threshold (jet $p_T > 15$ GeV, $|\eta| < 2.5$). If the central jet is overlapping with the identified electron or the anti-identified electron/muon, the central jet is removed from the jet counting. Without this procedure, the central jet veto efficiency would be higher in the W+jet /QCD control sample since the jet is already counted as the anti-id muon in the W+jet /QCD control sample.

6.4 Z+jet Fake Factors

For the fake factor, Z+jets sample has been considered, instead of the di-jets sample. Making use of the Z+jets sample for the fake factor has never been tried because the measurement in general requires large statistics. As one can imagine, Z+jet production cross section is much smaller than the di-jets (QCD) cross section. Nevertheless fairly large Z boson statistics have been available at the LHC, which makes the Z+jets fake factor possible. The procedure of the Z+jets fake factor measurement is summarized below.

6.4.1 Feature of Z+jet Fake Factor

The fake factor is measured using Z+jets sample. There are several advantages to using the Z+jets sample below:

- no trigger bias is expected in the measurement since the triggers (see Section 6.4.2) are fired by leptons from $Z \to \ell\ell$ decays,
- jet flavor composition in the Z+jets sample is expected to be similar to that in the W+jets sample ($gq' \to Zq'$ vs $gq' \to Wq''$), [1] which results in small sample dependence compared to that on the di-jets fake factor,
- jet kinematics like jet p_{T} in the Z+jets are expected to be similar to those in the W+jets because the center-of-mass energy of W and Z events is approximately identical,

Nevertheless there are a couple of limitations in the Z+jets fake factor measurement:

- statistics are limited (Z boson production cross section is small and the rate at which jets are misidentified as leptons is also small), in particular numerator statistics,
- larger EW contamination from diboson backgrounds, $W\gamma^{(*)}/WZ/Z\gamma^{(*)}/ZZ$ in the Z+jets sample.

Hence the systematic uncertainty on the Z+jets fake factor must be scrutinized comparing to the uncertainty on the di-jets fake factor. This is extensively discussed in Section B.1.4. Also the jet flavor composition is discussed in detail in Section B.2.

6.4.2 Z+jet selection

6.4.2.1 $Z \to \ell\ell$ selection

For electrons, in order to gain in acceptance, "medium" electron is defined by loosening fully identified electron selection criteria shown in Table 6.1. In particular the electron identification is loosened from the VeryTight likelihood to the cut-based Medium++, which results in 10 % improvement in single electron acceptance. The leading electron E_{T} is set to

[1] It means heavy flavor versus light flavor. One can imagine that heavy flavor composition is very different from the W+jets because of the W+charm process. This is true and is discussed further in Section B.2.

be 25 GeV without di-electron trigger, [2] `EF_2e12Tvh_loose1`, since the gain in acceptance from the di-electron trigger lowering lepton E_{T} is less than 10 %. In addition lowering electron E_{T} can increase the contamination of third electrons from $W\gamma^{(*)}/Z\gamma^{(*)}$ decays in the Z+"fake electron" sample, in particular photon conversions from the $Z\gamma$, in Z+fake electron sample.

For muons, "medium" muon is also defined but is identical to the fully identified muon shown in Table 6.3. The leading muon p_{T} is lowered to be 22 GeV with the di-muon trigger, `EF_mu18_tight_mu8_EFFS`, since the gain in acceptance is substantial (∼15-20 %), due to the extended η coverage from the di-muon trigger in the central region (see Section 4.2.1).

Since leptons from $Z \to \ell\ell$ decays are triggered by primary single/di-muon triggers, trigger bias is not expected in the fake factor measurement. After leptons selection, jet cleaning and overlap removals that are identical to those used in the standard analysis, are applied. Independently numerators and denominators for the fake factor calculation are also defined as shown in Table 6.1, 6.2, 6.3, 6.4, with proper overlap removal procedure summarized in Section 6.3.3. The lepton selection for $Z \to \ell\ell$ reconstruction is summarized in Table 6.7.

Table 6.7: lepton selection for $Z \to \ell\ell$ reconstruction.

lepton	$p_{\mathrm{T}}^{\mathrm{lead}}$[GeV]	triggers
electron	25	`EF_e24vhi_medium1`, `EF_e60_medium1`
muon	22	`EF_mu24i_tight`, `EF_mu36_tight`, `EF_mu18_tight_mu8_EFFS`

Pairs of two oppositely signed same flavor leptons are then selected to reconstruct Z bosons as shown in Figure 6.1.

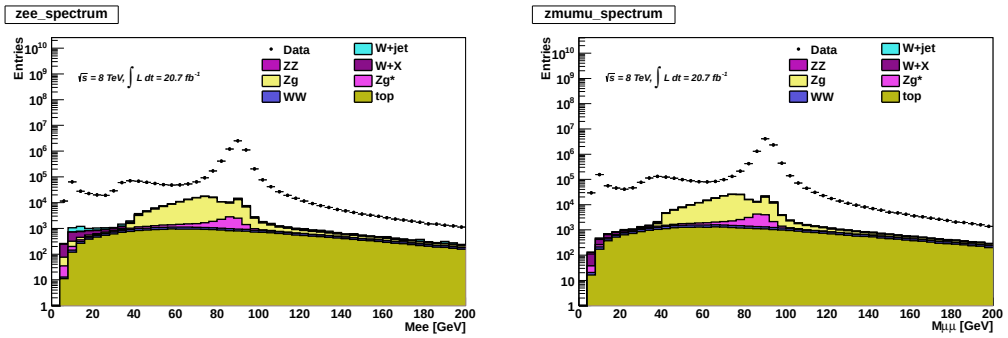

Figure 6.1: Invariant mass distributions for $Z \to ee$ (left) and $Z \to \mu\mu$ (right) after $Z \to \ell\ell$ selection. The Z+jets contribution is not explicitly shown but they can been seen as the difference between data and all other backgrounds. To suppress the contamination of diboson backgrounds, the Z mass window selection is applied later.

[2] the standard analysis uses `EF_2e12Tvh_loose1` trigger as well with the leading lepton $p_{\mathrm{T}} > 22$ GeV.

After $Z \to \ell\ell$ reconstruction, invariant mass of the two leptons are required to be within the Z mass window defined as 81 GeV $< M_{\ell\ell} <$ 107 GeV. However there is still a substantial diboson contamination in the Z+jets sample, in particular in Z+numerator sample, even after the cut on the Z mass window. Figure 6.2 shows m_{T}(lepton, $E_{\mathrm{T}}^{\mathrm{miss}}$) distributions for electrons and muons.

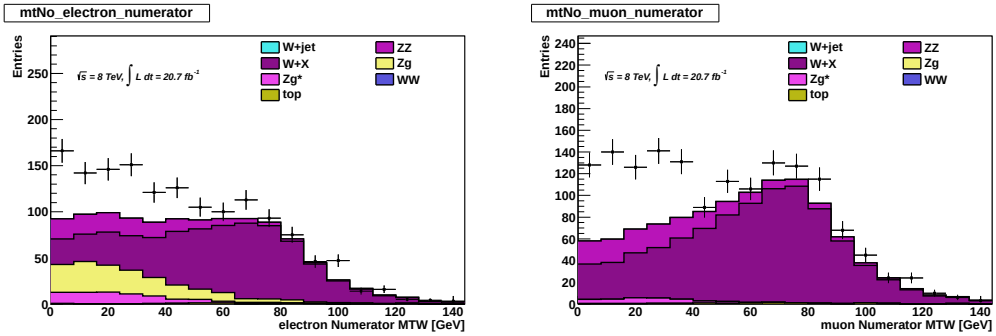

Figure 6.2: The m_{T}(lep, $E_{\mathrm{T}}^{\mathrm{miss}}$) distributions for electron channel (left) and for muon channel (right) after Z mass window selection where "METRefFinal" is used as missing E_{T}. The jacobian peak from W boson can be clearly seen around 80 GeV. At the high m_{T} region, WZ background is dominated in electron and muon channel. Further m_{T} selection is therefore needed to reduce the contamination of these background.

6.4.2.2 Diboson veto procedure

In order to further reduce the remaining contamination, ZZ and WZ veto cuts are applied, defining "loose" leptons that do not pass any identification and isolation requirements but do pass lepton $p_{\mathrm{T}} > 7$ GeV:

- ZZ **veto:** event is vetoed if there is another pair of oppositely signed same flavor leptons is within Z mass peak, $|M_Z - M_{\ell\ell}| < 15$ GeV,
- WZ **veto:** event is vetoed if there is an associated W boson candidate satisfying m_{T}(lep,$E_{\mathrm{T}}^{\mathrm{miss}}$) > 30 GeV.

The WZ veto is optimized to make the total uncertainty on the fake factor smallest as shown in Table 6.8, 6.9 by varying m_{T} cuts.

6.4.2.3 Fake factor Measurement

After ZZ and WZ veto, the fake factors are measured by taking the ratio of the number of numerators to the number of denominators as a function of p_{T} as shown in Figure 6.3. The fake lepton p_{T} distributions in Z+numerator and in Z+denominator control samples are shown in Figure 6.4 and Figure 6.5 by comparing two cases, $m_{\mathrm{T}} > 30$ GeV and > 100 GeV.

Table 6.8: Comparison of EW systematic uncertainty and statistical uncertainty varying m_{T} cuts from 20 GeV to 50 GeV in electron channel. The EW systematic uncertainty blows up rapidly while the statistical uncertainty goes down, when going to looser m_{T} veto cut. It is found that $m_{\mathrm{T}} >$ 30-40 GeV is optimal.

stat. $\pm$ *EW* syst.	$m_{\mathrm{T}} > 20$	$m_{\mathrm{T}} > 30$	$m_{\mathrm{T}} > 40$	$m_{\mathrm{T}} > 50$
$10 < E_{\mathrm{T}} < 15$	21.1 $\pm$ 9.9 %	17.6 $\pm$ 10.5 %	15.5 $\pm$ 10.2 %	15.5 $\pm$ 10.9 %
$15 < E_{\mathrm{T}} < 20$	41.8 $\pm$ 18.7 %	34.0 $\pm$ 19.2 %	40.1 $\pm$ 27.8 %	28.2 $\pm$ 20.1 %
$20 < E_{\mathrm{T}} < 25$	52.1 $\pm$ 18.8 %	52.1 $\pm$ 24.8 %	45.2 $\pm$ 25.4 %	72.5 $\pm$ 50.6 %
$E_{\mathrm{T}} > 25$	38.0 $\pm$ 23.7 %	29.6 $\pm$ 23.1 %	22.1 $\pm$ 20.2 %	20.5 $\pm$ 22.5 %

Table 6.9: Comparison of EW systematic uncertainty and statistical uncertainty varying m_{T} cuts from 20 GeV to 50 GeV in muon channel. The EW systematic uncertainty blows up rapidly while the statistical uncertainty goes down, when going to looser m_{T} veto cut. It is found that $m_{\mathrm{T}} >$ 30-40 GeV is optimal.

stat. $\pm$ *EW* syst.	$m_{\mathrm{T}} > 20$	$m_{\mathrm{T}} > 30$	$m_{\mathrm{T}} > 40$	$m_{\mathrm{T}} > 50$
$10 < p_{\mathrm{T}} < 15$	12.1 $\pm$ 2.3 %	10.2 $\pm$ 2.6 %	9.4 $\pm$ 3.0 %	9.3 $\pm$ 3.3 %
$15 < p_{\mathrm{T}} < 20$	20.6 $\pm$ 4.1 %	17.9 $\pm$ 5.1 %	17.3 $\pm$ 7.0 %	16.6 $\pm$ 8.1 %
$20 < p_{\mathrm{T}} < 25$	37.3 $\pm$ 8.9 %	28.6 $\pm$ 8.9 %	24.2 $\pm$ 9.4 %	28.1 $\pm$ 14.6 %
$p_{\mathrm{T}} > 25$	31.4 $\pm$ 13.2 %	34.1 $\pm$ 21.0 %	25.1 $\pm$ 18.4 %	32.4 $\pm$ 31.8 %

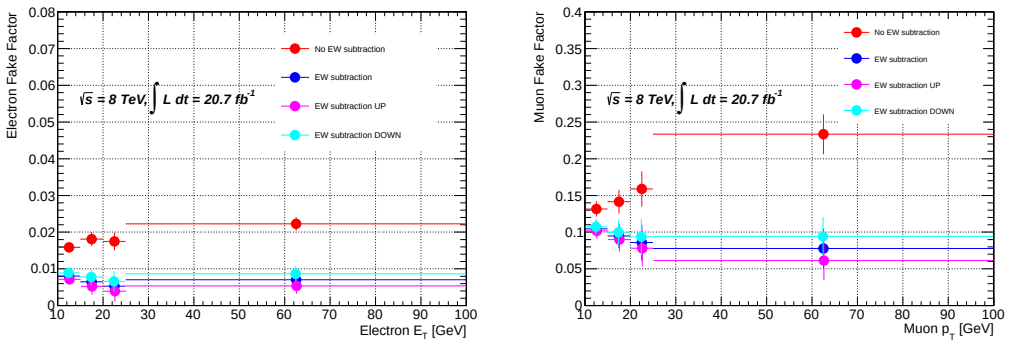

Figure 6.3: The Z+jets fake factor as a function of p_{T} in electron channel (left) and muon channel (right). The red dots are the fake factor before the EW subtraction, the blue dots are after the EW subtraction, and the others (light blue and magenta) are the variations of the EW subtraction. Since the statistics are very small above 25 GeV, all p_{T} bins above 25 GeV are merged.

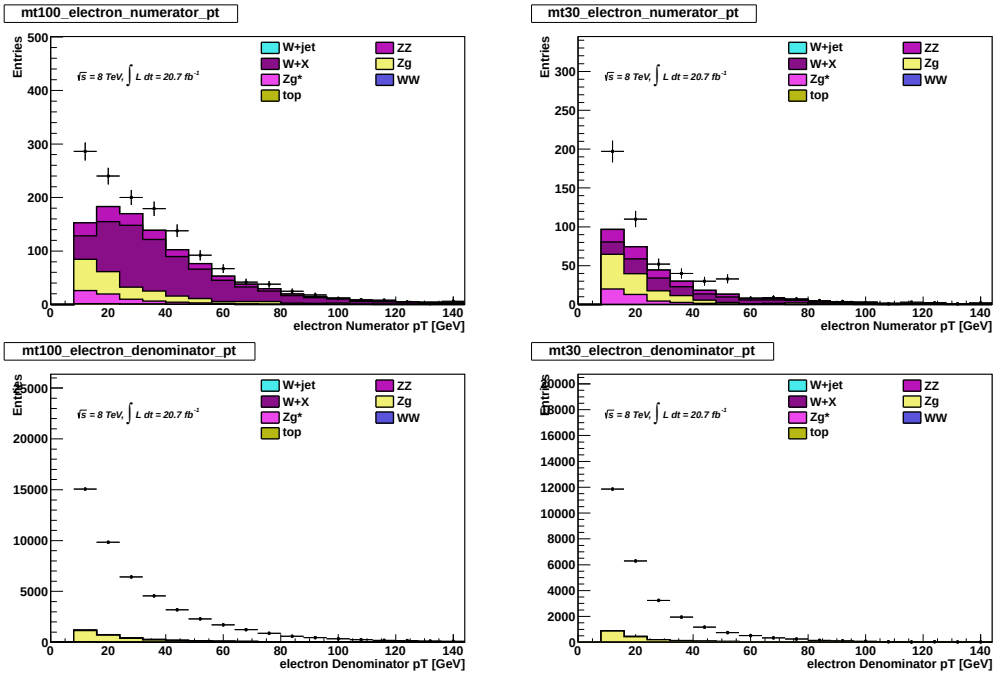

Figure 6.4: Comparison of electron E_{T} distributions after applying various m_{T} veto. The left two plots show E_{T} distribution for the numerator (top left) and for the denominator (bottom left) after applying $m_{\mathrm{T}} > 100$ GeV veto. The right two plots show E_{T} distribution for the numerator (top right) and for the denominator (bottom right) after applying $m_{\mathrm{T}} > 30$ GeV veto. In order to reduce real lepton contaminations in the Z+jets control sample, in particular in Z+numerator sample, the $m_{\mathrm{T}} > 30$ GeV is applied before measuring the fake factors. The remaining backgrounds are dominated by $Z\gamma$ in lower E_{T} whereas are dominated by $WZ/W\gamma^{*}$ in higher E_{T}.

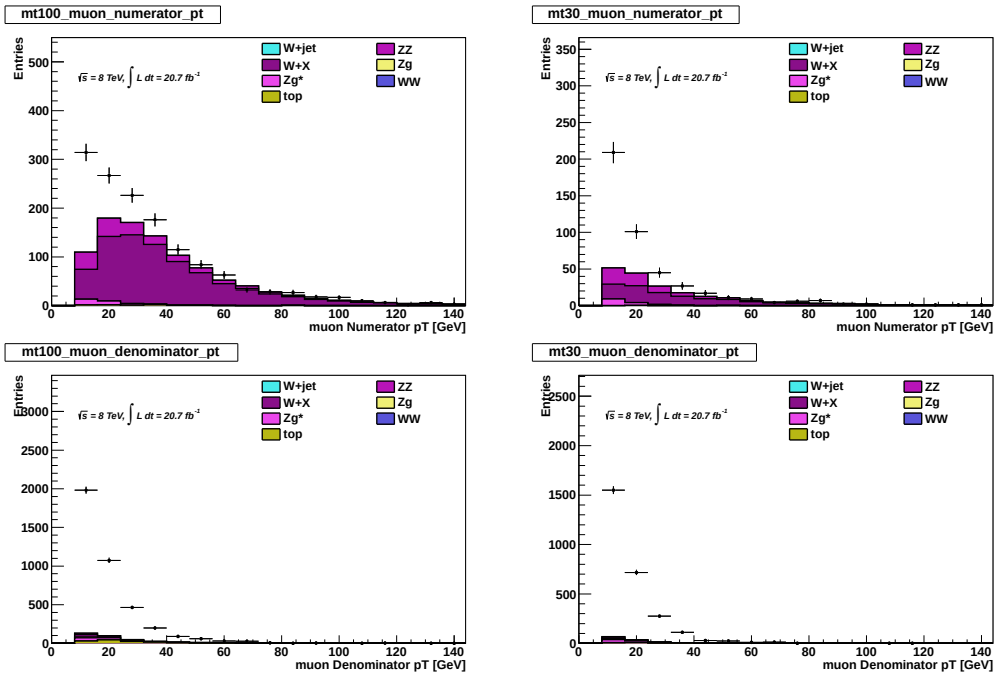

Figure 6.5: Comparison of muon p_{T} distributions after applying various m_{T} veto. The left two plots show p_{T} distribution for the numerator (top left) and for the denominator (bottom left) after applying $m_{\mathrm{T}} > 100$ GeV veto. The right two plots show p_{T} distribution for the numerator (top right) and for the denominator (bottom right) after applying $m_{\mathrm{T}} > 30$ GeV veto. In order to reduce real lepton contaminations in the Z+jets control sample, in particular in Z+numerator sample, the $m_{\mathrm{T}} > 30$ GeV is applied before measuring the fake factors. The remaining backgrounds are dominated by $WZ/W\gamma^{*}$.

Finally the η dependence of the fake factor from the di-jet measurement is injected to the Z+jet fake factors by taking the ratio of the p_{T} dependent fake factors:

$$f^{\mathrm{Z+jets}}_{(p_{\mathrm{T}},\eta)} = (f^{\mathrm{Z+jets}}_{p_{\mathrm{T}}} / f^{\mathrm{di\text{-}jets}}_{p_{\mathrm{T}}}) \times f^{\mathrm{Z+jets}}_{(p_{\mathrm{T}},\eta)}\,, \tag{6.7}$$

As is hard to take the η dependence directly from the Z+jets sample due to poor statistics, this approach (1D fake factor $\rightarrow$ 1D$\times$1D fake factor) is the best way to make the shape on the W+jets background more accurate. The injected η dependence is shown in Figure 6.6.

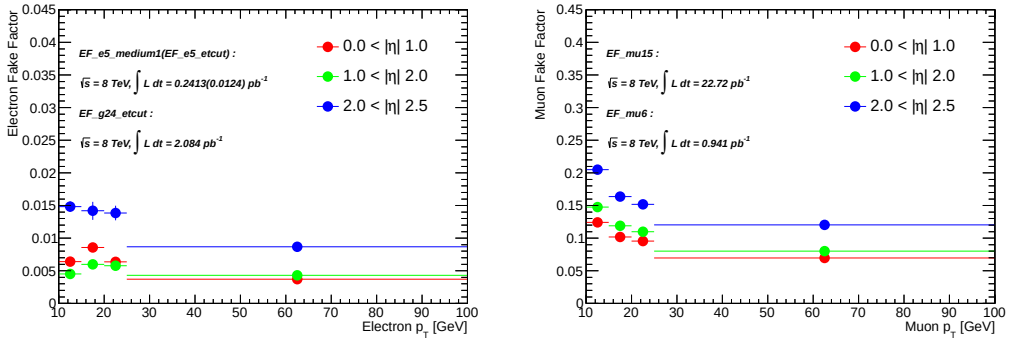

Figure 6.6: Plots show η dependence of fake factors taken from the di-jet enriched sample for electrons (left) and for muons (right). The fake factors tend to increase more than a factor of 2-3 at endcap region ($2.0 < |\eta| < 2.5$) because of detector geometry. The dependence is injected to the Z+jets fake factors to obtain more accurate shape estimate for the W+jets background.

6.4.3 Systematics

Systematic uncertainty associated with the fake factor measurement is the dominant source of uncertainty on the W+jets background. The fake factor uncertainty is divided into the following sources:

- The potential difference in fake factor between the Z+jets and W+jets is considered as sample dependence uncertainty. This is estimated by comparing the two fake factors in simulation. [3] This is the dominant systematic uncertainty on the fake factor.

- The uncertainty related to the third lepton contamination from diboson processes such as those $W\gamma^{(*)}/WZ/Z\gamma^{(*)}/ZZ$ in the Z+jet sample. This is estimated by varying the diboson subtractions.

These are each described in more detail below.

[3] The difference are in fact corrected for by correction factors based on simulation. The uncertainty on the correction factor as sample dependence is then evaluated by comparing several generators (see Section 6.5).

6.4.3.1 Sample dependence

The fake factor is measured in the Z+jet sample and is applied to the W+jets control sample ($N_{\mathrm{id+anti-id}}$). Differences in jet kinematics and heavy flavor fraction may cause the fake factor to be different in these two samples. A systematic uncertainty account for this sample dependence. This uncertainty is evaluated in simulation by comparing the two fake factors.

For electrons, the W+jets background is dominated by light-flavor (for instance, charged pion track overlapping with neutral pion cluster in EM calorimeter), and the contribution of heavy flavor is found to be small. The flavor composition is studied in detail, which is found in Section B.2. Figure 6.7 shows the comparison of the electron fake factors between the Z+jets and W+jets in simulation, $(f_l^{\mathrm{Z+jet}} - f_l^{\mathrm{W+jets}})/f_l^{\mathrm{Z+jet}}$ as a function of E_{T}. The fractional difference from the two samples is found to be $\sim$ 20 %.

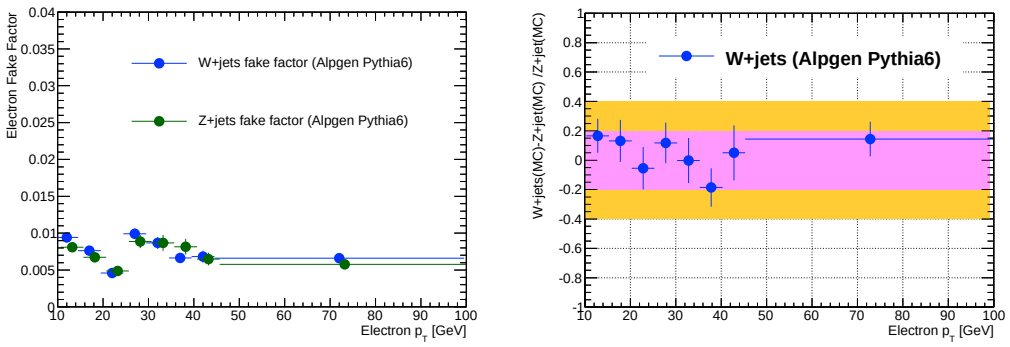

Figure 6.7: Comparison of electron fake factors between the Z+jets and W+jets samples (left). The fractional difference between the Z+jets and W+jets electron fake factors (right). The yellow band represents the sample dependence expected from the di-jets fake factor, while the pink band represents the sample dependence expected from the Z+jets fake factor. The sample dependence for the Z+jet fake factor is $\sim$ 20 % that is only 50 % of that for the di-jet fake factor.

For muons, W+jets background is dominated by heavy flavor (for instance, (semi-)leptonic decay of charm or bottom meson from W_c and W_{bb}/W_{cc} processes). The effect of light flavor is found to be smaller than that of heavy flavor, depending on p_{T} range. The flavor composition is studied in detail, which is found in Section B.2. Figure 6.8 shows the comparison of the muon fake factors between the Z+jets and W+jets in simulation, $(f_l^{\mathrm{Z+jet}} - f_l^{\mathrm{W+jets}})/f_l^{\mathrm{Z+jet}}$ as a function of p_{T}. The fractional difference from the two samples is found to be $\sim$ 20 %.

6.4.3.2 Lepton contamination in Z+jet sample

The Z+jet sample enhances jets misidentified as leptons. However there is still real lepton contamination from diboson processes such as those $W\gamma^{(*)}/WZ/Z\gamma^{(*)}/ZZ$ in the Z+jets

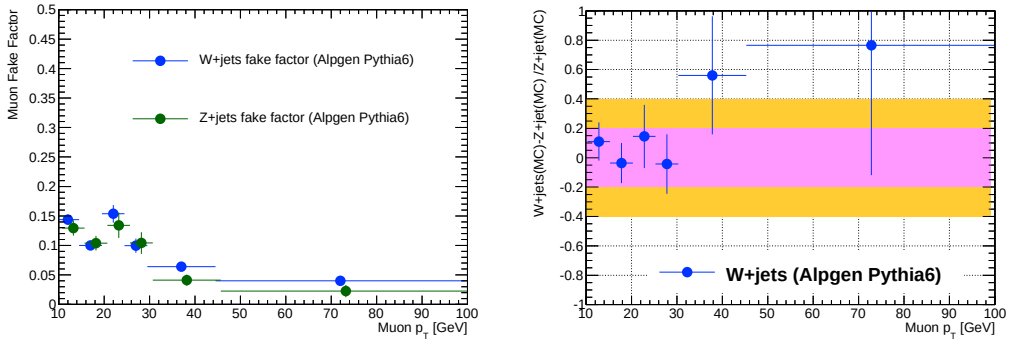

Figure 6.8: Comparison of muon fake factors between the Z+jets and W+jets samples (left). The fractional difference between the Z+jets and W+jets muon fake factors (right). The yellow band represents the sample dependence expected from the di-jets fake factor, while the pink band represents the sample dependence expected from the Z+jets fake factor. The sample dependence for the Z+jet fake factor is $\sim$ 20 % that is only 50 % of that for the di-jet fake factor.

sample. The lepton contamination from those events will bias the fake factor measurement. To reduce this bias, the EW veto (ZZ and WZ veto defined in Section 6.4.2.2) is applied to the Z+jets sample. The EW veto rejects 80 % of real lepton contamination, while retaining 70-80 % of the Z+jets sample. It has been checked that the EW veto does not bias the fake factor as shown in Figure 6.9.

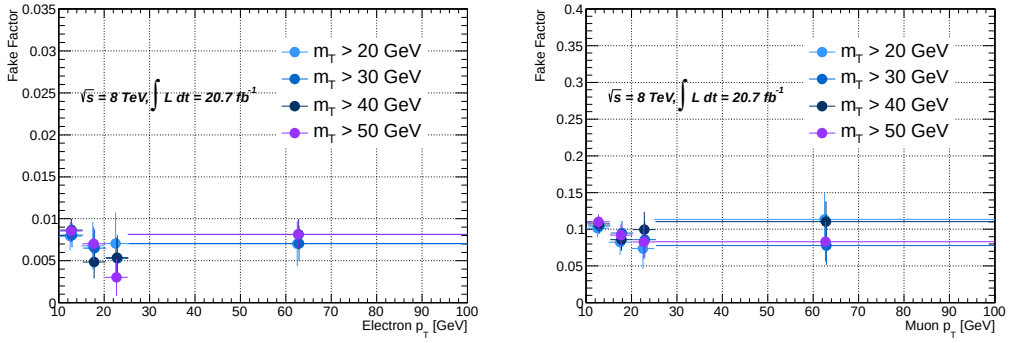

Figure 6.9: The Z+jets fake factor as a function of p_{T} in various m_{T} cuts to see the stability of the fake factors in electron channel (left) and muon channel (right) separately. Since the statistics are very small above 25 GeV, all p_{T} bins above 25 GeV are merged.

The remaining dibosons contribution is subtracted from the observed data using simulation. Figure 6.3 shows the estimated fake factor with/without the EW background

subtraction. The uncertainty due to the level of residual EW background is evaluated by varying the overall diboson cross sections by ±10%. The 10 % is set to be conservative compared to the uncertainties on the cross section evaluated for individual diboson processes [172]. The EW uncertainty accounts for uncertainties associated with those dibosons cross sections, and the modeling of simulated leptons from those dibosons satisfying the denominator selection. The EW uncertainty is in general smaller at lower lepton p_{T}, while it increases rapidly at higher p_{T}.

6.4.3.3 Trigger bias and pileup uncertainty

The trigger bias is not expected in the Z+jets measurement since electrons and muons used in the $Z \to \ell\ell$ reconstruction are defined to be tighter than trigger requirement. Also the pileup dependence appeared in the di-jets measurement is mostly cancelled out as can be seen in Equation 6.7, and the remaining uncertainty is expected to be less than a few %. Since the pileup uncertainty is much smaller than other uncertainties, the uncertainty is not included in the total systematic uncertainty.

6.5 Correction Factors

6.5.1 OS W+jets versus SS W+jets

In the previous publication, the W+jets background in the signal region ($N_{\text{id+id}}^{\text{W+jet(OS)}}$) was estimated using the W+jets control sample ($N_{\text{id+anti-id}}$) and fake factor obtained from di-jets sample ($f_{di-jets}^{incl.}$) as:

$$N_{\text{id+id}}^{\text{W+jet(OS)}} = f_{W+jets}^{incl.} \cdot N_{\text{id+anti-id}}^{\text{W+jet(OS)}} = f_{di-jets}^{incl.} \cdot \frac{f_{W+jets}^{incl.}}{f_{di-jets}^{incl.}} N_{\text{id+anti-id}}^{\text{W+jet(OS)}} \tag{6.8}$$

Similarly the W+jets estimate in same sign region ($N_{\text{id+id}}^{\text{W+jet(SS)}}$) is expressed as:

$$N_{\text{id+id}}^{\text{W+jet(SS)}} = f_{W+jets}^{incl.} \cdot N_{\text{id+anti-id}}^{\text{W+jet(SS)}} = f_{di-jets}^{incl.} \cdot \frac{f_{W+jets}^{incl.}}{f_{di-jets}^{incl.}} N_{\text{id+anti-id}}^{\text{W+jet(SS)}} \tag{6.9}$$

The same sign region was used as a validation region for the fake factor ($f_{di-jets}^{incl.}$), assuming the ratio of the fake factors ($\frac{f_{W+jets}^{incl.}}{f_{di-jets}^{incl.}}$) is unity and the deviation from unity is accounted for as the sample dependence systematic uncertainty.

The di-jets fake factor is replaced with the Z+jets fake factor when the Z+jets fake factor is introduced. The W+jets background in signal region ($N_{\text{id+id}}^{\text{W+jet(OS)}}$) is otherwise estimated in the same way as:

$$N_{\text{id+id}}^{\text{W+jet(OS)}} = f_{W+jets}^{incl.} \cdot N_{\text{id+anti-id}}^{\text{W+jet(OS)}} = f_{Z+jets}^{incl.} \cdot \frac{f_{W+jets}^{incl.}}{f_{Z+jets}^{incl.}} N_{\text{id+anti-id}}^{\text{W+jet(OS)}} \tag{6.10}$$

$$N_{\text{id+id}}^{\text{W+jet(SS)}} = f_{W+jets}^{incl.} \cdot N_{\text{id+anti-id}}^{\text{W+jet(SS)}} = f_{Z+jets}^{incl.} \cdot \frac{f_{W+jets}^{incl.}}{f_{Z+jets}^{incl.}} N_{\text{id+anti-id}}^{\text{W+jet(SS)}} \tag{6.11}$$

However these Equations are not accurate because the W+jets fake factor is different between OS and SS. The W+jets fake factor is therefore split into OS and SS, and the ratios, $f_{W+jets}^{OS}/f_{Z+jets}^{incl.}$ and $f_{W+jets}^{SS}/f_{Z+jets}^{incl.}$, are evaluated as "**correction factors**" in simulation. The Equations 6.10 and 6.11 can be then expressed as:

$$N_{\text{id+id}}^{\text{W+jet(OS)}} = f_{W+jets}^{OS} \cdot N_{\text{id+anti-id}}^{\text{W+jet(OS)}} = f_{Z+jets}^{incl.} \cdot \frac{f_{W+jets}^{OS}}{f_{Z+jets}^{incl.}} N_{\text{id+anti-id}}^{\text{W+jet(OS)}} \tag{6.12}$$

$$N_{\text{id+id}}^{\text{W+jet(SS)}} = f_{W+jets}^{SS} \cdot N_{\text{id+anti-id}}^{\text{W+jet(SS)}} = f_{Z+jets}^{incl.} \cdot \frac{f_{W+jets}^{SS}}{f_{Z+jets}^{incl.}} N_{\text{id+anti-id}}^{\text{W+jet(SS)}} \tag{6.13}$$

In this approach, the sample dependence is evaluated for OS and SS separately by comparing several generators that accounts for how well the correction factors are understood. The Equations 6.12 and 6.13 are new procedures used for the W+jets background estimate.

6.5.2 Correction Factors

6.5.2.1 OS/Z and SS/Z correction factors

To obtain the W+jets predictions in OS and SS separately, the two correction factors, $f_{W+jets}^{OS}/f_{Z+jets}^{incl.}$ and $f_{W+jets}^{SS}/f_{Z+jets}^{incl.}$, in Equations 6.12 and 6.13 are independently computed in simulation. Figure 6.10 and 6.11 show the OS W+jets and SS W+jets fake factors comparing with the di-jets and Z+jets fake factors.

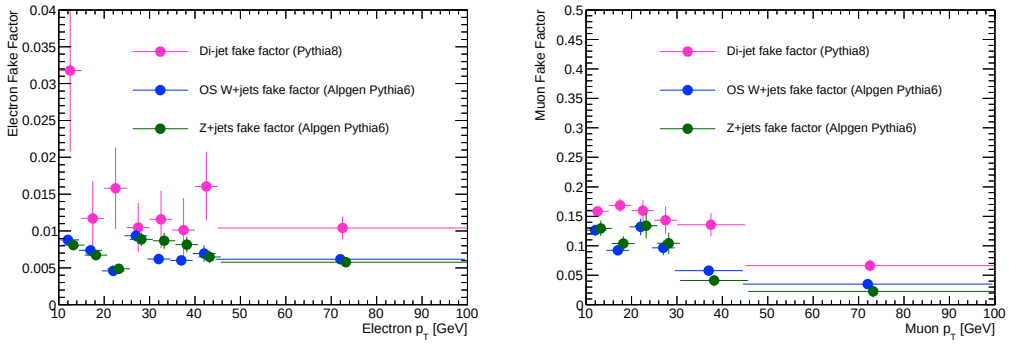

Figure 6.10: Comparison of the fake factors among the OS W+jets, di-jets, Z+jets samples in electron channel (left) and muon channel (right). Alpgen+Pythia6 sample is used for the OS W+jets and Z+jets fake factors, while `Pythia8` is used for the di-jets fake factor.

And Figure 6.12 shows direct comparison of the OS W+jets and SS W+jets fake factors in simulation. It is found that the SS W+jets fake factors are more than 20 % higher than

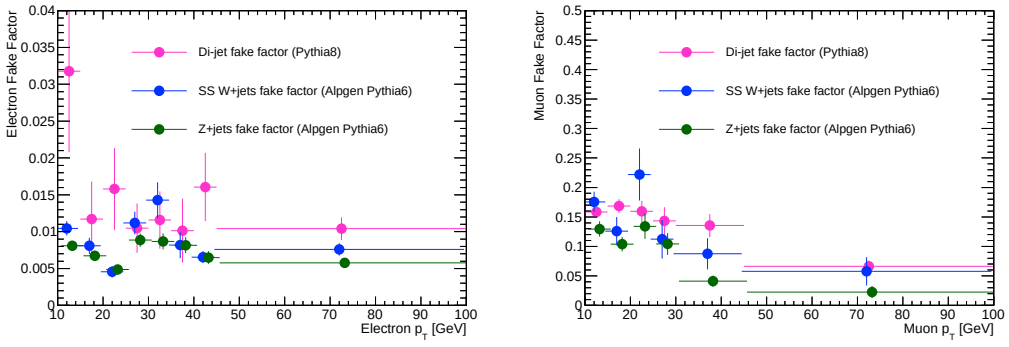

Figure 6.11: Comparison of the fake factors among the OS W+jets, di-jets, Z+jets samples in electron channel (left) and muon channel (right). Alpgen+Pythia6 sample is used for the OS W+jets and Z+jets fake factors, while `(mu-filtered) Pythia8` is used for the di-jets fake factor.

the OS W+jets fake factors. The difference in the fake factors arises from the difference in the flavor composition, which is discussed in detail in Section B.2.

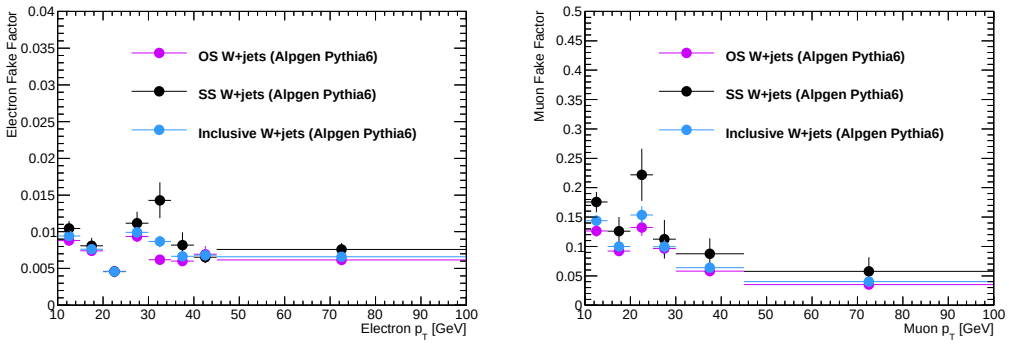

Figure 6.12: Comparison of the fake factors between the OS W+jets and SS W+jets samples in electron channel (left) and muon channel (right). Alpgen+Pythia6 sample is used for the OS W+jets and SS W+jets fake factors.

Using individual fake factors in Figures 6.10, 6.11, and 6.12, the correction factors, $f^{OS}_{W+jets}/f^{incl.}_{Z+jets}$ and $f^{SS}_{W+jets}/f^{incl.}_{Z+jets}$, are computed. Figure 6.13 shows the correction factors. $f^{OS}_{W+jets}/f^{incl.}_{Z+jets}$ is quite consistent with unity (, namely no correction) within the statistical uncertainty for both electrons and muons, whereas $f^{SS}_{W+jets}/f^{incl.}_{Z+jets}$ is 25 % correction for electrons and 40 % correction for muons.

Since the Alpgen+Pythia6 generator is well validated in data (see Figure B.9), the Alpgen+Pythia6 is used to derive the central value of the correction factors. The sam-

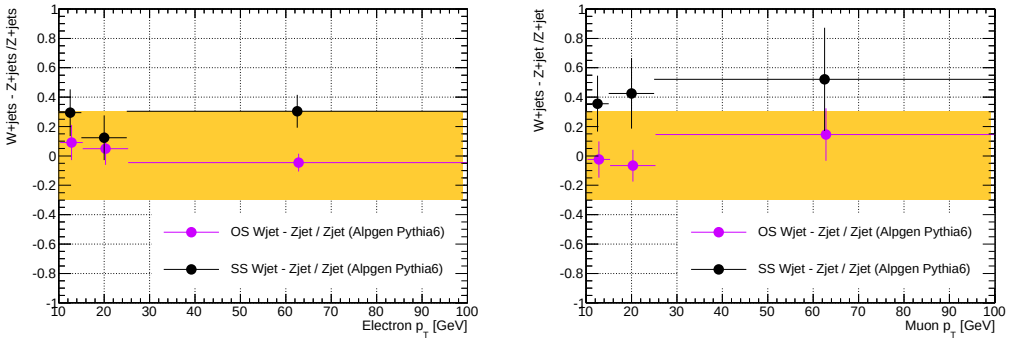

Figure 6.13: Deviation of correction factors from unity, $(f^{OS}_{W+jets}/f^{incl.}_{Z+jets}) - 1$ and $(f^{SS}_{W+jets}/f^{incl.}_{Z+jets}) - 1$, for electrons (left) and muons (right). Yellow band represents 30 % correction as reference, and does not indicates something special. The difference between OS and SS arises from the difference in the flavor composition that is discussed in Section B.2.

ple dependence is then evaluated by comparing with other generators with different ME and parton shower modeling such as those Alpgen+Herwig and Powheg+Pythia8 . Tables 6.10 and 6.11 show the comparison of the correction factors between generators for each p_{T} bin. Generally the correction factors are consistent within statistical fluctuations, and they do not have dependence much on ME and parton shower modelings.

To deal with statistical fluctuations on the correction factors, the comparison is finally made by merging p_{T} bins. The resulting systematic uncertainties and correction factors are summarized in Table 6.12. The correction factor in OS is quite consistent with the unity within the statistical uncertainty meaning that they do not change the W+jets prediction in OS. On the other hand, the correction factor in SS is not consistent with the unity within the statistical uncertainty but the unity (no correction) is still covered by the systematic uncertainty.

6.5.2.2 SS/OS correction factor

In addition to the two correction factors, the W+jets fake factor ratio, SS/OS ratio, is also computed using the W+jets simulation to see the direct difference in the two fake factors. Figure 6.14 shows the deviation of the SS/OS ratio from the unity. Also the generator comparison of the ratio is found in Table 6.13. Note that the SS/OS correction factor is not used in the analysis but is of special interest to see p_{T} dependence.

6.5.3 Data Validation

The correction factors derived from simulation are validated in the low p_{T} WW control region, defined as $10 < p_{\mathrm{T}}^{\mathrm{sub}} < 15$ GeV, $55 < M_{\ell\ell} < 110$ GeV after $p_{\mathrm{T}}^{\ell\ell}$ cut. The high purity of the W+jets is guaranteed in SS, whereas the WW contamination is substantial in OS.

Table 6.10: Comparison of correction factors between generators for electrons.

$f^{OS}_{W+jets}/f^{incl.}_{Z+jets}$

	Alpgen+Pythia6	Alpgen+Herwig	Powheg+Pythia8
$10 < E_{\mathrm{T}} < 15$	1.09 ± 0.12	0.95 ± 0.16	0.87 ± 0.09
$15 < E_{\mathrm{T}} < 25$	1.04 ± 0.31	0.72 ± 0.13	0.62 ± 0.08
$E_{\mathrm{T}} > 25$	0.95 ± 0.06	0.86 ± 0.07	0.87 ± 0.10
E_{T} average	0.99 ± 0.05	0.86 ± 0.06	0.80 ± 0.06

$f^{SS}_{W+jets}/f^{incl.}_{Z+jets}$

	Alpgen+Pythia6	Alpgen+Herwig	Powheg+Pythia8
$10 < E_{\mathrm{T}} < 15$	1.30 ± 0.16	1.13 ± 0.24	1.21 ± 0.13
$15 < E_{\mathrm{T}} < 25$	1.12 ± 0.15	0.95 ± 0.22	0.57 ± 0.09
$E_{\mathrm{T}} > 25$	1.31 ± 0.11	1.11 ± 0.11	1.09 ± 0.14
E_{T} average	1.25 ± 0.08	1.09 ± 0.09	0.95 ± 0.06

Table 6.11: Comparison of correction factors between generators for muons.

$f^{OS}_{W+jets}/f^{incl.}_{Z+jets}$

	Alpgen+Pythia6	Alpgen+Herwig	Powheg+Pythia8
$10 < p_{\mathrm{T}} < 15$	0.97 ± 0.12	1.72 ± 0.28	1.17 ± 0.13
$15 < p_{\mathrm{T}} < 25$	0.93 ± 0.11	1.21 ± 0.21	1.23 ± 0.17
$p_{\mathrm{T}} > 25$	1.14 ± 0.18	0.84 ± 0.17	1.50 ± 0.36
p_{T} average	1.00 ± 0.08	1.12 ± 0.12	1.21 ± 0.10

$f^{SS}_{W+jets}/f^{incl.}_{Z+jets}$

	Alpgen+Pythia6	Alpgen+Herwig	Powheg+Pythia8
$10 < p_{\mathrm{T}} < 15$	1.35 ± 0.19	1.19 ± 0.26	1.23 ± 0.15
$15 < p_{\mathrm{T}} < 25$	1.43 ± 0.24	1.68 ± 0.46	1.52 ± 0.25
$p_{\mathrm{T}} > 25$	1.52 ± 0.35	0.63 ± 0.20	1.95 ± 0.62
p_{T} average	1.40 ± 0.14	0.93 ± 0.15	1.33 ± 0.13

Table 6.12: Corrections factors and corresponding systematic uncertainties. Alpgen+Pythia6 is used to derive the central value and the systematic uncertainty is evaluated by comparing with other generators. The systematic uncertainty accounts for the difference in the flavor composition among samples.

	$f^{OS}_{W+jets}/f^{incl.}_{Z+jets}$	$f^{SS}_{W+jets}/f^{incl.}_{Z+jets}$
electrons	0.99 ± 0.05(stat) ± 0.19(syst)	1.25 ± 0.08(stat) ± 0.30(syst)
muons	1.00 ± 0.08(stat) ± 0.21(syst)	1.40 ± 0.14(stat) ± 0.47(syst)

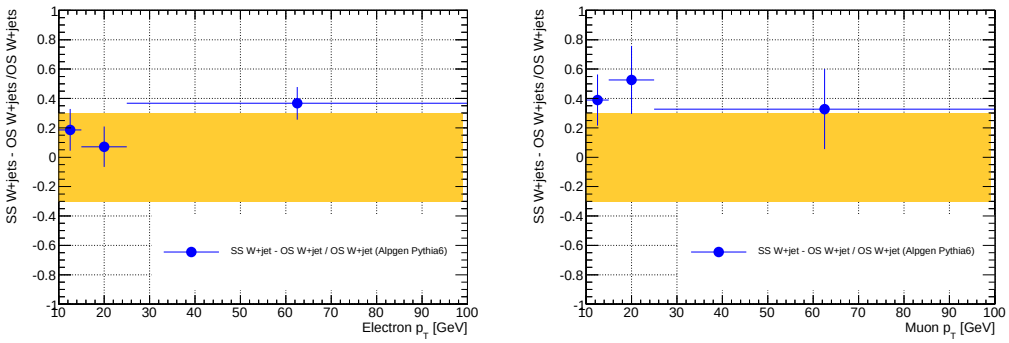

Figure 6.14: Deviation of the SS/OS ratio from unity, $(f^{SS}_{W+jets}/f^{OS}_{W+jets}) - 1$, for electrons (left) and muons (right). Yellow band represents 30 % correction as reference, and does not indicates something special. The difference between OS and SS arises from the difference in the flavor composition that is discussed in Section B.2.

It is hard to say something conclusive from this validation due to the limited statistics in SS but the agreement of data/simulation looks improved with the corrections as shown in Figure 6.15. Given that the correction factors for OS are ~ 1, the correction factors do not change pictures much in OS.

Another data/simulation comparison is made using the SS/OS ratio in the low $p_{\mathrm{T}}WW$ control region. The W+jets fake factors for OS and SS in data can be directly computed by using $N_{\text{id+anti-id}}$ and $N_{\text{id+id}}$ samples as follows:

$$f^{OS}_{W+jets} = (N^{\mathrm{OS}}_{\text{id+id}} - N^{\mathrm{EW(OS)}}_{\text{id+id}} - N^{\mathrm{QCD}}_{\text{id+id}})/(N^{\mathrm{OS}}_{\text{id+anti-id}} - N^{\mathrm{EW(OS)}}_{\text{id+anti-id}} - N^{\mathrm{QCD}}_{\text{id+anti-id}}) \quad (6.14)$$

$$f^{SS}_{W+jets} = (N^{\mathrm{SS}}_{\text{id+id}} - N^{\mathrm{EW(SS)}}_{\text{id+id}} - N^{\mathrm{QCD}}_{\text{id+id}})/(N^{\mathrm{SS}}_{\text{id+anti-id}} - N^{\mathrm{EW(SS)}}_{\text{id+anti-id}} - N^{\mathrm{QCD}}_{\text{id+anti-id}}) \quad (6.15)$$

where $N^{\mathrm{EW}}_{\text{id+id}}$ and $N^{\mathrm{EW}}_{\text{id+anti}-\text{id}}$ include all other backgrounds except for the W+jets/QCD backgrounds.

Table 6.13: Comparison of correction factors between generators.

$f^{SS}_{W+jets}/f^{OS}_{W+jets}$ for electrons

	Alpgen+Pythia6	Alpgen+Herwig	Powheg+Pythia8
$10 < E_{\mathrm{T}} < 15$	1.19 ± 0.14	1.19 ± 0.28	1.39 ± 0.12
$15 < E_{\mathrm{T}} < 25$	1.07 ± 0.14	1.32 ± 0.33	0.93 ± 0.14
$E_{\mathrm{T}} > 25$	1.37 ± 0.11	1.29 ± 0.12	1.24 ± 0.14

$f^{SS}_{W+jets}/f^{OS}_{W+jets}$ for muons

	Alpgen+Pythia6	Alpgen+Herwig	Powheg+Pythia8
$10 < p_{\mathrm{T}} < 15$	1.39 ± 0.17	0.68 ± 0.16	1.05 ± 0.10
$15 < p_{\mathrm{T}} < 25$	1.53 ± 0.23	1.39 ± 0.39	1.24 ± 0.17
$p_{\mathrm{T}} > 25$	1.33 ± 0.27	0.75 ± 0.22	1.30 ± 0.35

To extract pure W+jets component, other contributions such as those QCD and EW backgrounds are subtracted from data. The SS/OS ratio is then computed by taking the ratio of the two fake factors. The ratio can be a good quantity for the validation because there is no room for the Z+jets fake factor.

The comparison of the SS/OS ratio between data and simulation is found in Table 6.14. The SS/OS ratios in data are consistent with those in MC within the large uncertainty that is dominated by WW background subtraction in OS and by statistical uncertainty in SS.

Table 6.14: The data/MC comparison of the SS/OS ratio in the low p_T WW control region, where the Alpgen+Pythia6 is used and only stat uncertainty is taken into account for MC. The uncertainty is dominated by the other background contamination and the statistical uncertainty in data.

	Data	MC
electrons	0.82 ± 0.30	1.19 ± 0.14
muons	2.22 ± 0.79	1.39 ± 0.17

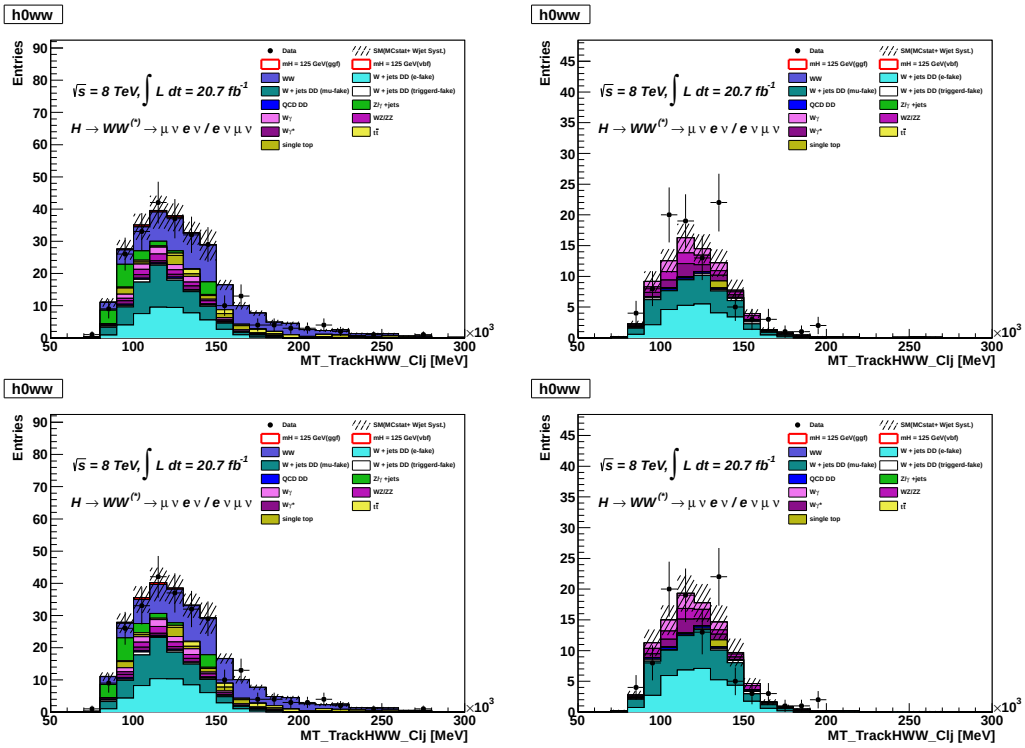

Figure 6.15: The low $p_{\mathrm{T}}WW$ validation region defined as $10 < p_{\mathrm{T}}^{\mathrm{sub}} < 15$ GeV, $55 < M_{\ell\ell} < 100$ GeV after $\mathbf{p}_{\mathrm{T}}^{\ell\ell}$ cut. The top plots are before corrections and the bottom plots are after corrections.

6.6 W+jets Control Sample

6.6.1 Control Sample Definition

Data-driven W+jets control sample ($N_{\text{id+anti-id}}$) is used to obtain the W+jets prediction in the signal region ($N_{\text{id+id}}$) multiplying the fake factors as discussed in Section 6.2. The W+jets control sample is defined as events that have one `id` lepton and one `anti-id` lepton. The control sample is collected with the primary triggers that are used in the standard analysis (see Table 3.2): `EF_e24vhi_medium1`, `EF_e60_medium1`, `EF_2e12Tvh_loose1`, and `EF_e12Tvh_medium1_mu8` for ee and $e\mu$+μe channels, and `EF_mu24i_tight`, `EF_mu36_tight`, `EF_mu18_mu8_EFFS`, and `EF_e12Tvh_medium1_mu8` for $\mu\mu$ and $e\mu$+μe channels. Nevertheless there is a small bias on the W+jets control sample when using those triggers due to some requirements on the triggers such as `medium1` and `i`. This is further discussed in the next Section B.4.

There is also a contribution from multiple `anti-id` lepton events that have one `id` lepton and more than one `anti-id` leptons, to the W+jets control sample. It is possible to include such multiple `anti-id` lepton events by replacing one of the `anti-id` leptons with reconstructed jet when treating the other `anti-id` lepton as fake lepton. The contribution of the multiple `anti-id` lepton events to the control sample was investigated, and was found to be $<$ a few % in 0 jet bin, $<$ 10 % in 1 jet bin, and $\sim$ 20 % in 2 jet bin. Given the large systematic uncertainty on the fake factor (30-40 %) and small impact of the W+jets background in the VBF signal region, the events are not taken into account as the W+jets control sample in the current analysis scheme.

Kinematic distributions of the W+jets control sample is investigated by splitting into low p_{T} and high p_{T} (sub-leading $p_{\text{T}} > 15$ GeV) and by overlaying the expectation from the W+jets simulation for shape comparison. The shape modeling of the W+jets background is further discussed in Section B.3. The higher Z+jets contamination (20-30 %) is expected in $\mu\mu$ channel but otherwise the purity of the W+jets background in the control sample is more than 90 % depending on the cut stage or signal region.

Figure 6.16 and 6.17 show kinematic distributions after $\mathbf{p}_{\text{T}}^{\ell\ell}$ cut in 0 jet for μe and $e\mu$ channels, respectively. In terms of the shape modeling, data shows reasonable agreement with simulation even though statistics in simulation in low p_{T} $e\mu$ channel is limited. After $\Delta\phi_{\ell\ell}$ cut, the EW contamination will be negligible, less than a few %, in μe and $e\mu$ channels. Figure 6.18 and 6.19 show kinematic distributions after b-veto requirement in 1 jet for μe and $e\mu$ channels, respectively. After $\Delta\phi_{\ell\ell}$ cut, the EW contamination will be negligible, less than a few %, in μe and $e\mu$ channels. Nevertheless the QCD contamination remains in lower MAX $m_{\text{T}}(W)$ distribution in $e\mu$channel, which will be correctly subtracted using the QCD control sample ($N_{\text{anti-id+anti-id}}$. The detailed procedure of the QCD subtraction from the W+jets control sample is presented in Section 6.7.

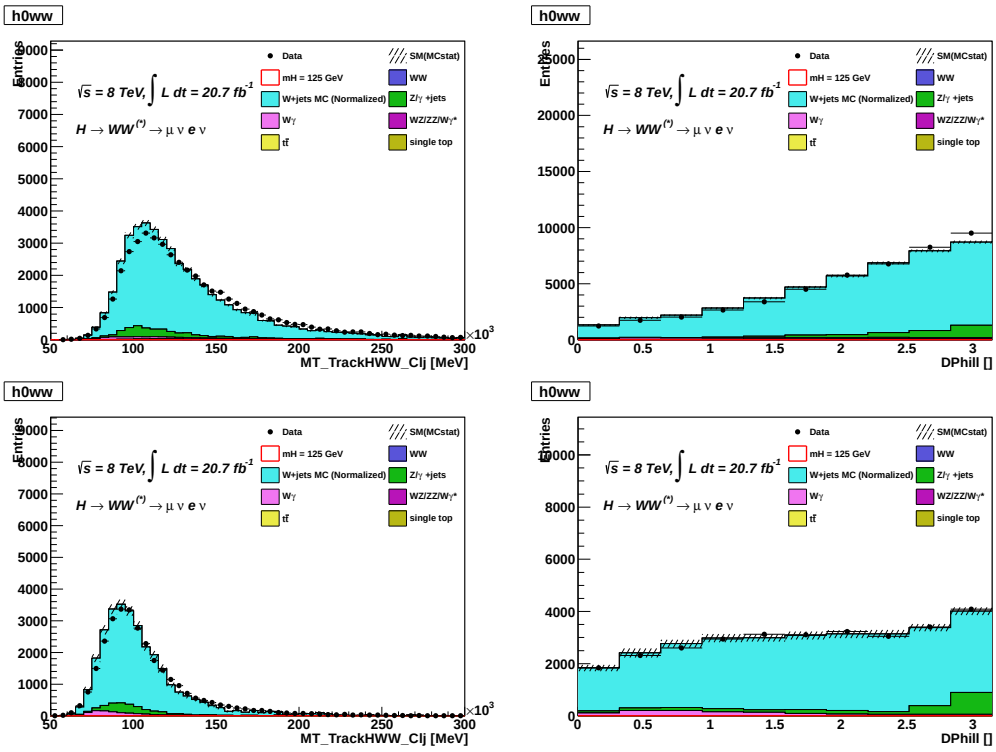

Figure 6.16: Kinematics of the W+jets control sample for μe channel in 0 jet after $p_{\mathrm{T}}^{\ell\ell}$requirement. The top plots are m_{T} (left) and $\Delta\phi_{\ell\ell}$ (right) in high p_{T}. The bottom plots are m_{T} (left) and $\Delta\phi_{\ell\ell}$ (right) in low p_{T}. The expectation from the W+jets simulation is also shown for comparison.

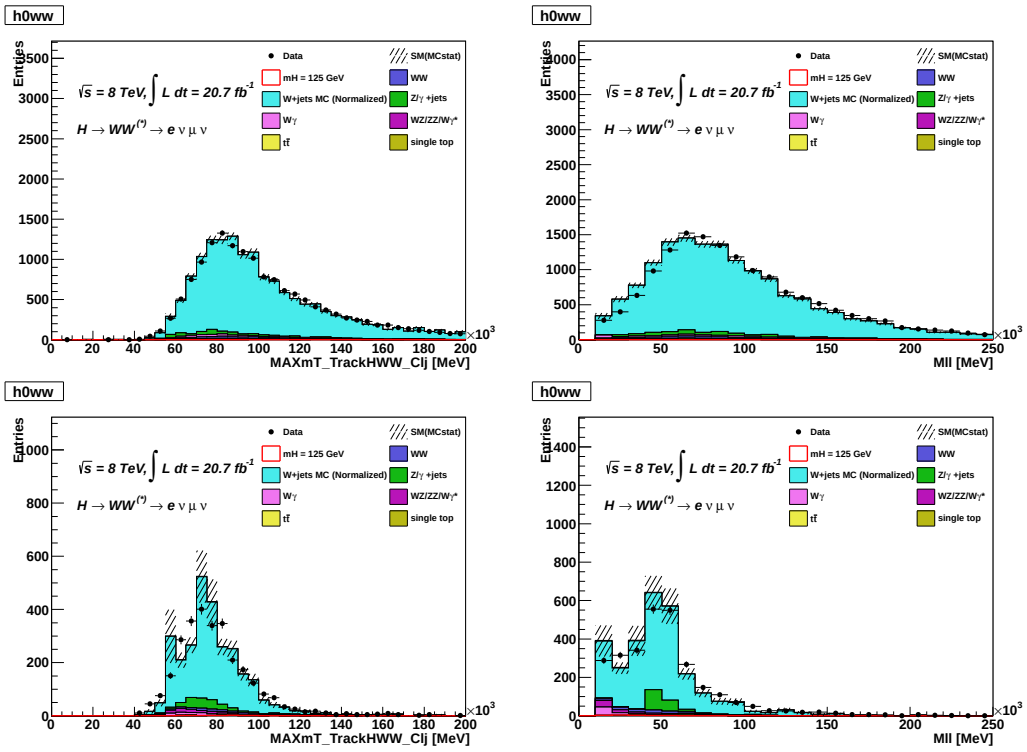

Figure 6.17: Kinematics of the W+jets control sample for $e\mu$ channel in 0 jet after $p_{\mathrm{T}}^{\ell\ell}$requirement. The top plots are $m_{\mathrm{T}}(W)$(MAX) (left) and $M_{\ell\ell}$ (right) in high p_{T}. The bottom plots are $m_{\mathrm{T}}(W)$(MAX) (left) and $M_{\ell\ell}$ (right) in low p_{T}. The expectation from the W+jets simulation is also shown for comparison.

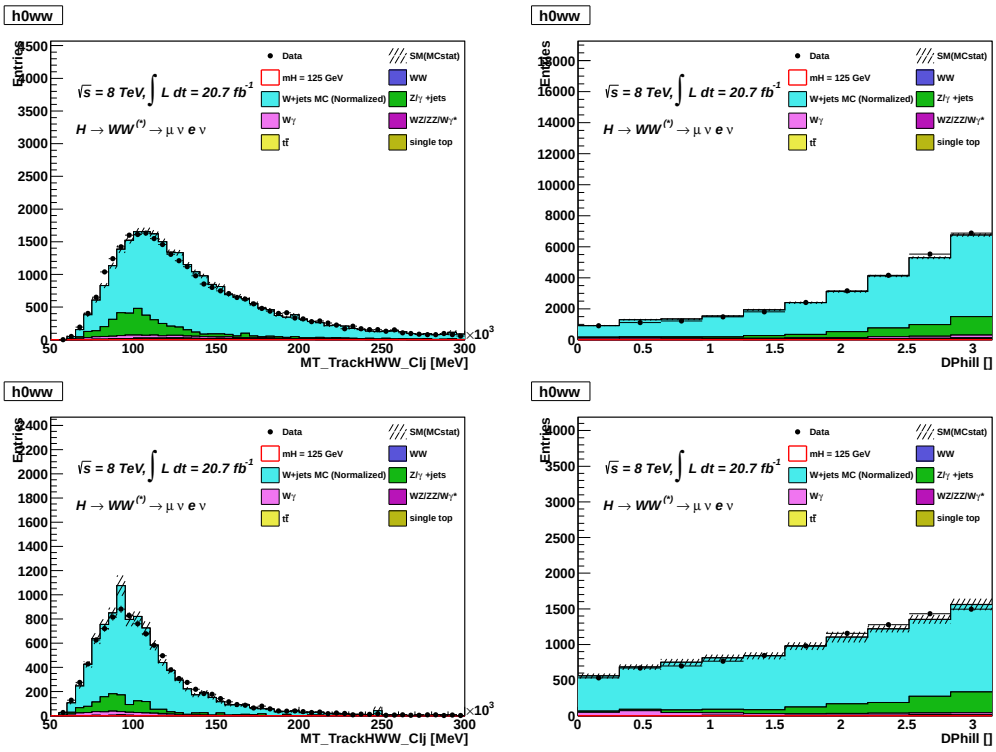

Figure 6.18: Kinematics of the W+jets control sample for μe channel in 1 jet after b-veto requirement. The top plots are m_{T} (left) and $\Delta\phi_{\ell\ell}$ (right) in high p_{T}. The bottom plots are m_{T} (left) and $\Delta\phi_{\ell\ell}$ (right) in low p_{T}. The expectation from the W+jets simulation is also shown for comparison.

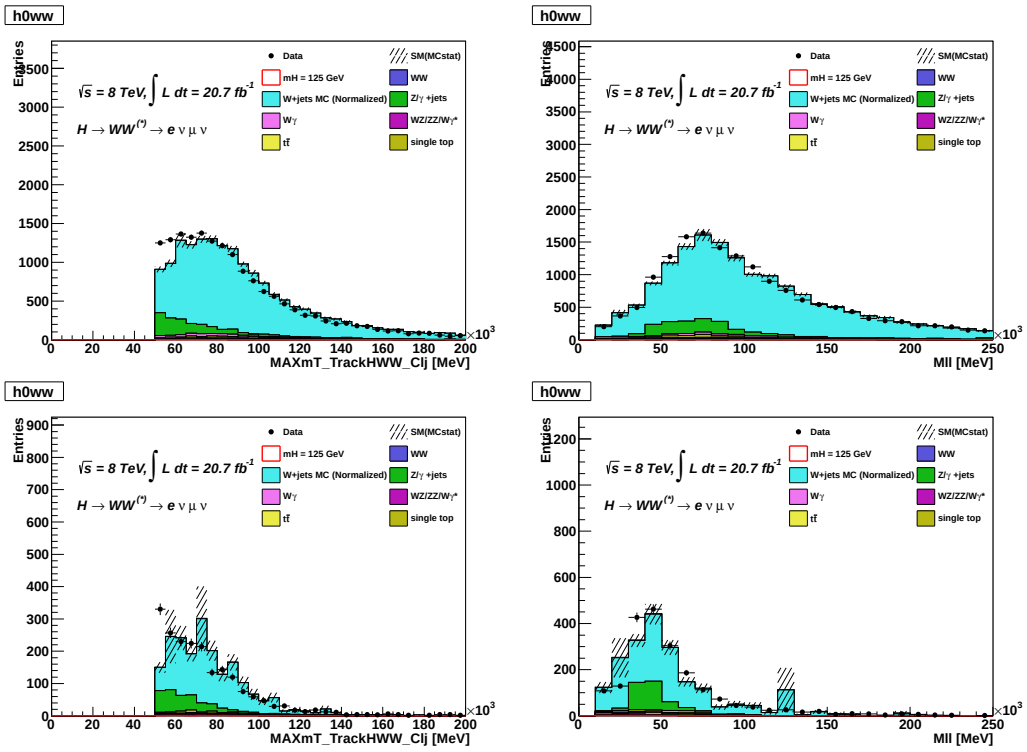

Figure 6.19: Kinematics of the W+jets control sample for $e\mu$ channel in 1 jet after b-veto requirement. The top plots are $m_{\mathrm{T}}(W)$(MAX) (left) and $M_{\ell\ell}$ (right) in high p_{T}. The bottom plots are $m_{\mathrm{T}}(W)$(MAX) (left) and $M_{\ell\ell}$ (right) in low p_{T}. The expectation from the W+jets simulation is also shown for comparison.

6.6.2 Run Dependence

The stability of the W+jets control sample against run period is investigated by comparing the yield of the control sample for each lepton flavor channel through 2012 data taking. Figure 6.20 shows the yield of the control sample per pb^{-1} versus period for OS events. The comparisons are made after the jet veto requirement for 0 jet, after the one jet requirement for 1 jet, and after two jet requirement for 2 jet. No significant run dependence is observed, and it is found that the yield is stable within the run period used in the analysis. Any deviation arises from the pileup effect, change in trigger configuration, and change in performance of jet reconstruction.

It is worth noting the fact that the acceptance of the sub-leading muon, namely $e\mu$ or $\mu\mu$ channel, increases with higher jet multiplicity. This is because the larger contribution of fake leptons from $t\bar{t}$ events in the control sample. In practice the contribution is not subtracted from the control sample as it is from real fake lepton. To do this, only leptonic decays of $t\bar{t}$ events with two real leptons in the final state are subtracted from the control sample.

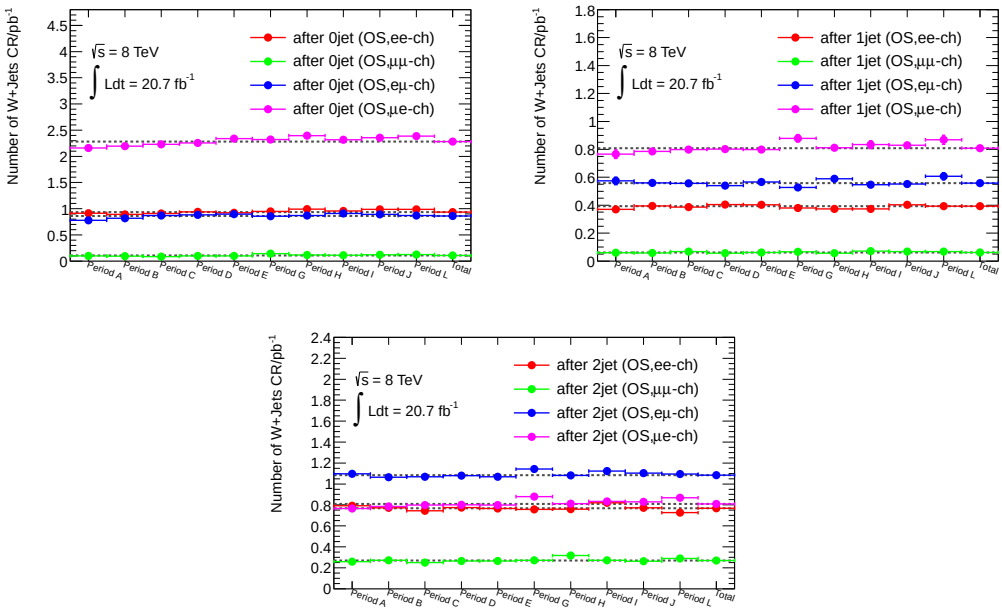

Figure 6.20: OS W+jet control region yields per pb^{-1} as a function of run period. The yields are shown after the jet veto requirement, one jet requirement, and two jets requirement for each channel.

6.7 QCD Estimation

6.7.1 QCD in the Fake Factor Method

As an extension of the fake factor method, it is possible to obtain data-driven QCD background estimation. The data-driven QCD estimation uses the QCD control sample defined as events that have two `anti-id` leptons ($N_{\text{anti-id+anti-id}}$). For these events, the fake factor based on the di-jets sample is applied twice to obtain the QCD prediction in the signal region ($N_{\text{id+id}}$):

$$N_{\text{QCD Bkg}} = f^2 \times N^{\text{QCD}}_{\text{anti-id+anti-id}}, \tag{6.16}$$

where f is the di-jets fake factor and $N^{\text{QCD}}_{\text{anti-id+anti-id}}$ is the number of QCD events with two leptons satisfying the `anti-id` definition, and where the EW contamination is not explicitly shown. The QCD enters the W+jet control sample when one of the jets satisfies `id` lepton definition and the other satisfies the `anti-id` lepton definition ($N^{\text{QCD}}_{\text{id+anti-id}}$). The QCD in the W+jets control sample is in principle double counted because there are two possible combinations (`id + anti-id` versus `anti-id + id`), which can be explicitly expressed as:

$$N^{\text{QCD}}_{\text{id+anti-id}} = 2 \times f \times N^{\text{QCD}}_{\text{anti-id+anti-id}}, \tag{6.17}$$

The QCD contamination in the W+jet prediction is finally written by combining the above Equations 6.16 and 6.17, and Equation 6.5 as:

$$N^{\text{QCD in W+jets}}_{\text{id+id}} = f \times N^{\text{QCD}}_{\text{id+anti-id}} = 2 \times f^2 \times N^{\text{QCD}}_{\text{anti-id+anti-id}} = 2 \times N_{\text{QCD Bkg}}. \tag{6.18}$$

Note that the formulation above ignores the fact that the QCD factor factor can be quite different from the Z+jets (or di-jets) fake factor due to the difference in flavor composition and jet p_{T} , which will be addressed in Section B.5.2.

6.8 Summary of the W+jets Systematic Uncertainty

The W+jets/QCD backgrounds are estimated in a data-driven way using the fake factor method. The W+jets fake factor is derived in Z+jets sample, and the W+jets control sample is constructed by events that have one identified lepton and one anti-identified lepton. The fake factors are applied to the W+jets control sample to obtain the W+jets prediction in the signal region. The Z+jets fake factor may not be accurate due to the difference in the jet flavor composition between the Z+jets and W+jets sample. A dedicated correction factors are evaluated separating into OS and SS to correct the difference in the flavor composition. The correction factors are further applied to obtain the final W+jets prediction in the signal region (OS) and SS region. The systematic uncertainties on the fake factors are evaluated by varying EW contamination in the Z+jets sample and by comparing the correction factors using several generators (central value is derived in Alpgen + Pythia6). The systematic uncertainties on the fake factors are summarized in Table 6.15 and Figure 6.21.

Table 6.15: Summary of systematic uncertainties (quoted as percentages) on the Z+jets fake factor measurement. Same-sign and opposite-sign uncertainties are quoted separately because the correction factor uncertainties differ. For the correction factor uncertainties, the statistical, correlated systematic, and uncorrelated systematic components quoted in Table 7.5 are summed in quadrature.

	electrons				muons			
	stat.	*EW* syst.	corr. factor	**total**	stat.	*EW* syst.	corr. factor	**total**
$10 < p_T < 15$	18	11	20	**29 (OS)**	10	3	22	**25 (OS)**
			25	32 (SS)			35	37 (SS)
$15 < p_T < 20$	34	19	20	**44 (OS)**	18	5	22	**29 (OS)**
			25	46 (SS)			35	40 (SS)
$20 < p_T < 25$	52	25	20	**61 (OS)**	29	9	22	**37 (OS)**
			25	63 (SS)			35	46 (SS)
$p_T > 25$	30	23	20	**43 (OS)**	34	21	22	**46 (OS)**
			25	45 (SS)			35	53 (SS)

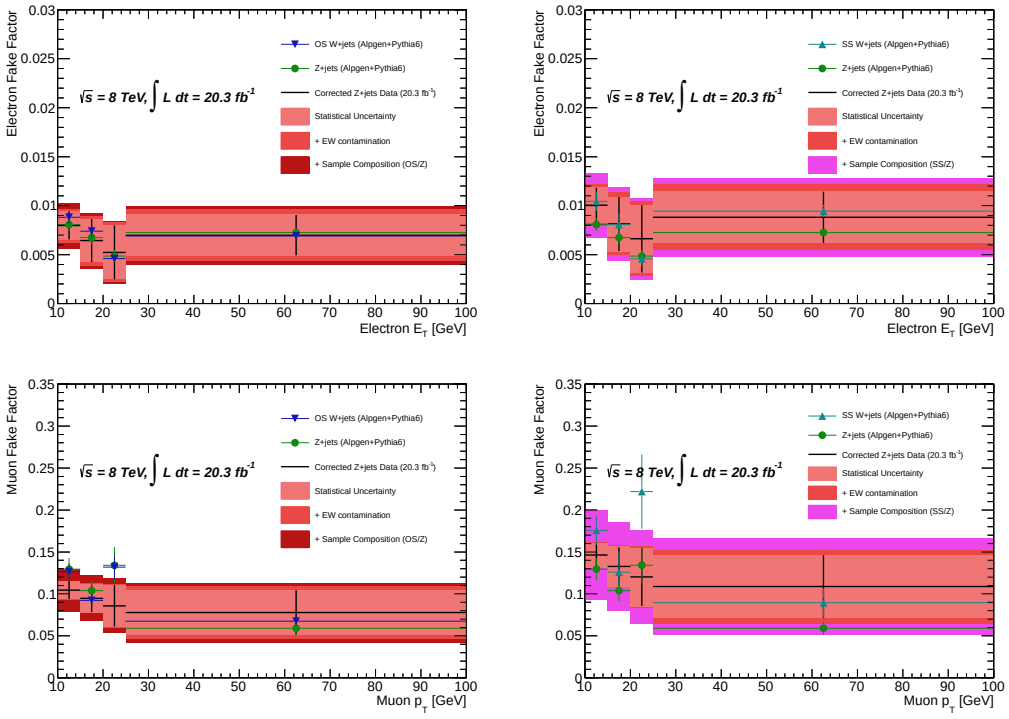

Figure 6.21: Summary of fake factor and corresponding systematics for OS electrons (top left), SS electrons (top right), OS muons (bottom left), and SS muons (bottom right). The correction factors summarized in Table 6.15 are applied to data Z+jets fake factor. All systematic uncertainties are added in quadrature.

Chapter 7

Modeling of Same Sign Backgrounds

7.1 Introduction

The "non-WW" dibosons (VV) such as those $W\gamma, Z\gamma, W\gamma^*, WZ$, $Z\gamma^*$, and ZZ, are the second largest backgrounds in the signal region. The Same Sign (SS) events that pass the same selection criteria as the signal region but are required to be same signed two leptons, provide a good validation region for those backgrounds, since the SS events are dominated by VV (and W+jets) backgrounds. Adding the SS region to the simultaneous fit as another control region allows the fit to obtain more robust predictions of those backgrounds. The same sign control region (SS CR) is designed to set the summed normalization of all the VV backgrounds. The SS CR is built from events that pass all the signal region cuts up to the $\Delta\phi_{\ell\ell}$ with the same charge requirement.

The γ, γ^*, or Z in those diboson processes equally produces a lepton of either charge relative to the charge of the lepton from the W. The normalization and kinematic distributions for the SS region from these VV backgrounds are thus identical in the different lepton flavor channels ($e\mu$+μe) final states to the signal region (OS) in a good approximation. Since the phase space of the signal and control regions is identical, potential extrapolation uncertainties are negligible compared to other sources of uncertainties, thus the extrapolation uncertainties on the SS CR are not considered unlike WW or top control regions. While in the same lepton flavor channels (ee+$\mu\mu$), the SS populations are not identical to the OS, for instance WZ process. The SS CR is therefore used only for different lepton flavor channels ($e\mu$+μe).

Another dominant process which contributes to the SS region is the W+jets background with one fake lepton. Its contribution is not symmetric between SS and OS as discussed in Section 6.5. The W+jets background needs to be predicted separately for the SS region and signal region. Dedicated corrections factors to both the OS and SS W+jets prediction have been introduced and described in Section 6.5. The W+jets background is

subtracted from the SS data to obtain a collective normalization factor for the VV backgrounds. Tables 7.1 and 7.2 show the expected and observed event yields in the $N_{\text{jet}} = 0$ and $= 1$ channels, respectively.

Table 7.1: The expected and observed event yields in the SS control region in the $N_{\text{jet}} = 0$ channel. The W+jets background is estimated using the data-driven method. The $H \to \tau\tau$ contribution is included in the "Signal" column, and the "NF" column illustrates the ratio of the "data-non-VV" to the VV.

	Signal [125 GeV]	$WZ/ZZ/W\gamma$	$W\gamma$	$W\gamma^*$	WZ	ZZ	Z+jets	W+jets	Total Bkg.	Observed	Data/MC	NF
$e\mu$+μe	2.14 ± 0.39	348.67 ± 8.51	173.13 ± 7.46	115.32 ± 3.77	56.39 ± 1.61	3.83 ± 0.14	20.86 ± 2.60	162.86 ± 4.38	541.11 ± 9.95	531	0.98 ± 0.05	0.96 ± 0.08
$e\mu$	1.27 ± 0.29	156.76 ± 5.36	67.05 ± 4.57	56.32 ± 2.53	31.51 ± 1.18	1.88 ± 0.10	7.51 ± 1.56	76.04 ± 4.02	246.06 ± 6.91	272	1.11 ± 0.07	1.16 ± 0.13
μe	0.87 ± 0.26	191.91 ± 6.62	106.08 ± 5.90	59.01 ± 2.79	24.88 ± 1.08	1.94 ± 0.10	13.35 ± 2.08	86.82 ± 1.73	295.04 ± 7.15	259	0.88 ± 0.06	0.81 ± 0.10

Table 7.2: The expected and observed event yields in the SS control region in the $N_{\text{jet}} = 1$ channel. The W+jets background is estimated using the data-driven method. The $H \to \tau\tau$ contribution is included in the "Signal" column, and the "NF" column illustrates the ratio of the "data-non-VV" to the VV.

	Signal [125 GeV]	$WZ/ZZ/W\gamma$	$W\gamma$	$W\gamma^*$	WZ	ZZ	Z+jets	W+jets	Total Bkg.	Observed	Data/MC	NF
$e\mu$+μe	1.93 ± 0.35	120.32 ± 4.35	53.18 ± 3.58	30.02 ± 2.12	34.29 ± 1.27	2.84 ± 0.12	13.96 ± 5.93	58.49 ± 2.71	200.06 ± 7.86	193	0.96 ± 0.08	0.93 ± 0.14
$e\mu$	1.00 ± 0.25	57.30 ± 2.80	19.37 ± 2.14	16.19 ± 1.52	20.11 ± 0.98	1.63 ± 0.09	2.16 ± 0.92	31.87 ± 2.48	96.24 ± 3.88	104	1.08 ± 0.11	1.12 ± 0.20
μe	0.93 ± 0.25	63.02 ± 3.32	33.81 ± 2.87	13.82 ± 1.47	14.18 ± 0.80	1.21 ± 0.08	11.80 ± 5.86	26.61 ± 1.09	103.82 ± 6.83	89	0.86 ± 0.11	0.75 ± 0.20

The normalization factor (NF) is obtained from the ratio of the "data-non-VV" to the expected VV yield predicted by simulaion. The resulting NF is taken from the $e\mu$+μe channel and it is 0.96 ± 0.07 (stat.) and 0.93 ± 0.13 (stat.) in the $N_{\text{jet}} = 0$ and $= 1$ channels, respectively. Figures 7.1 and 7.2 show the $m_{\ell\ell}$, $\Delta\phi_{\ell\ell}$, m_{T} and $p_{\text{T}}^{\ell\ell}$ distributions for the 0-jet $e\mu$+μe $e\mu$ and μe channels, and the corresponding distributions for the 1-jet are shown in Figures 7.3 and 7.4. The dedicated NFs have been applied to the VV background.

In the following sections the systematic uncertainties on W+jets and VV backgrounds are discussed. The treatment of the uncertainty on the W+jets background is a bit complicated, since the correlation between OS and SS regions needs to be taken into account. In practice the W+jets systematics due to flavor composition are split into correlated and uncorrelated uncertainties. On the other hand the uncertainties on VV backgrounds are common between OS and SS since they are uncertainties on production cross section. A special treatment is also required for the $W\gamma$ background because this background arises from conversion (photon faking electron), so a dedicated systematic uncertainty to account for the conversion modeling is specially introduced for the $W\gamma$ background.

In the simultaneous fit, the relative contributions of the individual VV processes are still allowed to float under gaussian constraint within the uncertainty on their cross sections.

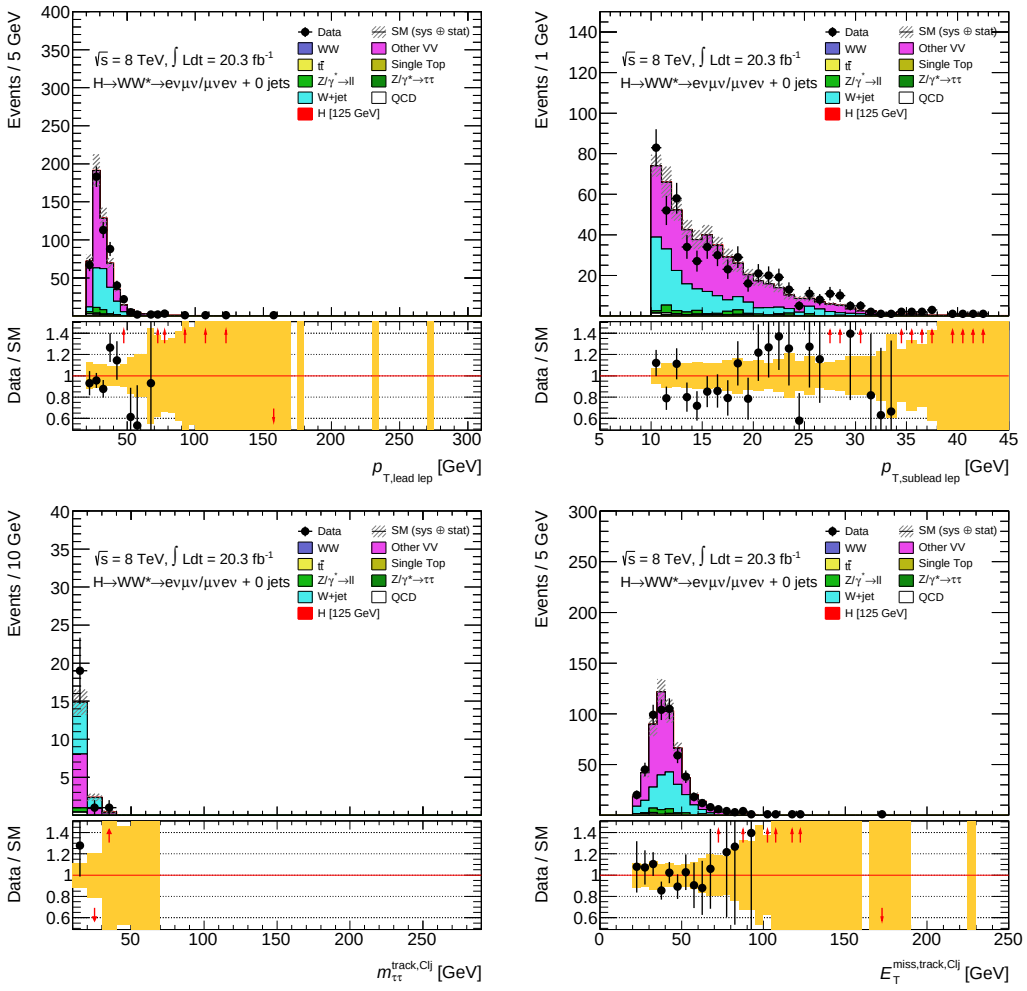

Figure 7.1: Kinematic distributions for same sign control region : $p_{\mathrm{T}}^{\mathrm{lead}}$ (top left), $p_{\mathrm{T}}^{\mathrm{sub}}$ (top right), $m_{\tau\tau}$ (bottom left), and $E_{\mathrm{T}}^{\mathrm{miss}}$ (bottom right).

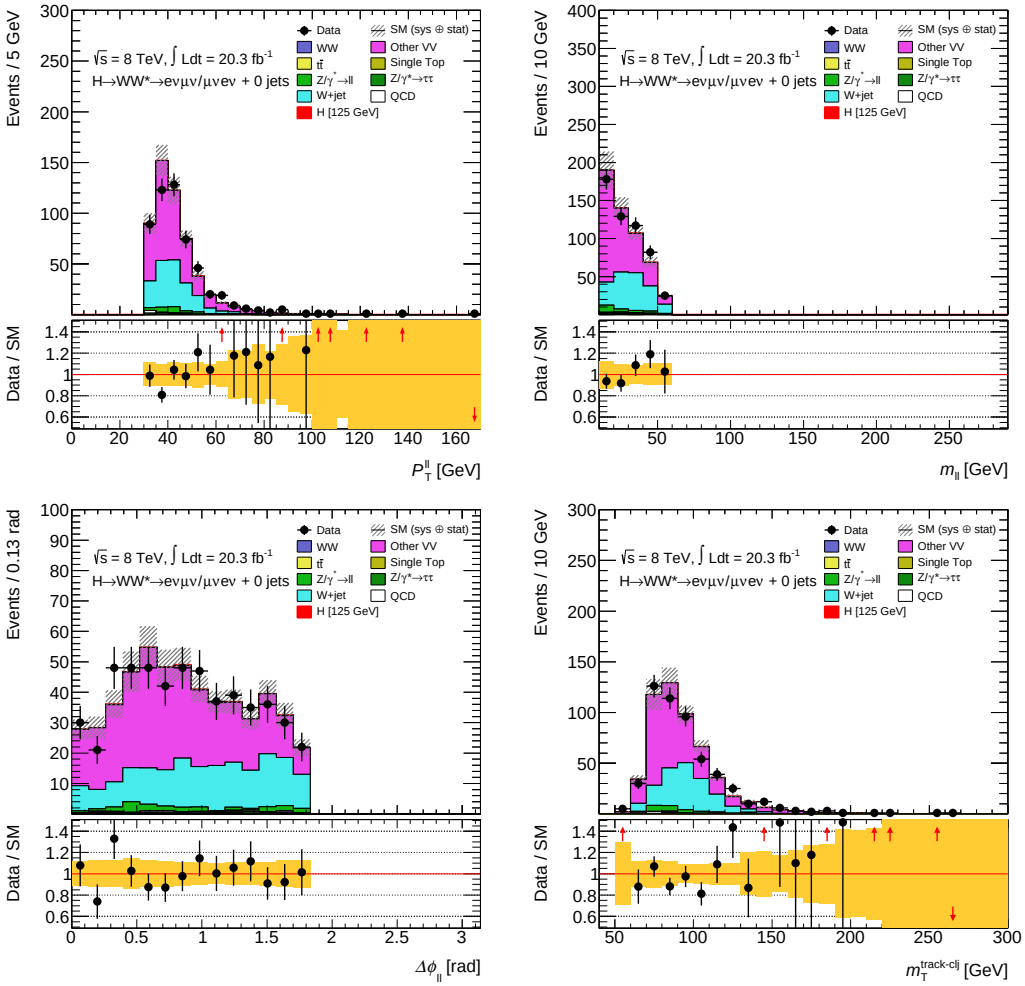

Figure 7.2: Kinematic distributions for same sign control region : $p_{\mathrm{T}}^{\ell\ell}$ (top left), $m_{\ell\ell}$ (top right), $\Delta\phi_{\ell\ell}$ (bottom left), and m_{T} (bottom right).

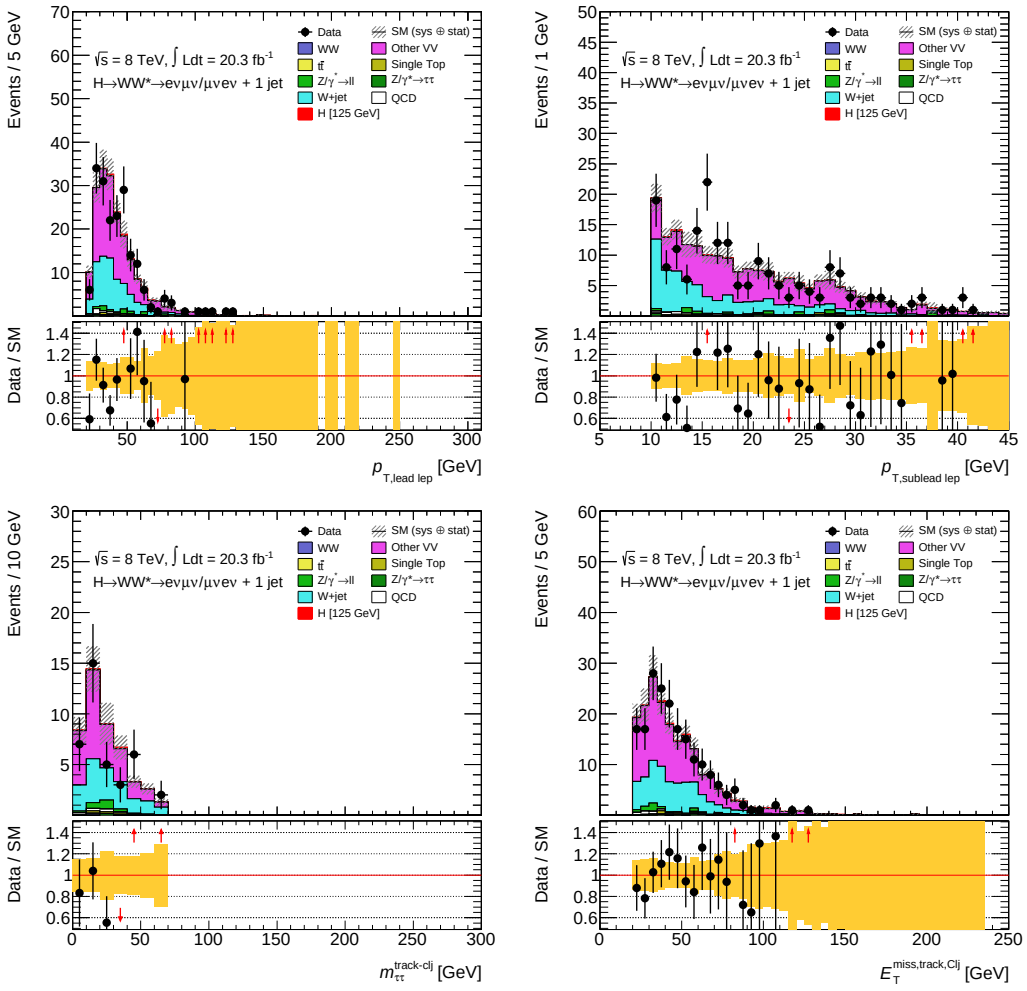

Figure 7.3: Kinematic distributions for same sign control region : $p_{\mathrm{T}}^{\mathrm{lead}}$ (top left), $p_{\mathrm{T}}^{\mathrm{sub}}$ (top right), $m_{\tau\tau}$ (bottom left), and $E_{\mathrm{T}}^{\mathrm{miss}}$ (bottom right).

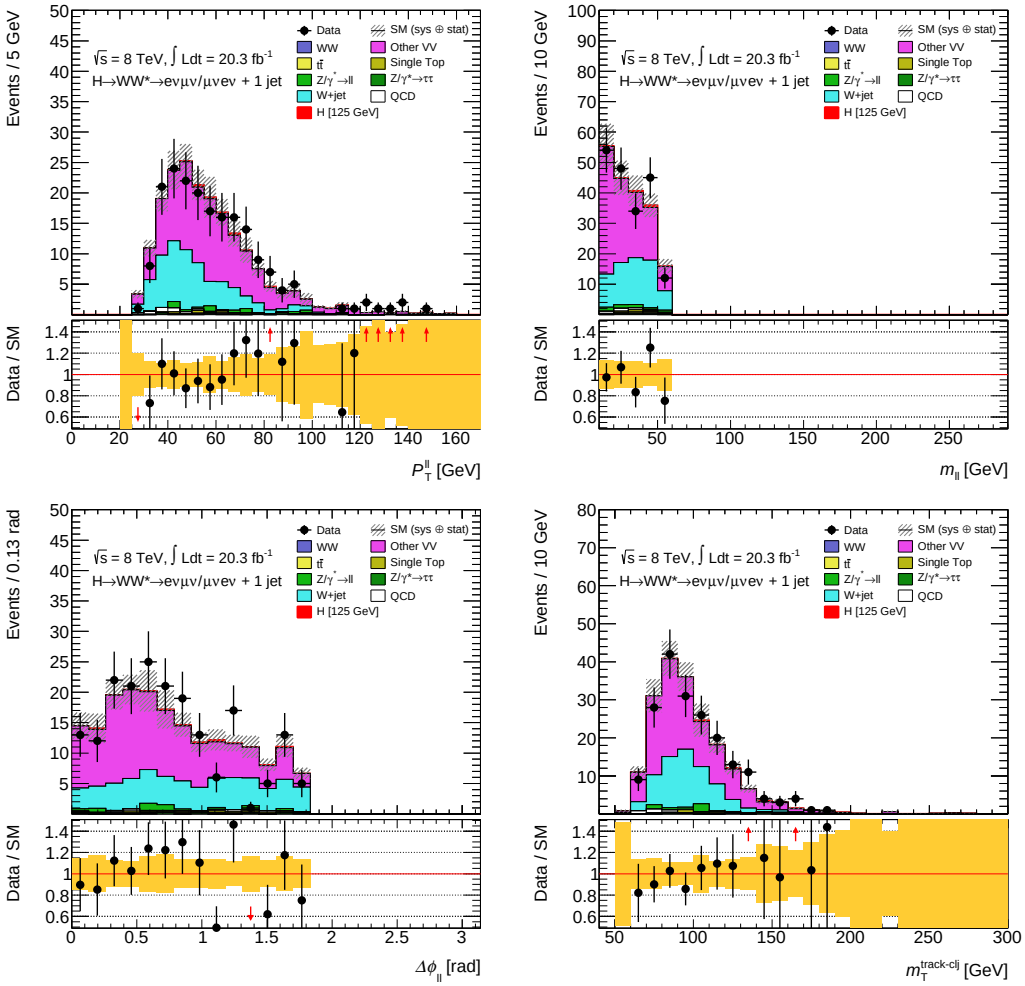

Figure 7.4: Kinematic distributions for same sign control region : $p_{\mathrm{T}}^{\ell\ell}$ (top left), $m_{\ell\ell}$ (top right), $\Delta\phi_{\ell\ell}$ (bottom left), and m_{T} (bottom right).

7.2 Dibosons backgrounds

7.2.1 Theoretical Uncertainties on Dibosons

The non-WW diboson (VV) processes that include $W\gamma/Z\gamma$, $W\gamma^*/WZ$, $ZZ/Z\gamma^*$, and $Z\gamma$, are the second largest backgrounds in the signal region. The size of these backgrounds increases at lower sub-leading lepton p_{T} and lower $m_{\ell\ell}$. For 0-jet different flavor signal regions, the sum of VV backgrounds is normalized to data in the SS CR. For individual VV components, the theoretical uncertainties on NLO cross sections are evaluated by comparing to MCFM [174] generator at truth level.

$W\gamma/Z\gamma$ backgrounds

The uncertainties and correction factor referred to as "k-factor" on the $W\gamma$ background are evaluated for each jet bin. The procedure of the calculation is described in [175]. For the $W\gamma$ production, there are infrared divergences at low photon p_{T} that must be regularized with a minimum p_{T} cut at generator level. Also there are collinear divergences that arise from photons close to the other objects like lepton or jet. These are avoidable divergences by defining minimum ΔR cut. The cuts imposed at generator level are summarized as follows :

- $p_{\mathrm{T}}^{\gamma} > 8$ GeV,
- $\Delta R(\ell, \gamma) > 0.25$,
- $\Delta R(\mathrm{jet}, \gamma) > 0.1$,

where ΔR is defined as $\sqrt{\Delta\phi^2 + \Delta\eta^2}$. The comparison of Alpgen to MCFM is made after these cuts are imposed. The k-factor is calculated for inclusive sample, which is 1.15, and the difference in normalization for each jet bin is taken as theoretical uncertainty, which is 11% for the 0-jet, 53% for the 1-jet, and 100% for the $\geq$2-jet. The large uncertainty on the $\geq$1-jet bins is due to the fact that the MCFM is an NLO generator that is not able to compute the uncertainty directly for $\sigma_{\geq 2jet}$, so the uncertainty on the 1-jet bin is evaluated as a fractional difference between $\sigma_{\geq 2-jet}$ and $\sigma_{\geq 1-jet}$. An additional PDF uncertainty of 3.1% is also considered for this process. The $Z\gamma$ background can also contributes to both signal region and SS CR, but it requires one lepton is out of acceptance, so the size of this background is small compared to the $W\gamma$ background. The $Z\gamma$ background is thus treated as a part of Z+jets backgrounds in the analysis. For the $W\gamma$ background the additional uncertainty is considered to account for conversion modeling (photon faking electron). The conversion is discussed a bit more in the next Section.

$W\gamma^*/WZ$ backgrounds

The $W\gamma^*/WZ$ processes lead to the same final state. These processes are each defined by separating in $m_{\ell\ell}$ at 7 GeV, high mass sample is called WZ process and low mass sample is called $W\gamma^*$ process. The WZ background is generated by Powheg and $W\gamma^*$ background

is generated by Sherpa with ≤ 1 parton included in the matrix element. The dedicated k-factor is calculated for Sherpa comparing to MCFM generator at truth level. However the MCFM is unstable in the region $m_{\gamma^*} < 0.5$ GeV, the k-factor is calculated above $m_{\gamma^*} > 0.5$ GeV (and up to 7 GeV). The m_{γ^*} dependent k-factor is shown in Figure 7.5.

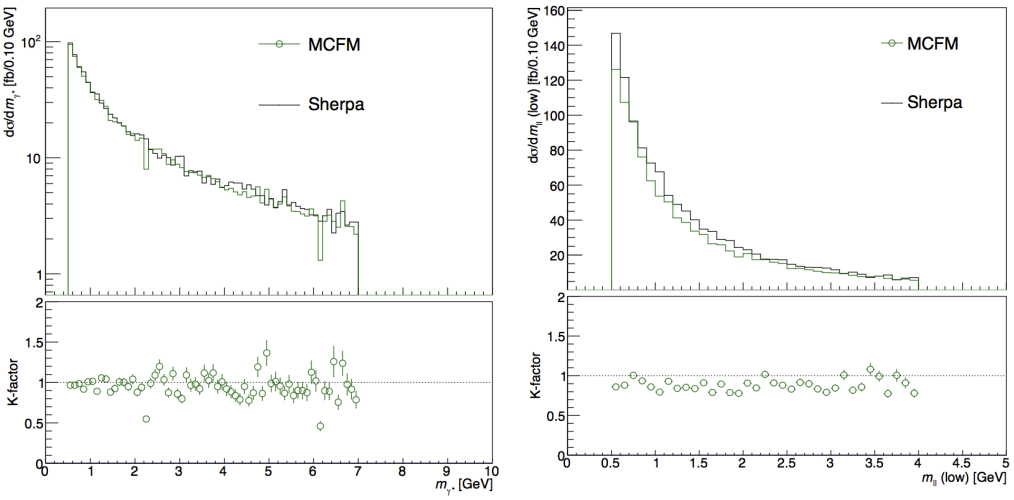

Figure 7.5: Invariant mass of the γ^* for Sherpa $W\gamma^*$ and $Z\gamma^*$ comparing to the MCFM in the region $0.5 < m_{\gamma^*} < 7$ GeV ($W\gamma^*$) and $0.5 < m_{\gamma^*} < 4$ GeV ($Z\gamma^*$) after dilepton selection. The ratio plots below show the resulting k-factors that are independent of m_{γ^*}.

The resulting k-factor is 0.94 ± 0.07. In addition to the k-factor, jet bin dependent correction factors are calculated for normalization, which are summarized in Table 7.3.

Table 7.3: The jet bin dependent correction factors, C, applied to the $W\gamma^*$ sample, and multiplied by the k-factor. Relative scale uncertainties are shown.

N_{jets}	C	k-factor $\times$ C
0	$0.905 \pm 6.5\%$	$0.854 \pm 9.9\%$
1	$1.09 \pm 30\%$	$1.03 \pm 31\%$
≥ 2	$1.95 \pm 26\%$	$1.84 \pm 27\%$

The $W\gamma^*$ background is validated in a dedicated validation region (VR), which is discussed in Appendix C.

$Z\gamma^*/ZZ$ backgrounds

The $Z\gamma^*/ZZ$ processes lead to the same final state. These processes are each defined by separating in $m_{\ell\ell}$ at 4 GeV, high mass sample is called ZZ process and low mass sample is called $Z\gamma^*$ process. The ZZ background is generated by Powheg and $Z\gamma^*$ background

is generated by Sherpa with ≤ 1 parton included in the matrix element. Similar to $W\gamma^*$, the dedicated k-factor is calculated for Sherpa comparing to the MCFM generator at truth level. The m_{γ^*} dependent k-factor is also shown in Figure 7.5. The resulting k-factor is 0.88 ± 0.048. This background is only $\sim 1\%$ contribution in the SS CR, but $Z\gamma^*$ is more important when deriving fake factor for the W+jets background using the Z+jets sample (see Chapter 6).

7.2.2 Conversion Modeling

The $W\gamma$ background may not be accurately modeled in simulation, since this background arises from conversion (photon faking electron). A dedicated validation region, $Z\gamma$ validation region (VR), is defined to investigate the modeling of the conversion. The $Z\gamma$ validation region is composed of the events with $Z \to \mu\mu$ in association with final state photon radiation. Instead of reconstructed photons, reconstructed electrons are used for the $Z \to \mu\mu\gamma$ reconstruction. Correlation of invariant mass between $m_{\mu\mu e}$ and $m_{\mu\mu}$ is shown in Figure 7.6 (left).

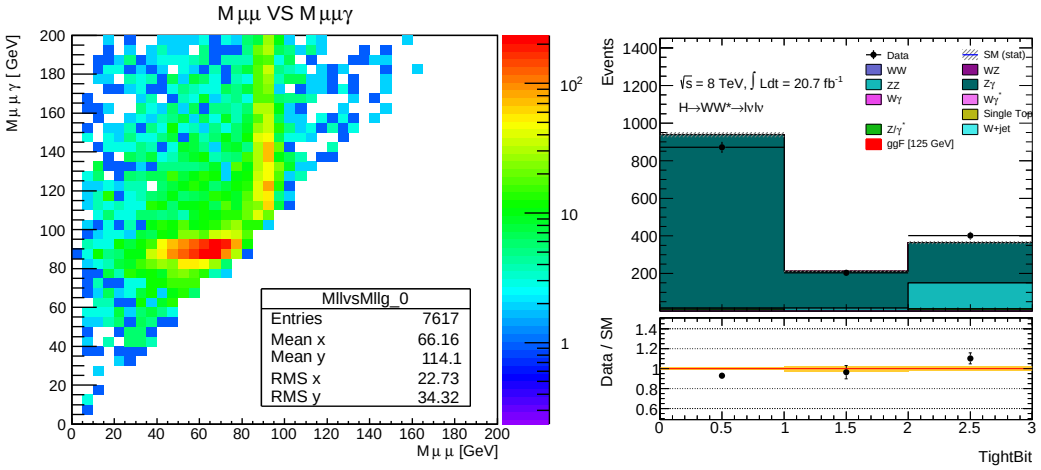

Figure 7.6: Correlation of invariant mass between $m_{\mu\mu\gamma}$ (x-axis) and $m_{\mu\mu}$ (y-axis).

A cut of $|m_{\mu\mu e} - m_z| < 15$ GeV is imposed to reduce $W\gamma^*/WZ$ backgrounds as well as $Z \to \mu\mu$+jet background, where a jet is misidentified as an identified electron, but to enhance converted electrons, which results in $\sim 90\%$ purity of $Z\gamma$ VR. To further increase the purity of the $Z\gamma$ events, the electrons are classifed into three regions using b-layer and conversion flag requirements in the electron identification as :

- Tight Bit 0 : fail both b-layer and conversion flag requirements,
- Tight Bit 1 : fail either b-layer or conversion flag requirement,
- Tight Bit 2 : pass both b-layer and conversion flag requirements,

where "Tight Bit 2" is identical to the electron used in the standard analysis. Only electrons that satisfy "Tight Bit 0" are used as $Z\gamma$ VR, which is almost 100% pure with the $Z \to \mu\mu\gamma$

events as shown in Figure 7.6 (right). Figure 7.7 shows electron p_{T} and η distribution in $Z\gamma$ VR.

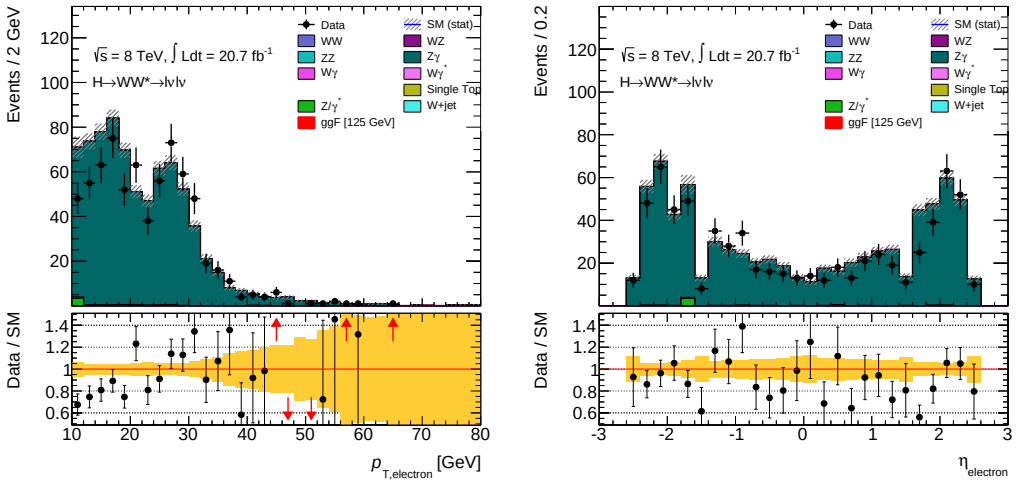

Figure 7.7: Kinematic distributions in the $Z\gamma$ VR : electron p_{T} distribution (left) and η distribution (right). A mis-modeling depends on electron p_{T} rather than electron η.

A mis-modeling on the conversion depends on electron p_{T} rather than η, thus the systematic uncertainty is derived as a function of electron p_{T}. The conversion systematic uncertainties are summarized in Table 7.4, which includes the agreement of data/simulation for other "Tight Bit" regions, but the numbers in the "Tight Bit 0" row are taken as the final systematics, since the contamination of ZZ background is about 40% in the "Tight Bit 2". The resulting systematic uncertainties vary 5-25% as a function of p_{T}.

Table 7.4: Comparison of normalization factor (data/simulation) as a function of electron p_{T} in the $Z\gamma$ enriched region. Only statistical uncertainty is displayed. The systematic uncertainty due to the conversion mis-modeling is taken from the numbers in the "Tight Bit 0"($Z\gamma$ VR).

Tight Bit	10-15	15-20	20-
Tight Bit 2 (pass both)	1.35 ± 0.19 (stat)	1.13 ± 0.19 (stat)	1.09 ± 0.12 (stat)
Tight Bit 1 (fail *b*-layer)	0.90 ± 0.26 (stat)	1.13 ± 0.26 (stat)	1.11 ± 0.13 (stat)
Tight Bit 1 (fail conversion flag)	0.66 ± 0.12 (stat)	0.72 ± 0.15 (stat)	0.64 ± 0.06 (stat)
Tight Bit 0 (fail both)	0.75 ± 0.07 (stat)	0.82 ± 0.07 (stat)	0.95 ± 0.03 (stat)

7.3 W+jets Correlation Model

Since the W+jets contamination in the SS region is 30 % for both 0-jet and 1-jet channels, it is essential to subtract the contamination correctly when the non-WW dibosons (VV) are normalized in the SS region. As discussed in Chapter 6, the W+jets prediction in SS region differs from the prediction in signal region (OS) due to the different flavor composition. Some compositions should be common between SS and OS, and the others should be unique in OS, since any SS events arise from quark charge flip or gluon splitting. As an example, the flavor composition of electron fake and muon fake is illustrated in Figure 7.8.

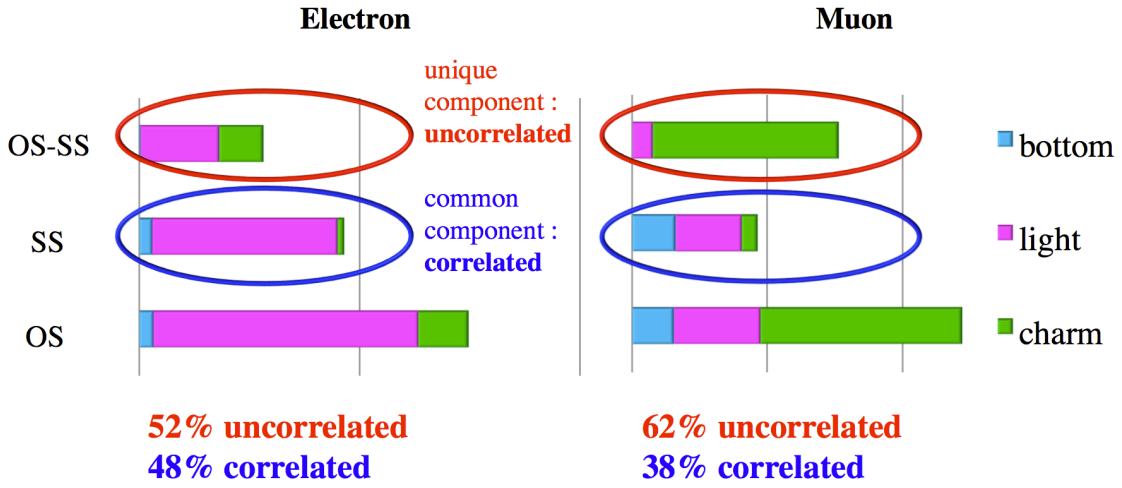

Figure 7.8: Schematic comparison of the flavor composition. The left figure shows the flavor composition in each sample (OS, SS, and OS-SS) for electrons. The right figure shows the same for muons. The correlated uncertainties are computed by taking the ratio of number of denominators ($N^{SS}_{den}/N^{OS}_{den}$) using numbers in Tables B.5 and B.6

From Figure 7.8, it is found that the unique component is mainly from W+charm and W+light for electrons, and is mostly from W+charm for muons. It is well justified that every processes appearing in SS has OS counterpart, but some fraction of OS is unique because of the OS/SS asymmetry caused by W+charm process etc. (See Section B.2) The SS events can be therefore considered as correlated component, whereas the unique component (i.e. OS-SS component) can be considered as uncorrelated component between OS and SS. The uncertainty on the W+jets backgroud should be also separated into correlated and uncorrelated uncertainties. The relationship of correlated and uncorrelated components, or the relationship of correlated and uncorrelated uncertainties, can be give by :

$$\sigma^2_{\mathrm{OS}} = \Delta(OS/Z)^2 = \rho^2 \cdot (\sigma^{OS}_{\mathrm{corr}})^2 + (\sigma^{OS}_{\mathrm{uncorr}})^2 + (\sigma^{OS}_{\mathrm{stat}})^2, \tag{7.1}$$

$$\sigma^2_{\mathrm{SS}} = \Delta(SS/Z)^2 = (\sigma^{SS}_{\mathrm{corr}})^2 + (\sigma^{SS}_{\mathrm{stat}})^2, \tag{7.2}$$

where $\Delta(OS/Z)$ and $\Delta(SS/Z)$ are uncertainties on the correction factors, OS/Z and SS/Z (see Section 6.5), and where ρ, σ_{corr}, and σ_{uncorr} are the fraction of correlated component, the correlated uncertainty, and the uncorrelated uncertainty, respectively. What is needed as an additional input is the ρ parameter that can be computed by taking the ratio of the number of denominators, $N_{den}^{SS}/N_{den}^{OS}$. The denominator ratio can be a good representation of the ρ. This approach can be simply justified by Equations below :

$$f^{\text{OS}} = f^{\text{SS}} \cdot \frac{N_{\text{den}}^{SS}}{N_{\text{den}}^{OS}} + f^{\text{OS-SS}} \cdot \frac{N_{\text{den}}^{OS-SS}}{N_{\text{den}}^{OS}}. \tag{7.3}$$

The three superscripts, "OS", "SS", and "OS-SS", can be replaced with "total", "corr", and "uncorr", respectively in this model. The Equation above can be then rewritten as follows :

$$f^{\text{total}} = f^{\text{corr}} \cdot \frac{N_{\text{den}}^{\text{corr}}}{N_{\text{den}}^{\text{total}}} + f^{\text{uncorr}} \cdot \frac{N_{\text{den}}^{\text{uncorr}}}{N_{\text{den}}^{\text{total}}} \tag{7.4}$$

The computed ρ is 0.48 for electrons and is 0.38 for muons. Also the resulting correlated and uncorrelated uncertainties, σ_{corr} and σ_{uncorr}, are summarized in Table 7.5. Note that the statistical uncertainty on the flavor composition is eventually added in quadrature to the uncorrelated uncertainty.

Table 7.5: Corrections factors and corresponding systematic uncertainties. Alpgen+Pythia6 is used to derive the central value and the systematic uncertainty is evaluated by comparing with other generators. The systematic uncertainty covers the differences among generators. In the second row the systematic on the OS correction factor is shown splitting into the systematic components that are correlated and uncorrelated with the SS correction factor systematic and the part. (Further study is found in Appendix C.1.)

	$f_{W+\text{jets}}^{\text{OS}}/f_{Z+\text{jets}}^{\text{incl.}}$	$f_{W+\text{jets}}^{\text{SS}}/f_{Z+\text{jets}}^{\text{incl.}}$
electrons	0.99 ± 0.05 (stat) ± 0.19 (syst) ± 0.11 (corr) ± 0.16 (uncorr)	1.25 ± 0.08 (stat) ± 0.30 (syst)
muons	1.00 ± 0.08 (stat) ± 0.21 (syst) ± 0.13 (corr) ± 0.17 (uncorr)	1.40 ± 0.14 (stat) ± 0.47 (syst)

The calculated uncertainties are treated as separated nuisance parameters in the simultaneous fit. In this case, the correlated uncertainty on OS W+jets background (SR) can be constrained by the SS W+jets background. In other word a part of the W+jets systematics is canceled because the W+jet background is determined in the SS region, while the other uncertainties are left because all the other uncertainties such as EW contamination, statistical uncertainty etc are treated as fully correlated between OS and SS. Similarly the improvement on the VV background is not expected to be large (only statistical improvement), since all the uncertainties are fully correlated between OS and SS. Therefore the SS CR improves the W+jets systematics rather than VV systematics. The procedure of the statistical analysis is further discussed in next Chapter 8.

Part III

Result and Conclusion

Chapter 8

Results

8.1 Signal Extraction

8.1.1 ggF 0-1 jet Signal Region

For the signal extraction the transverse mass of dilepton system m_{T} is used as final discriminant:

$$m_{\mathrm{T}} = \sqrt{(E_{\mathrm{T}}^{\ell\ell} + E_{\mathrm{T}}^{\mathrm{miss}})^2 - |\boldsymbol{p}_{\mathrm{T}}^{\ell\ell} + \boldsymbol{E}_{\mathrm{T}}^{\mathrm{miss}}|^2}, \tag{8.1}$$

where $E_{\mathrm{T}}^{\ell\ell}$ can be rewritten as $E_{\mathrm{T}}^{\ell\ell} = \sqrt{|\boldsymbol{p}_{\mathrm{T}}^{\ell\ell}|^2 + m_{\ell\ell}^2}$. For the missing transverse energy $E_{\mathrm{T}}^{\mathrm{miss}}$ (and $\boldsymbol{E}_{\mathrm{T}}^{\mathrm{miss}}$), track-based $\boldsymbol{p}_{\mathbf{T}}^{\mathbf{miss,\ jetCorr}}$ is used because of its higher resolution than calorimeter based $E_{\mathrm{T}}^{\mathrm{miss}}$ and better in the signal separation from backgrounds. Figure 8.1 shows the m_{T} distribution after all selections and before performing the fit (pre-fit) for 0-jet and 1-jet analyses where all lepton flavors, sub-leading lepton p_{T} bins ($p_{\mathrm{T}}^{\mathrm{sublead}}$ 10-15, 15-20, 20- GeV), and $m_{\ell\ell}$ bins ($m_{\ell\ell} < 30$, $m_{\ell\ell} > 30$ GeV) are combined, and Figures 8.2 and 8.3 are the same distributions for the 0-jet and 1-jet analyses but are split into lepton flavors, where the Data/SM ratios include signal yields predicted by the Standard Model ($\mu = 1$). The data excess is observed in both 0-jet and 1-jet m_{T} distributions. More quantitative discussions introducing the statistical tool are made in Section 8.3.1.

8.1.2 VBF Signal Region

For the signal extraction the BDT score is used as final discriminant. The last bin (highest score bin) is the most sensitive to the VBF signal, but last three bins are used as the signal region for the VBF signal extraction. Figure 8.4 shows BDT score before performing the fit (pre-fit) for different flavor channel and same flavor channels in the VBF analysis. The data excess is observed at the high BDT score. More quantitative discussions introducing the statistical tool are made in Section 8.3.2.

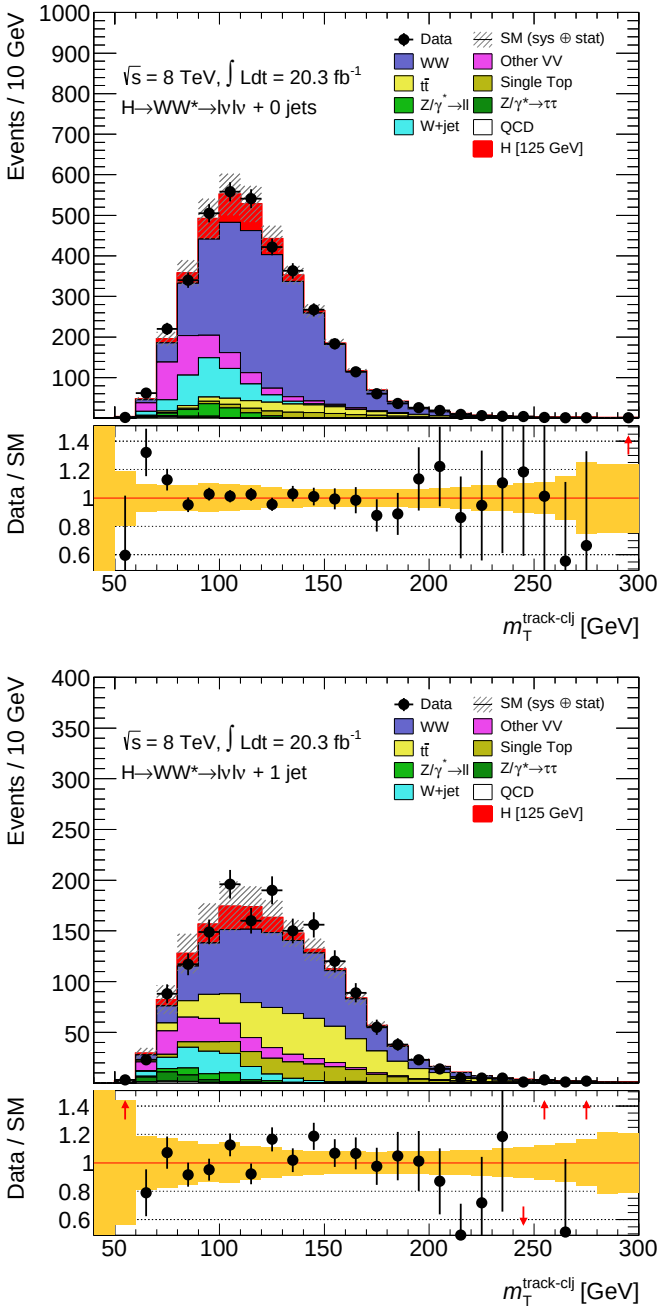

Figure 8.1: m_{T} distribution for all flavor channels ($e\mu$+μe+ee+$\mu\mu$) combined for the 0-jet analysis (top) and 1-jet analysis (bottom) after all selections and before performing the fit (pre-fit). The Data/SM ratio includes signal yields predicted by the Standard Model ($\mu = 1$). The yellow band includes both statistical and systematic uncertainties.

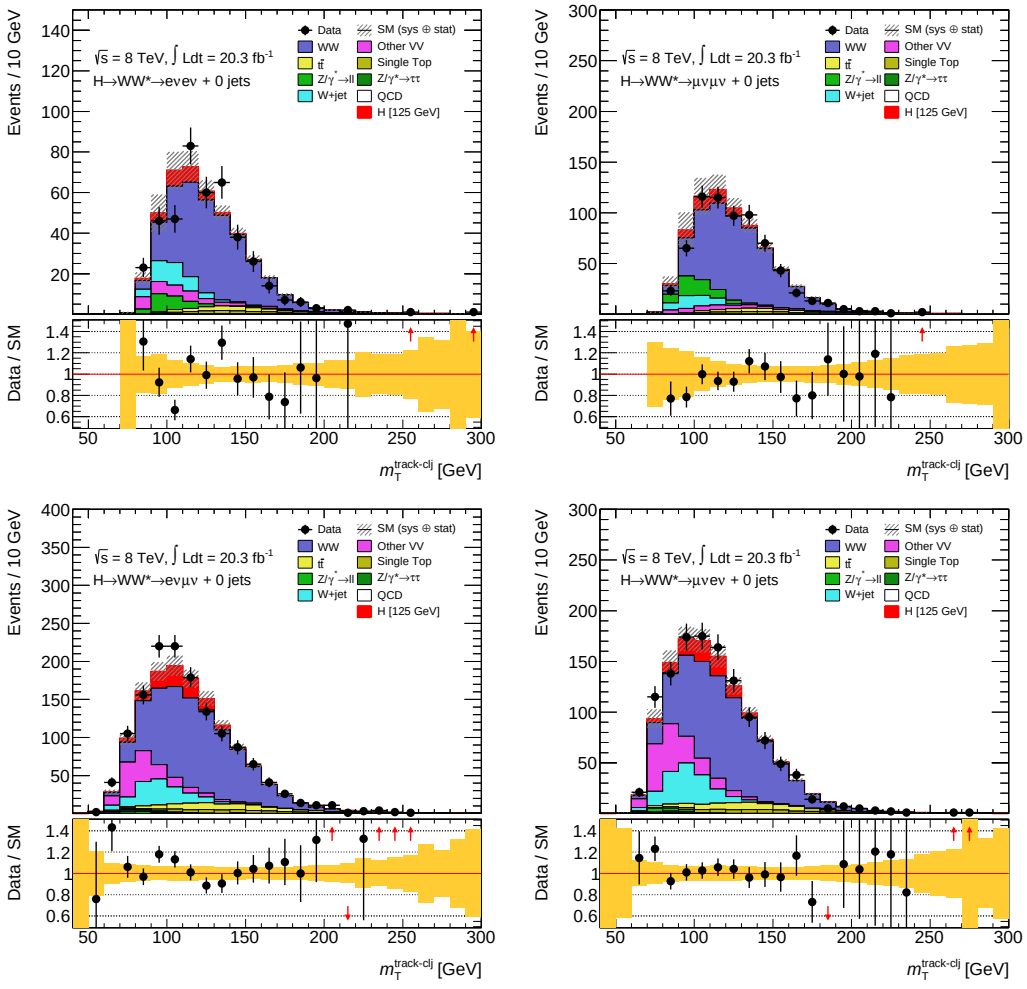

Figure 8.2: m_{T} distribution for all flavor channels ($ee, \mu\mu, e\mu, \mu e$) for the 0-jet analysis after all selections and before performing the fit (pre-fit). The Data/SM ratio includes signal yields predicted by the Standard Model ($\mu = 1$). The yellow band includes both statistical and systematic uncertainties.

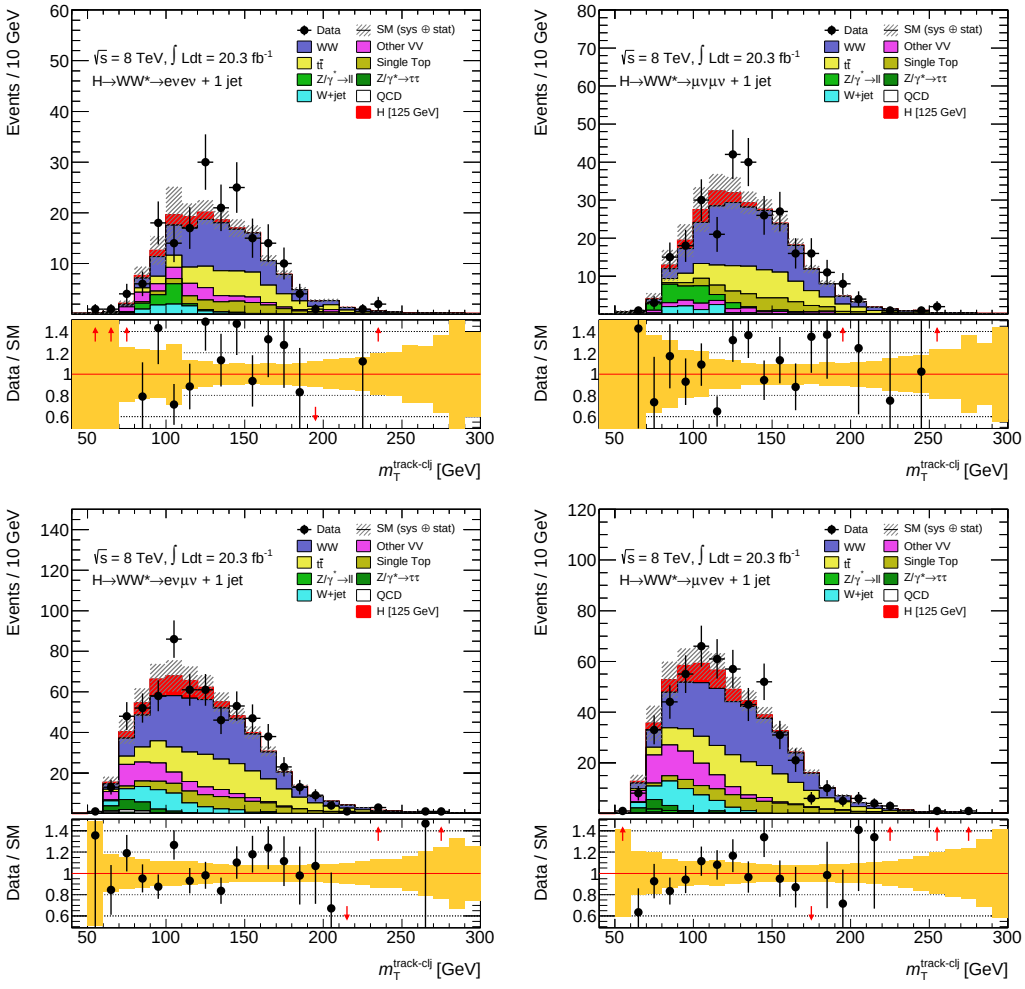

Figure 8.3: m_{T} distribution for all flavor channels ($ee, \mu\mu, e\mu, \mu e$) for the 1-jet analysis after all selections and before performing the fit (pre-fit). The Data/SM ratio includes signal yields predicted by the Standard Model ($\mu = 1$). The yellow band includes both statistical and systematic uncertainties.

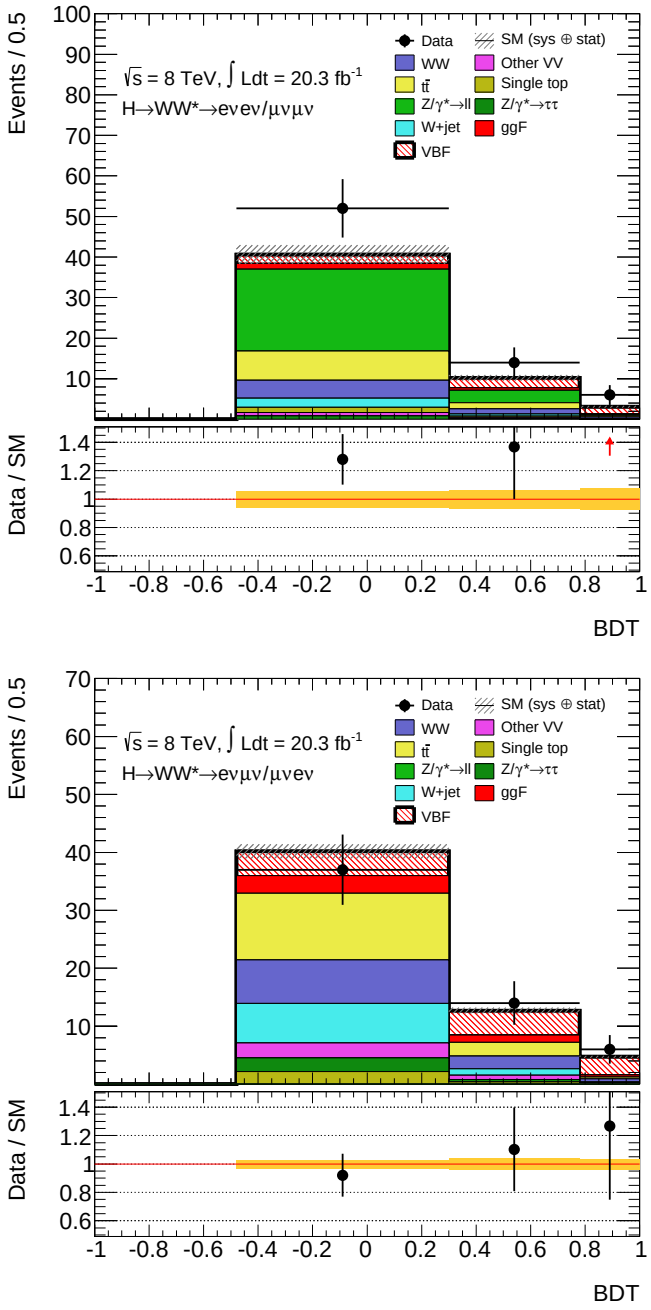

Figure 8.4: BDT score for different flavor channel (top) and same flavor channel (bottom) after all selections and before performing the fit (pre-fit). The Data/SM ratio includes signal yields predicted by the Standard Model ($\mu = 1$). The yellow band includes only statistical uncertainty, and no systematic uncertainty is displayed.

8.2 Fitting Procedure

8.2.1 Profile Likelihood

In the ggF analysis, each m_{T} distribution is firstly remapped to give a flat signal distribution across the full $0 < m_{\mathrm{T}} < \infty$ range where the m_{T} distribution is binned into 10 bins for the 0-jet analysis and into 6 bins for the 1-jet analysis. The remapping is motivated by the wide variation of signal and background shapes in the various signal region. For example, the VV backgrounds typically populate lower m_{T}, while the top and WW background enters at high m_{T}. In the VBF analysis, the highest 3 bins in the BDT score are used instead of the m_{T} distribution where no remapping is made.

The statistical analysis is performed using the likelihood function. The likelihood function condenses all details of the analysis into a single equation from the minimal set of information required to describe the analysis. A likelihood is constructed using the strength parameters. Both signals and backgrounds are equally parametrized in the likelihood as:

$$\mathcal{L}(\mu, \mu_b) = P(N|\mu s + \mu_b b_{\mathrm{SR}}^{\mathrm{exp}}) \times P(M|\mu_b b_{\mathrm{CR}}^{\mathrm{exp}}), \tag{8.2}$$

where $b_{\mathrm{SR}}^{\mathrm{exp}}$ and $b_{\mathrm{CR}}^{\mathrm{exp}}$ are expected background yields in the signal and control region predicted in simulation, and where μ and μ_b are the signal and background strength parameter, and M and N represent measured yield in signal region and control region. The expected signal and background yields can be allowed to vary within the relevant systematic uncertainties when introducing nuisance parameters θ. The nuisance parameters represent systematic uncertainties, and they are constrained by the probability density functions $N(\tilde{\theta}|\theta)$ (e.g. Gaussian, and Poisson), where $\tilde{\theta}$ represents an auxiliary measurement related to the nuisance parameter θ.

Expanding this simple likelihood to the complete form used in the analysis, a product over lepton flavors and jet multiplicity is explicitly written. Furthermore a product over the bins of final discriminant (m_{T} bins for the ggF and BDT bins for the VBF) is also present. The strength parameters μ_b are applied to the WW, VV, and different flavor $Z/\mathrm{DY} \to \tau\tau$ and same flavor $Z/\gamma^{*} \to ee/\mu\mu$ backgrounds in the 0-jet and 1-jet analyses, as well as the top background in the 1-jet and 2-jet analyses. The other backgrounds which do not have floating strength parameters, for instance, data-driven W+jets/QCD estimates are added to the Poisson expectations. The full likelihood can be written as:

$$\begin{aligned}\mathcal{L}(\mu,\vec{\theta}) = &\{\prod_{i}^{N_{\rm lep}}\prod_{j}^{N_{p_{\rm T}}}\prod_{k}^{N_{m_{\ell\ell}}}\prod_{l}^{N_{\rm jet}}\prod_{m}^{N_{\rm bin}} P(N_{ijklm}|\mu s^{\rm SR}_{ijklm} + \sum_{n}^{N_{\rm bg}}\mu_b b^{\rm SR}_{ijklmn})\}\\ &\times\{\prod_{o}^{N_{\rm lep}}\prod_{p}^{N_{\rm jet}}\prod_{q}^{N_{\rm CR}} P(M_{opq}|\mu s^{\rm CR}_{opq} + (\mu_b)_q b^{\rm CR}_{opq} + \sum_{r}^{N_{\rm bg-1}} b^{\rm CR}_{opqr})\}\\ &\times\{\prod_{s}^{N_\theta} N(\tilde{\theta_s}|\theta_s)\},\end{aligned} \tag{8.3}$$

where $N_{\rm lep}$ is the number of lepton flavors ($ee, \mu\mu, e\mu, \mu e$), $N_{p_{\rm T}}$ the number of sub-leading lepton $p_{\rm T}$ (10-15,15-20,20-) bins, $N_{m_{\ell\ell}}$ the number of $m_{\ell\ell}$ bins ($m_{\ell\ell}$ <30, $m_{\ell\ell}$ >30), $N_{\rm jet}$ the number of jet multiplicity, $N_{\rm bin}$ the number of bins in final discriminant, $N_{\rm CR}$ the number of control regions (WW, VV, top, $Z/\gamma^* \to \tau\tau$, and $Z/\gamma^* \to \ell\ell$), N_θ the number of nuisance parameters, and $N_{\rm bg}$ the number of types of backgrounds (WW, top, W+jets, VV, $Z/\gamma^* \to \tau\tau$, $Z/\gamma^* \to \ell\ell$, etc) where "bg-1" in the second term indicates that it does not include the background itself being considered. s denotes the Higgs signal and b denotes the background. $s^{\rm SR}$ and $s^{\rm CR}$ (or $b^{\rm SR}$ and $b^{\rm CR}$) are used according to the region being considered. μ_b does not appear in the $\sum^{N_{\rm bg-1}}$ term since only the background being considered is scaled in its control region. The product over $m_{\ell\ell}$ and sub-leading lepton p_T is explicitly written out to emphasize the 3D fit (bins of sub-leading lepton $p_{\rm T} \otimes m_{\ell\ell} \otimes m_{\rm T}$) used in the 0-1 jet different flavor analysis. The signal contamination in the control region is also taken into account in this formalization. Since the signal (μ) is also treated as a floating parameter, the change in signal yield can affect μ_b.

The signal and background expectations are functions of the nuisance parameters. These functions are parametrized such that the response of s and b to each θ is factorized from the nominal value of the expected rate, s_0 (or b_0) namely $s = s_0 \times \prod \nu(\theta)$ (or $b = b_0 \times \prod \nu(\theta)$), where $\nu(\theta)$ depends on systematic source, type of the $\nu(\theta)$, that is $\nu_{\rm stat}(\theta)$, $\nu_{\rm flat}(\theta)$, and $\nu_{\rm shape}(\theta)$. The statistical uncertainty is constrained by the Poisson probability given by:

$$P(\tilde{\theta}|\lambda(\theta)) = \frac{(\lambda(\theta))^{\tilde{\theta}}}{\tilde{\theta}!}\exp(-\lambda(\theta)). \tag{8.4}$$

For example, an uncertainty σ_{b_0} on an expected yield b_0, $\tilde{\theta}$ and $\nu_{\rm stat}(\theta)$ are $\tilde{\theta} = \lambda = b_0^2/\sigma_{b_0}^2$ and $\nu_{\rm stat}(\theta) = \theta$ ($b = b_0 \cdot \theta$). The systematic uncertainties on the W+jets/QCD backgrounds or theoretical uncertainties on the background normalization, are also constrained by the Poisson probability. For flat systematics that do not change the $m_{\rm T}$ or BDT shape (e.g. overall systematics like luminosity, cross sections, etc), $\nu(\theta)$ takes the form $\nu_{\rm flat}(\theta) = \kappa^\theta$, where κ is determined by measuring $\mu_{\rm flat}$ at $\theta = \pm 1$. In this case the θ is constrained by the Gaussian probability and κ^θ distributes log-normally. For shape systematics that can potentially change the $m_{\rm T}$ or BDT shape, the shape variation is firstly separated into a flat

component ($\nu_{\text{flat}}(\theta)$) and purely shape component ($\nu_{\text{shape}}(\theta)$), such that varying pure shape component of s or b has no effect on the expected rate. The flat component is treated as a flat systematic uncertainty, and the pure shape component uses vertical linear interpolation to estimate the variation (e.g. WW shape systematic uncertainty, see Section 5.6.2). The shape component is distributed as $\nu_{\text{shape}}(\theta) = 1 + \epsilon\theta$, satisfying $\nu_{\text{shape}}(\theta < \frac{-1}{\epsilon}) = 0$. ϵ is determined by measuring $\nu_{\text{shape}}(\theta)$ at $\theta = \pm 1$ with Gaussian constraint, and the same θ is shared between $\nu_{\text{shape}}(\theta)$ and $\nu_{\text{flat}}(\theta)$. The treatment of each nuisance parameter in this analysis is detailed in [176].

8.2.2 Test statistic and p-values

For statistical computations (e.g. compatibility test for data vs background-only or background+signal hypothesis), the profile likelihood ratio test statistic $\tilde{q}_\mu$ is used [177]. First the profile likelihood ratio is constructed as:

$$\tilde{\lambda}(\mu) = \begin{cases} \frac{L(\mu, \hat{\hat{\vec{\theta}}}(\mu))}{L(\hat{\mu}, \hat{\vec{\theta}})} & \hat{\mu} \geq 0, \\ \frac{L(\mu, \hat{\hat{\vec{\theta}}}(\mu))}{L(0, \hat{\hat{\vec{\theta}}}(0))} & \hat{\mu} < 0 \end{cases} \tag{8.5}$$

where $\hat{\mu}$ and $\hat{\vec{\theta}}$ are the parameters that maximize the likelihood, and $\hat{\hat{\vec{\theta}}}(0)$ and $\hat{\hat{\vec{\theta}}}(\mu)$ are the conditional maximum likelihood of $\vec{\theta}$ given a strength parameter of 0 or μ. Using the profile likelihood ratio, the test statistic $\tilde{q}_\mu$ is given by:

$$\tilde{q}_\mu = \begin{cases} -2\ln\tilde{\lambda}(\mu) & \hat{\mu} \leq \mu \\ 0 & \hat{\mu} > \mu \end{cases} = \begin{cases} -2\ln\frac{L(\mu, \hat{\hat{\vec{\theta}}}(\mu))}{L(0, \hat{\hat{\theta}}(0))} & \hat{\mu} < 0\ , \\ -2\ln\frac{L(\mu, \hat{\hat{\vec{\theta}}}(\mu))}{L(\hat{\mu}, \hat{\vec{\theta}})} & 0 \leq \hat{\mu} \leq \mu\ , \\ 0 & \hat{\mu} > \mu\ . \end{cases} \tag{8.6}$$

The modified frequentist method CLs is used to compute 95% confidence intervals on the signal strength parameter μ. In this case the test statistic is one sided with the constraint $0 < \hat{\mu} < \mu$. The test statistic $\tilde{q}_\mu$ can be computed for $\hat{\theta}_\mu$ (or $\hat{\theta}_0$) that maximizes the likelihood for background+signal (or background-only) hypothesis. The p-value p_μ (or p_b) is derived from the sampling distribution $f(\tilde{q}_\mu|\mu, \hat{\theta}_\mu)$ (or $f(\tilde{q}_\mu|0, \hat{\theta}_0)$) given by:

$$p_\mu = \int_{\tilde{q}_{\mu,\text{obs}}}^{\infty} f(\tilde{q}_\mu|\mu, \hat{\theta}_\mu) d\tilde{q}_\mu \tag{8.7}$$

$$p_b = \int_{\infty}^{\tilde{q}_{\mu,\text{obs}}} f(\tilde{q}_\mu|0, \hat{\theta}_0) d\tilde{q}_\mu \tag{8.8}$$

CLs is then constructed as the ratio of p-values, $\text{CLs} = p_\mu / 1 - p_b$. The 95% CL upper limit on μ is the solution to $\text{CLs} = 0.05$. For computing statistical significance, the background-only p-value is computed from the test statistic q_0, with a different constraint $\hat{\mu} > 0$:

$$p_0 = \int_{q_{0,\mathrm{obs}}}^{\infty} f(q_0|0,\hat{\theta}_0)dq_0 \tag{8.9}$$

One can extract the statistical significance Z from p_0 by translating from the gaussian tail probability $Z = \Phi^{-1}(1-p_0)$, where Φ^{-1} is the quantile of the standard Gaussian. Asymptotic formulae are employed to approximate the sampling distributions. This procedure is covered in [178].

8.2.3 Normalization Factors

As a validation of the fitting for this analysis, comparisons of the background normalization factors (NF) are made between pre-fit and post-fit, namely before and after the fit. Table 8.1 shows the post-fit NFs comparing to the pre-fit NFs. The post-fit NFs are compatible with the pre-fit NFs within the uncertainty. The large uncertainty on the WW 1-jet NF is due to the large subtraction of top background. Similarly the large uncertainty on the VV 0-jet and VV 1-jet NFs are due to the large subtraction of the W+jets background. The W+jets systematics (20-60%) are propagated to the uncertainties on the VV NFs.

Table 8.1: Comparison of the Normalization factors (NF) before and after the fitting.

NF	pre-fit	post-fit
WW 0-jet	1.22±0.10	1.22
WW 1-jet	1.06±0.23	1.11
top 0-jet	1.08±0.08	1.02
top 1-jet	1.04±0.07	1.03
$Z/\gamma^* \to \tau\tau$ 0-jet	1.00±0.02	0.99
$Z/\gamma^* \to \tau\tau$ 1-jet	1.06±0.04	1.05
VV 0-jet	0.92±0.18	0.99
VV 1-jet	0.96±0.25	0.88

8.3 Results

8.3.1 ggF 0-1 jet Result

Statistical tests for the ggF 0-1 jet analysis are performed. Figure 8.5 shows p_0 curve. The p_0 is the given probability for the background-only scenario. The solid curve is observed p_0 and the dashed curve is expected p_0 in the presence of the SM Higgs boson with a given m_{H}, where the cross section is normalized to the Standard Model cross section. In case of no signal, the solid line should fluctuates around 0σ line. The observed significance at $m_{\mathrm{H}} = 125$ GeV is 4.61 σ (4.25 σ expected). The excess of events is quantified as signal strength μ. Figure 8.5 also shows signal strenth as a function of m_{H}.

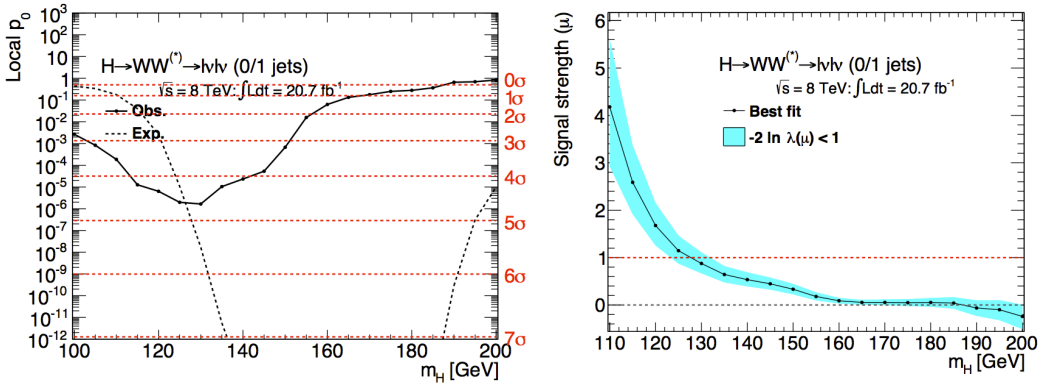

Figure 8.5: Results of p_0 significance (left) and signal strength μ (right) for the ggF 0-1 jet analysis. (Left) The solid line represents observed significance as a function of m_{H}. The dashed line represents expected significance for a given m_{H}. (Right) The solid line represents observed signal strength μ and shaded cyan band represents 1σ error band.

The observed μ value for $m_{\mathrm{H}} = 125$ GeV is:

$$\mu^{\mathrm{obs}}_{0-1\mathrm{jet}} = 1.14^{+0.32}_{-0.27} = 1.14^{+0.20}_{-0.20}(\mathrm{stat.})\ ^{+0.24}_{-0.19}(\mathrm{syst.}), \tag{8.10}$$

where the measurement with an accuracy of $\sim 30\%$ is achieved. The uncertainties on the signal strength are categorized and listed in Table 8.2. The leading uncertainties are the statistical uncertainty on the signal region and the uncertainty on the signal yield and acceptance. The uncertainties on the backgrounds and objects are dominated by the WW extrapolation, the W+jets systematics, and the $Z/\gamma^* \to \ell\ell$ systematics for same flavor analysis.

8.3.2 VBF Result

Statistical tests for the VBF signal are performed by taking into account the ggF signal as a part of background. Figure 8.6 shows p_0 curve and signal strength μ as a function of m_{H}. The observed significance at $m_{\mathrm{H}} = 125$ GeV is 4.08. σ (2.92 σ expected).

Table 8.2: Leading uncertainties on the signal strength μ for the ggF 0-1 jet analysis. The statistical uncertainties on the control regions are included in the each background systematic uncertainty.

Category	Source	Uncertainty, up (%)	Uncertainty, down (%)
Statistical	Signal region statistics	+13	−13
Theoretical	Signal yield and acceptance	+14	−11
Theoretical	WW extrapolation	+11	−11
Experimental	W+jets systematics	+7	−7
Theo./Exp.	$Z/\gamma^* \to \ell\ell$ systematics	+6	−6
Theo./Exp.	VV systematics	+4	−4
Experimental	Luminosity	+4	−3
Others	Other bkg. and object	+7	−6
Total		+28	−24

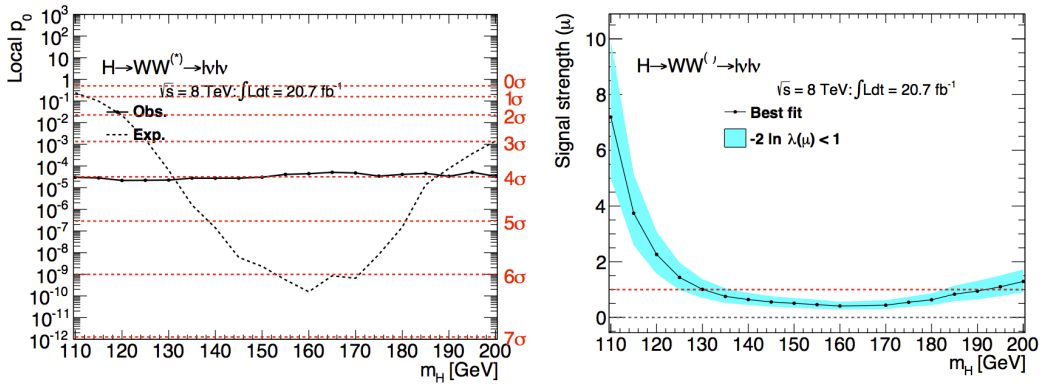

Figure 8.6: Results of p_0 significance (left) and signal strength μ (right) for the VBF analysis. (Left) The solid line represents observed significance as a function of m_{H}. The dashed line represents expected significance for a given m_{H}. (Right) The solid line represents observed signal strength μ and shaded cyan band represents 1σ error band.

The observed μ value for $m_{\mathrm{H}} = 125$ GeV is:

$$\mu_{\mathrm{VBF}}^{\mathrm{obs}} = 1.58^{+0.63}_{-0.53} = 1.58^{+0.53}_{-0.53}(\mathrm{stat.})\ ^{+0.35}_{-0.30}(\mathrm{syst.}), \tag{8.11}$$

where the measurement with an accuracy of $\sim 40\%$ is achieved. The uncertainties on the signal strength are categorized and listed in Table 8.3. The total uncertainty is dominated by the statistical uncertainty on the signal region.

Table 8.3: Leading uncertainties on the signal strength μ for the VBF analysis.

Category	Source	Uncertainty, up (%)	Uncertainty, down (%)
Statistical	Signal region statistics	+30	−30
Statistical	Control region statistics	+17	−16
Theoretical	Signal yield and acceptance	+15	−09
Others	Other bkg. and object (e.g. JES/JER)	+17	−17
Total		+41	−39

8.3.3 Combined Result

Statistical tests for the combined analysis including 2011 and 2012 ggF 2-jet analyses, are performed. Figure 8.7 shows p_0 curve and signal strength μ as a function of m_{H}. The observed significance at $m_{\mathrm{H}} = 125$ GeV is 5.81 σ (5.51 σ expected). The observed μ value for $m_{\mathrm{H}} = 125$ GeV is:

$$\mu^{\mathrm{obs}}_{\mathrm{Comb}} = 1.15^{+0.24}_{-0.22} = 1.15^{+0.16}_{-0.16}(\mathrm{stat.})\ ^{+0.18}_{-0.15}(\mathrm{syst.}). \tag{8.12}$$

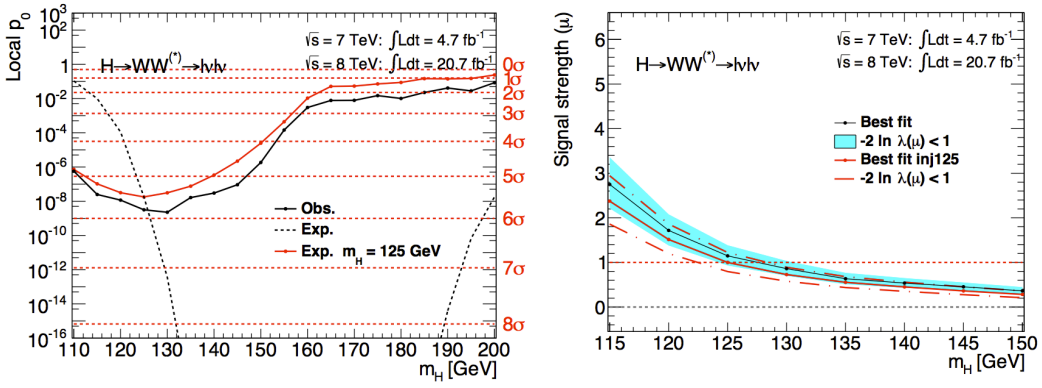

Figure 8.7: p_0 significance (left) and signal strength μ (right) for the combination. The red solid line represents expected p_0 and signal strength assuming the SM Higgs boson with a mass of $m_{\mathrm{H}} = 125$ GeV.

8.3.4 Signal Profiling

The measurement of the signal strengths for combined analysis do not give direct information on the relative contributions of the different production mechanism. Furthermore fixing the ratios of the production cross sections for the various processes to the values predicted by the Standard Model may conceal differences between data and theoretical predictions, therefore the signal strengths of different production processes contributing to the $H \to WW^*$ decay channel are determined by profiling signals for individual production processes. Two signal strength parameters, μ_{ggF} and $\mu_{\mathrm{VBF+VH}} = \mu_{\mathrm{VBF}} = \mu_{\mathrm{VH}}$, are introduced where the $H \to WW^* \to \ell\nu\ell\nu$ decay branching fraction is fixed to the nominal value and is treated as common parameter, and cross section ratio ($\sigma_{\mathrm{VBF}}/\sigma_{\mathrm{VH}}$) is still fixed to the values predicted by the Standard Model. This should be reasonable approach as both the VH and VBF production processes are similar. The effect of the fixed ratios is negligibly small since the contamination of the VH process to the ggF or VBF signal region is less than 1%. The two parameters scale the theoretical prediction to those observed for a given m_{H} (here m_{H} is fixed to be 125 GeV). Figure 8.8 shows likelihood contours in the μ_{ggF} and $\mu_{\mathrm{VBF+VH}}$ plane for $m_{\mathrm{H}} = 125$ GeV.

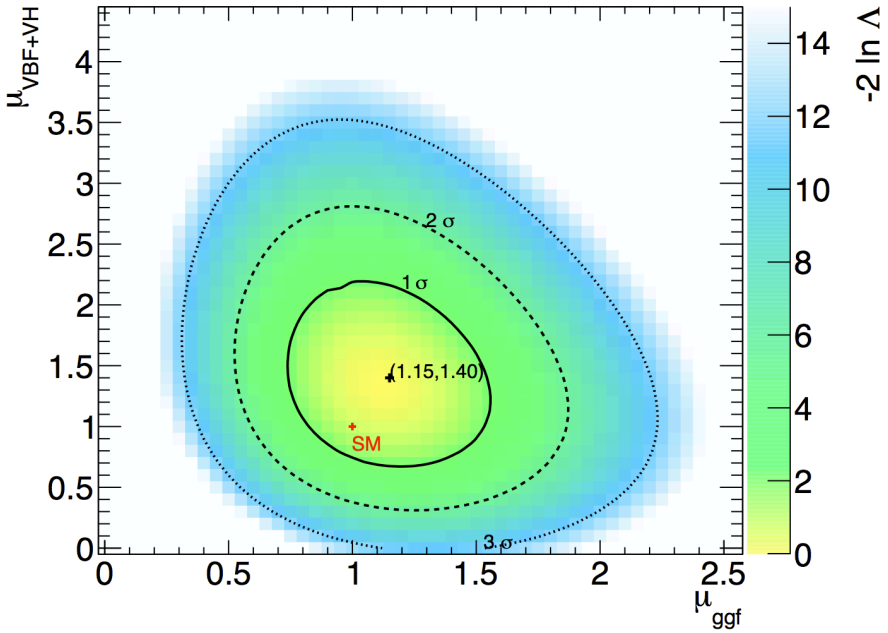

Figure 8.8: Likelihood contours in the μ_{ggF} and $\mu_{\mathrm{VBF+VH}}$ plane for $m_{\mathrm{H}} = 125$ GeV. The best-fit values to data and the 68% (solid) and 95% CL (dotted), as well as the SM prediction (1,1) are explicitly shown.

The best-fit μ values for $m_{\mathrm{H}} = 125$ GeV are:

$$\begin{aligned}\mu_{\mathrm{ggF}} &= 1.15^{+0.30}_{-0.26} = 1.15^{+0.18}_{-0.18}(\mathrm{stat.})^{+0.23}_{-0.19}(\mathrm{syst.}),\\ \mu_{\mathrm{VBF+VH}} &= 1.36^{+0.55}_{-0.47} = 1.36^{+0.45}_{-0.41}(\mathrm{stat.})^{+0.32}_{-0.24}(\mathrm{syst.}).\end{aligned} \tag{8.13}$$

Here one may realize the fact that the best-fit value of μ_{Comb} is the same as μ_{ggF}. For the μ_{Comb}, both ggF and VBF signals are treated as the same signal, whereas for the μ_{ggF} they are treated independently in the fit. In other words the fit model is different between the two cases, thus it does not make sense to consider the relation between the two.

The signal strength ratio ($\mu_{\mathrm{VBF+VH}}/\mu_{\mathrm{ggF}}$) can be also a good observable due to the fact that there is no assumption made on the Higgs boson branching ratio, so the ratio gives direct information about the ratio of the Higgs production cross section. The best-fit ratio for $m_{\mathrm{H}} = 125$ GeV is calculated as:

$$\mu_{\mathrm{VBF+VH}}/\mu_{\mathrm{ggF}} = 1.18^{+0.56}_{-0.49} = 1.18^{+0.43}_{-0.40}(\mathrm{stat.})^{+0.36}_{-0.28}(\mathrm{syst.}). \tag{8.14}$$

8.3.5 Coupling Fits

In the measurements of the signal strength μ, the production and decay modes cannot be treated independently [179, 180]. However it is possible to deal with both production and decay modes more consistently in leading order (LO) [56] based on the following assumptions.

- The signals observed in the different search channels originate from a single narrow resonance with a mass of 125 GeV. The case of several, possibly overlapping, resonances in this mass region is not considered.
- The width of the assumed Higgs boson near 125 GeV is neglected, i.e. the zero-width approximation is used. Hence the product $\sigma \times BR(X \to H \to VV)$ can be decomposed in the following way for all channels including fermion channels:

  $$\sigma \times BR(X \to H \to VV) = \frac{\sigma_X \cdot \Gamma_{VV}}{\Gamma_H}, \tag{8.15}$$

  where σ_X, Γ_{VV}, and Γ_H represent the production cross section through the initial state X, the partial decay width into the final state VV, and the total width of the Higgs boson.
- Only the Standard Model particles contributes to the total decay width, namely the BSM contributions are not considered.
- Only modifications of couplings strengths, i.e. of absolute values of couplings, are taken into account, while the tensor structure of the couplings is assumed to be the same as in the Standard Model, in other words, the Higgs boson is assumed to be a CP-even scalar as in the Standard Model. This assumption has been tested [18, 181] by the ATLAS and CMS experiments.

The LO-motivated coupling scale factors κ_j are defined in a way that the cross section σ_j and the partial width Γ_j (associated with the Standard Model particle j) scale with the factor κ_j^2 when compared to the corresponding SM prediction [56, 179]. For example one can consider the case of $gg \to H \to WW$:

$$\sigma \times \mathrm{BR}(gg \to H \to WW) = \sigma_{\mathrm{SM}}(gg \to H) \cdot \mathrm{BR}_{\mathrm{SM}}(H \to WW) \cdot \frac{\kappa_g^2 \cdot \kappa_W^2}{\kappa_H^2}. \tag{8.16}$$

In the fits the effective scale factor κ_g for $gg \to H$ process can be decomposed into more fundamental coupling scale factors κ_t and κ_b, since the ggF produces the Higgs boson through t-quark or b-quark loop:

$$\begin{aligned} \kappa_g^2 &= \frac{\kappa_t^2 \cdot \sigma_{ggH}^{tt} + \kappa_t\kappa_b \cdot \sigma_{ggH}^{tb} + \kappa_t^2 \cdot \sigma_{ggH}^{bb}}{\sigma_{ggH}^{tt} + \sigma_{ggH}^{tb} + \sigma_{ggH}^{bb}}, \\ &= 1.06 \cdot \kappa_t^2 - 0.07 \cdot \kappa_t\kappa_b + 0.01 \cdot \kappa_b^2. \end{aligned} \tag{8.17}$$

where interference term $\kappa_t\kappa_b$ is explicitly included. Similarly the VBF cross section can be expressed as:

$$\begin{aligned} \kappa_{\mathrm{VBF}}^2 =& \frac{\kappa_W^2 \cdot \sigma_{\mathrm{VBF}}^{WW} + \kappa_Z^2 \cdot \sigma_{\mathrm{VBF}}^{ZZ}}{\sigma_{\mathrm{VBF}}^{WW} + \sigma_{\mathrm{VBF}}^{ZZ}}, \\ =& 0.74 \cdot \kappa_W^2 + 0.26 \cdot \kappa_Z^2. \end{aligned} \tag{8.18}$$

Also the total decay width scale factor κ_H is expressed as:

$$\begin{aligned} \kappa_H^2 &= \sum_{jj=WW,ZZ,b\bar{b},\cdots} \frac{k_j^2 \Gamma_{jj}^{\mathrm{SM}}}{\Gamma_H^{\mathrm{SM}}}, \\ &= 0.57 \cdot \kappa_b^2 + 0.22 \cdot \kappa_W^2 + 0.09 \cdot \kappa_g^2 + 0.06 \cdot \kappa_\tau^2 + 0.03 \cdot \kappa_Z^2 + 0.03 \cdot \kappa_c^2. \end{aligned} \tag{8.19}$$

A simplification made by assuming common coupling scale factors κ_F for all fermions and κ_V for all vector boson as:

$$\begin{aligned} \kappa_F &= \kappa_t = \kappa_b = \kappa_\tau = \kappa_g, \\ \kappa_V &= \kappa_W = \kappa_Z. \end{aligned} \tag{8.20}$$

As only Standard Model particles are considered in this model, the ggF process depends directly on the fermion scale factor κ_F^2. Using this simplification the Equation 8.16 can be rewritten as:

$$\sigma \times \mathrm{BR}(gg \to H \to WW) \sim \frac{\kappa_F^2 \cdot \kappa_V^2}{0.75 \cdot \kappa_F^2 + 0.25 \cdot \kappa_V^2}. \tag{8.21}$$

Similarly the VBF production mode is written as:

$$\sigma \times \mathrm{BR}(qq' \to qq'H \to WW) \sim \frac{\kappa_V^2 \cdot \kappa_V^2}{0.75 \cdot \kappa_F^2 + 0.25 \cdot \kappa_V^2}. \tag{8.22}$$

Figure 8.9 shows the correlation of the coupling scale factors κ_F and κ_V.

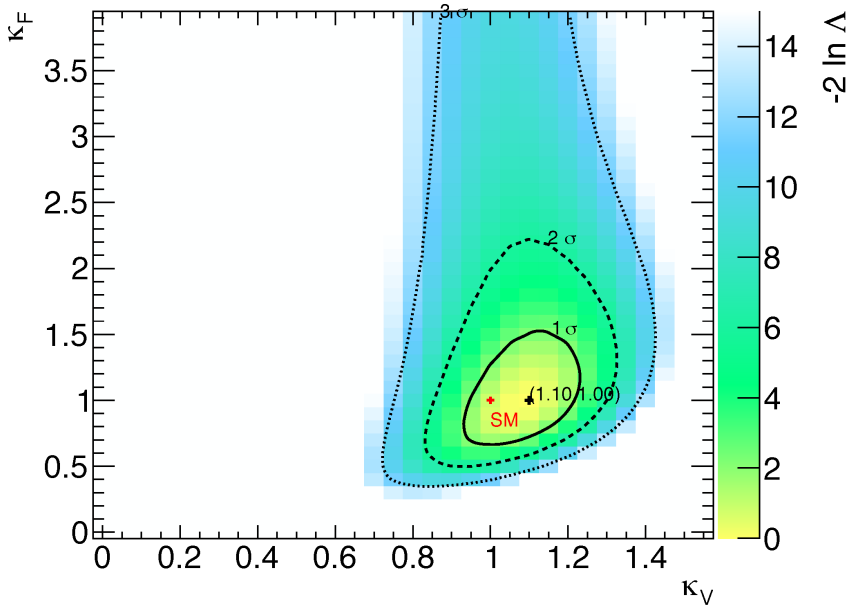

Figure 8.9: Likelihood contours in the κ_V and κ_F plane for $m_{\mathrm{H}} = 125$ GeV. The best-fit values to data and the 68% (solid) and 95% CL (dotted), as well as the SM prediction (1,1) are explicitly shown.

The low sensitivity to the high values of κ_F is due to the functional behavior of the ggF yield shown in Equation 8.21. The $\sigma \times \mathrm{BR}(gg \to H \to WW)$ is in fact κ_F independent in the $\kappa_F \to \infty$. The sensitivity to the high κ_F is therefore driven by $\mu_{\mathrm{VBF+VH}}$ that rapidly vanishes in the $\kappa_F \to \infty$, due to the increase of the total width $(0.75 \cdot \kappa_F^2 + 0.25 \cdot \kappa_V^2)$ and the consequent reduction of the WW branching fraction.

The best-fit values of κ_V and κ_F are:

$$\begin{aligned} \kappa_V &= 1.08^{+0.11}_{-0.11} = 1.08^{+0.07}_{-0.08}(\mathrm{stat.})^{+0.08}_{-0.07}(\mathrm{syst.}), \\ \kappa_F &= 1.00^{+0.32}_{-0.24} = 1.00^{+0.24}_{-0.18}(\mathrm{stat.})^{+0.22}_{-0.15}(\mathrm{syst.}). \end{aligned} \tag{8.23}$$

Similar to the signal strength ratio, the κ_F/κ_V ratio (referred to as λ_{FV} in [180]) can be also a good observable (i.e. no assumption made on the total width). The best-fit value for $m_{\mathrm{H}} = 125$ GeV is calculated as:

$$\kappa_F/\kappa_V = 0.93^{+0.31}_{-0.24} = 0.93^{+0.23}_{-0.18}(\text{stat.})^{+0.22}_{-0.15}(\text{syst.}). \quad (8.24)$$

8.3.6 Summary of Observables

In summary, the measured and presented physical quantities related to the Higgs boson couplings are summarized in Table 8.4. All the observables discussed above are compatible with the values predicted by the Standard Model.

Table 8.4: Summary of measured physical quantities related to the Higgs couplings: μ, κ, and λ.

Observables	Values
μ_{ggF}	$1.15^{+0.18}_{-0.18}(\text{stat.})^{+0.23}_{-0.19}(\text{syst.})$ (see Section 8.3.4)
$\mu_{\text{VBF+VH}}$	$1.36^{+0.41}_{-0.45}(\text{stat.})^{+0.32}_{-0.24}(\text{syst.})$ (see Section 8.3.4)
$\mu_{\text{VBF+VH}}/\mu_{\text{ggF}}$	$1.18^{+0.43}_{-0.40}(\text{stat.})^{+0.36}_{-0.28}(\text{syst.})$ (see Section 8.3.4)
κ_V	$1.08^{+0.07}_{-0.08}(\text{stat.})^{+0.08}_{-0.07}(\text{syst.})$ (see Section 8.3.5)
κ_F	$1.00^{+0.24}_{-0.18}(\text{stat.})^{+0.22}_{-0.15}(\text{syst.})$ (see Section 8.3.5)
$\lambda_{FV}(=\kappa_F/\kappa_V)$	$0.93^{+0.23}_{-0.18}(\text{stat.})^{+0.22}_{-0.15}(\text{syst.})$ (see Section 8.3.5)

The observables related to the ggF production process start being limited by the systematic uncertainties, in particular the uncertainties related to the signal yields (e.g. QCD scale and PDF, as well as the jet-bin-uncertainties) and uncertainties related to the background estimation. However it is still possible to reduce the uncertainty on the WW normalization with more statistics, and the uncertainty on the WW extrapolation by defining a closer control region to the signal region. Also the W+jets background that is reducible background will be reduced by tightening the lepton selection. Therefore the increased statistics will give substantial improvements to the ggF analysis, but even incorporating those improvements the measurement will be again reaching the limit on the signal uncertainty which is $\sim 20\%$ in total. The higher order calculation of the signal cross section, especially higher order QCD correction is thus necessary in the future measurement.

On the other hand, the observables related to the VBF production process are still dominated by the statistical uncertainty. The impact of the signal uncertainty is relatively small compared to the ggF analysis due to no QCD vertices in the leading order. Thus the analysis with the higher statistics obviously improves the measurement (presumably up to $\sim 15\%$ due to the uncertainty on the signal) in the future.

8.4 Compatibility of Signal Strength

8.4.1 Comparison of Individual Measurements

The combined signal strength is decomposed into the individual channels to see the compatibility. The individual measurements are summarized in Table 8.5 (observed and expected) and Figure 8.10 (observed). All the individuals are compatible within their uncertainties.

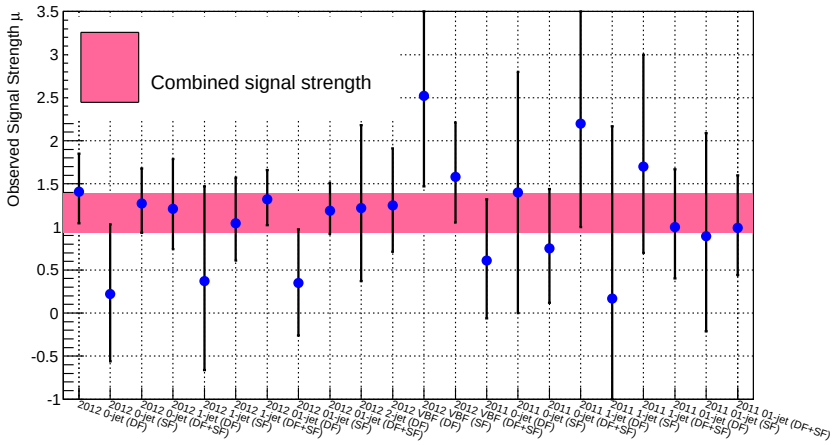

Figure 8.10: Observed signal strength for individual and combined (band) analyses.

Table 8.5: Observed and expected signal strength for individual analyses: different flavor (DF), same flavor (SF), and combined (DF+SF). The central value of the expected signal strengths are set to be $\mu = 1$ for $m_{\mathrm{H}} = 125$ GeV.

Channel	DF(obs)	SF(obs)	DF+SF(obs)	DF(exp)	SF(exp)	DF+SF(exp)
2012 0-jet	$1.41^{+0.44}_{-0.37}$	$0.22^{+0.81}_{-0.78}$	$1.27^{+0.41}_{-0.34}$	$1.00^{+0.38}_{-0.32}$	$1.00^{+0.84}_{-0.79}$	$1.00^{+0.36}_{-0.31}$
2012 1-jet	$1.21^{+0.58}_{-0.47}$	$0.37^{+1.10}_{-1.03}$	$1.04^{+0.53}_{-0.43}$	$1.00^{+0.53}_{-0.44}$	$1.00^{+1.20}_{-1.10}$	$1.00^{+0.50}_{-0.41}$
2012 0-1 jet	$1.32^{+0.34}_{-0.30}$	$0.35^{+0.62}_{-0.61}$	$1.19^{+0.32}_{-0.27}$	$1.00^{+0.30}_{-0.26}$	$1.00^{+0.66}_{-0.63}$	$1.00^{+0.28}_{-0.25}$
2012 2 jet	$1.22^{+0.96}_{-0.85}$	-	-	$1.00^{+0.94}_{-0.85}$	-	-
2012 VBF	$1.25^{+0.66}_{-0.54}$	$2.52^{+1.31}_{-1.05}$	$1.58^{+0.63}_{-0.53}$	$1.00^{+0.67}_{-0.55}$	$1.00^{+1.13}_{-0.87}$	$1.00^{+0.59}_{-0.49}$
2011 0-jet	$0.61^{+0.71}_{-0.67}$	$1.40^{+1.40}_{-1.40}$	$0.75^{+0.69}_{-0.63}$	$1.00^{+0.76}_{-0.68}$	$1.00^{+1.36}_{-1.25}$	$1.00^{+0.70}_{-0.63}$
2011 1-jet	$2.20^{+1.50}_{-1.20}$	$0.17^{+2.00}_{-1.70}$	$1.70^{+1.30}_{-1.00}$	$1.00^{+1.17}_{-1.01}$	$1.00^{+1.89}_{-1.61}$	$1.00^{+1.04}_{-0.90}$
2011 0-1 jet	$1.00^{+0.67}_{-0.60}$	$0.89^{+1.20}_{-1.10}$	$0.99^{+0.61}_{-0.55}$	$1.00^{+0.63}_{-0.58}$	$1.00^{+1.07}_{-1.00}$	$1.00^{+0.57}_{-0.53}$

8.4.2 Comparison to Previous Analysis

A comparison of the signal strengths to the previous analysis [3] is made, even though both analyses use the same data set recorded in 2011-2012. Table 8.6 shows the comparison of the signal strength presented in this thesis to the previous one.

Table 8.6: Comparison of signal strengths between the two analyses.

	The analysis presented here	Previous analysis
μ_{ggF}	1.15±0.30 ($\Delta\mu/\mu = 25\%$)	0.82±0.36 ($\Delta\mu/\mu = 44\%$)
$\mu_{\text{VBF+VH}}$	1.36±0.55 ($\Delta\mu/\mu = 40\%$)	1.66±0.79 ($\Delta\mu/\mu = 47\%$)

Many improvements are incorporated into this analysis. For example, another 50% of data is added from trigger/lepton optimization. The individual improvements for the ggF analysis are summarized in Table 8.7. The total improvement on significance is $> 50\%$.

Table 8.7: List of improvements made for the ggF analysis since previous results. Note that some of those numbers are outdated.

Improvements	Z (Exp.)	$\Delta Z/Z_{\text{prev.}}$ (%)
Previous Results	2.80	-
Increase MC Statistics	2.84	1.3%
Lepton optimization, Add dilepton trigger	3.04	8.5%
Updates on W+jets systematics	3.15	12.5%
$m_{\text{T}}(E_{\text{T}}^{\text{miss}}) \rightarrow m_{\text{T}}(\boldsymbol{p}_{\text{T}}^{\text{miss, jetCorr}})$	3.43	22.5%
Doubling the m_{T} bins	3.62	29.2%
Add low $p_{\text{T}}^{\text{sublead}}$ bin (10-15 GeV)	3.73	33.2%
Add SS CR method for VV backgrounds	3.87	38.2%
Updated b-tagging efficiency	3.93	40.3%
$E_{\text{T}}^{\text{miss}}$ optimization	4.23	51.1%
Add ggF 2-jet analysis	4.36	55.7%

8.4.3 Comparison to CMS

It is interesting to compare the result with other $H \to WW^*$ analysis. The most relevant way is to compare with the CMS $H \to WW^*$ result [182]. Figure 8.11 shows 2-dimensional contours, "κ_v versus κ_f" and "μ_{ggF} versus μ_{VBF}". Table 8.8 shows comparison of the observed signal strength μ in the CMS to that in the ATLAS. The CMS obtained slightly lower μ values but both are well agreed within the uncertainty.

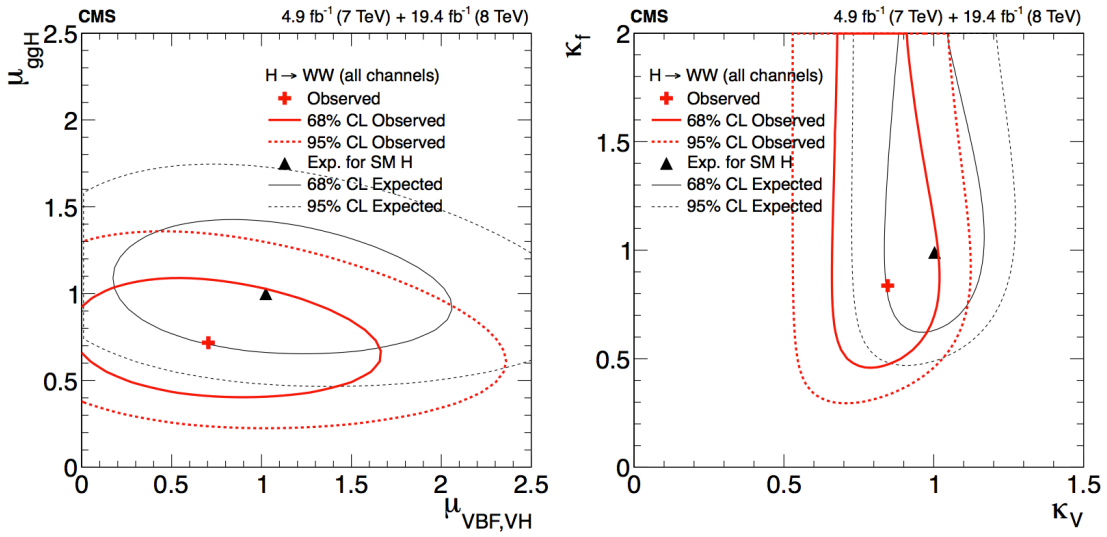

Figure 8.11: Likelihood profiles on μ_{ggF} and $\mu_{\mathrm{VBF,VH}}$ at 68% (solid) and 95% CL (dotted). The expected (black) and observed (red) distributions for $m_{\mathrm{H}} = 125.6$ GeV are shown. (This figure is taken from [182].)

Table 8.8: Comparison of the CMS results to the ATLAS (presented in this thesis): observed $\sigma/\sigma_{\mathrm{SM}}$ (μ) and significance for each category at $m_{\mathrm{H}} = 125$ GeV. The CMS result is taken from [182].

Category	$\sigma/\sigma_{\mathrm{SM}}$ (CMS)	exp./obs. (CMS)	$\sigma/\sigma_{\mathrm{SM}}$ (ATLAS)	exp./obs. (ATLAS)
ggF Category	$0.76^{+0.21}_{-0.21}$	5.2/4.0 σ	$1.15^{+0.30}_{-0.26}$	4.6/5.0 σ
VBF Category	$0.62^{+0.58}_{-0.47}$	2.1/1.3 σ	$1.36^{+0.55}_{-0.47}$	2.5/3.4 σ

Chapter 9

Conclusion

On 4th July 2012, the ATLAS and CMS collaborations announced that they had each observed a Higgs boson with a mass of approximately 125 GeV. The discovery opened up a new era in understanding the nature of electroweak symmetry breaking. The major focus of physics analysis at the LHC now is the measurement of the properties of the Higgs boson. In this thesis, the measurements of the couplings using the $H \to WW^* \to \ell\nu\ell\nu$ final state are presented with the full Run-I pp collision data corresponding to 20.3 fb^{-1} of $\sqrt{s} = 8$ TeV and 4.5 fb^{-1} of 7 TeV, recorded by the ATLAS at the LHC. The $H \to WW^* \to \ell\nu\ell\nu$ channel is sensitive to the coupling measurement through gluon-gluon fusion (ggF) and vector boson fusion (VBF) production processes. The precise measurement is possible only in understanding all the Standard Model processes, since the analysis suffers from many backgrounds. The analysis adopted several enhanced techniques on the background estimation to attain a substantially better sensitivity of the measurement.

The result presented in this thesis supersedes the previous measurement in accuracy, owing to optimizations of selection of physics objects and improvements of the modeling of backgrounds. The observed excess of the inclusive production for $m_{\mathrm{H}} = 125$ GeV is about 6 σ that is large enough to claim the discovery of the $H \to WW^*$ decay, and the corresponding signal strengths for individual production processes are:

$$\mu_{\mathrm{ggF}} = 1.15^{+0.18}_{-0.18}(\mathrm{stat.})^{+0.23}_{-0.19}(\mathrm{syst.}),$$

$$\mu_{\mathrm{VBF+VH}} = 1.36^{+0.41}_{-0.45}(\mathrm{stat.})^{+0.32}_{-0.24}(\mathrm{syst.}).$$

Furthermore the coupling to fermions and weak bosons are each extracted, introducing κ_F and κ_V. The measured κ_V and κ_F are:

$$\kappa_V = 1.08^{+0.11}_{-0.11} = 1.08^{+0.07}_{-0.08}(\mathrm{stat.})^{+0.08}_{-0.07}(\mathrm{syst.}),$$

$$\kappa_F = 1.00^{+0.32}_{-0.24} = 1.00^{+0.24}_{-0.18}(\mathrm{stat.})^{+0.22}_{-0.15}(\mathrm{syst.}).$$

The measured couplings via these production processes are consistent with the Standard Model prediction. [1]

The observables related to the ggF analysis (e.g. μ_{ggF}) start being limited by systematic uncertainties. However it is still possible to reduce the uncertainty on the WW normalization with more statistics, and the uncertainty on the WW extrapolation by defining a closer control region to the signal region. Also the W+jets background will be reduced by tightening the lepton selection. Therefore the increased statistics will bring substantial improvements. Without having higher order calculation of the QCD correction on the signal production, the analysis will eventually be reaching the limit on the signal uncertainty which is $\sim$ 20%. On the other hand, the observables related to the VBF analysis (e.g. μ_{VBF}) is still limited by the statistical uncertainty. Therefore the analysis with the higher statistics obviously achieves better measurement (presumably up to 15% due to the uncertainty on the signal) in the future.

In the Run II (2015-2018) we expect $\sim$100 fb^{-1} of 13-14 TeV data set. This corresponds to 10 times higher statistics of the Higgs boson signal when taking into account the increased signal production cross section. Therefore it might be interesting to look into other Higgs production processes and decay modes (e.g. $bbH/ttH \to b\bar{b}$ or $\gamma\gamma$). Also it might be interesting to continue to perform: (1) search for the BSM Higgs boson predicted in the MSSM [183–187] and (2) search for the invisible decay of the Higgs boson [188].

[1] The final published numbers may be slightly different from the numbers in this thesis.

Appendix A

Additional Materials for $H \to WW^* \to \ell\nu\ell\nu$ Analysis

A.1 ggF 2-jet analysis

A.1.1 Event Selection

The ggF production still present signal yield in 2-jet bin. A dedicated selection for the 2-jet analysis based on the events orthogonal to the VBF and VH analyses is required. Since the contribution from same flavor channel is tiny, only different flavor ($e\mu$+μe) channel is considered. The selection of events satisfying the preselection and containing at least two selected jets is similar to the 0-1 jet analysis. In addition to the preselection described in Section 5.4.1, the followings are required:

- $\boldsymbol{p}_{\mathbf{T}}^{\mathbf{miss,\ jetCorr}} > 20$ GeV
- b-jet veto (see Section 5.4.2)
- $Z \to \tau\tau$ veto (see Section 5.4.2)
- Non-VBF(VH) selection:
  - VBF cut-based veto: fail of either $\Delta Y_{jj} > 3.6$, $m_{jj} > 600$ GeV, CJV or OLV,
  - VBF BDT veto: fail of either CJV, OLV or BDT score > -0.48,
  - VH veto: fail of either $\Delta y_{jj} < 1.2$ or $|m_{jj} - 85\ \text{GeV}| < 15$ GeV,
- The event must pass the same cuts on $m_{\ell\ell}$ and $\Delta\phi_{\ell\ell}$ as well as 0-jet analysis.

The selection must be orthogonal to other analyses since the priority of VBF (and VH) is high. Table A.1 shows fraction for each Higgs production after all signal region criteria. As can be seen in this table, the contribution from other production modes (VBF and VH) is 25 % even after VBF and VH veto applied. Table A.2 shows expected signal and background counts for the 2-jet analysis.

Table A.1: The expected number of events and fraction for each production mode (ggF, VBF and VH) after all signal region selection criteria.

Production process	ggF	VBF	VH
Number of events	34.04 ± 0.25	6.88 ± 0.11	4.53 ± 0.29
Signal composition [%]	74.9	15.1	10.0

Table A.2: The expected number of signal and background counts for the 2-jet analysis.

	Signal $H \to WW$	WW	$WZ/ZZ/W\gamma$	$t\bar{t}$	Single Top	$Z(\tau\tau)$ +jets	W+jets	QCD	Total Bkg.
Missing E_{T}	415.89 ± 3.80	8107.26 ± 12.27	1246.34 ± 10.92	57508.99 ± 28.96	5328.11 ± 6.72	12798.86 ± 46.85	2475.16 ± 20.28	756.48 ± 3.53	88677.83 ± 66.05
at least two jets	119.95 ± 2.65	963.67 ± 4.15	264.16 ± 4.97	49665.85 ± 27.19	2814.62 ± 4.90	2204.29 ± 22.39	704.93 ± 11.79	194.40 ± 1.73	56927.25 ± 39.61
b-jet veto	61.95 ± 2.07	693.58 ± 3.49	174.73 ± 3.99	2621.99 ± 6.29	317.98 ± 1.80	1502.96 ± 17.59	228.37 ± 6.82	117.46 ± 1.39	5729.99 ± 22.96
$Z \to \tau\tau$ veto	42.19 ± 1.52	401.23 ± 2.66	98.76 ± 3.07	1640.11 ± 4.98	197.01 ± 1.41	417.81 ± 9.28	126.12 ± 4.98	68.99 ± 1.01	2967.64 ± 12.60
Non-VBF	38.33 ± 1.52	390.09 ± 2.63	97.64 ± 3.06	1623.59 ± 4.95	193.97 ± 1.38	412.64 ± 9.24	124.03 ± 4.93	67.80 ± 1.00	2926.46 ± 12.52
VH veto	31.57 ± 1.12	351.23 ± 2.50	86.98 ± 2.91	1457.22 ± 4.70	172.12 ± 1.29	368.31 ± 8.78	107.47 ± 4.64	62.36 ± 0.96	2619.57 ± 11.87
$m_{\ell\ell} < 55$ GeV	18.45 ± 0.76	53.83 ± 0.98	21.85 ± 1.51	229.06 ± 1.86	25.87 ± 0.51	228.01 ± 6.80	30.03 ± 3.68	52.22 ± 0.89	648.25 ± 8.31
$\Delta\phi_{\ell\ell} < 1.8$	12.62 ± 0.72	39.13 ± 0.83	16.20 ± 1.35	181.54 ± 1.65	21.08 ± 0.42	78.78 ± 4.00	15.31 ± 3.04	41.64 ± 0.80	397.41 ± 5.68

A.1.2 Background Estimation

Figures A.1 shows schematic view of the extraction of the main backgrounds in the ggF 2-jet analysis.

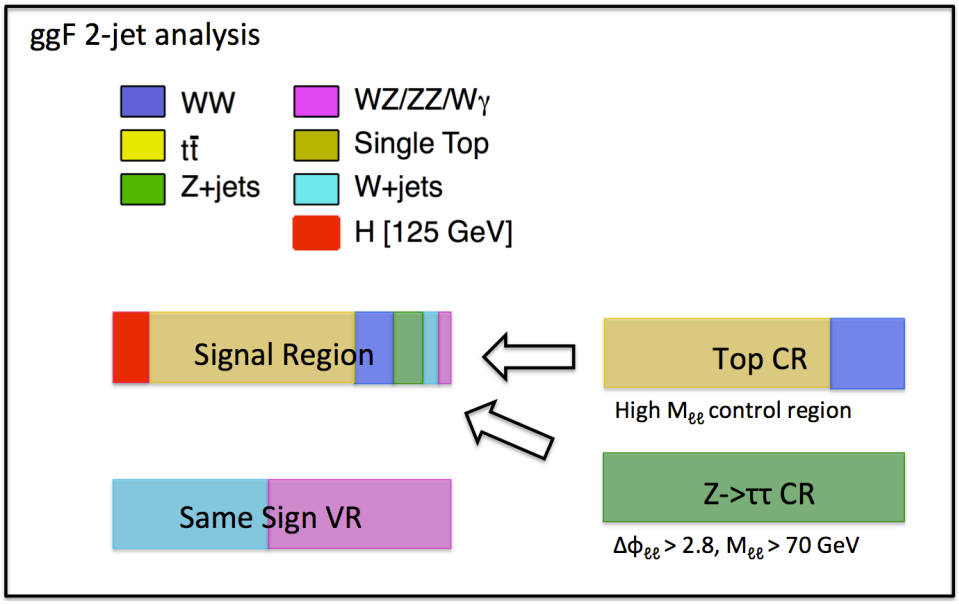

Figure A.1: Schematic view of the extraction of the main backgrounds for the ggF 2-jets analysis. Some backgrounds are normalized to data in dedicated control regions.

Top background

The top background is estimated using MC and is normalized in a high $m_{\ell\ell}$ control region. For the high $m_{\ell\ell}$ control region the following selection criteria are added in addition to the preselection described in Section 5.4.1:

- $\boldsymbol{p}_{\mathbf{T}}^{\mathbf{miss,\ jetCorr}} > 20$ GeV,
- b-jet veto (see Section 5.4.2),
- Non-VBF(VH) selection,
- $m_{\ell\ell} > 80$ GeV.

The purity of this control region is $\sim 70\%$ and the remaining contamination is mostly WW background. Similar to the signal region, the b-jet veto is applied to the control region, which allow for cancelling b-tagging related systematic uncertainties. The resulting normalization factor is 1.07 ± 0.03(stat.). For the systematics, the shape systematic uncertainty is evaluated by comparing several generators in truth level, in addition to the experimental and theoretical uncertainties that are small compared to the uncertaities on the b-tagged control region for the 1-jet. The resulting shape systematic uncertainty is at most 4 % level.

$Z/\gamma^* \to \tau\tau$ background

The $Z/\gamma^* \to \tau\tau$ background is estimated using MC and is normalized in a $Z/\gamma^* \to \tau\tau$ control region that is defined as:

- $\boldsymbol{p}_{\mathbf{T}}^{\mathbf{miss,\ jetCorr}} > 20$ GeV,
- b-jet veto (see Section 5.4.2),
- Non-VBF(VH) selection,
- $m_{\ell\ell} < 70$ GeV,
- $\Delta\phi_{\ell\ell} > 2.8$ radians.

The definition and procedure of systematic evaluation for the $Z/\gamma^* \to \tau\tau$ control region is mostly the same as the 0-1 jet analysis. The resulting normalization factor is 1.07 ± 0.03(stat.).

W+jets/QCD background

The W+jets/QCD backgrounds are estimated using the same data-driven method as is employed in the ggF 0-1 jet analysis.

VV background

For VV backgrounds fully MC-based estimation is employed since they remain small in the signal region. These backgrounds can be validated in Same Sign region.

WW background

The WW background is estimated using MC prediction. The WW control region is not established due to large top contamination in potential WW enriched region, and the size of this background is not large compared to the 0-1 jet analysis.

A.2 7 TeV (2011) analysis

In the previous sections only 8 TeV (2012) analysis is discussed. The addition of 7 TeV (2011) analysis incorporating all improvements made in the 8 TeV analysis, improves the sensitivity on the measurement. For the 7 TeV analysis, the following lepton flavor and jet-bin channels are considered :

- $e\mu$+μe and ee+$\mu\mu$ $N_{\text{jet}} = 0$ and $= 1$ ggF-enriched,
- $e\mu$+μe and ee+$\mu\mu$ $N_{\text{jet}} \geq 2$ VBF-enriched.

A.2.1 Physics Object

Physics objects for the 7 TeV analysis basically follow those for 8 TeV analysis but there are some differences due to changes in running condition, namely pileup condition. The different pileup condition induces changes in trigger and physics objects :

- trigger:
  1. single lepton (e and μ) triggers,
  2. period dependent thresholds,
- electrons:
  1. non-GSF,
  2. cut-based identification (tight++),
  3. tight isolation and impact parameter requirements (suppress W+jets/QCD contributions);

For the 7 TeV analysis, only single lepton triggers are used, since the trigger threshold in 2011 is lower than that in 2012, and the lower threshold allows for making the same lepton p_{T} configuration as 2012 (leading lepton $p_{\text{T}} > 22$ GeV and sub-leading lepton $p_{\text{T}} > 10$ GeV), while keeping high efficiency. The electron definition is slightly tightened due to the fact that the GSF electron is not available in 2011 that reduces background electron, mainly jet faking electron. The MC generators and processes used in the 7 TeV analysis are summarized in Table 5.3.

A.2.2 ggF analysis

The event selection of the 7 TeV analysis follows that of the 8 TeV, except for f_{recoil} that is set to be looser in 2011 due to lower level of pileup and lower contamination of Z/γ^* background, otherwise the event selection is identical. Background estimation also follow the procedures used in the 8 TeV analysis. One exception is the treatment of same sign backgrounds, namely the W+jets/QCD and non-WW diboson (VV) backgrounds. In the 7 TeV analysis the W+jets background is estimated using fake factor from di-jets enriched sample, while the 8 TeV analysis using the fake factor from the Z+jets enriched sample. This is due to the lack of the Z+jets statistics in the 7 TeV analysis. Furthermore the same sign (SS) control region is not used for the VV background estimate in the 7 TeV analysis due to the limited statistics in SS region, so the SS region is used only for purpose of validation of those backgrounds. The background treatment for the 7 TeV analysis is listed in Table A.2.2, along with that for the VBF analysis.

Table A.3: Background treatment listing for the 7 TeV analysis. The estimation procedures for various background processes are given in four categories : normalized using a control region (CR); data-driven estimate (Data); normalized using the MC (MC); and normalized using the MC, but validated in a control region (MC+VR). The "($e\mu$+μe)" indicates that the control region is defined in different flavor data set instead of same flavor data set for reasons of purity and/or statistics.

Channel	WW	Top	$Z/\gamma^* \to \tau\tau$	$Z/\gamma^* \to ee/\mu\mu$	W+jets/QCD	VV
$N_{\text{jet}} = 0$						
$e\mu$+μe	CR	CR	CR	MC	Data	MC+VR
ee+$\mu\mu$	CR ($e\mu$+μe)	CR ($e\mu$+μe)	CR ($e\mu$+μe)	Data	Data	MC+VR
$N_{\text{jet}} = 1$						
$e\mu$+μe	CR	CR	CR	MC	Data	MC+VR
ee+$\mu\mu$	CR ($e\mu$+μe)	CR ($e\mu$+μe)	CR ($e\mu$+μe)	Data	Data	MC+VR
$N_{\text{jet}} \geq 2$						
$e\mu$+μe	MC	CR	CR	MC	Data	MC+VR
VBF						
$e\mu$+μe	MC	CR	CR ($e\mu$+μe +ee+$\mu\mu$)	MC	Data	MC+VR
ee+$\mu\mu$	MC	CR	CR ($e\mu$+μe +ee+$\mu\mu$)	Data	Data	MC+VR

A.2.3 VBF analysis

For the 7 TeV analysis, the BDT trained for 8 TeV is applied to the 7 TeV data set due to higher statistics in 8 TeV. There are also additional benefits to this apart from the resulting increased sensitivity, such as being able to take the same theoretical uncertainties as for the 8 TeV analysis and to facilitate the combination of the two analyses. No changes are made to the event selection and background estimation, except for doing a counting experiment (namely one bin in the signal region) instead of a fit to BDT score (3 bins in signal region) as is done for the 8 TeV BDT analysis due to a lack of statistics in the signal region.

Appendix B

Additional Studies for Fake Backgrounds

B.1 Di-jet Fake Factors

Di-jets sample is extensively used for fake background estimations even for other methods such as 'Matrix Method'. However the di-jets fake factor is not mainly used for the W+jets estimation in this analysis because it is found that the Z+jets fake factor has smaller uncertainty. Nevertheless the di-jet fake factor is still partially used in this analysis for the QCD estimation and W+jets triggered fake correction that are discribed in Section 6.7 and B.4.

B.1.1 Electron Fake Factors

The fake factors are measured in data using a di-jet control sample. For electrons, the di-jet control sample is collected with the e/gamma supporting triggers:

- `EF_g24_etcut` (2.084 pb^{-1}),
- `EF_e5_etcut` (12.4 nb^{-1}),
- `EF_e5_medium1` (241.3 nb^{-1}),

where `EF_g24_etcut` (`EF_e5_etcut`) supporting trigger requires a reconstructed EM cluster with transverse energy E_{T} above 24 (5) GeV but makes no requirement on the electron identification, and where `EF_e5_medium1` trigger requires a reconstructed electron with transverse energy E_{T} above 5 GeV that satisfies the `medium1` electron identification requirements. Due to their large trigger rates, the e/gamma supporting triggers are heavily pre-scaled.

The `EF_e5_etcut` and `EF_e5_medium1` triggers are used below $E_{\text{T}} = 20$ GeV, while the `EF_g24_etcut` is used above $E_{\text{T}} = 20$ GeV. The following basic quality cuts are required: GRL, $E_{\text{T}}^{\text{miss}}$ cleaning, primary vertex quality cut, and LAr veto. The presence of electrons from W or Z bosons in the di-jet sample will bias the calculation of the fake factor. To

suppress this contamination, events used in the fake factor calculation are required to the followings:

- away side jet with $p_{\mathrm{T}} > 15$ GeV,
- $\Delta\phi$(electron, jet) > 0.7,

and events are vetoed if they satisfy the followings:

- m_{T}(electron, $E_{\mathrm{T}}^{\mathrm{miss}}$) > 30 GeV,
- $|M_Z - M_{\ell\ell}| < 13$ GeV,

where electrons are either `id` or `anti-id`.

The remaining W and Z contributions referred to as 'EW contamination', are subtracted from the di-jet sample using simulation. This contribution has been validated by comparing the data/simulation agreement in the Z peak. The di-jet p_{T} distributions for numerators and denominators with W and Z contaminations are shown in Figure B.1. There is no EW contamination in $E_{\mathrm{T}} < 20$ GeV due to the lack of `EF_e5_etcut` and `EF_e5_medium1` in simulation sample but the effect is covered by systematic uncertainty.

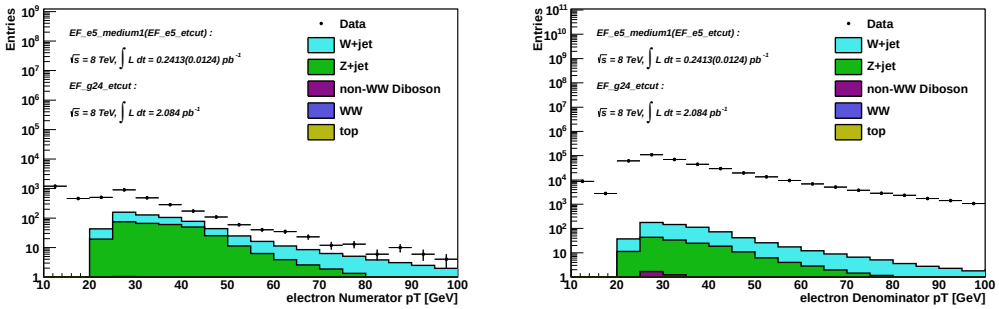

Figure B.1: Di-jet p_{T} distributions for electron numerators (left) and electron denominators (right) collected with e/gamma supporting triggers. W and Z contaminations are also illustrated but the contributions are negligibly small at the end of the selection.

To avoid a possible bias due to trigger threshold, the fake factors for 10-20 GeV electrons is calculated by a combination of supporting triggers (`EF_e5_etcut` and `EF_e5_medium1`). The electrons satisfying the identified electron selection are collected with the `EF_e5_medium1` trigger, while the sample of electrons satisfying the electron denominator definition are collected with the `EF_e5_etcut` trigger. The fake factor is then computed after correcting the denominator sample for the pre-scale of the `EF_e5_etcut` and `EF_e5_medium1` triggers. Making use of this combination increases the number of `id` objects and decreases the statistical uncertainty significantly. Measured di-jets fake factors for electrons as a function of E_{T} and η (1D and 2D) are shown in Figure B.2. Note that the sutracted EW contamination is larger at higher E_{T} whereas it remains small at lower E_{T}.

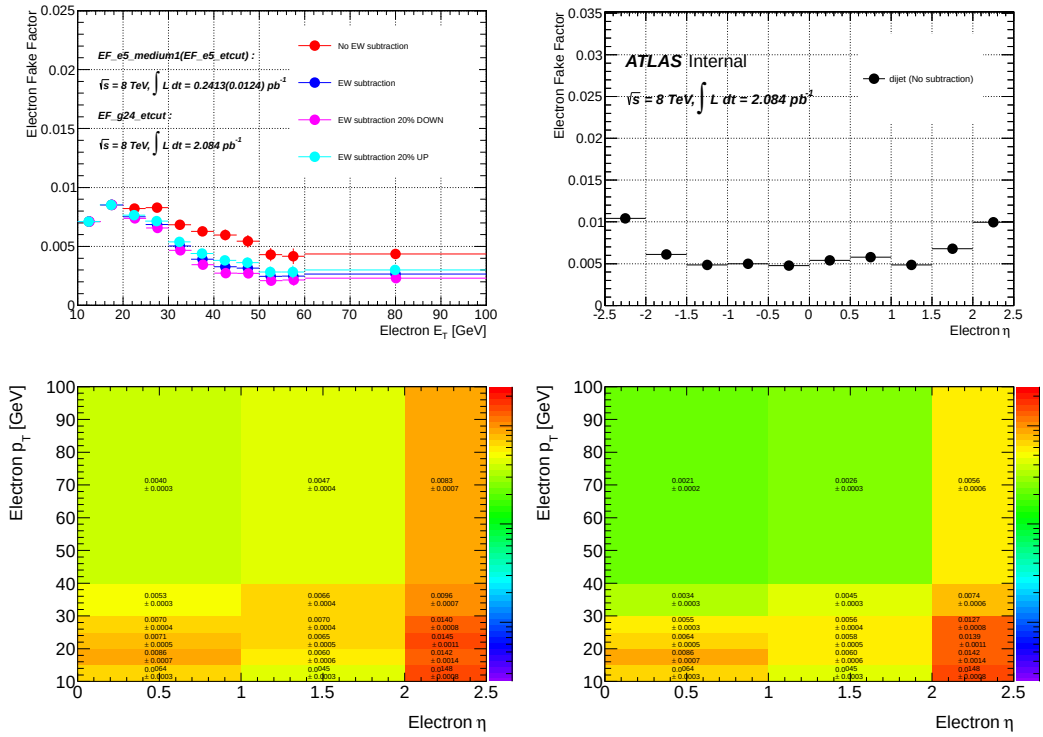

Figure B.2: The di-jets fake factor as a function of p_{T}(top left) and as a function of η (top right) in electron channel. The red points show the fake factor before the subtraction of the EW contamination in the di-jet data sample. The blue points show the fake factor after the subtraction and the change in fake factor by varying the amount of EW contamination by $\pm$ 20%. The top right plot shows the eta dependence before the subtraction of the EW contamination in the di-jet data sample. The bottom left and right plots show the 2-dimensional fake factor as functions of p_{T} and η before the subtraction of the EW contamination (left) and after the subtraction (right).

B.1.2 Muon Fake Factors

The fake factors are measured in data using a di-jet control sample. For muons, the di-jet control sample is collected with the Muon Combined Performance (MCP) supporting triggers:

- `EF_mu6` (0.941 pb^{-1}),
- `EF_mu15` (22.72 pb^{-1}),
- `EF_g24_etcut` (2.084 pb^{-1}),

where `EF_mu15` (`EF_mu6`) supporting trigger requires a reconstructed muon with transverse energy above 15 (6) GeV but makes no requirement on the muon impact parameters or

isolations, and where `EF_g24_etcut` supporting trigger requires a reconstructed EM cluster with transverse energy E_{T} above 24 GeV but makes no requirement on the presence of a muon. Due to their large trigger rates, the MCP supporting triggers are heavily pre-scaled but the available luminosity is normally larger than e/gamma supporting triggers.

The `EF_mu6` trigger is used below $p_{\mathrm{T}} = 15$ GeV and the `EF_mu15` is used above $p_{\mathrm{T}} = 15$ GeV. The fake factor calculation has been cross checked with the e/gamma supporting trigger, `EF_g24_etcut`. The following basic quality cuts are required: GRL, $E_{\mathrm{T}}^{\mathrm{miss}}$ cleaning, primary vertex quality cut, and LAr veto. The presence of muons from W or Z bosons in the di-jet sample will bias the calculation of the fake factor. To suppress this contamination, events used in the fake factor calculation are required to the followings:

- away side jet with $p_{\mathrm{T}} > 15$ GeV,
- $\Delta\phi$(muon, jet) > 0.7,

and events are vetoed if they satisfy the followings:

- m_{T}(muon, $E_{\mathrm{T}}^{\mathrm{miss}}$) > 30 GeV,
- $|M_Z - M_{\mu\mu}| < 13$ GeV,

where muons are either `id` or `anti-id`.

The remaining W and Z contributions referred to as 'EW contamination', are subtracted from the di-jet sample using simulation. This contribution has been validated by comparing the data/simulation agreement in the Z peak. This contribution has been validated by comparing the data/simulation agreement in the Z peak and high m_{T}. The di-jet p_{T} distributions for numerators and denominators with W and Z contaminations are shown in Figure B.3.

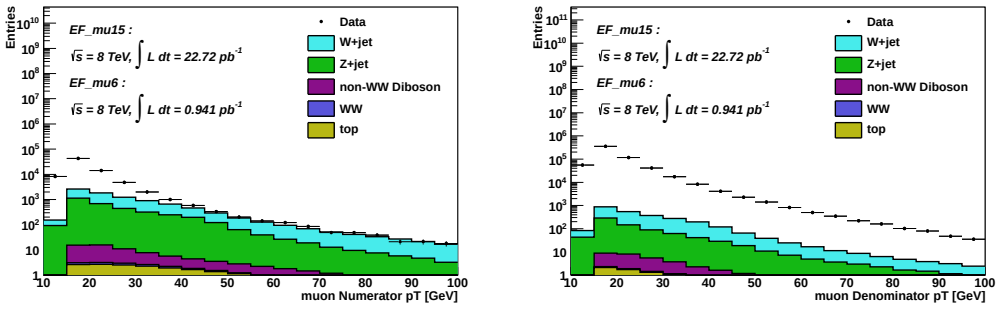

Figure B.3: Di-jet p_{T} distributions for muon numerators (left) and muon denominators (right) collected with MCP supporting triggers. W and Z contaminations are also illustrated but the contributions are negligibly small at the end of the selection.

To avoid a possible bias due to trigger threshold, the fake factors for 10-15 GeV muons have been calculated in a data set triggered by the `EF_mu6` trigger. Measured di-jets fake

factors for muons as a function of p_{T} and η (1D and 2D) are shown in Figure B.4. Note that the sutracted EW contamination is larger at higher p_{T} whereas it remains small at lower p_{T}.

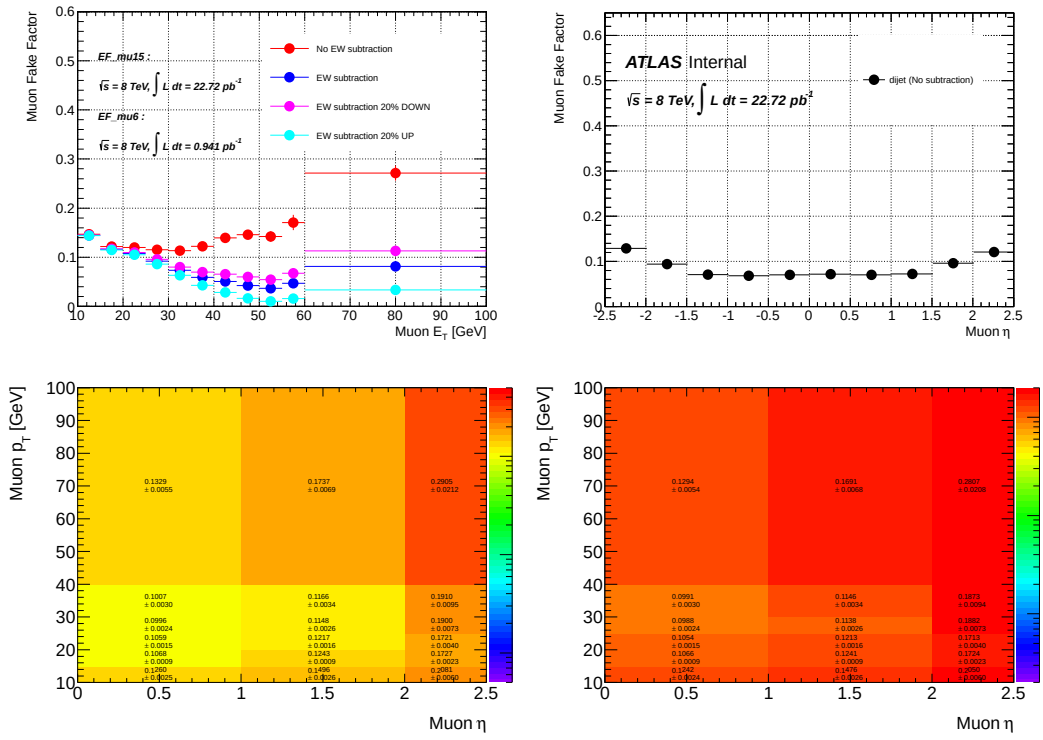

Figure B.4: The di-jets fake factor as a function of p_{T}(top left) and as a function of η (top right) in muon channel. The red points show the fake factor before the subtraction of the EW contamination in the di-jet data sample. The blue points show the fake factor after the subtraction and the change in fake factor by varying the amount of EW contamination by $\pm$ 20%. The top right plot shows the eta dependence before the subtraction of the EW contamination in the di-jet data sample. The bottom left and right plots show the 2-dimensional fake factor as functions of p_{T} and η before the subtraction of the EW contamination (left) and after the subtraction (right).

B.1.3 Systematics

Systematic uncertainty associated with the fake factor measurement is the dominant source of uncertainty on the W+jets /QCD background. The fake factor uncertainty is divided into the following sources:

- The difference in fake factor between the di-jet and W+jets samples. This is estimated by comparing the two fake factors: di-jets and W+jets fake factors in simulation. This

is the dominant systematic uncertainty on the fake factor.

- The effect of pileups on the fake factor due to different run conditions during data taking. This is estimated by studying the fake factor as a function of $< \mu >$ (Average number of interactions per bunch crossing).

- The uncertainty associated to the real lepton contamination from W/Z events in the di-jet samples. This is estimated by varying the W/Z subtraction in the di-jet samples.

These are each described in more detail below and final uncertainty on the di-jets fake factor is summarized in Table B.1 and B.2

Table B.1: Summary of the fake factor uncertainties in 15 - 20 GeV bin for electrons. The individual contributions are added in quadrature to obtain total uncertainty.

Source	Electron		
η range	$\lvert\eta\rvert < 1.0$	$1.0 < \lvert\eta\rvert < 2.0$	$2.0 < \lvert\eta\rvert < 2.47$
Fake Fator	0.0086	0.0060	0.0142
Sample Dependence	60.0%	60.0%	60.0%
Statistical Error	8.1%	10.0%	9.8%
Pile-Up Error	10.4%	4.4%	7.7%
EW-Contamination	2.4%	2.3%	0.8%
Total Uncertainty	61.4%	61.0%	61.3%

Table B.2: Summary of the fake factor uncertainties in 15 - 20 GeV bin for muons. The individual contributions are added in quadrature to obtain total uncertainty.

Source	Muon		
η range	$\lvert\eta\rvert < 1.0$	$1.0 < \lvert\eta\rvert < 2.0$	$2.0 < \lvert\eta\rvert < 2.5$
Fake Factor	0.102	0.119	0.163
Sample Dependence	40.0%	40.0%	40.0%
Statistical Error	0.8%	0.8%	1.3%
Pile-Up Error	10.3%	7.0%	5.4%
EW-Contamination	0.8%	0.8%	0.9%
Total Uncertainty	41.3%	40.6%	40.4%

B.1.3.1 Sample dependence

The fake factor is measured in the di-jet sample and is applied to the W+jets control sample ($N_{\text{id+anti-id}}$). Differences in jet kinematics and heavy flavor fraction may cause the

fake factor to be different in these two samples. A systematic uncertainty accounts for this sample dependence. This uncertainty is evaluated in simulation by comparing the two fake factors.

For electrons, W+jets background is dominated by light flavor (for instance, charged pion track overlapping with neutral pion cluster in EM calorimeter) and the contribution of heavy flavors is found to be small. The flavor composition is studied in detail, which is found in Section B.2. Figure B.5 shows the comparison of electron fake factors between the di-jet and W+jets in simulation, $(f_l^{\mathrm{di-jet}} - f_l^{\mathrm{W+jets}})/f_l^{\mathrm{di-jet}}$ as a function of E_{T}. The fractional difference from the two samples is found to be $\sim 60\%$.

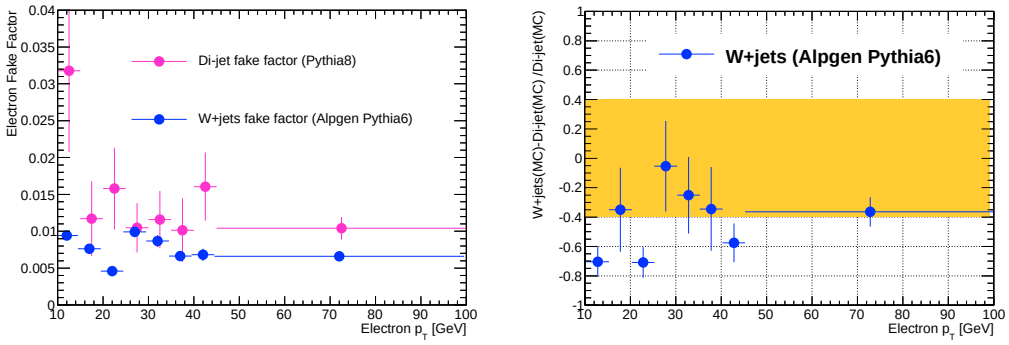

Figure B.5: Comparison of electron fake factors between the di-jets and W+jets samples (left). The fractional difference between the two fake factors (right). The overlaid yellow band is a 40 % uncertainty as a reference. A 60 % uncertainty is assigned in overall E_{T}.

For muon, W+jets background is dominated by heavy flavor (for instance, (semi-)leptonic decay of charm or bottom meson from W_c and W_{bb}/W_{cc} processes). The effect of light flavor is found to be smaller than that of heavy flavor, depending on p_{T} range. The flavor composition is studied in detail, which is found in Section B.2. Figure B.6 shows the comparison of muon fake factors between the di-jet and W+jets in simulation, $(f_l^{\mathrm{di-jet}} - f_l^{\mathrm{W+jets}})/f_l^{\mathrm{di-jet}}$ as a function of p_{T}. The fractional difference is found to be $\sim 40\%$.

B.1.3.2 Lepton contamination in di-jets sample

The di-jet sample enhances jets misidentified as leptons. However there is still real lepton contamination from W and Z bosons in the di-jet sample. The lepton contamination from W/Z events will bias the fake factor measurement. To reduce this bias, the EW veto is applied to the di-jet sample. The EW veto rejects 80-90 % of W/Z contamination, while retaining more than 90 % of the di-jet samples. It has been checked that the EW veto does not bias the fake factor.

The remaining W/Z contribution is subtracted from the observed data using simulation. The normalizations of the W/Z contributions are obtained from dedicated control samples

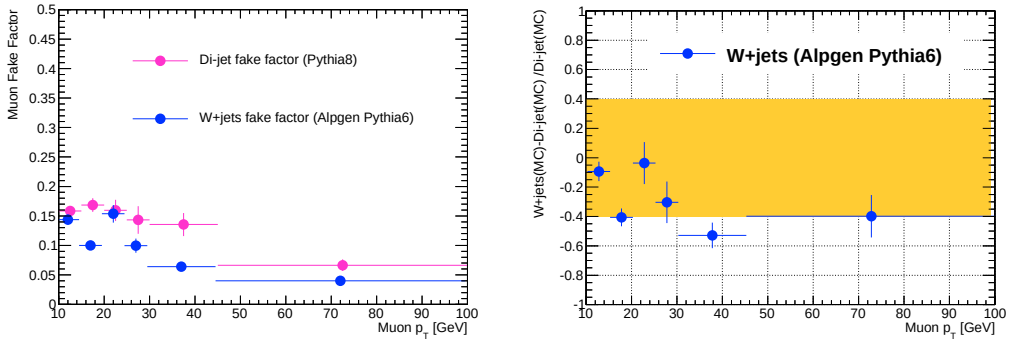

Figure B.6: Comparison of muon fake factors between the di-jets and W+jets samples (left). The fractional difference between the two fake factors (right). The overlaid yellow band is a 40 % uncertainty as a reference. A 40 % uncertainty is assigned in overall p_{T}.

that are defined as $|m_{ll} - m_Z| < 13$ GeV for Z bosons and as $m_T > 30$ GeV for W bosons. It is found that the evaluated normalization factors ($N_{data}/N_{simulation}$ per W/Z) are close to unity. Figure B.2 and B.4 show the estimated fake factor with/without the EW background subtraction. The uncertainty due to the level of residual EW background is evaluated by varying the normalization factors by ±20%. This uncertainty accounts for uncertainties associated with the W and Z cross sections, and the modeling of simulated leptons from W and Z bosons satisfying the denominator selection. The uncertainty is found to be negligible at lower p_{T}.

For electrons, the uncertainty for $E_{\mathrm{T}} < 20$ GeV cannot be evaluated due to the lack of simulation samples. The uncertainty is instead taken from the next p_{T} bin where higher EW contamination is expected. This approach is very conservative but the impact of this uncertainty is still negligibly small compared to the sample dependence.

B.1.3.3 Trigger bias

For electrons, the `etcut` triggers are used to select electron denominators, and the `medium1` triggers are used to select fully identified electrons. The `etcut` triggers are highly prescaled, but are expected to be no bias from the triggers since only E_{T} cut is applied to the reconstructed EM cluster. The fully identified electron selection is normally tigher than `medium1` but the bias remains in $E_{\mathrm{T}} < 25$ GeV where Very Tight LH identification is used. The bias is evaluated by adding the cut-based Medium++ to the Very Tight LH identification, and it is found that the bias is at most $\sim$ -5 % (see Section 4.5.1). This is a negligible bias comapred to the sample dependence uncertainty (40-60 %). The uncertainty is thus not included in the fake factor systematics.

For muons, the `EF_mu6` and `EF_mu15` triggers are used to measure the fake factor. Since they do not make any requirements on the impact parameters or isolations, they are unbiased with respect to both muon numerator and denominator definitions. The trigger bias

on the muon fake factor is thus expected to be negligible, and is not included in the fake factor systematics.

B.1.3.4 Pileup uncertainty

The systematic due to variations in the fake factor from differing levels of pileup is investigated by calculating the fake factor in a high pileup and low pileup di-jet samples. The di-jet sample has been divided into two subsets based on $< \mu >$ (average number of interactions per crossing). If the number of interactions is above (below) twenty, the event is classified as the high (low) pileup sample. The results are shown in Figures B.7. As expected, the fake factors decrease with increased pileups. This is primarily due to the increase in isolation energy from the higher event activity in the high pileup events. The level of systematic uncertainty is at most 10 % depending on p_{T} and η.

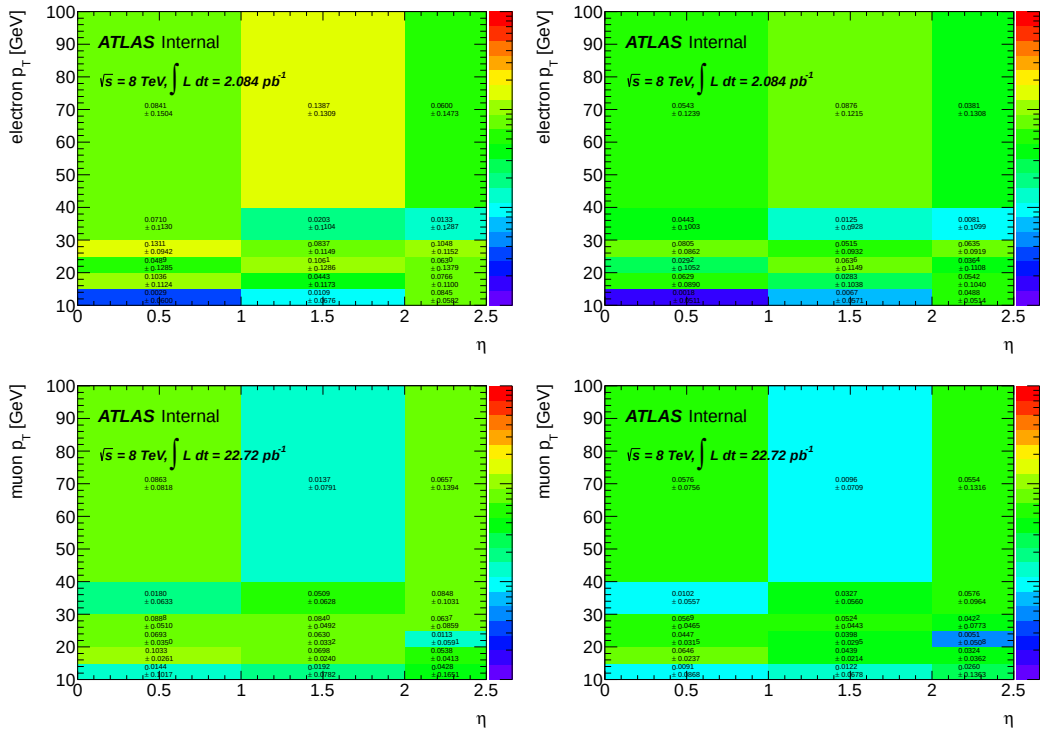

Figure B.7: Pileup dependence (relative) uncertainty on the di-jets fake factor for electrons (top) and for muons (bottom). The fake factor is measured in data with high pileup (left) and low pileup (right).

B.1.4 Z+jet vs Di-jet Fake Factors

Comparisons of the Z+jets and the di-jets fake factors in both data and simulation are made to see the compatibility between the fake factors, and to obtain the p_{T} threshold on the Z+jets fake factor. As discussed above, the Z+jet fake factor has shown its better performance than the di-jet fake factor in terms of sample dependence systematic uncertainty. Nevertheless it is not obvious that the Z+jets fake factor is still better at higher p_{T} region where larger statistical uncertainty and EW uncertainty are expected. Considering two points below, the p_{T} threshold on the Z+jets fake factor is determined:

1. size of total systematic uncertainty,

2. reliability and compatibility,

B.1.4.1 Comparison of systematic uncertainties

The systematic uncertainties on the Z+jets fake factor is compared to the uncertainty on the di-jets fake factor. Table B.3 and B.4 show the comparison of the total and individual systematic uncertainties.

Table B.3: Comparison of systematic uncertainty on the di-jet and Z+jets fake factor in electron channel.

stat. $\pm$ *EW* syst. $\pm$ sample dependence (total) %	di-jet	Z+jets
$10 < p_T < 15$	2.9 $\pm$ 1.9 $\pm$ 60.0 (60.1) %	17.6 $\pm$ 10.5 $\pm$ 20.0 (28.6) %
$15 < p_T < 20$	5.0 $\pm$ 1.9 $\pm$ 60.0 (60.1) %	34.0 $\pm$ 19.2 $\pm$ 20.0 (43.8) %
$20 < p_T < 25$	3.9 $\pm$ 1.9 $\pm$ 60.0 (60.1) %	52.1 $\pm$ 24.8 $\pm$ 20.0 (61.1) %
$p_T > 25$	3.6 $\pm$ 4.2 $\pm$ 60.0 (60.1) %	29.6 $\pm$ 23.1 $\pm$ 20.0 (42.5) %

Table B.4: Comparison of systematic uncertainty on the di-jet and Z+jets fake factor in muon channel.

stat. $\pm$ *EW* syst. $\pm$ sample dependence (total) %	di-jet	Z+jets
$10 < p_T < 15$	1.1 $\pm$ 1.8 $\pm$ 40.0 (40.1) %	10.2 $\pm$ 2.6 $\pm$ 20.0 (22.6) %
$15 < p_T < 20$	0.5 $\pm$ 1.8 $\pm$ 40.0 (40.1) %	17.9 $\pm$ 5.1 $\pm$ 20.0 (27.3) %
$20 < p_T < 25$	0.9 $\pm$ 1.8 $\pm$ 40.0 (40.1) %	28.6 $\pm$ 8.9 $\pm$ 20.0 (36.0) %
$p_T > 25$	1.6 $\pm$ 4.2 $\pm$ 40.0 (40.2) %	34.1 $\pm$ 21.0 $\pm$ 20.0 (44.8) %

For electrons, the total systematic uncertainty on the Z+jets is smaller than the uncertainty on the di-jets in overall p_{T} range, assuming 20 % sample dependene as shown in Figure 6.7. For muons, the total systematic uncertainty on the Z+jets is smaller than the uncertainty on the di-jets in $p_T < 25$ GeV, while they are compatible in $p_{\mathrm{T}} > 25$ GeV, assuming 20 % sample dependence as shown in Figure 6.8.

B.1.4.2 Compatibility of fake factors

The Z+jets and di-jets fake factors are compared using both data and simulation. Figure B.8 shows the comparison of the Z+jets and di-jets fake factors in data and simulation. It is found that the Z+jets fake factor is compatible with di-jet fake factor in data, whereas they are not in simulation, even though they are not expected to be compatible due to sample dependence.

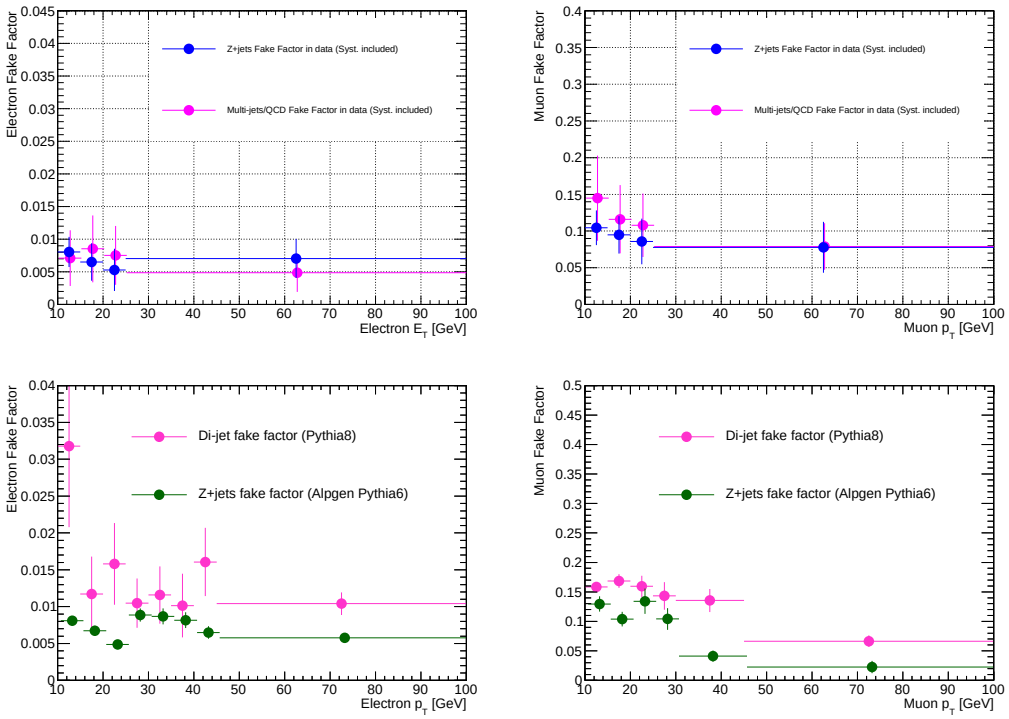

Figure B.8: Comparison of Z+jets fake factor and di-jet fake factor for electrons (left) and muons (right) in data (top) and simulation (bottom). Data fake factors include both statistical uncertainty and systematic uncertainty, while simulated fake factors include only statistical uncertainty in simulation. Alpgen+Pythia6 generator is used for Z+jets simulation, and `Pythia8` (or `mu-filtered Pythia8`) is used for di-jets simulation.

Figure B.9 shows the comparison of data and simulated fake factors in Z+jets and di-jets samples.

In overall the agreement on data/simulation looks better in the Z+jets fake factor. The Z+jets fake factor in data is consistent with that in simulation, while the di-jets fake factor does not well. This is probably due to the fact that the parton shower modeling in di-jets simulation (`Pythia8`) is imperfect, while the parton shower modeling is better in Z+jets

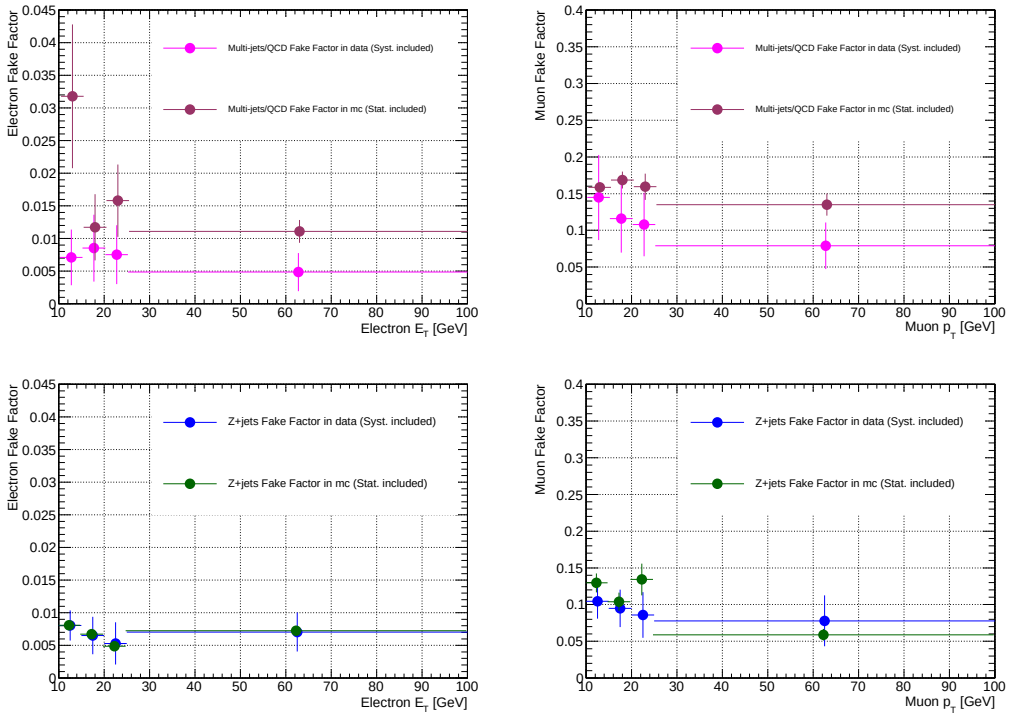

Figure B.9: The comparison of data and simulated fake factors in di-jets (top) and Z+jets (bottom) samples. Data fake factors include both statistical uncertainty and systematic uncertainty, while simulated fake factors include only statistical uncertainty in simulation. Alpgen+Pythia6 generator is used for Z+jets simulation, and `Pythia8` (or `mu-filtered Pythia8`) is used for di-jets simulation.

simulation (`Pythia6`). [1]

In summary, Z+jets fake factor is feasible and is better for the analysis, even at higher p_{T} range when all p_{T} bins above 25 GeV are merged. The Z+jets fake factor is therefore used in overall p_{T} range with 4 bins (10-15, 15-20, 20-25, 25- GeV).

[1] Unfortunately no other di-jet simulation sample available for now.

B.2 OS/SS Asymmetry and Flavor Composition

Motivated by the difference between the OS W+jets fake factor and SS W+jets fake factor, flavor composition studies are performed based on MC to understand behaviors in fake factors. Not only the difference between the OS W+jets and the SS W+jets, the flavor compostion also explains any differences in fake factors among samples such as the di-jet, the Z+jets, OS W+jets, and SS W+jets. In this section, OS/SS asymmetry is introduced first, the flavor composition for each sample is then shown.

B.2.1 OS/SS Asymmetry

It is well known the fact that there is a charge asymmetry in W+jets production in pp collision. This is because a u-quark tends to be in the initial state rather than a d-quark. However the OS/SS asymmetry is not exactly the same as the charge asymmetry. Figure B.10 shows typical tree level diagram in W+jets production.

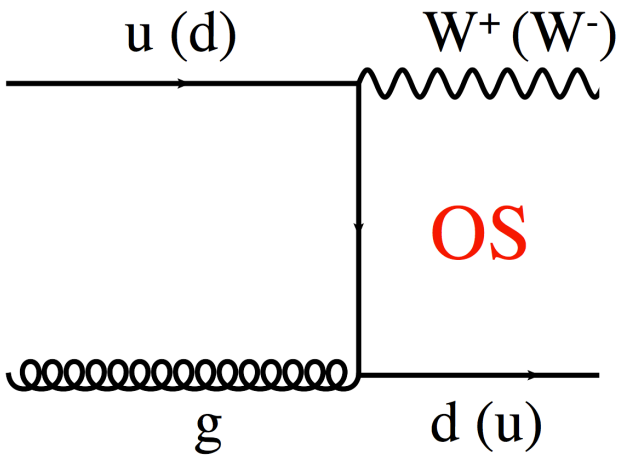

Figure B.10: Tree level diagram for $qg \to Wq'$ production.

In this diagram, the W+jet tends to be opposite sign (OS) regardless of the initial state quark in ME level. The W^+ is always produced in association with d-quark ($ug \to W^+d$), whereas the W^- is always produced in association with u-quark ($dg \to W^-u$) in the context of first generation. Similary the W+charm ($sg \to Wc$ and $sg \to Wcg$) goes in OS even if it associates with final state gluon. On the other hand, the $W + b\bar{b}$ can equally go into OS and SS because b-quark (or $\bar{b}$-quark) always comes from gluon splitting. Figure B.11 shows typical tree level diagrams in W+charm and $W + b\bar{b}$ productions.

Extending the discussion above to the analysis, the situation will be more complicated since quarks can be observed as jets. The situation will be much more complicated when considering reconstructed fake leptons (`id` or `anti-id` leptons) since it is not obvious whether or not these leptons can keep track of the final state quark charge, namely jet charge. A

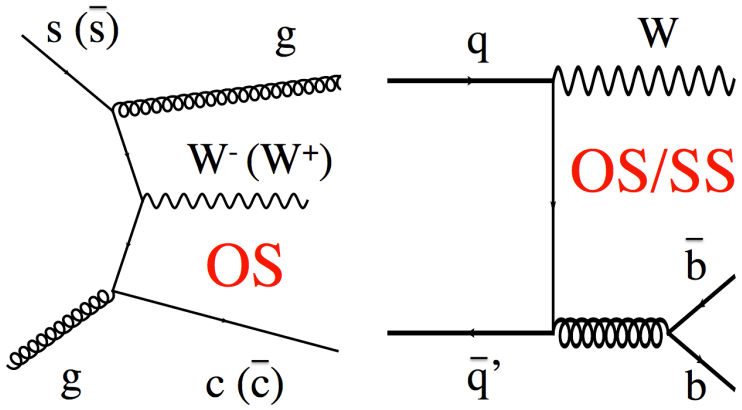

Figure B.11: Tree level diagram for $qg \to Wq'$ production. Tree level diagram for $q\bar{q} \to W + g(\to b\bar{b})$ production.

quark charge flip (for instance, OS $\to$ SS or vice versa) can happen when the quark goes into fake lepton. In addition the probability of the charge flip strongly depends on the tightness of lepton selection. It is therefore essential to understand the feature of quark charge flip when the OS/SS asymmetry in the W+jets production is considered.

B.2.2 Flavor Composition in W+charm Production

A simple test is made to learn the OS/SS asymmetry using W+charm samples (Alpgen+Pythia6 $WcNp0 - WcNp4$). All tree level diagrams (ME level) included in the W+charm samples are found in [155]. The W+charm process should tend to be OS unless there are charge flipped quarks or quarks from gluon splitting. Figure B.12 shows p_{T} distributions for `anti-id` leptons splitting into OS and SS. In muon channel, the OS/SS asymmetry can be seen as the asymmetry in normalization, meaning that the normalization in OS is about 10 times higher than that in SS. The `anti-id` muons in OS are mostly from leptonic decay of charm mesons, whereas the `anti-id` muons in SS are mostly from gluon splitting in which the OS/SS ratio is expected to be unity. On the other hand, most of the `anti-id` electrons are from gluon splitting, as a result, the asymmetry is less clear compared to muon case. The difference between the `anti-id` muon and `anti-id` electron is explained by the fact that the tightness of lepton selection is quite different between them. In fact the definition of the `anti-id` electron is looser than that of the `anti-id` muon, so that the `anti-id` electrons tend to be more "real" jets (or fragments of jets) rather than "real" leptons.

B.2.3 Flavor Composition in $W + b\bar{b}$ Production

Another simple test is made to learn the case that the OS/SS is symmetric using $W + b\bar{b}$ samples (Alpgen+Pythia6 $WbbNp0 - WbbNp3$). All tree level diagrams (ME level) included in the $W + b\bar{b}$ samples are found in [155]. The $W + b\bar{b}$ process should tend to be symmetric in OS and SS as far as the b-quarks from the gluon splitting go into fake leptons. Figure B.13 shows p_{T} distributions for `anti-id` leptons splitting into OS and SS. In muon channel, most of the `anti-id` muons are from leptonic decay of b-mesons which makes the composition symmetric between OS and SS within stat uncertainty. On the contrary there is an asymmetry from light flavor component such as those charged kaon and charged pion in electron channel. The asymmetry is from the process shown in Figure B.10 in association with an additional final state gluon ($ug \to Wd + g(\to b\bar{b})$).

From the simple tests above, it is worthwhile summarizing several things:

- SS events are always produced by either gluon splitting or quark charge flip,
- `anti-id` muons are mostly from leptonic decay of heavy flavor mesons if heavy flavor mesons exist in event,
- `anti-id` electrons are mostly from a fragment of gluon or quark jet rather than leptonic decay of heavy flavor mesons in event,
- the difference between electrons and muons is related to the tightness of the lepton selection,
- the OS/SS asymmetry is caused by not only W+charm, but also light flavors (charged pions and kaons) that is clearly shown in electrons.

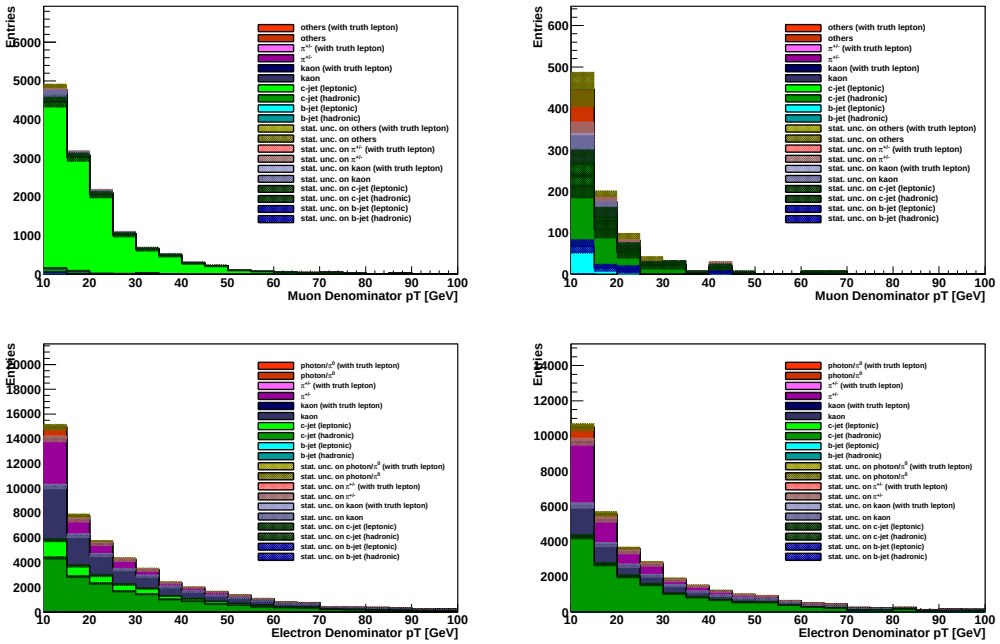

Figure B.12: Flavor composition as a function of `anti-id` lepton p_{T} in W+charm process (Alpgen+Pythia6). The top left is for `anti-id` muon in OS and the top right is for `anti-id` muon in SS. The OS composition is dominated by leptonic decay of charm mesons, whereas the SS composition is dominated by a fragment of gluon splitting. The bottom left is for `anti-id` electron in OS and the bottom right is for `anti-id` electron in SS. Both the OS and SS compositions are dominated by a fragment of gluon splitting or non-leptonic decay of charm mesons. The leptonic decay event is defined as the event that has a truth lepton around heavy flavor quark/meson/baryon. Otherwise, the event is classified as hadronic decay.

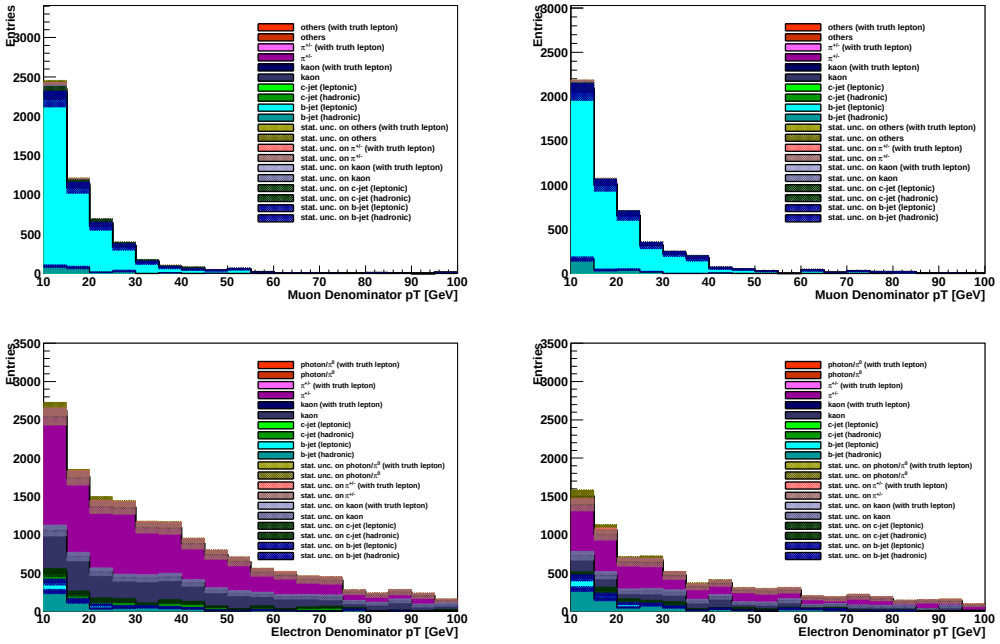

Figure B.13: Flavor composition as a function of `anti-id` lepton p_{T} in $W + b\bar{b}$ process (Alpgen+Pythia6). The top left is for `anti-id` muon in OS and the top right is for `anti-id` muon in SS. THe `anti-id` muons are dominated by leptonic decay of b-mesons in both OS and SS. The contribution of the b-mesons is quite symmteric between the OS and SS. The bottom left is for `anti-id` electron in OS and the bottom right is for `anti-id` electron in SS. Both OS and SS are dominated by a fragment of final state u/d quark or gluon. The OS/SS asymmetry in the light flavors is caused by $gq \to Wq' + g(\to b\bar{b})$ diagram. The leptonic decay event is defined as the event that has a truth lepton around heavy flavor quark/meson/baryon. Otherwise, the event is classified as hadronic decay.

B.2.4 Flavor Composition in Inclusive W+jets Production

B.2.4.1 Flavor composition in electron channel

Figure B.16 shows comparison of flavor composition between OS and SS in W+jets sample. The light flavors (pions and kaons) are dominant components for both OS and SS in the denominator sample. The contribution from leptonic decay of c-mesons is also not negligible ($\sim$ 30 %) in the OS numerator sample due to the W+charm production that induces a part of the OS/SS asymmetry. Furthermore, the OS/SS asymmetry also arises from light flavors (charged pions and kaons) due to the main W+jets diagram ($qg \to Wq'$) shown in Figure B.10. While the contribution from leptonic decay of b-mesons and neutral pions ($\pi^0 \to \gamma\gamma$) , referred to as 'neutral components', is symmetric between OS and SS. In other words, the "relative" contribution from the neutral components is larger in SS.

The fake factors for each component are also shown in Figure B.14, where a large hierarchy from the quark type can be seen. The largest fake factor comes from the leptonic decay of b-mesons, and the light flavor fake factors tends to be smaller. Moreover it is found that the fake factors for each component are identical regardless of fake lepton charge, which means that any differences in inclusive fake factors (for instance, OS W+jets versus SS W+jets) can be fully explained by the differences in flavor composition. The number of denominators and numerators in OS and SS are found in Table B.5. The relatively larger contribution from the neutral components leads to larger SS W+jets fake factor.

Figure B.17 shows comparison of flavor composition between the OS W+jets and Z+jets sample. The light flavor compositions in the Z+jets sample are similar to those in the OS W+jets sample. The difference between the two samples is the composition in heavy flavor. A larger charm contribution can be seen in the OS W+jets composition because of W+charm process, whereas a larger bottom contribution can be seen in the Z+jet composition. As a result, total heavy flavor contribution (b-mesons and c-mesons) in the Z+jets sample is similar to that in the OS W+jets, which makes the Z+jets fake factor close to the OS W+jets fake factor. The similar light flavor/heavy flavor ratio between the two samples implies that the flavor compositions in both samples are dominated by the main diagram ($qg \to Wg'$ or $qg \to Zq$) shown in Figure B.10.

Table B.5: Number of denominators and numerators for each component in electron channel.

OS	c-quarks	b-quarks	charged pions	neutral pions	kaons	total
N_{den}	12689±193	390±47	661085±1239	67080±695	287728±776	1028972±1630
N_{num}	1147±60	318±38	3097±92	2112±120	783±46	7457±173
Fake Factor	0.09±0.004	0.81±0.13	0.0046±0.0002	0.031±0.002	0.0027±0.0002	0.0072±0.0002
SS	c-quarks	b-quarks	charged pions	neutral pions	kaons	total
N_{den}	1188±69	433±50	297028±895	67069±696	119766±521	485484±1250
N_{num}	148±27	289±41	1576±72	2250±126	379±36	4642±157
Fake Factor	0.12±0.03	0.66±0.13	0.0053±0.0003	0.033±0.002	0.0031±0.0003	0.0095±0.0003

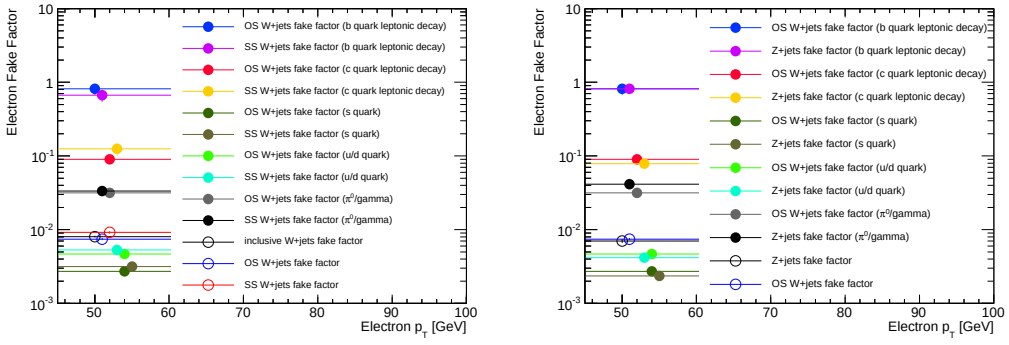

Figure B.14: Comparison of electron fake factors for each component (Alpgen+Pythia6). The left plot is the comparison of OS W+jets fake factor and SS W+jets fake factor in each component. The right plot is the comparison of OS W+jets fake factor and Z+jets fake factor in each component. There is a large hierarchy in fake factor from quark types (in order of b-quark > c-quark > light-quark). The fake factors are identical in each component regardless of fake lepton charge. The inclusive fake factor is close to the light flavor fake factor since the inclusive sample is dominated by light flavors. The larger b-quark fake factor and nueutral pion fake factor lead to larger SS fake factor at the end.

B.2.4.2 Flavor composition in muon channel

Figure B.18 shows comparison of flavor composition between OS and SS in W+jets sample. Regardless of charge, the heavy flavors (charm and bottom) are dominant components in both the denominator and numerator samples except for the lowest p_{T} bin. The light flavors are also enhanced in the numerator sample due to d_0 impact parameter and track isolation requirements that are not required for the denominator sample but are required for the numerator sample. Particularly the d_0 impact parameter is sensitive to the heavy flavors as discussed in Section 4.6.2. Similarly to the electron case, the OS/SS asymmetry arises from leptonic decay of c-mesons in W+charm process as well as light flavors. On the other hand the contribution from leptonic decay of b-mesons and "others"(muons from calorimeter including pion decay in-flight) is symmetric between OS and SS in normalization. In other words, the "relative" contribution from the neutral components is larger in SS.

The fake factors for each component are also shown in Figure B.15, where a large hierarchy from the quark type can be seen. The largest fake factor is from the light flavors and the fake factors from the leptonic decay of heavy flavor mesons are smaller. Moreover the fake factors for each component are roughly consistent between OS and SS (and between OS W+jets and Z+jets). So the similar discussion to the electron case can be applied to the muon case. The number of denominators and numerators in OS and SS are found in Table B.6. From Table B.6 it is found that OS fake factor is smaller than SS fake factor because of the higher charm fraction in OS, which has a lower fake factor than all the others.

Figure B.19 shows comparison of flavor composition between the OS W+jets and Z+jets

sample. The light flavor compositions in the Z+jets sample are similar to those in the OS W+jets sample. The difference between the two samples is mainly from the composition in heavy flavor. A larger charm contribution can be seen in the OS W+jets because of the W+charm process, whereas a larger bottom contribution can be seen in the Z+jet sample. As a result, total heavy flavor contribution in the Z+jets sample is also similar to that in the OS W+jets, which makes the Z+jets fake factor close to the OS W+jets fake factor.

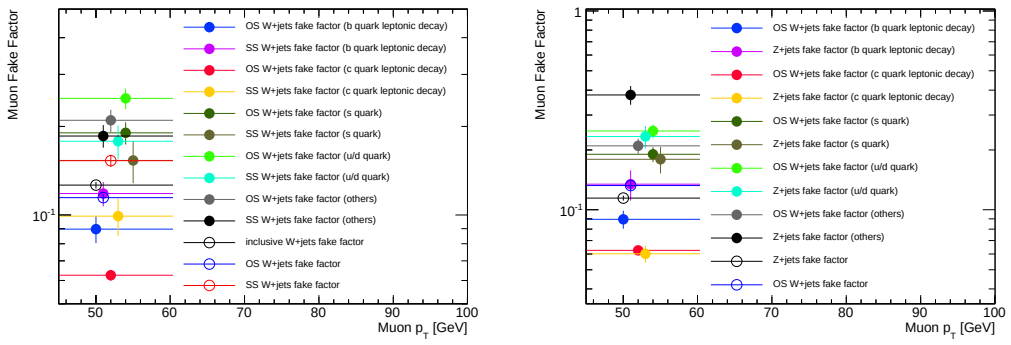

Figure B.15: Comparison of muon fake factors for each component (Alpgen+Pythia6). The left plot is the comparison of OS W+jets fake factor and SS W+jets fake factor in each component. The right plot is the comparison of OS W+jets fake factor and Z+jets fake factor in each component. There is a large hierarchy in fake factor from quark types (in order of light-quark > b-quark > c-quark). The fake factors are mostly identical in each component regardless of fake lepton charge. The inclusive fake factor is close to the fake factor in heavy flavor since the inclusive sample is dominated by heavy flavors. The larger fraction of c-quark in OS which has smaller fake factor than any other components, leads to SS fake factor higher than OS fake factor.

Table B.6: Number of denominators and numerators for each component in muon channel.

OS	c-quarks	b-quarks	charged pions	kaons	others	total
N_{den}	29859±298	6067±181	4118±136	3056±95	5661±200	48761±434
N_{num}	1866±75	544±54	1024±74	580±46	1186±93	5200±157
Fake Factor	0.06±0.01	0.09±0.01	0.25±0.02	0.19±0.02	0.20±0.02	0.107±0.004
SS	c-quarks	b-quarks	charged pions	kaons	others	total
N_{den}	2420±95	6314±186	2345±106	1510±75	5949±209	18538±322
N_{num}	240±33	747±67	417±51	231±36	1104±89	2739±131
Fake Factor	0.10±0.02	0.11±0.01	0.18±0.03	0.15±0.02	0.19±0.02	0.147±0.008

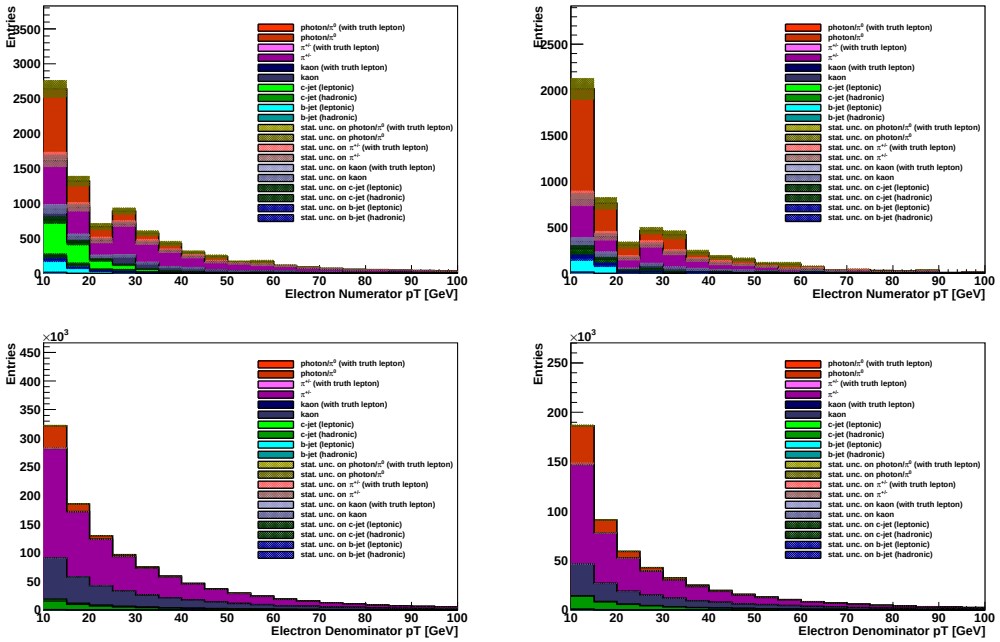

Figure B.16: Comparison of flavor composition between OS and SS in W+jet sample (Alpgen+Pythia6). The top left is for `id` electron in OS and the top right is for `id` electron in SS. The bottom left is for `anti-id` electron in OS and the bottom right is for `anti-id` electron in SS. The `anti-id` is dominated by light flavor components in both OS and SS. The OS/SS asymmetry can be seen in leptonic decay of c-mesons, charged pion, and kaon components whereas leptonic decay of b-mesons and neutral pion components are symmetric between OS and SS in normalization. Neverthless a relative contribution of the b-mesons and the neutral pions is higher in SS which makes SS fake factor higher than OS fake factor.

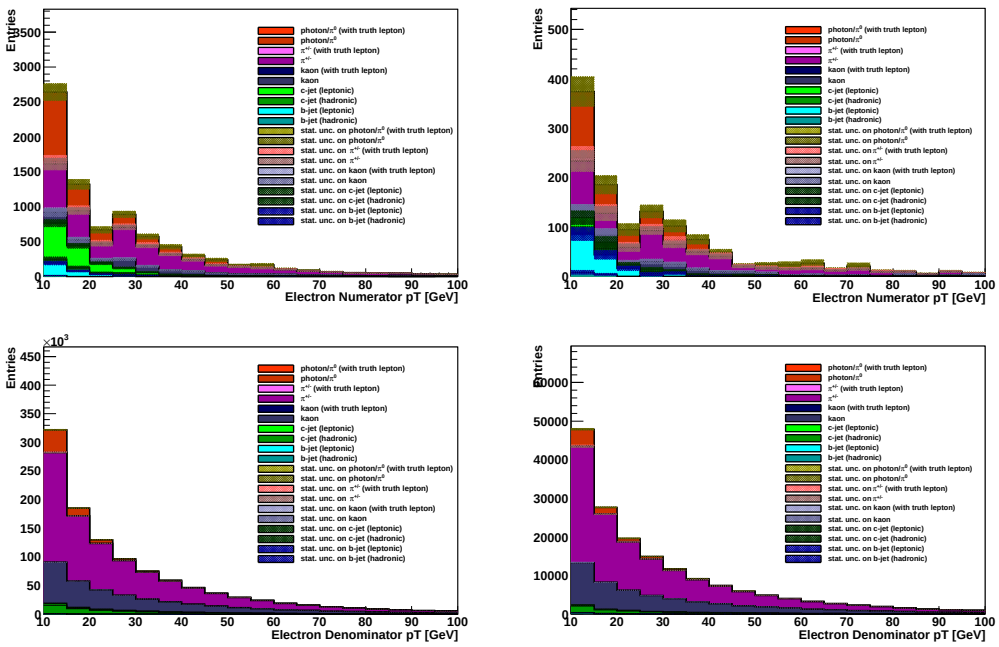

Figure B.17: Comparison of flavor composition between OS W+jets sample and Z+jets sample (Alpgen+Pythia6). The top left is for `id` electron in OS W+jets and the top right is for `id` electron in Z+jets sample. The bottom left is for `anti-id` electron in OS W+jets sample and the bottom right is for `anti-id` electron in Z+jets sample. The fraction of light flavor components (pions and kaons) in Z+jets sample is similar to that in OS W+jets sample. A larger charm contribution is seen in OS W+jets because of the W+charm process whereas a larger bottom contribution is seen in Z+jet sample due to the fact that the electron PID strongly enhances the b-quark composition.

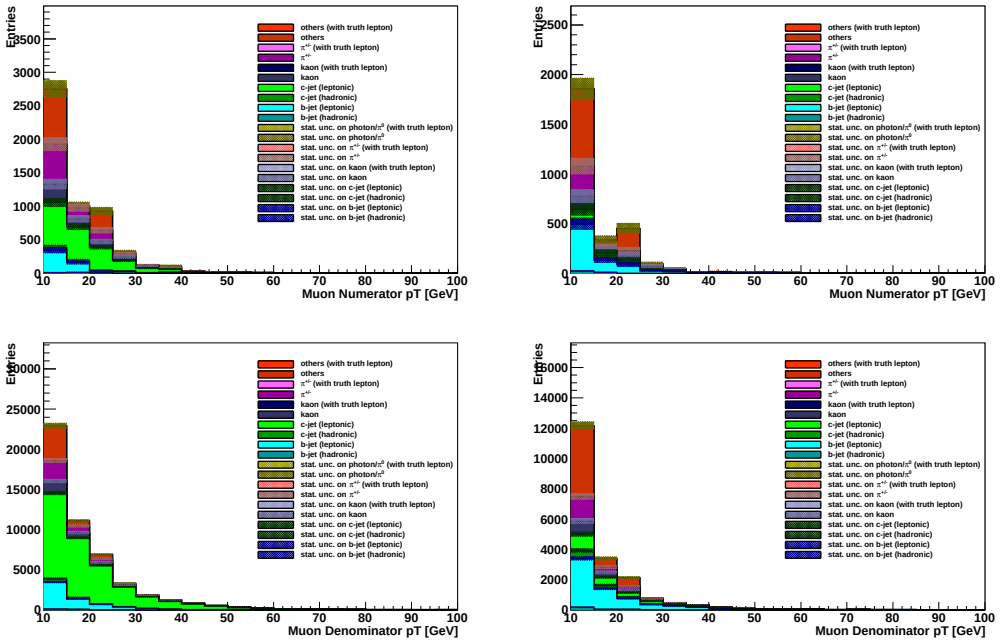

Figure B.18: Comparison of flavor composition between OS and SS in W+jet sample (Alpgen+Pythia6). The top left is for `id` muon in OS and the top right is for `id` muon in SS. The bottom left is for `anti-id` muon in OS and the bottom right is for `anti-id` muon in SS. The `anti-id` is dominated by heavy flavor components in both OS and SS except for the lowest p_T bin. The OS/SS asymmetry can be seen in leptonic decay of c-mesons, charged pion, and kaon components whereas leptonic decay of b-mesons and others components are symmetric between OS and SS in normalization. Neverthless a relative contribution of the b-mesons and others is higher in SS which makes SS fake factor higher than OS fake factor.

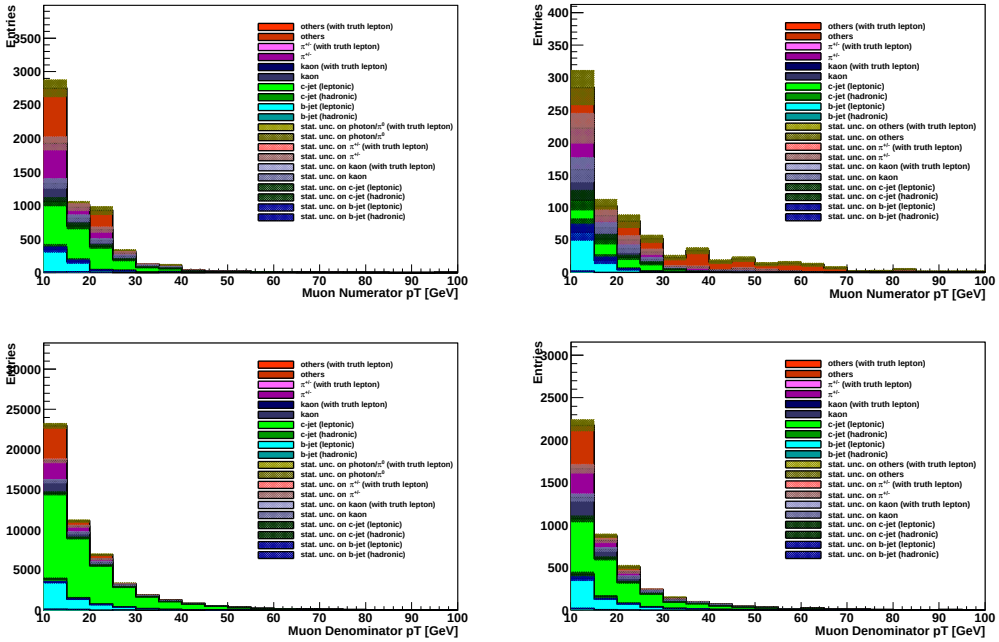

Figure B.19: Comparison of flavor composition between OS W+jets sample and Z+jets sample (Alpgen+Pythia6). The top left is for `id` muon in OS W+jets and the top right is for `id` muon in Z+jets sample. The bottom left is for `anti-id` muon in OS W+jets sample and the bottom right is for `anti-id` muon in Z+jets sample. The fraction of non-heavy flavor components (pions and kaons) in Z+jets sample is similar to that in OS W+jets sample. A larger charm contribution is seen in OS W+jets because of the W+charm process whereas a larger bottom contribution is seen in Z+jet sample.

B.3 W+jets Shape Modeling

It is not obvious that the data-driven W+jets background defined as events that have one `id` lepton and one `anti-id` lepton scaled by the dedicated fake factor, can model kinematic shapes of the W+jets background correctly. To validate the shapes of the data-driven W+jet background, comparisons of the kinematic distributions are made using the W+jets simulation.

Figures B.20 and B.21 show the comparisons of the kinematic distributions where black dots are the W+jets prediction in simulation and red dots are the data-driven W+jets prediction. Since the statistics of the W+jets simulation are quite limited due to its very large cross section, some high cross section weight events with large statistical uncertainty can be seen in simulation, while the data-driven prediction has sufficient statistics. This is one of the reasons why the data-driven method is preferred for the W+jets prediction. In overall, the kinematic shapes of the data-driven W+jets prediction look reasonable.

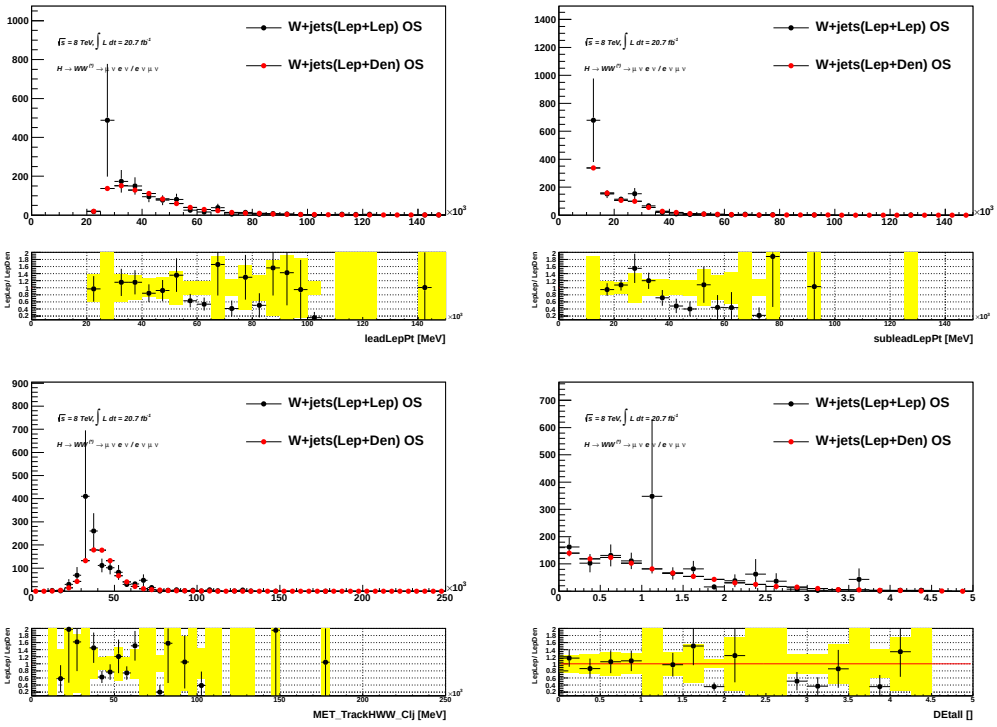

Figure B.20: Comparison of the data-driven W+jets and W+jets simulation in kinematic shapes for $e\mu$+μe channel. Alpgen+Pythia6 sample is used for the W+jets simulation, and data-driven W+jets control sample is scaled by the dedicated Z+jets fake factor.

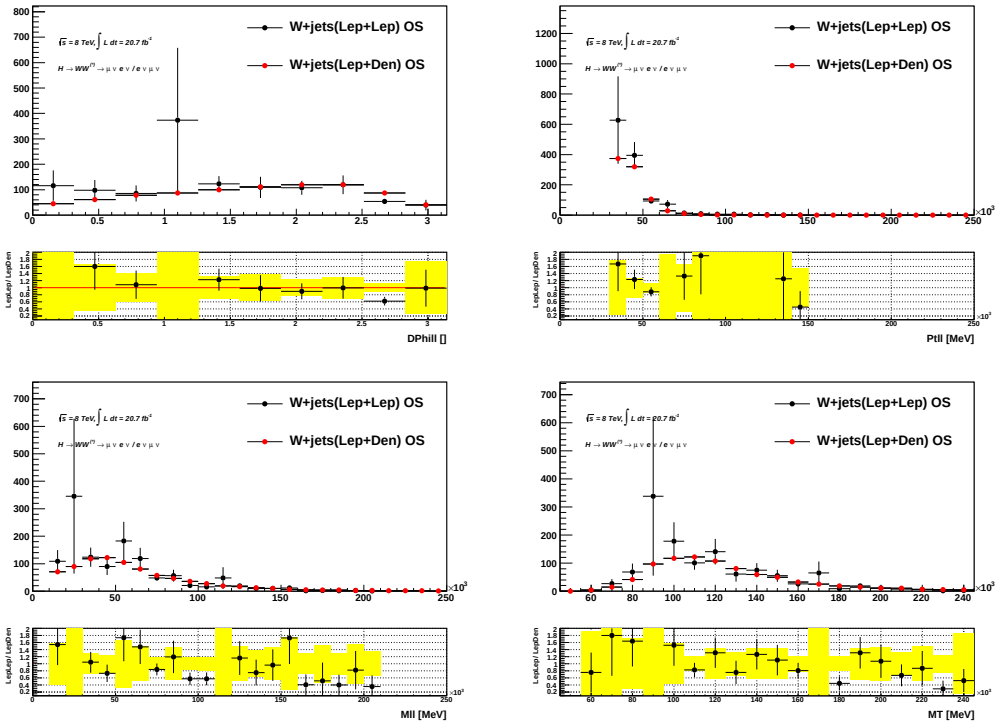

Figure B.21: Comparison of the data-driven W+jets and W+jets simulation in kinematic shapes for $e\mu$+μe channel. Alpgen+Pythia6 sample is used for the W+jets simulation, and data-driven W+jets control sample is scaled by the dedicated Z+jets fake factor.

B.4 Triggered Fake Correction

There exists a small bias on the W+jets control sample with the current definition of `anti-id` leptons (see Section 6.3.1 and 6.3.2). This is because the `anti-id` electron is orthogonal to the trigger selection due to `medium1`, and because the trigger selection is not a superset of the `anti-id` muon due to different isolation requirements. To correct for the bias, triggered `anti-id` lepton (triggered denominator) that can pass trigger selection is additionally and exclusively defined. Events that contain one triggered `anti-id` lepton and one `id` lepton are then added to the W+jets control sample. The contribution from the triggered W+jets background is ∼10 % in overall, and it is dependent on the signal region. The definition of the triggered anti-id leptons (triggered denominator) are summarized below.

B.4.1 Triggered Anti-id Electron Definition

In the standard analysis, the following triggers are used in electron channel: `EF_e24vhi_medium1`, `EF_e60_medium1`, `EF_2e12Tvh_loose1`, and `EF_e12Tvh_medium1_mu8`, where "`medium1`" is compatible with isEM Medium++ and "`i`" indicates track isolation, Ptcone20/$p_{\mathrm{T}} < 0.10$. Nevertheless (non-triggered) `anti-id` electron defined in Table 6.2 cannot pass the trigger selection due to the requirement of isEM Medium++ veto (and looser track isolation) in the `anti-id` electron. To correct for this bias, triggered `anti-id` electron is defined by requiring isEM Medium++ and by loosening other cuts as shown in Table B.7.

Table B.7: Definition of the triggered `anti-id` electron (triggered electron denominator).

Triggered Anti-id Electron
Author 1 or 3
$p_{\mathrm{T}} > 15$ GeV
$\lvert\eta\rvert < 2.47$, excluded crack region ($1.37 < \lvert\eta\rvert < 1.52$)
$\lvert z_0 \sin\theta\rvert < 1.2$ mm, $d_0/\sigma(d_0) < 9$
$N_{hits}^{SCT} + N_{hits}^{Pixel} \geq 4$
isEM Medium++
Ptcone and Etcone cuts Removed
Fails the identified electron

Isolation cuts are removed from the triggered `anti-id` electrons to make the definition as loosened as possible. Otherwise the EW contamination is too large to define the W+jets control sample (W+triggered `anti-id` sample). The bias therefore still remains on the W+jets control sample due to the trigger isolation. To avoid the trigger isolation bias on the W+jets control sample, events that pass only dilepton triggers to which trigger isolation is not imposed are used to collect the W+jets control sample (W+triggered `anti-id` sample).

The remaining bias from inefficiency of the di-leton triggers (ORing single/dilepton versus only dilepton trigger) is expected to be negligible, at most < a few % that is simply

computed as "0.10 (triggered `anti-id` contribution in total) × 0.20 (inefficiency of the dilepton trigger)".

B.4.2 Triggered Anti-id Muon Definition

In the standard analysis, the following triggers have been used in muon channel: `EF_mu24i_tight`, `EF_mu36_tight`, `EF_mu18_mu8_EFFS`, and `EF_e12Tvh_medium1_mu8`, where "`i`" indicates track isolation, Ptcone20/$p_{\mathrm{T}} < 0.12$. Nevertheless (non-triggered) `anti-id` muons shown in Table 6.4 sometimes do not pass the `EF_mu24i_tight` trigger because there is no track isolation requirement in the `anti-id` muon definition. To correct for this bias, triggered `anti-id` muon is defined by changing Etcone cut to Ptcone cut as shown in Table B.8. The bias is then completely removed from the W+jets control sample (W+triggered `anti-id` sample).

Table B.8: Definition of the triggered `anti-id` muon (triggered muon denominator).

Triggered Anti-id Muon Definition
STACO Combined Muon
$p_{\mathrm{T}} > 25$ GeV
$\lvert\eta\rvert < 2.5$
d_0 Impact Parameter Requirements Removed
$\lvert z_0 \sin\theta\rvert < 1$ mm
Ptcone30/$p_{\mathrm{T}} < 0.12$
Fails the identified muon selection

B.4.3 Fake Factors for Triggered Anti-id Leptons

The fake factors for the triggered `anti-id` lepton is measured by using the di-jets sample. In practice the procedure of the fake factor measurement is the same as what is used for non-triggered `anti-id` leptons as described in Section B.1. It is also possible to use the Z+jets sample for the fake factor measurement. The larger uncertainty on the di-jets fake factor than that on the Z+jets fake factor does not matter much since the contribution of the triggered `anti-id` leptons to the W+jets control sample is not large. Also the triggered `anti-id` leptons are mainly used for the QCD estimation where the di-jets fake factor is essential.

The fake factor increases with the triggered `anti-id` lepton because the number of denominators ($N_{\mathrm{anti-id}}$) decreases due to tighter lepton definition. This can be seen in the comparison of the denominator p_{T} distributions (non-triggered versus triggered `anti-id`) as shown in Figure B.22. Also dedicated fake factors for the triggered `anti-id` lepton (1D and 2D) and corresponding EW uncertainty (2D) are shown in Figure B.23 for electrons and in Figure B.24 for muons. According to the decrease of the number of denominators, resulting fake factor increase by roughly a factor of 10, depending on p_{T} bin.

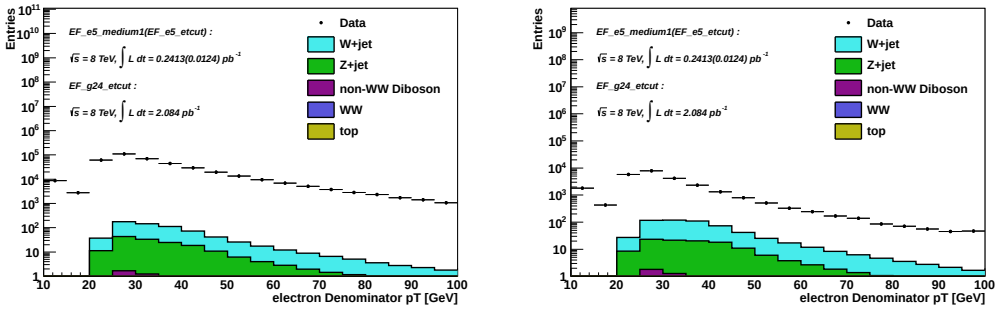

Figure B.22: Di-jet p_{T} distributions for non-triggered (left) and triggered electron denominators (right) collected with e/gamma supporting triggers. W and Z contaminations are also illustrated but the contributions are negligibly small at the end of the selection.

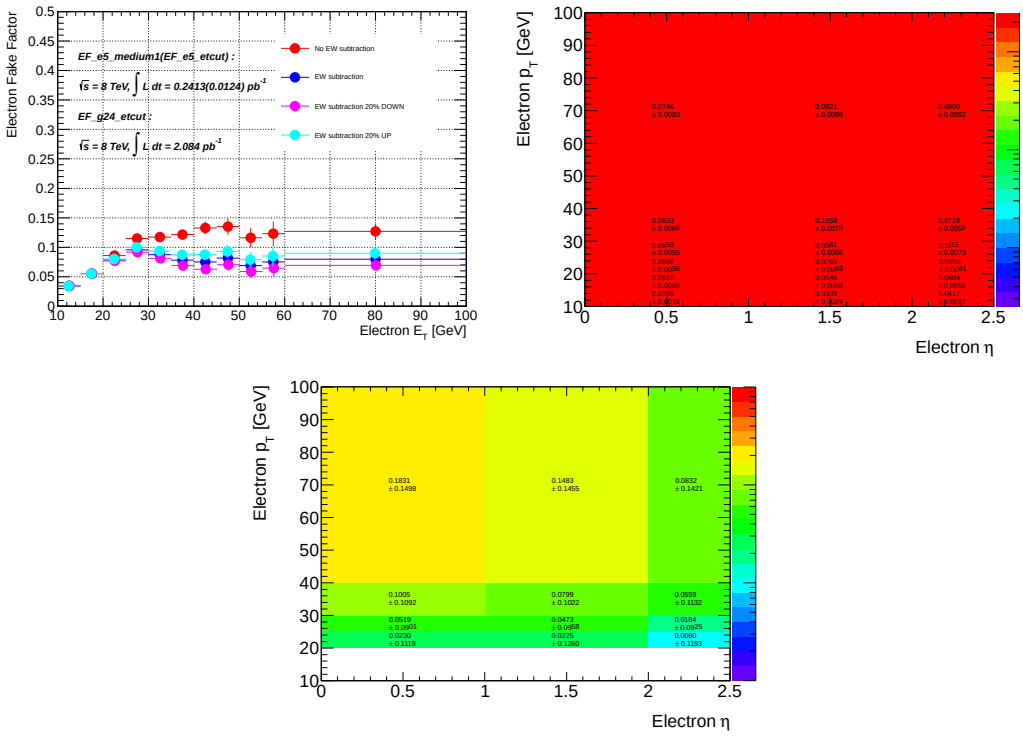

Figure B.23: 1D (top left) and 2D fake factors (top right) for triggered `anti-id` electrons. And the EW contamination systematic uncertainties (bottom) for triggered `anti-id` electrons. The EW contamination is not evaluated below 20 GeV due to the lack of e5 triggers in MC. The uncertainty on 15-20 bin is thus taken from next bin (higher bin).

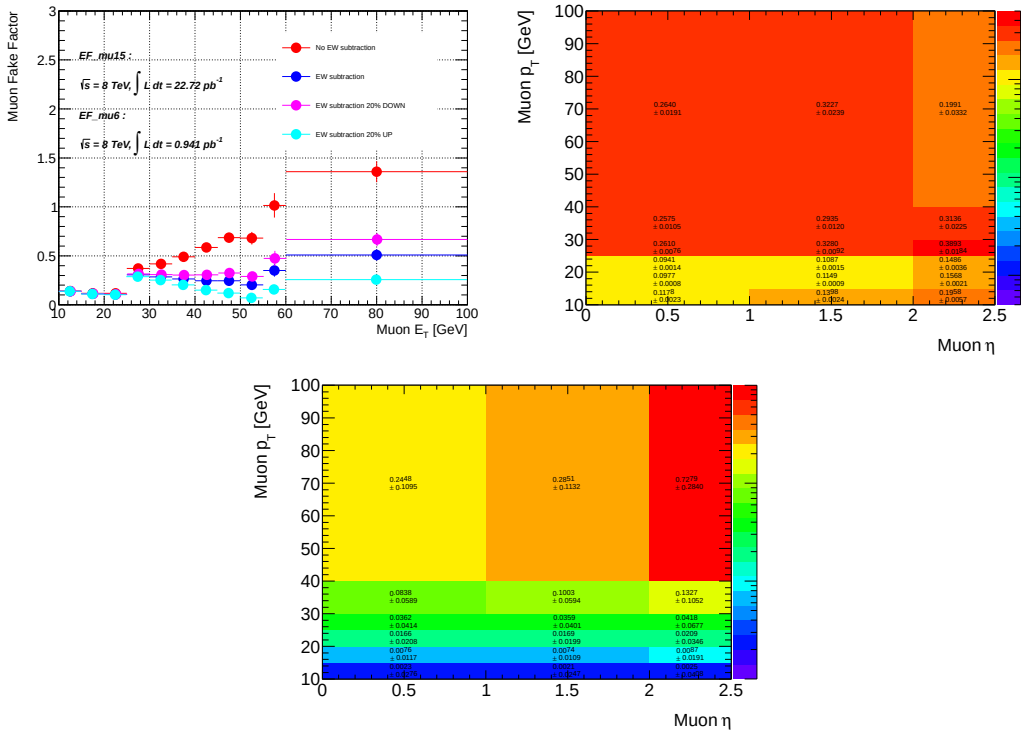

Figure B.24: 1D (top left) and 2D fake factors (top right) for triggered `anti-id` muons. And the EW contamination systematic uncertainties (bottom) for triggered `anti-id` muons.

B.4.4 W+jets Control Sample for Triggered Anti-id Leptons

In addition to the fake factor, dedicated W+jets control sample is also defined as events that have one triggered `anti-id` lepton and one `id` lepton. The statistics of the control sample for the triggered `anti-id` is smaller than that for the non-triggered `anti-id` due to its small contribution to the W+jets control sample. Also the EW contamination, in particular the $W\gamma$ background, is relatively larger due to the fact that the tighter lepton definition enhaces more either ture electrons or conversions rather than jets misidentified as leptons. The remaining contribution needs to be subtracted from the control sample to avoid double counting of the EW background. Figure B.25 shows kinematic distributions of the W+jets control sample for the triggered `anti-id` leptons.

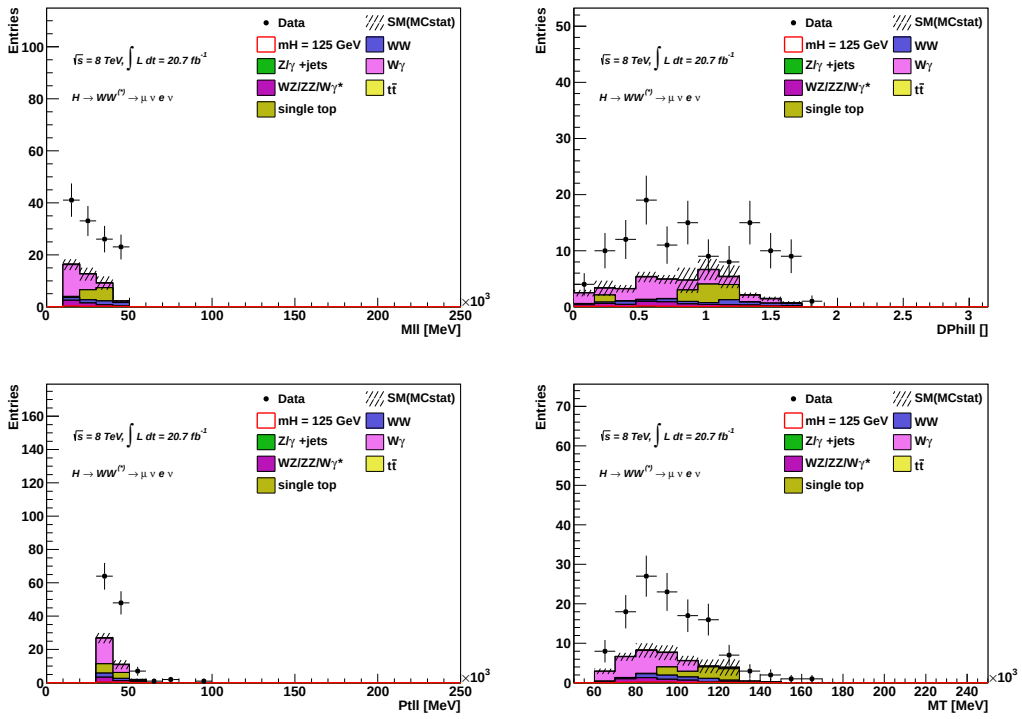

Figure B.25: Kinematic distributions of the W+jets control sample for the triggered `anti-id` leptons. The statistics of the control sample is smaller and the EW contamination in the control sample is larger compared to the W+jets control sample for the non-triggered `anti-id` leptons.

B.5 QCD Estimation

B.5.1 QCD Subtraction from W+jets Control Sample

Before having a QCD prediction, it is necessary to subtract the QCD contamination from the W+jets control sample. The W+jets control sample can be written as:

$$N_{\text{id+ anti-id}} = N^{\text{W+jet}}_{\text{id+ anti-id}} + N^{\text{QCD}}_{\text{id+ anti-id}} + N^{\text{EW}}_{\text{id+ anti-id}}. \tag{B.1}$$

To obtain the pure W+jets prediction in the signal region, the QCD and EW backgrounds are subtracted off, and the Z+jets (or di-jets) fake factor is applied as:

$$N^{W+jet}_{\text{id+id}} = f \cdot N^{\text{W+jet}}_{\text{id+anti-id}} \tag{B.2}$$

$$= f \cdot \left(N_{\text{id+anti-id}} - N^{\text{QCD}}_{\text{id+anti-id}} - N^{\text{EW}}_{\text{id+anti-id}} \right) \tag{B.3}$$

where $N^{\text{EW}}_{\text{id+anti-id}}$ is obtained from simulation. Using Equation 6.17 to substitute for $N^{\text{QCD}}_{\text{id+anti-id}}$, the QCD contribution to the W+jets control sample can be evaluated using the data driven QCD estimate with two `anti-id` leptons ($N_{\text{anti-id+anti-id}}$). However the fake factor can be quite different between the W+jets and QCD backgrounds due to the differences in the jet p_{T} spectrum and flavor composition. Hence the fake factor appeared in Equation 6.17 is labelled as f'' instead of f. The pure W+jets prediction is then expressed as:

$$N^{W+jet}_{\text{id+id}} = f \cdot \left(N_{\text{id+ anti-id}} - 2 \times f'' \times N^{\text{QCD}}_{\text{anti-id+anti-id}} - N^{\text{EW}}_{\text{id+anti-id}} \right) \tag{B.4}$$

Since the electron and muon fakes are separated in the analysis, the QCD contamination must be subtracted independently from the `id` μ + `anti-id` electron sample and `id` electron + `anti-id` μ sample, etc. f'' depends on the `anti-id` definition as well as the presence of other lepton in the event because the presence of the other lepton can dramatically change the jet flavor composition. One can rewrite f'' as:

$$f'' = c''^{\text{away-side anti-id}}_{\text{near-side}} \times f, \tag{B.5}$$

where the near-side refers to the `anti-id` lepton definition to which the fake factor is applied, and the away-side refers to the other lepton in the event, meaning that c^e_μ, for instance, refers to a `anti-id` muon and `id` electron in the event. Since there are triggered and non-triggered `anti-id` definitions as well as `id` definitions, a different correction is required for each lepton definition and away-side lepton definition. The procedure to split the electron and muon fakes by subtracting the QCD contribution, for example, from the W+jets with electron fake is given as:

$$N^{\text{W+jet electron fake}}_{\text{id } \mu\text{+predicted-id e}} = f \cdot \left(N_{\text{id } \mu\text{+ anti-id e}} - c''^{\mu}_{e} \times f \times N^{\text{QCD}}_{\text{anti-id } \mu \text{ +anti-id e}} - N^{\text{EW}}_{\text{id } \mu\text{+ anti-id e}} \right), \tag{B.6}$$

where $N^{\text{W+jet electron fake}}_{\text{id } \mu\text{+predicted-id e}}$ is the pure W+jets contribution with electron fake to the signal region. The μ and e terms are reversible when predicting the amount of W+jets background

with the muon fake. The $N^{\text{QCD}}_{\text{anti-id }\mu\text{+anti-id e}}$ is the events with a pair of two `anti-id` leptons. Note that the order does not indicate the leading and sub-leading lepton but indicates electron and muon fakes. Also when correcting the f to the OS or SS fake factor to account for differences in jet flavor composition for fake leptons with the same charge as the W and opposite charge of the W, it is important to apply these corrections to the subtraction of QCD as well.

In the QCD subtraction from the W+jets control sample, the $N^{\text{QCD}}_{\text{anti-id }\mu\text{+anti-id e}}$ term is used twice. Once to subtract from the electron fakes, and once to subtract from the muon fakes, which accounts for the double counting of the QCD contamination in the W+jets control sample. To summarize, the correction term is either for an electron or muon, and the electron or muon can be for a triggered `anti-id` or a non-triggered `anti-id` definition. The away-side lepton can be either lepton flavor, and either `id`, `anti-id`, or triggered `anti-id`. Combining these together, there are $2{\times}2 \times 2 \times 3 = 24$ different correction terms defined.

At the end, the $N^{\text{QCD}}_{\text{anti-id }\mu\text{+anti-id e}}$ term is once more used to predict the QCD background in the signal region by modifying Equation 6.16 as:

$$N^{\text{QCD}}_{\text{id+id}} = f' \cdot f'' \cdot (N_{\text{anti-id+anti-id}} - N^{\text{W+jet}}_{\text{anti-id+anti-id}} - N^{\text{EW,MC}}_{\text{anti-id+anti-id}}) \tag{B.7}$$

where f' refers to the di-jets fake factor corrected for the presence of an away-side `id` lepton, and f'' referes to the di-jets fake factor corrected for the presence of an away-side `anti-id` lepton. Schematic view of those fake factor measurements is illustrated in Figure B.26.

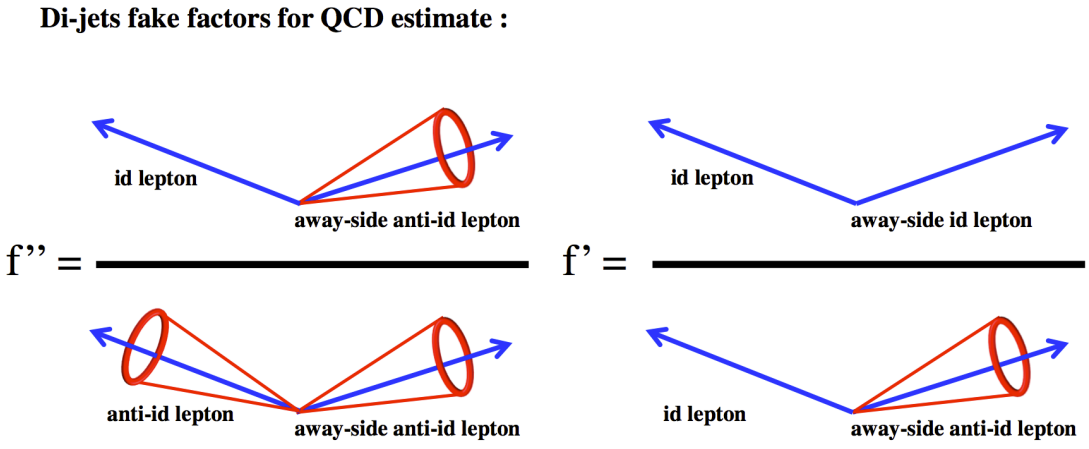

Figure B.26: Schematic view of di-jets fake factor measurements for the data-driven QCD estimate. f' refers to the di-jets fake factor corrected for the presence of an away-side `id` lepton (left). f'' refers to the di-jets fake factor corrected for the presence of an away-side `anti-id` lepton (right).

B.5.2 QCD Correction

The di-jets fake factors, f' and f'', for the QCD subtraction/prediction are dependence on the away-side lepton flavor and lepton definition due to the change in the jet flavor composition. The requirements on the away-side object can greatly enhance the heavy flavor contributions. Hence the correction factors, c' and c'', that are derived in simulation, must be determined for each away-side lepton condition.

Looking at $N^{QCD}_{\text{id+anti-id}}$, for example, one realize that one `id` lepton biases the other jet that ends up as a `anti-id` lepton, so one can label the fake factor of the second jet as:

$$f' = c'^{\text{away-side id}}_{\text{near-side}} \cdot f, \tag{B.8}$$

where f is the di-jets fake factor that is the ratio of the total count of `id` leptons (N), to the total count of `anti-id` leptons (D) in di-jets sample in data. When requirements are placed on away-side object in the event, the composition of the N and D samples changes, which are referred to as N^{bias} and D^{bias}. The c can be then rewritten as:

$$c = \frac{1}{f} \cdot \frac{N^{\text{bias}}}{D^{\text{bias}}}. \tag{B.9}$$

The N^{bias} and D^{bias} can be split into three flavor components, c-quark, b-quark and light flavor (LF). Then the c can be further rewritten as:

$$c = \frac{1}{f} \cdot \frac{N^{\text{bias}}_{LF} + N^{\text{bias}}_{b} + N^{\text{bias}}_{c}}{D^{\text{bias}}_{LF} + D^{\text{bias}}_{b} + D^{\text{bias}}_{c}}, \tag{B.10}$$

where N^{bias}_{LF} (D^{bias}_{LF}) is the number of light flavor jet faking `id` lepton (`anti-id` lepton) with away-side lepton, N^{bias}_{c} (D^{bias}_{c}) is the number of c-quark jet faking `id` lepton (`anti-id` lepton) with away-side lepton, N^{bias}_{b} (D^{bias}_{b}) is the number of c-quark jet faking `id` lepton (`anti-id` lepton) with away-side lepton. Each component is, for example N^{bias}_{LF}, estimated by introducing the jet ratio as:

$$N^{\text{bias}}_{LF} = N_{LF} \cdot \frac{J^{\text{away-side}}_{LF}}{J^{\text{jet-unbiased}}_{LF}} = N_{LF} \cdot \xi_{LF}, \tag{B.11}$$

where ξ_{LF} is the ratio of the number of LF jets with away-side `id` or `anti-id` requirement to the number of LF jets without away-side requirements. The above is for the LF component but one can also factorize $N^{\text{bias}}_{c,b}$ and $D^{\text{bias}}_{c,b}$ into $N_{c,b} \cdot \xi_{c,b}$ and $D_{c,b} \cdot \xi_{c,b}$.

ξ physically corresponds to the change in jet composition after requiring one `id` or `anti-id` lepton in an event. $\xi = 1$ means no change, and ξ larger or smaller than 1 means an increase or decrease, respectively, of that flavor jet. Plugging Equation B.11 for all flavors into Equation B.10, the equation can be written as:

$$c = \frac{1}{f} \cdot \frac{N_{LF} \cdot \xi_{LF} + N_{b} \cdot \xi_{b} + N_{c} \cdot \xi_{c}}{D_{LF} \cdot \xi_{LF} + D_{b} \cdot \xi_{b} + D_{c} \cdot \xi_{c}}, \tag{B.12}$$

where N_{LF}, N_b, N_c, D_{LF}, D_b, D_c, ξ_{LF}, ξ_b, and ξ_c are measured in the di-jets simulation. The largest uncertainty comes from using an away-side muon due to the limited muon MC

statistics. ξ_{LF}, ξ_b, and ξ_c for an away-side electron are shown in Figure B.27, and ξ averaged over all jet p_{T} is summarized in Table B.5.2. Due to the poor statistics, the ξ averaged over jet p_{T} is used.

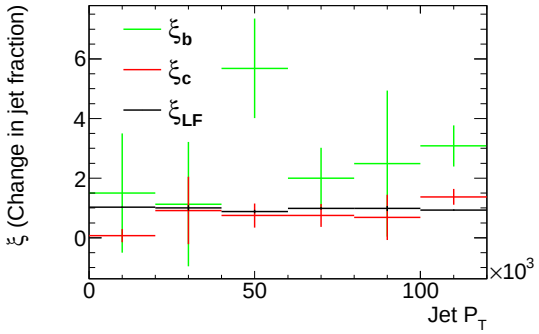

Figure B.27: The change in the awayside jet fractions for an awayside electron as a function of the jet p_{T}. An $\xi = 1$ indicates no change, and being larger than 1 indicates an increase in that jet flavor. The bottom (green), charm (red), and light flavor (black) jets.

Table B.9: Awayside jet corrections (ξ) from a numerator and denominator for the electron and muon. ξ is change in bottom, charm, and LF jets averaged over all jet p_{T} by having an awayside muon or electron numerator or denominator. $\xi = 1$ means no change in jet composition.

Lepton definition	Flavor		
Mean (ξ)	bottom	charm	Light Flavor (LF)
Electron Numerator	3.0 ± 0.5	1.1 ± 0.2	0.94 ± 0.01
Electron Denominator	1.15 ± 0.03	1.05 ± 0.01	0.995 ± 0.002
Electron Triggerable Denominator	3.40 ± 0.11	1.13 ± 0.04	0.928 ± 0.004
Muon Numerator	8.0±0.2	1.18±0.04	0.82±0.005
Muon Denominator	7.0±0.1	1.26±0.01	0.82±0.002

The largest systematic uncertainty on the correction (c) arises from varying the b-quark and c-quark fractions up and down by 50% and the simulation statistical uncertainties. The uncertainties and correction factors for the electron are shown in Figure B.28, and uncertainties for the correction factors and f used in the analysis are in Table B.10 for 10 GeV correction factors. All uncertainties are added in quadrature to get the total uncertainty on the QCD background.

It is found that the correction factors for some of the `anti-id` leptons are very similar each other as shown in Figure B.29. The difference in the correction factors, for example, between triggered `anti-id` muon and non-triggered `anti-id` muon is less than 5 %. Hence it is possible to make a simplification to reduce the number of correction factors. To reduce

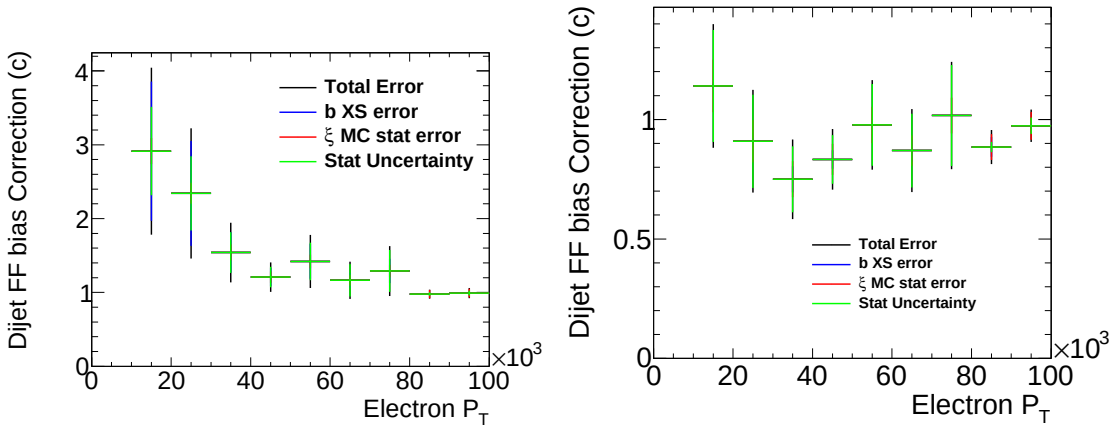

Figure B.28: QCD correction to the fake factor for flavor composition. The correction for the non-triggereable denominator (left) and triggered denominator (right) electrons in events with a muon numerator. The uncertainties from each component are shown and is dominantly the b-cross-section for the non-triggereable denominator.

Table B.10: Ralative uncertainties on f and the QCD correction factors for 10-15 GeV leptons in the different flavor.

Sources	Uncertainties		
	$c^{\mu}_{\text{e anti-id trig}}$	$c^{\mu}_{\text{e anti-id}}$	c^{e}_{μ}
b-XS	0.00	0.32	0.03
c-XS	0.04	0.04	0.00
jet p_{T}	0.20	0.20	0.20
MC Stat	0.21	0.21	0.03
ξ Stat	0.10	0.06	0.25
Pileup	0.10	0.10	0.10
EW Contamination	0.05	0.05	0.05
Total	0.33	0.45	0.34

the very large number of corrections, the away-side `id` lepton is used for both the away-side `id` and away-side `anti-id` leptons as:

$$c''^{\text{away-side anti-id}}_{\text{near-side}} = c'^{\text{away-side id}}_{\text{near-side}}. \tag{B.13}$$

The one exception is the effect of the away-side non-triggered electron on the muon, which is roughly 10% different as shown in Figure B.29. For the non-triggered electron on muon, its own correction factor is used.

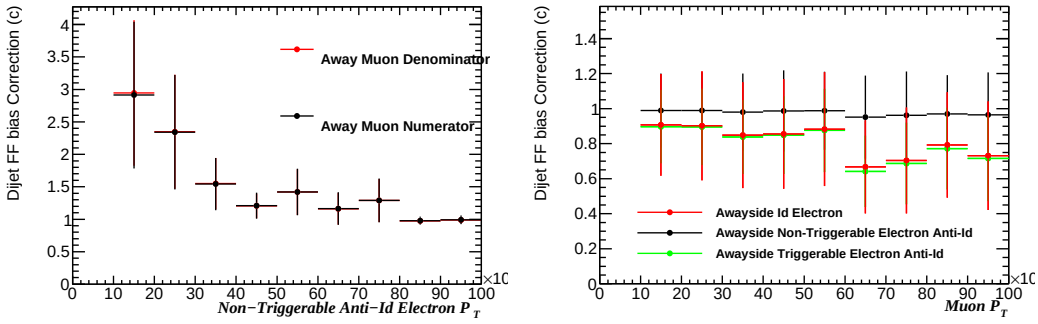

Figure B.29: QCD corrections comparing the effect of an awayside `id` lepton (red) and an away-side `anti-id` lepton (black and green). The effect of an awayside `anti-id` vs an away-side `id` lepton is small except for the non-triggerable electron `anti-id` effect on the muon.

Finally the correction factors are validated in data using low $E_{\mathrm{T}}^{\mathrm{miss}}$ region ($\max m_{\mathrm{T}}(W)$ <20 GeV). The comparison of the correction factors between data and simulation is found in Table B.11.

Table B.11: QCD correction terms derived in data from the $\max m_{\mathrm{T}}(W) < 20$ GeV. The simulation is corrected for the difference in dilepton and single lepton triggers. The QCD uncertainties are the sum in quadrature of all the systematics, and the data uncertainties are statistical only.

Correction Term	Channel	data	simulation
$c^{\mu}_{\text{e anti-id}}$	$e\mu$	2.33 ± 0.17	2.1±0.9
c^{e}_{μ}	$e\mu$	1.07 ± 0.10	1.2±0.4
$c^{\mu}_{\text{e anti-id trig}}$	μe	1.75 ± 0.10	1.6±0.7

B.5.3 QCD Control sample

Data-driven QCD control sample ($N_{\text{anti−id+anti−id}}$) is used to obtain the QCD prediction/subtraction in the signal region ($N_{\text{id+id}}$) multiplying the fake factors as discussed in Section 6.7.1. The QCD control sample is defined as events that have two `anti-id` leptons. The control sample is collected with the primary triggers that are used in the standard analysis (see Table 3.2): `EF_e24vhi_medium1`, `EF_e60_medium1`, `EF_2e12Tvh_loose1`, and `EF_e12Tvh_medium1_mu8` for ee and $e\mu$+μe channels, and `EF_mu24i_tight`, `EF_mu36_tight`, `EF_mu18_mu8_EFFS`, and `EF_e12Tvh_medium1_mu8` for $\mu\mu$ and $e\mu$+μe channels.

The trigger acceptance for QCD control sample is different from the W+jets control sample due to the isolation and identification that is cut on in the trigger. Most of the W+jets control sample trigger on the generally higher p_{T} lepton from the W for which the offline requirements are tighter than the trigger's. The W+jets control sample then uses a non-triggerable `anti-id` definition to predict W+jets in the signal region. On the other hand, the QCD control sample has both leptons coming from jets, which means that both leptons need a looser isolation or identification to extrapolate into the signal region. The dilepton triggers make looser requirements on the leptons. Therefore the QCD events are mainly accepted through the dilepton triggers, which use the triggered `anti-id` definition summarized in Section B.4.

The purity of the QCD control sample is very high over all jet multiplicity bins. The contamination of the EW backgrounds are subtracted out, and additionally the W+jets simulation is subtracted to remove event in which the prompt lepton from the W satisfies the `anti-id` definition.

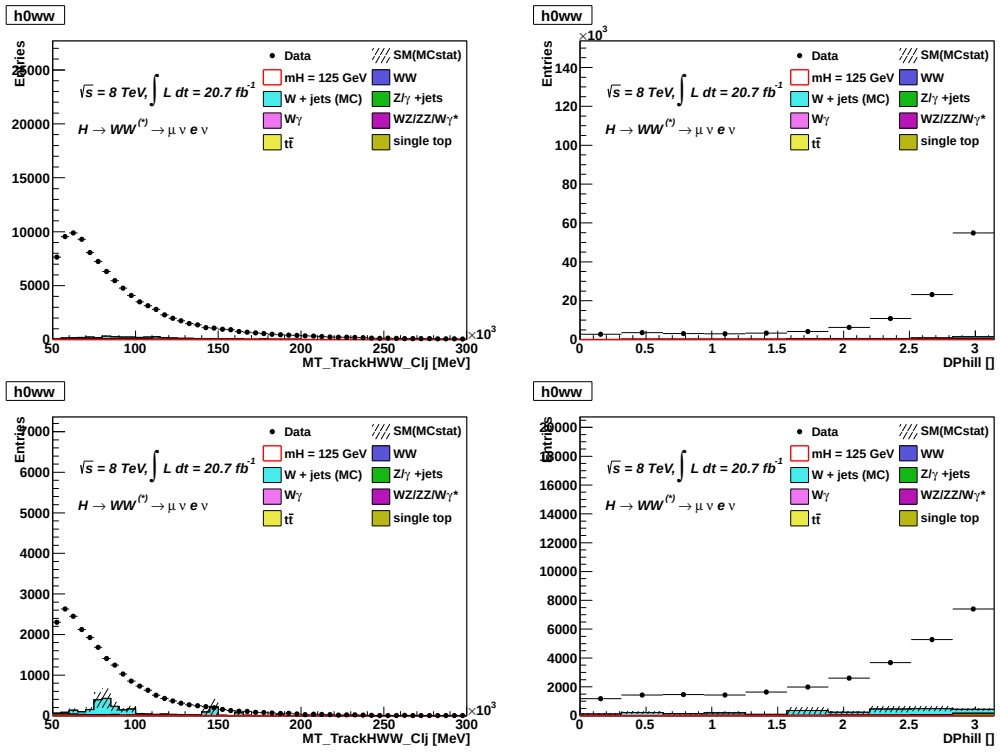

Figure B.30: Kinematics of the QCD control sample for μe channel after $M_{\ell\ell}$ requirement. The QCD events are represented as data events - all other simulations. The top plots are m_{T} (left) and $\Delta\phi_{\ell\ell}$ (right) in high p_{T}. The bottom plots are m_{T} (left) and $\Delta\phi_{\ell\ell}$ (right) in low p_{T}.

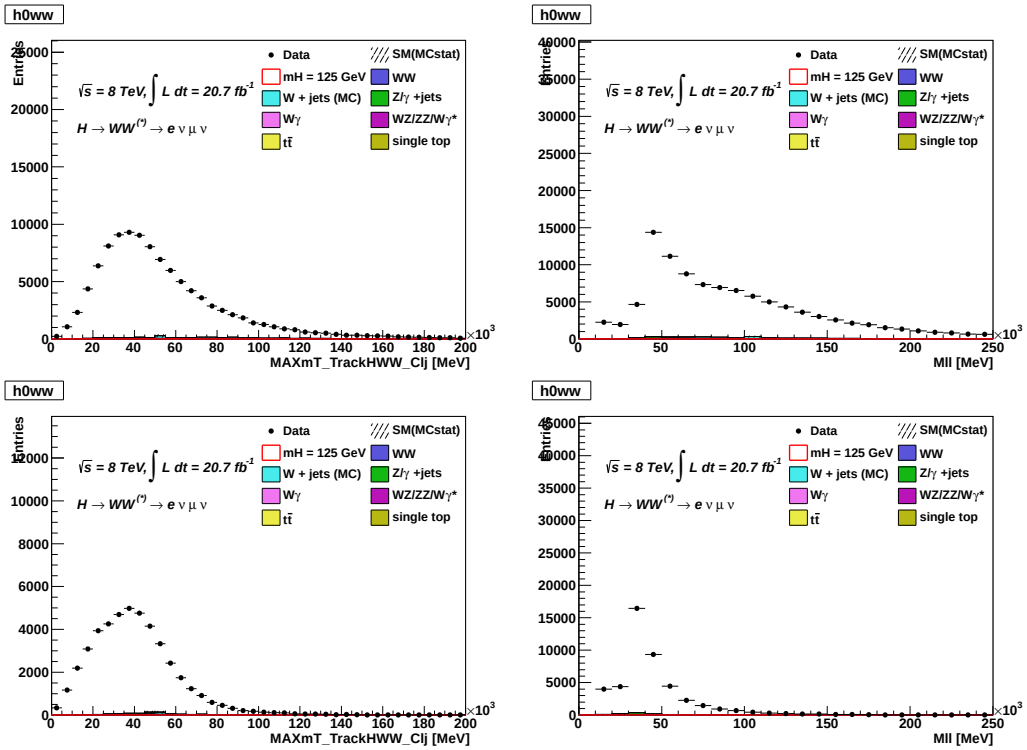

Figure B.31: Kinematics of the QCD control sample for $e\mu$ channel after $M_{\ell\ell}$ requirement. The QCD events are represented as data events - all other simulations. The top plots are $m_{\mathrm{T}}(W)$(MAX) (left) and $M_{\ell\ell}$ (right) in high p_{T}. The bottom plots are $m_{\mathrm{T}}(W)$(MAX) (left) and $M_{\ell\ell}$ (right) in low p_{T}.

Appendix C

Additional Material for Modeling of Same Sign Backgrounds

C.1 Heavy Flavor Cross Section Variations

It is not obvious that the W+jets fake factors are stable against parton distribution functions (PDFs) for heavy flavor. In order to check the stability against the heavy flavor cross section, the cross section of the W+charm and $W+b\bar{b}$ processes is each varied from 50% to 200% as shown in Figure C.1 and C.2. The resulting differences are less than 20% and are well covered by the systematic uncertainty on the correction factors currently assigned.

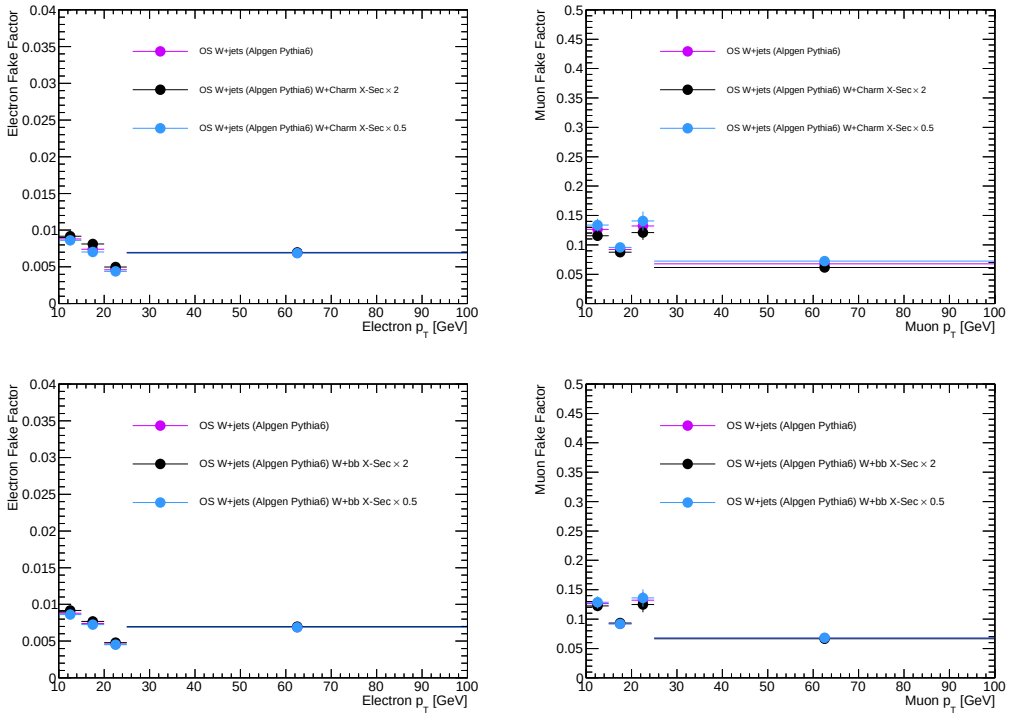

Figure C.1: Comparison of the fake factors varying the heavy flavor cross section by 50% or 200%. No strong dependence on the heavy flavor cross section is observed and the variations are well covered by the systematic uncertainty currently assigned on the W+jets correction factors. Alpgen+Pythia6 sample is used.

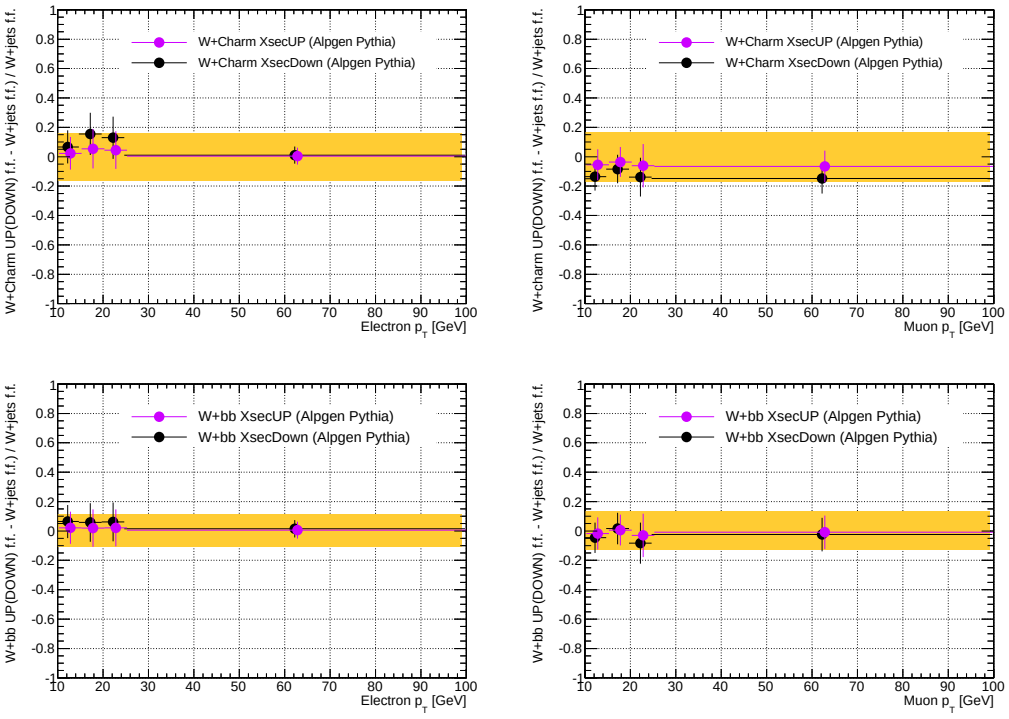

Figure C.2: Relative difference of the fake factors varying the heavy flavor cross section by 50% or 200%. No strong dependence on the heavy flavor cross section is observed and the variations are well covered by the systematic uncertainty currently assigned on the W+jets correction factors. Alpgen+Pythia6 sample is used.

Appendix D

Additional materials for Results

D.1 Results

D.1.1 ggF Results

The m_{T} distributions of each signal region ($m_{\ell\ell}$:[10-30, 30-55] $\otimes$ $p_{\mathrm{T}}^{\mathrm{sub}}$:[10-15, 15-] $\otimes$ flavor:[$e\mu$,μe]) for ggF 0-jet and ggF 1-jet different flavor analyses are shown in Figure D.1, D.2, D.3, and D.4. Also Table D.1 and D.2 show full cutflow for different flavor and same flavor channels comparing observed data to expected signal and background counts.

D.1.2 VBF Results

Table D.3 show full cutflow for different flavor and same flavor channels comparing observed data to expected signal and background counts.

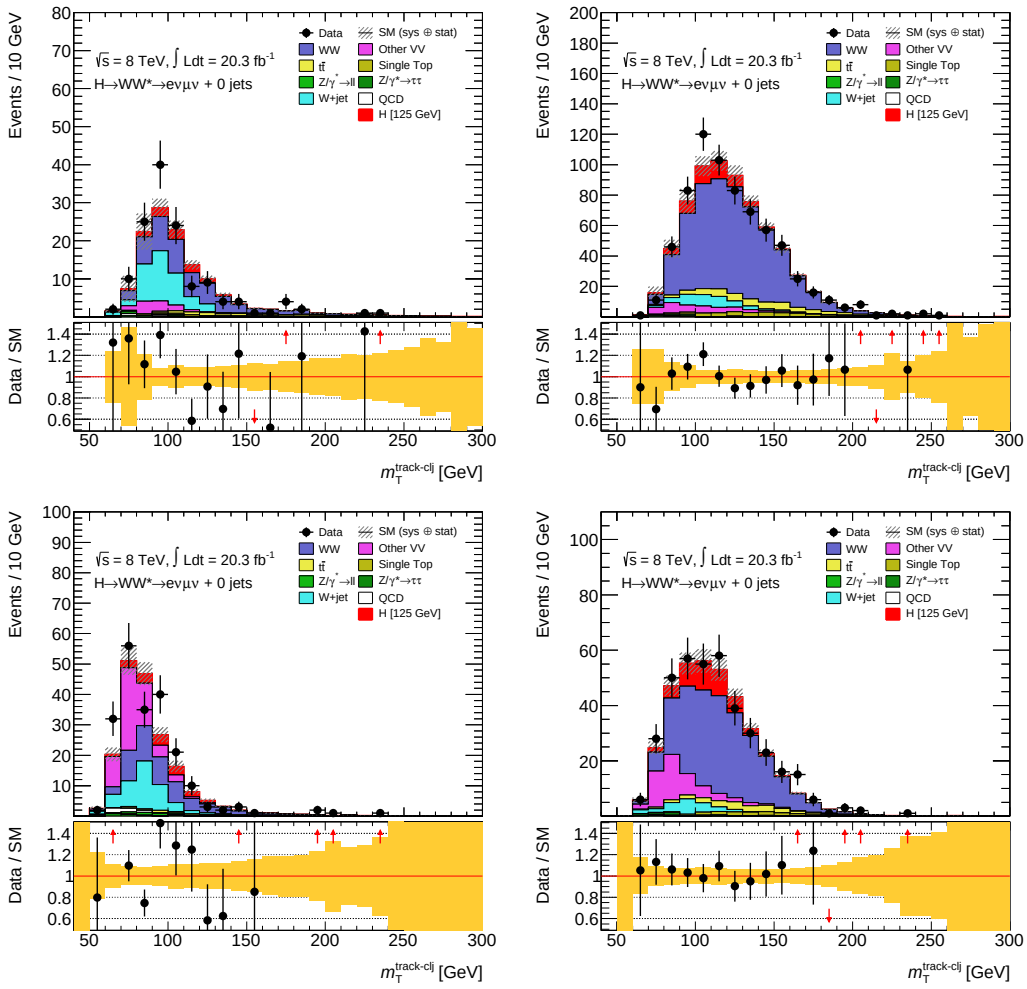

Figure D.1: m_{T} distribution for each sub-divisions in the 0-jet $e\mu$ channel : $p_{\mathrm{T}}^{\mathrm{sub}}$ = 10-15 GeV and $m_{\ell\ell} > 30$ GeV (upper left), $p_{\mathrm{T}}^{\mathrm{sub}}$ >15 GeV and $m_{\ell\ell} > 30$ GeV (upper left), $p_{\mathrm{T}}^{\mathrm{sub}}$ = 10-15 GeV and $m_{\ell\ell} < 30$ GeV (lower left), $p_{\mathrm{T}}^{\mathrm{sub}}$ >15 GeV and $m_{\ell\ell} < 30$ GeV (lower right).

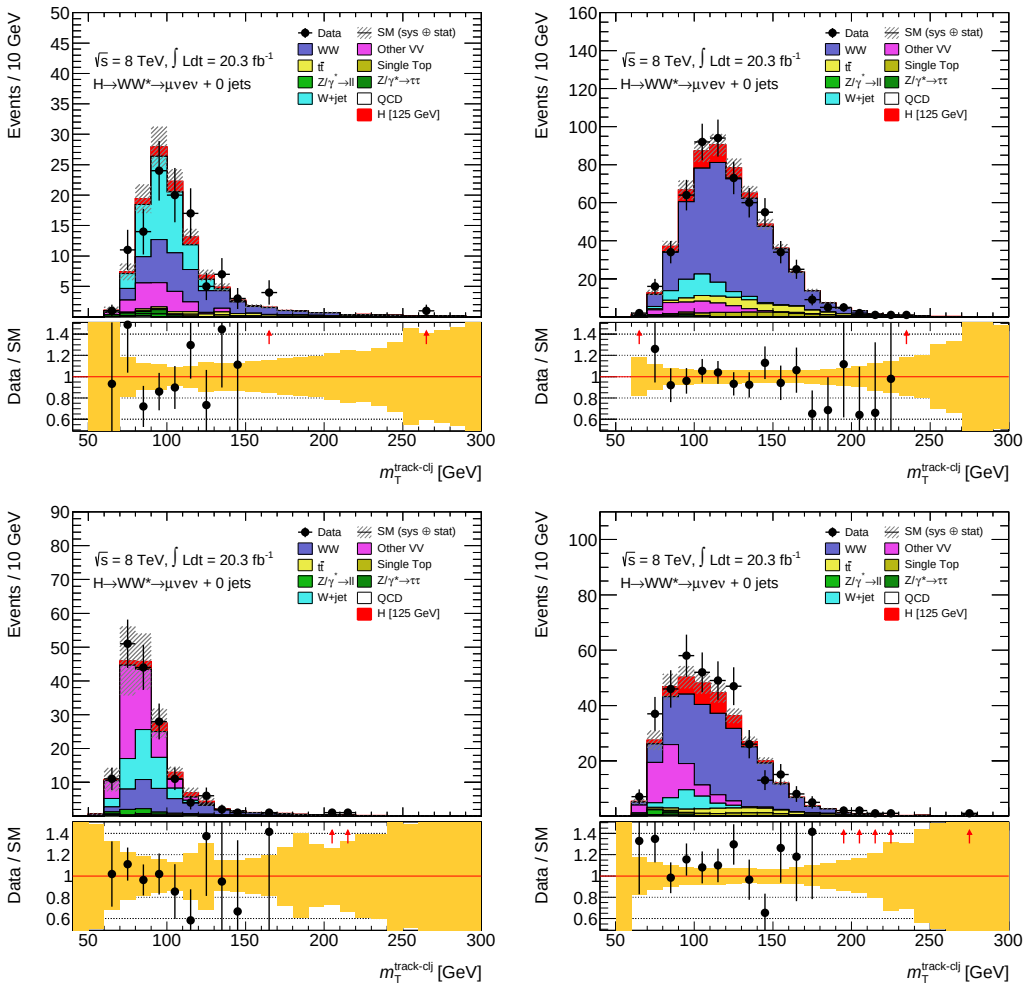

Figure D.2: m_{T} distribution for each sub-divisions in the 0-jet μe channel : $p_{\mathrm{T}}^{\mathrm{sub}}$ = 10-15 GeV and $m_{\ell\ell} > 30$ GeV (upper left), $p_{\mathrm{T}}^{\mathrm{sub}}$ >15 GeV and $m_{\ell\ell} > 30$ GeV (upper left), $p_{\mathrm{T}}^{\mathrm{sub}}$ = 10-15 GeV and $m_{\ell\ell} < 30$ GeV (lower left), $p_{\mathrm{T}}^{\mathrm{sub}}$ >15 GeV and $m_{\ell\ell} < 30$ GeV (lower right).

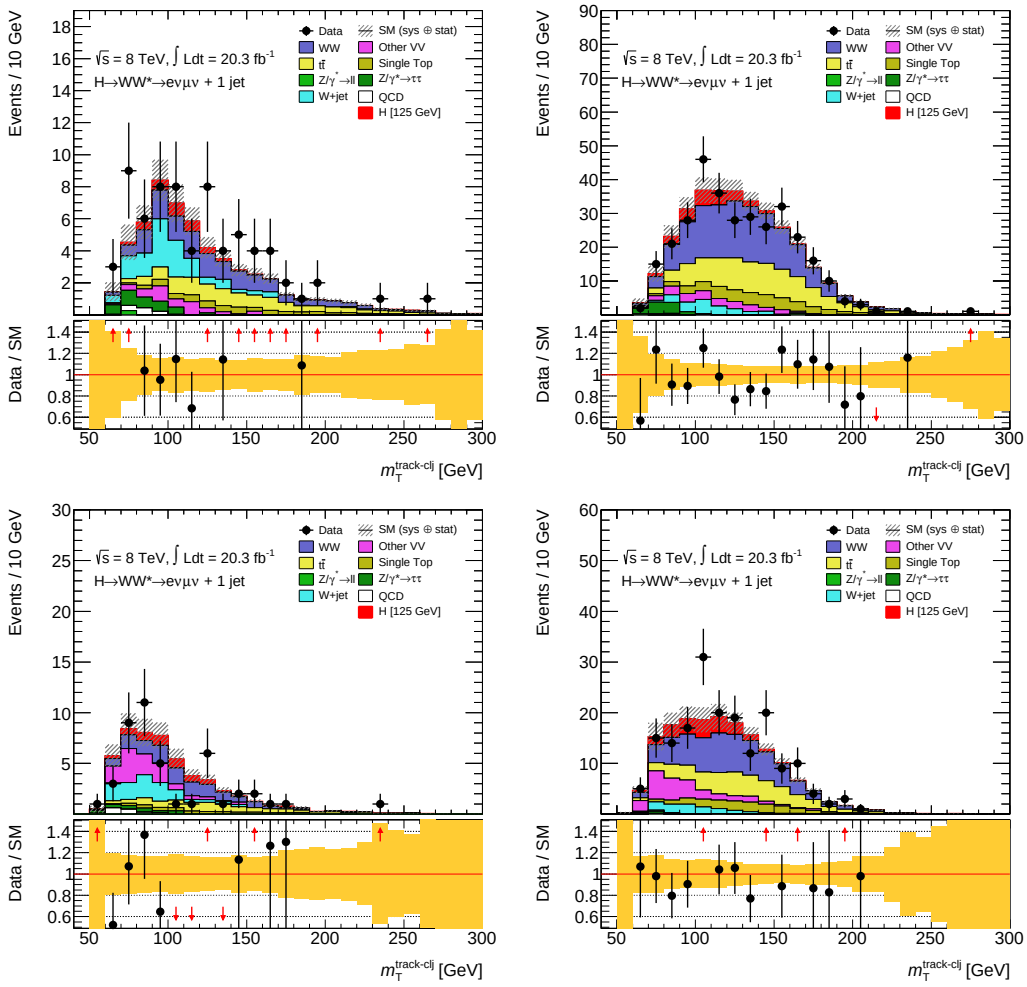

Figure D.3: m_{T} distribution for each sub-divisions in the 1-jet $e\mu$ channel : $p_{\mathrm{T}}^{\mathrm{sub}}$ = 10-15 GeV and $m_{\ell\ell} > 30$ GeV (upper left), $p_{\mathrm{T}}^{\mathrm{sub}}$ >15 GeV and $m_{\ell\ell} > 30$ GeV (upper left), $p_{\mathrm{T}}^{\mathrm{sub}}$ = 10-15 GeV and $m_{\ell\ell} < 30$ GeV (lower left), $p_{\mathrm{T}}^{\mathrm{sub}}$ >15 GeV and $m_{\ell\ell} < 30$ GeV (lower right).

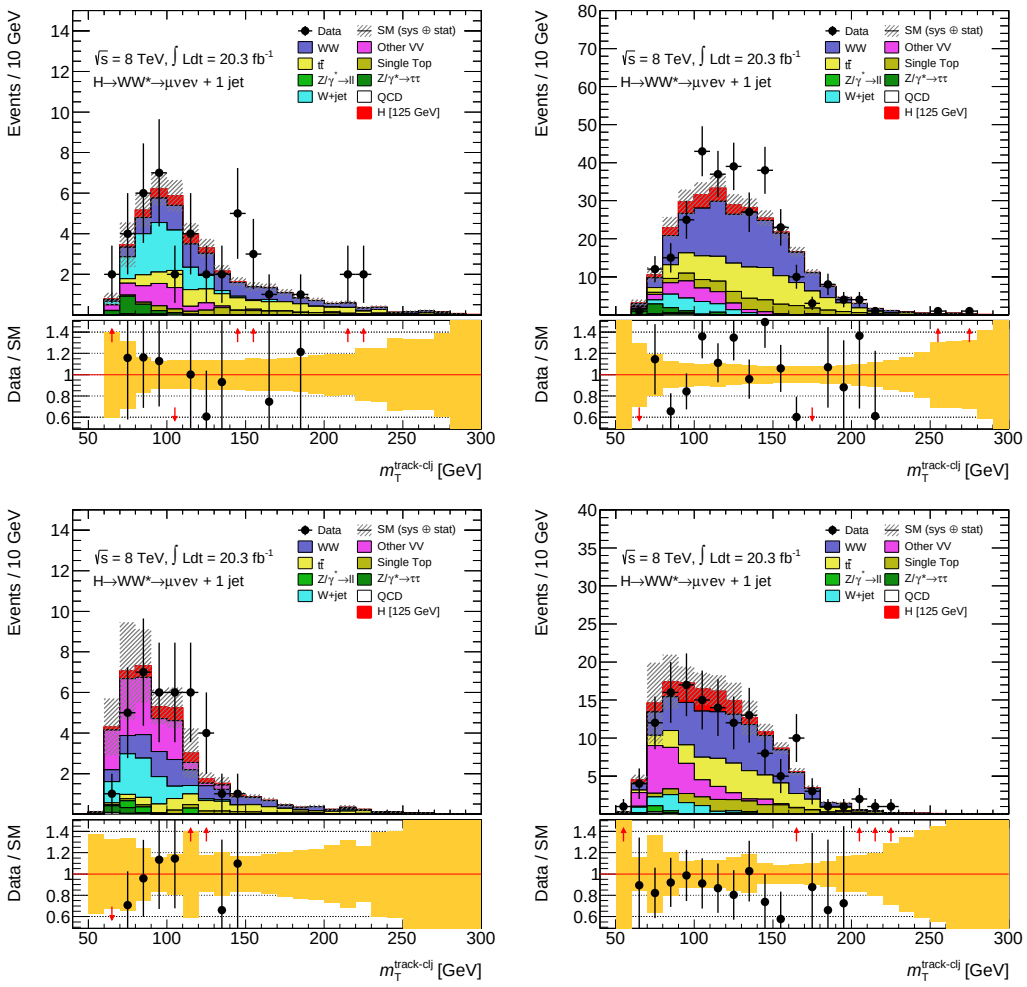

Figure D.4: m_{T} distribution for each sub-divisions in the 1-jet μe channel : $p_{\mathrm{T}}^{\mathrm{sub}}$ = 10-15 GeV and $m_{\ell\ell} > 30$ GeV (upper left), $p_{\mathrm{T}}^{\mathrm{sub}}$ >15 GeV and $m_{\ell\ell} > 30$ GeV (upper left), $p_{\mathrm{T}}^{\mathrm{sub}}$ = 10-15 GeV and $m_{\ell\ell} < 30$ GeV (lower left), $p_{\mathrm{T}}^{\mathrm{sub}}$ >15 GeV and $m_{\ell\ell} < 30$ GeV (lower right).

Table D.1: Full cutflow for the 8 TeV ggF $N_{\text{jet}} = 0$ and $= 1$ $e\mu$+μe signal and control regions. Uncertainties are statistical only. The Data/MC ratio does not include signal yields.

	Signal [125 GeV]	WW	Other VV	$t\bar{t}$	Single Top	$Z \to \ell\ell + \gamma$/jets	$Z \to \tau\tau + \gamma$/jets	W+jets	QCD	Total Bkg.	Observed	Data/MC
	851.34 ± 2.69	11523.52 ± 14.62	4806.33 ± 21.81	59889.72 ± 28.84	5748.70 ± 7.26	2535.47 ± 88.71	52129.75 ± 95.82	3545.57 ± 49.47	7857.39 ± 10.74	148036.45 ± 145.55	157557	1.06 ± 0.00
lepton p_{T}	815.21 ± 2.64	11378.76 ± 14.53	4290.11 ± 20.45	59380.15 ± 28.72	5703.64 ± 7.21	907.92 ± 37.06	44756.46 ± 88.89	6237.25 ± 39.43	3447.42 ± 7.51	136101.72 ± 111.32	142926	1.05 ± 0.00
Scale factors				NF = 1.05	NF = 1.05							
OS leptons	789.33 ± 2.26	11340.06 ± 14.51	2149.80 ± 14.51	62291.28 ± 30.18	5936.77 ± 7.15	573.68 ± 35.18	44632.41 ± 88.77	3715.91 ± 30.57	2228.36 ± 6.17	132868.28 ± 107.11	136013	1.02 ± 0.00
$m_{\ell\ell} > 10, 12$ GeV	781.70 ± 2.25	11321.85 ± 14.50	2041.01 ± 13.99	62214.96 ± 30.16	5930.55 ± 7.15	564.81 ± 35.13	44603.03 ± 88.74	3726.42 ± 30.39	2176.42 ± 6.10	132579.07 ± 106.94	135675	1.02 ± 0.00
Z veto (SF)	781.70 ± 2.25	11321.85 ± 14.50	2041.01 ± 13.99	62214.96 ± 30.16	5930.55 ± 7.15	564.81 ± 35.13	44603.03 ± 88.74	3726.42 ± 30.39	2176.42 ± 6.10	132579.07 ± 106.94	135675	1.02 ± 0.00
Scale factors				NF = 1.05	NF = 1.05		NFs applied					
$E_{\text{T,[rel],(clj)}}^{\text{miss,(track)}} > [40], (20)$	591.34 ± 1.78	9121.65 ± 13.02	1490.91 ± 12.12	37927.21 ± 23.54	4365.61 ± 6.12	182.73 ± 20.80	12055.96 ± 45.16	2331.82 ± 19.04	599.99 ± 3.54	68075.88 ± 61.28	69244	1.02 ± 0.00
Z VR (incl)	781.70 ± 2.25	11321.85 ± 14.50	2041.01 ± 13.99	62214.96 ± 30.16	5930.55 ± 7.15	564.81 ± 35.13	44603.03 ± 88.74	3726.42 ± 30.39	2176.42 ± 6.10	132579.07 ± 106.94	135675	1.02 ± 0.00
Z VR (incl), $E_{\text{T,rel}}^{\text{miss}} > 40$ GeV	289.34 ± 1.17	4951.87 ± 9.59	591.84 ± 7.60	25385.75 ± 19.26	2659.49 ± 4.72	18.02 ± 2.27	1045.55 ± 12.89	851.95 ± 9.59	46.30 ± 1.35	35550.77 ± 28.43	36392	1.02 ± 0.01
Top VR (incl)	70.54 ± 0.82	598.37 ± 3.44	148.36 ± 3.52	45582.02 ± 25.85	3663.46 ± 5.45	23.27 ± 7.15	1157.16 ± 14.39	538.20 ± 10.51	122.17 ± 1.37	51833.00 ± 33.06	51833	1.00 ± 0.00
Scale factors		NF = 1.22	NFs applied	NF = 1.09	NF = 1.09							
0j: jet veto	322.34 ± 1.08	7094.13 ± 12.68	735.86 ± 8.35	822.98 ± 3.52	408.04 ± 2.03	115.77 ± 15.75	5562.51 ± 31.74	1334.92 ± 12.62	236.82 ± 2.67	16311.04 ± 40.85	16410	1.01 ± 0.01
0j: $\Delta\phi_{\ell\ell,MET} > 1.57$	321.93 ± 1.07	7088.89 ± 12.68	733.42 ± 8.34	814.95 ± 3.50	406.11 ± 2.03	115.02 ± 15.74	5527.12 ± 31.66	1333.39 ± 12.57	230.25 ± 2.66	16249.16 ± 40.76	16326	1.00 ± 0.01
0j: $p_{\text{T},\ell\ell} > 30$ GeV	272.65 ± 0.90	5674.72 ± 11.35	569.33 ± 7.36	732.84 ± 3.32	364.25 ± 1.88	59.99 ± 10.24	782.68 ± 11.70	1054.39 ± 8.76	27.86 ± 1.83	9266.07 ± 22.79	9334	1.01 ± 0.01
0j: $m_{\ell\ell} < 55$ GeV	232.51 ± 0.68	1666.01 ± 6.12	349.37 ± 6.02	141.18 ± 1.45	79.31 ± 0.85	27.85 ± 4.47	349.94 ± 7.80	426.61 ± 6.16	12.39 ± 1.71	3052.66 ± 14.08	3411	1.12 ± 0.02
0j: $E_{\text{T,rel}}^{\text{miss,track}} > 40$ GeV (SF)	232.51 ± 0.68	1666.01 ± 6.12	349.37 ± 6.02	141.18 ± 1.45	79.31 ± 0.85	27.85 ± 4.47	349.94 ± 7.80	426.61 ± 6.16	12.39 ± 1.71	3052.66 ± 14.08	3411	1.12 ± 0.02
0j: $\Delta\phi_{\ell\ell} < 1.8$	208.81 ± 0.64	1498.84 ± 5.81	320.74 ± 5.80	132.69 ± 1.41	75.21 ± 0.81	18.45 ± 2.37	12.31 ± 1.59	277.65 ± 5.02	9.17 ± 1.63	2345.06 ± 10.30	2642	1.13 ± 0.02
0j: $f_{\text{recoil}} < 0.1$ (SF)	208.81 ± 0.64	1498.84 ± 5.81	320.74 ± 5.80	132.69 ± 1.41	75.21 ± 0.81	18.45 ± 2.37	12.31 ± 1.59	277.65 ± 5.02	9.17 ± 1.63	2345.06 ± 10.30	2642	1.13 ± 0.02
0j: low p_{T}	42.90 ± 0.27	184.45 ± 2.02	145.25 ± 3.97	20.08 ± 0.54	9.89 ± 0.29	8.88 ± 1.68	6.10 ± 1.10	163.11 ± 4.13	5.66 ± 1.55	543.42 ± 6.62	614	1.13 ± 0.05
0j: high p_{T}	165.91 ± 0.57	1314.38 ± 5.44	175.49 ± 4.22	112.61 ± 1.30	65.32 ± 0.76	9.57 ± 1.67	6.21 ± 1.16	114.54 ± 2.85	3.51 ± 0.51	1801.63 ± 7.89	2028	1.13 ± 0.03
0j: $0.75 \cdot m_{\text{H}} \leq m_{\text{T}} \leq m_{\text{H}}$	133.57 ± 0.46	658.19 ± 3.84	78.37 ± 2.72	39.92 ± 0.77	21.41 ± 0.47	3.92 ± 1.09	2.34 ± 0.67	132.73 ± 2.90	0.82 ± 0.60	937.70 ± 5.78	1129	1.20 ± 0.04
0j: SSCR	2.14 ± 0.39	2.47 ± 0.21	323.93 ± 5.79	0.59 ± 0.09	0.47 ± 0.07	19.38 ± 2.50	2.74 ± 0.82	173.78 ± 4.23	5.49 ± 0.67	528.86 ± 7.67	531	1.00 ± 0.05
0j: Z VR	386.65 ± 1.38	7214.82 ± 11.60	995.33 ± 10.00	871.96 ± 3.57	434.15 ± 2.08	391.87 ± 28.61	33159.70 ± 78.58	2014.69 ± 22.54	1196.29 ± 4.74	46278.81 ± 88.17	48505	1.05 ± 0.01
0j: Z VR ($E_{\text{T,rel}}^{\text{miss}}$)	169.30 ± 0.71	3873.77 ± 9.38	326.20 ± 5.79	516.23 ± 2.79	261.27 ± 1.58	13.79 ± 2.01	637.09 ± 9.95	466.62 ± 5.90	27.12 ± 1.21	6122.08 ± 16.47	6123	1.00 ± 0.01
0j: Z VR ($p_{\text{T},\ell\ell}$)	158.62 ± 0.64	3562.40 ± 9.01	289.10 ± 5.46	487.52 ± 2.71	248.42 ± 1.53	8.33 ± 1.57	25.60 ± 1.97	399.15 ± 4.78	2.22 ± 0.90	5022.73 ± 12.28	5032	1.00 ± 0.01
0j: Z VR ($E_{\text{T,rel}}^{\text{miss,track}}$)	128.64 ± 0.60	2994.43 ± 8.29	171.12 ± 4.04	426.30 ± 2.53	220.22 ± 1.38	3.79 ± 1.15	1.58 ± 0.57	237.47 ± 3.69	-0.58 ± 0.87	4054.34 ± 10.46	4057	1.00 ± 0.02
0j: Z VR (f_{recoil})	82.39 ± 0.48	2179.35 ± 7.09	110.24 ± 3.26	186.12 ± 1.67	119.90 ± 1.03	2.46 ± 0.92	0.35 ± 0.28	154.95 ± 2.98	-0.29 ± 0.72	2753.08 ± 8.67	2780	1.01 ± 0.02
0j: WW CR (no SF $E_{\text{T,rel}}^{\text{miss,track}}$)	49.79 ± 0.54	2056.20 ± 6.84	115.44 ± 3.02	217.93 ± 1.81	120.17 ± 1.19	23.66 ± 8.04	339.47 ± 7.61	298.43 ± 4.32	6.08 ± 0.53	3177.38 ± 14.21	3255	1.02 ± 0.02
Scale factors		NF = 1.22	NFs applied	NF = 1.09	NF = 1.09							
0j: WW CR	28.25 ± 0.43	1948.64 ± 6.66	98.77 ± 2.79	216.46 ± 1.81	119.48 ± 1.14	9.14 ± 1.71	105.87 ± 4.21	182.42 ± 3.08	1.98 ± 0.48	2682.75 ± 9.33	2711	1.01 ± 0.02
0j: WW CR (SF f_{recoil})	28.25 ± 0.43	1948.64 ± 6.66	98.77 ± 2.79	216.46 ± 1.81	119.48 ± 1.14	9.14 ± 1.71	105.87 ± 4.21	182.42 ± 3.08	1.98 ± 0.48	2682.75 ± 9.33	2711	1.01 ± 0.02
0j: WW VR	0.56 ± 0.18	1111.45 ± 5.04	48.69 ± 1.93	187.29 ± 1.68	83.73 ± 0.80	0.66 ± 0.37	0.52 ± 0.31	53.96 ± 1.47	0.95 ± 0.12	1487.25 ± 5.91	1381	0.93 ± 0.03
Scale factors		NF = 1.06	NFs applied	NF = 1.03	NF = 1.03		NFs applied					
1j: one jet	192.93 ± 1.17	2781.31 ± 7.38	492.04 ± 6.43	8138.04 ± 10.76	2238.43 ± 4.32	62.47 ± 13.54	5648.41 ± 28.58	662.57 ± 12.00	334.25 ± 2.22	20357.52 ± 37.14	20595	1.01 ± 0.01
1j: b-jet veto	166.05 ± 1.03	2430.73 ± 6.86	419.22 ± 5.95	1599.27 ± 4.80	546.78 ± 2.34	53.43 ± 12.54	4923.90 ± 26.48	534.83 ± 10.58	268.17 ± 2.00	10776.32 ± 32.94	10854	1.01 ± 0.01
1j: Max lepton-MT (DF)	141.18 ± 0.94	2285.49 ± 6.65	363.05 ± 5.53	1528.02 ± 4.69	522.81 ± 2.27	40.33 ± 11.15	1988.44 ± 17.23	476.35 ± 7.17	62.35 ± 0.98	7266.84 ± 24.00	7365	1.01 ± 0.01
1j: $Z \to \tau\tau$ veto (DF)	119.78 ± 0.77	1683.65 ± 5.71	273.89 ± 4.89	1095.34 ± 3.96	384.21 ± 1.95	18.85 ± 5.39	690.52 ± 10.62	310.95 ± 5.50	31.70 ± 0.77	4489.10 ± 15.78	4573	1.02 ± 0.02
1j: $m_{\ell\ell} < 55$ GeV	100.25 ± 0.59	491.15 ± 3.07	138.06 ± 3.70	294.00 ± 2.05	109.78 ± 1.09	5.82 ± 1.31	382.53 ± 7.85	128.61 ± 4.00	18.61 ± 0.59	1568.55 ± 10.40	1655	1.06 ± 0.03
1j: $E_{\text{T,rel}}^{\text{miss,track}} > 35$ GeV (SF)	100.25 ± 0.59	491.15 ± 3.07	138.06 ± 3.70	294.00 ± 2.05	109.78 ± 1.09	5.82 ± 1.31	382.53 ± 7.85	128.61 ± 4.00	18.61 ± 0.59	1568.55 ± 10.40	1655	1.06 ± 0.03
1j: $\Delta\phi_{\ell\ell} < 1.8$	87.25 ± 0.49	422.03 ± 2.85	118.27 ± 3.42	266.64 ± 1.95	101.00 ± 1.00	4.56 ± 1.17	22.33 ± 1.93	88.02 ± 2.89	6.06 ± 0.39	1028.91 ± 6.18	1128	1.10 ± 0.03
1j: $f_{recoil} < 0.10$ (SF)	87.25 ± 0.49	422.03 ± 2.85	118.27 ± 3.42	266.64 ± 1.95	101.00 ± 1.00	4.56 ± 1.17	22.33 ± 1.93	88.02 ± 2.89	6.06 ± 0.39	1028.91 ± 6.18	1128	1.10 ± 0.03
1j: low p_{T}	13.89 ± 0.19	47.66 ± 0.95	31.06 ± 1.82	32.98 ± 0.68	11.84 ± 0.38	1.26 ± 0.60	6.83 ± 1.09	38.34 ± 2.06	3.07 ± 0.27	173.04 ± 3.27	196	1.13 ± 0.08
1j: high p_{T}	73.36 ± 0.45	374.37 ± 2.69	87.21 ± 2.89	233.66 ± 1.83	89.16 ± 0.93	3.30 ± 1.01	15.50 ± 1.60	49.67 ± 2.02	2.99 ± 0.28	855.87 ± 5.25	932	1.09 ± 0.04
1j: $0.75 \cdot m_{\text{H}} \leq m_{\text{T}} \leq m_{\text{H}}$	48.81 ± 0.37	144.85 ± 1.67	41.28 ± 1.98	75.59 ± 1.04	29.40 ± 0.61	0.80 ± 0.44	2.44 ± 0.69	39.94 ± 1.73	0.54 ± 0.19	334.85 ± 3.44	407	1.22 ± 0.06
1j: SSCR	1.91 ± 0.35	1.00 ± 0.13	116.23 ± 3.40	1.36 ± 0.14	1.83 ± 0.43	4.75 ± 1.18	0.83 ± 0.37	62.15 ± 2.60	2.95 ± 0.25	191.09 ± 4.49	193	1.01 ± 0.08
1j: Z VR	225.66 ± 1.31	2961.14 ± 7.41	663.88 ± 7.66	8967.03 ± 11.45	2495.32 ± 4.62	113.38 ± 15.97	8168.62 ± 33.20	878.37 ± 15.33	672.07 ± 3.18	24919.82 ± 43.22	25759	1.03 ± 0.01
1j: Z VR ($E_{\text{T,rel}}^{\text{miss}}$)	74.30 ± 0.69	1368.80 ± 5.18	176.36 ± 3.97	4508.62 ± 8.01	1197.11 ± 3.13	2.79 ± 0.84	256.61 ± 5.88	192.68 ± 4.69	13.12 ± 0.51	7716.09 ± 13.20	7763	1.01 ± 0.01
1j: Z VR ($E_{\text{T,rel}}^{\text{miss,track}}$)	52.65 ± 0.61	1042.27 ± 4.54	109.54 ± 3.10	3592.30 ± 7.15	964.07 ± 2.76	1.06 ± 0.51	2.79 ± 0.68	110.39 ± 3.41	0.35 ± 0.20	5822.78 ± 10.07	5863	1.01 ± 0.01
1j: Z VR (f_{recoil})	31.57 ± 0.48	726.45 ± 3.80	69.29 ± 2.43	1960.89 ± 5.28	612.86 ± 2.18	0.75 ± 0.41	1.05 ± 0.36	67.40 ± 2.64	0.08 ± 0.18	3438.76 ± 7.77	3477	1.01 ± 0.02
1j: WW CR (no SF $E_{\text{T,rel}}^{\text{miss,track}}$)	4.28 ± 0.38	1159.92 ± 4.75	126.15 ± 3.06	827.09 ± 3.46	266.92 ± 1.52	15.42 ± 8.67	81.35 ± 3.52	152.06 ± 3.07	12.81 ± 0.43	2641.72 ± 11.97	2646	1.00 ± 0.02
Scale factors		NF = 1.06	NFs applied	NF = 1.03	NF = 1.03		NFs applied					
1j: WW control region	4.28 ± 0.38	1159.92 ± 4.75	126.15 ± 3.06	827.09 ± 3.46	266.92 ± 1.52	15.42 ± 8.67	81.35 ± 3.52	152.06 ± 3.07	12.81 ± 0.43	2641.72 ± 11.97	2646	1.00 ± 0.02
1j: WW control region (SF f_{recoil})	4.28 ± 0.38	1159.92 ± 4.75	126.15 ± 3.06	827.09 ± 3.46	266.92 ± 1.52	15.42 ± 8.67	81.35 ± 3.52	152.06 ± 3.07	12.81 ± 0.43	2641.72 ± 11.97	2646	1.00 ± 0.02
1j: Top CR (no SF $E_{\text{T,rel}}^{\text{miss,track}}$)	26.71 ± 0.56	347.02 ± 2.72	73.34 ± 2.43	6599.58 ± 9.73	1707.21 ± 3.67	8.27 ± 4.55	720.87 ± 10.78	127.60 ± 5.67	66.08 ± 0.97	9649.97 ± 17.07	9741	1.01 ± 0.01
1j: Top CR	16.96 ± 0.47	244.87 ± 2.23	49.19 ± 1.99	4674.09 ± 8.17	1434.80 ± 3.31	5.32 ± 4.17	204.04 ± 5.62	90.46 ± 3.85	12.32 ± 0.40	6715.10 ± 12.27	6717	1.00 ± 0.01
1j: Top CR (SF f_{recoil})	21.45 ± 0.51	304.55 ± 2.55	58.95 ± 2.18	5783.48 ± 9.11	1485.23 ± 3.41	3.01 ± 1.82	187.71 ± 5.74	107.77 ± 4.20	15.65 ± 0.45	7946.34 ± 12.65	7934	1.00 ± 0.01

Table D.2: Full cutflow for the 8 TeV ggF $N_{\text{jet}} = 0$ and $= 1$ $ee{+}\mu\mu$ signal and control regions. Uncertainties are statistical only. The Data/MC ratio does not include signal yields.

	Signal [125 GeV]	WW	Other VV	$t\bar{t}$	Single Top	$Z \to \ell\ell + \gamma$/jets	$Z \to \tau\tau + \gamma$/jets	W+jets	QCD	Total Bkg.	Observed	Data/MC
	913.38 ± 2.99	11968.71 ± 15.03	10290.00 ± 24.00	60864.97 ± 29.01	5846.84 ± 7.32	16567081.31 ± 8163.91	55564.19 ± 99.41	21993.57 ± 162.28	11913.82 ± 11.20	16745523.40 ± 8166.24	17068931	1.02 ± 0.00
lepton p_{T}	879.86 ± 2.95	11829.38 ± 14.94	9779.67 ± 22.96	60378.04 ± 28.89	5804.62 ± 7.28	16225683.08 ± 8120.74	49080.33 ± 93.44	18535.11 ± 152.08	7998.49 ± 9.04	16389088.72 ± 8122.81	16554616	1.01 ± 0.00
Scale factors				NF = 1.05	NF = 1.05							
OS leptons	850.52 ± 2.55	11799.62 ± 14.92	7748.74 ± 18.53	63360.16 ± 30.36	6047.50 ± 7.27	16192345.92 ± 8112.88	48995.52 ± 93.36	18826.16 ± 148.73	6901.81 ± 8.46	16356025.43 ± 8114.88	16519905	1.01 ± 0.00
$m_{\ell\ell} > 10, 12$ GeV	828.40 ± 2.54	11742.00 ± 14.89	7564.33 ± 18.00	63107.21 ± 30.30	6026.80 ± 7.26	16162912.14 ± 8112.57	48934.46 ± 93.31	22169.52 ± 144.80	2429.08 ± 5.10	16324885.54 ± 8114.50	16379188	1.00 ± 0.00
Z veto (SF)	770.61 ± 2.17	9216.56 ± 13.18	2668.65 ± 12.48	49903.22 ± 26.94	4761.06 ± 6.41	1835968.42 ± 2031.24	47132.54 ± 91.55	7870.28 ± 73.28	2193.88 ± 4.70	1959714.62 ± 2034.90	2012653	1.03 ± 0.00
Scale factors				NF = 1.05	NF = 1.05	NFs applied	NFs applied					
$E_{\text{T,[rel],(clj)}}^{\text{miss,(track)}} > [40], (20)$	288.42 ± 1.13	4075.19 ± 8.78	642.13 ± 6.66	18651.80 ± 16.46	2046.97 ± 4.21	41142.35 ± 264.49	1062.35 ± 13.00	836.17 ± 14.18	45.04 ± 0.72	68502.00 ± 265.96	70601	1.03 ± 0.01
Z VR (incl)	57.79 ± 1.31	2525.43 ± 6.92	4895.68 ± 12.97	13203.99 ± 13.87	1265.75 ± 3.41	14326943.72 ± 7854.16	1801.91 ± 18.06	14299.23 ± 124.89	235.20 ± 1.98	14365170.93 ± 7855.20	14366535	1.00 ± 0.00
Z VR (incl), $E_{\text{T,rel}}^{\text{miss}} > 40$ GeV	7.19 ± 0.57	1021.82 ± 4.41	1652.23 ± 7.94	5358.01 ± 8.83	563.14 ± 2.21	311269.08 ± 1030.37	41.80 ± 2.56	401.40 ± 20.17	5.12 ± 0.34	320312.60 ± 1030.65	320307	1.00 ± 0.00
Top VR (incl)	26.97 ± 0.47	284.44 ± 2.40	71.22 ± 2.31	18435.23 ± 16.39	1620.44 ± 3.64	2830.42 ± 67.36	83.10 ± 3.85	196.69 ± 6.68	6.15 ± 0.26	23527.68 ± 69.93	24022	1.02 ± 0.01
Scale factors		NF = 1.22		NF = 1.09	NF = 1.09	NFs applied						
0j: jet veto	171.45 ± 0.67	3247.40 ± 8.66	366.46 ± 5.08	419.48 ± 2.51	211.99 ± 1.38	31818.84 ± 235.84	684.27 ± 10.37	503.98 ± 11.14	29.22 ± 0.60	37281.66 ± 236.56	38015	1.02 ± 0.01
0j: $\Delta\phi_{\ell\ell,MET} > 1.57$	171.23 ± 0.67	3243.99 ± 8.66	363.49 ± 5.07	416.93 ± 2.50	211.57 ± 1.38	29252.31 ± 223.43	621.31 ± 9.88	492.62 ± 10.79	25.84 ± 0.57	34628.06 ± 224.15	35425	1.02 ± 0.01
0j: $p_{T,\ell\ell}$ >30 GeV	160.75 ± 0.65	3000.77 ± 8.34	316.87 ± 4.78	395.56 ± 2.44	202.05 ± 1.33	6862.84 ± 101.33	21.05 ± 1.79	396.06 ± 6.67	2.60 ± 0.29	11197.81 ± 102.05	11656	1.04 ± 0.01
0j: $m_{\ell\ell} < 55$ GeV	146.88 ± 0.58	1252.63 ± 5.39	182.73 ± 3.88	109.55 ± 1.28	64.22 ± 0.78	4900.17 ± 34.13	8.70 ± 1.13	250.57 ± 5.27	1.98 ± 0.27	6770.54 ± 35.22	6785	1.00 ± 0.01
0j: $E_{\text{T,rel}}^{\text{miss,track}} > 40$ GeV (SF)	120.94 ± 0.53	1093.77 ± 5.05	109.99 ± 2.81	99.39 ± 1.22	58.92 ± 0.73	661.66 ± 14.81	0.28 ± 0.20	133.48 ± 3.34	0.53 ± 0.24	2158.02 ± 16.31	2197	1.02 ± 0.02
0j: $\Delta\phi_{\ell\ell} < 1.8$	117.00 ± 0.53	1064.88 ± 4.98	107.69 ± 2.79	96.47 ± 1.20	57.44 ± 0.68	649.95 ± 14.72	0.28 ± 0.20	122.28 ± 3.17	0.46 ± 0.24	2099.45 ± 16.17	2127	1.01 ± 0.02
0j: $f_{\text{recoil}} < 0.1$ (SF)	74.77 ± 0.42	783.77 ± 4.29	71.52 ± 2.25	40.86 ± 0.78	30.99 ± 0.50	90.37 ± 5.26	0.11 ± 0.11	78.54 ± 2.46	0.04 ± 0.23	1096.19 ± 7.62	1108	1.01 ± 0.03
0j: low p_{T}	13.07 ± 0.15	72.09 ± 1.29	19.64 ± 1.31	6.27 ± 0.30	4.41 ± 0.19	21.97 ± 2.53	0.00 ± 0.00	33.80 ± 1.70	-0.13 ± 0.22	158.03 ± 3.59	159	1.01 ± 0.08
0j: high p_{T}	61.70 ± 0.40	711.69 ± 4.09	51.88 ± 1.82	34.59 ± 0.72	26.58 ± 0.47	68.40 ± 4.61	0.11 ± 0.11	44.75 ± 1.78	0.17 ± 0.04	938.16 ± 6.73	949	1.01 ± 0.03
0j: $0.75 \cdot m_{\text{H}} \leq m_{\text{T}} \leq m_{\text{H}}$	58.27 ± 0.34	347.80 ± 2.85	32.52 ± 1.57	10.89 ± 0.40	8.31 ± 0.28	64.29 ± 4.54	0.11 ± 0.11	53.17 ± 1.98	-0.05 ± 0.22	517.04 ± 5.95	510	0.99 ± 0.05
0j: SSCR	0.89 ± 0.24	0.95 ± 0.13	57.91 ± 2.32	0.19 ± 0.05	0.31 ± 0.11	0.23 ± 0.18	0.00 ± 0.00	41.54 ± 1.94	0.14 ± 0.04	101.27 ± 3.03	89	0.88 ± 0.10
0j: Z VR	20.75 ± 0.61	1626.34 ± 5.57	2447.66 ± 8.35	173.32 ± 1.59	92.31 ± 1.01	11055491.90 ± 6875.07	1356.92 ± 16.09	10385.52 ± 102.39	143.34 ± 1.66	11071717.30 ± 6875.86	11014687	0.99 ± 0.00
0j: Z VR ($E_{\text{T,rel}}^{\text{miss}}$)	2.26 ± 0.25	784.30 ± 4.27	879.61 ± 5.42	102.15 ± 1.24	55.08 ± 0.79	250892.95 ± 918.49	27.97 ± 2.10	272.74 ± 17.17	3.15 ± 0.30	253017.95 ± 918.68	253043	1.00 ± 0.00
0j: Z VR ($p_{T,\ell\ell}$)	1.63 ± 0.23	704.91 ± 4.06	804.77 ± 5.18	95.63 ± 1.20	51.41 ± 0.75	33172.47 ± 385.89	1.97 ± 0.51	109.53 ± 7.37	0.02 ± 0.17	34940.71 ± 386.02	34951	1.00 ± 0.01
0j: Z VR ($E_{\text{T,rel}}^{\text{miss,track}}$)	1.25 ± 0.22	578.44 ± 3.69	681.70 ± 4.75	83.88 ± 1.12	44.89 ± 0.63	3198.08 ± 135.29	0.18 ± 0.18	40.82 ± 2.38	-0.15 ± 0.14	4627.85 ± 135.45	4623	1.00 ± 0.03
0j: Z VR (f_{recoil})	0.80 ± 0.19	419.83 ± 3.15	482.83 ± 3.95	36.26 ± 0.74	23.71 ± 0.43	434.59 ± 60.68	0.00 ± 0.00	21.87 ± 1.43	-0.08 ± 0.11	1418.99 ± 60.92	1419	1.00 ± 0.05
0j: WW CR (no SF $E_{\text{T,rel}}^{\text{miss,track}}$)	20.38 ± 0.25	801.34 ± 4.32	64.57 ± 1.96	83.01 ± 1.12	48.70 ± 0.67	1678.83 ± 66.70	9.69 ± 1.21	77.87 ± 2.94	0.39 ± 0.05	2764.40 ± 66.96	2637	0.95 ± 0.03
Scale factors		NF = 1.22		NF = 1.09	NF = 1.09	NFs applied						
0j: WW CR	7.02 ± 0.20	584.37 ± 3.70	44.34 ± 1.50	69.28 ± 1.02	39.98 ± 0.60	123.32 ± 21.44	0.39 ± 0.29	34.57 ± 1.72	0.07 ± 0.02	896.32 ± 21.91	863	0.96 ± 0.04
0j: WW CR (SF f_{recoil})	4.28 ± 0.18	428.54 ± 3.18	30.67 ± 1.24	29.28 ± 0.66	21.33 ± 0.44	6.29 ± 1.63	0.26 ± 0.26	22.19 ± 1.13	0.04 ± 0.02	538.60 ± 4.04	526	0.98 ± 0.04
0j: WW VR	0.47 ± 0.16	706.87 ± 4.06	44.63 ± 1.56	132.10 ± 1.41	61.21 ± 0.69	70.51 ± 19.15	0.21 ± 0.21	22.41 ± 0.91	0.06 ± 0.02	1038.00 ± 19.72	998	0.96 ± 0.04
Scale factors		NF = 1.06		NF = 1.03	NF = 1.03	NFs applied	NFs applied					
1j: one jet	77.13 ± 0.74	1122.13 ± 4.74	193.64 ± 3.57	3648.34 ± 7.19	966.67 ± 2.88	8334.16 ± 113.12	279.44 ± 6.16	177.59 ± 6.71	12.77 ± 0.37	14734.75 ± 113.90	15333	1.04 ± 0.01
1j: b-jet veto	66.47 ± 0.66	981.51 ± 4.40	164.97 ± 3.28	718.43 ± 3.21	242.13 ± 1.63	6867.41 ± 100.84	240.81 ± 5.66	137.07 ± 5.80	10.23 ± 0.32	9362.56 ± 101.38	9892	1.06 ± 0.02
1j: Max lepton-MT (DF)	66.47 ± 0.66	981.51 ± 4.40	164.97 ± 3.28	718.43 ± 3.21	242.13 ± 1.63	7464.26 ± 109.63	240.81 ± 5.66	137.07 ± 5.80	10.23 ± 0.32	9959.41 ± 110.12	9892	0.99 ± 0.01
1j: $Z \to \tau\tau$ veto (DF)	66.47 ± 0.66	981.51 ± 4.40	164.97 ± 3.28	718.43 ± 3.21	242.13 ± 1.63	7464.26 ± 109.63	240.81 ± 5.66	137.07 ± 5.80	10.23 ± 0.32	9959.41 ± 110.12	9892	0.99 ± 0.01
1j: $m_{\ell\ell} < 55$ GeV	57.87 ± 0.51	354.63 ± 2.65	79.44 ± 2.41	224.16 ± 1.79	83.52 ± 1.04	3466.06 ± 24.07	167.80 ± 4.68	73.11 ± 4.32	7.79 ± 0.28	4456.50 ± 25.24	5123	1.15 ± 0.02
1j: $E_{\text{T,rel}}^{\text{miss,track}} > 35$ GeV (SF)	42.62 ± 0.43	295.28 ± 2.42	49.72 ± 1.84	191.55 ± 1.65	71.81 ± 0.86	198.40 ± 8.79	1.75 ± 0.51	37.49 ± 1.98	0.20 ± 0.05	846.20 ± 9.70	959	1.13 ± 0.04
1j: $\Delta\phi_{\ell\ell} < 1.8$	38.57 ± 0.41	267.79 ± 2.30	44.91 ± 1.75	177.45 ± 1.59	67.35 ± 0.82	197.91 ± 9.20	1.50 ± 0.49	30.27 ± 1.77	0.17 ± 0.05	787.34 ± 9.98	888	1.13 ± 0.04
1j: $f_{recoil} < 0.10$ (SF)	23.15 ± 0.28	189.85 ± 1.95	29.73 ± 1.43	97.17 ± 1.18	43.37 ± 0.65	26.18 ± 2.95	0.85 ± 0.35	17.39 ± 1.31	0.02 ± 0.03	404.57 ± 4.26	467	1.15 ± 0.05
1j: low p_{T}	4.37 ± 0.10	22.99 ± 0.67	6.92 ± 0.72	14.15 ± 0.44	5.85 ± 0.28	8.05 ± 1.26	0.17 ± 0.17	6.63 ± 0.84	0.01 ± 0.01	64.76 ± 1.89	64	0.99 ± 0.13
1j: high p_{T}	18.78 ± 0.26	166.86 ± 1.83	22.81 ± 1.23	83.02 ± 1.09	37.52 ± 0.58	18.13 ± 2.67	0.68 ± 0.30	10.76 ± 1.00	0.02 ± 0.02	339.80 ± 3.82	403	1.19 ± 0.06
1j: $0.75 \cdot m_{\text{H}} \leq m_{\text{T}} \leq m_{\text{H}}$	15.97 ± 0.22	59.43 ± 1.09	11.30 ± 0.92	22.93 ± 0.57	10.68 ± 0.35	13.65 ± 2.53	0.00 ± 0.00	11.17 ± 0.97	0.00 ± 0.01	129.15 ± 3.14	143	1.11 ± 0.10
1j: SSCR	0.76 ± 0.26	0.22 ± 0.06	22.73 ± 1.44	0.39 ± 0.07	0.30 ± 0.27	0.00 ± 0.00	0.02 ± 0.02	13.77 ± 1.23	-0.05 ± 0.04	37.38 ± 1.92	34	0.91 ± 0.16
1j: Z VR	18.71 ± 0.75	653.93 ± 3.53	1527.66 ± 7.70	1874.64 ± 5.23	545.44 ± 2.18	2413668.33 ± 3258.62	317.73 ± 6.59	2821.04 ± 59.90	65.40 ± 0.92	2421474.16 ± 3259.19	2476415	1.02 ± 0.00
1j: Z VR ($E_{\text{T,rel}}^{\text{miss}}$)	3.17 ± 0.40	291.34 ± 2.43	515.72 ± 4.62	945.26 ± 3.66	256.97 ± 1.45	49491.46 ± 423.51	8.08 ± 0.96	89.91 ± 9.01	1.45 ± 0.14	51600.19 ± 423.66	51512	1.00 ± 0.01
1j: Z VR ($E_{\text{T,rel}}^{\text{miss,track}}$)	1.78 ± 0.31	213.39 ± 2.09	380.63 ± 3.94	747.25 ± 3.26	201.96 ± 1.24	1694.06 ± 102.52	0.39 ± 0.21	20.93 ± 2.00	0.05 ± 0.04	3258.67 ± 102.69	3319	1.02 ± 0.04
1j: Z VR (f_{recoil})	0.65 ± 0.19	147.38 ± 1.74	246.13 ± 3.14	408.93 ± 2.41	128.95 ± 1.01	224.22 ± 44.89	0.23 ± 0.14	11.90 ± 1.21	0.00 ± 0.02	1167.74 ± 45.13	1149	0.98 ± 0.05
1j: WW CR (no SF $E_{\text{T,rel}}^{\text{miss,track}}$)	0.92 ± 0.29	385.61 ± 2.76	46.91 ± 1.65	333.42 ± 2.19	100.28 ± 0.87	1342.06 ± 67.71	2.55 ± 0.58	31.37 ± 1.67	0.59 ± 0.08	2242.78 ± 67.85	2057	0.92 ± 0.03
Scale factors		NF = 1.06		NF = 1.03	NF = 1.03	NFs applied	NFs applied					
1j: WW control region	0.56 ± 0.21	269.58 ± 2.31	30.30 ± 1.31	243.08 ± 1.87	73.99 ± 0.75	52.69 ± 17.37	0.23 ± 0.23	14.19 ± 0.84	0.03 ± 0.01	684.08 ± 17.71	651	0.95 ± 0.04
1j: WW control region (SF f_{recoil})	0.44 ± 0.19	185.36 ± 1.92	19.63 ± 1.02	129.58 ± 1.37	44.25 ± 0.57	9.14 ± 8.51	0.23 ± 0.23	9.29 ± 0.61	0.02 ± 0.01	397.50 ± 8.93	371	0.93 ± 0.05
1j: Top CR (no SF $E_{\text{T,rel}}^{\text{miss,track}}$)	10.55 ± 0.34	139.60 ± 1.75	28.63 ± 1.40	2956.73 ± 6.50	731.11 ± 2.40	1308.84 ± 46.66	38.57 ± 2.45	40.54 ± 3.38	2.54 ± 0.17	5246.56 ± 47.41	5441	1.04 ± 0.02
1j: Top CR	5.65 ± 0.24	80.50 ± 1.30	14.11 ± 0.95	1765.23 ± 5.01	525.19 ± 2.01	47.06 ± 9.36	0.47 ± 0.22	16.73 ± 1.99	-0.00 ± 0.06	2449.28 ± 11.11	2457	1.00 ± 0.02
1j: Top CR (SF f_{recoil})	4.14 ± 0.19	71.68 ± 1.26	11.52 ± 0.88	1289.21 ± 4.29	376.34 ± 1.71	24.03 ± 13.09	0.33 ± 0.19	9.94 ± 1.60	0.04 ± 0.03	1783.09 ± 14.06	1791	1.00 ± 0.03

Table D.3: Event yields in the VBF BDT $e\mu$+μe (top) and ee+$\mu\mu$ (bottom) signal region. The Data/MC ratio does not include signal yields.

$e\mu$+μe	VBF [125 GeV]	VH [125 GeV]	ggF [125 GeV]	WW	$WZ/ZZ/W\gamma$	$t\bar{t}$	Single Top
≥2j: Fit region	11.52 ± 0.14	0.10 ± 0.05	4.59 ± 0.08	8.58 ± 0.33	3.35 ± 0.57	19.07 ± 0.61	3.52 ± 0.27
≥2j: −0.48 <BDT< 0.30	4.19 ± 0.09	0.08 ± 0.05	3.03 ± 0.06	5.99 ± 0.28	2.53 ± 0.49	16.97 ± 0.59	3.16 ± 0.27
≥2j: 0.30 <BDT< 0.78	4.21 ± 0.09	0.02 ± 0.02	1.21 ± 0.04	2.06 ± 0.16	0.75 ± 0.28	1.85 ± 0.14	0.29 ± 0.04
≥2j: 0.78 <BDT< 1.0	3.12 ± 0.07	0.00 ± 0.00	0.36 ± 0.02	0.53 ± 0.07	0.06 ± 0.06	0.26 ± 0.05	0.07 ± 0.02
≥2j: 0.30 <BDT< 1.0	7.33 ± 0.11	0.02 ± 0.02	1.56 ± 0.04	2.60 ± 0.18	0.82 ± 0.28	2.10 ± 0.15	0.37 ± 0.04

$Z \to \ell\ell$+jets	EW $Z \to \ell\ell$+jets	$Z \to \tau\tau$+jets	EW $Z \to \tau\tau$+jets	W+jets	QCD	Total Bkg.(+ggF)	Observed	Data/MC
0.02 ± 0.02	0.00 ± 0.00	4.16 ± 0.53	0.66 ± 0.20	3.82 ± 0.85	2.11 ± 0.17	49.89 ± 1.40	57	1.14 ± 0.15
0.02 ± 0.02	0.00 ± 0.00	3.85 ± 0.52	0.18 ± 0.09	3.38 ± 0.81	1.84 ± 0.16	40.94 ± 1.31	37	0.90 ± 0.15
0.00 ± 0.00	0.00 ± 0.00	0.26 ± 0.06	0.36 ± 0.15	0.43 ± 0.26	0.27 ± 0.06	7.48 ± 0.47	14	1.87 ± 0.51
0.00 ± 0.00	0.00 ± 0.00	0.06 ± 0.04	0.12 ± 0.09	0.01 ± 0.02	0.00 ± 0.00	1.48 ± 0.15	6	4.06 ± 1.71
0.00 ± 0.00	0.00 ± 0.00	0.32 ± 0.07	0.48 ± 0.17	0.44 ± 0.26	0.27 ± 0.06	8.95 ± 0.50	20	2.23 ± 0.51

ee+$\mu\mu$	VBF [125 GeV]	VH [125 GeV]	ggF [125 GeV]	WW	$WZ/ZZ/W\gamma$	$t\bar{t}$	Single Top
≥2j: Fit region	6.38 ± 0.11	0.06 ± 0.04	2.20 ± 0.05	4.94 ± 0.25	1.21 ± 0.27	12.04 ± 0.48	2.11 ± 0.22
≥2j: −0.48 <BDT< 0.30	2.17 ± 0.06	0.06 ± 0.04	1.48 ± 0.04	3.53 ± 0.22	0.89 ± 0.22	10.67 ± 0.47	1.83 ± 0.21
≥2j: 0.30 <BDT< 0.78	2.47 ± 0.07	0.00 ± 0.00	0.56 ± 0.03	1.14 ± 0.12	0.30 ± 0.15	1.18 ± 0.11	0.24 ± 0.06
≥2j: 0.78 <BDT< 1.0	1.74 ± 0.06	0.00 ± 0.00	0.16 ± 0.01	0.26 ± 0.05	0.02 ± 0.02	0.19 ± 0.05	0.04 ± 0.01
≥2j: 0.30 <BDT< 1.0	4.21 ± 0.09	0.00 ± 0.00	0.72 ± 0.03	1.40 ± 0.13	0.32 ± 0.15	1.37 ± 0.12	0.28 ± 0.06

$Z \to \ell\ell$+jets	EW $Z \to \ell\ell$+jets	$Z \to \tau\tau$+jets	EW $Z \to \tau\tau$+jets	W+jets	QCD	Total Bkg.(+ggF)	Observed	Data/MC
29.18 ± 2.25	0.55 ± 0.14	2.03 ± 0.32	0.15 ± 0.08	1.24 ± 0.51	0.16 ± 0.04	55.80 ± 2.42	72	1.29 ± 0.16
24.61 ± 2.18	0.42 ± 0.12	1.74 ± 0.32	0.05 ± 0.05	0.99 ± 0.47	0.16 ± 0.04	46.38 ± 2.33	52	1.12 ± 0.17
4.21 ± 0.54	0.08 ± 0.04	0.28 ± 0.08	0.09 ± 0.05	0.28 ± 0.19	-0.00 ± 0.00	8.35 ± 0.63	14	1.68 ± 0.47
0.36 ± 0.11	0.05 ± 0.05	0.01 ± 0.01	0.00 ± 0.00	-0.03 ± 0.02	-0.00 ± 0.00	1.07 ± 0.14	6	5.61 ± 2.41
4.57 ± 0.55	0.13 ± 0.07	0.29 ± 0.08	0.09 ± 0.05	0.25 ± 0.19	-0.00 ± 0.00	9.42 ± 0.64	20	2.12 ± 0.50

Bibliography

[1] ATLAS Collaboration, *Observation of a new particle in the search for the Standard Model Higgs boson with the ATLAS detector at the LHC*, Phys. Lett. B **716** (2012) 1–29.

[2] CMS Collaboration, *Observation of a new boson at a mass of 125 GeV with the CMS experiment at the LHC*, Phys. Lett. B **716** (2012) 30–61.

[3] ATLAS Collaboration, *Measurements of the properties of the Higgs-like boson in the $WW^{(*)} \to \ell\nu\ell\nu$ decay channel with the ATLAS detector using 25 fb^{-1} of proton-proton collision data*, ATLAS-CONF-2013-030 . http://cds.cern.ch/record/1527126.

[4] ATLAS Collaboration, *Measurements of Higgs boson production and couplings in diboson final states with the ATLAS detector at the LHC*, Phys. Lett. B **726** (2013) 88–119.

[5] F. Englert and R. Brout, *Broken symmetry and the mass of gauge vector mesons*, Phys. Rev. Lett. **13** (1964) 321–323.

[6] P. W. Higgs, *Broken symmetries and the masses of gauge bosons*, Phys. Rev. Lett. **13** (1964) 508–509.

[7] G. Guralnik, C. Hagen, and T. Kibble, *Global conservation laws and massless particles*, Phys.Rev.Lett **13** (1964) 585–587.

[8] ATLAS Collaboration, *Search for a fermiophobic Higgs boson in the diphoton decay channel with the ATLAS detector*, Eur. Phys. J. C **72** (2012) 2157.

[9] CMS Collaboration, *Search for a fermiophobic Higgs boson in pp collisions at $\sqrt{s} = 7$ TeV*, JHEP **09** (2012) 111.

[10] CMS Collaboration, *Searches for HIggs bosons in pp collisions at $\sqrt{s} = 7$ and 8 TeV in the context of four-generation and fermiophobic models*, Phys. Lett. B **06** (2013) 43.

[11] Saurabh D. Rindani, *Strong gauge boson scattering at the LHC*, arXiv:0910.5068 [hep-ph].

[12] ATLAS Collaboration, *Cavern background measurements and comparison with simulation*, ATLAS-COM-MUON-2013-003. http://cds.cern.ch/record/1513176.

[13] ATLAS Collaboration, *Electron performance measurements with the ATLAS detector using the 2011 LHC proton-proton collison data*, ATLAS-COM-PHYS-2013-1448. http://cds.cern.ch/record/1612217.

[14] ATLAS Collaboration, *Electron reconstruction and identification efficiency measurements with the ATLAS detector using the 2011 LHC proton-proton collision data*, Eur. Phys. J. C **74** (2014) 2941.

[15] K. Yoshihara, D. Schaefer, R. Polifka, L. Ma for HWW working group, *Object Selections in the $H \to WW^* \to \ell\nu\ell\nu$ analysis with 20 fb^{-1} of data collected with the ATLAS detector at $\sqrt{s} = 8$ TeV*, Tech. Rep. ATL-COM-PHYS-2013-1504, CERN, Geneva, 2014. http://cds.cern.ch/record/1624408.

[16] K. Yoshihara, D. Schaefer, L. Yuan, J. Machado Miguens for HWW working group, *Background estimates in the $H \to WW^* \to \ell\nu\ell\nu$ analysis with 20* fb^{-1} *of data collected with the ATLAS detector at* $\sqrt{s} = 8$ TeV, Tech. Rep. ATL-COM-PHYS-2013-1630, CERN, Geneva, 2014. http://cds.cern.ch/record/1636127.

[17] ATLAS Collaboration, *Measurement of the Higgs boson mass from the $H \to \gamma\gamma$ and $H \to ZZ^* \to 4\ell$ channels with the ATLAS detector using 25 fb^{-1} of pp collision data*, arXiv:1406.3827 [hep-ex].

[18] ATLAS Collaboration, *Evidence for the spin-0 nature of the Higgs boson using ATLAS data*, Phys. Lett. B **726** (2013) .

[19] http://en.wikipedia.org/wiki/Spontaneous_symmetry_breaking.

[20] http://philsci-archive.pitt.edu/9295/1/Spontaneous_symmetry_breaking_in_the_Higgs_mechanism.pdf.

[21] http://www.physik.uni-leipzig.de/~zierenberg/work/zierenberg_spontaneousSymmetryBreaking.pdf.

[22] http://guava.physics.uiuc.edu/~nigel/courses/569/Essays_Fall2007/files/xianhao_xin.pdf.

[23] J. Goldstone, *Field theories with superconductor solutions*, Il Nuovo Cimento **19(1)** (1961) 154–164.

[24] J. Goldstone, A. Salam, S. Weinberg, *Broken symmetries*, Phys. Rev. **126** (1962) 965–970.

[25] http://en.wikipedia.org/wiki/Higgs_mechanism.

[26] http://www.theorie.physik.uni-muenchen.de/lsfrey/teaching/archiv/sose_09/rng/higgs_mechanism.pdf.

[27] S. Weinberg, *Physical Processes in a Convergent Theory of the Weak and Electromagnetic Interactions*, Phys. Rev. Lett. **27(24)** (1971) 1688–1691.

[28] S. Weinberg, *General Theory of Broken Local Symmetries*, Phys. Rev. D **7(4)** (1973) 1068–1082.

[29] ATLAS Collaborations, *Physics at a High-Luminosity LHC with ATLAS*, ATL-PHYS-PUB-2013-007 (2013) .

[30] S. L. Glashow Nucl. Phys. **B22** (1961) 579.

[31] S. Weinberg Phys. Rev. Lett. **19** (1967) 1264.

[32] A. Salam, Elementary Particle Theory,. Almqvist and Wiksells, Stockholm, 1968.

[33] ATLAS Collaboration, *Search for the bb decayof the Standard Model Higgs boson in associated W/ZH production with the ATLAS detector*, ATLAS-CONF-2013-079. http://cds.cern.ch/record/1563235.

[34] ATLAS Collaboration, *Evidence for Higgs Boson Decays to the $\tau^+\tau^-$ Final State with the ATLAS Detector*, ATLAS-CONF-2013-108. http://cds.cern.ch/record/1632191.

[35] CMS Collaboration, *Evidence for the direct decay of the 125 GeV Higgs boson to fermions*, Nature Physics (2014) .

[36] M. Peskin, D. Schroeder, *An Introduction to Quantum Field Theory*, .

[37] J. Bjorken, S. Drell, *Relativistic Quantum Mechanics.*, .

[38] Max Baak, Roman Kogler, *The global electroweak Standard Model fit after the Higgs discovery*, arXiv:1306.0571 [hep-ph].

[39] ATLAS Collaboration, *Measurement of WW Production in pp colisions at $\sqrt{s} = 7$ TeV with the ATLAS Detector and limits on anomalous WWZ and $WW\gamma$ couplings*, Phys. Rev. D **87** (2013) 112001.

[40] ATLAS Collaboration, *Measurement of the WW production cross-section in $\sqrt{s} = 7$ TeV pp collisions at ATLAS and limits on anomalous gauge couplings*, Phys. Lett. B **712** (2012) 289–308.

[41] ATLAS Collaboration, *Measurement of the $t\bar{t}$ production cross-section using $e\mu$ events with b-tagged jets in pp collisions at $\sqrt{s} = 7$ and 8 TeV with the ATLAS detector*, submitted to Eur. Phys. J. C (2014) , arXiv:1406.5375 [hep-ex].

[42] ATLAS Collaboration, *Measurement of the cross section for associated production of a top quark and a W boson at $\sqrt{s} = 8$ TeV with the ATLAS detector*, ATLAS-CONF-2013-100. http://cds.cern.ch/record/1600799.

[43] ATLAS Collaboration, *Measurement of the $t-$channel single top-quark production cross section in pp collisions at $\sqrt{s} = 7$ TeV with the ATLAS detector*, Phys. Lett. B **717** (2012) 330–350.

[44] ATLAS Collaboration, *Measurement of the $W\ell\nu$ and $Z/\gamma^* \to \ell\ell$ production cross sections in proton proton collisions at $\sqrt{s} = 7$ TeV with the ATLAS detector*, JHEP12(2010)060 (2010) .

[45] ATLAS Collaboration, *Measurement of the low-mass Drell-Yan differential cross section at $\sqrt{s} = 7$ TeV using the ATLAS detector*, JHEP **06** (2014) 112.

[46] ATLAS Collaboration, *Measurement of the $W\gamma$ and $Z\gamma$ Production in pp collisions at $\sqrt{s} = 7$ TeV with the ATLAS Detector at the LHC*, Phys. Rev. D **87** (2013) 112003.

[47] ATLAS Collaboration, *Measurement of WZ Production in Proton-Proton Collisions at $\sqrt{s} = 7$ TeV with the ATLAS detector*, Eur. Phys. J. C **72:2173** (2012) .

[48] ATLAS Collaboration, *Measurement of ZZ production in pp collisions at $\sqrt{s} = 7$ TeV with the ATLAS detector and limits on anomalous ZZZ and $ZZ\gamma$ couplings*, JHEP03(2013)128 (2013) .

[49] ATLAS Collaboration, *Measurement of differential production cross-sections for a Z boson in association with b-jets in 7 TeV proton-proton collisions with the ATLAS detector*, arXiv:1407.3643 [hep-ex].

[50] ATLAS Collaboration, *Measurement of the production of a W boson in association with a charm quark in pp collisions at $\sqrt{s} = 7$ TeV with the ATLAS detector*, JHEP **05** (2014) 068.

[51] ATLAS Collaboration, *Measurement of the cross-section for W boson production in association with b-jets in pp collisions at $\sqrt{s}$=7 TeV with the ATLAS detector*, JHEP **06** (2013) 084.

[52] https://atlas.web.cern.ch/Atlas/GROUPS/PHYSICS/CombinedSummaryPlots/SM/ATLAS_c_SMSummary_TotalXsect_rotated/ATLAS_c_SMSummary_TotalXsect_rotated.pdf.

[53] ATLAS Collaboration, *Standard Model cross-section summaries for July 2014*, ATLAS-COM-PHYS-2014-575. http://twiki.cern.ch/twiki/bin/view/AtlasPublic/StandardModelPublicResults.

[54] LHC Higgs Cross Section Working Group, *Handbook of LHC Higgs Cross Sections: 1. Inclusive Observables*, CERN-2011-002 (2011) .

[55] LHC Higgs Cross Section Working Group, *Handbook of LHC Higgs Cross Sections: 2. Differential Distributions*, CERN-2012-002 (2012) .

[56] LHC Higgs Cross Section Working Group, *Handbook of LHC Higgs Cross Sections: 3. Inclusive Observables*, CERN-2013-004 (2013) .

[57] A. Djouadi and M. Spira and P. M. Zerwas, *Production of Higgs bosons in proton colliders: QCD corrections*, Phys. Lett. B **264** (1991) 440.

[58] S. Dawson, *Radiative corrections to Higgs boson production*, Nucl. Phys. **B359** (1991) 283.

[59] Spira, M. and Djouadi, A. and Graudenz, D. and Zerwas, P. M., *Higgs boson production at the LHC*, Nucl. Phys. **B453** (1995) 17, arXiv:hep-ph/9504378.

[60] R. Harlander and W. B. Kilgore, *Next-to-next-to-leading order Higgs production at hadron colliders*, Phys. Rev. Lett. **88** (2002) 201801, arXiv:hep-ph/0201206 [hep-ph].

[61] C. Anastasiou and K. Melnikov, *Higgs boson production at hadron colliders in NNLO QCD*, Nucl. Phys. **B646** (2002) 220, arXiv:hep-ph/0207004 [hep-ph].

[62] V. Ravindran, J. Smith, W. L. van Neerven, *NNLO corrections to the total cross-section for Higgs boson production in hadron hadron collisions*, Nucl. Phys. **B665** (2003) 325, arXiv:hep-ph/0302135 [hep-ph].

[63] S. Catani, D. de Florian, M. Grazzini, and P. Nason, *Soft-gluon re-summation for Higgs boson production at hadron colliders*, JHEP **0307** (2003) 028, arXiv:hep-ph/0306211.

[64] U. Aglietti, R. Bonciani, G. Degrassi, and A. Vicini, *Two loop light fermion contribution to Higgs production and decays*, Phys. Lett. **B595** (2004) 432, arXiv:hep-ph/0404071 [hep-ph].

[65] S. Actis, G. Passarino, C. Sturm, and S. Uccirati, *NLO Electroweak Corrections to Higgs Boson Production at Hadron Colliders*, Phys. Lett. **B670** (2008) 12, arXiv:0809.1301 [hep-ph].

[66] C. Anastasiou, R. Boughezal, and F. Petriello, *Mixed QCD-electroweak corrections to Higgs boson production in gluon fusion*, JHEP **0904** (2009) 003, arXiv:0811.3458 [hep-ph].

[67] D. de Florian, M. Grazzini, *Higgs production through gluon fusion: updated cross sections at the Tevatron and the LHC*, Phys. Lett. **B674** (2009) 291, arXiv:0901.2427 [hep-ph].

[68] J. Baglio and A. Djouadi, *Higgs production at the lHC*, JHEP **1103** (2011) 055, arXiv:1012.0530 [hep-ph].

[69] P. Bolzoni, F. Maltoni, S.-O. Moch, and M. Zaro, *Higgs production via vector-boson fusion at NNLO in QCD*, PRL **105** (2010) 011801, arXiv:arXiv:1003.4451 [hep-ph].

[70] M. L. Ciccolini, A. Denner, and S. Dittmaier PRL **99** (2007) 161803, arXiv:0707.0381 [hep-ph].

[71] M. L. Ciccolini, A. Denner, and S. Dittmaier Phys. Rev. **D77** (2008) 013002, arXiv:0710.4749 [hep-ph].

[72] Arnold, K. and Bahr, M. and Bozzi, Giuseppe and Campanario, F. and Englert, C. and others, *VBFNLO: A Parton level Monte Carlo for processes with electroweak bosons*, Comput.Phys.Commun. **180** (2009) 1661–1670, arXiv:0811.4559 [hep-ph].

[73] Rodolfo A. Diaz, R. Martinez, *The Custodial Symmetry*, arXiv:hep-ph/0302058 [hep-ph].

[74] J.L. Diaz-Cruz, D.A. Lopez-Falcon, *Probing the mechanism of EWSB with a rho parameter defined in terms of Higgs couplings*, Phys. Lett. B **568** (2003) 245–253.

[75] https://twiki.cern.ch/twiki/bin/view/LHCPhysics/CrossSectionsFigures.

[76] J. C. Romao, S. Andringa, *Vector Boson decays of the Higgs boson*, Eur. Phys. J. C **7** (1999) .

[77] A. Djouadi, J. Kalinowski, and M. Spira, *HDECAY: A program for Higgs boson decays in the standard model and its supersymmetric extension*, Comput. Phys. Commun. **108** (1998) 56, arXiv:hep-ph/9704448.

[78] William J. Marciano, Cen Zhang, and Scott Willenbrock, *Higgs decay to two photons*, Phys. Rev. D **85** (2012) 013002.

[79] John Ellis, Mary K. Gaillard, Dimitri V. Nanopoulos, *A Historical Profile of the Higgs Boson*, arXiv:1201.6045 [hep-ph].

[80] CERN, *LEP design report*, tech. rep., CERN, 1984. CERN-LEP-84-01.

[81] SLD Collaboration. http://www-sld.slac.stanford.edu/sldwww/sld.html.

[82] G. Abbiendi et al., *Search for the standard model Higgs boson at LEP*, Phys. Lett. **B565** (2003) 61, arXiv:hep-ex/0306033.

[83] Dawson, S. and Jackson, C. B. and Reina, L. and Wackeroth, D., *Exclusive Higgs boson production with bottom quarks at hadron colliders*, Phys. Rev. **D69** (2004) 074027, arXiv:hep-ph/0311067.

[84] T. Altonen et al., *Combination of Tevatron searches for the standard model Higgs boson in the W^+W^- decay mode*, Phys. Rev. Lett. **104** (2010) 061802, arXiv:1001.4162 [hep-ex].

[85] http://lepewwg.web.cern.ch/LEPEWWG/plots/summer2010/.

[86] CDF Collaboration, *Combined search for the standard model Higgs boson decaying to a bb pair using the full CDF data set*, Phys. Rev. Lett. **109** (2012) .

[87] D0 Collaboration, *Combined search for the standard model Higgs boson decaying to bbbar using the D0 Run II data set*, Phys. Rev. Lett. **109** (2012) .

[88] ATLAS Collaboration, *Study of the spin properties of the Higgs-like boson in the $H \to WW^{(*)} \to e\nu\mu\nu$ channel with 21 fb^{-1} of $\sqrt{s} = 8$ TeV data collected with the ATLAS detector*, ATLAS-CONF-2013-031 . http://cds.cern.ch/record/1527127.

[89] Alan J. Barr, Ben Gripaios, and Christopher G. Lester, *Measuring the Higgs boson mass in dileptonic W-boson decays at hadron colliders*, JHEP07(2009)072 (2009) .

[90] L. Evans and P. Bryant (editors), *LHC Machine*, JINST **3** (2008) .

[91] Pettersson, Thomas Sven, Lefevre P, *The Large Hadron Collider : conceptual design*, . CERN-AC-95-05.

[92] CERN PhotoLab/Accelerators, *The four main LHC experiments*, . CERN-AC-9906026.

[93] http://www.atlas.ch/photos/lhc.html.

[94] ATLAS Collaboration, *ATLAS detector and physics performance : Technical Design Report, 1*, tech. rep., CERN, 1999. ATLAS-TDR-014, CERN-LHCC-99-014.

[95] ATLAS Collaboration, *ATLAS detector and physics performance : Technical Design Report, 2*, tech. rep., CERN, 1999. ATLAS-TDR-015, CERN-LHCC-99-015.

[96] ATLAS Collaboration, *The ATLAS Experiment at the CERN Large Hadron Collider*, JINST **3** (2008) .

[97] ATLAS Collaboration Collaboration, *Studies of the performance of the ATLAS detector using cosmic-ray muons*, Eur. Phys. J. **C71** (2011) 1593.

[98] CMS Collaboration, *CMS technical proposal*, tech. rep., CERN, 1994. CERN-LHCC-894-38.

[99] LHCb Collaboration, *LHCb technical proposal*, tech. rep., CERN, 1998. CERN-LHCC-98-004.

[100] ALICE Collaboration, *ALICE: Technical proposal for a Large Ion collider Experiment at the CERN LHC*, tech. rep., CERN, 1997. CERN-LHCC-95-71.

[101] K. Schindl., *The injector chain for the LHC.*, tech. rep., CERN, 1999. CERN-OPEN-99-052.

[102] http://te-epc-lpc.web.cern.ch/te-epc-lpc/machines/pagesources/Cern-Accelerator-Complex.jpg.

[103] http://www.lhc-closer.es/1/1/1/0.

[104] ATLAS Collaboration, *Luminosity Determination in pp Collisions at sqrt(s)=7 TeV Using the ATLAS Detector at the LHC.*, Eur.Phys.J. **C71** (2011) 1630.

[105] https://twiki.cern.ch/twiki/bin/view/AtlasPublic/AtlasTechnicalPaperListOfFigures.

[106] ATLAS Collaboration, *ATLAS inner detector: Technical Design Report, 1*, tech. rep., CERN, Geneva, 1997. CERN-LHCC-97-016.

[107] ATLAS Collaboration, *ATLAS inner detector: Technical Design Report, 2*, tech. rep., CERN, Geneva, 1997. CERN-LHCC-97-017.

[108] ATLAS Collaboration Collaboration, *ATLAS pixel detector electronics and sensors*, JINST **3** (2008) P07007.

[109] ATLAS Collaboration Collaboration, *The barrel modules of the ATLAS semiconductor tracker*, Nucl. Instrum. Meth. **A568** (2006) 642–671.

[110] ATLAS Collaboration Collaboration, *The ATLAS semiconductor tracker end-cap module*, Nucl. Instrum. Meth. **A575** (2007) 353–389.

[111] ATLAS Collaboration Collaboration, *The silicon microstrip sensors of the ATLAS semiconductor tracker*, Nucl. Instrum. Meth. **A578** (2007) 98–118.

[112] ATLAS Collaboration Collaboration, *The ATLAS Transition Radiation Tracker (TRT) proportional drift tube: design and performance*, JINST **3** (2008) P02013.

[113] ATLAS Collaboration Collaboration, *The ATLAS TRT Barrel Detector*, JINST **3** (2008) P02014.

[114] ATLAS Collaboration Collaboration, *The ATLAS TRT end-cap detectors*, JINST **3** (2008) P10003.

[115] ATLAS Collaboration, *Commissioning of the ATLAS Muon Spectrometer with Cosmic Rays*, Eur.Phys.J. **C70** (2010) 875–916.

[116] http://www.hep.ph.ic.ac.uk/~wstirlin/plots/plots.html.

[117] ATLAS Collaboration Collaboration, *Performance of the ATLAS Trigger System in 2010*, Eur. Phys. J. C. **C72** (2012) 1849.

[118] ATLAS Collaboration, *Performance of the ATLAS Electron and Photon Trigger in p-p Collisions at $\sqrt{s} = 7$ TeV in 2011*, ATLAS-CONF-2012-048. http://cds.cern.ch/record/1450089.

[119] ATLAS Collaboration Collaboration, *Electron Performance measurements with the ATLAS detector using the 2010 LHC proton-proton collision data*, Eur. Phys. J. **C72** (2012) 1909.

[120] ATLAS Collaboration, *Alignment of the ATLAS Inner Detector and its Performance in 2012*, ATLAS-CONF-2014-047. http://cds.cern.ch/record/1304982.

[121] ATLAS Collaboration, *Study of alignment-related systematic effects on the ATLAS Inner Detector tracking*, ATLAS-CONF-2012-141. http://cds.cern.ch/record/1483518.

[122] ATLAS Collaboration, *Performance of the ATLAS Inner Detector Track and Vertex Reconstruction in the High Pile-Up LHC Environment*, ATLAS-CONF-2012-042. http://cds.cern.ch/record/1435196.

[123] ATLAS Collaboration, *Alignment of the ATLAS Inner Detector Tracking System with 2010 LHC proton-proton collisions at* $\sqrt{s} = 7$ *TeV*, ATLAS-CONF-2011-012. http://cds.cern.ch/record/1204071.

[124] ATLAS Collaboration, *Performance of the ATLAS Detector using First Collision Data*, JHEP09(2010)056 (2010) .

[125] R. Fruehwirth, *Application of Kalman filtering to track and vertex fitting*, Nucl. Instrum. Meth. (1987) .

[126] ATLAS Collaboration, *Performance of primary vertex reconstruction in proton-proton collisions at* $\sqrt{s} = 7$ *TeV*, ATLAS-CONF-2010-069. http://cds.cern.ch/record/1281344.

[127] Cacciari, Matteo and Salam, Gavin P. and Soyez, Gregory, *The anti-k_t jet clustering algorithm*, JHEP **04** (2008) 063, arXiv:0802.1189 [hep-ph].

[128] T. Sjostrand, S. Mrenna, and P. Z. Skands, *PYTHIA 6.4 physics and manual*, JHEP **0605** (2006) 026.

[129] T. Sjostrand, S. Mrenna, and P. Z. Skands, *A Brief Introduction to PYTHIA 8.1*, CERN-LCGAPP **04** (2007) 1, arXiv:0710.3820.

[130] https://twiki.cern.ch/twiki/bin/view/AtlasPublic/JetEtmissApproved2013JESUncertainty.

[131] ATLAS Collaboration, *Pile-up subtraction and suppression for jets in ATLAS*, ATLAS-CONF-2013-083. http://cds.cern.ch/record/1570994.

[132] ATLAS Collaboration, *Tagging and suppression of pileup jets with the ATLAS detector*, ATLAS-CONF-2014-018. http://cds.cern.ch/record/1700870.

[133] ATLAS Collaboration, *Calibration of the performance of b-taggingfor c and light-flavour jets in the 2012 ATLAS data*, ATLAS-CONF-2014-046. http://cds.cern.ch/record/1741020.

[134] ATLAS Collaboration, *Calibration of b-tagging using dileptonic top pair events in a combinatorial likelihood approach with the ATLAS experiment*, ATLAS-CONF-2014-004. http://cds.cern.ch/record/1664335.

[135] ATLAS Collaboration, *Performance of Impact Parameter-Based b-tagging Algorithms with the ATLAS Detector using Proton-Proton Collisions at* $\sqrt{s} = 7$ *TeV*, ATLAS-CONF-2010-091. http://cds.cern.ch/record/1299106.

[136] ATLAS Collaboration, *Performance of the ATLAS Secondary Vertex b-tagging Algorithm in 7 TeV Collision Data*, ATLAS-CONF-2010-042. http://cds.cern.ch/record/1277682.

[137] ATLAS Collaboration, *Performance of Missing Transverse Momentum Reconstruction in ATLAS studied in Proton-Proton Collisions recored in 2012 at 8 TeV*, ATLAS-CONF-2013-082. http://cds.cern.ch/record/1570993.

[138] ATLAS Collaboration, *Pile-up Subtracion and Suppresion for Missing* E_{T}, ATLAS-CONF-2014-019. http://cds.cern.ch/record/1702055.

[139] Lampl, W and Laplace, S and Lelas, D and Loch, P and Ma, H and Menke, S and Rajagopalan, S and Rousseau, D and Snyder, S and Unal, G, *Calorimeter Clustering Algorithms: Description and Performance*, ATL-LARG-PUB-2008-002. ATL-COM-LARG-2008-003.

[140] ATLAS Collaboration, *Improved electron reconstruction in ATLAS using the Gaussian Sum Filter-based model for bremsstrahlung*, ATLAS-CONF-2012-047. http://cds.cern.ch/record/1449796.

[141] ATLAS Collaboration, *Expected electron performance in the ATLAS experiment*, ATLAS-PHYS-PUB-2011-006. http://cds.cern.ch/record/1345327.

[142] ATLAS Collaboration, *Electron performance measurements with the ATLAS detector using the 2010 LHC proton-proton collision data*, The European Physical Journal C **72** (2012) no. 3, 1–46. http://dx.doi.org/10.1140/epjc/s10052-012-1909-1.

[143] ATLAS Collaboration, *Description and Performance of the Electron Likelihood Tool at ATLAS using 2012 LHC Data*, ATLAS-COM-PHYS-2013-378. http://cds.cern.ch/record/1537410.

[144] ATLAS Collaboration, *Measurement of the inclusive isolated prompt photon cross section in pp collisions at sqrt(s) = 7 TeV with the ATLAS detector*, Phys.Rev. **D83** (2011) 052005, arXiv:1012.4389 [hep-ex].

[145] ATLAS Collaboration, *Calorimeter isolation and pile-up*, ATLAS-COM-PHYS-2012-467. http://cds.cern.ch/record/1444890.

[146] ATLAS Collaboration, *Performance Studies for e/gamma Calorimeter Isolation*, ATLAS-COM-PHYS-2011-1186. http://cds.cern.ch/record/1379530.

[147] ATLAS Collaboration, *Preliminary results on the muon reconstruction efficiency, momentum resolution, and momentum scale in ATLAS 2012 pp collision data*, ATLAS-CONF-2013-088. http://cdsweb.cern.ch/record/1580207.

[148] ATLAS Collaboration, *Muon reconstruction efficiency in reprocessed 2010 LHC proton-proton collision data recorded with the ATLAS detector*, ATLAS-CONF-2011-063. https://cdsweb.cern.ch/record/1345743.

[149] ATLAS Collaboration, *A measurement of the muon reconstruction efficiency in 2010 ATLAS data using jpsi decays*, ATLAS-CONF-2012-125. https://cds.cern.ch/record/1474642.

[150] ATLAS Collaboration, *Muon Momentum Resolution in First Pass Reconstruction of pp Collision Data Recorded by ATLAS in 2010*, ATLAS-CONF-2011-046. https://cdsweb.cern.ch/record/1338575.

[151] S. Hassani et al Collaboration, *A muon identification and combined reconstruction procedure for the ATLAS detector at the LHC using the (MUONBOY,STACO,MuTag)reconstruction packages*, Nucl. Instrum. Meth. **A572** (2007) 77–79.

[152] ATLAS Collaboration, *A muon identification and combined reconstruction procedure for the ATLAS detector at the LHC at CERN*, ATLAS-CONF-2003-011. http://cds.cern.ch/record/681410.

[153] ATLAS Collaboration, *Electron efficiency measurements with the ATLAS detector using the 2012 proton-proton collisino data*, ATLAS-CONF-2014-032. http://cds.cern.ch/record/1706245.

[154] Michael H. Seymour, Marilyn Marx, *Monte Carlo Event Generators*, arXiv:1304.6677 [hep-ph].

[155] M. L. Mangano et al., *ALPGEN, a generator for hard multi-parton processes in hadronic collisions*, JHEP **0307** (2003) 001.

[156] G. Corcella et al., *HERWIG 6: an event generator for hadron emission reactions with interfering gluons (including super-symmetric processes)* , JHEP **0101** (2001) 010.

[157] Butterworth, J. M. and Forshaw, Jeffrey R. and Seymour, M. H., *Multiparton interactions in photoproduction at HERA*, Z. Phys. **C72** (1996) 637, arXiv:hep-ph/9601371.

[158] LHC Higgs Cross Section Working Group, S. Dittmaier, C. Mariotti, G. Passarino, and R. Tanaka (Eds.), *Handbook of LHC Higgs cross sections: 2. Differential distributions*, arXiv:1201.3084 [hep-ph].

[159] D. de Florian et al., *Transverse-momentum resummation: Higgs boson production at the Tevatron and the LHC*, JHEP **11** (2011) 064, arXiv:1109.2109 [hep-ph]. For Higgs boson $p_{\mathrm{T}} > m_H$, the calculation is switched from NLO+NLL to NLO.

[160] E. Bagnaschi, G. Degrassi, P. Slavich and A. Vicini, *Higgs production via gluon fusion in the POWHEG approach in the SM and in the MSSM*, JHEP **1202** (2012) 88, arXiv:1111.2854 [hep-ph].

[161] T. Binoth, M. Ciccolini, N. Kauer and M. Kramer, *Gluon-induced W-boson pair production at the LHC*, JHEP **0612** (2006) 046, hep-ph/0611170v1.

[162] H.-L. Lai and others, *New parton distributions for collider physics*, Phys. Rev. **D82** (2010) 074024, arXiv:1007.2241 [hep-ph].

[163] P. M. Nadolsky et al., *Implications of CTEQ global analysis for collider observables*, Phys. Rev. **D78** (2008) 013004.

[164] A. Sherstnev and R. S. Thorne, *Parton distributions for the LHC*, Eur. Phys. J. **C55** (2009) 553.

[165] ATLAS Collaboration, *The ATLAS simulation infrastructure*, Eur. Phys. J. **C70** (2010) 823, arXiv:1005.4568 [physics.ins-det].

[166] S. Agostinelli et al., *GEANT 4, A Simulation Toolkit*, Nucl. Instrum. Meth. **A506** (2003) 250.

[167] S. Alioli, P. Nason, and C. Oleari, and E. Re, *NLO Higgs boson production via gluon fusion matched with shower in POWHEG*, JHEP **0904** (2009) 002, arXiv:0812.0578 [hep-ph].

[168] P. Nason and C. Oleari, *NLO Higgs boson production via vector-boson fusion matched with shower in POWHEG*, JHEP **1002** (2010) 037, arXiv:0911.5299 [hep-ph].

[169] S. Frixione and B. Webber JHEP **0308** (2003) 007.

[170] B. P. Kersevan and E. Richter-Was, *The Monte Carlo event generator AcerMC version 2.0 with interfaces to PYTHIA 6.2 and HERWIG 6.5*, arXiv:hep-ph/0405247 (2004) .

[171] B. Mellado, X. Ruan, and Z. Z.hang, *Extraction of top backgrounds in the Higgs boson search with the $H \to WW^{(*)} \to \ell\ell + E_{\mathrm{T}}^{\mathrm{miss}}$ decay with a full-jet veto at the LHC*, Phys. Rev. D **84** (2011) .

[172] HWW working group, *Theoretical studies for the $H \to WW^* \to \ell\nu\ell\nu$ analysis with the ATLAS detector at $\sqrt{s} = 8$ TeV*, Tech. Rep. ATL-COM-PHYS-2013-1541, CERN, Geneva, 2014. http://cds.cern.ch/record/1627073.

[173] The ATLAS Collaboration, *Measurement of the WW cross section in $\sqrt{s} = 7$ TeV pp collisions with ATLAS*, Phys. Rev. Lett. **107** (2011) 041802, arXiv:1104.5225.

[174] Campbell, John M. and Ellis, R. Keith, *An update on vector boson pair production at hadron colliders*, Phys. Rev. **D60** (1999) 113006, arXiv:hep-ph/9905386.

[175] I. Stewart and F. Tackmann, *Theory uncertainties for Higgs mass and other searches using jet bins*, Phys. Rev. **D85** (2012) 034011, arXiv:1107.2117 [hep-ph].

[176] A. Aaron, *Discovery of a Higgs Boson with the ATLAS Detector*, CERN-THESIS-2013-047. http://cds.cern.ch/record/1553771.

[177] ATLAS Collaboration Collaboration, *Asymptotic formulae for likelihood-based tests of new physics*, Eur. Phys. J. C. **C71** (2011) .

[178] G. Cowan, K. Cranmer, E. Gross, and O. Vitells, *Asymptotic formulae for likelihood-based tests of new physics*, Eur.Phys.J. **C71** (2011) 1554.

[179] ATLAS Collaboration, *Combined coupling measurements of the Higgs-like boson with the ATLAS detector using up to 25 fb^{-1} of proton-proton collision data*, ATLAS-CONF-2013-034. http://cds.cern.ch/record/1528170.

[180] ATLAS Collaboration, *Updated coupling measurements of the Higgs boson with the ATLAS detector using up to 25 fb^{-1} of proton-proton collision data*, ATLAS-CONF-2014-009. http://cds.cern.ch/record/1670012.

[181] CMS Collaboration, *Measurement of the properties of a Higgs boson in the four-lepton final state*, Phys. Rev. D **89** (2014) .

[182] CMS Collaboration, *Measurement of Higgs boson production and properties in the WW decay channel with leptonic final states*, JHEP01(2014)096 (2014) .

[183] ATLAS Collaboration, *Search for charged Higgs bosons in the τ+jets final state with pp collision data recorded at $\sqrt{s} = 8$ TeV with the ATLAS experiment*, ATLAS-CONF-2013-090. http://cdsweb.cern.ch/record/1595533.

[184] ATLAS Collaboration, *Search for Higgs bosons in Two-Higgs-Doublet models in the $H \to WW \to e\nu\mu\nu$ channel with the ATLAS detector*, ATLAS-CONF-2013-027. http://cdsweb.cern.ch/record/1525887.

[185] ATLAS Collaboration, *Search for flavor changing neutral currents in $t \to cH$, with $H \to \gamma\gamma$, and limit on the tcH coupling*, ATLAS-CONF-2013-081. http://cdsweb.cern.ch/record/1565103.

[186] J.F. Gunion, H.E. Haber, G. Kane, and S. Dawson, *The Higgs Hunter's Guide*, Addison-Wesley (1990) .

[187] T.P. Cheng and L.-F. Li, *Neutrino masses, mixings, and oscillations in SU(2)⊗U(1) models of electroweak interactions*, Phys. Rev. D **22** (1980) 2860–2868.

[188] ATLAS Collaboration, *Search for invisible decay of a Higgs boson produced in association with a Z boson in ATLAS*, ATLAS-CONF-2013-011. http://cdsweb.cern.ch/record/1523696.